Dissertation zur Erlangung des Doktorgrades

der Fakultät für Chemie und Pharmazie

der Ludwig-Maximilians-Universität München

Tuning the Structure and Properties of Nitrogen-rich Covalent Organic Frameworks by Molecular Design and Solid State Reactions

Frederik Haase

aus

Gießen, Deutschland

2018

Erklärung

Diese Dissertation wurde im Sinne von § 7 der Promotionsordnung vom 28. November 2011 von Frau Professor Dr. Bettina V. Lotsch betreut.

Eidesstattliche Versicherung

Diese Dissertation wurde eigenständig und ohne unerlaubte Hilfe erarbeitet.

München, ..13.04.2018......

.........Frederik Haase........

Dissertation eingereicht am: 08.03.2018

1. Gutachterin: Prof. Dr. Bettina Lotsch

2. Gutachter: Prof. Dr. Konstantin Karaghiosoff

Mündliche Prüfung am: 09.04.2018

"Damit das Mögliche entsteht, muss immer wieder das Unmögliche versucht werden."

- Hermann Hesse

Brief (Sept. 1960) an Wilhelm Gundert Quelle: Mein Hermann Hesse - Ein Lesebuch. Hrsg. Udo Lindenberg, 2008, Suhrkamp Verlag, S. 26

Acknowledgements

Table of Contents

1.   Summary

Covalent organic frameworks (COFs) are based on two- or three-dimensional covalently extended networks that are crystalline, porous and solely composed of light elements. These characteristics promise inherently functional materials that might be applied in gas storage, gas separation, sensing and catalysis. However, the greatest utility in COFs arises from the modular synthetic approach involving the use of molecular building blocks. The separation of the synthesis of the final solid-state material and the precursors enables organic chemistry to design and incorporate various functionalities into COFs. Multitopic building blocks can be constructed and purified by molecular synthesis, which can then be assembled through specialized reversible reactions that allow the crystallization of the COF.

Results

This thesis explores the design of COFs with regard to their in-plane- and out-of-plane structure and the modification of the COF linkages. The molecular design of the covalently connected structure of COFs was exploited by the systematic variation of molecular building blocks in two COF platforms. The thereby altered composition of the COFs was accompanied by changes in the optoelectronic properties, studied with photocatalysis. COFs present the best platform to elucidate structure-property-activity relationships regarding photocatalytic hydrogen evolution, as their highly tailorable structures make the development of rational series of compounds straightforward. In the first platform, the nitrogen substitution patterns were systematically altered to study possible descriptors for the photocatalytic hydrogen evolution activity. This platform is based on an aryl-triaryl-azine COF (ATA-COF), of which five were synthesized (chapter 4.2 and chapter 4.3). All obtained COFs showed remarkably similar optical band gaps, but drastically varied in their photocatalytic hydrogen evolution performance. With the help of theory, it was possible to pinpoint a descriptor based on the vertical radical anion stabilization energy for the photocatalytic hydrogen evolution activity of these frameworks. The second platform is based on a benzene triazine imine system (BTI-COFs), modified by the introduction of hydroxyl groups into the precursors. The use of these additional functionalities has dramatic effects on the optical band gap of these materials (chapter 4.4), and thereby the light absorption abilities. Hydroxyl groups reduce the band gap and increase the polarity of the pore walls, enabling a significantly improved photocatalytic production of hydrogen. These examples of photocatalytic hydrogen evolution show the feasibility of tuning properties in COFs with a large degree of control.

On the non-covalent tier of design in COFs, the work in this thesis elucidated the alteration of the stacking pattern in a system of two triazine based COFs by changing the shape of the precursors (chapter 5.2). Several design principles have been proposed for the improvement of the stacking in COFs, but only few had an impact on the actual discernable crystalline structure. For the first time, the investigations into the crystalline structure clearly showed a defined mode of stacking (slip-stacking) as derived by significant changes in the X-ray powder diffraction pattern. The stacking structure could be determined by refinement of X-ray diffraction data in conjunction with electron diffraction and theoretical calculations. Simulations of stacking disorder in COFs helped elucidate the origin of the usually observed high symmetry unit cells that are often falsely attributed to eclipsed stacking. With the help of theoretical calculations, it was possible to pinpoint the origin of the slip-stacking to donor-acceptor type stacking through layer alternation in the COF, a new design principle for well-stacked COFs. This work shows that not only the in-plane and the molecular connectivity, but also the supramolecular arrangement can be altered by design of the building blocks.

The functional groups created as the COF linkages can be designed, by choosing from available reactions, that tend to be prone to bond cleavage under certain conditions. Interestingly, these functional groups can be altered after the synthesis of the COFs. This thesis shows two reactions for altering the COF linkages to possibly alleviate the disadvantages imbued by the presence of reversible COF linkages. The first reaction is the transformation of imine based COFs to their corresponding thiazoles by reaction with elemental sulfur (chapter 6.2). As this reaction proceeds without bond breakage in the COF backbone, the crystallinity and the porosity of the COF is seen to be retained. Although characterization of *post*-synthetic modification of solid state material is challenging, the combined use of orthogonal techniques is necessary to elucidate the structure. Combined results from diffraction, infrared spectroscopy and solid state NMR, in conjunction with theoretical NMR chemical shift calculations proved the transformation of the imine to the thiazole linkage and the structure of the resulting COF. One of the properties altered by the transformation is the improved contrast and stability in the transmission electron microscope (TEM), which allowed unprecedented investigations into the real structure of this COF. The imaging of COF crystallites showed the presence of defects and inter-grown grain boundaries that have not been observed in COFs so far. The second reaction that has been explored is the transformation of aromatic azines into the corresponding stilbenes (chapter 6.3). The reaction is shown to proceed in the COF albeit with loss of crystallinity. A possible explanation for this behavior can be found in the mechanism of the stilbene formation and the geometric arrangement of the azine groups during the reaction. Since the azine pyrolysis reaction proceeds through an intermolecular mechanism, backbone linkages are broken and the ordered structure is lost. These results show how a judicious choice of post-synthetic linkage modification may help in altering the COF linkages, while maintaining order and therefore present a guiding principle for the design of arrested linkage COFs.
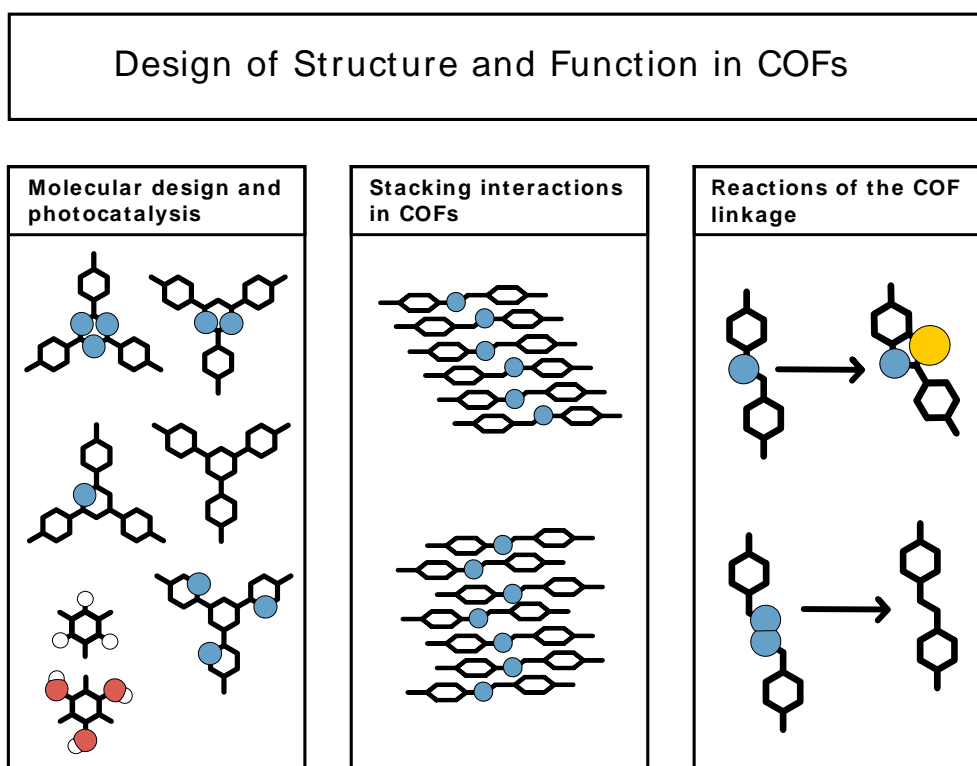
Figure 1-1: Overview of the approaches to designing and tuning the structure and properties of COFs in this thesis.

2.   General Introduction to Covalent Organic Frameworks

COFs are a rapidly developing class of organic solids, which possesses the unusual properties of crystallinity, porosity and covalent connectivity in two or more dimensions, while being based on only light elements (H, B, C, N, and O).[1] COFs are synthesized in a modular approach, where first classical organic chemistry is used to synthesize multifunctional building blocks that are then reacted under reversible solvothermal conditions that enable error correction and defect healing for crystallization of the COFs (Figure 2-1).

These materials exhibit a variety of properties that make them amenable to applications as discussed in chapter 2.1. The development of COFs follows the ongoing trend of designing highly functional porous materials and the synthesis of complex and ordered solid-state metastable materials by a versatile chemical approach, as discussed in chapter 2.1. COFs are crystalline, covalently linked complex materials, which require special design considerations to enable crystallization. General principles of crystallization in COFs are explored in chapter 2.4, whereas the so far developed reversible reactions for forming COFs are discussed in chapter 2.2. The molecular building blocks employed in the synthesis also influence and enable the design of the COFs and these geometric considerations for designing COFs can be found in chapter 2.3.
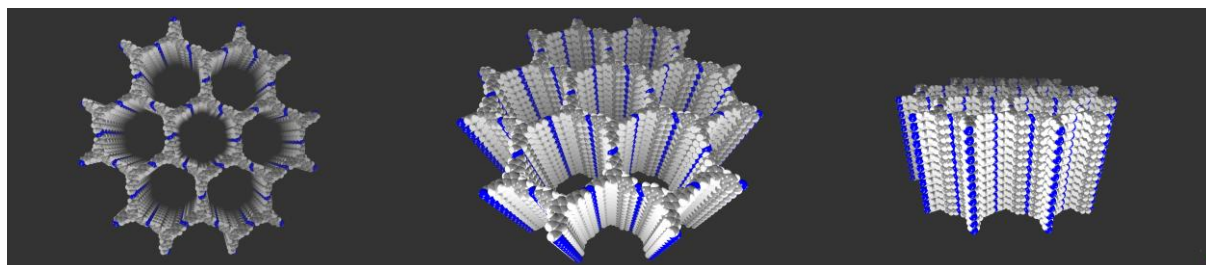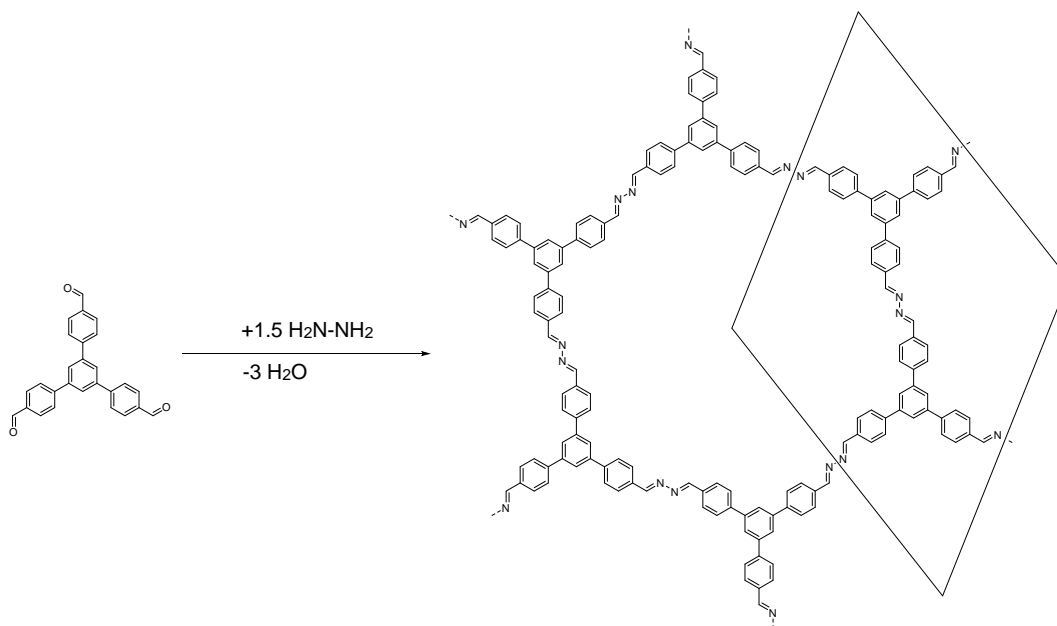
Figure 2-1: Schematic representation of the synthesis of N_0-COF[2] and 3D models of sections of the crystalline structure.

2.1.   The development of COFs

The development of COFs by Omar Yaghi in 2005[1] cumulates the quest of pushing the limits of functionality and tailorability of porous and nonporous ordered solid-state materials.

2.1.1.   Tailorable ordered porous solids

Porosity is a feature of solid state materials, where accessible voids are present in the material. These voids can display a variety of possible functions depending on the surface area, the pore size and the pore functionalization. The high internal surface area of porous materials is coincident with the presence of a large number of adsorption sites for atoms and molecules, which make porous materials prime targets as adsorbents for gas storage, separation and removal of pollutants. The capacity and selectivity of the adsorption process in a pore are key features and can be tailored by pore size, surface area and surface functionality modulation. Porous materials such as activated carbon possess surface areas >3000 m^2/g,[3] but due to their disordered and inert nature they are difficult to tailor for applications where selective adsorption is necessary. In sensing and catalysis, defined chemical environments are of great importance, as selectivity and catalytic activity need to be specific to the target analyte or reaction. The search for defined porous materials whose properties can be tailored thus continues.

Zeolites, which are crystalline and porous, are a technologically relevant material that can be considered the opposite of activated carbons in terms of defined porosity. The naturally occurring zeolites are tectoalumosilicates consisting of a network of silica and alumina tetrahedra and octahedra. They are synthesized under hydrothermal conditions from low molecular weight silica and alumia precursors and a mineralizer such as fluoride (F^-) or hydroxide (OH^-) ions and organic structure directing agents that aid the formation of the porous structure. This naturally occurring class of inorganic crystalline material exhibits microporous voids with extreme analyte specificity and with excellent catalytic performance due to their confined environment. The catalytic activity in conjunction with their stability have led to the use of zeolites in industrial synthesis of branched hydrocarbons[4] and gas separations.[5] However, while zeolites have well-defined microporous structures, tuning their properties is difficult, as the achievable pore sizes are small and the surfaces of the pores cannot be readily tuned.
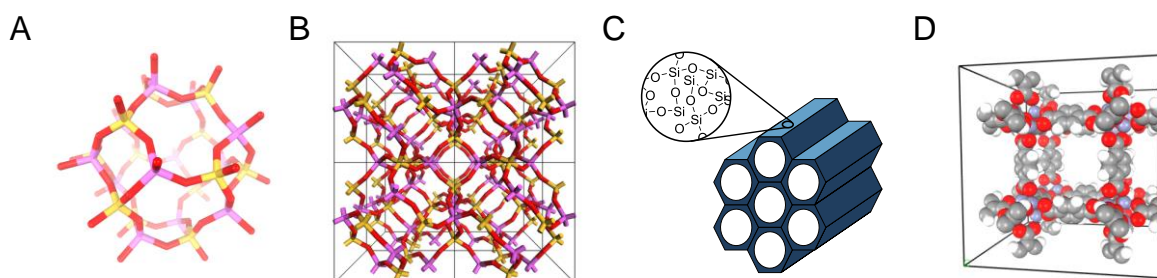
Figure 2-2: Structure of porous ordered solids: A: Sodalite A cage; B: Sodalite A network structure (sodium and chlorine atoms are omitted for clarity);[6] C: Schematic representation of MCM-41;[7] D: Representation of one unit cell of MOF-5.[8]

In order to obtain larger pore sizes, new classes of porous materials have been developed, where mesoporous silica such as MCM-41[7] and SBA-15[9] represent an important step. These materials are synthesized by the self-assembly of surfactants into mesophases, which are then cast into periodic mesostructured powders or monoliths by condensing silica precursors around the ordered mesophase.

This approach allows the tuning of the pore topology and the pore size through the choice of surfactant and pore sizes up to 50 nm can be achieved. The pores are well defined and ordered, while the pore walls are amorphous or show ordering incommensurate with the pores. The pore properties can be tuned during the synthesis or by post-synthetic grafting of functionalities onto the pore walls. The template approach has the benefit of being applicable to a variety of inorganic host materials.

This development sparked interest in other porous materials like metal organic frameworks.[10] MOFs are sometimes considered hybrid zeolites as they are crystalline porous materials in which metal atoms or inorganic clusters are bridged by organic ligands. The use of rigid ligands, strong ionic directional ligand-metal linkages and highly symmetrical metal nodes allowed the synthesis of materials with permanent porosity, meaning structures that could maintain their integrity upon solvent removal and evacuation. This class of materials shows extremely high surface areas, well-defined crystalline structures and open accessible pores. The low temperature solvothermal synthesis of MOFs allows the introduction of highly functional and fragile linkers, making the synthesis of MOFs highly modular. Ligands can be designed using conventional organic synthesis and functional groups can thereby be introduced by using predesigned building blocks. MOFs have demonstrated application in gas sorption, separation and sensing, where metal centers sometimes improve or enable catalysis or adsorption. However, often the metal center only acts as a structure-forming agent and the comparatively weak coordinative metal-ligand bonds make MOFs prone to degradation.[11]

To overcome these drawbacks, purely organic porous materials have come into focus, where the porosity and pore wall functionalities can be controlled and tailored. Purely organic porous materials have long been known as molecular crystals that possess voids. A prominent example is Dianin's compound, an organic molecular crystal that tends to form clathrates and can be synthesized with permanent porosity that is accessible to guest molecules.[12] Similarly, many other organic molecules have been designed with porosity,[13] which results from structures that are not able to pack densely and thus voids remain in the interstitial space,[14] or by the introduction of intermolecular forces such as hydrogen bonding.[15, 16] Porosity can also be introduced into molecular systems by the defined design of molecules that consist of "one pore", which then pack to form a porous solid.[13] These materials exhibit intrinsic and extrinsic porosity: the intrinsic porosity can be tailored readily by the design of the cage, while the extrinsic porosity is dependent on molecular packing and therefore difficult to design.
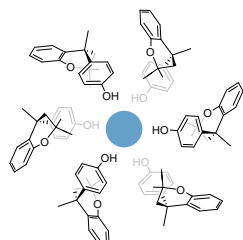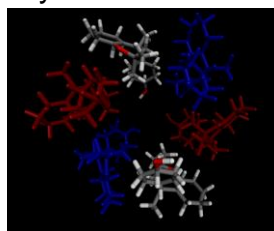
| porous molecular crystal | porous cage | PIM | PCP |
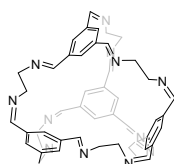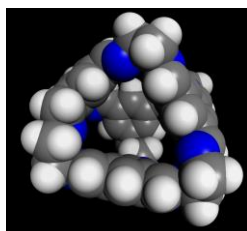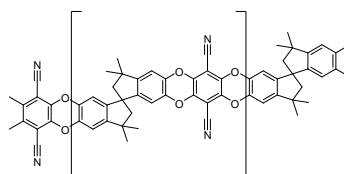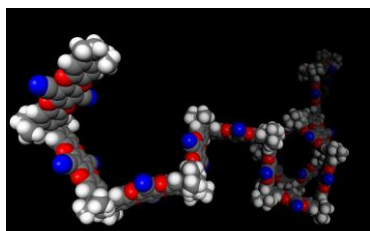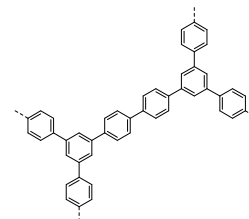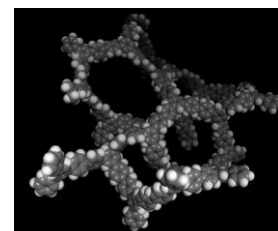
Figure 2-3: Examples of porous organic solids: molecular crystals that possess accessible voids as in Dianin's compound;[12] crystallized molecular porous cages, CC1;[17] polymers of intrinsic microporosity, PIM-1;[18] hypercrosslinked porous conjugated polymers, CMP-M1.[19]

Amorphous organic polymers can also be designed to be porous and two classes of materials are especially important: porous conjugated polymers (PCPs)[20] and polymers of intrinsic micro-porosity (PIMs).[21-23] PCPs are heavily cross-linked polymers that are synthesized by irreversible reactions, which generate porous solids due to the rigid building blocks that do not allow the pores to collapse. These polymers are synthetically accessible through a wide range of reactions and can be especially stable due to the robust bonds that are formed in the synthesis. However, their monolithic and disordered nature makes the design of defined pore sizes difficult. PIMs, on the other hand, are linear polymers, which are amorphous, glassy and contain rigid backbones that cannot densely pack in the solid state, leading to high free volume. They are linear, soluble and thermally stable polymers, which makes them easily processable for applications such as developing membranes, where the amorphous and monolithic nature of the PIMs is beneficial. The processability of PIMs is a feature that is largely lacking in all other discussed materials.

Among these materials, COFs are the continuation of the search for stable polymeric organic materials that are highly tailorable in their structures and properties, especially concerning their pores.

2.1.2. Controlling covalently linked crystalline materials

Crystalline hybrid and organic materials gained significant attention in recent years with the development of hybrid perovskites for solar cells,[24, 25] porous metal organic frameworks,[26-28] organic molecular semiconductors[29, 30] and organic/hybrid superconductors.[31-34] These compounds are composed of molecular units assembled by weak ionic and/or van-der-Waals interactions. Furthermore, several complex materials based on extended covalently linked structures have been proposed in recent years for their intriguing properties,[35-38] and the variability of carbon based materials promised a virtually infinite number of extended structures based on carbon alone or in combination with other elements. However, only a handful of carbon allotropes have been obtained so far, as synthetic access to these extended strongly bound solids is elusive.[39] The diverse properties of these materials may be observed in the few carbon allotropes that are already known: graphite, diamond, lonsdaleite, fullerenes, carbon nanotubes and graphene. Examples of these properties are the mechanical softness (graphite),[40] hardness (diamond, lonsdaleite)[41] and extreme tensile strength

(graphene, carbon nanotubes)[42-44] or their electronic properties as semiconductors (fullerene, carbon nanotubes),[45, 46] metals (graphite, carbon nanotubes[46, 47] and Dirac metal in graphene[48]) or being used for their large band gap (diamond).[49] Further, a large number of carbon allotropes have been predicted with interesting electronic properties, magnetic properties and porosity (Figure 2-4). These materials are metastable in the entire phase diagram and they require synthesis conditions under kinetic control to achieve the complex molecular motifs. This however presents a significant challenge, as order and thereby crystallinity are difficult to impart without reversibility, a hallmark of thermodynamic control. The solution to this problem is the use of "partial" thermodynamic control, meaning employing a thermodynamically controlled reaction to assemble kinetically trapped preassembled motifs.
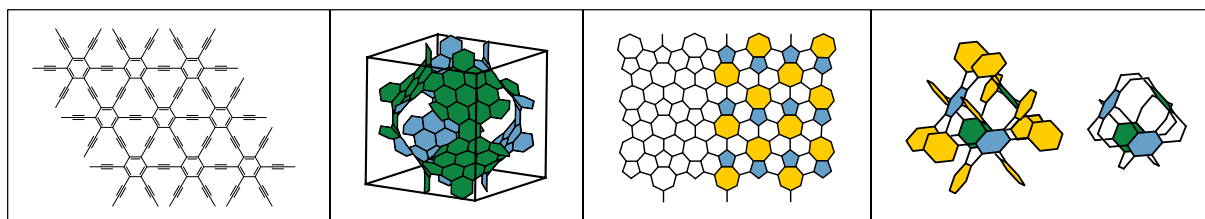
Figure 2-4: Predicted carbon allotropes with physical properties of interest: graphyne,[35] negatively curved cubic carbon crystals with octahedral symmetry,[36] Phagraphene,[37] and fragments from "polybenzene"[38]

A prime example of this approach is the synthesis of carbon nitrides. Initially, carbon nitrides have been extensively investigated, due to the prediction of exceptional hardness of the cubic variant (β-C_3N_4)[50, 51] and then for their promising application as photocatalysts.[52] Graphitic carbon nitride, as well as the related, not fully condensed polymers melon ($[C_6N_7(NH_2)(NH)]_n$) and melam are synthesized by reaction in a controlled atmosphere of decomposition gases (especially NH_3) that ensure reversibility. The crystallization of these materials is possible at moderate temperatures, whereas at high temperatures they decompose to graphite and nitrogen gas. Similarly, the synthesis of covalent phosphorousoxynitride (PON) networks is performed in the presence of NH_4Cl acting as a mineralizer that allows crystallization of these covalently connected solids.[53-55] Carbon nitrides and phosphorousoxynitrides show how novel covalently linked solids can be synthesized by reversible reactions that allow strongly bound solids to crystallize. The approach of using molecular precursors in reversible reactions has been used for the synthesis of the carbon nitrides C_2N[56] and C_3N.[57] Both materials are synthesized by condensation reaction of molecular precursors (Figure 2-5) and lie at the intersection of the merging fields of classical inorganic chemistry and COFs. C_2N can be synthesized from two precursors, hexaketocyclohexane and hexaaminobenzene under ambient conditions, while C_3N is synthesized by self-condensation of hexaaminobenzene trihydrochloride at high temperatures. The precursors are synthesized by classical molecular organic synthesis and are then assembled to carbon nitrides under reversible conditions allowing crystallization. These complex materials might be difficult or impossible to synthesize directly from the elements, however, formation by a condensation reaction of complex precursors is possible. Consequently, reversible reactions with molecular precursors can be used to synthesize new solid-state materials such as COFs that can bridge the gap between classical crystalline solid-state materials and metastable organic materials.
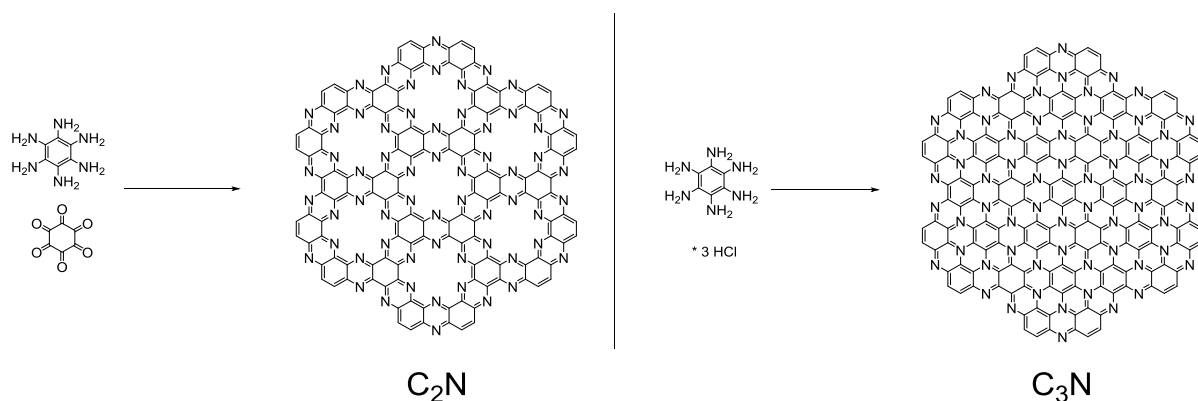
Figure 2-5: Synthesis of inorganic carbon nitrides C$_2$N [56] and C$_3$N [57] from molecular precursors.

2.2.   COF forming reactions

The crystallization of COFs requires microscopically reversible reaction chemistry. In addition, it is necessary for the formed linkage to be rigid and directional, to obtain materials with permanent porosity. These features further help in designing COFs since the prediction of the structure becomes straightforward. Over time a myriad of reactions capable of producing COFs have been developed as shown in Figure 2-6.

The early days of COF chemistry was dominated by boron based reversible reactions to form, for example, boroxine and boronate ester based COFs.[1] As the field matured, other reactions were adopted, with imine forming reactions being the most common. The chemistry based on boronic acids has the advantage that precursors are synthetically accessible and that the boron based linkages show good reversibility leading to high crystallinity. However, the high reversibility also makes these COFs prone to hydrolysis.[58] Despite this, the chemistry of boron and other semi-metals has continued to be of interest to the COF community.
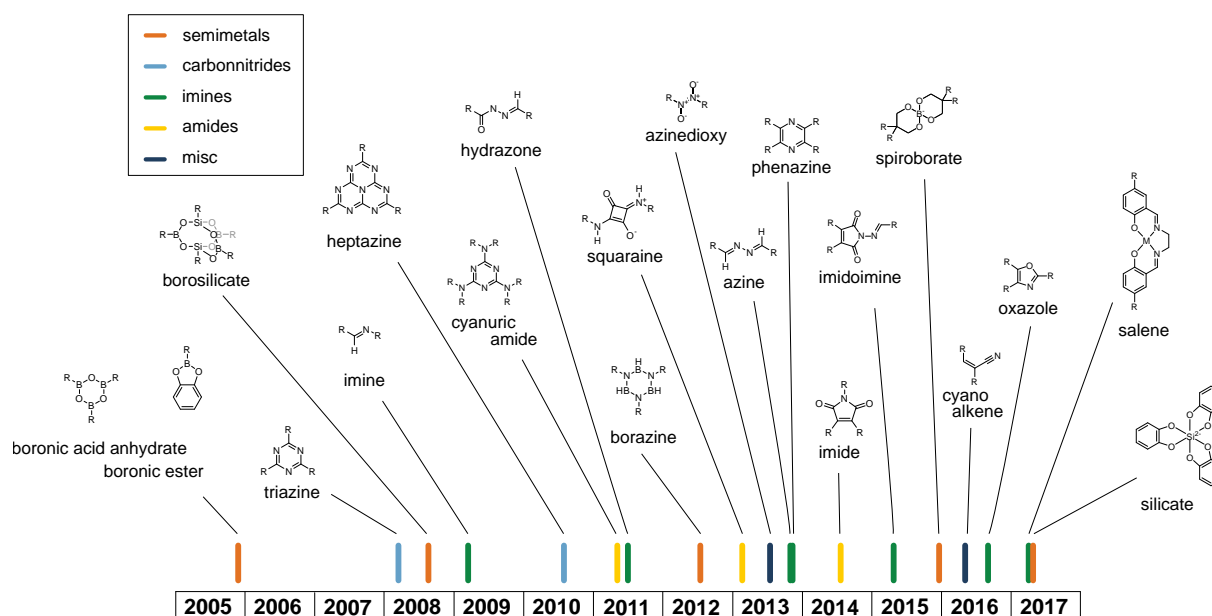
Figure 2-6: Different COF producing linkages and their respective time of first publication.

The borazine linked COFs can be formed from the condensation of an amine borohydride adduct (R-NH$_2$·BH$_3$).[59] The development of the borosilicate linkage is especially intriguing as it possesses a trigonal bipyramidal geometry that could expand the otherwise linear or 2D nature of the connecting linkages.[60] Also, the borosilicate linkage is a rare example of a COF node that is nonlinear and composed of two different organic precursors and this could allow the synthesis of anisotropic structures. This type of linkage, synthesized from a boronic acid and a silane triol, has been used only as a trigonal node.

Use of such semimetallic elements pushes COFs towards the field of metal organic frameworks (MOF) as the covalency is expected to be lower with semimetallic elements than with other COF linkages. This holds especially true for the recently developed COF linkages using anionic spiroborate centers[61] and the anionic hexacoordinate silicon-based COF.[62] Based on these motifs, further linkages could be envisioned that are more "inorganic" in nature such as defined organosilicate clusters. MOF and COF chemistry have been combined to link a metal organic cluster based building block by COF chemistry.[63]

One of the most common linkage type is the iminic nitrogen-carbon bond formed by the condensation of amines with aldehydes (Figure 2-7). These linkages show great synthetic variability and are easily accessible.[64] Instead of simple amines, other nitrogen functionalities can be used as precursors such as those based on H$_2$N-N derived functionalities to form for example, hydrazone COFs[65] and azine COFs.[66] The azine linkage is a special case of a diamine linker with zero length, which essentially makes dimers of aldehydes and thereby can only be employed with tritopic and higher functionalized aldehydes to form COFs. Special COF linkages such as the aminoimide[67] have been explored as well, but the limited synthetic utility severely restricts the available linkers.
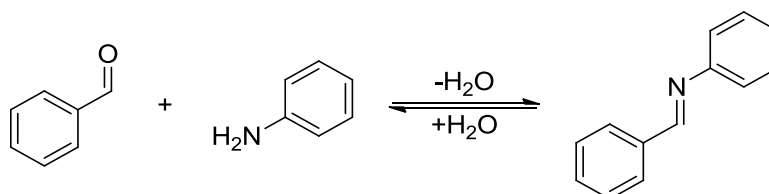
Figure 2-7: Reversible condensation reaction of an aldehyde with an amine to form the imine bond.

An intriguing COF linkage is the oxazole, which can be synthesized by the reaction of an aldehyde with an *ortho*-hydroxy amine, which cyclizes oxidatively to the oxazole during COF formation.[68] The demonstration of a pyrazine based COF, synthesized from *ortho*-diamines with *ortho*-diketones[69] shows a method to synthesize highly annulated and extended two-dimensional π-systems. However, the synthetically demanding precursors limit the versatility of this approach considerably.

Instead of the iminic nitrogens as linking groups, also acid amides and imides have been investigated for the formation of COFs with examples of amides,[70] imides,[71] squaraines[72] or cyanuric amide leading to crystalline materials.[73] These three reactions can be formally grouped as the reaction of a carboxylic acid or acid chloride with an amine to form the desired bond. The cyanuric amide linkage presents an interesting case as it can be described as a reversible nucleophilic aromatic substitution.[73] The synthesis of imide COFs is unusual as they were synthesized by the use of base catalysis using isoquinoline and not by the addition of aqueous acid.[71]

The class of carbonnitride based COF linkages are unusual in their synthesis conditions, as the heptazine[74] linkage is similar to the synthesis of classical carbon nitride polymers such as melon. They are synthesized by the condensation of nitriles with diamino triazine terminated building blocks.

The structurally related triazine linkage is obtained by an ionothermal melt, usually based on zinc chloride at high temperatures (up to 500°C).[75] These harsh conditions severely limit the scope of usable functional groups and while many materials have been reported based on this reaction only three of these materials can be considered crystalline and thereby COFs.[75-78]

A COF linkage that is difficult to group with other COF reaction chemistry is the nitrosyl dimerization reaction wherere an azinedioxy group is formed.[79] This reaction marks the limit of COF chemistry with extremely weak azinedioxy bonds, which are covalent but create very labile materials. Cyano vinyl COFs are obtained by a Knoevenagel reaction of aldehydes with cyanomethyl groups.[80] This chemistry is special as the products of these reactions are COFs that are not linked by heteroatoms, but by carbon atoms only.

2.3. Geometric requirements for building COFs

COFs can be designed by a step-by-step approach as outlined by Diercks et al.,[81] where first a topology and thereby the underlying net is chosen (Figure 2-8, step 1). This net is then deconstructed into the underlying geometric units whose molecular equivalents are then designed (Figure 2-8, step 2). Here, the design needs to take into account the connectivity of the building block as well as the geometry. The angles between the connecting points need to be considered, as several topologies are often available for one kind of vertex. Only by choice of optimal geometric constraints can the desired net be obtained. Usually nodes are deconstructed to organic building blocks with the appropriate shape, but in some cases the COF linkage itself can provide a node such as boronic anhydrides (for a comprehensive list see chapter 2.2). Based on the building blocks and the topology, the network is constructed (Figure 2-8, step 3), where at desired locations the COF linkage is inserted (Figure 2-8, step 4). By depolymerization of the framework into its constituents the building block of the framework can be obtained (Figure 2-8, step 5).
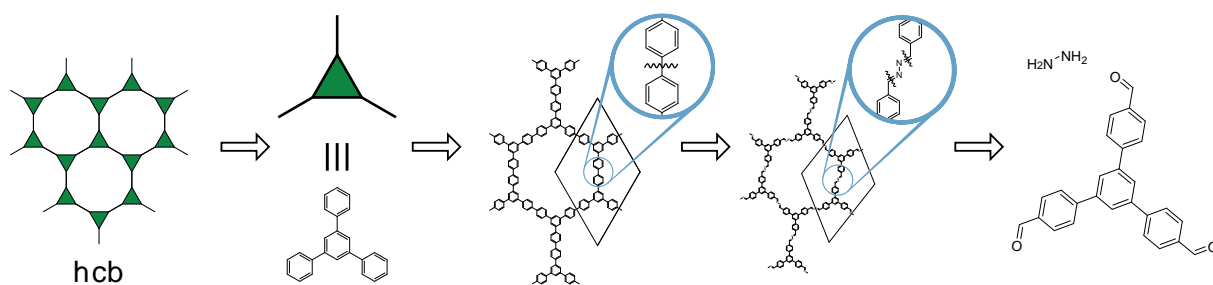
Figure 2-8: Schematic of the retrosynthesis in designing COFs from the net to the building block: 1. deciding the net; 2. picking building block structures to realize the nodes; 3. constructing the framework; 4. insertion of reversible bonds at the desired positions; 5. "depolymerization" to the building blocks.

2.3.1. Nets and building blocks in COFs

Of the many topologies that exist, only eight different nets have been demonstrated in COFs.[81] Four of the five topologies based on vertices connected by only one edge have been realized in two-dimensional COFs (Figure 2-9). In three dimensions the number of possible nets are much larger, but only four of these nets been demonstrated (Figure 2-10).
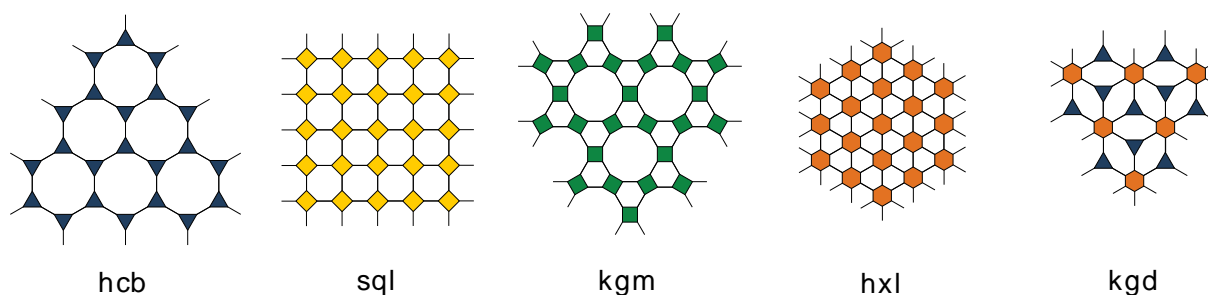
Figure 2-9: Schematic of prominent two-dimensional nets that could be used in COF. All but the last have been demonstrated experimentally: **hcb** net;[1] **sql** net;[82] **kgm** net;[83] **hxl** net;[84] **kgd** net.
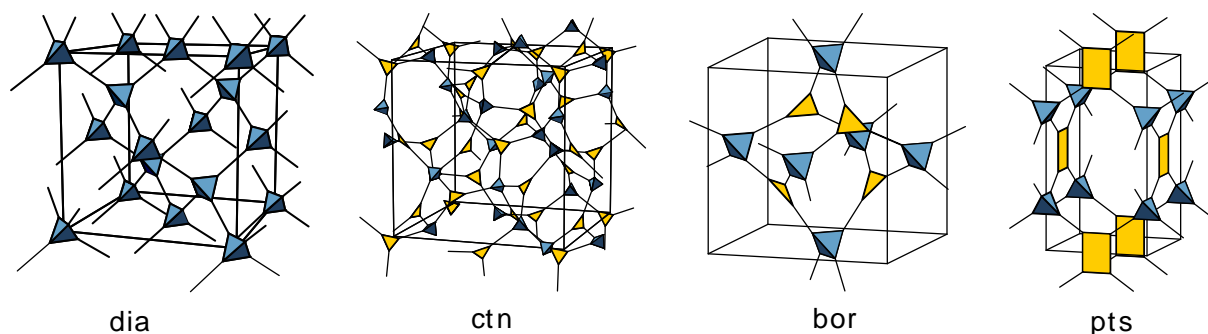
Figure 2-10: Schematic of three dimensional nets that have been demonstrated in COF: **dia** net, [70, 85-88] **cnt** net[89] **bor** net[89] and **pts** net.[90, 91]

2.3.2.   From 2D to 3D

COFs can be classified by the dimensionality of the covalent connectivity, with connectivity in two and three dimensions leading to COFs (with the exception of woven COFs see chapter 2.4). The organic nature of COFs makes the design of rigid flat structures straightforward.[92, 93] 2D COFs become bulk 3D materials by stacking of the individual layers (Figure 2-11, left). There are two main approaches of generating 3D COFs: the use of out of plane building blocks (Figure 2-11, right) and the combination of building blocks that cannot form 2D structures due to geometric constraints (Figure 2-11, middle). While the former approach has been successfully applied to COFs, the latter has not been demonstrated so far.
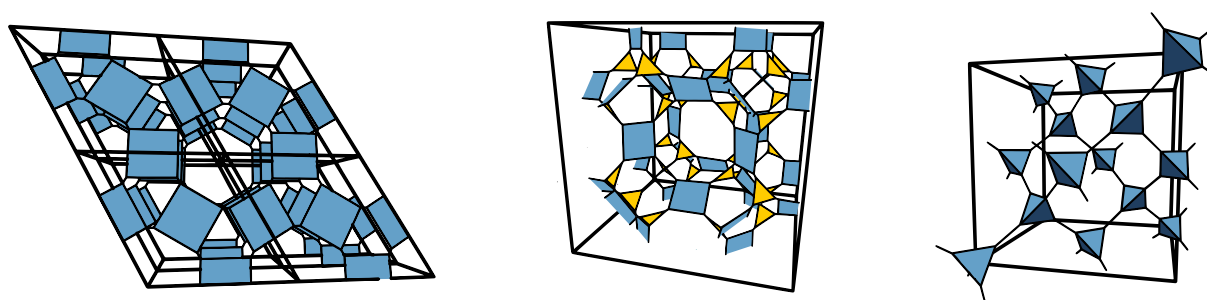
Figure 2-11: Fundamentally different ways of approaching the geometry and topology of COFs: Left a hexagonal 2D COF composed of planar fourfold linkers; middle a 3D COF composed of 3 and 4 fold planar linkers; right a 3D COF generated from tetrahedral building blocks.

The first approach is straightforward, but limited as the number of available geometries of purely organic building blocks is small. This is in stark contrast to the number of geometries available in MOF chemistry, based on a rich set of 3D nodes, formed by metal linker clusters.[94-97] The three dimensional nature of the building block needs to be supported not only by symmetry of the organic

backbone, but it also has to be rigid and directional. A variety of building blocks with very high point symmetries is possible that could be used to produce three dimensional building blocks.[98-100] However, their synthesis is often prohibitively complicated and this severely limits the synthetically useful geometries. Successfully synthesized 3D COFs are all based on tetrahedral building blocks that use either a tetra phenyl methane, tetraphenylsilane or an adamantane motif.[70, 85-91] The design of three dimensional COFs promises a route to organic materials with building blocks that are fully accessible from the pore. This would be of interest in cases where the functional groups are otherwise blocked by adjacent layers or the π-systems need to be isolated, such as for porphyrins where the catalytic activity of an exposed metal site is of importance.[91, 101, 102] Additionally, 2D COFs are limited in the one dimensional topology of their channels. Examples from metal organic frameworks show, that it is possible to design porous materials with many types of pore topologies and shapes, such as bottle shaped pores.[103-106] Different kinds of pores can be designed in a single 2D COF (see chapter 2.3.5), but since the channels are isolated from each other, transport from one pore to another is only possible via the surface of the crystallite thereby reducing their utility. Open 3D COFs could alleviate these restrictions, but are difficult to make because of interpenetration. Interpenetration occurs when the pore topology is compatible to the topology of the COF backbone, leading to the growth of an additional COF net inside the pore, until the pore is filled (Figure 2-12).[70, 86-88]
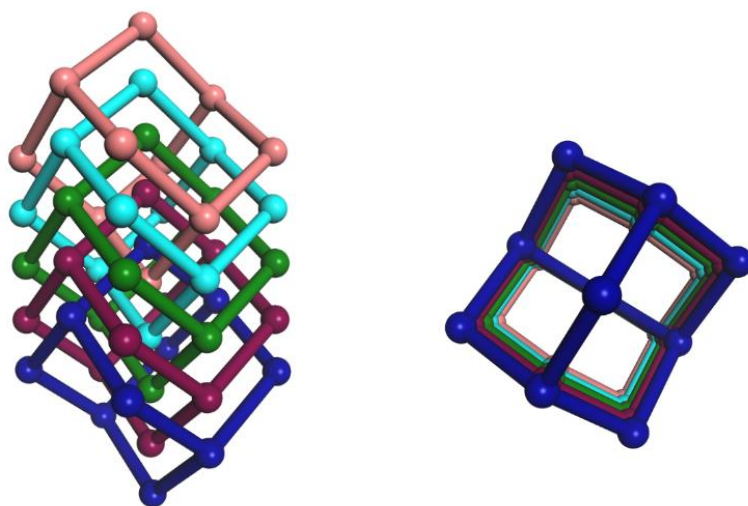
Figure 2-12: Schematic of interpenetration of a **dia** net based structure, demonstrated in an adamantane cage, a subsection of the **dia** net.

Most COFs based on the **dia** net[70, 86-88] and the **pts** net[90, 91] are interpenetrated, but not all. In a very small pore **dia** COF, interpenetration is not possible since the nodes are too large to interpenetrate the pores.[85] COFs based on the **bor** net[89] or the **cnt** net[89] do not suffer from interpenetration, as the topology of the pore and the COF backbone are not compatible for interpenetration (Figure 2-10). While interpenetration is mainly an issue of three dimensional materials, it can also be observed in two-dimensional materials. A highly interpenetrated hydrogen bonded organic framework was observed where slabs of layers are interpenetrated by a further slab of the interpenetrating layers (Figure 2-13).[15] Similarly, interpenetration is seen to occur in the simulation of the COF-5 crystallization and has been argued to be one of the factors leading to low crystallinity in 2D COFs.[107] Interpenetration in 2D COFs has however not been observed so far experimentally.
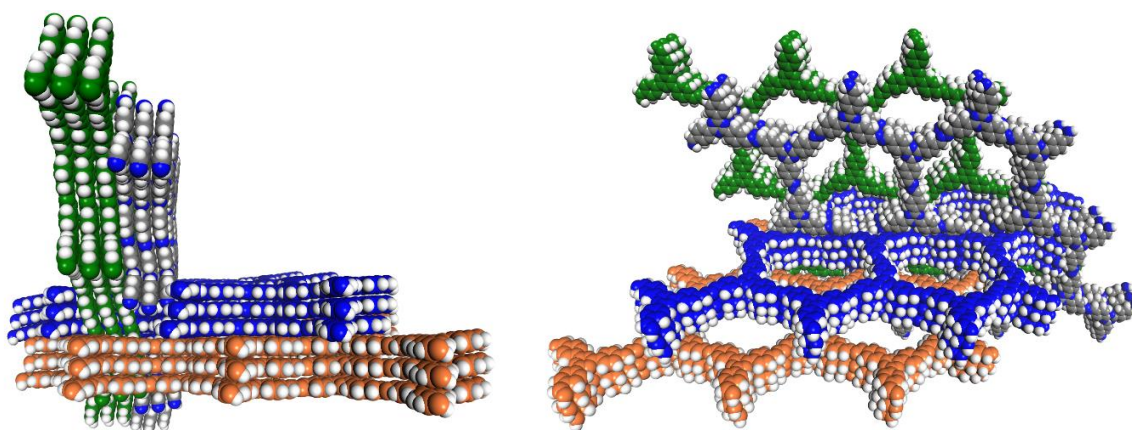
Figure 2-13: Schematic of interpenetration in a 2D hexagonal layered material as described by Zentner et al.[15] applied to the N$_3$-COF.

2.3.3. Rigid and flexible building blocks

The two-dimensional nets are well compatible with typical organic rigid building blocks and based on these nets, a multitude of isoreticular nets with a wide range of building blocks and functionalities have been synthesized. The ability to expand the pore sizes in an isoreticular manner demonstrates the tailorability of COF structures.[108-110] Typically, building blocks are based on molecules that are completely conjugated in their sp and sp^2 carbons based backbone, as in aromatic and polyaromatic moieties alkyne or vinylic groups.[92, 93, 111] Special functional groups are required for C4 symmetrical building blocks that would be difficult to synthesize based on purely carbon-carbon bonded backbones. These are however readily available as flat and rigid porphyrins[72, 81, 91, 102, 112-114] and phthalocyanins.[115-119]
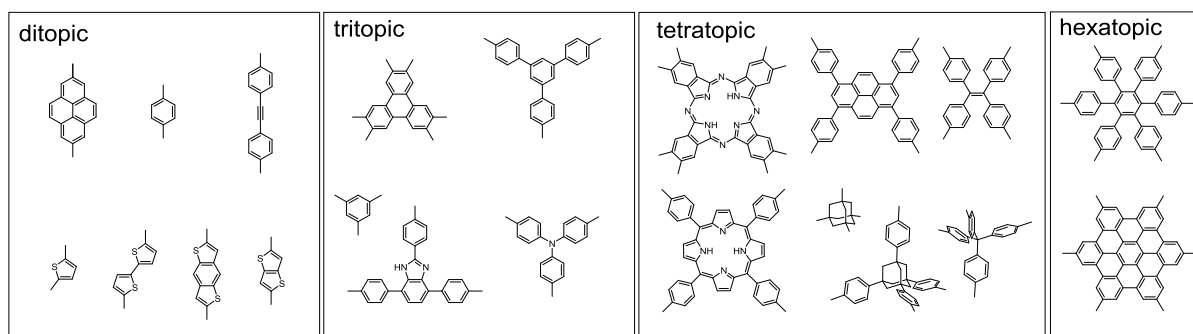
Figure 2-14: Common building blocks used for the synthesis of COFs.

Typically high symmetry building blocks are employed, as often these are more synthetically accessible in addition to the increased difficulty in crystallizing low symmetry building blocks (see chapter 2.4). A notable example of an unsymmetrical COF is the use of a T-shaped benzimidazole linkage, which still produced a rather crystalline "brick-wall" type COF.[120]

As previously discussed, flexibility is a factor in reducing the crystallinity of COFs and therefore mostly sp and sp^2 based building blocks have been employed for the synthesis of COFs. However, several examples of sp^3 carbons in the COF backbone have been demonstrated (Figure 2-15). These are especially important for three dimensional COFs, all of which have been based on tetrahedral adamantane or tetraphenyl methane building blocks.[70, 86-91] These moieties contain sp^3-carbons, but are rigid and the molecule does not gain considerable degrees of conformational freedom. Less prominent are the examples of triphenyl cyclononane[61] and spiroborate,[121] which are expected to be

more flexible, but still possess considerable rigidity due to their cyclic or bicyclic nature. Two examples of COFs have been demonstrated with flexible ditopic cyclohexane units that possess considerable flexibility to transform from the boat to the chair conformer: one based on dicarboxy cyclohexane[70] and another on a disubstituted piperazine.[73] These examples show that absolute rigidity is not a prerequisite for the formation of a crystalline materials, but the low number of demonstrated flexible COFs in addition to the results from chapter 2.4.2 suggest that flexibility may increase the difficulty of crystallizing a COF.
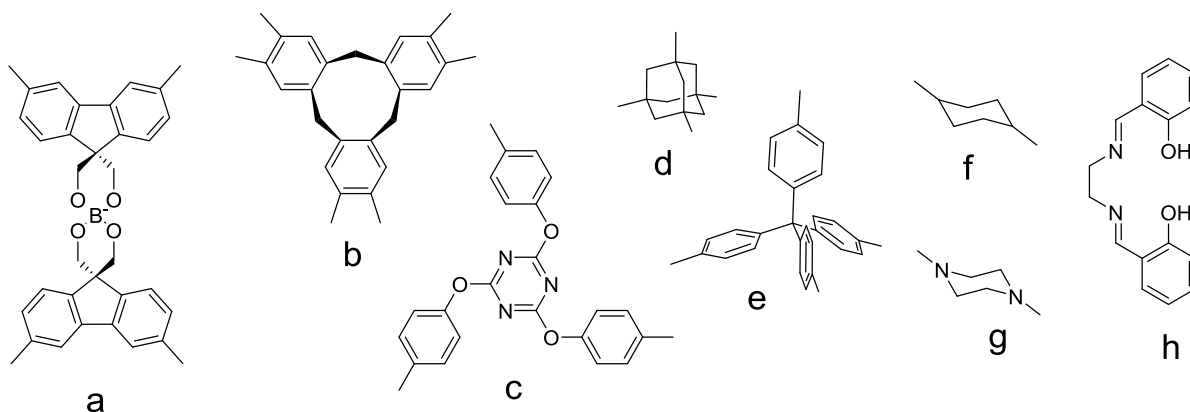
Figure 2-15: Flexible linkers and linkages in COFs: a, spiro borate linkage;[61] b, cyclohexanonane based linker;[121] c, aryl ether bond;[122] d, adamantane linker;[85] e, tetraphenylmethane linker;[79] f, cyclohexane linker;[70] g, piperazine linker;[73] h, salen ligand as COF linkage.[123]

2.3.4. Structurally responsive COFs

The previous section showed how flexible building blocks can be included in COFs, but also common motifs such as imine bonds lead to considerable flexibility. This flexibility can not only be detrimental but can also be used for function in the material. Responsive structures represent a powerful tool to imbue functionality into materials by design.[124-129] The phenomenon of flexibility and the associated phenomena of breathing and gating are well studied in MOFs for sorption and sensing applications.[130, 131] In COFs flexibility and the resulting applications are a nascent field and first examples have shown that COFs are also capable of structural changes upon guest addition or removal. A clear example of structural transformation was observed in COF-1, where a partial removal of the incorporated guest molecule (mesitylene) led to a change in the stacking structure from staggered to eclipsed (Figure 2-16).[132] In the staggered structure, the mesitylene guest is sandwiched between layers of the boronic anhydride COF, thereby leading to a favorable interaction. Upon removal of the mesitylene by heating, this stabilization is lost when the mesitylene-COF interaction is overcome and the layers correspondingly rearrange to reform the thermodynamically favored state by stacking in an approximately eclipsed fashion.
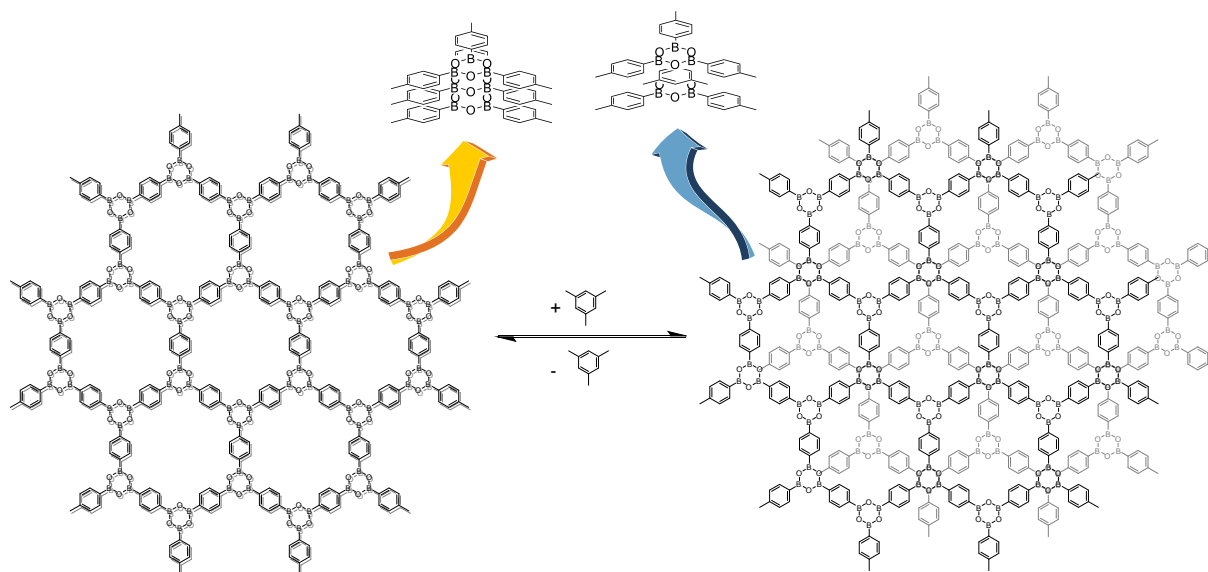
Figure 2-16:Schematic of the changing stacking structure of COF-1 upon solvent addition from eclipsed to staggered. [132]

Other structural flexibility has been observed in three dimensional COFs based on the **dia** net. Investigation of a 3D imine COF with rotation electron diffraction, showed two different structures depending on the temperature, presenting the first observation of a thermally induced phase transition in COFs.[86] The crystal polymorphs at 89 K exhibit rectangular pores based on the $I\bar{4}2d$ symmetry, while at higher temperature of 298 K $Imma$ symmetry is observed with square pores. These structural variations result from the conformation and twisting of the backbone, while the topology and the interpenetration of the network remain the same. In the same COF a strong hysteresis loop and steep adsorption was observed at one point in the Argon sorption isotherm, which could point to guest induced structural transformations and/or rearrangement/reorientation of Argon packing. Similar observations have been previously made in 3D COFs.[64]

The first clear proof of guest induced breathing in a 3D COF was seen by addition of tetrahydrofuran (THF) to an imine COF, which caused a conformational change of the structure.[133] In this structure the conformation of rotating imine "pedals" could be reversibly changed by the ad- and desorption of THF (Figure 2-17). The addition of THF led to a larger pore volume, an expansion of and slacker framework structure together with less dense packing of the layers. This structural transformation was deduced from drastic changes in the XRPD pattern and could also be induced and characterized by Xenon adsorption. ^{129}Xe NMR was able to show the transformation and coexistence of both structures in an intermediate range. Similar to the previously described COFs, a gate opening effect was observed at very high partial pressures of the nitrogen sorption isotherms, which could be explained by the same structural changes.
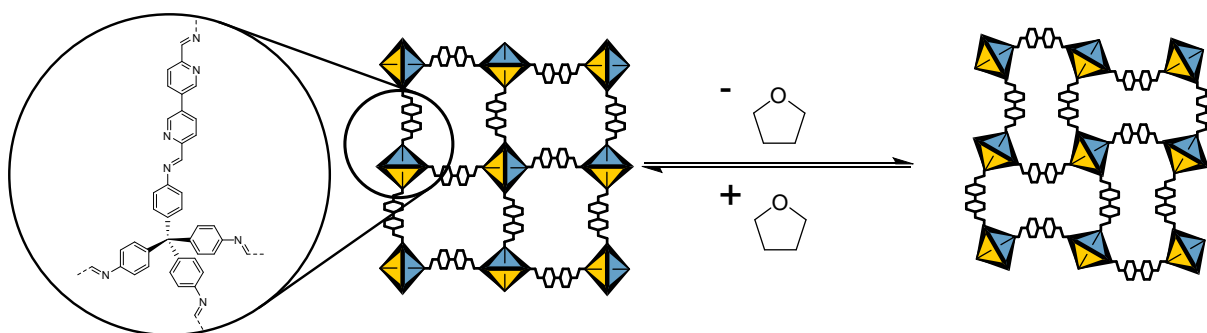
Figure 2-17: Schematic of structural transformation in a breathing 3D imine COF.[133]

2.3.5. Design of pores: two kinds of pores in two-dimensional COFs

Since the synthesis of two-dimensional COFs is often more straightforward than 3D COFs, strategies have been devised to produce different kinds of pores in a single 2D COF. A direct approach to generating different kinds of pores is the combination of intrinsic pores and extrinsic pores. Macrocyclic linkers provide a strategy to produce intrinsic pores, by pre-designation of the shape of a pore as a molecular building unit. These linkers are then additionally able to generate extrinsic pores by the linking reaction between the building blocks. This has been demonstrated based on the previously discussed semi-aliphatic macrocycle cyclononane and with a series of C3 and C4 symmetrical linkers (Figure 2-19).
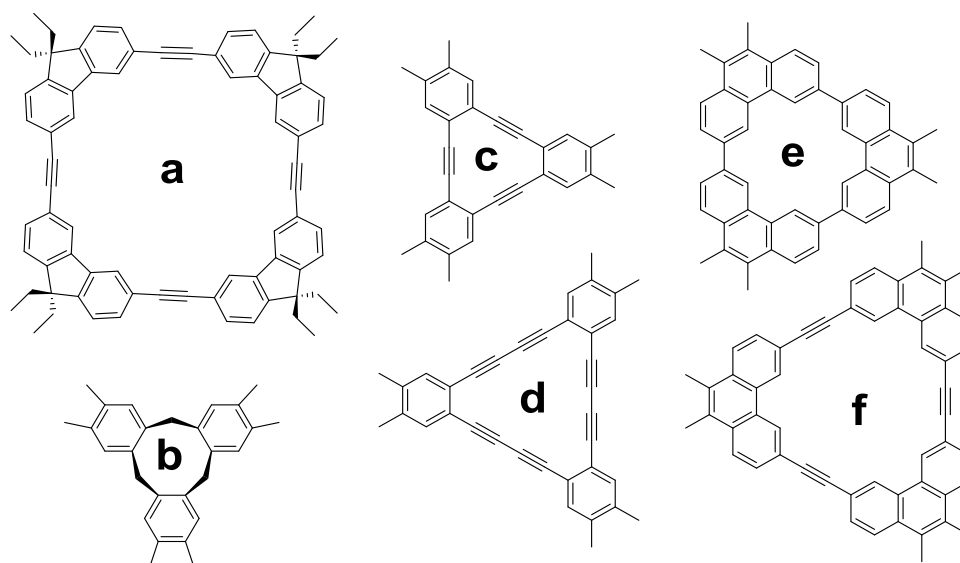
Figure 2-18: Schematic of macrocyclic COF building blocks: a, C4 fluorene –alkine tetramer;[61] b: C3 bowl shaped cyclo nonane building block;[121] c,d: C3 phenyl alkyne trimers;[134] e: C3 phenanthrene trimer;[135] f, C3 phenanthrene alkyne trimer.[136]

A further approach that does not rely on the elaborate synthesis of precursor macrocycles is the generation of two or even three kinds of pores by asymmetry. One example is the unsymmetrical elongation of triformyl benzene that leads to the formation of different pore sizes due to self-sorting during the synthesis of the COF (Figure 2-19, A).[137] Altering the symmetry can be employed by using a tetratopic linker that is not C4 symmetrical, but shows a 120° and a 60° angle, to induce the formation of a kagome (**kgm**) net instead of a **sql** net (see chapter 2.4.2; Figure 2-19, B).[83] Based on the **kgm** net, further desymmetrization can be used to introduce three kinds of pores by combining two linear linkers of different lengths. The linkers do not form two COFs but form a single COF by

self sorting into a structure with three differently sized pores (Figure 2-19, C).[138] Lastly, a two linkers can be used for the formation of three different kinds of pores by using an asymmetric bent geometry (Figure 2-19, D).[139]
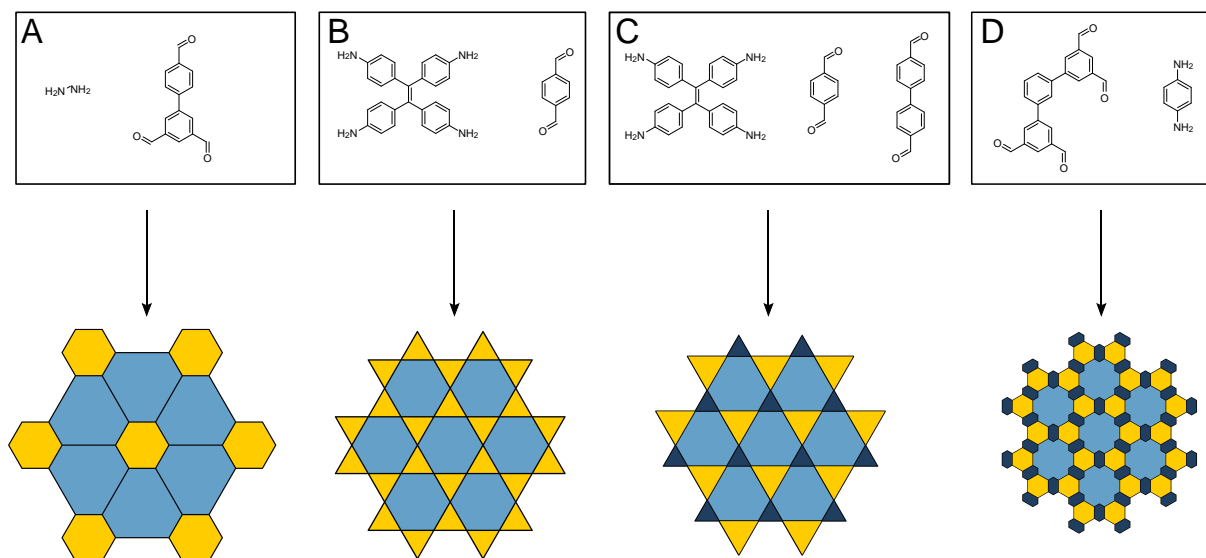
Figure 2-19: Strategies of synthesizing COFs with differently sized and shaped pores: **A** desymmetrized vertex design;[137] **B**: kagome COF with two kinds of pores;[83] **C**: three linkers kagome COF with three kinds of pores;[138] **D**: three kinds of pores from two linkers.[139]

2.4.   Formation principles of ordered complex covalent solids

Simple covalent solids such as diamond, graphite and boron nitride are formed by high temperature synthesis that allows for direct covalent bond cleavage and reformation, and thereby crystallization of the materials. However, this direct approach can be implemented with complex molecular building blocks, only if some bonds are by design much weaker than others and would be cleaved discriminately. Nitrosyl dimerization reaction for the synthesis of COFs is an example for this strategy. The covalent nitrogen-nitrogen bond in the azinedioxy moiety is especially weak (83-126 kJ/mol)[86] and can be homolytically cleaved under ambient conditions.[79] Nevertheless, this approach leads to very unstable materials. Therefore, reactions that allow reversible bond opening under mild conditions without relying on direct bond cleavage are needed. The first ordered complex organic solids were assembled as molecular crystals using weak van-der-Waals interactions. Over time, strategies have been developed to form stronger reversible linkages, such as hydrogen bonds, metal-ligand interactions and finally covalent bonds. Crystallization is known to become more difficult with increasing bond strength and therefore, the synthesis of COFs with their strong covalent bonds present the pinnacle of this development (Figure 2-20).
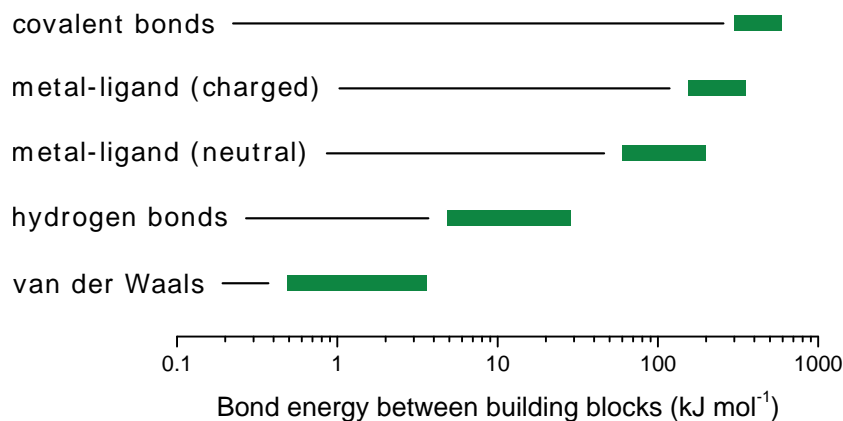
Figure 2-20: Approximate bond strengths of bonds that are used for the synthesis of complex solids based on molecular building blocks.[140-143]

In addition to the reversible covalent bond formation, two more strategies exist, which lead to ordered materials: a single reaction pathway and separate crystallization and covalent bond formation (Figure 2-21). COFs are not designed solely relying on one of these strategies, but in conjunction with each other to obtain crystalline materials depending on the COF.
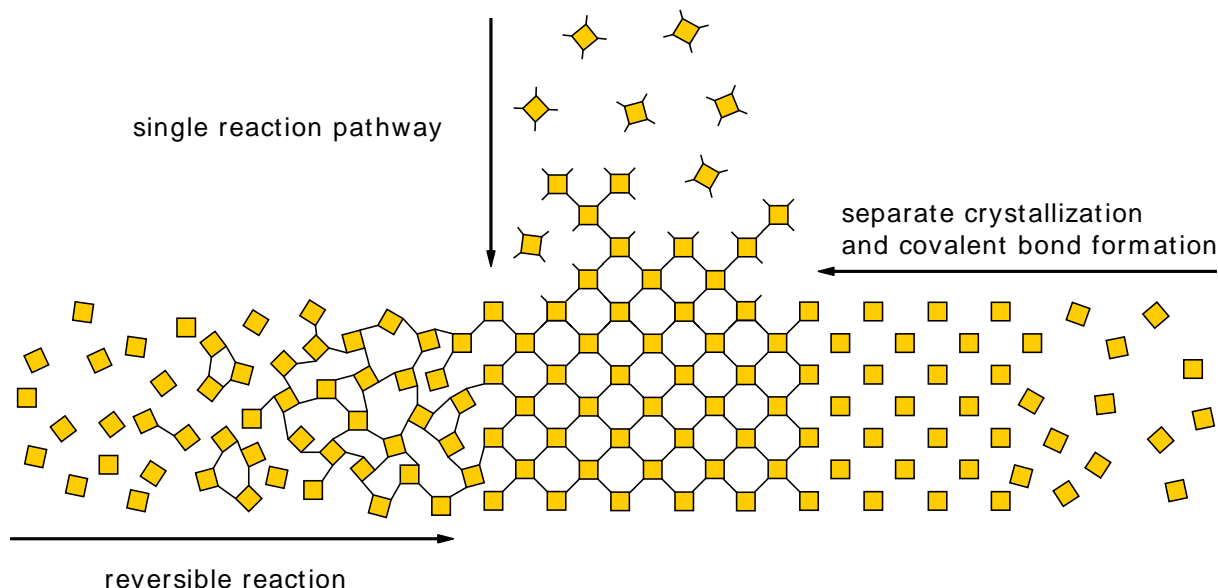
Figure 2-21: Three approaches to forming a crystalline covalently bound polymer

2.4.1. Crystallinity through reversible covalent bond formation

The generally accepted explanation for the crystallinity of COFs is the reversibility of covalent bond formation.[1, 59, 60, 62] The reversible opening and closing of the COF linkage in the COF forming reactions (Figure 2-22) allows the slow rearrangement, defect healing and thereby crystallization into an ordered lattice. The rearrangement allows an initially formed amorphous solid to crystallize over time.[144] This mechanism seems to be prominent for some imine based COFs, whereat the formation of the initial amorphous polymer is fast and the defect healing occurs only over time.[144] In some boronic ester based COFs another mechanism dominates the COF formation: sheet-like oligomers and small crystallites form under reversible control in suspension and then precipitate by aggregation, from which point on improvement of the crystallinity is negligible.[145] Knowledge of these mechanisms opens the door to tailoring the synthesis conditions of COFs specifically.

Based on the reversible COF formation mechanism, many reversible reactions have been developed for the synthesis of COFs and these are discussed in chapter 2.2.
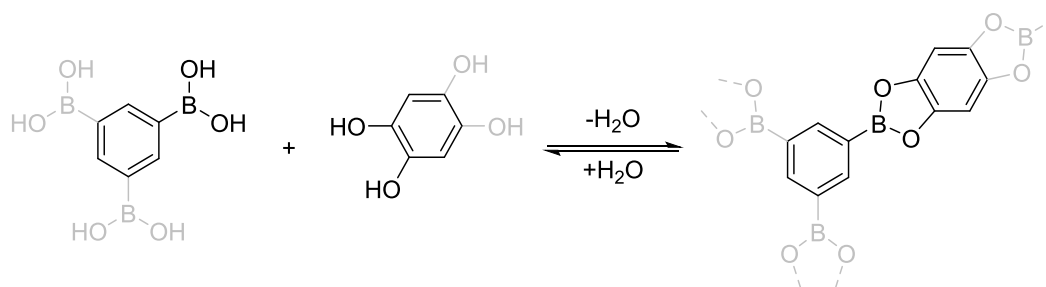
Figure 2-22: Reversible condensation reaction of a boronic acid with a catechol to form the boronic ester, archetypical for the reaction used in many boron based COFs.

Besides the design of new reversible reactions, methods have been developed to improve the crystallinity by influencing the reversibility. One of the most straightforward means developed by Dichtel and coworkers[144] is the addition of increased amounts of water to favor the back reaction and therefore improve crystallization. Mechanistic investigation into the formation of imine COFs showed rapid condensation into an amorphous polymer by the catalysis of acetic acid which enabled the forward reaction. However, only upon addition of sufficient amounts of water for the back-reaction and error correction, crystallization is possible. Alternatives to the imine forming catalyst acetic acid have been explored, as acetic acid is an ineffective catalyst for the transamination reaction.[146] The use of a Lewis acid instead of the usual Brønsted acid for the condensation of imine COFs leads to significantly improved crystallinity and porosity as determined by a higher BET surface area and a narrower pore size distribution. The Lewis acids employed for these studies were transition metal triflates (M = Sc, In, Yb, Eu), which showed extremely fast conversion to the corresponding COFs (in the range of minutes), at low loadings and low temperatures, while producing high surface area and high crystallinity. Scandium triflate performed especially well as a transamination catalyst due to the low ionic radius of Sc^{3+}. However, these findings were not generalizable as some COFs performed better with the acetic acid catalyst than with the triflate catalysts.

The mechanism of imine condensation showed that a fast polymerization occurs to an amorphous polymer that slowly crystallizes. In boronate COFs, the precipitation of the COF hinders further crystallization. Both these mechanisms suggest that crystallinity can be improved by slowing the initial reaction speed, so kinetic intermediates are not trapped. Consequently, several approaches have been developed to slow down the reaction speed. Dichtel and coworkers[58] showed that the use of amines protected as benzophenone imines slows the initial reaction speed by a slow deprotection of the benzophenone imine and thus gives rise to higher crystallinity. Work by Bein and coworkers[147] improved the crystallization by the addition of a mono-dentate linker in the synthesis of a boronic ester COF. The introduction of the monodentate modulator leads to sharper reflections in XRPD, increased the BET area, as well as drastically increased the domain sizes as observed by TEM. The improved crystallization originates from the modulators' rapid attachment and detachment to the growing COF crystallite, which slows the rate of growth by reversibly inhibiting the attachment of new linkers. Banerjee and coworkers[148] slowed the imine formation reaction by supplying the amine as a salt of toluene sulfonic acid (TSA), to improve the crystallinity of a set of twelve COFs. TSA acts as a catalyst for the imine formation instead of the commonly used acetic acid. Additionally, the anilinium species needs to be deprotonated before reacting to the imine, limiting the supply of the amine to the reaction. This can also be interpreted as a regulation of the equilibrium reaction by favoring the back reaction by the protonation of the amine. This so-called "terra cotta" process

improved the surface areas two to three times, in comparison to the conventional solvothermal methods. Instead of chemically slowing the reaction by adding inhibitors, it is also possible to limit COF growth by slowly supplying the COF precursors to a preformed suspension of COF nanoparticles. In this experiment by Dichtel and coworkers, precursors were slowly added through a syringe pump to nucleate colloidal COF nanoparticles[149] that led to homoepitaxial growth of the COF crystallites.[150] This result is in agreement with earlier findings that some imine COF thin films could only be crystallized by the slow addition of precursors.[151]

2.4.2. Single reaction pathway: Crystallinity through low degrees of freedom during synthesis

Reversibility is not the only strategy for forming ordered structures; if kinetically controlled reactions occur only at well-defined positions with low or very low conformational degrees of freedom, order can also be achieved. The nucleation and growth need to be sufficiently slow, such that larger crystallites can form with only vacancies as possible defects. This has not been shown to be a predominant mechanism in the growth of COFs so far, but many examples point towards the importance of a single reaction pathway for the formation of crystalline COFs. This is especially of importance for COFs based on reactions with low reversibility, where the single reaction pathway compensates for a lack or diminished capability for error correction. Conversely, low conformational flexibility might be desirable for creating crystalline COFs, but it would also prohibit functional frameworks based on guest or stimuli induced flexibility as discussed in chapter 2.3.
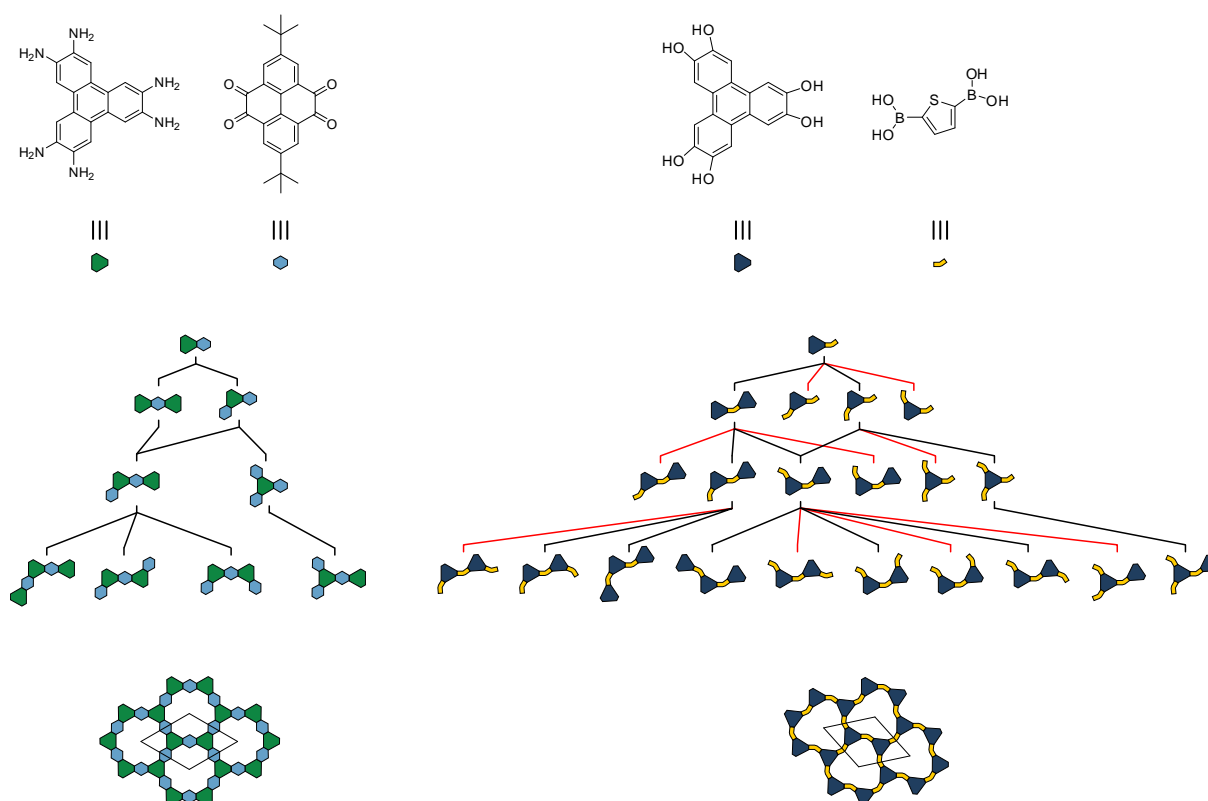
Figure 2-23: Reaction pathways for the formation of oligomers, which are compatible with the periodic structure of the periodic product. Left: The formation of phenazines, where all reaction pathways lead to desirable products.[69] Right: The angled nature of the thiophene based building block leads to many conformers, only some of which are compatible with the periodic structure of the final COF (compatible shown as black, incompatible as red pathways).[152]

A single conformer pathway can easily be imagined for pyrazine based COFs[69] as these materials can be designed with only one possible reaction pathway due to exceptional conformational rigidity in the annulated nature of the COF (Figure 2-23 left). In comparison, work by Dinca and coworkers[152] has shown that the introduction of nonlinear angled or offset linkers can drastically reduce the crystallinity of COFs. Angled linkers are able, in terms of the reaction pathways, to generate a large number of conformers, not all of which would lead to a structure that can be periodically and covalently connected (Figure 2-23). Misorientation of the linkers can be healed if sufficient reversibility is possible; however, reversibility might be limited in boronic ester based COFs due to the precipitation of aggregates from solution after the initial stages of COF formation.[145] These examples show how easy crystallization is necessary for the generation of appreciable crystallinity in COFs.

The pyrazine COF is an example of extremes of conformational rigidity, but the reduction of possible conformers can be used as a design principle to improve crystallinity in more flexible systems. Boronic ester and boronic acid anhydride based COFs are examples of a COF linkage that allows rotation around the C-B bond, but as the dihedral angles of these building blocks are close to 0°, only a low number of energetically favorable conformers exist (Figure 2-24; Figure 2-25, A).[1] In comparison, imine-linked COFs have the possibility to crystallize with imine bonds in different directions (Figure 2-25, E), increasing the conformational degrees of freedom.
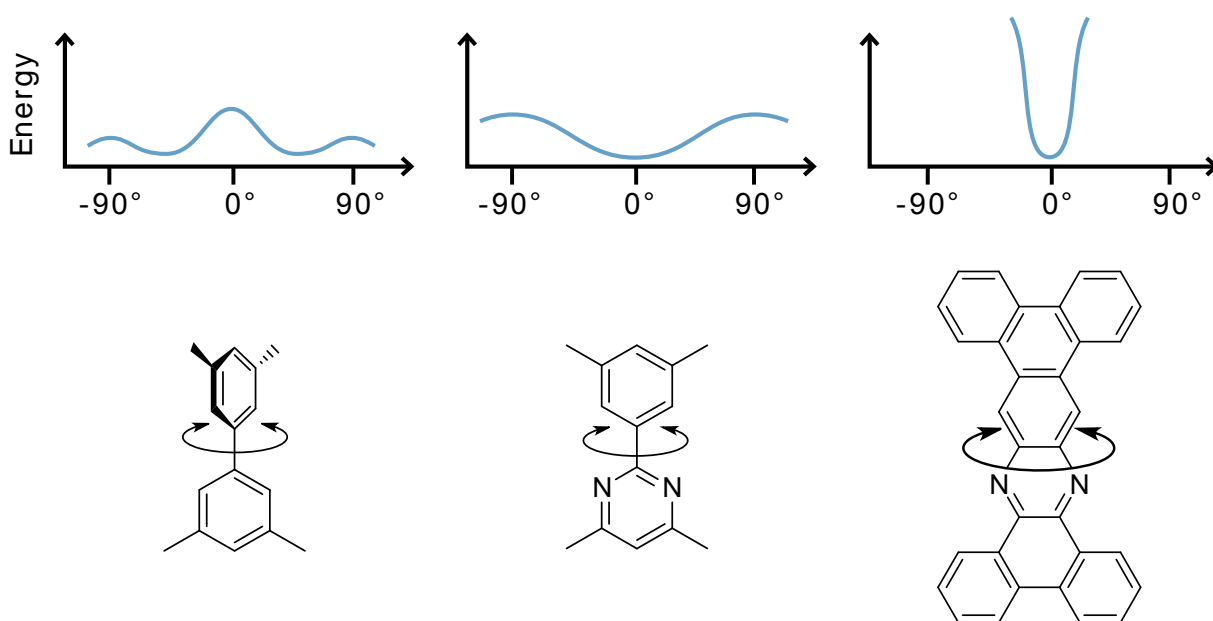
Figure 2-24: Schematic of energy barriers for the torsion in aromatic systems.

Low conformer structures are also observed in covalent triazine frameworks, where the flat triazine-phenyl moieties (Figure 2-25, B) lead to only few possible conformers in comparison to twisted biphenyls (Figure 2-25, C). In these systems, low reversibility of the nitrile trimerization is compensated by the low number of conformers. This might explain why only a few simple CTFs based on rigid and low conformer building blocks display crystallinity,[75-78] while the majority are amorphous.[113, 153-155]
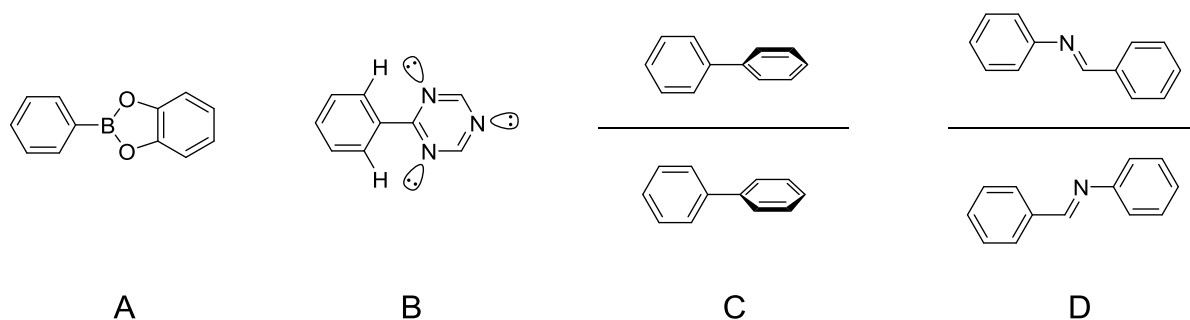
Figure 2-25: Structural motifs with low (A, B) and high (C, D) number of conformers: A: boronic ester linkage. B: triazine-phenyl linkage; C: biphenyl linkage; D: imine linkage.

Conformers might lead to disorder and low crystallinity, but they can also lead to crystallographic polymorphism. Surface COFs (sCOF) based on pyrene building blocks have been shown to exhibit such polymorphism, where two polymorphs based on the direction of imine groups can be identified (Figure 2-26).[156] "Heterodromous" imine bonds lead to the rhombohedral structure, while homodromous imines lead to a parallelogram structure. In addition, this sCOF displays a third polymorph based on a different topology of the underlying net, the rhombohedral and parallelogram structures are based on the square net, while the third polymorph is based on the kagome net. As the density of these structures is different, with the kagome showing the lowest density, the formation of each polymorph can be influenced by adjusting the precursor concentration during synthesis.
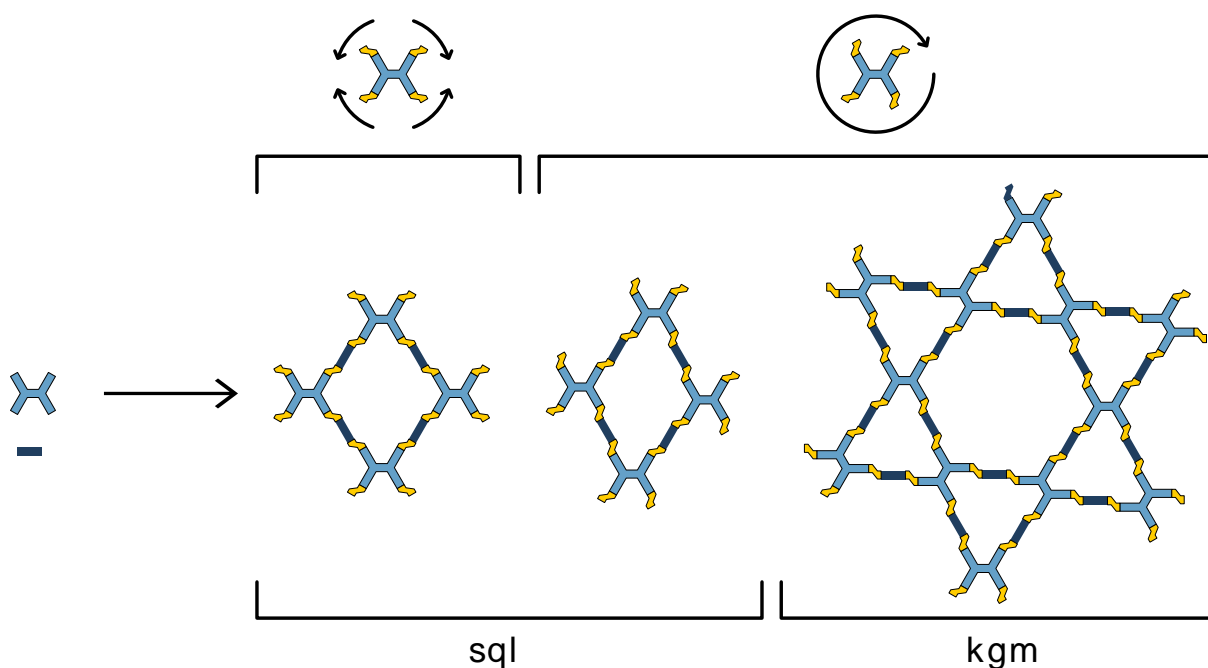
Figure 2-26: Different polymorphs of an imine – pyrene surface COF, where three polymorphs were observed.[156]

This poses an interesting relation to bulk COFs, which could also display such polymorphisms. This however has not been observed so far, possibly because the differences between the rhombohedral structure and the parallelogram might be too small to resolve with the currently achievable crystallinity in COFs. The polymorphism considering the underlying net has been indirectly observed in COFs based on building blocks with 120° and the 60° angles (Figure 2-27) that would be ideal for both **sql** and **kgm** nets. Some of the COFs based on these building blocks form the kagome net and some form the square net. COFs based on the tetraphenyl ethylene (TPE) building block crystallize in

a kagome net,[83, 138, 157, 158] while pyrene based COFs produce a square net.[66, 159-161] This observed difference could be related to the stacking of the building blocks, as pyrenes tend to slip-stack,[162] while TPE prefers eclipsed stacking.[83] A square lattice would be able to coherently slip-stack in one direction, as all pyrene building blocks are co-aligned, whereas in kagome nets the building blocks are rotated in three different orientations making uniform slip-stacking difficult.
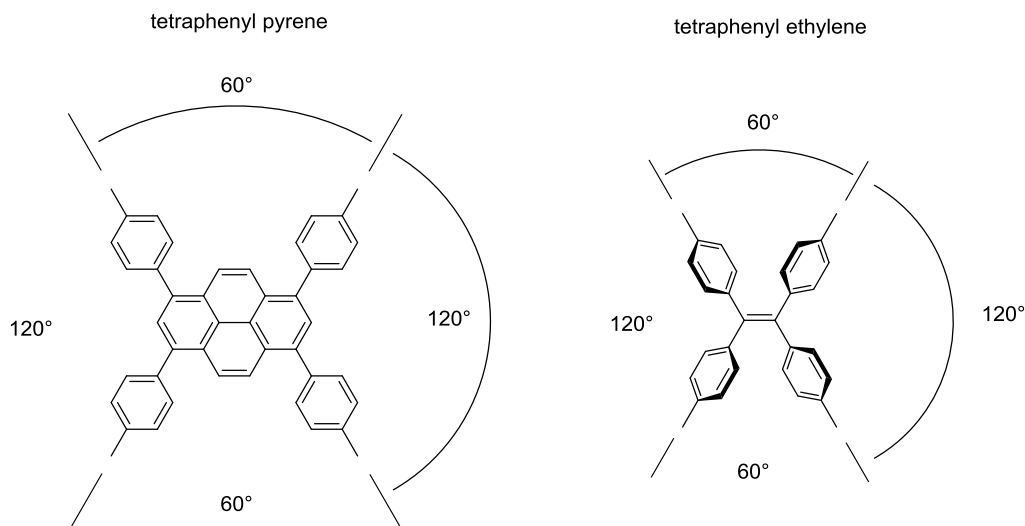
Figure 2-27: Schematic picture of common COF building blocks based on 60° and 120° angles between the linking groups.

In imines, the number of conformers can be reduced by designing the building block with intramolecular hydrogen bonds. The conformational direction of the imines can be locked by using an *ortho*-hydroxy aldehyde building block (Figure 2-28, A). However, locking the direction of the imine only leads to a reduction in the number of conformers, if the hydroxy bearing phenyl cannot rotate freely. An elegant strategy to reduce conformers in imine COFs has been demonstrated by Jiang and coworkers,[163] where two building blocks based on dihydroxy-terephthalaldehyde were used. The difference between the building blocks lies in the substitution pattern of the hydroxy groups, where hydroxy groups in *para* positions show the conformational offset (Figure 2-28, B), while the hydroxy groups in *ortho* position lead to a straight connection (Figure 2-28, C).

The influence of the degrees of freedom during COF synthesis discussed here are based on the in-plane structure of COFs. The out-of-plane structure that is created in 2D COFs by stacking can also lead to singular or many reaction pathways, depending on the choice of building blocks. Means of reducing the stacking degrees of freedom are discussed in chapter 5.1.
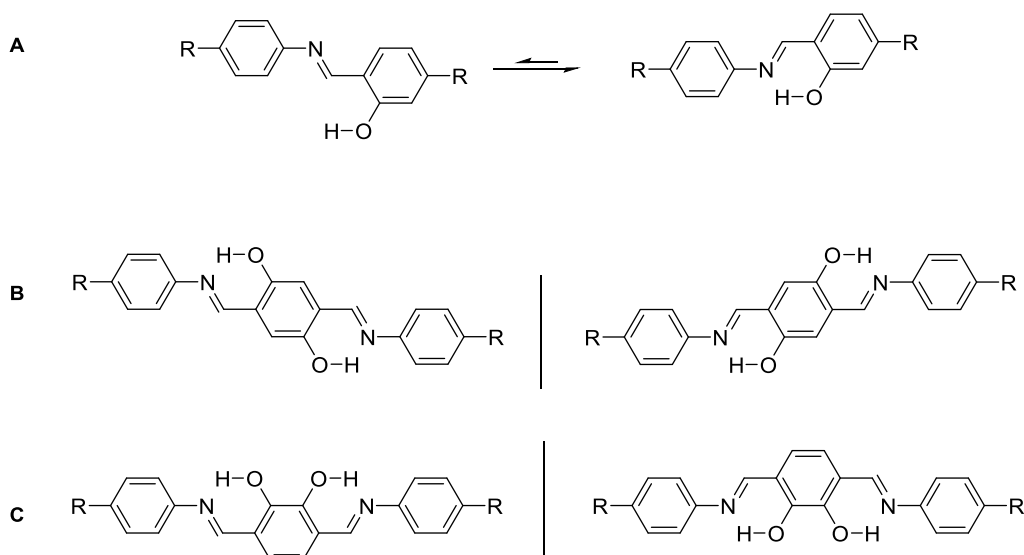
Figure 2-28: Directing imine conformers by hydrogen bonding. **A**: preferred conformer on the right, due to hydrogen bonding between the imine and the hydroxyl groups. **B,C**: using hydroxyl groups to create a linear linker from a normally offset linker.[163]

2.4.3. Pre-orientation of reaction substrates: separate crystallization and polymerization

A third path has been explored for the synthesis of strongly connected complex and metastable solids in a variety of material classes. This is based on the pre-orientation of a reaction substrate to ensure the correct reaction connectivity or conformer. In principle, this approach is widely used for the synthesis of ordered solids based on templating leading to laminar or porous materials. The used surfactants or hard templates arrange the reaction precursors in a mesoscopically defined manner that lead to defined long range order.[164] This approach has been used for the synthesis of mesoporous inorganic solids with a wide variety of structures with amorphous pore walls.[165, 166] Two-dimensional polymers can be synthesized by self-templating in combination with cross-linking to form defined lamellar sheets. Linear polymers are pre-oriented by hydrophobic effects to form lamellar structures in which polymerizable functional groups are in close proximity. Upon polymerization, the existing morphology is locked in place.[167, 168] These examples show how pre-orientation can induce long range order, while not influencing short range order. Pre-orientation strategies can also be used to induce short range order and crystalline materials that would otherwise be difficult or impossible to produce. Examples of this approach are the synthesis of 'unfeasible" zeolites[169] and linear polyimide polymers.[170] Crystalline zeolites have been synthesized by pre-orienting exfoliated crystalline layers by the addition of a modulator that determines layer registry. These are then linked with reactive silanes to form the predefined crystalline material.[169, 171] By this method, synthesis of zeolites that have been deemed not feasible to be synthesized in a typical hydrothermal synthesis is possible. Similarly, it is possible to synthesize linear crystalline polyimide polymers by the defined preassembly of the carboxylic acid and the amine precursors into ionic co-crystals. The pre-oriented intermediate can condense into polymers with much higher crystallinity than the direct method would produce. These examples show how control over pre-orientation can lead to crystalline ordered solids.

Pre-orientation has been used to synthesize crystalline two-dimensional polymers, by allowing molecular precursors to arrange into a molecular crystal, and then crosslinking the molecules in a single crystal to single crystal (topotactic) reaction. This approach generates polymeric single crystals from molecular single crystals by an irreversible reaction. Examples of such reactions include

anthracene dimerization, or the [4+2]-cycloaddition of anthracenes with alkynes, both of which can be triggered photochemically in the solid state.[172-174] While this approach is elegant, it is limited by the low accessibility and designability of these structures, as molecular crystals with reactive functional groups in close proximity in the solid state are required. The prediction of the packing molecules and thereby the crystalline structure is not straightforward and therefore these strategies can be quite limited.
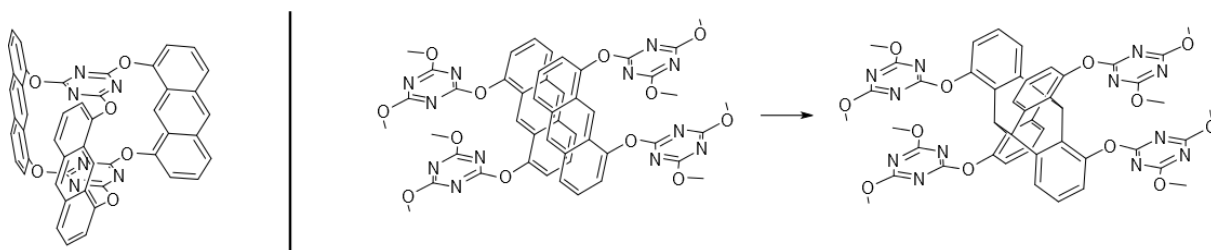
Figure 2-29: Schematic representation of the polymerization of a molecule in the solid state. Left: Trifunctional anthracene designed by Kory et al.[175] Face-to-face arrangement of the same molecule in the crystal structure and the subsequent polymerization reaction by dimerization of the anthracene units.

Similarly, anthracene units were pre-oriented by the growth of a COF where they are arranged in a face-to-face fashion by stacking in the two-dimensional COF. The close proximity in the solid state then allows photodimerization transforming a two-dimensional COF into a nominally three dimensional COF. This approach shows how COFs can be used to design rationally pre-oriented functional groups.[176]

The utilization of pre-orientation to improve the crystallinity in a COF was again showed by Banerjee and coworkers[148] who used TSA to pre-orient their amine precursors. Single-crystal X-ray diffraction structure solution of the TSA salt showed a laminated hydrogen-bonded network, with a separation of 5-7 Å of the amine units induced by TSA. The space between the amines matches the approximate size of the aldehyde reactant, which reacts with the amine by displacing TSA (Figure 2-30). The amine is deprotonated and condenses with the aldehyde, THB-CHO to form the imine, which is possible since the weak hydrogen bond is replaced with the stronger covalent bond. The TSA salt crystal structure is converted slowly into COF layers, which then stack due to hydrophobic and π-π interactions. Crystallinity is only observed upon washing, indicating residual TSA in the pores, as suggested by the mechanism.
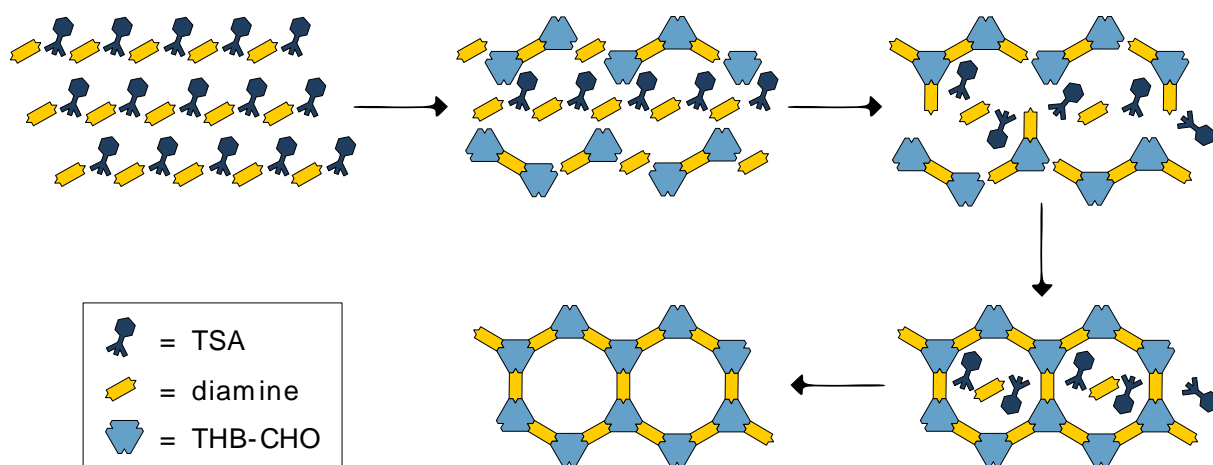
Figure 2-30: Schematic of the mechanism of the pre-orientation of diamines with help of TSA. TSA is replaced by THB-CHO and then reacts.

Bein and coworkers[83] have shown a method of introducing pre-orientation, with a COF layer directing the precise growth of the next layer by providing defined molecular docking sites. The pre-orientation is achieved by using propeller shaped building blocks that influence the stacking landscape such that a single minimum exists. The newly added molecules are guided to defined positions, where they react to form a highly crystalline COF (Figure 2-31). The stacking landscape of other COFs can present multiple degenerate or energetically similar minima that would lead to in-plane mismatches during the growth of a layer and thereby lower crystallinity. This example can be considered also as a type of single reaction pathway. Similarly, many of the described strategies for improving stacking and thereby crystallinity, as described in chapter 5.1, can be considered pre-orientation.
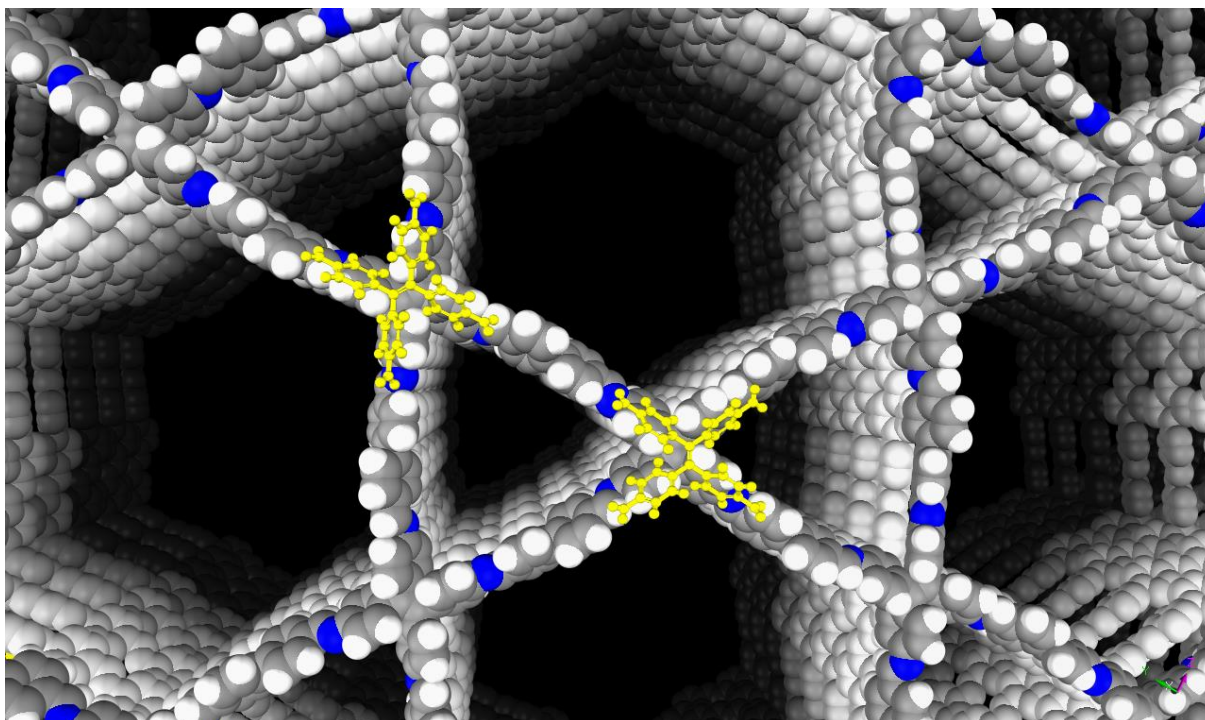
Figure 2-31: Pre-orienting molecules on an already grown 4PE-2P COF surface.[83] The possible position of the molecules are confined to a single energy minimum per underlying building block in the stacking energy landscape. This pre-orientation could serve as a molecular motif during the crystallization and growth of the COF.

Three-dimensional COFs can be synthesized from linear covalent chains by using metal coordination bonds as a means to arrange the chains in a way such that an interwoven structure is results (Figure 2-32).[177, 178] The interlocking of individual chains in the synthesis of a COF is a result of pre-orienting the linkers, by chemistry previously pioneered for the synthesis of catenanes.[179] The linear building blocks used for the synthesis of these COFs are essentially pre-woven by the quasi-tetrahedral arrangement of two V-shaped building blocks that are assembled by a metal ion binding in the grooves of two building blocks. The pre-orientation of the linear building blocks into a quasi-tetrahedral building block facilitates interweaving during the synthesis of the COF, and is also retained in the crystalline COF. The necessity of pre-orienting the building block has been demonstrated by performing the COF reaction and the building block assembly simultaneously, which lead to no observed crystallinity.[178] The crystalline COF could also be demetallated, to remove the orienting effect of the metal, which leads to a significant loss of crystallinity.[177] However, upon reintroducing the metal, it is possible to recover the crystallinity fully, which demonstrates that the topology of the COF is maintained upon demetallation and that the woven COF achieved its structure only through pre-orientation.

The chemical conversion of COF linkages can be considered a pre-orientation of the building blocks by the reversible reaction, which are then reacted in place by an irreversible reaction. Such transformations are discussed in section 6.1.
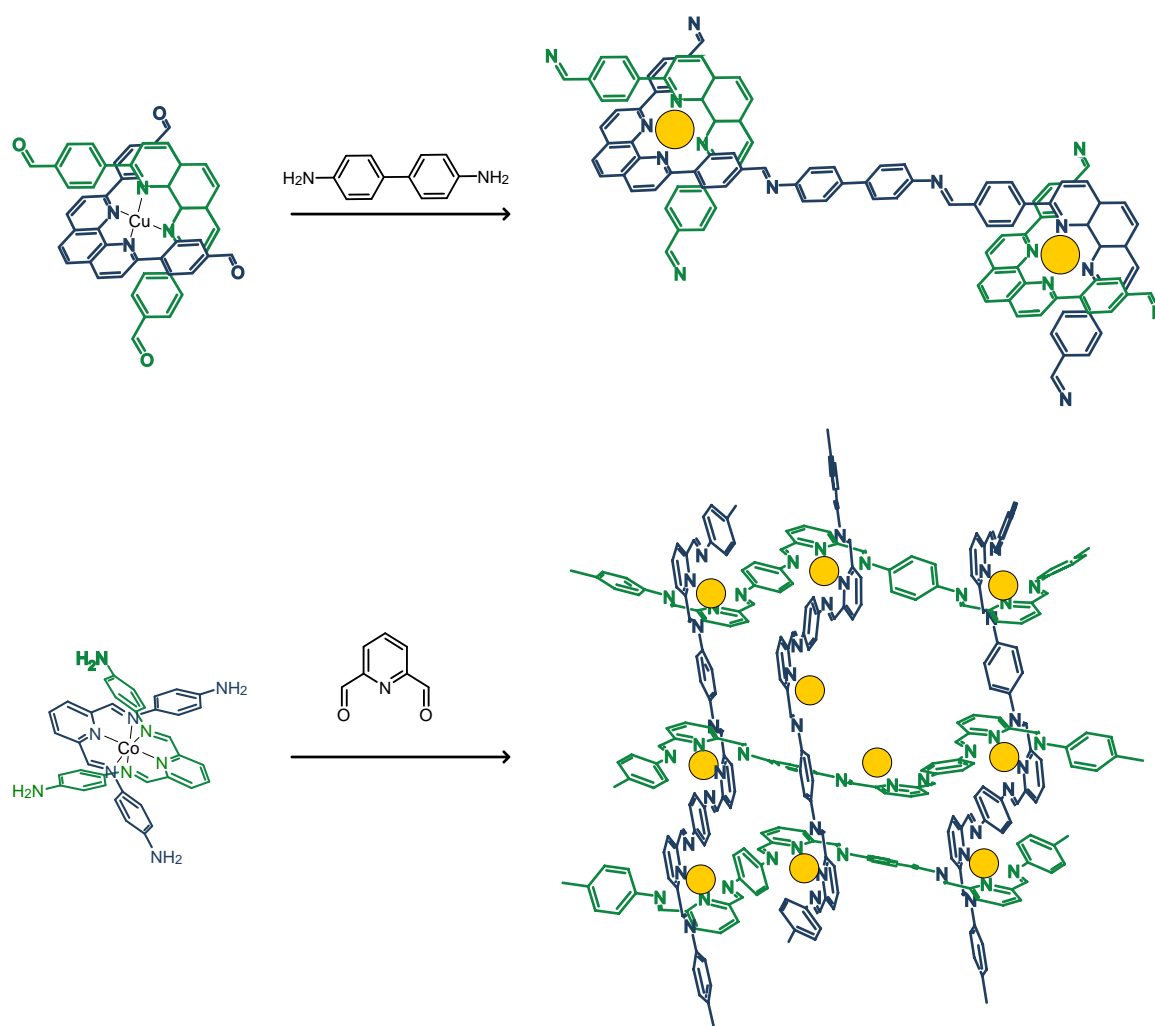
Figure 2-32: Woven COFs generated from linear polymers. Top: COF-505, the first woven COF.[177] Bottom: COF-112, a diiminopyridine woven COF[178]

2.5.   Application of COFs

Due to their inherent porosity and usually aromatic backbone, COFs have been used for a variety of applications. One of the most explored uses is the COF's porosity for sorption applications. As COFs contain no metals, their densities are fundamentally lower than those of metal organic frameworks (lowest reported: 0.17 g/cm^3, COF-108[89]). COFs are therefore useful for sorption applications where mass is a critical factor such as gas storage in mobile applications. Gas storage in COFs by physisorption has been investigated with hydrogen,[89, 180, 181] methane,[182, 183] and carbon dioxide.[184-186] The addition of functional groups into COF pores makes chemisorption of reactive gasses possible. The adsorption of ammonia[187] for example is enabled by Lewis acidic sites in boron based COFs and sulfur dioxide could be adsorbed in amine containing COFs.[188, 189] The defined pore diameters of COFs allow tuning the selectivity for gases and therefore can be used for separation of gas mixtures, such as of H_2/CH_4,[190] H_2/N_2[190] and CO_2/CH_4.[191] Mixtures of H_2/D_2 can be separated by designing a small pore COF with cryogenically flexible functional groups that allow quantum

sieving of the two isotopes.[192] The high surface area and porosity of COFs can also be used for the adsorption of nongaseous molecules or ions such as the adsorption of mercury ions from wastewater[193, 194] or the temporary trapping of guest molecules for drug delivery.[88, 195, 196] Because of their accessible pores COFs have been employed for sensing, where fluorescence quenching was used to detect guest molecules.[66, 67, 194, 197-201] The heterogeneous, but tailorable organic nature of COFs and their high surface area makes them a versatile platform for organic catalysis, as seen with the reported Suzuki cross coupling reaction by incorporation of monometallic palladium into the pores.[202-204] The Lewis basic nitrogen functionalities of imine groups in the COF backbone are able to catalyze Knoevenagel condensation,[85, 205, 206] where aldehydes and C-H acidic compounds condense to form a C=C bond. The tunability of COFs allows the facile introduction of chiral side groups, which can be used for asymmetric organocatalysis[207-209] or chiral separation columns.[210-212] Energy storage and battery applications have been investigated in COFs with the development of redox active COFs[151, 213-215] and with the use of COFs for the retention of polysulfides[216-219] that could enable the development of long lasting lithium sulfur batteries.

Most COFs are based on π-systems that are either conjugated or favor charge transport by π-π interactions; it is thus possible to design COFs as organic semiconductors that display hole,[116, 220] electron[115] or ambipolar transport properties.[221] The extended stacked structures in 2D COFs often enable conductivity that can be improved by including donor and acceptor moieties into the framework's backbone.[222] A different strategy is using the COF backbone as an electron donor and including an electron acceptor into the pores.[223] Photoexcited charge separation, photoconductivity[223, 224] and ambipolar charge separation have been demonstrated in COFs and have been utilized to build field effect transistors.[225, 226] In addition to electronic conduction, it has been shown that COFs can be used for ionic conduction, especially proton conduction[227-230] and lithium ion conduction.[61, 231]

The aromatic backbones of COFs and the charge percolation in combination with their porosity makes them tunable photoabsorbers with high accessible surface areas that can be employed for photocatalysis. Application of COFs for photocatalytic hydrogen evolution is discussed in chapter 3.

These very diverse examples of applications and properties show the versatility of COFs and the possibility of designing the properties of these functional materials.

# 3.	Research Objective

The current state of research in the synthesis of COFs is still fairly limited to a moderate number of examples, in spite of the modular synthesis allowing for a systematic variation of structures and properties. The variability and ability to use dissimilar building blocks to construct structurally similar COFs makes the fine-tuning of the structure and the properties possible. Higher-level structural features such as the geometry of building blocks and the resulting nets are routinely controlled, but fine-tuning of desired properties and allied strategies such as structure-property relationships are often lacking. In particular, the study of collective properties that only manifest in the solid state such as the photocatalytic activity of COFs and their stacking require fine-tuning of the building blocks. Furthermore, additional properties including stability are mostly addressed by choice and design of the precursors, fundamentally limiting the properties of COFs.

The aim of this thesis is to develop design principles for the structure and properties of COFs based on the variation of building blocks and through post-synthetic modifications (Figure 1-1). The focus lies on two-dimensional COFs (2D COFs), which are defined by their covalent connectivity in two dimensions with only weaker stacking interactions in the third direction to give rise to layered materials. These COFs offer three levels of control over the structure and thereby properties can be distinguished (Figure 3-1). The first level controls the molecular makeup of the building blocks and thereby the covalent structure in a layer. The second level concerns the out-of-plane structure and the resulting stacking in COFs. The third level deals with post-synthetic modification that produce with structural and property changes that cannot be incorporated by simple building block design alone, and therefore have to be incorporated after the COF synthesis.
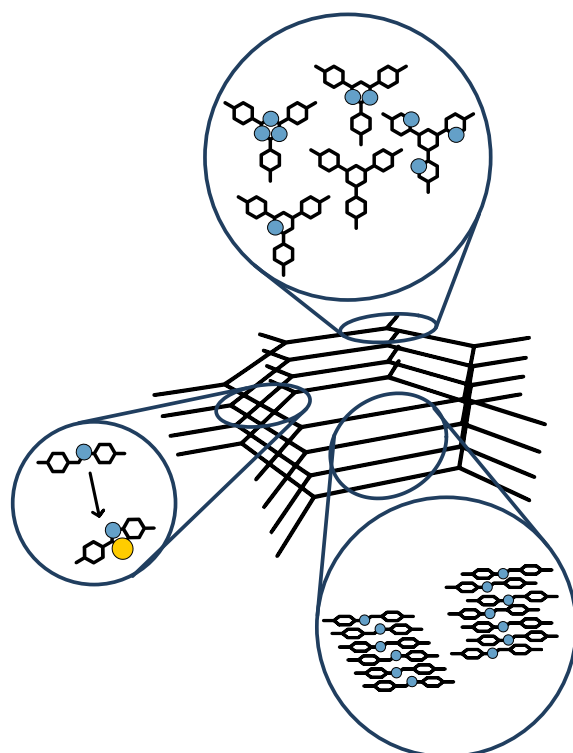
Figure 3-1: Controlling the structure and properties of COFs on different levels.

Controlling structure-property relationships in COFs, the first level is especially important as the electronic and geometric features of the in-plane structure play a large role in determining the properties of the resulting framework. The design of structural motifs readily translates to the in-plane

structure and, thus, may be used to alter the optoelectronic properties of COFs. In this thesis, this change in optoelectronic properties by in-plane design of COFs will be used to modify and optimize the photocatalytic properties of COFs. Different molecular functional groups will be explored to modify photocatalytic hydrogen evolution and thereby enable the extraction of structure-activity relationships that can guide the design of next generation photocatalysts. The in-plane structural design is versatile and largely rational. In contrast, the out-of-plane structure is based on non-covalent interactions, increasing the difficulty of the control of these supramolecular features. The out-of-plane structure has significant importance for the optoelectronic properties, nevertheless, controlling it is especially challenging. This thesis will investigate means of improving the inter-layer registry as well as design principles for defined stacking polytypes. The COF linkages are formed during the synthesis of the COF, but their presence can induce undesirable chemical or physical properties that are disadvantageous for applications like photocatalytic hydrogen evolution, where hydrolytic stability is important. The COF linkages cannot be altered substantially by building block design, as they are required for obtaining crystallinity and porosity. Hence, alteration of these moieties can only be obtained after the synthesis of the COF. Therefore, rational and crystallinity preserving transformation of these linkages is highly desirable. This thesis will investigate post-synthetic strategies for altering the structures of COFs to obtain materials that cannot be synthesized directly by reversible reactions.

4.   Photocatalytic Hydrogen Evolution with COFs

Photocatalytic hydrogen evolution with COFs presents a promising approach for generating solar fuels, since the inherent properties of COFs align with many requirements for the design of a successful photocatalyst. The factors determining the photocatalytic ability of a COF are the efficiency of light absorption, the efficiency of charge separation and transport, the choice of hydrogen evolution electrocatalysts or the design of active sites on the COF backbone. The crystalline nature of COFs enables, especially in 2D COFs, charge percolation either through the π-conjugated network structure and/or through layers by means of π-π interaction between the individual layers. The porosity of the COFs additionally makes a large specific surface area available, which is beneficial for catalysis and enables better permeation of solvents and sacrificial electron donor. In addition, the products of photocatalysis can get transported to and from the catalytically active sites efficiently. The modular and molecular nature of COFs make them amenable to molecular design, where the ability to fine tune the optoelectronic and structural properties of the otherwise heterogeneous framework can lead to stable systems.

4.1.   Introduction

The use of fossil fuels in locomotion as well as heat and electricity generation is unsustainable since fossil fuels represent a finite resource. Even not considering the implications of depletion out of natural gas, oil and coal reserves, the anthropogenic carbon dioxide emissions cause significant global warming and pollution that lead to unacceptable ecological and economic damage.[232] The stepwise replacement of fossil resources by renewable sources has focused on generation of electricity through biomass, geothermal, wind, hydroelectric, solar-thermal and photovoltaic means.[233, 234] However, the intermittency at which solar and wind energy are available limits their exploitation, since the storage of electrical energy to cover low supply, high demand times and transportation is expensive.[235] Transportation accounts for the majority of energy consumption from fossil fuels and this limits the utilization of renewable technologies in general.[234] Therefore, the unpredictable and discontinuous availability of renewable energy is currently prohibitive for the widespread adaptation of these technologies and for consumer acceptance of renewable products.[235] One strategy to introduce renewable energy that can be stored and transported efficiently is the replacement of fossil fuels with CO_2 neutral renewable fuels. Commercially viable strategies based on the utilization of biomass are already available, however these pose ethical challenges as the production of these fuels often competes with food crops for arable land[236] leading to an increase in the basic sustenance cost of the poor. An alternative could be synthetic fuels based on CO_2 reduction,[237] or on technologies that circumvent the actual formation of CO_2 altogether such as the electrochemical generation and storage of H_2 gas. The benefit of a hydrogen based technology is the absence of direct CO_2 emissions, as H_2 can be used for combustion or in efficient fuel cells, leading to water as the only byproduct.[238] The generation of renewable fuels from photovoltaic electrical energy would currently be possible at high efficiency albeit at high cost.[232] A strategy to circumvent this problem is the direct use of sunlight for the production of "solar fuels" by photocatalysis (also termed artificial photosynthesis),[232, 237, 239] such as the production of hydrogen by the water splitting reaction:

$$2\ H_2O \rightarrow 2\ H_2 + O_2$$
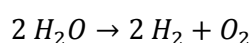
4.1.1. Photocatalysis

Photocatalysis describes the process of driving a thermodynamically uphill reaction with light. The energy supplied by light is thereby stored in the reaction products, that can be separated from the photocatalyst and used as fuel.[240] A requirement for a photocatalytic system is a suitable band gap for the material to be able to absorb light (Figure 4-1). Wavelengths shorter than the band gap are absorbedto produce electron hole pairs. The excess energy is lost as heat by a process called thermalization. Light with energy lower than the band gap is not absorbed and therefore not available for the photocatalytic reaction. The electrochemical requirements of the water splitting reaction need to be taken into account as well. The thermodynamically required energy to split water is 1.23 eV. However, charge separation, overpotentials for the respective reactions and appropriately high current densities for application limit the minimum energy required to at least 2.0 eV for single absorber materials, which in turn leads to maximum efficiencies of less than 10%.[232]
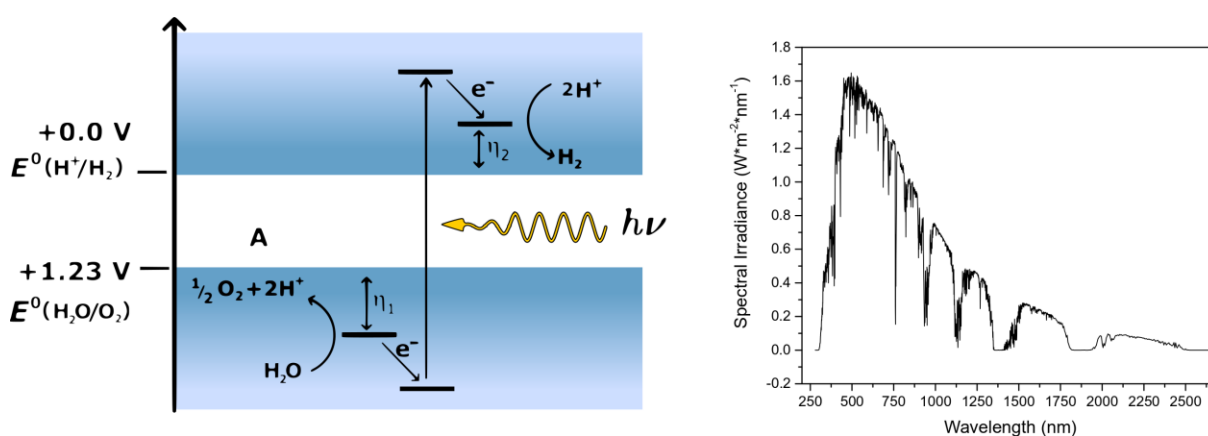
Figure 4-1: Left: Energy diagram for the photocatalytic water splitting reaction. A single photon excites an electron from the valence band to the conduction band, generating an electron hole pair at a potential that allows both the reduction and the oxidation of water to hydrogen and oxygen, respectively. The thermodynamically required potential for water splitting is negative and positive of 0.0 and 1.23 V, respectively. η_i: overpotential for the hydrogen and oxygen evolution reactions. Right: Spectral irradiance of the sun at AM1.5 G conditions.

Additionally, the band positions of the photoabsorber are required to straddle the water oxidation and reduction potentials. By being reducing enough to generate hydrogen from electrons and oxidizing enough to generate oxygen from holes, water can be split with a single photocatalyst. However, the use of a single photoabsorber can result in kinetically demanding photocatalytic systems that lead to recombination. The stringent requirements of the size of the band gap and the band position can be circumvented by employing a combination of semiconductors, where two semiconductors share the required potential. While one semiconductor has holes oxidizing enough to produce oxygen, the other generates electrons reducing enough for hydrogen evolution. Such combinations constitute so called Z-schemes (Figure 4-2). Due to the utilization of two semiconductors with smaller band gaps, a larger fraction of the solar spectrum can be used to drive the desired reaction. This allows for further increase in the efficiency (23-32%),[241-244] even though this scheme requires the absorption of twice the number of photons. In addition to these photoelectrochemical requirements, a high stability is required for commercially water splitting photocatalysts, as the materials should be operational for years to offset production costs, during which the systems need to resist degradation in the electrolyte and sunlight.[232]

4.1.2. Setup

Photocatalytic water splitting can be performed by building an electrochemical cell in which the oxidation and reduction sites are separate. This has the benefit of physically separating hydrogen and oxygen generation locations. The problem with these setups is the high initial cost of the device architecture.[232, 245] An alternative, cheaper method is the use of semiconductors in colloidal suspension (Figure 4-2). These systems often feature a co-catalyst fused to the surface of the colloidal particles, and this acts as the hydrogen or oxygen evolution electrocatalyst to reduce the overpotential for production of hydrogen and oxygen.[246-248] In this architecture, the semiconductor absorbs the light and the charges are separated, facilitated by the semiconductor/co-catalyst interface.[249, 250] The electron residing on the co-catalyst reduces protons to hydrogen, while the hole in the semiconductor or on another co-catalyst oxidizes water to oxygen. The drawback of colloidal photocatalytic systems lies with the production of hydrogen and oxygen in the same headspace that can lead to explosive mixtures.[232] The mixed hydrogen and oxygen now needs to be separated, increasing the cost and reducing the efficiency of these setups. However such set-ups can still be much cheaper than non-colloidal setups requiring rigid devices.[245] A major difficulty arising from the direct contact of oxygen, hydrogen and the catalyst is the back reaction that is catalyzed by most water splitting catalysts as well.[251, 252] At too high concentration the back reaction and the forward reaction are in equilibrium, with no net energy gains from the photocatalysis reaction. This issue however can be avoided by the removal of the reaction products.[232]

More complex setups such as Z-schemes are also possible in solution (Figure 4-2, right) and are especially useful if the band positions of a semiconductor are not sufficient to perform both oxygen and hydrogen evolution (or if the overpotential of one part of the reaction represents a significant bottleneck). As an example, a colloidal Z-scheme was realized by mixed suspensions of Pt/TiO_2 (anatase) and TiO_2 (rutile),[253] where rutile is able to oxidize water and anatase is able to perform water reduction. Both systems were electrochemically coupled by the use of the IO_3^-/I^- redox mediator. This example shows how materials can practically be used to perform only one half-reaction of photocatalytic water splitting. Such Z-schemes present one of the reasons why often only one of the half-reactions are studied in photocatalysis, in order to avoid the difficulties associated with the kinetics of the other half reaction. In such cases, the catalytically inactive charges are extracted by a sacrificial electron acceptor or electron donor,[254, 255] as they otherwise would accumulate in the material increasing recombination. Common hole scavengers are alcohols such as methanol or larger molecules such as ethylenediaminetetraacetic acid (EDTA) and triethanolamine (TEoA). Electron scavengers added to the oxygen evolution reaction are silver ions (Ag^+) or peroxodisulfate ($S_2O_8^{2-}$).
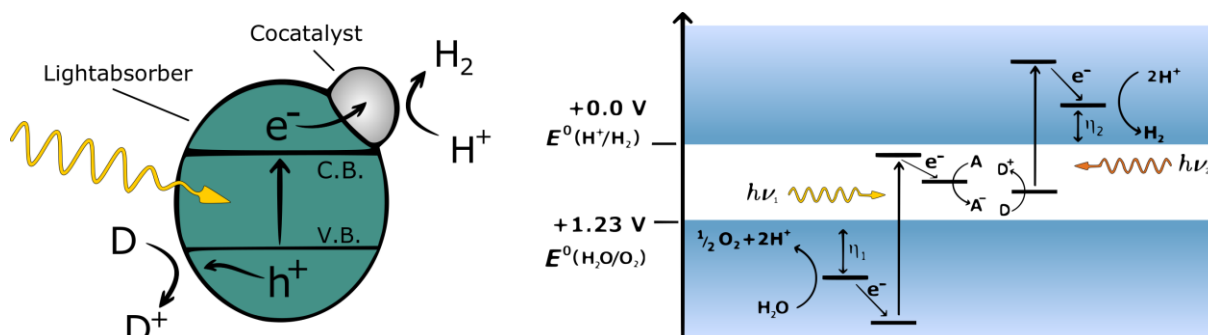
Figure 4-2: Left: Schematic of a colloidal semiconductor particle with an attached co-catalyst, that is used to generate hydrogen from protons, with holes being quenched by a sacrificial electron donor (D). Right: Redox mediator coupled Z-scheme for water splitting with two semiconductors.

4.1.3. Photocatalysis in organic extended solids

Many types of semiconductors have been used for photocatalytic hydrogen evolution,[256] with inorganic semiconductors based on transition metals especially in focus since the beginning of the field, which started with the seminal paper on photoelectrocatalytic water splitting on TiO_2.[257-259] However, some transition metal based photocatalystsare expensive, due to the use of rare elements and their properties are difficult to tune. In contrast, photocatalytic systems based on molecular light absorbers and catalysts display versatile structure and are extremely tunable in their absorption features as well as their electrocatalytic abilities.[260] However, many molecular systems typically suffer from limited stability. Conjugated polymers are robust in comparison to molecular systems while still being tunable. [261, 262] The conjugation increases the material's conductivity and thus allows charges generated from the excitation by light to travel through the material to catalytically active sites.[263, 264]

Organic polymer photocatalysts have gained significant attention in recent years. They can be produced cheaply, are purely based on abundant elements, highly robust and in some cases tailorable (Figure 4-3). One of the most prominent examples of polymeric photocatalysis is the demonstration of photocatalytic hydrogen evolution in the polymeric carbon nitride, melon, by Antonietti, Domen and coworkers,[265] as well as full water splitting with g-C_3N_4.[266] Based on the pioneering results obtained with this material, many works on heptazine and triazine based carbon nitride materials followed.[248, 262, 266-268] While carbon nitrides are in principle organic materials, they are formed in high temperature condensation reactions that do not allow the targeted introduction of diverse building blocks and therefore make tuning the properties of carbon nitrides very similar to tuning in inorganic semiconductors.

PTI   CTF-1   P7
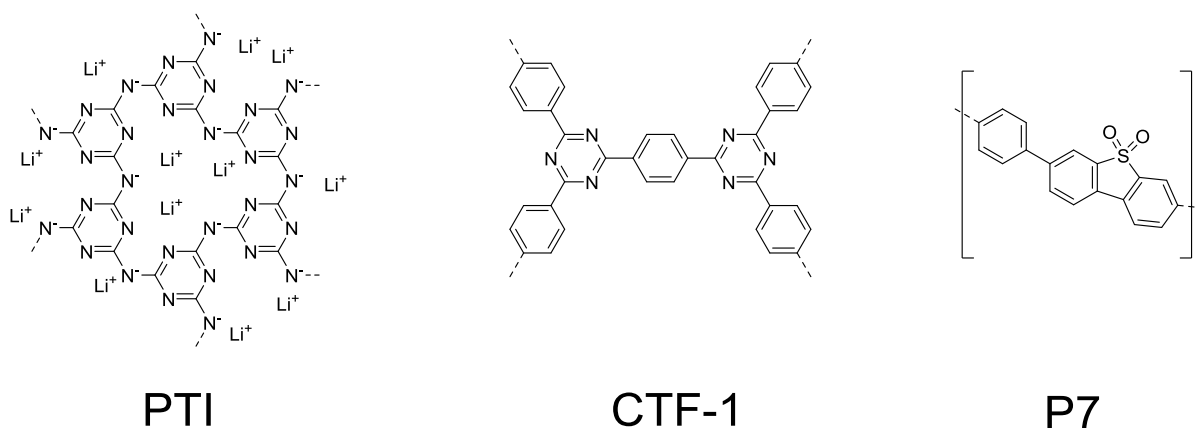
Figure 4-3: Examples of the organic based materials that have been used for photocatalytic hydrogen evolution. From left to right: polytriazine imide (PTI);[267] CTF-1[269] and an organic polymer P7.[270]

Conjugated linear and cross-linked polymers have also been successfully employed for photocatalytic hydrogen evolution, such as covalent triazine frameworks, porous and linear polymers.[270, 271] While polymers generally exhibit great degrees of tunability, they are lacking a defined inter-chain structure. Such limitations lead to difficulty in designing intra chain charge transport, which is an important means for enhancing charge mobility in conducting polymers.[272] The lack of order in these systems also hinders the design of pore voids for optimal mass transport and makes active site engineering difficult. Covalent triazine frameworks (CTFs) present a triazine rich material that can be synthesized as crystalline and porous solids. This class of materials has been used as polymers[273-276] or as oligomers[269] for photocatalytic hydrogen evolution. CTFs are very robust due to their bonding through triazines, but the synthesis is performed under harsh condition in either a $ZnCl_2$ melt[269] or

catalyzed by a superacid [276] that significantly limits the crystallinity and the functional group tolerance.

4.1.4.   Photocatalysis with COFs

COFs unite the beneficial properties of robustness, tunability, porosity and crystallinity.[92] The highest degree of control over the structure of covalently bound organic solids can be exerted in COFs, be it intramolecular[2, 92, 277] (chapter 4.2, 4.3 and 4.4) or intermolecular[83, 162, 209, 278-281] arrangement of the structure (chapter 5.2). These features make COFs ideal platforms for the targeted design of efficient photocatalysts.[282] The first proof of photocatalytic hydrogen evolution in a COF was given by Stegbauer et al.[283] who showed that a triazine based hydrazone COF could produce hydrogen photocatalytically in appreciable quantities. The material showed some degradation over the course of the photocatalysis experiment, which points towards the important point of stability of the photocatalyst, because COFs are not as inherently stable as CTF or other polymers. However, recent advances have produced COFs that are more stable towards typical photocatalytic conditions in water than the earlier generations of COFs. Air, water, acid and base stable COFs can be routinely generated now,[66, 70, 110, 284] which is key to developing commercially viable photocatalysts. Further methods to enhance the stability of COFs are discussed in this thesis (chapter 6.2).

Important developments in the field of COF photocatalysis besides the work presented in this thesis is the demonstration of the use of a COF cadmium sulfide quantum dot (CdS QD) hybrid as a photocatalytic system.[285] The COF served as a support for the CdS QDs thereby reducing electron–hole pair recombination. This work showed that the incorporation of CdS QDs into a keto-enol-imine COF improves the hydrogen evolution efficiency dramatically with respect to the pure quantum dots and with respect to the bare COF. More recently N_2-COF (chapter 4.2) was shown to be an active photocatalyst with molecular co-catalysts, instead of the commonly used heterogeneous metallic platinum for hydrogen evolution.[286] Further, an acetylene COF was shown to be photocatalytically active and the activity could be tuned by changing a diphenyl acetylene to a diphenyl diacetylene structure.[287]

4.1.5.   This work

The work shown in this chapter follows the work of Stegbauer et al.[283] on photocatalytic COFs based on triazine moieties (TFPT–COF) and was motivated by the tailorability that can be imbued into COFs by precursor design and synthesis. Two platforms of two-dimensional COFs were chosen for the design of efficient photocatalytic hydrogen evolving systems (Figure 4-4): the aryl triaryl azine system (ATA-COFs) as well as the benzene triazine imine system (BTI-COFs).
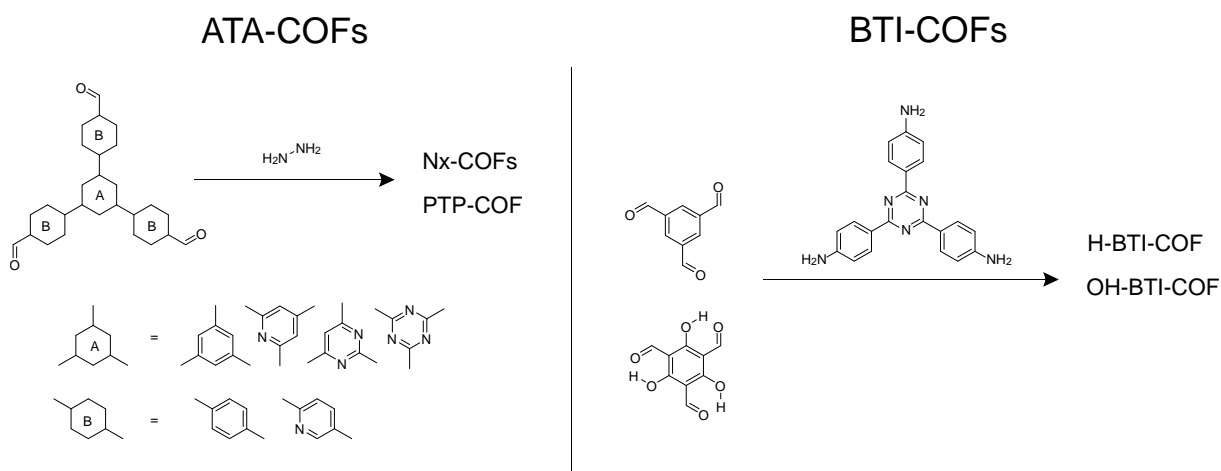
Figure 4-4: Schematic representation of the base structure of the two investigated COF systems for photocatalysis. Left: ATA-COFs; Right BTI-COFs.

The ATA-COF platform (Chapter 4.2 and 4.3) was investigated as means to create a series of COFs to study the effect of nitrogen substitution on photocatalytic hydrogen evolution, as previous studies on nitrogen rich compounds showed promising photocatalytic hydrogen evolution capabilities.[248, 267, 269, 283] The ATA-COFs also served as a platform with similar optical properties and this allowed the investigation of the influence of nitrogen substitution on the electronic and structural properties and in turn their influence on the photocatalytic hydrogen evolution process.

The BTI-COF platform in contrast was used to alter the optical properties of the COF in order to enhance light absorption and thereby improve photocatalytic hydrogen evolution activity(Chapter 4.4).

4.2.   A tunable azine-covalent organic framework platform for visible light-induced hydrogen generation

This work was published and sections of this chapter were reproduced from:

Vijay S. Vyas, Frederik Haase and Bettina V. Lotsch proposed the idea and designed the experiments. Vijay S. Vyas and Bettina V. Lotsch wrote the manuscript. Vijay S. Vyas carried out the synthesis and photocatalysis experiments. Frederik Haase helped in synthesis, photocatalysis and structure simulation of the COFs. Linus Stegbauer performed the sorption experiments. Filip Podjaski performed electrochemistry for determining the band potential of COFs. Gökcen Savasci and Christian Ochsenfeld performed the theoretical calculations.

Supplementary information for this chapter can be found in section 9.4.

Here we show that as a direct consequence of molecular engineering, a triphenylarene platform can readily be tuned for photocatalytic water reduction. Using a series of triphenylarylahldehydes with the central aryl ring containing 0-3 nitrogen atoms as building blocks, two-dimensional (2D) azine-linked COFs were synthesized which reflect the structural variations of the triphenylarene platform. Investigation of these COFs as a new generation of polymeric photocatalysts show progressively enhanced hydrogen evolution with increasing nitrogen content in the frameworks. This work demonstrates the potential of organic materials in solar energy conversion where a vast array of organic building blocks and bond-forming reactions provide an extensive toolbox for the systematic fine-tuning of their structural and physical properties[2] thus making way for the application of COFs in photocatalytic water splitting.[283]

4.2.1.   Results

Design, Synthesis and Characterization of COFs.

A progressive substitution of alternate carbons in the central aryl ring of the triphenylaryl platform (Fig 1a, green dots) by nitrogen atoms leads to a change in the electronic and steric properties of the central ring, i.e. $N = 0$ (phenyl), $N = 1$ (pyridyl), $N = 2$ (pyrimidyl) and $N = 3$ (triazine). As a consequence of the substitution of the C-H moiety with nitrogen atoms, a change in dihedral angle between the central aryl ring and the peripheral phenyl rings is expected, which in turn leads to varied degrees of planarity in the platform. This was corroborated by density functional theory (DFT) calculations at the PBE0-D3/Def2-SVP level as evident by the decreasing dihedral angles in the energy minimized structures of precursor aldehydes N_x-CHO (Table 1). Additionally, this results in a progressive decrease in electron density in the central aryl ring of the COF platform (Figure 4-5a) as the number of nitrogen atoms increase from 0 to 3.
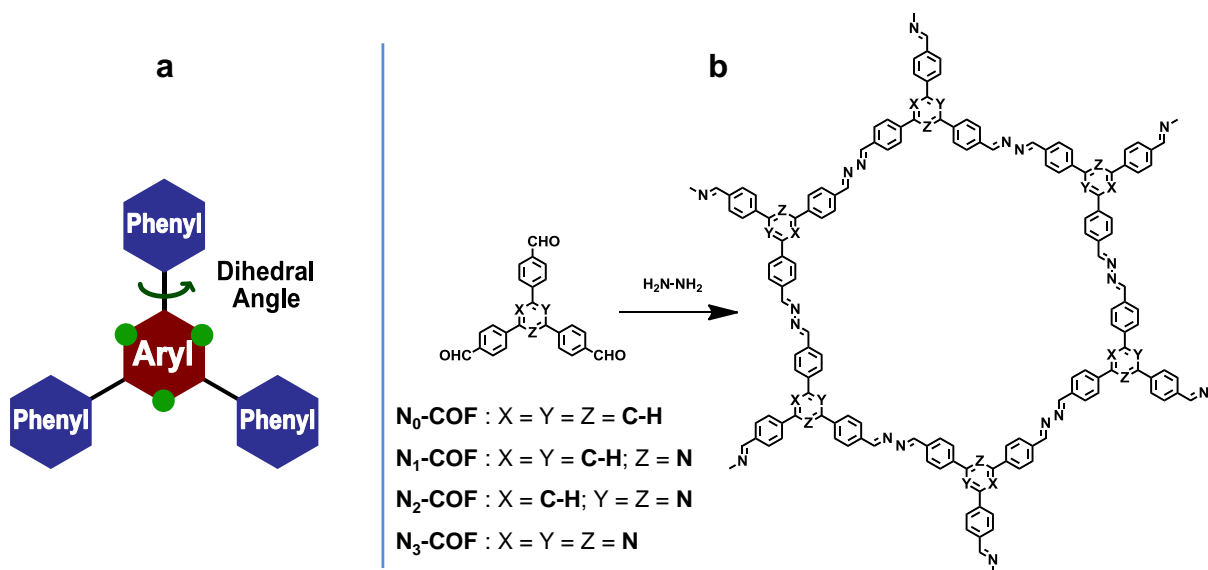
Figure 4-5: Design and synthesis of the N_x-COFs. (a) A tunable triphenylarene platform for photocatalytic hydrogen evolution. Replacement of 'C-H' by 'nitrogen atoms' at the green dots lead to variation of angle between central aryl and peripheral phenyl rings leads to varied planarity in the platform. (b) Synthesis of Nx-COFs from Nx-CHO and hydrazine.

Encouraged by the theoretical calculations, we decided to synthesize **N_x-COFs** (x = 0, 1, 2, 3) by azine formation reaction[66, 288] of the aldehydes with hydrazine and investigate the translation of chemical and structural variation in the precursors to the overall order and optoelectronic properties of the resulting COFs, with the consequent influence on photocatalytic hydrogen production.

Table 1: DFT geometry optimizations of precursor aldehydes at the PBE0-D3/Def2-SVP level. Dihedral angles between central aryl and peripheral phenyl rings show increased planarity in the precursor aldehydes along the series N_0 to N_3-CHO. Blue dots denote nitrogen atoms.

Aldehyde	N_0-CHO	N_1-CHO	N_2-CHO	N_3-CHO
A (°)	38.7	38.9	16.7	0.0
B (°)	38.7	20.0	0.5	0.0
C (°)	38.7	20.9	17.9	0.0

The precursor aldehydes (**N_x-CHO**) were synthesized as described in the Supplementary Methods. **N_x-CHO** as well as their precursors were characterized using ^{1}H and ^{13}C spectroscopy (Figure S 2, S 3, S 4, S 5, S 6, S 7, S 8, S 9, S 10, S 11, S 12, S 13, S 14, S 15). **N_x-COFs** were synthesized in quantitative yields by a condensation reaction between the corresponding trialdehydes with hydrazine in the presence of 6 M acetic acid using 1:1 mesitylene/dioxane as solvent at 120 ˚C for 72 hours (Figure 4-5b and Figure S 1). FT-IR spectra of the Nx-COFs were compared with the corresponding aldehydes and hydrazine (Figure S 16, S 17, S 18, S 19) and show the disappearance of aldehydic C−H and C=O stretches and the appearance of the azine C=N stretch at 1622 cm^{-1}. These observations

were further corroborated by the complementary Raman spectra (Figure S 20) which showed characteristic Raman signals at 1000–1010 cm^{-1} for the ν(N–N) stretch, 1540–1560 cm^{-1} for ν_{sym}(C=N) stretch and at 1600–1625 cm^{-1} for ν_{asym} (C=N) stretch.[289] The composition and local structures of the **N_x-COFs** were further confirmed by XPS (Figure S 80) and ^{13}C cross-polarization magic angle-spinning (CP-MAS) solid-state NMR (ssNMR) spectroscopy. As seen in Figure 4-5 and Figure S 50, S 53, S 56, S 59, the characteristic aldehyde carbonyl ^{13}C resonance located at $\approx$ 190 ppm in the precursor aldehydes disappears with the concomitant appearance of the azine C=N peak at $\approx$ 160 ppm, thereby attesting the conversion of the precursors into the respective COFs. The molecular structure of the building blocks remains intact during COF formation as evident by the largely unchanged chemical shifts of the peripheral phenyl rings as well as the central aryl ring that shows characteristic peaks in the NMR. Thus, for example, the C3 symmetric carbon in the central triazine ring in the N3-CHO at 171 ppm shows minimal shift and appears at ~168 ppm in **N_3-COF**. Similarly, the characteristic ^{13}C NMR peak of the central pyridine/pyrimidine ring in N1-CHO and N2-CHO at 119 ppm and 112 ppm, respectively, can easily be spotted in the corresponding COFs due to their upfield nature (Figure 4-6). The assignment of these peaks was done using 2D HMQC NMR of N_1 and N_2 aldehydes (Figure S 8, S 11).
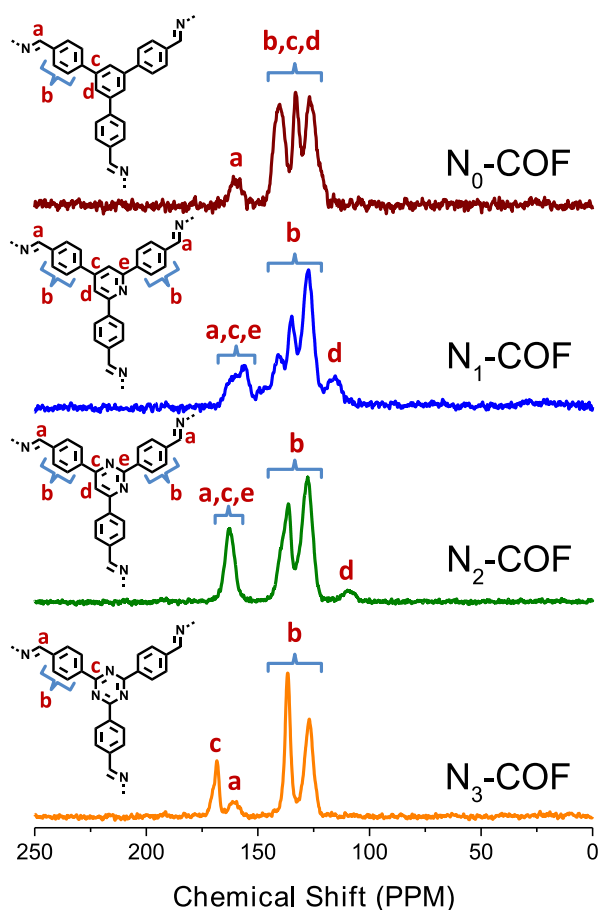
Figure 4-6: ^{13}C cross-polarization magic angle-spinning solid-state NMR of the Nx-COFs. The azine C=N peak (marked a) appears at $\approx$ 160 ppm while the phenyl peaks (marked b) and characteristic central aryl peaks (marked c,d,e) show nominal changes with respect to their precursor aldehydes.

X-ray powder Diffraction, Gas Sorption and Electron Microscopy.

In order to gain insight into the structural details and morphology of the COFs, X-ray powder diffraction (XRPD), gas sorption, scanning electron microscopy (SEM) and transmission electron

microscopy (TEM) analyses were performed. XRPD of N_x-COFs indicated the formation of crystalline networks with 2D honeycomb-type lattices as evident by the presence of an intense 100 reflection at $2\theta = 3.52°$ and reflections at 6.0, 7.1, and 9.5° corresponding to the 110, 200, and 120 reflections, respectively (Figure 4-7). The observed reflections match well with the calculated patterns (Figure S 42, S 43, S 44, S 45) obtained from structural simulations performed for an AA eclipsed layer stacking (Figure S 34, S 35, S 36, S 37, S 38, S 39, S 40, S 41) using the Materials Studio v6.0.0 program (Accelrys). It should be noted that a slight lateral offset of the layers is expected for the stacked structures,[290] which however cannot be distinguished from the eclipsed topology by XRPD due to substantial peak broadening. Thus, for practical reasons, the eclipsed structure is used as simplified working model.[291] Interestingly, as we traverse the series from N_0 to N_3-COF, the XRPD peaks become sharper with the appearance of prominent stacking peaks for N_2 and N_3-COF at $2\theta = 26°$ arising from the d-spacing between the (001) lattice planes. Thus, the variation in planarity in the precursor aldehydes as a function of the dihedral angles translates well into the crystallinity of the resulting COFs. The unit cell parameters were obtained by Pawley refinements for all COFs and the results are included in Table S 9.4-1.
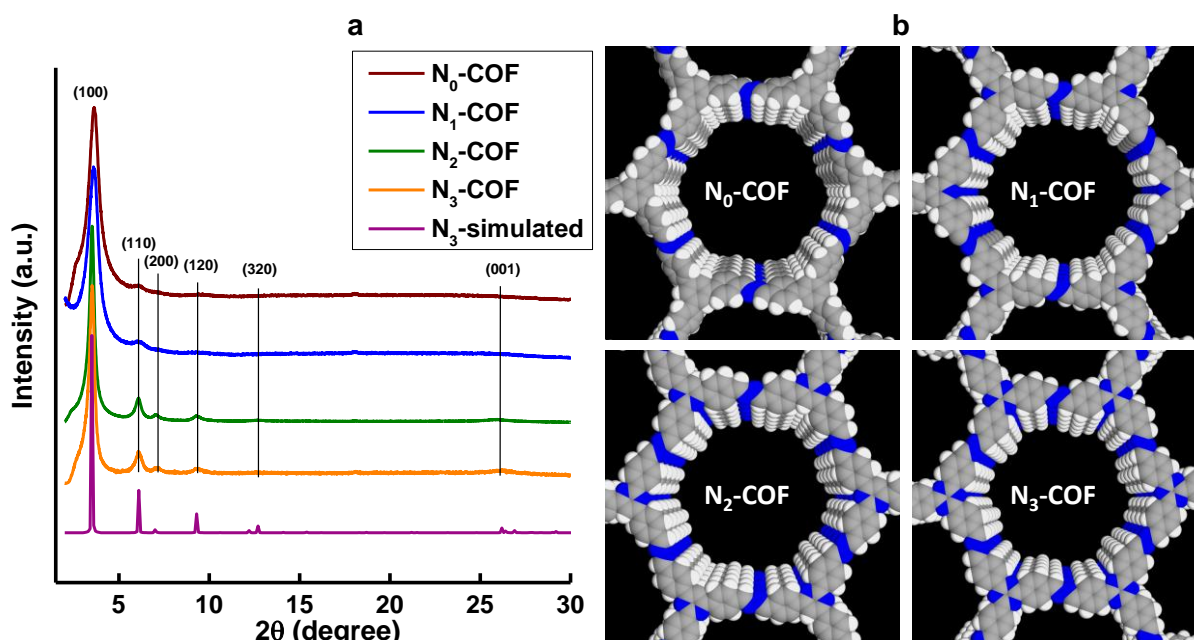
Figure 4-7: Structure and stacking analysis of the N_x-COFs. (a) XRPD patterns of the N_x-COFs compared with the simulated pattern calculated for the representative N_3-COF. (b) View of extended stacks of N_x-COFs in space filling model along the stacking direction (nitrogen – blue, carbon – gray, hydrogen - white). Note that an eclipsed stacking arrangement was assumed for simplicity.

The permanent porosities evaluated by measuring the argon adsorption isotherm at 87 K (Figure S 46) reveal that the Brunauer−Emmett−Teller (BET) surface area of symmetrical and unsymmetrical N_x-COFs show a deviation from the trend expected from the increasing level of planarity from N_0 to N_3-CHO. Thus, while XRPD shows a similar yet lower degree of crystallinity for N_0 and N_1-COF in comparison to that observed for N_2 and N_3-COF, a further demarcation is seen in the BET area of the symmetrical and unsymmetrical COFs. Interestingly, the BET surface area of the symmetrical N_0-COF was found to be 702 m^2 g^{-1}, which is significantly higher than that of the unsymmetrical N_1-COF with a BET area of 326 m^2 g^{-1}. Likewise, in case of comparatively planar N_2 and N_3-COF, the symmetrical N_3-COF showed a higher BET area of 1537 m^2 g^{-1} as compared to the unsymmetrical N_2-COF with a BET area of 1046 m^2 g^{-1}. Thus, the lowering of symmetry leads to a lower degree of order

and hence lower BET surface area. Accordingly, a narrow pore size distribution for the most crystalline N_3-COF was calculated by the non-local density functional theory (NLDFT) method with a peak maximum at ≈ 24 Å, which is in excellent agreement with the pore size established from the structural analysis and simulations. The maximum at 24 Å is accompanied by a minor peak in the PSD at ≈ 16 Å, which becomes more prominent in the other N_x-COFs (x = 0 - 2; Figure S 47), likely resulting from an increasing degree of lateral layer offsets and stacking disorder in the less crystalline materials.

SEM images show a change in morphology from purely ball-like agglomerates in N_0-COF to elongated ones in N_1-COF followed by transformation to rod-like morphology in N_2 and N_3-COF (Figure 4-8a-d and Figure S 21). The structure and morphology of N_x-COFs was further investigated by TEM analysis where hexagonal pores are clearly visible in N_2 and N_3-COF (Figure 4-8 e,f and Figure S 24, S 25). Selected area electron diffraction (SAED) along the [001] zone axis of the multilayers of N_3-COF is consistent with a nanocrystalline, hexagonally ordered in-plane structure composed of crystalline domains with sizes around 50-100 nm. TEM analysis of N_0 and N_1-COF, however, did not show any crystalline domains possibly due to instability in the electron beam (Figure S 22, S 23).

The thermal stability of the COFs was investigated by thermogravimetric analysis (TGA), suggesting that the COFs are stable up to ≈ 350 °C in argon. TGA analysis in air shows total decomposition of all the COFs at temperatures above 550°C, thus indicating the absence of any metal residues (Figure S 26, S 27, S 28, S 29, S 30, S 31, S 32, S 33).
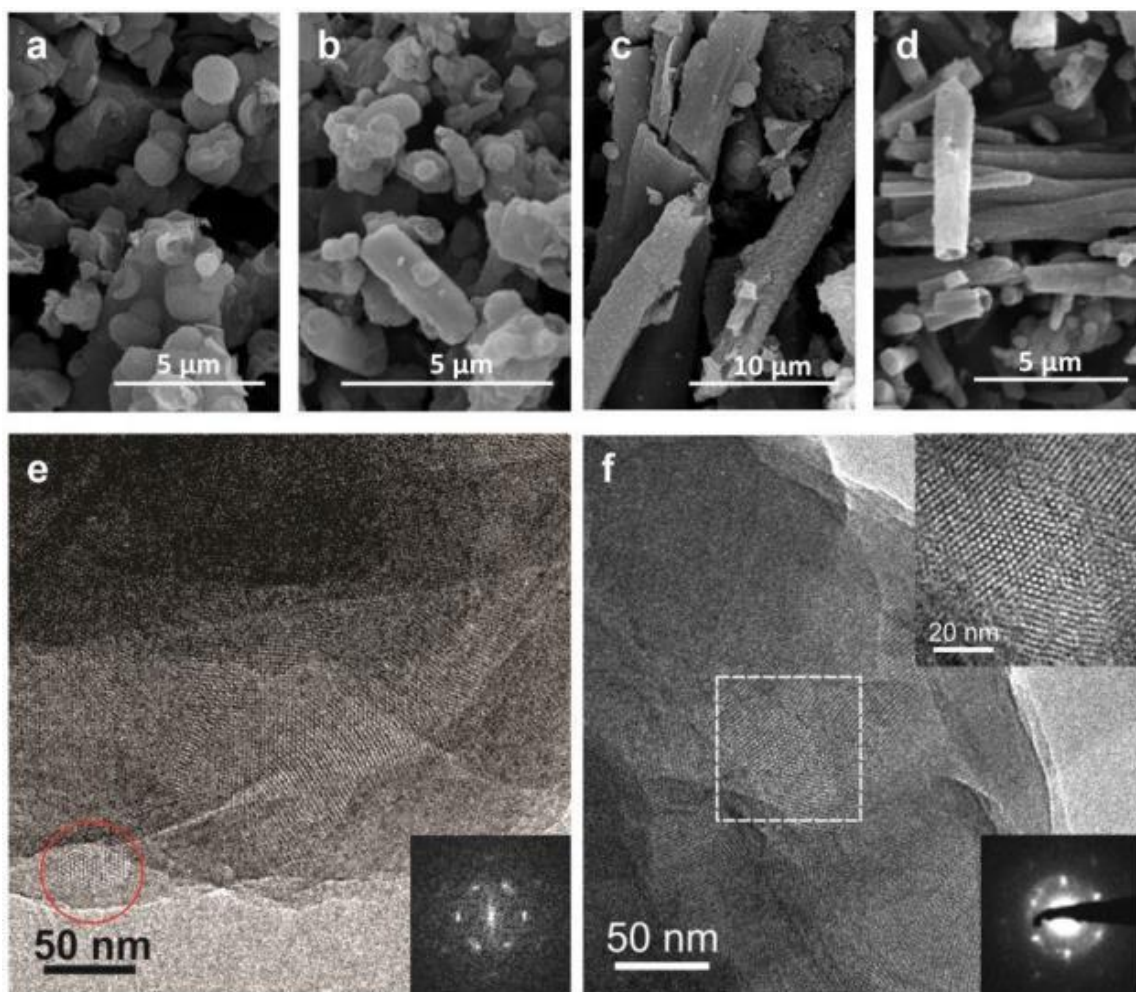
Figure 4-8: SEM and TEM images of N_x-COFs. (a) SEM images of N_0-COF, (b) N_1-COF, (c) N_2-COF, (d) N_3-COF indicating morphological variation along the series. (d) TEM image of N_2-COF showing hexagonal pores, with Fast Fourier Transform (FFT) of the marked area (red circle) in the inset. (e) TEM image of N_3-COF with enlarged Fourier filtered image (top right inset) of the marked area and representative SAED pattern (inset bottom right).

Optical properties and photocatalysis.

The diffuse reflectance absorption spectrum reveals that all the COFs absorb light in the ultraviolet and blue parts of the visible region and show similar absorption profiles with an absorption edge at ~465-475 nm (Figure 4-9a), thereby suggesting an optical band gap of $\approx 2.6 - 2.7$ eV as determined by the Kubelka-Munk function. These values are red shifted by $40 - 60$ nm in comparison to the solid-state absorption spectra of the precursor aldehydes and can be attributed to the introduction of the azine group and a higher degree of conjugation resulting from delocalization along as well as across the plane in the extended frameworks.[292] As seen in Figure 4-9a, unsymmetrical N_1 and N_2-**CHO** show a slightly red shifted absorption in comparison to the symmetrical N_0 and N_3-**CHO**. DFT calculations performed on the precursor aldehydes also indicate a similar trend in the optical band gaps of symmetrical and unsymmetrical aldehydes (Supplementary Table. 4). In order to understand the differences in absorption spectra of symmetrical and unsymmetrical aldehydes in the solid state, the absorption spectra of the precursors were additionally recorded in dilute (8 µM) dichloromethane solutions. The absorption profiles (Figure 4-9b) are marked by a clear difference between the symmetrical N3-CHO with one absorption band and the unsymmetrical N_1 and N2-CHO with twin absorption bands arising from the non-planar and hence non-fully conjugated phenyl-aryl ring

systems. The two bands in the absorption spectrum of N0-CHO are rationalized by absorptions from the two types of ring systems that are essentially decoupled due to strong out-of-plane torsion of the peripheral phenyl rings. The increase in planarity leading to a higher degree of conjugation (hence red-shift) along the series N_0 to N_3 is partly compensated by the increase in electron deficient character of the central aryl ring (hence blue-shift), thereby resulting in minimal changes in the optical band gap upon network formation. The similar optical gap makes the N_x-COF ensemble an ideal model platform for photocatalysis experiments, as their relative activities will not be governed by differences in their light harvesting capability.
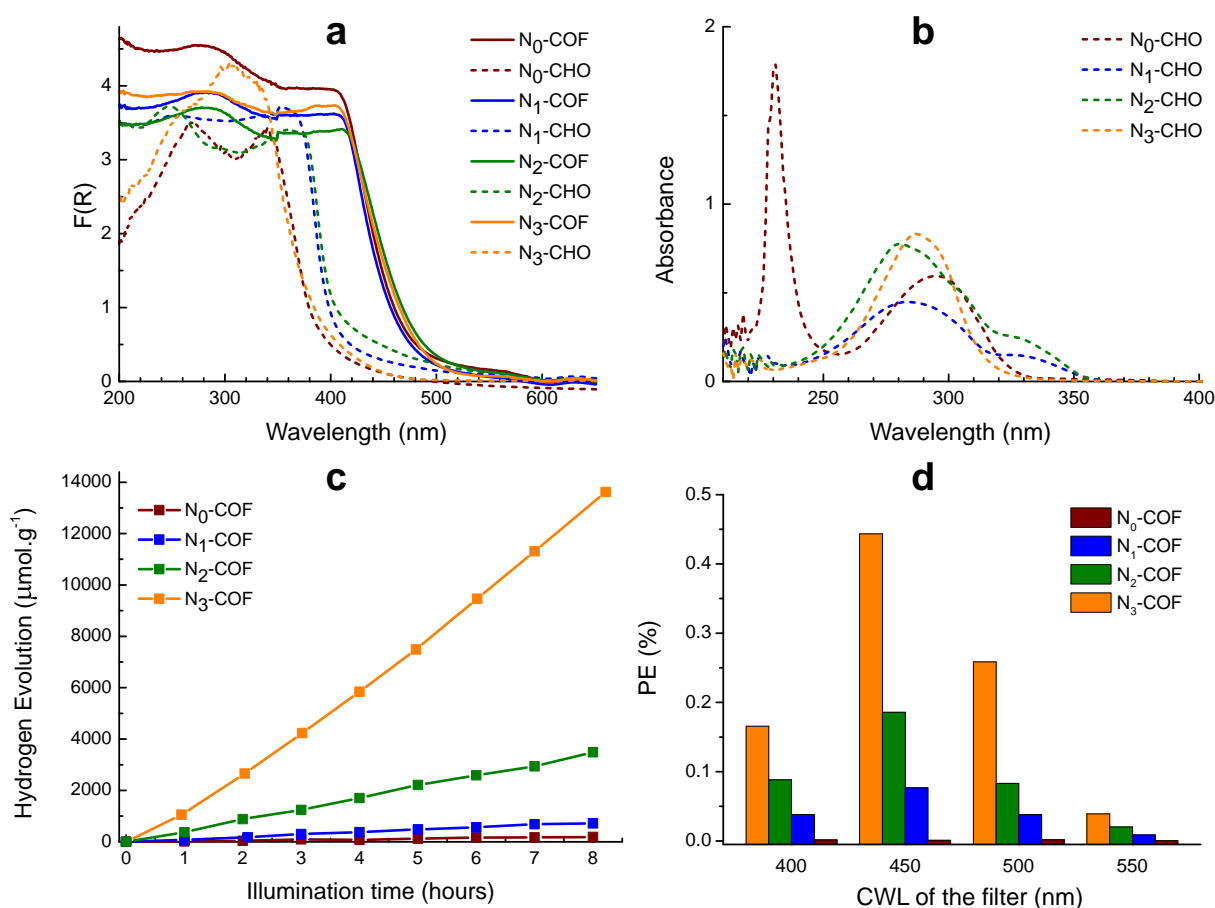
Figure 4-9: Optical and photocatalytic properties of N_x-COFs. (a) Diffuse reflectance absorption spectra of N_x-CHO and N_x-COFs recorded in solid state. (b) Absorption spectra of precursor aldehydes N_x-CHO in dichloromethane at 22 °C. (c) Hydrogen production monitored over 8 h using N_x-COFs as photocatalyst in the presence of triethanolamine as sacrificial electron donor. (d) Photonic efficiency measured with four different band pass filters with central wavelengths (CWL) at 400, 450, 500 and 550 nm.

The N_x-COFs were next evaluated as photocatalysts for visible light-induced hydrogen evolution. The hydrogen evolution experiments were performed by taking a suspension of the COFs in phosphate buffered saline (PBS) at pH 7 and irradiating with visible light ($\geq$ 420 nm) at 25 °C. Hexachloroplatinic acid was added for the *in situ* formation of the Pt co-catalyst[293] to reduce the overpotential for hydrogen evolution, and triethanolamine (TEoA) was used as sacrificial electron donor.[294, 295]

Notably, all COFs evolve hydrogen in the test period of 8 hours (Figure 4-9c). Interestingly though, the N_x-COFs show about four fold increase in hydrogen evolution with each substitution of C-H by N in the central aryl ring of the COF platform. Thus, at the end of 8 hours the average amount of hydrogen produced by N_0, N_1, N_2 and N_3-COF was 23, 90, 438 and 1703 µmol h^{-1} g^{-1}, respectively.

The amount of hydrogen evolved from the most active **N₃-COF** is competitive with carbon nitride photocatalysts and outperforms benchmark systems such as Pt-modified amorphous melon (720 µmol h^{-1} g^{-1}),[267] "g-C$_3$N$_4$" (840 µmol h^{-1} g^{-1}),[296] or crystalline poly(triazine imide) (864 µmol h^{-1} g^{-1}).[267] Photocatalysis lasting up to 48 hours using **N₃-COF** showed that the amount of hydrogen evolved was about four times higher than the amount of hydrogen present in the COF (Figure S 62), thus ascertaining that the primary hydrogen source is water rather than decomposition products of the COF. After photocatalysis, the COFs were isolated and checked for stability. The FT-IR (Figure S 48, S 51, S 54, S 57) and ssNMR (Figure S 50, S 53, S 56, S 59) spectra of the **N$_x$-COFs** obtained after photocatalysis did not show any significant structural change in the material, thus indicating the retention of molecular connectivity of the framework during photocatalysis. The framework crystallinity was preserved to a large extent in the post-photocatalysis recovered COFs, although a partial loss of the long-range order was observed by XRPD (Figure S 49, S 52, S 55, S 58). Such a decrease in long range order has been attributed to the delamination of framework layers.[283, 297] In addition, the TEM images obtained from the post-photocatalysis sample (Figure S 61) clearly demonstrate the retention of hexagonally ordered crystalline domains in addition to the uniform distribution of platinum nanoparticles that are formed *in -situ* during photocatalysis as observed in the SEM images (Figure S 60). Photocatalysis experiments performed in the absence of hexachloroplatinic acid did not show measurable amounts of hydrogen, thus underlining the role of platinum as electrocatalyst and microelectrode to mediate the electron transfer process.[293] Long-term studies performed with ascorbic acid as sacrificial electron donor revealed that the **N₃-COF** is stable in light for over 120 hours, showing sustained hydrogen evolution (Figure S 63). In order to quantify the spectral distribution of the photocatalytic activity of the four COFs, the photonic efficiency (PE) was calculated using four different band pass filters with central wavelengths (CWL) at 400, 450, 500 and 550 nm (Figure 4-9d, Table S 9.4-2, Figure S 64, S 65). These measurements clearly indicate that **N₃-COF** shows the best PE over the entire spectral range, with the maximum of 0.44% with a 450 nm band pass filter.

Theoretical calculations

In order to rationalize the observed trend and to provide insights into the change in band gaps and band positions along the **N$_x$**-series, Kohn-Sham band gaps were calculated at the PBE0-D3/def2-SVP level for the precursor aldehydes (**N$_x$-CHO**;Figure S 66, Figure S 67 and Table S 9.4-4), model phenylazines (**N$_x$-PhAz**; Figure S 68, Figure S 69 and Table S 9.4-5) and two sets of hexagons with different terminations (aldehydes **N$_x$-HxAl** and hydrazones **N$_x$-HxHz**; Figure S 70, Figure S 71, Figure S 72, Figure S 73 and Table S 9.4-6, 16), serving as representative semi-extended model systems (Figure 4-10). The hexagons (**N$_x$-HxAl** and **N$_x$-HxHz**) were stacked up to three layers for probing the role of stacking on the band gaps and positions (Figure S 75, Figure S 76 and Table S 9.4-9, Table S 9.4-8).
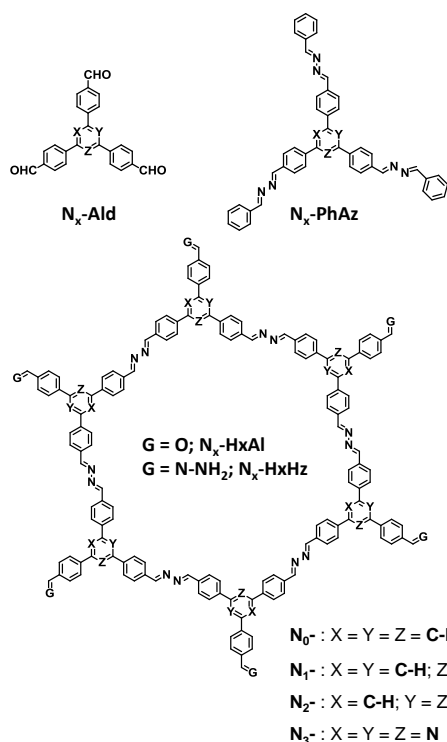
Figure 4-10: General structure of the model systems used for theoretical calculations.

Kohn-Sham band gaps calculated for the oligomers (Figure 4-11 a, b) do not show significant variation on going from the N_0- to the N_3-model systems, which is in line with the experimentally observed optical spectra of the COFs that show minor differences in their absorption edge (see Figure 4-9a). Also, as observed by Zwijnenburg and co-workers,[292] the stacked hexagons of N_3-COF both with hydrazone (N_3-HxHz) and aldehyde terminations (N_3-HxAl) show a decrease in the band gap with increasing numbers of layers (Figure 4-11 c).

The observed steady decrease in LUMO energy in these calculations for the N_x-COFs with increasing nitrogen content suggests a decreased thermodynamic driving force for electrons to move to the platinum co-catalyst. This trend, however, does not account for the differences in the observed hydrogen evolution activities. Instead, the lowering of the HOMO along the N_x-series may lead to an increase in the oxidizing power of the hole.[298] This increase in thermodynamic driving force may therefore facilitate hole removal from the COF by the sacrificial electron donor most efficiently in N_3-COF.[299]

Additionally, molecular orbitals for the model systems were extracted and compared for the extended COF systems. While HOMO-LUMO distributions are often invoked in the literature to rationalize exciton delocalization, charge separation and the location of potential charge transfer sites,[300-302] it has to be stressed that orbitals are not observables and hence, such model considerations need to be taken with care. Also, since DFTB+ orbitals did not always agree with orbitals from DFT calculations in the case of our 7-hexagon model systems, orbital data from DFTB+ calculations may be of limited use here. Nevertheless, unit cells of the N_x-COFs were optimized on the DFTB+/mio-1-0 level of theory using periodic single point calculations and molecular orbitals were subsequently calculated on the same level of theory. Across the different N_x-COFs, the HOMO is localized solely on the azine linker unit (Figure S 77), while the LUMO is delocalized across the conjugated pi-system of the framework (Figure S 78). When associating the HOMO with the charge transfer sites for holes, we

may infer that efficient hole quenching is possible through hydrogen bonding interactions with the sacrificial donor TEoA via the azine moiety for all COFs.

For smaller clusters calculated on a higher level of theory (PBE0-D3/def2-SVP), we find that the HOMOs of hydrazone terminated model hexagons are exclusively located at these terminations, while the LUMO is distributed along the hexagon with the maximum delocalization found for the planar **N_3-HxHz** model (Figure S 72, Figure S 73). In order to check the reliability of these model systems, even larger molecular clusters with 1248 atoms were modeled for the **N_3-**system to reduce the influence of terminating groups on the electronic structure of the innermost aryl core. However, the terminal hydrazone moieties still strongly localize the HOMO, whereas the LUMO in the 7-hexagon system is still centered on the innermost hexagon, despite the vicinal hexagons (Figure S 74). This suggests an efficient HOMO-LUMO separation for oligomers with electron-rich terminal groups, which could assist the charge separation process upon excitation. Note, however, that the HOMO and LUMO do not necessarily correspond to the orbitals participating in the brightest transitions and further calculations are necessary to pinpoint the orbital contributions to the optical absorptions involved in the photocatalytic process.
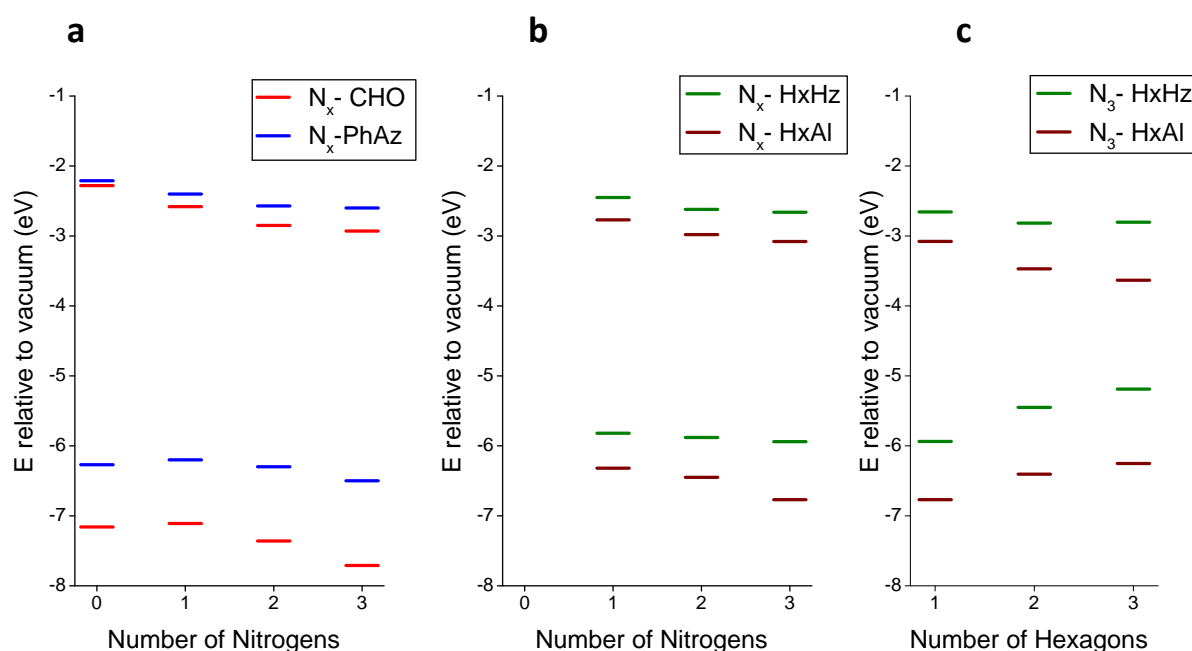
Figure 4-11: Kohn-Sham HOMO and LUMO energies of different model systems with N_x central core. (a) N_x-CHO and N_x-PhAz; (b) hexagons with hydrazone (N_x-HxHz) and aldehyde terminations (N_x-HxAl); (c) stacked hexagon layers of N_3-COF with hydrazone (N_3-HxHz) and aldehyde terminations (N_3-HxAl).

Since orbital considerations as non-observables are always difficult as discussed above, an alternative approach was pursued in considering the possible reaction intermediates. The stability of reactive intermediates formed during the photocatalytic process appears as a more reliable descriptor to rationalize the observed trend in the photocatalytic activity across the series of COFs. Hence, the energies and relative stabilities of radical anions of hydrazone-terminated N_x-hexagons were calculated as outlined in Figure 4-12.
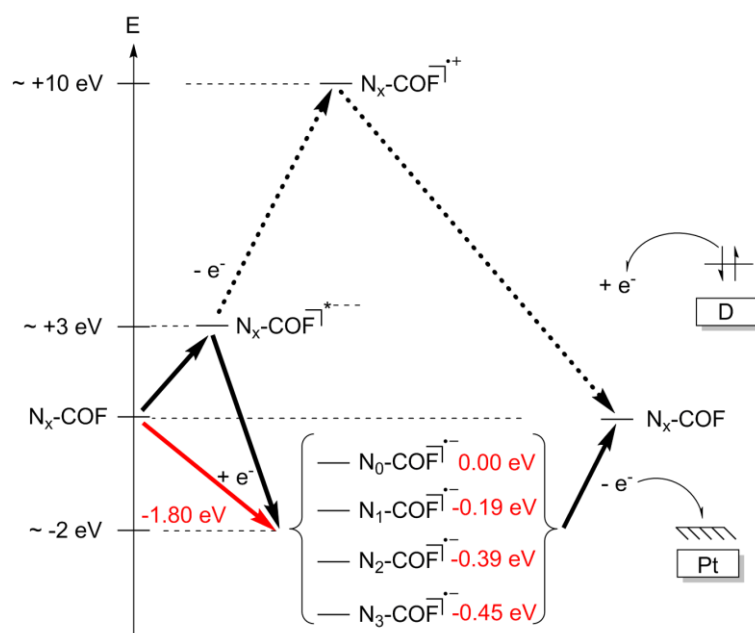
Figure 4-12: Schematic representation of two possible pathways after photoexcitation of N_x-COFs. Quenching the hole on the COF by the sacrificial electron donor leads to a radical anionic state for the COF (radical anion pathway – red arrow). The opposite order leads to the radical cationic pathway (dotted black arrows). Energies in red depict calculated vertical electron affinities as differences in total energies between radical anionic and neutral states of N_x-HxHz model systems at PBE0-D3/def2-SVP level.

Electron affinities of the N_x systems in the order of -2 eV were computed (see Table S 9.4-10), whereas the ionization potential for N_3-HxHz is estimated in the regime of roughly +10 eV in vacuum, thus rendering the formation of a radical cation during the photocatalytic process less likely. Considering the formation of a radical anion as the rate determining step, which is most favored for the N_3 system and least facile for the N_0 system, the observed energetics of the radical anion upholds the observed trend. On one hand, this finding emphasizes the role of the sacrificial electron donor that needs to swiftly remove the hole from the COF leading to the formation of a radical anion. On the other hand, it underlines the importance of the electron-poor character of the triazine building block, which is efficient at stabilizing the negative charge generated on the COF and at transferring it to the nearest platinum site. This trend is fully in line with the observed hydrogen evolution activity and we therefore reason that the formation of the radical anion is crucial for the photocatalytic process, as exemplified by N_x-COFs.

4.2.2. Discussion

While the above calculations are fully in line with the observed exponential increase in hydrogen production across the N_x series, the latter cannot be pinpointed to a single property change of the COFs but rather has to be ascribed to a complex interplay of several factors. For example, an increase in surface area may play a key role in the photocatalytic activity by providing a greater number of exposed active sites. However, in the present case, only a weak correlation with the surface area of the N_x-COFs could be established, thus suggesting that surface area is not the central factor determining the photocatalytic activity (see Table S 9.4-3).

Further, as observed earlier,[292] stacking likely plays a key role in the observed red-shift of absorption spectra of the COFs as compared to the spectra of the aldehyde building blocks. In addition, as a consequence of the decreased dihedral angle along the series and hence improved crystallinity,

enhanced structural definition and layer registry, most facile exciton migration within the COF plane and also along the well stacked aryl rings is expected for **N₃-COF**, which is in line with the observed trend in photocatalytic activity.[303, 304] While the exciton dynamics in such materials is expected to be complicated and dependent on both structural and electronic factors, it is interesting that a logarithmic plot of dihedral angles obtained from the geometry optimized precursor aldehydes against hydrogen production of the respective COFs shows a linear relationship (Figure S 79). Regarding electronic factors, the computed increase in stabilization of the radical anions in the most nitrogen-rich COFs nicely correlates with the observed trend. The stabilization of the anion radical likely enhances the charge separation, thereby increasing the probability of successful electron migration to a nearby Pt co-catalyst. The relevance of the anion radical for hydrogen evolution likewise shifts the focus to the sacrificial electron donor, whose interaction with the COF likely determines how quickly the hole can be quenched. Therefore, our results suggest that tuning the interfacial interactions between the COF and the electron donor may be a promising route to optimize the hydrogen evolution efficiencies further in such systems.

In summary, we have synthesized a new COF platform that can be tuned for visible light induced hydrogen evolution from water. Systematic variation in the properties of our four structurally related COFs clearly indicates that tuning the electronic and structural properties of the precursors has a significant impact on the photocatalytic activity of the resulting COFs. We have thus shown that engineering the building blocks and, hence, the electronic properties of photofunctional COFs opens new avenues to tunable, tailor-made supramolecular photocatalysts. Hydrogen evolution resulting from a crystalline COF that retains its structure during photocatalysis is an important stepping stone on the way to full water splitting by organic frameworks with embedded photophysical functions, and at the same time holds much room for further improvement through rational band gap and catalytic site engineering by tailoring the molecular building blocks.

4.2.3.   Experimental

Synthesis of Nₓ-COFs

All COFs were prepared by a procedure identical to the one described here for the synthesis of **N₃-COF.** In a Biotage® 5 mL high precision glass vial, was suspended **N₃-CHO** (50 mg, 0.13 mmol) in a mixture 1.0 mL of mesitylene, 1.0 mL of 1,4-dioxane and 100 μL aqueous 6M acetic acid. To the suspension was then added hydrazine hydrate (10 μL, 50-60% solution, Sigma Aldrich). The vial was then sealed and heated in an oil bath at 120 °C for 3 days at autogenous pressure. Thereafter, the vial was opened and the suspension was filtered and washed with chloroform (2 x 5 mL), acetone (2 x 5 mL) and THF (2 x 5 mL). The solid was dried in an oven at 60 °C to afford **N₃-COF** as light yellow powder. Anal. Calcd. for $(C_{24}N_6H_{15})_n$: C, 74.40; N, 21.69; H, 3.90. Found: C, 72.36; N, 21.32; H, 4.07. ^{13}C CP-MAS NMR (100 MHz) δ ppm 168.39, 159.55, 136.61, 126.96.

Photocatalysis

All photocatalysis experiments were performed in a double-walled glass reactor, where the outer compartment is circulated with water kept at a constant temperature (25 °C) through a thermostat. The reactor was top-irradiated through a quartz window with a xenon lamp (Newport, 300 W) equipped with a water filter and a dichroic mirror (900 nm > λ > 420 nm). For each experiment, the photocatalyst (COF) (5 mg) was suspended in a phosphate buffer solution (PBS, 10 mL of 0.1 M solution at pH 7) containing TEoA (100μl; 0.738 mmol). For long term experiments, ascorbic acid was used instead of TEoA. Hexachloroplatinic acid (5 μL, 8 wt% aqueous solution, Aldrich) was

added for the *in situ* formation of platinum as the co-catalyst. The actual loading with Pt as determined by the ICP analysis of COFs after photocatalysis was 2.14wt%, 1.70wt%, 0.94wt% and 0.68wt% for **N₀, N₁, N₂** and **N₃-COF**, respectively. The headspace was subjected to several cycles of evacuation and argon backfill prior to the experiment. In the course of the experiment, the headspace of the reactor was periodically sampled and the components were quantified by gas chromatography (Thermo Scientific TRACE GC Ultra) equipped with a TCD detector using argon as the carrier gas. For long term photocatalysis experiments, the head space of the reactor was evacuated and purged with argon every 24 hours to avoid hydrogen buildup and the photocatalysis was resumed. After the photocatalysis experiment, the COFs were recovered by filtration, washed with water, and then dried at 100 °C. The photonic efficiency of the photocatalysts were determined under irradiation using band-pass filters with central wavelengths (400, 450, 500, 550 nm; Thorlabs). For this purpose, 10 mg of COF was suspended in buffer (PBS, 10 mL of 0.1 M solution at pH 7) containing TEoA (1000µl; 7.38 mmol) and Hexachloroplatinic acid (10 µL, 8 wt% aqueous solution, Aldrich). The power of the incident light was obtained from a thermo power sensor (Thorlabs). The photonic efficiency was then calculated using the equation $PE = 2 \cdot [H_2]/I$ where $[H_2]$ is the average hydrogen evolution rate and I is the incident photon flux.

Calculations

Structures for all investigated building blocks were optimized on the PBE0-D3/Def2-SVP level of theory. Kohn-Sham band gaps were obtained from single point calculations on the same level of theory. Excitation energies for optimized building blocks were calculated on the TD-PBE0-D3/Def2-SVP level of theory. Excitations with the largest oscillator strength were selected for each optimized building block to compute the difference densities. Calculations for precursor aldehydes and model compounds were done using the Turbomole program package in version 6.3.1.[305] Calculations for the hexagons with different terminations were done using the FermiONs++ program package.[306, 307] Periodic calculations for optimizations and single points were performed using the DFTB+ program package. [308]

4.3. Structure-property-activity relationships in a pyridine containing azine-linked covalent organic framework for photocatalytic hydrogen evolution

This work was published, section of this chapter were reproduced from:

<u>Frederik Haase</u> proposed the idea, designed the experiments, synthesized the precursors and COFs, performed the photocatalytic measurements and wrote the manuscript. Tanmay Banerjee performed and interpreted the photoluminescence experiments. Gökcen Savasci and Christian Ochsenfeld performed the theoretical calculations. Bettina V. Lotsch supervised the research.

Supplementary information for this chapter can be found in section 9.5.

In the previous chapter we could show that in aryl triphenyl azine COFs (N_x-COFs) a stepwise increase in the nitrogen content of the central aromatic ring can lead to a progressive increase in photocatalytic hydrogen evolution, thus showing the extent to which tunability is possible and effective in adjusting the structure-property-activity relationships in such materials. The changes in the photocatalytic hydrogen evolution activity in a series of N_x-COFs featuring gradually increasing nitrogen content in the central aryl ring (no nitrogen for phenyl to three nitrogens for triazine, Figure 4-4) were traced back to intrinsic electronic factors of the building blocks as well as structural, geometric and morphology-related features. The electronic factors that can possibly influence the hydrogen evolution rate are the band gap of the materials, the absolute HOMO and LUMO levels with respect to the hydrogen evolution potential, and the (de)localization of the frontier orbitals as a qualitative indicator for charge carrier delocalization in the excited state. The radical anion stabilization energy (RASE) was found to be a possible descriptor of the hydrogen evolution (HE) activity of the N_x-COFs. In addition, morphological features such as crystallinity and surface area also correlate with the HE activity, which are higher in the N_2/N_3-COFs and lower in the N_0/N_1 COFs. While in the N_x-COF series, the rather gradual evolution of structural, morphology-related and electronic features with increasing nitrogen content provides an excellent model system for studying the structure-property-activity relations in such systems, the interplay and relative weight of such features can still be highly complex.

We thus intended to explore a related COF with a different distribution of nitrogen across the building blocks. To this end, we substituted the peripheral rather than the central aryl ring with nitrogen atoms, starting with the same number of nitrogens as in the N_3-COF to gauge the differences resulting from the placement of the nitrogen atoms within the precursor aldehyde (Figure 4-4). The resulting PTP-COF (Figure 4-13) indeed shows photocatalytic hydrogen evolution in the presence of TEoA as the sacrificial electron donor and a platinum co-catalyst. To put the findings of this study into context, comparison of the photocatalytic activity is made relative to the N_x-COF series and specifically to the isoelectronic N_3-COF.

4.3.1.   Results

The PTP-CHO building block was synthesized from tribromobenzene (Figure 4-13) through a two-step cross-coupling reaction and a subsequent formylation. For the purification of PTP-CHO, the derivatization into a dimethyl acetal was necessary to remove impurities. This linker was consequently used for the synthesis of PTP-COF under solvothermal conditions. Solvent screening was done and a 1:1 mixture of butanol and dimethylacetamide (Figure S81) led to the highest crystallinity with the most resolved peaks in the XRPD (Figure 4-14A).
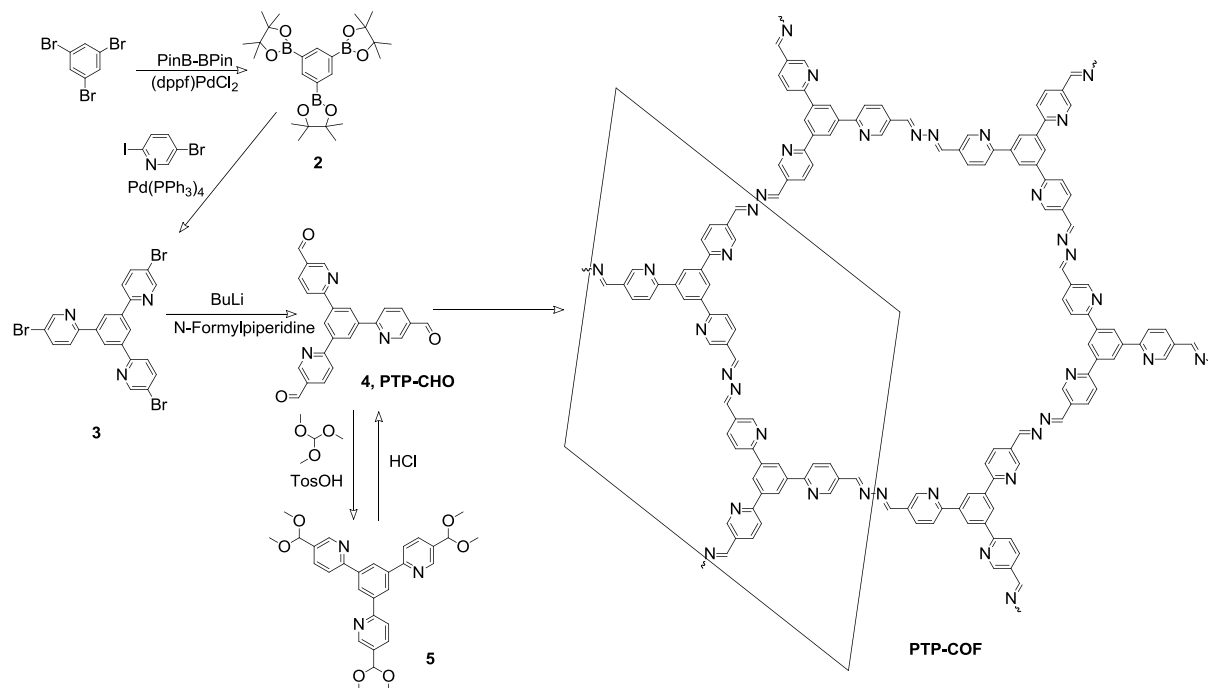
Figure 4-13: Synthesis of precursor PTP-CHO and PTP-COF. The in-plane unit cell is indicated on the right.

First, the IR spectrum of PTP-COF was compared to that of PTP-CHO (Figure 4-14B, Figure S82). Loss of the characteristic aldehyde (-CH=O) vibration at 1685 cm^{-1} and the appearance of the azine vibration (-CH=N-) at 1622 cm^{-1} is diagnostic of the conversion of the precursor aldehyde into the COF. The presence of a small residual aldehyde vibration either indicates small amounts of residual starting materials, oligomeric fragments or aldehyde-terminated surface groups of the PTP-COF particles.

To further corroborate the structure, we measured solid-state cross-polarization and polarization-inversion (CPPI) ^{13}C NMR of PTP-COF to help identify the signals in the NMR spectrum (Figure 4-14C).[309] With increasing inversion time, the intensity of carbons attached directly to hydrogens is reduced relative to those carrying no protons. Based on the CPPI sequence and comparison with known compounds from the literature, we assigned the peaks to the respective carbons. The retention of the molecular structure of the building blocks is evident from the ^{13}C NMR spectrum. The formation of the azine linkage is visible from the peak at 161 ppm, while only a small residual peak is seen at 191 ppm from unreacted aldehyde (Figure S83). The presence of the pyridine ring can be seen by the characteristic pyridine signal at 120 ppm, assigned to the carbon in *meta* position to the pyridine nitrogen (peak no. 8).

Figure 4-14: A: XRPD of PTP-COF with the corresponding Pawley refinement and the difference curve; B: ATR-IR spectrum shows the formation of PTP-COF from the precursor PTP-CHO; C: ^{13}C CPPI ssNMR measurement of the PTP-COF. In this experiment quarternar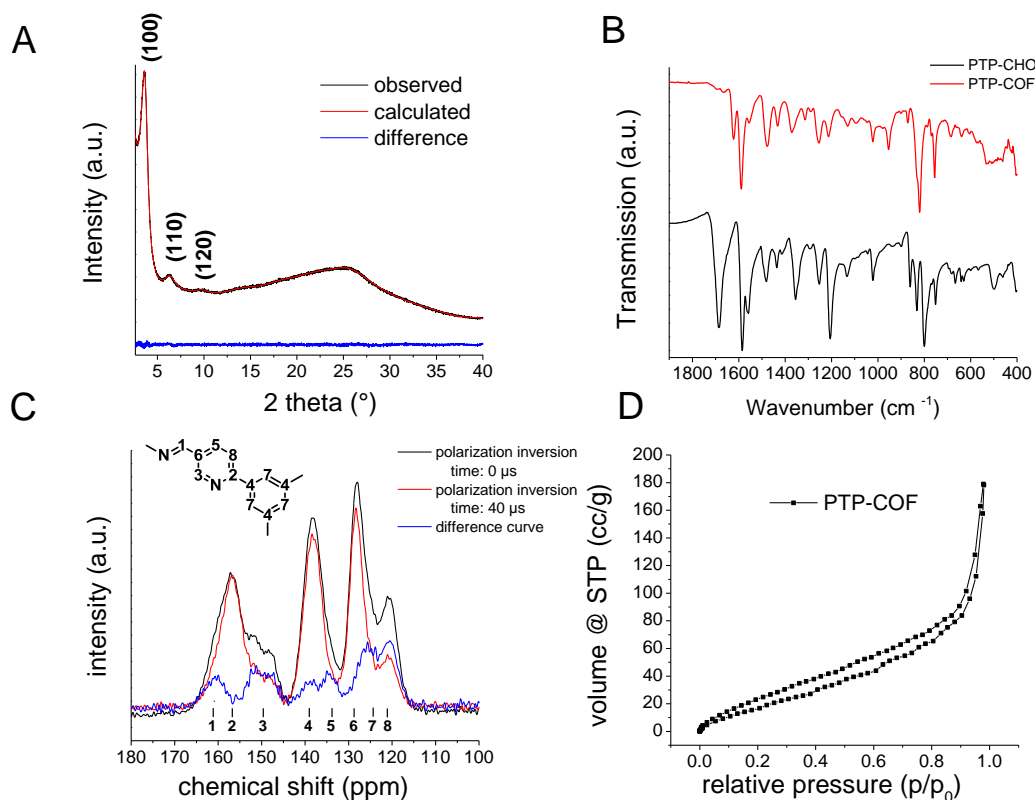y carbons stay constant in magnitude, while tertiary are decreasing with increased inversion times. The blue difference curve thus indicates the position of tertiary carbons. Assignment was based on a CPPI experiment and in comparison to literature known compounds. D: Nitrogen sorption isotherm of PTP-COF.

XRPD of PTP-COF shows three peaks (Figure 4-14A) that can be attributed to the (100), (110) and (120) planes at 3.68, 6.36 and 9.72 °2θ, respectively. Additionally, a broad feature in the region 20-30° is evident that may be attributed to a broad distribution of stacking distances in the PTP-COF or PTP-oligomers, or more generally to amorphous material. A unit cell was constructed based on the geometrical considerations of the precursor molecules and their expected connectivity (Figure 4-15). This led to a $P\bar{3}$ unit cell whose initial unit cell parameters were obtained from a force field optimization and then refined against the experimentally observed powder pattern by means of a Pawley fit (Rwp: 1.191). The thus obtained unit cell parameters are $a=b=27.75$ Å, $\alpha=\beta=90°$ and $\gamma=120°$. The unit cell parameter c and therefore the stacking distance could not be refined, as there is only a very broad feature visible in the expected region. This feature was not included in the structural model and only phenomenologically modelled with a background function (see method section ESI). Hence, c was kept at 3.55 Å as obtained from the force field geometry optimized unit cell in Materials Studio. Rietveld analysis showed that the model fits to the structure (Figure S84, Table S9.5-1).
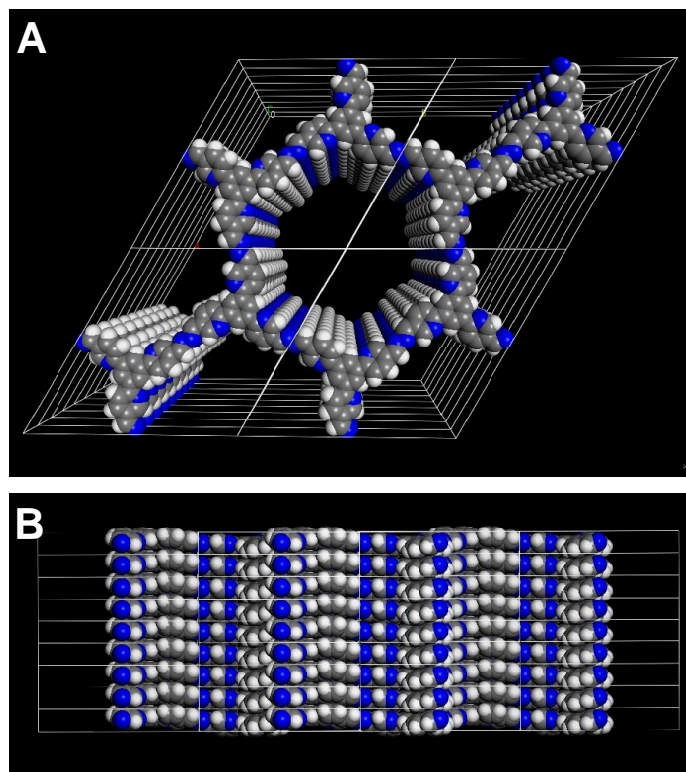
Figure 4-15: Illustration of the 3D structure that was used to model the PTP-COF. Perpendicular to (A) and along (B) the a-b plane.

To rationalize the observed low crystallinity, we analyze the geometry of the C3 symmetric phenyl tripyridine (PTP) core (Figure 4-13). Our previous studies showed that lower dihedral angles (i.e. increased planarity) between the peripheral and the central aryl rings entail improved stacking in the COF system, ultimately leading to higher crystallinity.[2] The PTP linker was chosen with the pyridine nitrogen in a position towards, rather than away from the central phenyl ring, so as to decrease the number of close hydrogen contacts between adjacent rings and to lower the dihedral angle. To corroborate the dihedral angles we calculated optimized geometries for the PTP-CHO building block and the N_x-CHO building units (Table S9.5-2, Figure S89, Figure S90) on the PBE0-D3/def2-TZVP level of theory. The PTP-CHO building block shows lower average dihedral angles (17.0°) than the N_1-CHO and N2-CHO building blocks (18.8° and 29.8°, respectively). The pyridine core in the N_1-CHO building block reduces the dihedral angle (29.8°) of two adjacent phenyl ligands in comparison to the N_0-CHO building block (39.1°). Three pyridine ligands attached to the phenyl core in PTP-CHO building block result in even higher overall planarity due to the threefold presence of this interaction. 1,4-repulsions of hydrogen atoms between the core and the ligands are decreased in all of the three attached ligands, causing the average dihedral angle to be in the range of that of the N_2-CHO building block; only the N_3-CHO has a lower dihedral angle of 0.0°. We tried to quantify this influence on the crystallinity by calculating the number of theoretically possible conformers of the precursors N_3-CHO and PTP-CHO. Analysis of the torsion angles in PTP-CHO and N_3-CHO shows a different number of distinct, but energetically degenerate conformers for both molecules. The torsion angle between the aldehyde and the adjacent aryl ring (angles B and D) gives two main conformers at 0° and 180° in PTP-CHO and N_3-CHO (Figure 4-16, blue curves). However, analysis of the torsion angle of the central aryl ring to the peripheral aryl ring (angles A and C) reveals a different trend (Figure 4-16, red curves). The torsion angle distribution shows four conformations in PTP-CHO, while N_3-CHO has only two, which are symmetry equivalent, thus leading to only one preferred torsion angle at 0° (Figure 4-16 A). We thus estimated the number of distinct conformers to

- 53 -

be $2^3*4^3 = 512$ and $2^3=8$ for PTP-CHO and N_3-CHO, respectively. If these conformers were to be observed as an individual entity, most of them would be symmetrically equivalent or degenerate. However, considered as a defect in an extended COF crystal, the degeneracy is lifted. Furthermore, such a defect will not only change the (average) occupancy of nitrogen at a certain position in space, but it also induces changes with the stacking, with regard to the stacking offset and the layer to layer distance, and can thus lead to an increased amount of disorder.
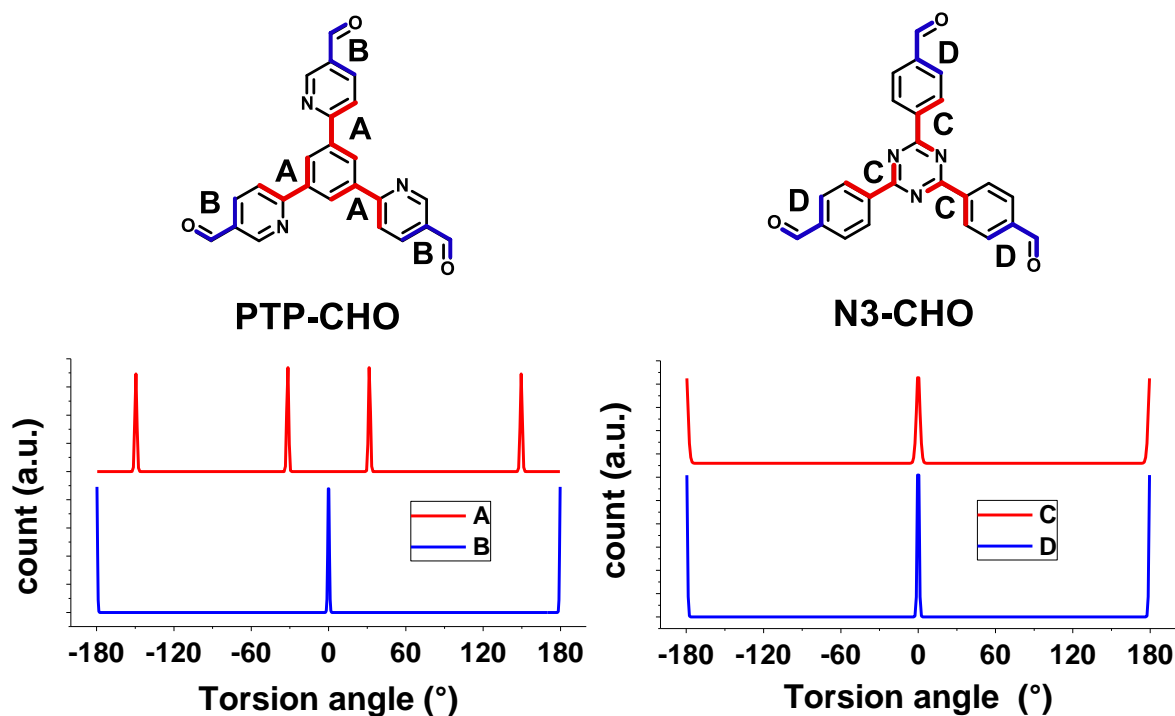
Figure 4-16: Conformer search in Materials Studio for PTP-CHO and N_3-CHO for the torsion angles displayed. The minimization was based on a coarse force field optimization to find the local minima.

The BET surface area of the material is 84.21 m²/g and therefore extremely low for a COF, as seen from Argon sorption analysis (Figure 4-14D and Figure S85). The low sorption capacity and thus possibly obstructed pores of the COF may either be attributed to its low crystallinity and the ill-defined stacking in the material, or due to residuals present in the pores, or both. As discussed above, such residuals could be the precursor molecule, PTP-CHO, which might explain the small residual aldehyde signal in ssNMR (191 ppm, Figure S83) and in IR (1683 cm⁻¹, Figure 4-14B). However, the small amount of molecular PTP-CHO should be washed away during the work-up in the synthesis of the COF. A more likely possibility thus is the presence of a broad distribution of chemically related oligomeric species with similar, yet not identical, chemical shifts, since the ssNMR signals of PTP-COF are rather broad in comparison to other COFs (Figure 4-14C).[2, 196]

A comparison of the morphologies of PTP-COF *vs* N_3-COF shows differences between the two.[2] While N_3-COF is composed of aggregated particulates in the range of several hundred nanometers, PTP-COF is composed of two parts – large, nearly perfectly spherical particles of relatively uniform size distribution of around 1 µm, and additional substantial areas of agglomerates (Figure 4-17, Figure S 86).

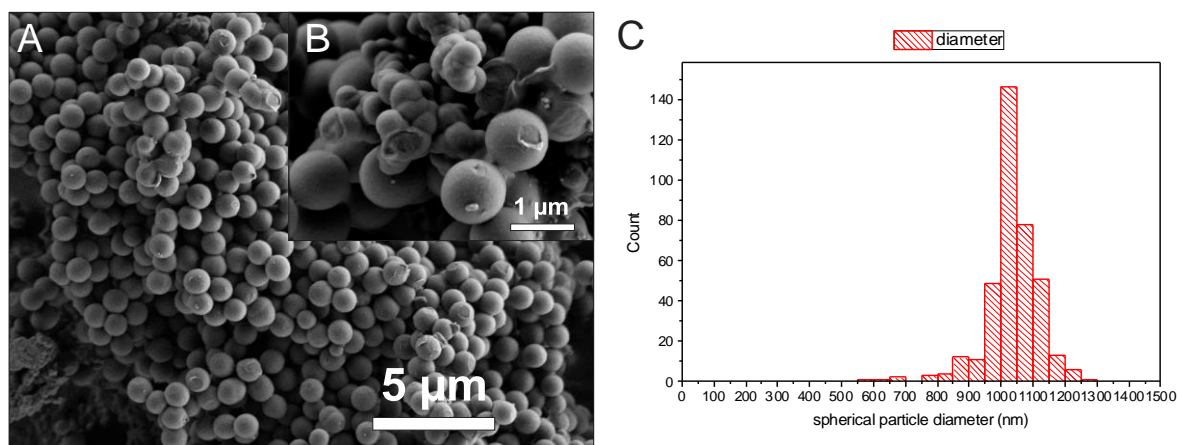Figure 4-17: SEM images of PTP-COF (A, B), showing the two distinct phases (B) - a compact intergrowth of small particles and the other nearly spherical particles with a narrow size distribution (C).

Photocatalytic hydrogen evolution was tested with PTP-COF under AM1.5 G conditions with triethanolamine as a sacrificial electron donor (SED) and platinum nanoparticles as the electrocatalyst. The platinum nanoparticles were generated and deposited *in situ* onto the photocatalyst by photo-reduction of added aqueous solution of hydrochloroplatinic acid into the reaction vessel. Triethanolamine was chosen as the sacrificial electron donor due to its ability to participate in hydrogen bonds with the PTP-COF. Such hydrogen bonding interactions may be more pronounced in PTP-COF than in N_3-COF due to the more basic character of the pyridine rings as compared to the triazine ring and it should facilitate close contact between the SED and the COF. We expect this close contact to enable an efficient hole quenching upon excitation of the photocatalyst. The thus tested PTP-COF produced hydrogen steadily over the course of over 15 h with no reduction in the observed rate (Figure 4-18A). An initial activation period can be observed in the hydrogen evolution, which could be attributed to the formation of platinum nanoparticles. The HE rate was 83.83 μmol/h/g, comparable to that of N_1-COF (90 μmol/h/g), but an order of magnitude lower than that of N_3-COF (1703 μmol/h/g).[2]

The observed lower HE rate of PTP-COF compared to N_3-COF is apparently unexpected if one considers the light harvesting properties of COFs as a decisive factor in determining the photocatalytic activity. This is because compared to the N_x-COFs, all of which show an absorption edge at 2.7 eV, PTP-COF has an extended absorption in the visible region with a measured absorption edge corresponding to a band gap of 2.1 eV (Figure 4-18A, Tauc-plot). Note, however, that stark differences in the HE activity are observed also within the N_x-COF series in spite of their similar band gaps, which puts the influence of the band gap on the catalytic activity into perspective.
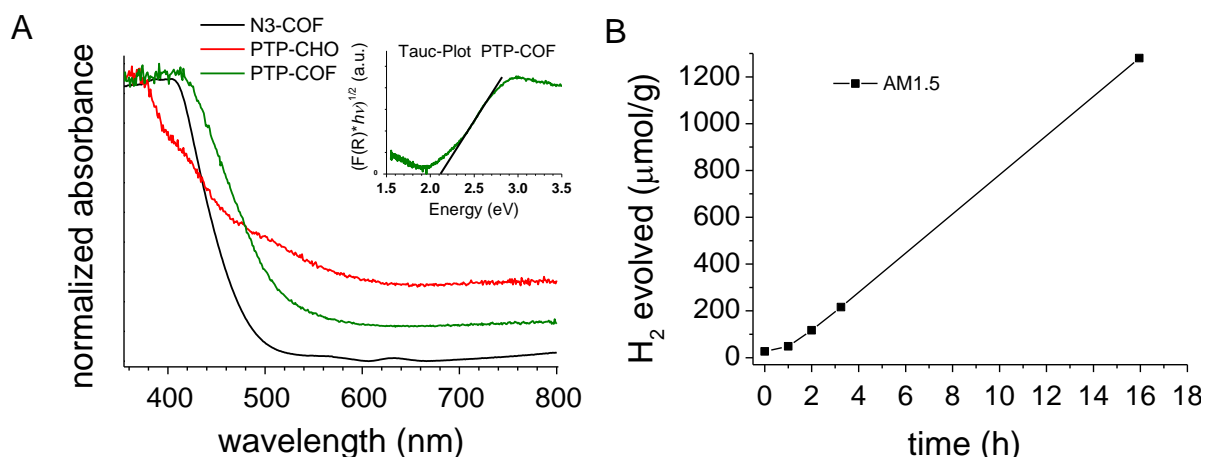
Figure 4-18: UV-Vis diffuse reflectance spectra of PTP-CHO and PTP-COF; B: hydrogen evolution under AM1.5 G conditions. After an initial activation period of about an hour, a linear increase in hydrogen evolution is seen.

To characterize the excited state properties of PTP-COF, we carried out time-resolved photoluminescence (PL) measurements. When excited at 380 nm, PTP-COF reveals a broad unresolved emission band over the whole visible spectral range from 425 nm to 800 nm (Figure 4-19A). Distinct peaks can be identified around 470-530 nm, at 630 nm and a shoulder at approximately 740 nm. The quantum yield of emission of the PTP-COF solid was found to be quite high at 4.15%, comparable for example to that of anthracene based emissive 2D COFs (5.4%) reported by Jiang and coworkers.[176]
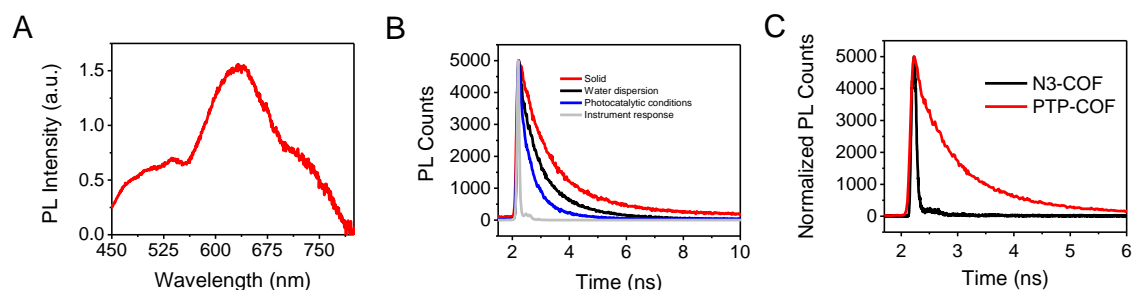
Figure 4-19: Emission properties of PTP-COF. A: Emission spectrum of PTP-COF powder (λ_{exc} = 380 nm); B: TCSPC decay trace of PTP-COF under different conditions (λ_{exc} = 375 nm, λ_{em} = 650 nm), and C; TCSPC decay trace of PTP-COF and N3-COF in water (λ_{exc} = 375 nm). The instrument response function is deliberately omitted for clarity. Three-exponential fits and the average lifetimes are shown in Table S9.5-3.

In order to understand the processes underlying hydrogen evolution better, we measured the absolute emission quantum efficiency of PTP-COF under different experimental conditions using an integrating sphere. As compared to 4.15% when measured as a solid, the quantum yield decreases steadily to 2.09% when measured as a water dispersion and finally to 0.87% when measured under photocatalytic conditions, i.e., after illumination (AM 1.5) in the presence of the sacrificial electron donor triethanolamine and the platinum precursor. Photoluminescence lifetimes recorded under the same conditions using time-correlated single-photon counting method (TCSPC) show an accompanied decrease in the fluorescence lifetime as well - from solid to water dispersion to photocatalytic conditions, as shown in Figure 4-19B. The TCSPC decay traces were subsequently fit to a three-exponential decay function (Table S9.5-3) and the radiative and non-radiative decay rates

were calculated from the quantum yield and the amplitude-weighted average lifetimes. Comparing the measurements of the water dispersion of the COF to those under photocatalytic conditions, the radiative decay rates of PTP-COF remain almost the same while the non-radiative decay rates, possibly corresponding to charge transfer steps of the hydrogen evolution process, increase considerably under photocatalytic conditions in the presence of the SED and Pt-cocatalyst. It must however be noted that this tri- exponential fit of the TCSPC decay may not reflect the underlying physics appropriately and has only been used to gain qualitative information on the radiative and non-radiative rates.

Fluorescence decay of N_3-COF as a water dispersion was recorded as well. In this case an external frequency doubled 400 nm laser beam from a Ti:Sa oscillator with a pulse width of ~ 100 fs was used as the excitation source. On comparison with the fluorescence decay of PTP-COF in water, N_3-COF in water (Figure 4-19C) can be seen to have a much shorter lifetime. Also, the emission quantum yield of N_3-COF (<0.5%, measured as a water dispersion) is much less than PTP-COF (2.09%, measured as a water dispersion). Relative to the radiative rates, the non-radiative rates thus seem to be more pronounced in N_3-COF, in line with its higher observed photocatalytic activity compared to PTP-COF.

4.3.2.   Discussion

PTP-COF was designed as an extension of the N_x-COF series. However, it turned out to differ considerably in its geometric, electronic and morphological properties, thus making the comparison to the N_x-COF series challenging. While PTP-COF is isoelectronic to N_3-COF and adopts a similar crystal structure as far as can be inferred from the XRPD, many structural and electronic features differ significantly. Most obvious differences can be found in the lower crystallinity, the significantly lower porosity and the different morphology. These features – particularly the low surface area of PTP-COF - might directly affect the ability of PTP-COF to produce hydrogen effectively under photocatalytic conditions in comparison to the N_x-COFs. The lower crystallinity can be seen as extensive peak broadening in the XRPD and a low number of observable reflections, in addition to the absence of a pronounced "stacking peak" (00l). This observation can be rationalized by considering the lower symmetry of PTP-COF compared to N_3-COF, which can already be seen in the precursor aldehyde PTP-CHO as compared to N_3-CHO. This reduction in symmetry leads to a higher number of molecular arrangements that can in turn lead to disorder in PTP-COF. Most prominently, the in-plane conformers, while conserving the connectivity of the PTP-COF, can influence the out-of-plane stacking interactions, which then could cause stacking disorder.

Another factor that might be influencing the stacking in the COFs can easily be observed in single crystals of PTP-H and N_3-H molecules (Figure 4-16). While N_3-H stacks in a face-to-face fashion with a slight offset, the stacking of PTP-H is governed by donor-acceptor interactions between the pyridine and the phenyl rings. Such an interaction could lead to additional stacking minima that lead to disorder and a reduction in crystallinity and porosity.
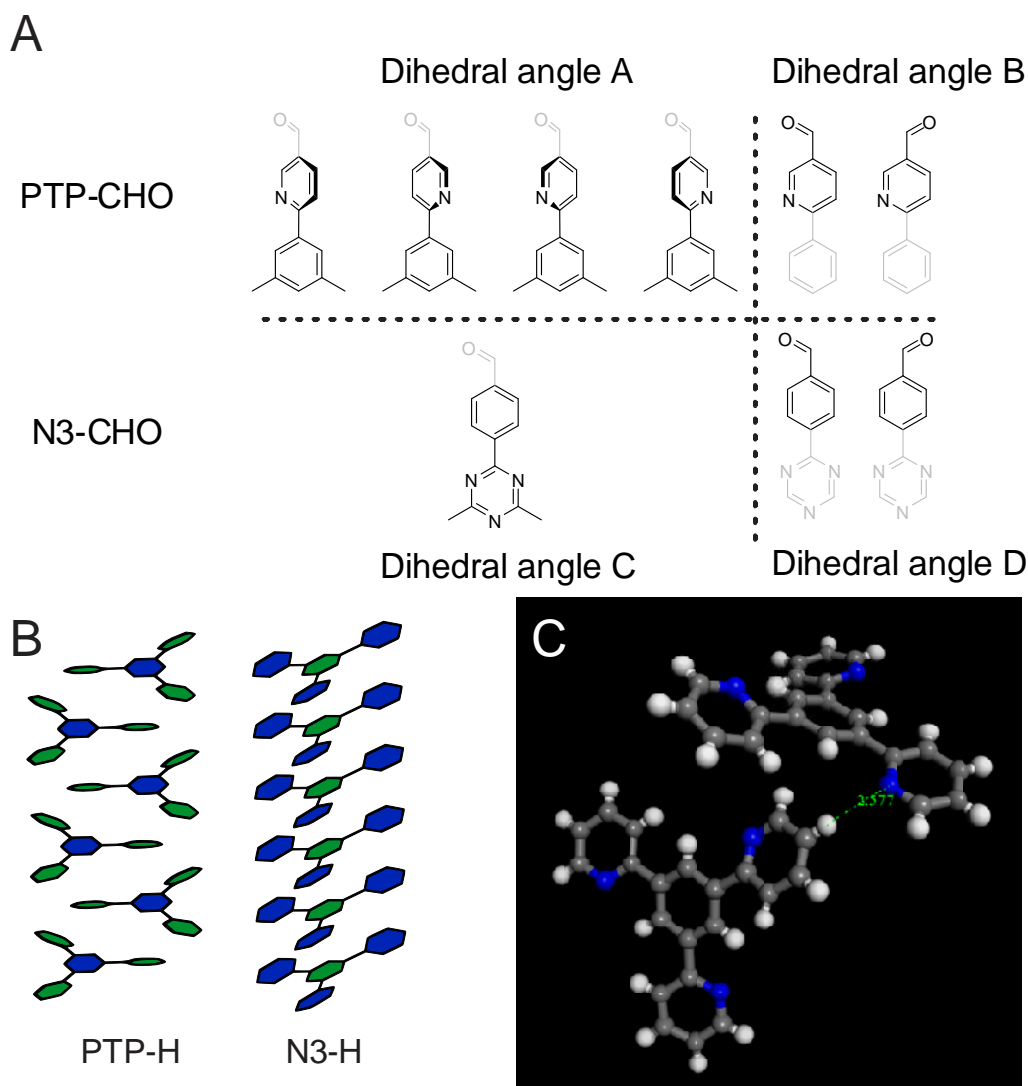
Figure 4-20: A: Schematic representation of the different conformers at the torsion angles A,B,C and D in PTP-CHO and N₃-CHO as indicated in Figure 4-16. B: Schematic representation of the stacking in single crystal structure solutions of PTP-H[310] and the N₃-H[311] cores, showing the different stacking modes. Green hexagons represent the nitrogen containing aryl rings and the blue hexagons represent the phenyl rings. C: Depiction of a hydrogen close contact in the PTP-H single crystal.[310]

A PTP-H single crystal shows another hint for the low porosity - an aryl hydrogen is in close proximity (2.58 Å) to the pyridine nitrogen (Figure 4-20C), indicating a tendency of this molecule to participate in hydrogen bonding. The pyridine moiety of the peripheral rings in PTP-CHO is more electron rich and hence more basic compared to triazine, the central aryl ring in the N_3 system, which could lead to bound molecules and oligomers being left in the pores after the synthesis of the COF, thus leading to a lowered surface area.

In line with low porosity and crystallinity, the morphological changes are from small aggregates that disperse reasonably well in water for the N_3-COF, to the large (1037±85 nm) smooth spheres of PTP-COF and macroscopic intergrown monoliths that do not disperse well in water for the PTP-COF, as was observed during the photocatalysis reaction. The morphology and the resulting dispersibility influences how efficiently light is absorbed and scattered in the suspension during photocatalysis and thereby how much catalyst is needed to absorb all light. These issues might however be addressed by mechanical methods of dispersion and reduction of particle size, such as ball milling and sonication.

The above solid-state properties will influence the ability of PTP-COF to produce hydrogen efficiently, independent of its optoelectronic properties. In fact, one may argue that the key feature determining the photocatalytic activity of a material is its specific surface area, which is extremely low in PTP-COF. Interestingly, when normalizing the observed HE activity against this surface area to extract an "effective HE activity", PTP-COF is indeed competitive with N_3-COF (0.995 μmol/h/m^2 vs 1.108 μmol/h/m^2).

Nevertheless, as in the N_x-COF series, there is evidence that a range of intrinsic factors influencing the HE activity of PTP-COF are also at play. For example, the longer PL lifetime and the higher quantum yield of PTP-COF compared to N_3-COF seem to imply smaller or less efficient non-radiative deactivation *via* charge transfer pathways during hydrogen evolution, *vs*. radiative recombination, in PTP-COF. This behavior has been reported before in carbon nitride based photocatalysts and is in line with the observed higher photocatalytic activity of N_3-COF compared to PTP-COF.[312, 313]
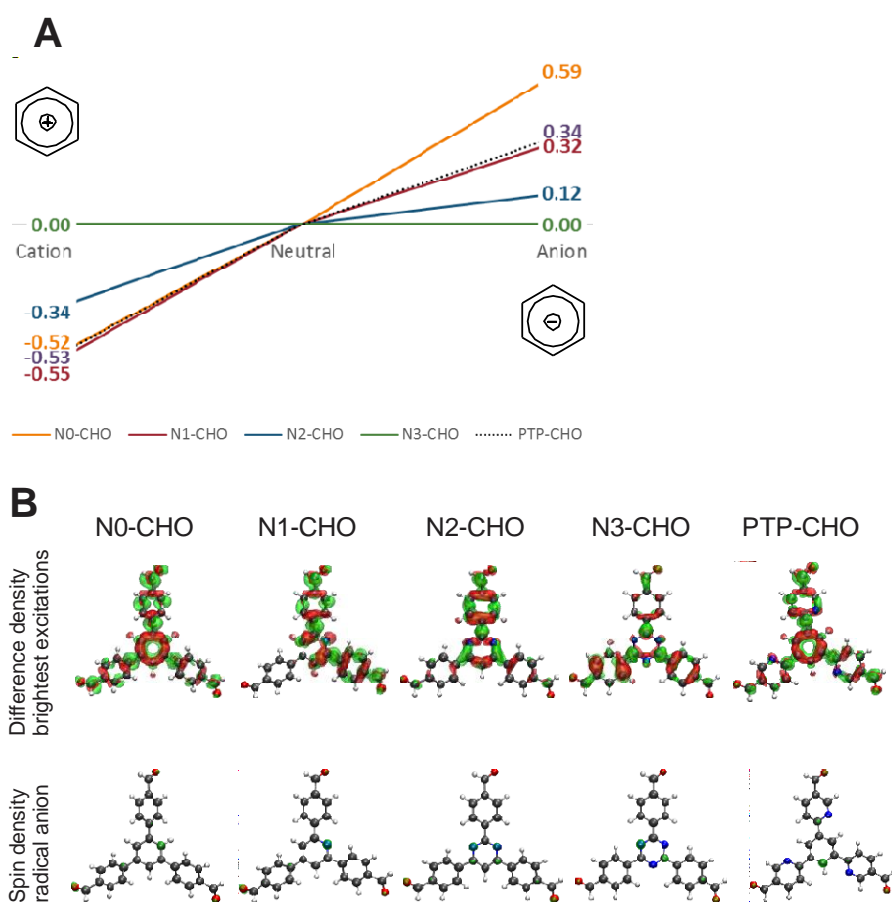

Figure 4-21: A: Comparison of vertical radical anion and radical cation stabilization energies of N_x-CHO molecules and PTP-CHO, where a lower energy corresponds to better stabilization. B: Difference densities of brightest excitations, spin densities underneath.

To further gauge the influence of intrinsic, i.e. optoelectronic factors, on the observed HE rates, we calculated molecular orbitals for all N_x-CHO building blocks and PTP-CHO on the PBE0-D3/def2-TZVP level of theory (Figure S91, Figure S92). The spatial extent and distribution of the frontier orbitals are often used to rationalize exciton delocalization, charge separation and the location of potential charge-transfer sites.[300, 301, 314] Using the delocalization of the HOMO/LUMO as a possible indicator for charge carrier separation in our investigated systems, the HOMO of the PTP-CHO building block shows a comparable localization as the HOMO of the N_1-CHO building block (Figure S91, Figure S92). Associating the HOMO with charge-transfer sites for holes, we may infer that the

hole delocalization is comparable between the two building blocks. Associating the LUMO with the charge-transfer site for electrons, we may deduce that due to differences in the LUMO spread across the building blocks, delocalization of the charge carrying species is less pronounced in PTP-CHO than in N_1-CHO. In addition, the LUMO of the PTP-CHO building block has the same spatial extent as the corresponding HOMO, which may point to more facile charge recombination in PTP-COF.

It has to be stressed, however, that orbitals are not observables and hence, such model considerations need to be taken with care. Therefore, an alternative approach was pursued in considering possible reaction intermediates during the photocatalytic process. Quenching the hole on the COF by a sacrificial electron donor would lead to a radical anionic state on the COF (Figure 4-21, reductive quenching; radical anionic pathway), which has been observed in a recent experimental study on N_x-model systems (unpublished results). The extraction of the electron from the photoexcited COF towards Pt (oxidative quenching) would lead to a radical cationic state on the COF, following a radical cationic pathway, accordingly.[2]

In order to investigate the relative stabilities of reaction intermediates within these two radical pathways, vertical radical stabilization energies (RASE) of the PTP-CHO building block and the N_x building block units were calculated at the PBE0-D3/def2-TZVP level of theory (Table S9.5-5). These RASE values, calculated on large subsections of the N_x-COFs, have been used in our previous work on the N_x-COFs.[2] These calculations showed the RASE to be a powerful descriptor of the HE efficiency in triphenyl aryl azine COFs. To extend these calculations to more generalized triaryl-aryl-azine COFs, we included the precursor aldehydes, PTP-CHO and N_x-CHO as model systems for PTP-COF and N_x-COFs, respectively. Comparison of radical stabilization energies with the series of N_x-CHO building blocks reveals that the radical anion of PTP-CHO has a similar stabilization as that of the N_1-CHO unit. The formation of a radical anion is most favored for the N_3-CHO system and least favored for the N_0-CHO system. If the formation of this radical anion is thus taken as the rate-determining step, the same trend in the computed energetics of the radical anion of the PTP-CHO, and the experimentally observed photocatalytic activity is seen - the observed HE activity of PTP-COF is similar to that of the N_1-COF. On one hand, the importance of the radical anion intermediate emphasizes the role of the sacrificial electron donor in being able to swiftly remove the hole from the COF, and on the other hand it underlines the importance of the electron-poor character of the building block in stabilizing the radical anion as best observed for the triazine building block. The introduced pyridine ligands in the PTP-CHO building block units are thus not as effective in stabilizing a negative charge (in order to transfer it to the nearest platinum site subsequently) as compared to the N_3-CHO unit.

Radical cation stabilizations show a very similar scenario for the PTP-CHO building block as for the N_0- and N_1-CHO building blocks (Figure 4-21), where all three investigated systems give very similar stabilization energies, yielding beneficial radical cations for all three systems. As the trend within the radical cation stabilization energies is contrary to the observed photocatalytic activities, we assume an anionic pathway during the photocatalytic process.

4.3.3. Conclusion

In summary, as for the N_x-COFs, we find a complex interplay between extrinsic, i.e. steric and morphology-related factors, and intrinsic, optoelectronic features – specifically the vertical radical anion stabilization energy – determining the photocatalytic activities of PTP-COF. Thus, the correlation with, or even prediction of the catalytic activity of a COF based only on its photophysical properties is challenging, given the plethora of "real structure" effects that may disguise the intrinsic

catalytic activitiy. The above findings thus show the importance of precisely controlling the structure, long-range order and morphology of a COF through dynamic covalent chemistry, such that the various factors determining the photocatalytic activity of a COF can ultimately be disentangled.

4.3.4.   Experimental

Synthesis

Synthesis of the molecular precursor compounds can be found in Section 9.2.1.

PTP-COF: PTP-CHO (0.127 mmol, 50.0 mg), hydrazine hydrate (50-60% in water, 0.191 mmol, 0.0108 ml), *n*-butanol (2.5 ml), N,N-dimethlyacetamide (2.5 ml) and aqueous acetic acid (6M, 0.182 ml) were added successively to a Biotage$^{©}$ precision glass vial, sealed and heated under autogenous pressure at 120 °C for 72 h. The reaction mixture was allowed to cool down and then filtered and washed thoroughly with ethanol, water, tetrahydrofuran and chloroform and then dried in high dynamic vacuum overnight.

Methods

Photocatalysis.

Photocatalysis experiments were performed in a glass reactor kept at a constant temperature (25 °C) with water circulated through a thermostat. The reactor was irradiated from the top through a quartz window with a xenon lamp (Newport, 300 W) equipped with a water filter and a dichroic mirror (AM1.5 G, Figure S88, 133mW/cm^2 (Thorlabs Thermo power sensor)). PTP-COF (5 mg) was suspended in PBS (10 ml of 0.1 M solution at pH 7) buffer containing triethanolamine (100 μl) and hexachloroplatinic acid (6 μl, 8 wt% in water) for *in situ* formation of platinum as the co-catalyst. Residual oxygen and nitrogen were removed by three cycles of evacuation and backfill with argon. For the determination of the evolved hydrogen, the headspace of the reactor was sampled periodically with a gas chromatograph (Thermo Scientific TRACE GC Ultra) equipped with a thermal conductivity detector (TCD) detector using argon as the carrier gas.

Steady-State and Time-Resolved Emission

Steady-State and Time-Resolved Emission data were collected at room temperature using an Edinburgh FLS980 spectrometer. For steady-state emission, samples were excited using light output from a housed 450 W Xe lamp passed through a single grating (1800 l/mm, 250 nm blaze) Czerny-Turner monochromator and finally a bandwidth slit. Emission from the sample was passed through a double grating (1200 l/mm, 500 nm blaze) Czerny-Turner monochromator (appropriate bandwidth) and finally detected by a peltier-cooled Hamamatsu R928P photomultiplier tube.

The dynamics of emission decay were monitored by using the FLS980's time-correlated single-photon counting capability (1024 channels; 10 or 20 ns window) with data collection for 5000 counts. For the longer lived PTP COF, excitation was provided by an Edinburgh EPL-375 picosecond pulsed laser diode (375 ± 6 nm, pulse width - 68 ps). For the short lived N_3-COF, a frequency doubled 400 nm (404 nm, ~100 fs, 85 MHz) laser beam from a Ti:Sa oscillator was used as the excitation source. A cooled microchannel plate photomultipler tube (MCP-PMT) was used as the detector. Kinetics were fit with a three-exponential function by using Edinburgh software package.

Emission quantum yield

Emission quantum yields were acquired using an integrating sphere incorporated into a spectrofluorometer (FLS980, Edinburgh Instruments). The samples were placed in the sphere and a movable mirror was used for direct or indirect excitation, making it possible to measure absolute emission quantum efficiency following the De Mello method.[315] No bandpass filters were used during quantum yield measurements. A 3 OD neutral density filter was used on the emission arm when measuring the scattering. This allowed the emission slits to be opened further for the emission spectrum to be accurately measured without detector saturation.

Quantum-Chemical Calculations

Structures for all investigated building block units were optimized on the PBE0-D3/def2-TZVP level of theory. Molecular orbitals, orbital energies, and Kohn-Sham Band-Gaps were obtained from single-point calculations on the same level of theory. Excitation energies for optimized building block units were calculated on the TD-PBE0/def2-TZVP//PBE0-D3/def2-TZVP level of theory. Excitations with the largest oscillator strength were selected for each optimized building block to compute difference densities. Vertical radical stabilization energies were calculated as total energy differences between radical anionic, radical cationic, and neutral states of investigated building blocks. Obtained as differences of single-points energies, PBE0/def2-TZVP level of theory was used. Spin densities were computed from the electron densities obtained on the same level of theory. All calculations were performed using the Turbomole program package in version 7.0.2.[316]

Conformation analysis

Conformers were calculated based on force fields (Forcite) in the BIOVA Materials Studio 2017 (17.1.0.48) Copyright © 2016 Dassault Systémes.

4.4. Tuning the optical band gaps of covalent organic frameworks for efficient solar light absorption and photocatalytic hydrogen evolution

Frederik Haase proposed the idea, designed the COF and the experiments, synthesized the COFs, interpreted the data and wrote the manuscript. Sebastian Vogel and Lars Grunenberg helped in the synthesis of the COFs and performed the photocatalysis experiments. Bettina V. Lotsch supervised the research.

This work focuses on maximizing light absorption by tuning the band gap of COFs by molecular design. COFs that were investigated so far for photocatalytic hydrogen evolution absorb only a small fraction of the solar spectrum due to their large band gaps. Therefore, tuning the band gap could be a possible strategy to improve the solar to hydrogen efficiency. The estimated minimum energy required for driving the overall photocatalytic water splitting reaction including overpotentials is approximately 2.0 eV[232] and therefore larger band gap materials cannot utilize much of the solar irradiation for photocatalysis. By using hydroxylated and non-hydroxylated building blocks for the synthesis of two isostructural triazine based COFs, the optical absorption onset can be altered and thereby the absorption of solar irradiation improved. The introduction of hydroxyl groups has a significant influence on the optical properties of the COFs and is shown to improve the hydrogen evolution quantum efficiency for illumination in the range of 450 nm to 500 nm, thus affecting the overall hydrogen evolution rates at AM1.5 G illumination.

4.4.1. Results and Discussion

The two COFs chosen for this study are both based on the triazine bearing TT-NH$_2$ building block, since triazines have previously been shown to be beneficial for photocatalytic hydrogen evolution in COFs,[283] CTFs[269, 273-275] and carbon nitrides.[248, 267] Two imine COFs were synthesized in this work designated H-BTI-COF and OH-BTI-COF (Figure 4-22), by combining two similar phenyl trialdehyde precursors, that differ only in the presence or absence of hydroxyl groups on the central aryl ring. The BIT-COFs that have also been described elsewhere,[148, 195, 216, 317, 318] were synthesized in mixtures of mesitylene and dioxane in the presence of aqueous acetic acid as a catalyst under autogenous pressure at 120°C for 72 h.
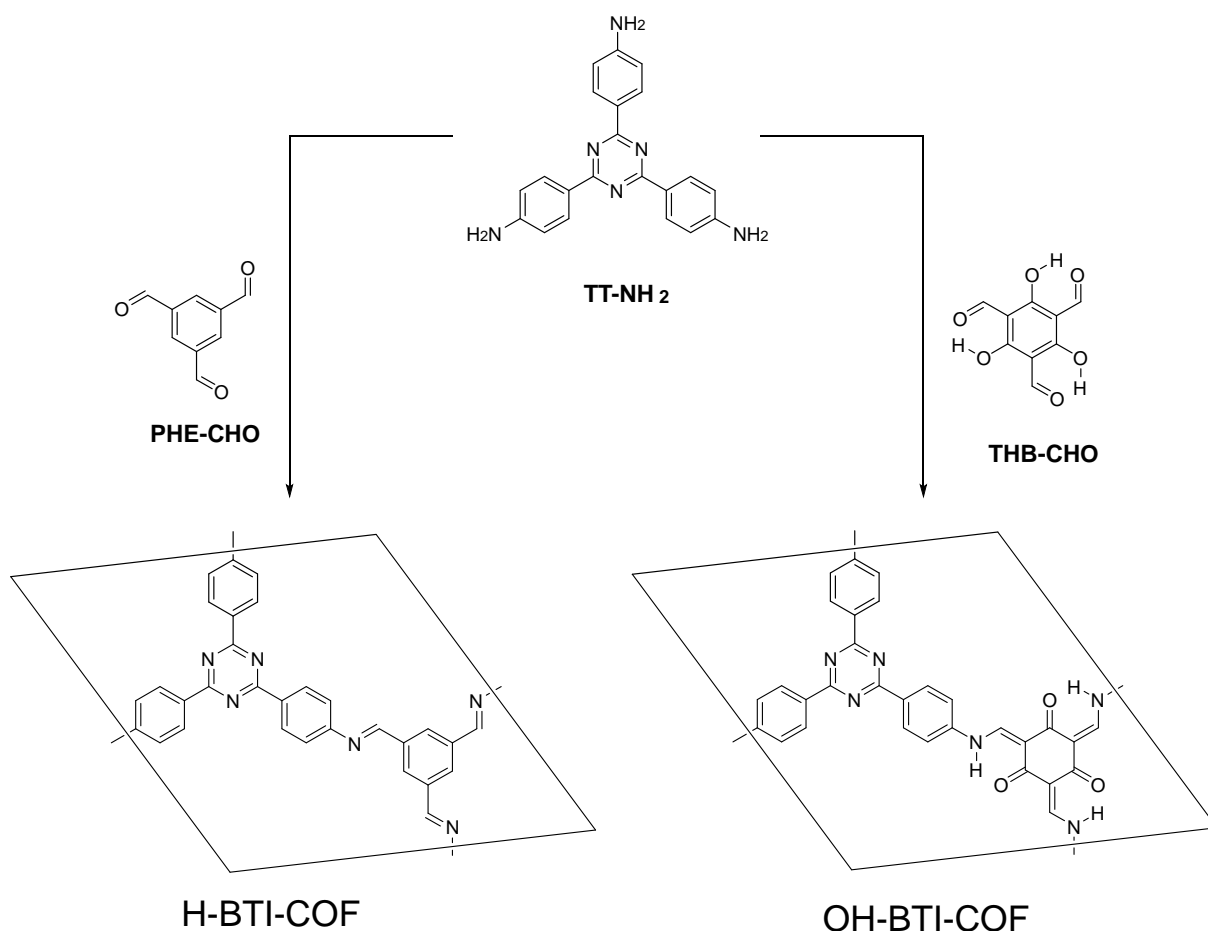
Figure 4-22: Reaction scheme for the synthesis of the H-BTI- and OH-BTI-COFs.

The obtained materials were characterized by FT-IR to confirm the condensation reaction to the polymeric imine and the keto-enamine for H-BTI- and OH-BTI-COFs, respectively (Figure 4-23). The characteristic aldehyde vibration (HC=O) present in the PHE-CHO precursor at 1695 cm^{-1} and in THB-CHO at 1637 cm^{-1} vanishes, including the N-H vibrations at 3300 – 3100 cm^{-1} for TT-NH$_2$. While these vibrations are largely absent in the COFs a new peak appeares at 1632 cm^{-1} and 1626 cm^{-1}, that corresponds to the imine bond in the H-BTI-COF and the OH-BTI-COF, respectively. The OH-BTI-COF shows keto-enol tautomerism, characteristic of the ortho hydroxyl imines based on THB-CHO,[110] which can be seen from additional vibrations present in the range from 1300-1200 cm^{-1}. These vibrations can be attributed to the C-O vibration from the hydroxyl groups and to C-N vibration from the keto-form of the COF.[110] The observed vibrations in both COFs indicate a successful condensation reaction between the aldehyde and the amine building blocks.
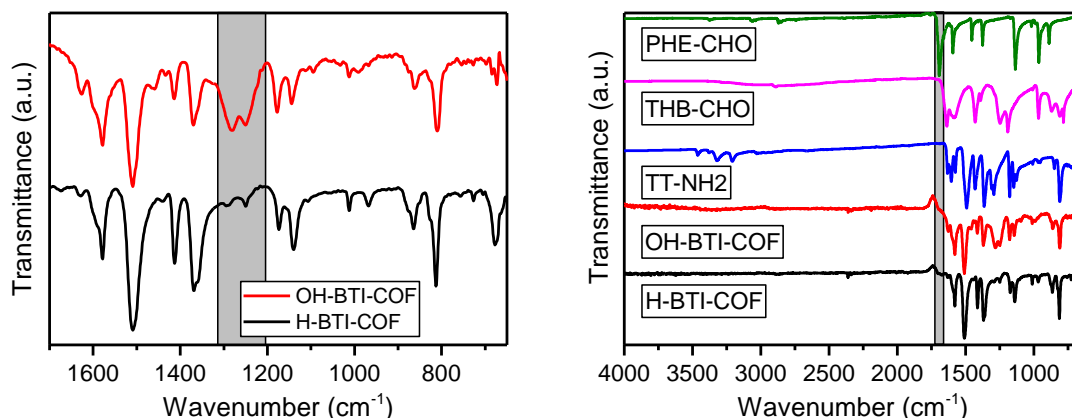
Figure 4-23: Left: FT-IR spectra of OH-BTI- and H-BTI-COFs. Right: comparison of the FT-IR spectrum of the molecular precursors with the COFs.

The BTI-COFs were further characterized with the help of ^{13}C solid state NMR to probe the formation of the framework and the retention of the molecular building units. The most characteristic observable peak results from the triazine carbon (**1, 7**) appearing in both COFs at 168 ppm. Further similarities are visible in the peaks in the region 150-145 ppm that can be assigned to the TT- phenyl carbons (**3, 8**) and in the region 115-112 ppm assigned to carbons **5**, and **10**. H-BTI-COF shows the presence of the characteristic imine carbon (**2**) at 153 ppm which confirms the condensation of the precursors. In addition, only a minor peak at 194 ppm resulting from residual aldehyde of the precursor or surface functional groups can be observed. OH-BTI-COF displays keto-enamine tautomerism which produces a significantly different ssNMR. The characteristic peaks resulting from the keto-enamine are located at 183 ppm for the keto functional group (**6**), at 140 ppm from the enamine carbon in proximity to the amine (**9**) and finally the adjacent enamine carbon (**11**) at 106 ppm. These spectra show the formation of an enamine based backbone for OH-BTI-COF.
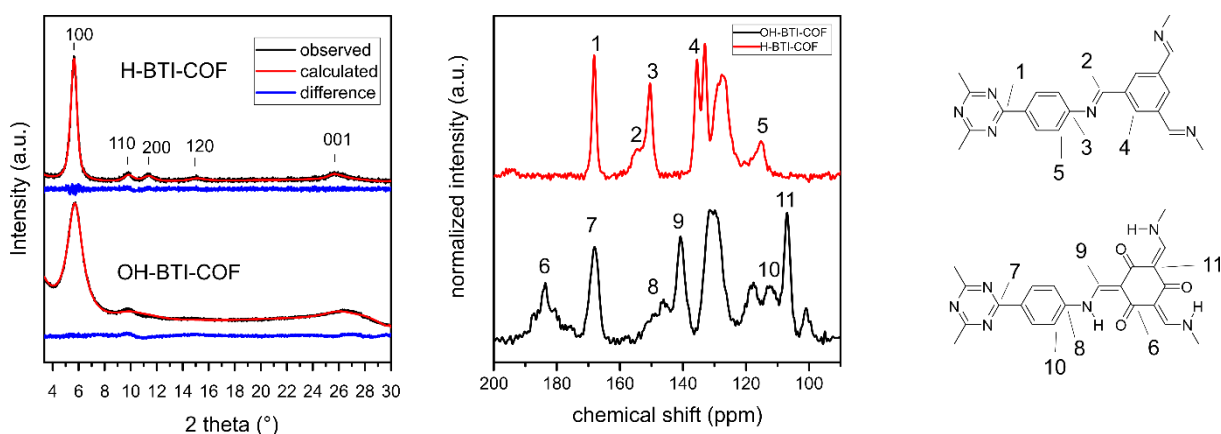

Figure 4-24: XRPD pattern of H-BTI and OH-BTI-COF and the Rietveld fit of the corresponding structural models.

The structure of H-BTI and OH-BTI-COF was evaluated by XRPD (Figure 4-24), which showed that both materials are crystalline, with hexagonal unit cells exhibiting only small differences in lattice parameters between the two (Table S 9.6-1). The OH-BTI-COF shows lattice parameters smaller by 0.276 Å for *a* and *b* and 0.153 Å for *c*. The lattice parameters in both cases indicate a structural similarity of the two COFs. However, a considerable difference with regard to the crystallinity is observed. While H-BTI-COF exhibits high crystallinity with four discernable in-plane reflections and a resolved stacking reflection (001), only two broad in-plane reflections are discernable for OH-BTI-

COF, which has a broad stacking reflection (001). The broad reflections of OH-BTI-COF indicate a higher degree of disorder or smaller crystallites. Geometric considerations as well as the molecular connectivity of the building blocks were used to construct structural models for the two COFs (Figure 4-25). The Rietveld refined models show a good fit to the experimentally obtained XRPD pattern (Figure 4-24).
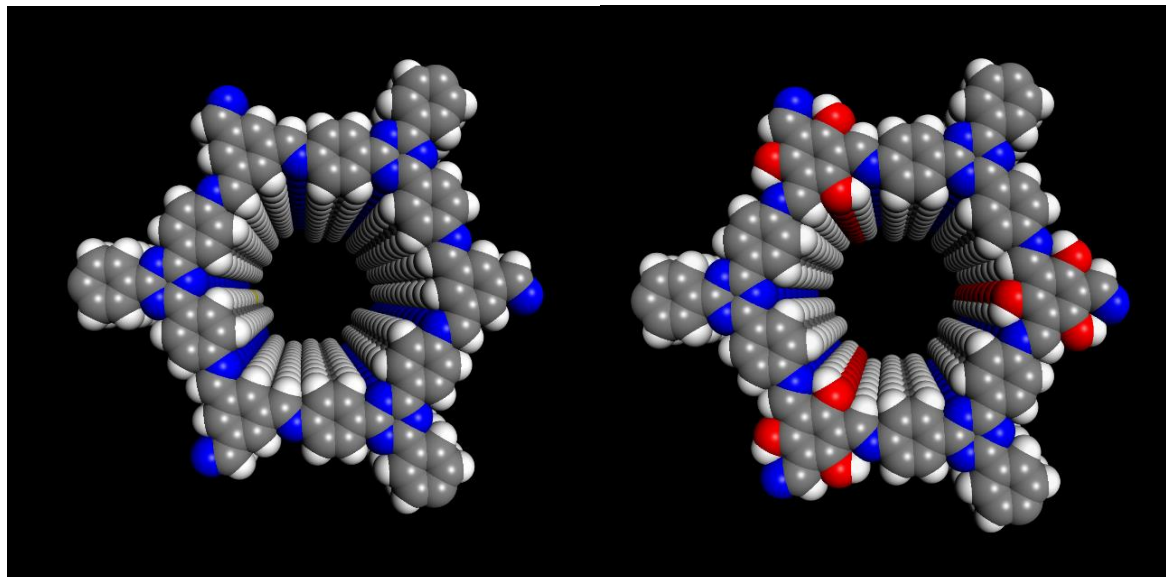

Figure 4-25: Representative image of a pore in the structural model of H-BTI-COF (left) and OH-BTI-COF (right). Carbons are shown in gray, hydrogen in white, nitrogen in blue and oxygen in red.

Sorption analysis of H-BTI-COF and OH-BTI-COF indicate that both materials are porous, with BET areas of 1516 m^2/g and 852 m^2/g, respectively. The lower surface area of OH-BTI-COF can be attributed to its lower crystallinity that may cause blocked pores, reducing the number of accessible surface area. Both the crystallinity and the porosity differences between the two COFs could be a result of the different nature of the COF linkages in both materials. The keto-enamine tautomerism present in OH-BTI-COF is able to stabilize the formed COF (chapter 6.1), however reversibility is reduced and thus the crystallinity. H-BTI-COF is based on a regular imine functional group and thus leads to higher crystallinity.

Further, both COFs were evaluated for their photocatalytic hydrogen evolution activity, which was performed using triethanolamine (TEoA) as the sacrificial electron donor and hexachloroplatinic(IV) acid as a precursor to the active hydrogen evolving electrocatalyst. Both COFs showed sustained hydrogen evolution albeit at different rates. The average rate of hydrogen evolution was 30 μmol h^{-1}g^{-1} for H-BTI-COF and 276 μmol h^{-1}g^{-1} for OH-BTI-COF, which is comparable to the performance of the N_2-COF[2] (438 μmol h^{-1}g^{-1}) at standard AM1.5 G conditions.
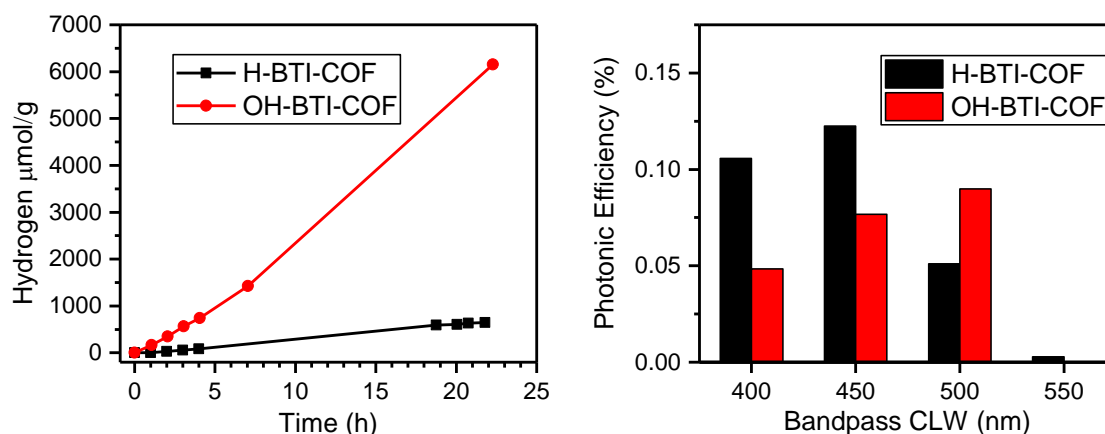
Figure 4-26: Hydrogen evolution performance of H-BTI-COF and OH-BTI-COFs under AM1.5 G illumination (left); Photonic efficiency of H-BTI and OH-BTI-COFs with different band pass filters with the central wavelength (CWL; Figure S 65) indicated on the ordinate. The photonic efficiency normalizes the yield of evolved hydrogen with respect to the incident number of photons.

The higher activity of OH-BTI-COF in comparison to H-BTI-COF is surprising since some of the qualitatively beneficial descriptors such as the surface area and crystallinity would point towards a lower hydrogen evolution rate for OH-BTI-COF (see chapter 4.2 & 4.3). However, the hydrogen evolution rate could be related to the band gap of the materials and thereby to the fraction of light energy of the incident solar spectrum that could be utilized for the photocatalytic reaction. The optical properties of H-BTI-COF and OH-BTI-COF were evaluated by diffuse reflectance absorption spectroscopy (Figure 4-27), which showed a significant red-shift of the absorption edge for OH-BTI-COF with respect to H-BTI-COF. The absorption edge of OH-BTI-COF was found to be redshifted also compared to some of the previously investigated highly active COFs such as the N_x-COFs and the PTP-COF. Optical band gaps of 2.38 eV and 2.81 eV were extracted from the Tauc plot for OH-BTI-COF and H-BTI-COF, respectively. To relate the changes in the band gap to the photocatalytic performance of the COFs, we tested whether activity for hydrogen evolution actually followed the absorption properties of the COFs by performing wavelength dependent photonic efficiency (PE) experiments. Measurement of PE using band pass filters with different central wavelengths showed that H-BTI-COF is a more efficient hydrogen evolution catalyst at lower wavelengths than OH-BT-COF. However, the OH-BTI-COF had a higher PE at 500 nm CWL, which also corresponds to the region of solar illumination with most intensity (Figure 4-1). This result shows that OH-BTI-COF can utilize the higher wavelength part of the solar spectrum more efficiently thereby being able to utilize a higher fraction of the incident light, which could be a reason for its improved hydrogen evolution efficiency. While the general trends agree between the hydrogen evolution rates and the PE measurements, there is a discrepancy between the observed performance differences between H-BTI and OH-BTI-COFs comparing PE with HE rates. To pinpoint the origin of this result further experiments are necessary.
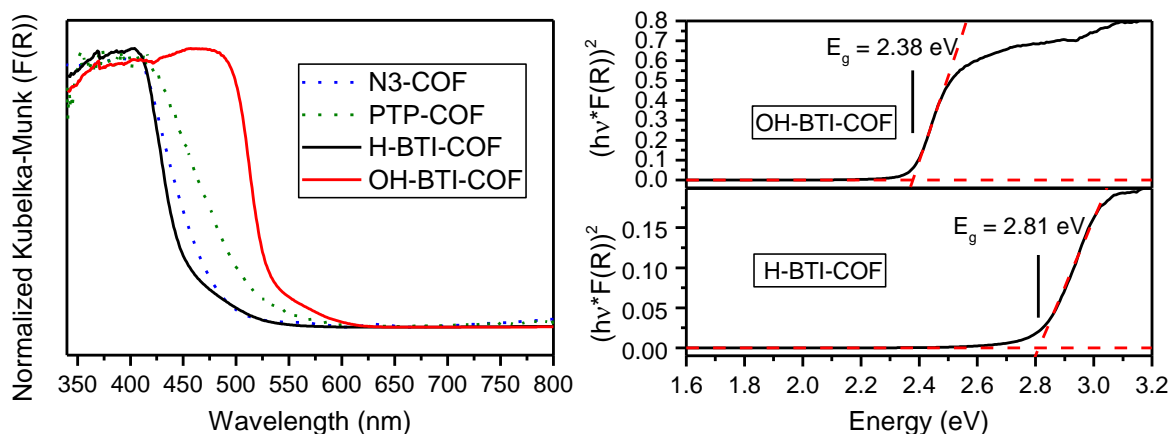
Figure 4-27: Left: Diffuse reflectance absorption spectra of H-BTI-COF, OH-BTI-COF, PTP-COF and N$_3$-COF. Right: optical band gap determination from the Tauc plot (calculated for a direct band gap).

Another possible factor improving the hydrogen evolution efficiency of OH-BTI-COF with respect to H-BTI-COF could be the increase in pore wall polarity,[189] which might improve the interaction of the platinum nanoparticles with the COF surface and its pores.[267] The hydroxyl group present in OH-BTI-COF can function as a hydrogen bond donor and acceptor, which might improve contact of the COF backbone with water molecules present in the pores and improved access of the sacrificial electron donor TEoA (Figure 4-28). In addition, the pore wall polarity might improve solvent penetration into the pores.[189]
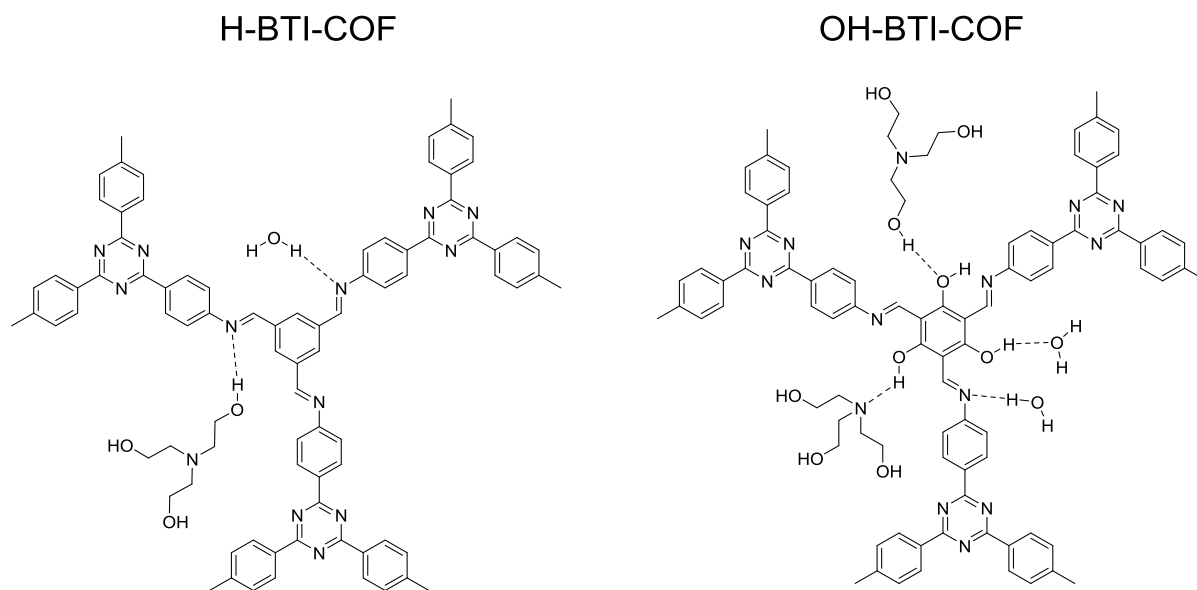

Figure 4-28: Possible binding motifs for hydrogen bonding in H-BTI-COF and OH-BTI-COF in the keto form.

4.4.2. Conclusion

Herein, we were able to synthesize two isostructural COFs with and without hydroxyl groups. This small variation significantly influences the crystallinity, porosity, optoelectronic and pore properties of these COFs. By this structural variation it was possible to manipulate the optical bandgap in these COFs to absorb a larger fraction of the incident solar light, compared to previously shown photocatalytically active COFs. The COFs were tested for photocatalytic hydrogen evolution, which showed that the small band gap OH-BTI-COF produces hydrogen at a significantly larger rate at

AM 1.5 G and has a higher photonic efficiency at higher wavelengths (550 nm) as compared to the larger band gap H-BTI-COF, which has higher photonic efficiencies at lower wavelengths (400-450 nm). These results show that band gap tuning in COFs is a viable strategy to improve the utilization of visible light for photocatalysts. On the other hand, it is important to note that the introduction of hydroxyl groups could be used to improve the pore polarity and possibly improve the charge transfer properties for photocatalytic hydrogen evolution.

4.4.3. Experimental

Synthesis

TT-NH2[196] and THB-CHO[110] were synthesized as previously reported. PHE-CHO and all other chemicals were obtained from commercial sources.

OH-BTI-COF: Briefly, OH-BTI–COF was synthesized by adding TT-NH2 (35 mg, 0.1 mmol) and TBA-CHO (21 mg, 0.1 mmol), mesitylene (1 ml), 1,4-dioxane (2 ml) and acetic acid (6 M, 100 µl) to a Biotage© high precision glass vial. The sealed vial was heated to 120°C for 72 h. The obtained precipitate was filtered off and thoroughly washed with ethanol, water, THF, chloroform and DCM. The sample was dried in high dynamic vacuum over night to yield of OH-BTI-COF as an orange red powder.

H-BTI-COF: Briefly, H-BTI–COF was synthesized by adding TT-NH2 (20 mg, 0.0564 mmol) and PHE-CHO (9.15 mg, 0. 564 mmol), mesitylene (0.286 ml), 1,4-dioxane (2.57 ml) and acetic acid (6 M, 214 µl) to a Biotage© high precision glass vial. The sealed vial was heated to 120°C for 72 h. The obtained precipitate was filtered off and thoroughly washed with ethanol, water, THF, chloroform and DCM. The sample was dried in high dynamic vacuum over night to yield H-BTI-COF as a pale yellow powder.

Photocatalysis

Photocatalytic hydrogen evolution experiments were performed in a top irradiated double walled, stirred cylindrical glass reactor, with a quartz window on top, that was kept at constant temperature (25°C) by water cooling. Triethanolamine (100 µL) and hexachloroplatinic acid (6.0 µL, 8 wt% in water) were added to a suspension of COF (5.0 mg) in 0.1M PBS (10 mL, pH 7) while stirring. The reactor was purged by argon by three successive cycles of evacuation and backfill with Ar. The reactor was irradiated with a Newport 500W xenon lamp (model 66904) equipped with a water filter and a dichroic mirror (AM1.5 G) or band pass wavelength filters. The illumination intensity for high intensities was quantified with a Thorlabs PM100D thermo power sensor. For low intensities for PE determination were measured for each band-pass filter with an Ocean Optics USB-4000-XR1-ES spectrometer. The headspace of the reactor was sampled periodically with a GC to determine the fraction of hydrogen.

5.   Stacking in two-dimensional COFs

Two-dimensional COFs are a subclass of COFs, where connectivity is in-plane via strong covalent bonds, but through weak intramolecular forces between the individual layers. Since the weak van-der-Waals, dipole-dipole and π -π interactions are short range and non-directional interactions, the exact stacking configuration is highly dependent on factors such as the shape of the building blocks, dipolar interactions and donor acceptor stacking. It is important to note that the exact stacking sequence is of great importance for optoelectronic, catalytic and gas sorption properties of these porous network materials. Interlayer forces can lead to a multitude of stacking sequences in COFs, which can be hard to characterize and are poorly understood due to the low levels of crystallinity observed in COFs. Consequently, detailed insights into the stacking geometries in COFs have remained largely elusive so far.

5.1.   Introduction

The organic nature of COFs leads to significant differences in the available geometries and nets that can be formed, in comparison to other framework materials such as MOFs. In COFs, the nodes are dominated by the linkers and not by the COF linkages. Only in some cases such as the boronic anhydride, the linking reaction itself provides a nonlinear node (see section 2.2 & 2.3). As such, flat building blocks with in-plane linking groups are far more common than those out-of-plane and therefore most COFs are designed to be two-dimensional. The dimensionality of a 2D COF is defined by the covalent connectivity in two dimensions and the noncovalent stacking in the third dimension by weak intermolecular forces, typically van-der-Waals interactions.[1] The design and synthesis of 2D COFs is straightforward as the rigidity requirements, for producing permanent porosity also favor the use of flat sp^2 carbon dominated molecules that tend to stack. On the other hand, the synthesis of 3D COFs often leads to significant interpenetration,[70] thereby reducing the dimensionality of the pores to one dimension despite the three dimensional nature of the backbone and thus reducing the utility of such designs. The molecular design of the precursors usually translates directly to the in-plane structure in COFs, while the interaction between different layers are more difficult to design. The challenge in rationally creating defined stacking interactions often lead to disordered stacking (Figure 5-1, B, C).[278]
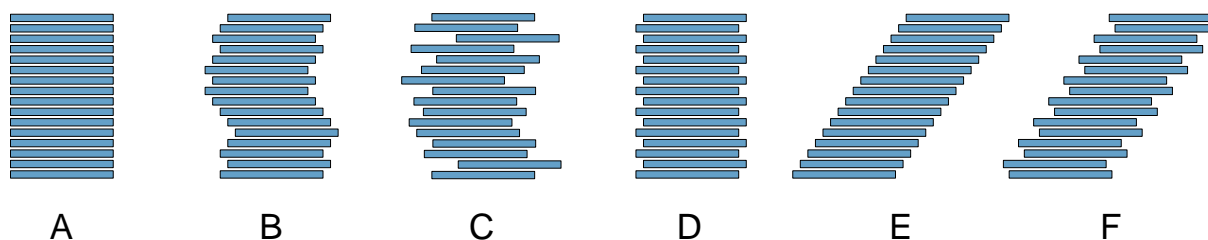

Figure 5-1: Different stacking modes: A: eclipsed or AA stacking; B: Random stacking in different directions with constant stacking vector length; C: Random stacking in different directions with random stacking vector length, also called turbostratic stacking; D: Staggered or AB stacking; E: Slip-stacking; F: Staggered slip-stacking.

Stacking polymorphs are well known and investigated in inorganic crystals composed of van der Waals or otherwise weakly stacked layered materials such as transition metal chalcogenides[319, 320] and transition metal halogenides.[321] In COFs, usually only the eclipsed or the staggered models are considered for structural refinement, as both these stacking geometries were present in the first two

reported COFs.[1] However, in recent years several more elaborate stacking models have been investigated and analyzed because of the utility of designing COFs with specific stacking interactions (Figure 5-2).

Strategies to introduce defined stacking in COFs have been developed, based on preformed motifs that are able to direct the weak interlayer interaction. How weak the interlayer interactions can be, is exemplified by the example of a boronic anhydride based COF, that changes its interlayer structure from staggered to eclipsed upon solvent guest removal.[132] One prominent example of guiding the stacking is the use of propeller-shaped building blocks, which can induce stacking without offset and lead to preferred, "locked-in" configurations (Figure 5-2, A).[83, 162] This motif can lead to perfectly eclipsed structure or slipped structure depending on the building blocks, by altering the stacking landscape in such a way that only one minimum remains to reduce the probability of random offset stacking. This strategy is based on the geometric features of the linkers to guide the stacking, by designing self-complementary building blocks. Another strategy is the introduction or control of shorter range forces for example, the use of donor and acceptor (DA) molecules that can stack in an alternating fashion (Figure 5-2, B) to improve crystallinity and stacking.[279] As an example, a porphyrin-amine building block could be combined with a mixture of fluorinated and non-fluorinated aldehydes, which self-sort into electron deficient and electron rich layers during crystallization. Although the alternation provides favorable interlayer interaction, this strategy allowed only for a small part of the inlayer structure to participate in donor acceptor stacking with the rest of the structure being dominated by homo-stacking.
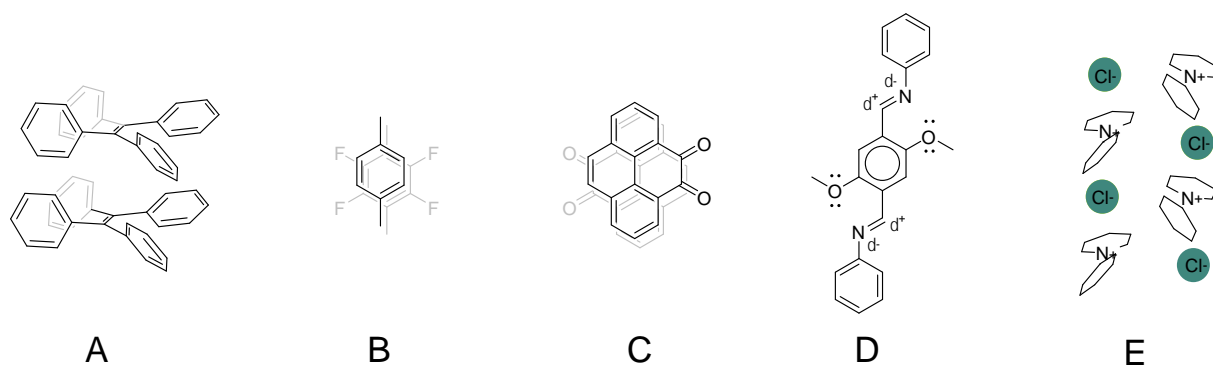

Figure 5-2: Molecular motifs influence the stacking in COF. A: lock-in through propeller shaped building blocks;[83, 162] B: donor acceptor π-stacking;[279] C: dipole-dipole induced stacking;[280] D: dipole reduction for improved stacking.[209] E: coulomb driven interlayer interaction [281]

Instead of designing two different layers, only one kind of layer can be used to gain favorable interaction between dipoles, by conformational flexibility or flexibility during crystallization. This was shown by the use of a pyrene-dione, which can stack in alternating directions (Figure 5-2, C).[280] This example shows how a dipole can be used to guide the stacking. However, in some cases parallel dipoles might cause repulsion and therefore favor random stacking. This is especially important in imine connected COFs based on C2 symmetrical amines or aldehydes. Layers that include a C2 or inversion symmetry between imine groups cannot align in an antiparallel fashion during crystallization. Therefore, reducing the dipole of the imines by introduction of electron donating methoxide groups at the electron deficient end of these structures can improve stacking (Figure 5-2, D).[209] An even stronger force to influence stacking is coulomb interactions between layers as exemplified by the use of a cationic COF backbone that then stacks in an alternating fashion with chloride counter ions (Figure 5-2, E).[281]

The planarity of building blocks play an important role in stacking in 2D COFs. At one end lies the previously discussed propeller shaped building blocks that generate a singular minimum for stacking. However, beneficial influence of flat building blocks on the crystallinity and stacking can be observed on the other end of the planarity scale as discussed with N_x-COFs in Chapter 4.2. This series shows how increased nitrogen content in the central aryl ring progressively planarizes the building blocks and thereby improves stacking. The seemingly contradictory results can be similarly observed in the offsets and distances in the structures of triphenyl aryl molecules, as determined by single crystal X-ray diffraction measurements (Figure 5-3, Table S 9.3-1). In this set only those molecules were considered where stacking is not significantly influenced by strong interlayer interactions and are stacking in a face to face fashion. The parameter space shows stunning trends in the stacking of these molecules: The molecules containing no nitrogen cluster around a layer offset of ~3.5 Å with a wide range of layer distances, which might indicate low interaction strength between the individual molecules. The triazine based molecules however stack with a relatively small range of interlayer distances, but with larger spread in terms of interlayer offset. This can be understood as strong intramolecular interactions leading to a tight stacking, which is localized in the intermolecular distance but not their offset due to the planar nature of the building blocks. The molecules containing one N are distributed above the threshold values for the layer distance and the offset that might arise from a combination of properties seen in the 0 N and 3 N cases. These examples show how a propeller shaped building block can lead to improved crystallinity through localization in plane while having less defined stacking distances.[83, 162] At the planar end of the scale, stronger interlayer interaction leads to more localized stacking distances, which can also improve crystallinity and stacking.[196, 278, 291]
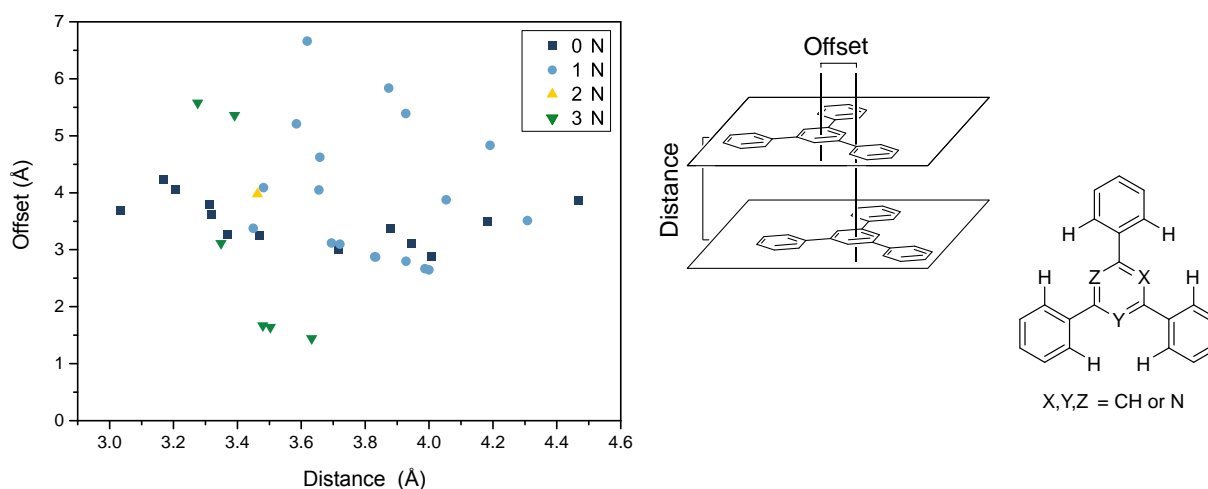

Figure 5-3: Scatter plot of the layer distances and the layer offsets obtained from single crystal structure solutions of triphenyl aryl molecules where the twist between two molecules is close to 0°. A list of structures used for this calculation can be found in the appendix (Table S 9.3-1).

The strategies described above influence the nature of stacking and improve the crystallinity of COFs, but in most cases, the nature of stacking could not be proven experimentally. Small crystallite sizes and the inherent strain in some COFs hinder solving of the exact structure by regular diffraction techniques, which are most relied on in determining the structure of COFs. Small crystallites and defects arise from incomplete error correction that lead to significant reflection broadening and overlap in the XRPD pattern (Figure 4-4). The resulting extractable information is diminished and allows only the refinement of average structures and stacking information is difficult to obtain.
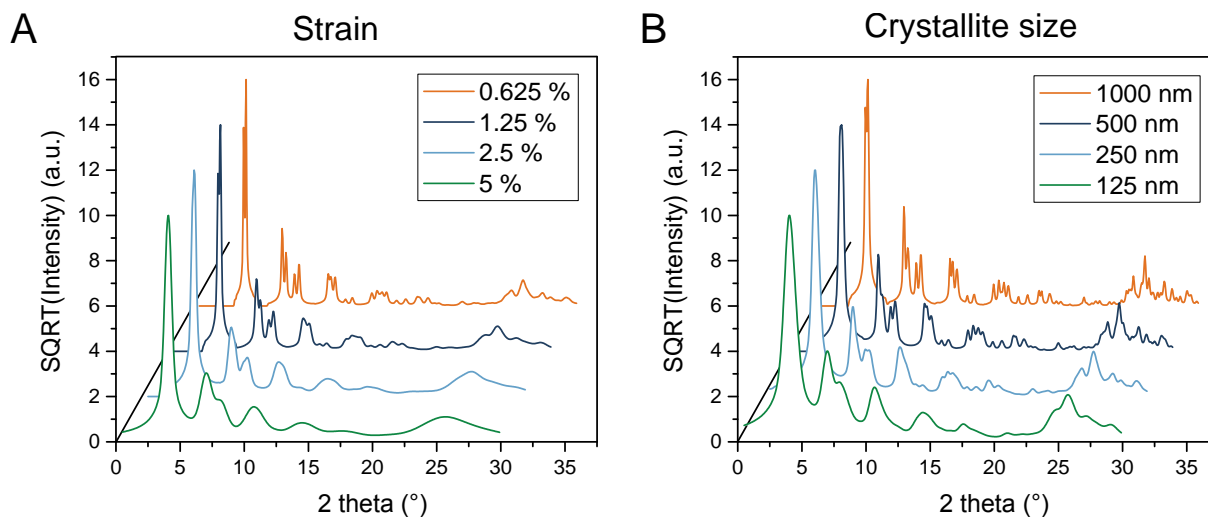
Figure 5-4: XRPD simulations of TTI-COF (Chapter 5.2) with different degrees of strain or crystallite size induced broadening.

Local analytical techniques such as ssNMR are largely insensitive to the stacking sequence. Therefore, early investigations were limited to differentiating between extreme cases of the staggered and the so-called "eclipsed" configuration.[1, 115, 322] The eclipsed configuration however contrasts with the prediction that a perfectly eclipsed stacking is not energetically favorable for flat π-stacked COFs, where the minima of the stacking landscape lie off center.[290, 323, 324] The COFs that are described by "eclipsed" (Figure 5-1 A) stacking are therefore often the result of an average structure solution that results from random or ordered offset stacking (Figure 5-1 B, C, D), that could not, or was not attempted to be resolved by XRPD. Uniform slip stacking as predicted by theory would lead to dramatic changes in the unit cell and thereby in the observed XRPD pattern. Bein and coworkers inferenced slip-stacking by evaluating intensity variations of reflections related to stacking in the XRPD data.[162] The TTI-COF described in this thesis (Chapter 5.2) showed drastic symmetry changes in its XRPD pattern, as would be expected from a slip-stacked COF unit cell and this has not been observed and attributed to slip-stacking before. A similar symmetry reduction can be observed in the XRPD of works by Jiang and coworkers[279] and Dichtel and coworkers[58] that may also be attributed to slip-stacking, but not investigated in their work. While slip-stacking was not directly observed by XRPD, it was still invoked to explain other experimental data such as sorption[71] or as theoretical predictions of the structure.[209, 280, 283]

5.2. Tuning the stacking behaviour of a 2D covalent organic framework through non-covalent interactions

Work on the structural characterization of the TTI-COF and the related TBI-COF resulted in two publications:

1. *Exploiting non-covalent interactions in an imine-based covalent organic framework for quercetin delivery*
    *Vijay S. Vyas, Medhavi Vishwakarma, Igor Moudrakovski, **Frederik Haase**,*
    Gökcen Savasci, Christian Ochsenfeld, Joachim P. Spatz, Bettina V. Lotsch
    *Adv. Mater. **2016**, 28, 8749–8754. DOI: 10.1002/adma.201603006*

Vijay S. Vyas, Medhavi Vishwakarma, Joachim P. Spatz and Bettina V. Lotsch proposed the idea and designed the experiments. Vijay S. Vyas carried out the synthesis and the quercetin loading experiments. Medhavi Vishwakarma performed the cell viability and drug delivery experiments. Vijay S. Vyas and Medhavi Vishwakarma wrote the manuscript. Igor Moudrakovski performed the ssNMR measurements. Frederik Haase solved the structure of the COF. Gökcen Savasci and Christian Ochsenfeld performed the theoretical calculations.

2. *Tuning the stacking behaviour of a 2D covalent organic framework through non-covalent interactions*
    ***Frederik Haase**, Kersting Gottschling, Linus Stegbauer, Luyia S. Germann,*
    Rico Gutzler, Viola Duppel, Vijay S. Vyas, Klaus Kern, Robert E. Dinnebier,
    Bettina V. Lotsch
    *Mater. Chem. Front. **2017**, 1, 1354−1361. DOI: 10.1039/c6qm00378h* - Published by
    The Royal Society of Chemistry.

Frederik Haase proposed the idea, synthesized the TTI-COF and precursors, analyzed the data and wrote the manuscript. Kersting Gottschling and Linus Stegbauer designed and synthesized the TBI-COF. Frederik Haase, Luzia S. Germann and Robert E. Dinnebier analysed the XRPD data. Viola Duppel recorded the TEM and SEAD images. Rico Gutzler performed the DFT calculations. Vijay S. Vyas, Klaus Kern, Robert E. Dinnebier, Bettina V. Lotsch supervised the research.

Sections of this chapter were reproduced from Publication 2.
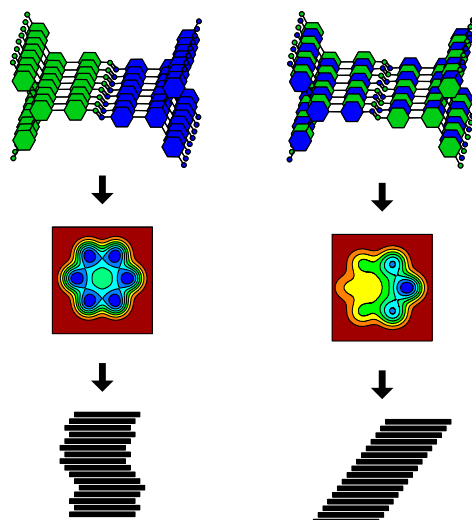
Inspired by the existing design principles, we have synthesized a COF in which the stacking can be rationally adjusted based on the geometry and non-covalent interactions of the building blocks. We demonstrate that individual layers can self-assemble to form DA-type stacks where imine bond polarization or similar interlayer interactions may be efficient in determining the polytype. To add evidence for our hypothesis, we "turned off" the possibility of DA stacking in a closely related system by introducing a propeller-shaped building block that causes the formation of an averaged eclipsed geometry. These two very similar systems allow us to gauge the influence of symmetry, geometry and polarity of the building blocks on the stacking characteristics of the COF. The stacking of the COFs was analyzed experimentally and theoretically and we provide evidence of well-defined slipped stacking in a COF for the first time based on a combination of Rietveld refinement of XRPD data and TEM.

5.2.1.   Results

Two imine COFs based on the triphenyl aryl unit were synthesized through the reaction of a triamine with a trialdehyde under solvothermal conditions in mesitylene/dioxane 1:1 and aqueous acetic acid as a catalyst (Figure 5-5).[196] The difference between these COFs lies in the nitrogen content of the triamine precursor, which is based on a central phenyl ring or a triazine ring in case of the TBI-COF or the TTI-COF, respectively. The successful condensation reaction was confirmed *via* the disappearance of N-H and C=O vibrations and the appearance of C=N vibrations through IR spectroscopy (Figure S1). The porosity of the structures was determined *via* argon physisorption (Figure S2), which showed BET surface areas of 1108 m^2/g for the TBI and 1403 m^2/g for the TTI-COF (Figure S3).

While both networks are crystalline (Figure 5-7), the TTI-COF has narrower line widths and shows a pronounced splitting of the (100), (110), (020) and (120) diffraction peaks as well as a discernable stacking peak (Figure 5-7) showing that this COF is highly crystalline. This unusual XRD pattern of TTI-COFs is distinct from previously reported, highly symmetrical frameworks.

To determine the structure of the two COFs, several structural models were considered to explain the observed powder patterns. We developed three models based on different stacking modes influencing the overall symmetry as well as the molecular conformations, which were compared to the experimental powder patterns using Pawley refinement[325] and Rietveld analysis.[326] The initial values of the cell parameters were obtained from the force field optimized structures, which were

constructed based on geometrical considerations, and the in-plane connectivity was derived from the topology of the molecular building blocks. All models are based on a honeycomb structure with a hcb net[197] (Figure 5-5).

High symmetry case: eclipsed stacking

For the eclipsed model C_3 symmetry was chosen for the in-plane structure. These individual layers were then stacked in a perfectly eclipsed fashion to form a one-layer cell with $P3$ symmetry and cell parameters $a = b \neq c$ and $\alpha = \beta = 90°$, $\gamma = 120°$. This type of model is simplistically assumed for most COFs in the absence of detailed structural information from the X-ray powder patterns.[1, 290, 324] While these COFs have an apparent high symmetry due to disorder,[1] only some COFs stack without any lateral offset between layers.[83] When this high symmetry cell is applied to the observed XRPD pattern of TTI-COF, stark differences between the simulated and the observed pattern are obvious and most prominently reflected by the different numbers of reflections (Figure 5-7, Rwp: 9.319). We therefore explored lower symmetry models for the TTI-COF. For the case of the TBI-COF the eclipsed model yielded a good fit (Rwp: 1.365), as no symmetry reduction is apparent.
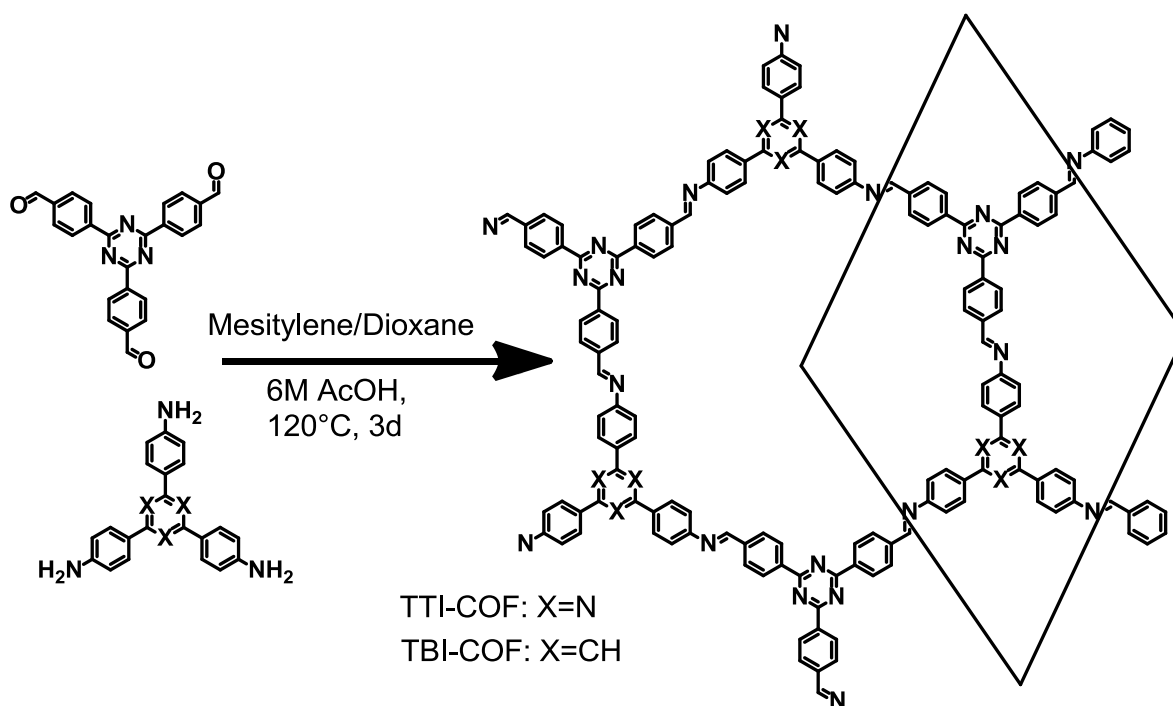
Figure 5-5: Schematic representation of the synthesis of TTI-COF and TBI-COF from a triamine and a trialdehyde.

Low symmetry layers: oblong pores

As a first lower symmetry model, the in-plane C_3 symmetry was removed and varying the conformation of the imine bonds lead to oblong pores (Figure S4), while the eclipsed layer stacking was retained. This structural modification leads to a Pm symmetry unit cell with $a \neq b \neq c$ and $\alpha = \beta = 90°$, $\gamma = 120°$. Pawley refinement of the oblong model shows a relatively good fit (Rwp: 5.359) to the observed powder pattern of the TTI-COF (Figure 5-7). However, when the structural model was constructed and the cell parameters were applied based on the Pawley refinement (Table S 9.7-1), the structure was compressed in the b direction, resulting in aromatic C-C bond lengths as small as 1.36 Å. The oblong model is only able to fit the experimental XRPD pattern with a marked reduction of the cell parameter b with respect to a, more than would be expected by the

conformational changes of the imine bonds. This strain disfavors the oblong model as a cause for the experimentally observed reduction in symmetry.

Shifted layer model: slipped stacking

Another conceivable way to lower the symmetry of the unit cell is to shift the individual pseudohexagonal layers along one direction. This model follows previous calculations on boronate ester COFs predicting that a slipped configuration in flat 2D COFs is energetically much more favorable than eclipsed stacking, which lacks experimental confirmation so far.[290, 323] This model was implemented in a $P1$ unit cell with the constraints $a = b \neq c$ and $\alpha = \beta$, $\gamma = 120°$. Pawley refinement with the slipped model showed the best fit (Rwp (Pawley): 4.461, Figure 5-7, bottom) of the three applied models (Table S 9.7-1). The lattice parameters of the slipped model Pawley refinement were implemented and showed no signs of strain such as unrealistically small bond lengths or angles. The one-layer geometry optimized unit cell was then refined using Rietveld analysis. Initially, the slipping direction was fixed with the constraint $a = b$. To explore other possible slipping directions, the parameter space of different directions and magnitudes of slipping at constant layer-layer distance was used for refinement and plotted against the layer offset (Figure 5-6). The obtained "landscape" of stacking, maps the hexagonal symmetry of the individual layers and reflects the fact that not all slipping directions fit the powder pattern equally well when comparing constant lateral offsets. The preferred slipping direction in this COF is along [1 0 0] and all equivalent directions ([1 1 0], [0 1 0], [-1 0 0], [-1 -1 0], [0 -1 0]) (Figure 5-6).
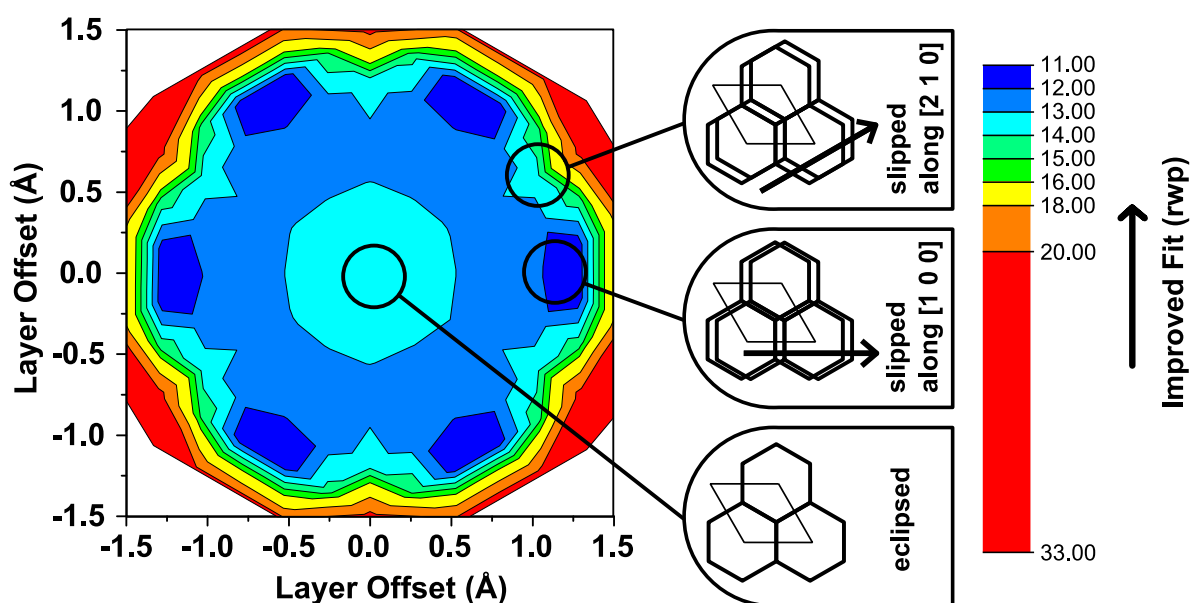
Figure 5-6: Contour plot of the relative quality of refinement (Rwp) of the slipping direction in the TTI-COF, by means of changing the α and β angles of the unit cell. To visualize the pseudo-hexagonal symmetry, the plot is shown in Cartesian coordinates, where the x-axis is collinear with the [1 0 0] and the y-axis with the [1 2 0] direction of the unit cell. The cartoon insets indicate the approximate stacking geometry of the respective positions in the refinement landscape.

The obtained models for the TTI-COF and the TBI-COF differ considerably despite the similarity of both COFs. To further confirm the models we performed periodic boundary condition DFT calculations in which the unit cells and atomic positions of the COFs were relaxed (Table S9.7-2). These showed a minimum for a slipped TTI-COF and a slipped TBI-COF. While the slipping in the TTI-COF is seen in the XRPD by the symmetry reduction, no such indication of slipping can be seen in the XRPD of the TBI-COF. In these DFT calculations the TTI-COF slips along [1 0 0] just as

observed in the XRPD refinement. The DFT based structure of the TBI-COF is slipped along [1 2 0], which is in contrast to the observed XRPD pattern showing *P*3 symmetry. In order to understand the difference between the DFT based structure and the observed powder pattern we performed DIFFaX simulations to find an explanation for the apparent higher symmetry obtained from the XRPD pattern (Figure 5-9).
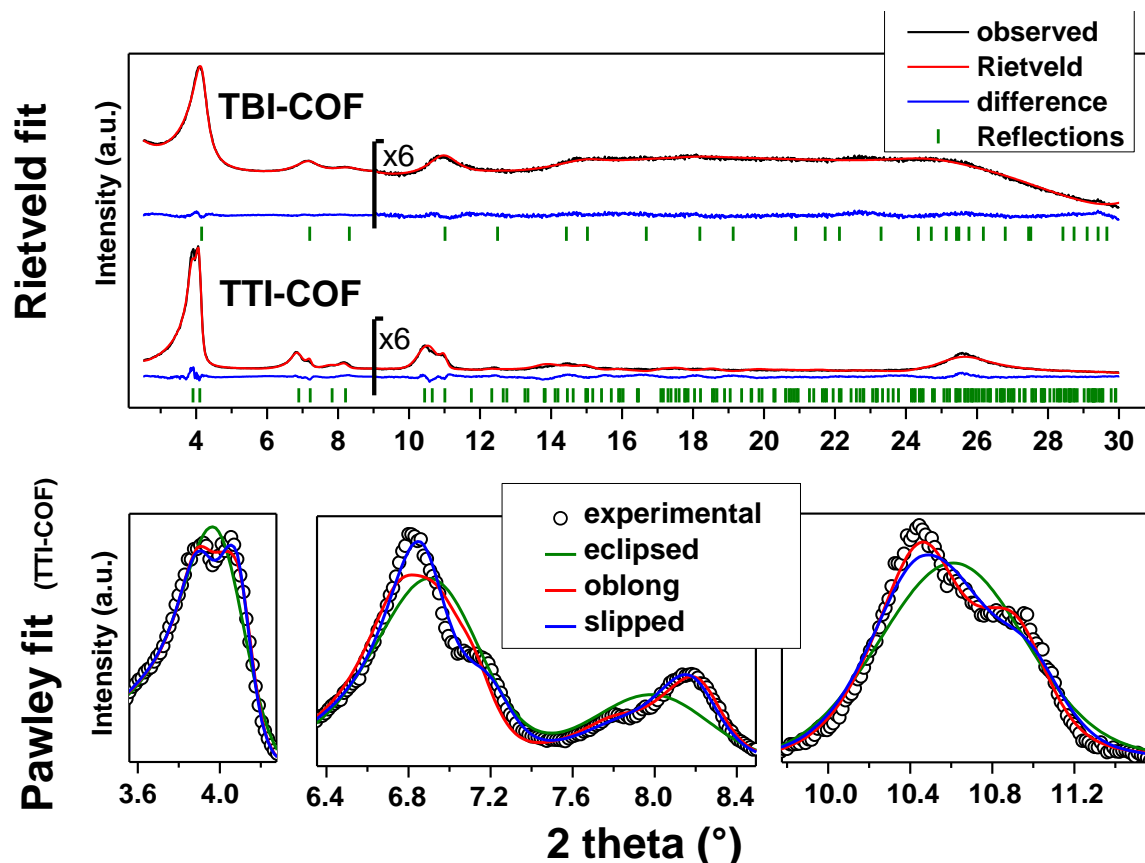

Figure 5-7: Top: XRPD patterns (λ = Cu Kα1) of the TBI-COF and the TTI-COF (black) with the final Rietveld fits of the COFs (red) and their respective difference curves (blue). Rwp (Rietveld) (see (1) in SI) values for the TTI-COF and the TBI-COF are 7.138 and 2.744, respectively. Bottom: XRPD pattern (λ = Cu Kα1) of the TTI-COF with eclipsed, oblong and slipped Pawley refinements with detail view of the reflections showing the reduction in symmetry.

In these simulations, as a simplified model subsequent layers of the structure had a chosen probability to slip in either one direction or the opposite, while the magnitude and the stacking offset was kept constant. When the probability of slipping in two directions becomes equal (0.5-0.5), the apparent symmetry of the simulated XRPD pattern increases to *P*3. Thus this simple model is able to rationalize the observed higher symmetry of the XRPD of TBI-COF, which can be attributed to disorder in the stacking of the TBI-COF. This confirms the often observed higher apparent symmetry of COFs, which results from an average structure due to the equal probability of energetically similar or equivalent slipping directions.[1, 290, 323, 324]
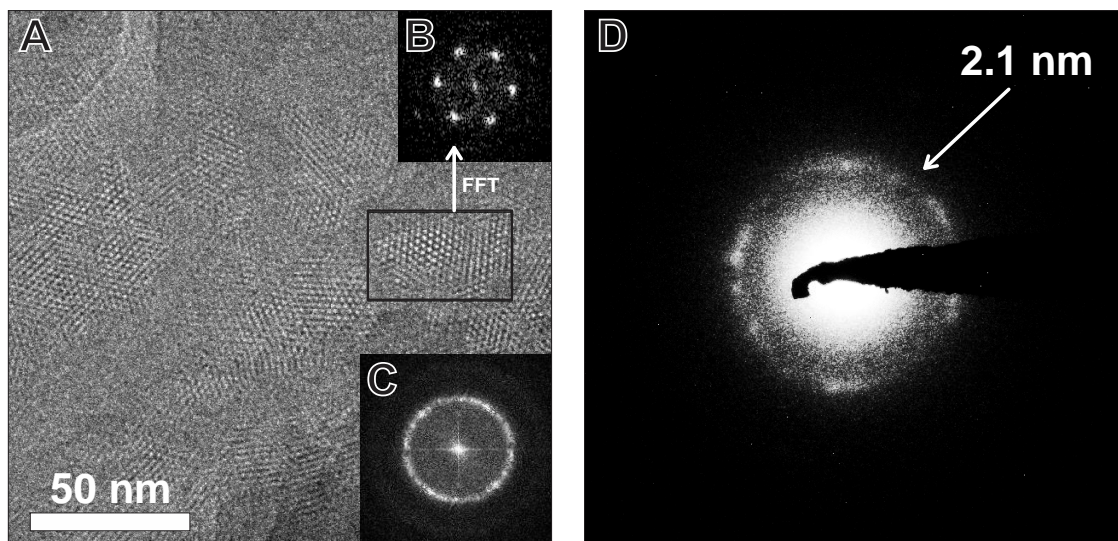
Figure 5-8: TEM image of the TBI-COF (A) with FFT of the entire image (C) and of the area indicated by the black rectangle (B). The SAED (D) shows the lattice spacing of the (100) and equivalent reflections, which are close to the value obtained by XRPD refinement (2.1 nm).

We performed transmission electron microscopy (TEM) and scanning electron microscope (SEM) experiments to confirm the results from XRPD and gain further insights into the local structural features of these COFs.
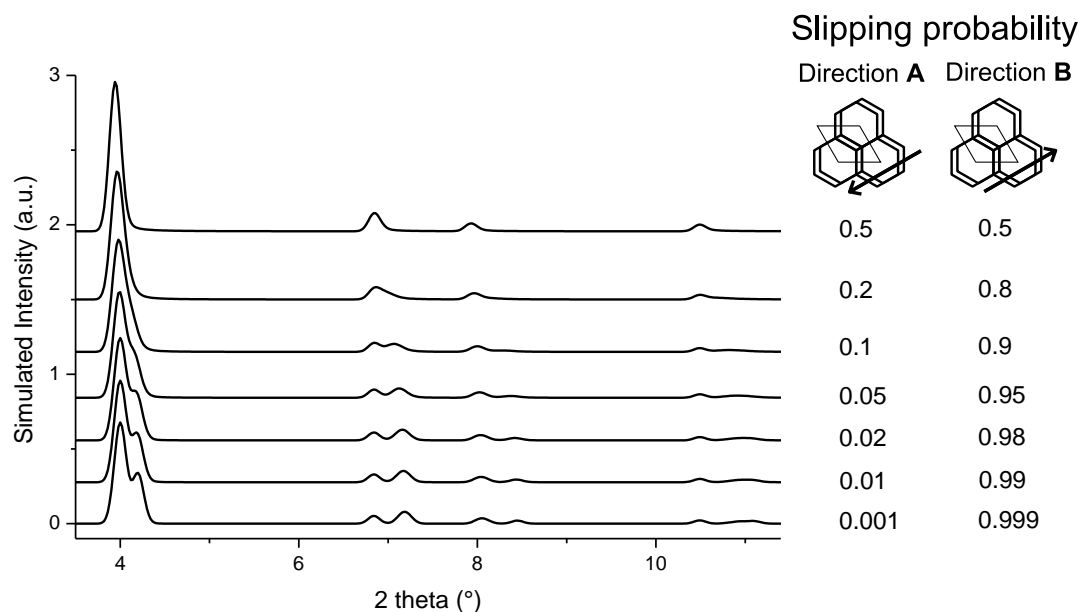

Figure 5-9: DIFFaX simulated XRPD pattern with varying degrees of disorder in the slipping direction [120] for the TBI-COF.

TEM images of the TBI-COF (Figure 5-8) show crystalline domains with domain sizes in the range of 30 nm up to 80 nm, which exhibit the hexagonal symmetry of the pores. The fast Fourier transform (FFT) and the selected area electron diffraction (SAED) patterns show the expected repeat distance of 2.1 nm that matches the (1 0 0) reflection obtained from the structural model based on the XRPD data. The morphology of the TBI-COF as observed in the SEM and TEM resembles individual slabs that are composed of smaller crystallites (Figure S5).
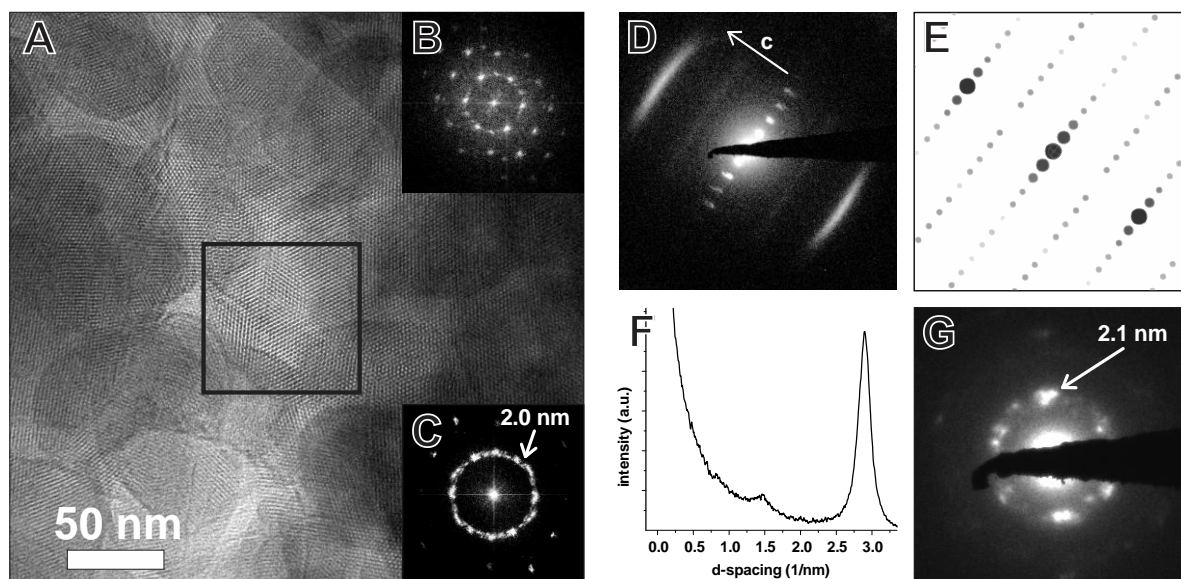
Figure 5-10: TEM image of the TTI-COF (A) with FFT of the area indicated by the black square (B) and of the entire image (C). The contrast-enhanced SAED (D, logarithmic contrast) shows a pattern taken along the [110] zone axis, which corresponds to the simulated SAED (E). Profile plot (F) along *c* corresponding to the [001] direction of the image D clarifies the streak features visible at 2.90 and 1.45 nm^{-1} corresponding to the (001) and (002) reflections, respectively. The SAED (G) shows the repeat distance of the (100) reflection with lattice spacing close to the value obtained by XRPD refinement (2.1 nm).

TEM of the TTI-COF shows significantly larger crystalline domains than the TBI-COF with crystallite sizes in the range of 50 nm up to 200 nm. The pseudo-hexagonal symmetry of the pores is apparent along the [001] zone axis, while the pore channels are visible when viewing in the direction along the a-b plane (Figure 5-10). The FFT and the SAED of the TTI-COF both show lattice spacing close to the values expected from XRPD. The microscopic morphology of the TTI-COF exposes large polycrystalline rods in which some crystallites show bending along the direction of the channels (Figure S5, Figure S6).
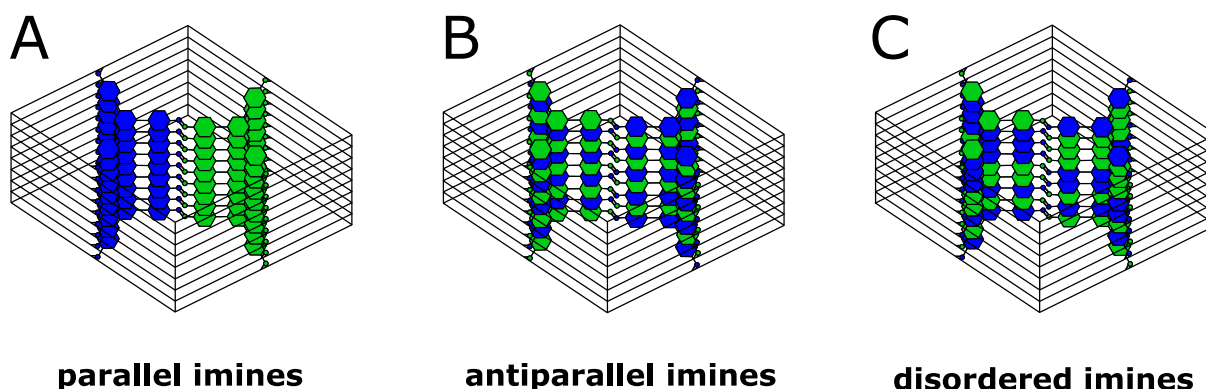
Figure 5-11: Three of the possible stacking motifs of the TTI-COF, where blue and green represent the amine and aldehyde building blocks, respectively.

The FFT shows the hexagonal pore structure of the COF along [001] (Figure 6B) as well as zone axes allowing the observation of 00*l* and *h-k*0 reflections simultaneously such as [110] (Figure 5-10 D). In addition to the sharp reflections from the (1-10) and higher order reflections, a prominent streak along (*hk*1) is visible at a distance of 2.90 nm^{-1} (3.5 Å) which is in excellent agreement with the expected layer-to-layer distance. Close inspection of the SAED reveals a further streak at the distance of 1.45 nm^{-1} (6.85 Å), which indicates the existence of two individual layers per unit cell along *c*. The

simulated SAED of a two-layer model fits well to the experimentally obtained SAED (Figure 5-10D, E; model: Figure 5-11, middle). In contrast to the simulation, the reflections (*hk*1) and (*hk*2) are smeared out to form streaks. The direction of these streaks indicates in-plane disorder as the cause of this diffuse reflection, since stacking disorder would cause streaks along c. A possible cause of in-plane disorder might be a random variation of the conformation of the imine linkages such as described in the oblong model. Since the SAED indicates two layers per unit cell, we developed possible models with different stacking geometries of imines with two layers per unit cell based on the structures of known molecular imines. From the crystal structures of molecular imine compounds three major geometric motifs are conceivable for the TTI-COF (Figure 5-11). Molecular imines have a variety of stacking modes, where sometimes one molecule exhibits different kinds of stacking in one crystal or differently stacked polymorphs exist for a single compound.[327] Ordered geometries include the direct slipped geometry where the imine orientation is the same for all molecules that are stacking (Figure 5-11 A),[328] and the antiparallel geometry with the imine orientation changing with a twofold axis from one layer to the next (Figure 5-11B).[329] These motifs are present in imines with different substituents and the influence of these might guide the stacking behavior.[327] A common motif for molecular imines with identical substituents is the disordered stacking leading to a pseudo inversion center on the imine bond (Figure 5-11C).[330-332] The symmetric substitution in the TTI-COF would point toward the disordered stacking, which however is not compatible with the observed SAED with clearly discernable streaks along (*hk*1) and (*hk*2).
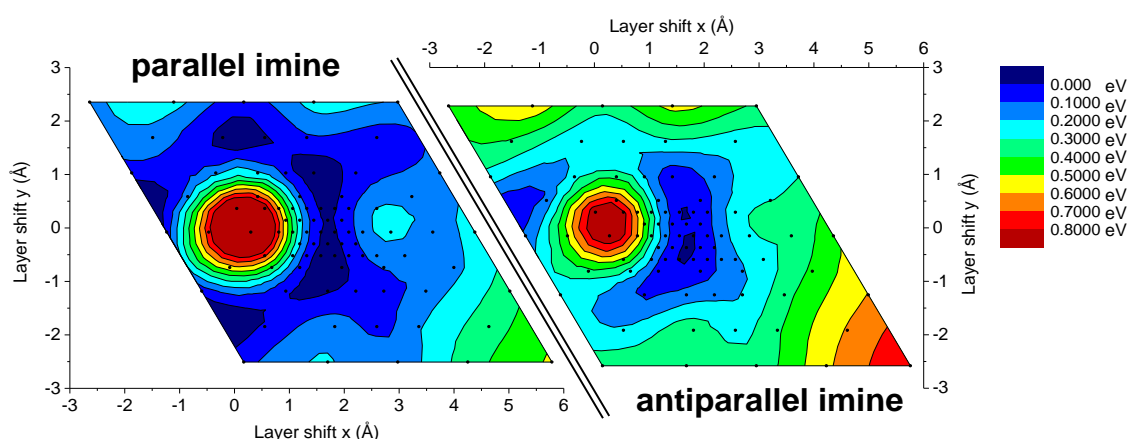

Figure 5-12: Energy landscape for slipping of the TTI-COF made of two extended layers that are slipped with respect to each other, while maintaining the stacking distance constant. The energy landscape was sampled in close proximity around the "ideal" offset, located at the center of each landscape. The layers were shifted with respect to each other at a constant distance between both layers. The obtained energies were normalized with respect to the lowest energy geometry. Values between data points were smoothed to aid the eye. A zero (0 Å, 0 Å) shift represents an eclipsed geometry.

To further narrow down the possible stacking geometries, we performed periodic boundary DFT calculations on two layer unit cells and compared whether the alignment of the imine bonds (Figure 5-11 A) or the antiparallel imine bond (Figure 5-11 B) are energetically more favorable. We relaxed the structures of the antiparallel imine and the parallel imine models and obtained two closely resembling slipped structures that match the obtained lattice parameters from Pawley refinement of the XRPD well (Table S9.7-2). The difference in total energy of these two structures was calculated and showed that the antiparallel configuration is more stable by approximately 0.32 eV (30.9 kJ/mol) per unit cell. This is not surprising, as an antiparallel stacking from one layer to the next leads to

donor – acceptor (DA) interactions between the more electron rich triazine triphenyl amine (TT-NH$_2$) and the electron poorer triazine triphenyl aldehyde (TT-CHO) across the layers, which is a well-known phenomenon for two flat molecules that have electron poor as well as electron rich character.[333] In addition, the antiparallel stacking creates antiparallel aligned dipoles, which stabilize the structure. The comparison of the parallel and the antiparallel stacking in the TBI-COF yielded only a negligible energetic difference of 0.04 eV (3.9 kJ/mol), which could be explained by a competition of the favorable DA stacking and the unfavorable geometric mismatch between the propeller shaped triphenyl benzene core (TB) and the flat triphenyl trizaine core (TT).
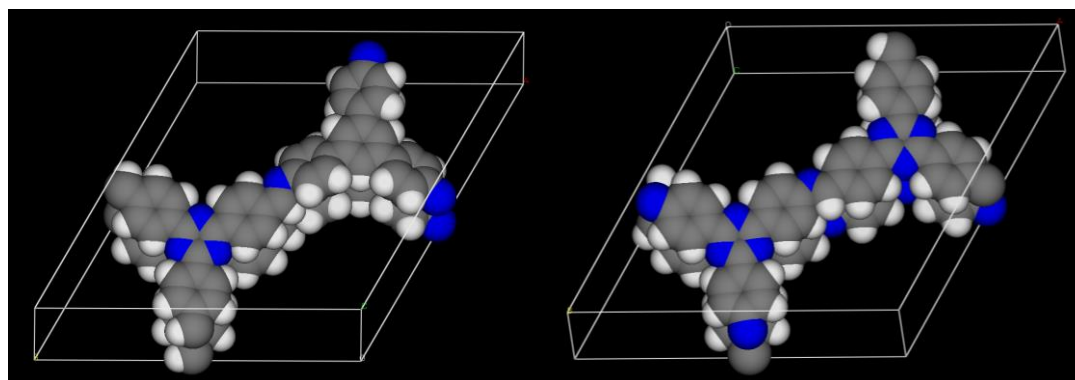
Figure 5-13: The DFT optimized structures of the TBI-COF (left, parallel) and the TTI-COF (right, antiparallel). Carbon atoms are shown in grey, nitrogen in blue and hydrogen in white.

To investigate the origin of the high crystallinity and the uniformly slipped geometry of the TTI-COF, we compared the energy landscape of stacking the layers with different offsets of the antiparallel and parallel imines (Figure 5-12), determined by DFT. In both energy landscapes, eclipsed stacking, corresponding to zero offset, is energetically non-favorable in contrast to the slipped geometry. The "parallel imine" stacking landscape shows a shallow and widespread minimum with multiple symmetry-related minima with a pseudo-hexagonal structure. Such an energy landscape might be expected to yield a random direction offset in stacking. In contrast, the "antiparallel imine" stacking landscape shows a reduced symmetry, which can be attributed to out of plane torsion of phenyl rings, which is more pronounced in the antiparallel imine case than in the parallel imine case (Figure S7). This torsion reduces the symmetry of one individual layer, but is also thereby able transfer the preferential slipping direction to the next layer, providing an explanation to the observed reduction in the symmetry by means of a uniform stacking direction. The comparison of both energy landscapes shows that in the case of the antiparallel imine bonds the minimum is steeper and less distributed than in the case of the parallel imine bonds. A steep minimum likely directs the crystallization process during the synthesis of the TTI-COF and therefore may be linked to the observed slipped stacking mode and the high crystallinity of the TTI-COF.

As the antiparallel stacked TTI-COF is the most stable configuration according to DFT, this structural model was used for the Rietveld refinement. The crystal structure consisting of two independent layers was refined using Rietveld methods, by refining the lattice parameters, atomic coordinates using rigid bodies for the layers and their shift with respect to each other. The final TTI-COF model is shown in Figure 5-13 and the corresponding refinement in Figure 5-7.

5.2.2. Discussion

As outlined above, the particular slip-stacking mode seen in the TTI-COF can be explained by an interplay of several factors that are different in the TBI-COF. Most notably, the TTI-COF is a flat

system, which allows the individual layers to slip freely, in contrast to out of plane elements, which can cause locking in of a structure.[83, 162] However, the flat structure alone does not seem to be sufficient for introducing uniform slipping, since many COFs are flat, but do not show the same layer offset in only one direction and hence, symmetry reduction, as observed in the TTI-COF.[1, 2, 290] Therefore, another factor influencing the stacking might be the self-complementary of the TTI-COF, which means that individual layers can form DA stacks just by alternation of the different building blocks along the c-direction (Figure 5-11). This feature is fairly unique, since it requires the use of two linkers with C_3-symmetry that have the same size, geometry, but different electronic structures. Generally, the parallel stacking of imines can be seen as a valid model for most imine COFs since conditions for self-complementary antiparallel stacking as outlined above are rarely met. If the size of the building blocks is different, then the contact during alternation would not be that intimate and the dipole of the imine bonds could not be aligned in a close, antiparallel fashion to enable favorable dipole-dipole interactions.[209, 280] In addition, the planarity of TTI-COF favors the DA stacking, which is in contrast to TBI-COF. The TBI-COF could be expected to stack with no offset between the layers (eclipsed) since it bears a propeller shaped building block.[83] However, the DFT calculations showed an energy minimum for an offset structure, which is why an averaged structure with an apparent zero layer offset is more likely for this COF. In principle, the TBI-COF could be expected to show an even more pronounced stacking in a DA fashion since a benzene core is more electron rich than the triazine core. However, the out-of-plane twisting of the TB system is likely to make efficient contact to the TT core in an adjacent layer difficult. Therefore, the lower crystallinity and the different observed stacking geometry of the TBI-COF is largely linked to the disturbance of planarity.

5.2.3.   Conclusion

In conclusion, we have synthesized two imine-COFs with similar molecular connectivity but distinctly different stacking geometries. While the TBI-COF adopts the archetypical random layer off-set as seen for most 2D COFs, giving rise to an average higher symmetry structure which is isostructural with eclipsed layer stacking, the TTI-COF shows an unusual slip-stacked geometry with uniform direction of the layer offset in each subsequent layer. SAED in conjunction with DFT calculations revealed a two-layer unit cell of the TTI-COF with antiparallel imines as a preferred stacking mode. The observed stacking preference of the TTI-COF directly translates into significantly increased domain sizes and crystallinity as compared to TBI-COF. DFT based energy landscapes for the stacking of the TTI-COF suggest that the alternate imine stacking creates steeper and deeper minima, which can be seen as the rationale for the uniform offset-stacking and the resulting improved overall crystallinity. In conclusion, the observed interlayer donor-acceptor type stacking interactions in TTI-COF may be used as a more general design principle based on non-covalent interactions that facilitate crystallization.

5.2.4.   Experimental

*T*ris(4-formylphenyl)*t*riazine (TT-CHO) and tris(4-aminophenyl)triazine (TT-NH2) were synthesized according to literature procedures.[196] All other chemicals were obtained from commercial sources.

Synthesis of the TTI-COF: TT-NH2 (0.0635 mmol, 22.5 mg), TT-CHO (0.0635 mmol, 25.0 mg), 1,4-dioxane (2.5 ml), mesitylene (2.5 ml), aqueous acetic acid (0.794 mmol, 6M, 0.132 ml) were added to a Biotage© precision glass vial, sealed and heated under autogenous pressure at 120°C for 72 h. After the reaction was allowed to cool down, the reaction mixture was filtered and washed thoroughly with ethanol, water, tetrahydrofuran and chloroform and then dried in high dynamic vacuum overnight.

6.   Chemical transformations of the COF linkage

The manipulation of COFs by post-synthetic modification has been demonstrated as a useful strategy for introducing additional functionality into COFs, be it by tethering side groups to the pore walls or by exchanging linkers reversibly in the preformed COF to incorporate labile linkers. These modifications are based on functionalizations that are orthogonal to the COF linkage reaction or utilize their reversibility. Manipulating the chemical nature of the reversible covalent bond presents a powerful tool to push the limits of COF utilization imposed by the reversibility of the COF linkage. Here we introduce strategies to alter the COF linkages in order to change their chemical and physical properties. This approach of approach of stabilization by modification of COFs has remained largely unexplored.

6.1.   Introduction

The defining features of COFs are the extended covalent connectivity and crystallinity, which are achieved currently by reversible reactions (reversible linkage COFs (RLCOFs)).[1, 169, 334] A high reversibility enables the synthesis of crystalline COFs by error correction and defect healing[278] but also increases the tendency of the COF linkages to be broken chemically or thermally. An extreme example for the tendency of weak bonds to be broken is the nitrosyl dimerization that has been used for the synthesis of COFs (Figure 6-1).[79] The formed azinedioxy bond is so weak (83-126 kJ/mol)[86] that the COFs can be simply recrystallized like molecular compounds from solution at room temperature. In addition, it was possible to synthesize large single crystals of this azinedioxy COF, which exemplifies how the weak bonding enables high reversibility and crystallinity. While most COF linkages are much stronger (i.e. imine: 418 kJ/mol)[86] they are still weak links by design. The prerequisite of a reversible bond formation inherently limits the chemical stability of COFs, some of which are labile towards mild conditions such as water, dilute acids or bases.[334] To increase the attractiveness for many applications chemical stability is a limiting factor.
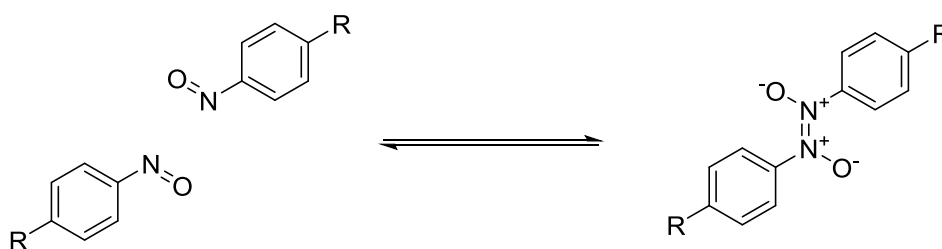
Figure 6-1: The nitrosyl dimerization reaction forming an azinedioxy moiety reversibly.

In an effort to balance crystallinity and stability, several ways have been devised to create stable but crystalline COFs. These can be separated into three categories: kinetic stabilization of the COF linkage, in situ stabilization by a reaction during COF formation, and lastly the stabilization of COFs by a subsequent reaction after the COF formation reaction by either a chemical or physical stimulus (Figure 6-2).
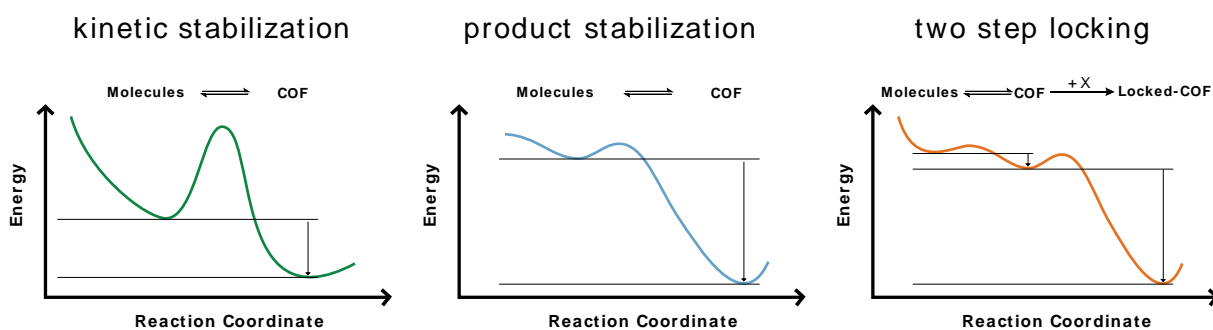
kinetic stabilization	product stabilization	two step locking

Figure 6-2: Schematic energy diagram of three strategies for generating stable COFs.

6.1.1. Kinetic stabilization

One method of stabilizing COFs against hydrolysis relies on the steric protection of the labile COF linkages. Boronate ester COFs are prone to attack by water from inside the pore and this access can be reduced by the introduction by aliphatic side chains.[335] The hydrophobic barrier created by the side chain hinders water from approaching the boronate ester. This example shows the introduction of kinetic barriers on purpose to stabilize COFs. However, steric stabilization may generally play a role in stabilizing 2D COFs as the linkages are sandwiched between layers. These provide protection from chemical attack from above and below the plane with the next layer presenting a physical barrier. In open framework 3D COFs no steric stabilization of this kind could be expected, thus exposing an inherently unstable bond to chemical attack.

6.1.2. In situ stabilization

The iminic nitrogen based functional groups, while more stable, can still get hydrolyzed with weak acids or bases.[284, 334] This was addressed by methods that stabilize the product of the COF linkage forming reaction. Most notable is the keto-enol stabilization approach pioneered by Banerjee and coworkers[284, 291, 336, 337] and the formation of oxazoles in situ.[68] These stabilization mechanisms reduce the back reaction by stabilizing the product. The intramolecular hydrogen bonding and the keto-enol tautomerism of imines based on o-hydroxy aldehydes can protect these bonds from hydrolysis.[291, 338, 339] This molecular motif has been used on many COF building blocks to stabilize the resulting COFs, but the most prominent example is the now widely used small molecule *triformyl phloroglucinol* that is able to perform the keto-enol tautomerism in its three subunits leading to a nonaromatic moiety (Figure 6-3). Similarly, the use of hydroxyl functional groups *ortho* to the amine stabilizes the network by cyclization to an oxazolane, which is subsequently oxidized to the oxazole in situ.[68]

The COFs resulting from these reactions showed improved chemical resistance but reduced crystallinity in comparison to non-stabilized COFs. A consequence of creating a more stable product is a reduction in reversibility, error-checking and thereby crystallinity, which leads to increased defect concentration, decreasing crystallite size and porosity.

keto - enol tautomerism   oxazole formation
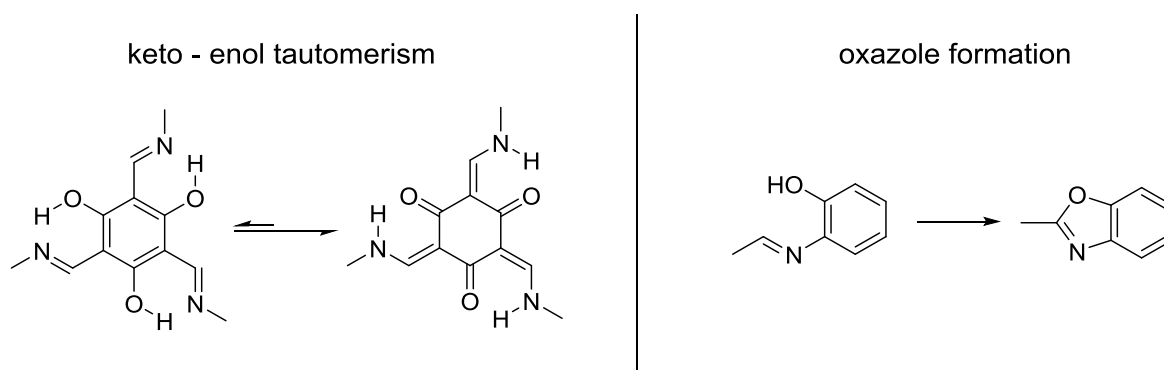
Figure 6-3 Stabilization mechanisms that were employed during crystallization to stabilize the resulting COF: keto-enol tautomerization in the triformylphloroglucinol linker (left);[284, 291] in situ formation of an oxazole from an ortho hydroxyl imine (right).[68]

6.1.3.   Triggered stabilization

In order to obtain crystalline and stable COFs, a highly reversible reaction and a stabilization mechanism are needed that are not affecting each other. The most straightforward approach to get stable and crystalline materials at low temperatures is the separation of the crystallization and the stabilization step. High reversibility can be ensured by performing an assembling reaction that uses only weak bonds allowing crystallization to obtain an unstable product. The second step takes into account the stabilization by chemical or physical stimuli inducing a topo tactic reaction that does not destroy the preformed order and creates bonds that are sufficiently stable, thereby locking the current crystalline state and protecting it from back reaction (Figure 6-4).
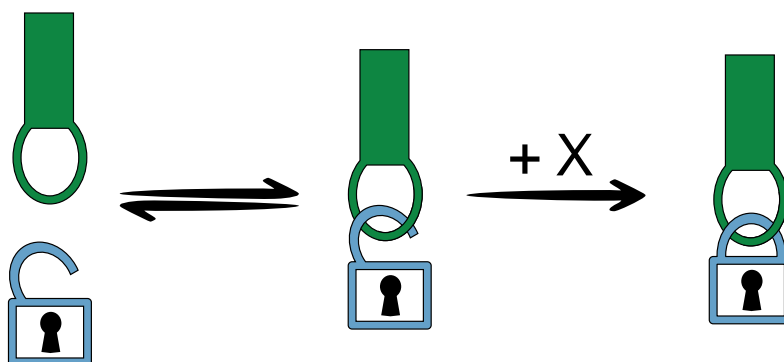
Figure 6-4: Schematic of how a reversible reaction can be locked with the help of a stimulus or reactant.

This approach has been used to generate compounds that cannot be synthesized in a direct route such as "unfeasible" zeolites[169] and molecular cages.[340] Crystalline metastable zeolites have been synthesized by chemically exfoliating a hydrothermally synthesized 3D zeolite into 2D sheets, crystallizing/reassembling them with additives into different stacking configurations and then locking the preoriented and predefined states through reaction with a reactive silane. The structure of the reassembled sheets is retained upon removal of the guest by calcination. Thereby, the synthesis of zeolites that would be difficult or impossible to produce with direct hydrothermal methods is possible. Another related example is the assembly of molecular cages where, similar to COFs, the synthesis proceeds through self-sorting of molecular precursors to obtain high yields of a certain cage configuration under thermodynamic control. The downside of this approach is again the low stability due to the undesired back reaction. The reversible linkage of the cage can be locked by transforming it

irreversibly by arresting *ortho*-hydroxy imines as carbamates thus inhibiting the back-reaction after the sorting reaction.[340]

A fundamentally similar, but chemically different approach is the crystallization of molecules with multiple anthracenes into molecular crystals and then inducing photodimerization in the solid state to covalently link the individual molecules to form highly crystalline 2D polymers.[175] The photodimerization itself can be reversed with the application of heat but this example shows that a very weakly bonded assembly can be polymerized topotactically into a strongly bonded material.
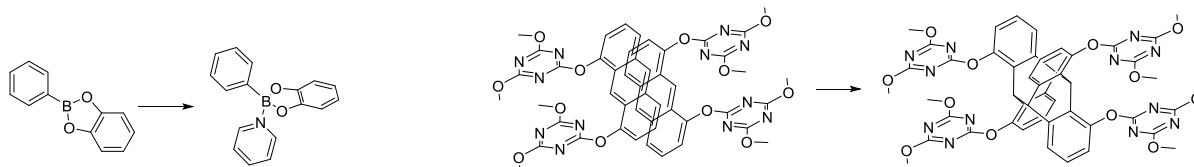
Figure 6-5 Two-step modification of a material to enhance stability. Left: sp^2-sp^3 transformation with pyridine in boronic ester COFs;[341] Right: photoinduced polymerization of molecular crystals by dimerization of anthracenes.[175]

In order to arrest COFs in their crystalline state (arrested linkage COFs: ALCOFs) the chemical linkage of the COF needs to be converted[334] from a reversible to an irreversible type of bond in a topochemical fashion. This approach was investigated at the beginning of research on COF chemistry with boroxine and boronate ester linkages that are especially prone to hydrolysis. The investigated means of stabilization were based on the fact that the sp^2-boron based molecules are prone to nucleophilic attack leading to bond cleavage and thus boronic ester linkages can be stabilized with nucleophiles to form sp^3 centers, such as by the addition of pyridines[341] or amines[342] to induce a coordinative saturation (Figure 6-5 left).

The first topotactic conversion of COF linkages was demonstrated by Waller et al.[334] where the imine linkage of two imine COFs were oxidized in mild and topotactic conditions to the corresponding amide linkages (Figure 6-6). The crystallinity was retained during this transformation reaction while the porosity was somewhat reduced (1250 -> 655 $m^2 g^{-1}$). The formed amide based COFs proved to be more stable with regard to chemical attack by acids such as 12M HCl and 1M NaOH at room temperature, showing that the chemical conversion of linkage groups is a viable strategy for stabilizing COFs. However, amide functional groups are still expected to be prone to hydrolysis under for example hot basic or strongly acidic conditions.[343] The possibility of amide bonds opening is further evidenced by amide type COFs that can be synthesized under reversible conditions such as imide-,[71] squaraine-,[72] cyanuric amide-[73] and the classical amide[70] linked COFs.
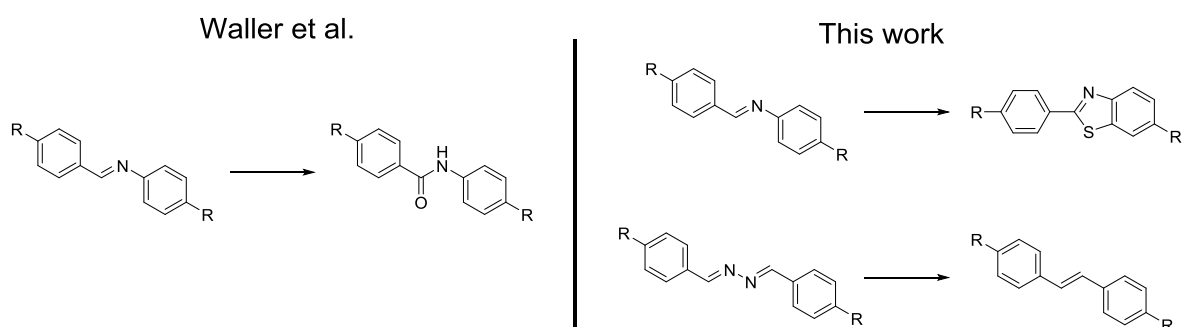
Figure 6-6: Chemical transformations in the COF backbone to lock the reversible bond: Oxidation of imines to amides.[334] (left), the oxidation and cyclization of imine to thiazole (top right) and the transformation of an azine bond to a stilbene (bottom right).

In this thesis two methods of altering the chemical linkages in COFs are presented, one based on the chemical conversion of two-dimensional imine-linked COFs into thiazole-linked COFs, while retaining its crystallinity and porosity, and the other based on the transformation of azine based COFs to their corresponding stilbenes, albeit with a loss of crystallinity.
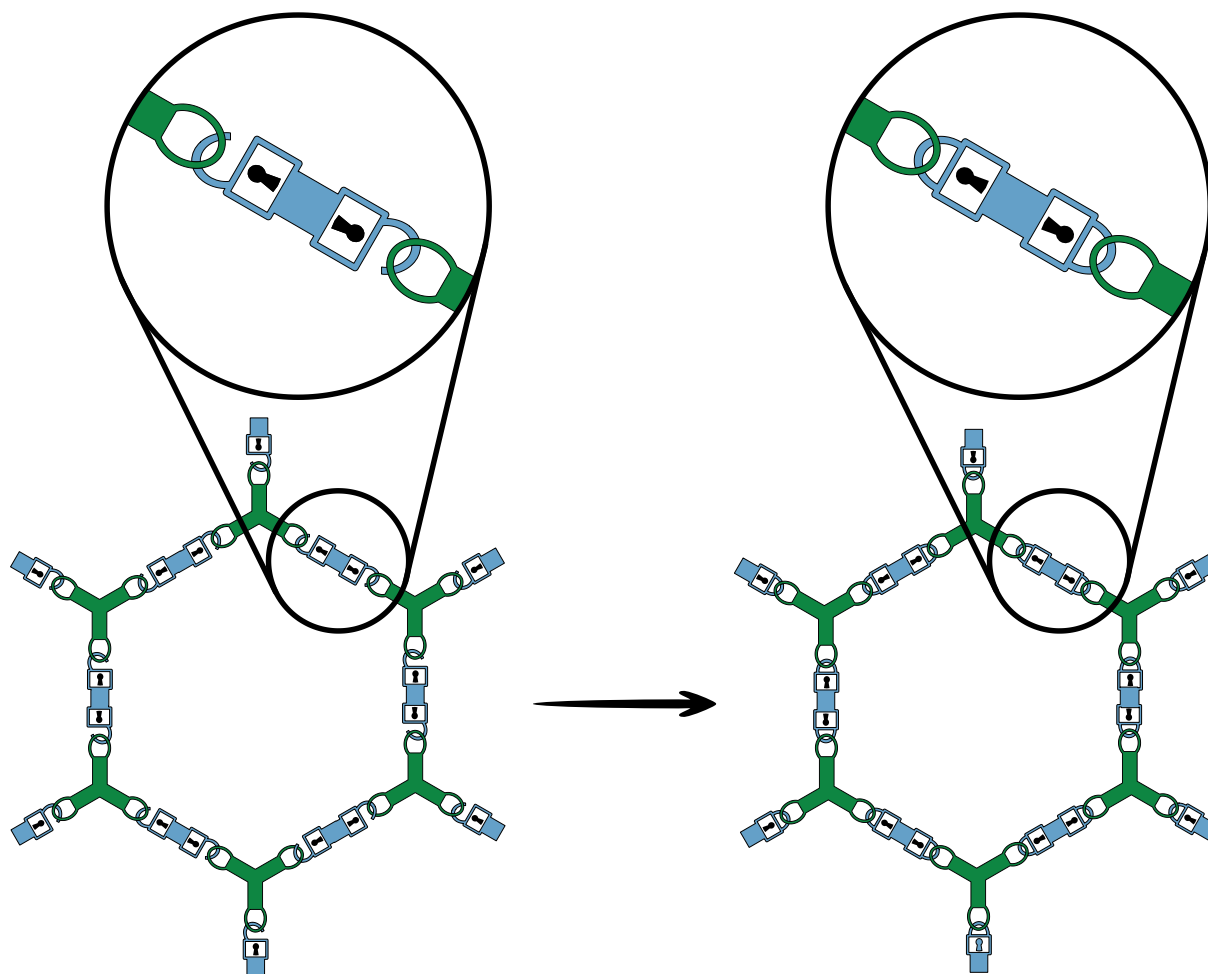

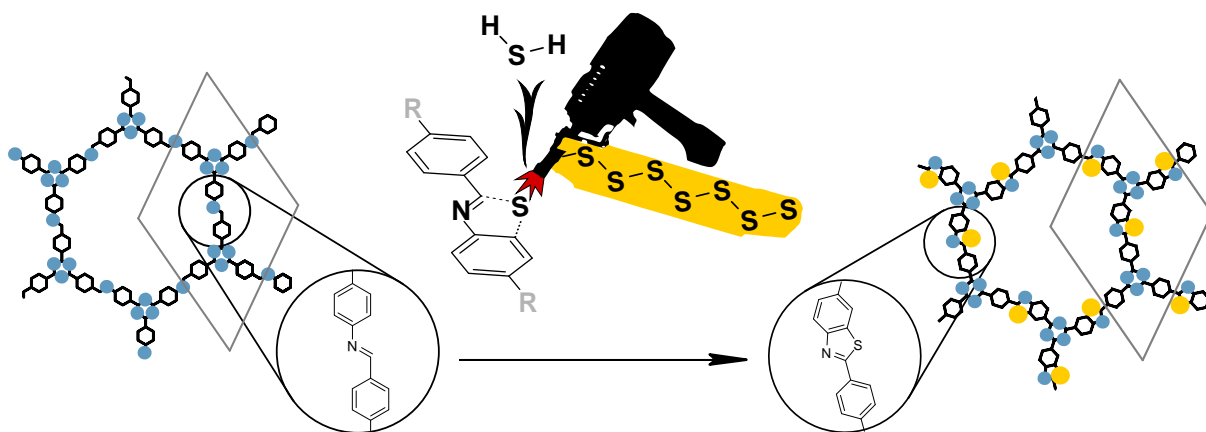Figure 6-7: Schematic section of a network structure that is locked without altering the topology of them material.

6.2.   Topochemical conversion of an imine- into a thiazole-linked covalent organic framework enabling real-structure analysis

This work has been submitted for publication:

In this work, we investigate the topochemical conversion of the imine-linked TTI-COF with elemental sulfur into a thiazole-linked COF through a post-synthetic locking strategy, thereby establishing a new class of thiazole-based COFs. This type of post-synthetic modification is fundamentally different from previous examples, such as the introduction of functionalities by tethering side groups [209] or heterogeneous linker exchange:[139] These approaches either do not change the reversible bond of the starting COFs, or they even utilize the reversibility to introduce functionality. The post-synthetic oxidation of an imine COF linkage to an amide, as reported recently, provides a direct transformation of the reversible bond of the COF;[334] however it was recently shown that even amides are, in principle, reversible enough to be used for the synthesis of COFs.[70] Modification of the imine linkage of the TTI-COF leads to excellent contrast and high electron beam stability of the sulfur-modified TTI-COF (TTT-COF), which enables imaging and analysis of in-plane defects with TEM, thus revealing details of real structure effects that have not been amenable to direct observation in any COF so far.

6.2.1. Results and Discussion

As pointed out by Yaghi et al., the promise of COFs lies in the fact that COFs, though being extended solids, are amenable to the versatile toolbox of molecular synthesis.[334] While this concept is particularly useful at the precursor level and hence formation of COFs, strategies for modifying the backbone of COFs once they are formed are extremely scarce.[334]
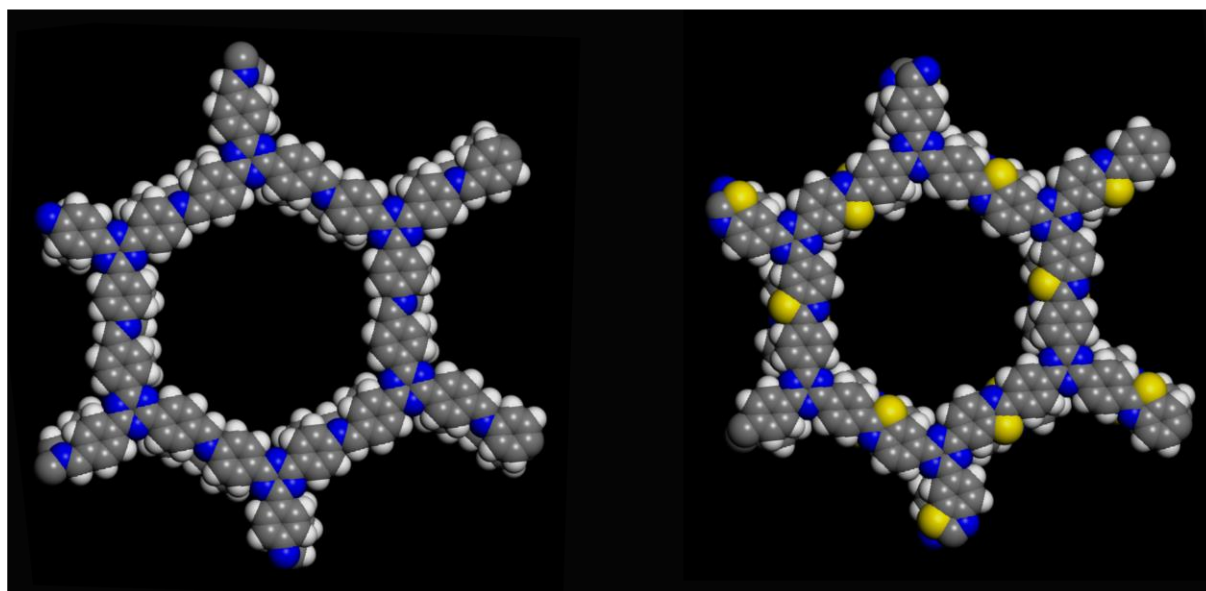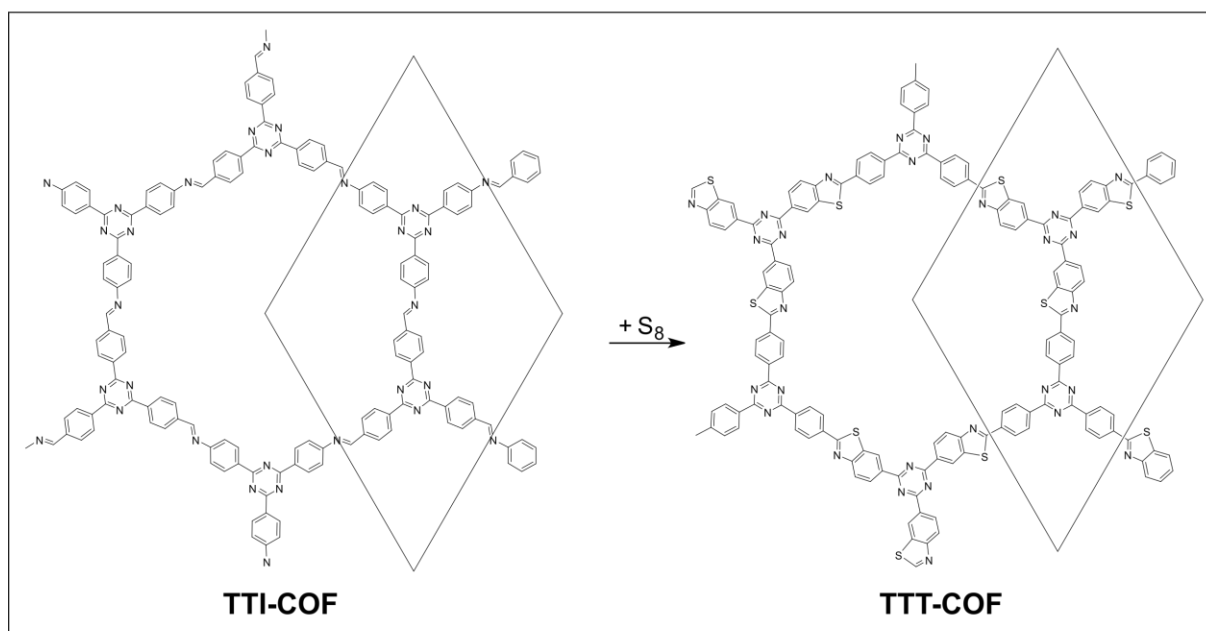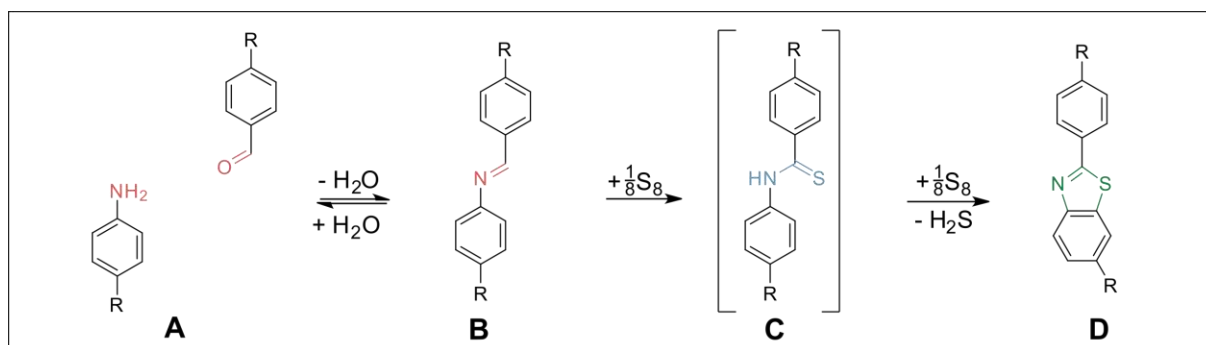
Figure 6-8: Top: Schematic of the reaction of an amine and an aldehyde (**A**) to form an imine (**B**), then a thioamide as an intermediate (**C**) by the action of elemental sulfur, and finally a thiazole (**D**). Middle: Schematic drawing of the sulfurization reaction of the TTI-COF to form the thiazole-based TTT-COF. Bottom: space filling model of one pore of the TTI-COF (left) and the TTT-COF (right).

We thus explored the post-synthetic reaction of COFs with elemental sulfur. At high temperatures, elemental sulfur reacts with aromatic imines to first oxidize the imine to a thioamide, and

subsequently oxidatively cyclizes the thioamide group to form a thiazole ring (Figure 6-8).[344] Thus, sulfur serves as an oxidant (being reduced to H_2S) and as a nucleophile, attaching first to the imine carbon and afterwards to the phenyl ring on the nitrogen side of the imine.

Transferring this reaction scheme to imine-linked TTI-COF, which was previously reported by us to show high thermal and chemical stability,[196, 278] we synthesized TTT-COF in two successive steps: First, TTI-COF was infiltrated with molten sulfur at 155 °C. At this temperature, sulfur has minimum viscosity, enabling mixing with the COF material. Subsequently, by using a thermal treatment at higher temperature (350°C), the conversion of the TTI-COF to the TTT-COF took place. After removal of the excess sulfur by Soxhlet extraction and under high vacuum, the obtained material was investigated by ^{13}C and ^{15}N solid state NMR (ssNMR) to probe the imine to thiazole conversion and retention of the framework structure (Figure 6-9). As shown in Figure 6-9 A and B, the ssNMR spectra of TTT-COF shows significant and well-defined changes as compared to the TTI-COF precursor. The loss of the carbon **3** and **4** signals at 151 ppm and 115 ppm (in TTI-COF) in the ^{13}C ssNMR spectra, together with the appearance of the **3'** signal at 156 ppm for the TTT-COF, indicate the conversion of the nitrogen bearing phenyl ring to the thiazole in TTT-COF. Small residual intensity at 151 ppm might indicate some unreacted TTI-COF. Furthermore, the characteristic imine carbon **2** is shifted in the thiazole **2'** as a shoulder to the triazine carbon **1'**.[345, 346] Also, the absence of a ^{13}C signal between 210 and 180 ppm[347] hints at the conversion of the imine to the thiazole and the absence of thioamides. ^{15}N ssNMR shows the triazine nitrogens, **6** and **6'**, at the same position for TTT-COF as for TTI-COF and a shift of the imine nitrogen **5** from −55 ppm to the thiazole **5'** at −71 ppm. As additional confirmation of the determined thiazole structure of the TTT-COF, the calculated NMR chemical shifts of excised fragments (Figure 6-9 A + B, Table S 3, Table S 4, Table S 5, Table S 6) are in good agreement with the experimental NMR spectra. ^{13}C and ^{15}N NMR chemical shifts were calculated with DFT on the B97-2/3/pcS-2//PBE-D3/def2-TZVP level of theory (Figure S 110, Figure S 111, Figure S 112, Figure S 113, Figure S 114), as we already applied this method successfully to other COF building blocks.[189]
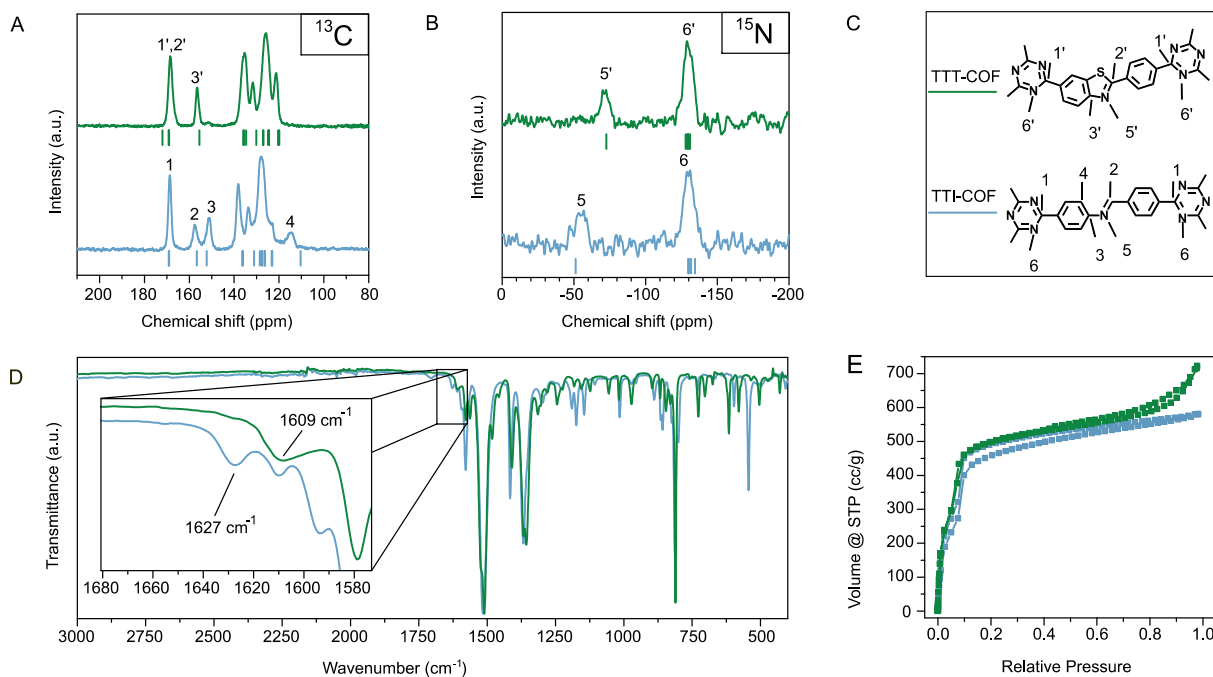
Figure 6-9: Characterization of the TTI-COF (black) and TTT-COF (red). (A) ^{13}C ssNMR demonstrating the conversion of the imine linkage to the corresponding thiazole. (B) ^{15}N ssNMR showing a shift in the imine nitrogen position (5 → 5'). Calculated $\Delta\delta$ values for the TTT and TTI-COF on B97-2/pcS-2 level of theory are shown as red and black dashes, respectively. (C) Assignment of the ^{13}C and the ^{15}N ssNMR signals to the respective ^{13}C and ^{15}N nuclei in the structures. (D): FT-IR spectra of TTI-COF (black) and TTT-COF (red). The inset shows an enlargement of the region characteristic for N=C vibrations (E) Argon sorption isotherms of TTI-COF and TTT-COF showing retention of porosity.

The FT-IR spectra further confirm the conversion of TTI-COF to TTT-COF, as evident by the disappearance of the characteristic imine (N=CH) vibration at 1627 cm^{-1} and the appearance of a new N=C vibration[346] of the thiazole at 1609 cm^{-1} (Figure 6-9 D, Figure S 117). Elemental analysis shows the presence of sulfur with an elemental composition close to the composition that would be expected from the thiazole model (Table S 7). In addition, energy dispersive X-ray spectroscopy (EDX/SEM; Figure S 119) of TTT-COF indicates homogeneous distribution of sulfur in all parts of the sample, thus verifying a uniform and regular incorporation of sulfur in the COF backbone. The XRPD confirms the complete absence of reflections originating from elemental sulfur, further validating that only chemically bound sulfur is present (Figure S 125).

Sorption analysis reveals retention of the porosity of the TTT-COF after sulfurization (Figure 6-9 E); the BET surface area of 1431 m²/g for the TTT-COF (theoretical surface area 1609 m²/g) being close to the BET surface area of 1362 m^2/g for the precursor TTI-COF (theoretical surface area 1970 m²/g) (Figure S 120). The ratio of experimental BET to theoretical surface area is seen to be improved upon sulfur incorporation. This not only indicates that the pores have not been blocked by sulfur deposits, but also that previously blocked pores might have been "cleaned" by oxidative or evaporative removal of guests in the pores. The pore size distribution was calculated from Argon isotherms using the QSDFT cylindrical pore model, which shows a reduction in the pore size from 2.3 nm in the TTI-COF to 2.2 nm in the TTT-COF (Figure S 121). This change in the pore size matches well with the reduction in lattice parameters observed in the XRPD and the expected pore size reduction by the bending of the linkers upon formation of the thiazole.

The structure and crystallinity of TTT-COF was then assessed with X-ray powder diffraction (XRPD), revealing a crystalline material with a hexagonal unit cell ($P6_3/m$) and a higher symmetry

than derived for the precursor TTI-COF (*P*1) (Figure S 122).[278] However, TTT-COF is quite similar to the randomly stacked TTI-COF (rs-TTI-COF, *P*6$_3$/m) (Figure 6-10 A), which is identical to the TTI-COF in terms of molecular connectivity, but shows random orientation of the stacking vector of the layers due to the altered synthesis conditions (see Methods section), and hence a higher apparent symmetry.[278] TTT-COF has reduced in-plane unit cell dimensions (24.478(5) Å vs 25.244(8) Å), and a larger interlayer stacking distance (*c* = 7.002(5) Å) than rs-TTI-COF (*c* = 6.905(7) Å) as is evident from Rietveld refinement (Table S 8, Figure S 122). The smaller *a* and *b* axis of the unit cell can be understood by the contraction induced by bending of the linker upon formation of the five-membered thiazole ring (Figure S 124). The larger stacking distance likely stems from the introduction of sulfur into the layers, also signaling a somewhat weaker interlayer interaction. This may explain the loss of the ordered slip-stacking that is present in TTI-COF (Figure S 122). Rietveld refinement of the XRPD pattern of TTT-COF was done using an imine model and a thiazole model; a significantly better fit was obtained for the thiazole model, which further confirms this structural feature in TTT-COF (Figure 6-10 B, Table S 9).
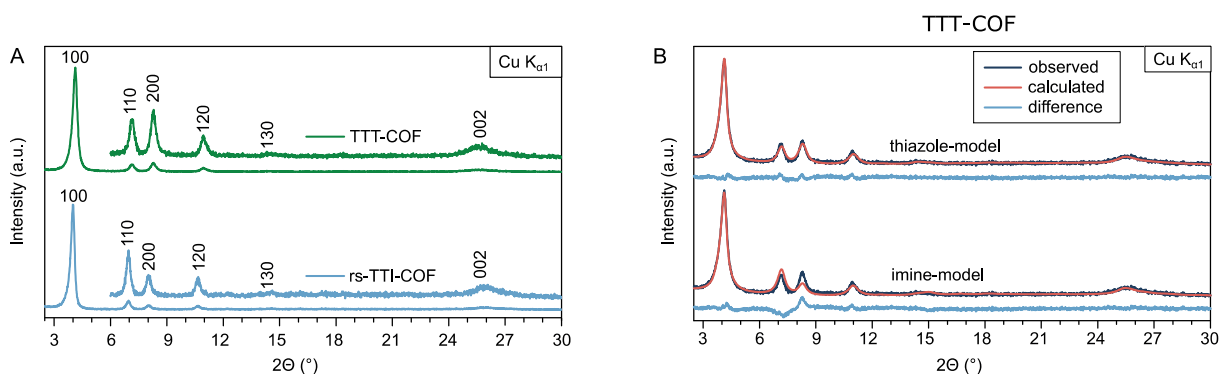
Figure 6-10: (A) XRPD patterns of the rs-TTI-COF and the TTT-COF showing retention of crystallinity upon transformation. (B) Comparison of the imine and thiazole models that were applied during Rietveld refinement of the XRPD TTT-COF. The thiazole model (top) shows a better fit than the imine model (bottom).

To demonstrate that the concept of imine to thiazole conversion in COFs can be generalized and transferred also to other COF systems, we performed the reaction on the pyrene-containing PBI-COF (*P*yrene tetra(phenyl) *biphenyl i*mine-COF, Figure S 115),[160] which was transformed to the PBT-COF (*P*yrene tetra(phenyl) *biphenyl* thiazole-COF, Figure S 115). In the PBI- and PBT-COFs the conversion is clearly evidenced by ^{13}C ssNMR as well, which shows the appearance of two peaks at 153.3 ppm and 166.8 ppm, with the latter corresponding to the characteristic thiazole carbon between the nitrogen and the sulfur (Figure S 116). Note that in the TTI- and TTT-COFs, this region is obstructed by the presence of the triazine carbon (**1** & **1'**, Figure 6-9 A). Similar to the TTI- to TTT-COF conversion, the PBI to PBT-COF conversion is evidenced by the disappearance of the vibration at 1622 cm^{-1} that corresponds to the characteristic imine stretch, and by the presence of a vibration at 1602 cm^{-1} in the PBT-COF that can be assigned to the thiazole moiety (Figure S 118).

As in the TTI-to-TTT transformation, crystallinity was retained during the transformation of the PBI-to PBT-COF (Figure S 126), while the in-plane lattice parameters *a* and *b* of the Rietveld-refined structures differ less between PBI- and PBT- COF (Figure S 126, Table S 10) as compared to the TTI- and TTT-COF (0.60 Å and 1.58 Å for the PB and the TT system, respectively). This effect is attributed to the lower degree of structural distortion during the sulfurization reaction, as seen in Figure S 127.

As the transformation of the imine-based TTI-COF to the thiazole-based TTT-COF is expected to significantly improve the chemical stability, we assessed the possibility of locking the reversible bond

by comparing the crystallinity before and after chemical treatment. Both materials were exposed to identical and extremely harsh conditions, to test the limits of stability of both COFs. Initially both COFs were treated with concentrated hydrochloric acid, after which both COFs showed no signs of degradation, testifying to the already excellent resistance to acids of TTI-COF. In contrast, other imine-based COFs have previously been reported to be labile under strongly acidic conditions.[334] The treatment of TTI-COF with KOH lead to a near complete loss of crystallinity, while the TTT-COF remained unaffected. Next, we tested reagents that are known to alter imine bonds: hydrazine is a particularly good nucleophile that enters the imine bond and replaces the amine, which then leads to a loss of order; sodium borohydride, a reagent that is used to reduce imine bonds could lead to a loss of rigidity, followed by a collapse of the structural order. In both cases the TTT-COF remains essentially unaffected, while the TTI-COF turns completely amorphous. This result shows that the imine bond has been locked as a thiazole, while the ordered structure of the TTT-COF is retained. The resilience of the TTT-COF to reactive conditions and reagents could enable a range of applications that were previously not accessible due to the lability of COFs.

Chemical stability
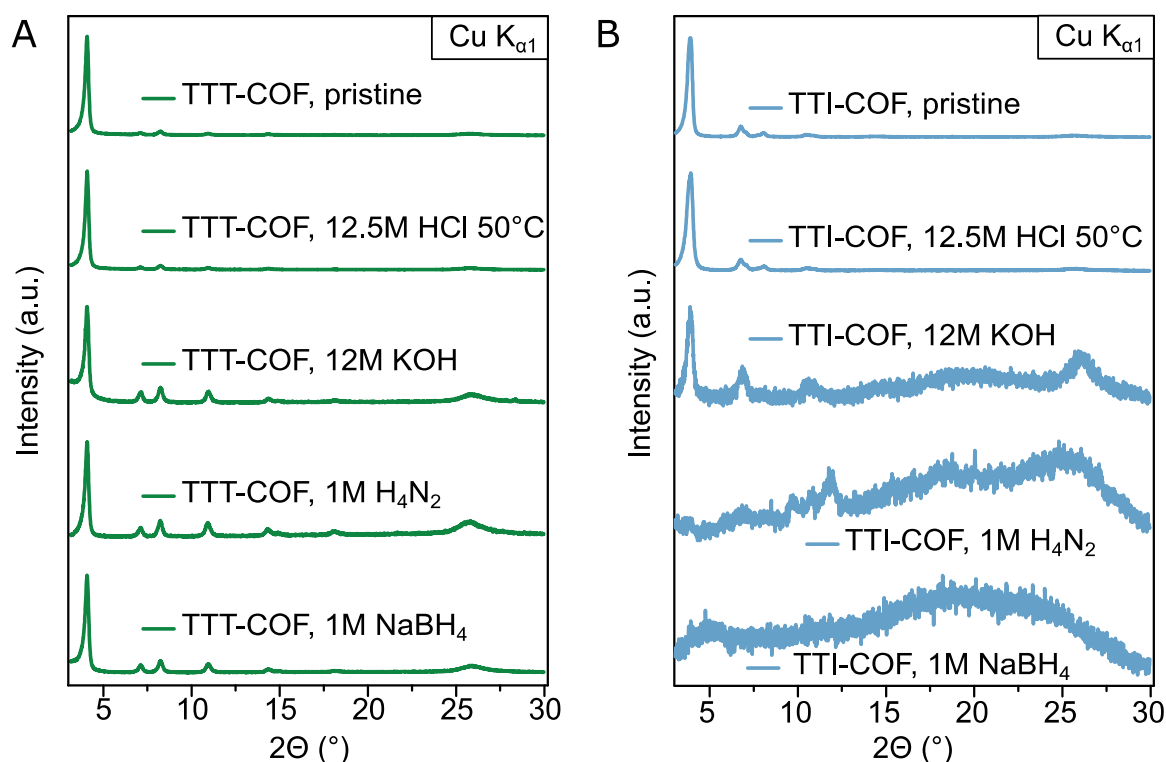
Figure 6-11: Chemical stability tests as judged by the crystallinity of the frameworks after exposure to various aggressive chemicals. The TTI- and TTT-COF samples were each exposed to identical conditions for 16 h, which showed a substantially higher stability of the TTT-COF against reactive conditions.

TEM investigations in COFs have so far primarily been used to confirm the periodic structure of COFs,[2, 177, 196, 278, 348] their nano- and micron-scale morphology,[337] and the presence of inorganic guests.[2, 349] However, the low contrast in COFs and their low electron beam stability generally render a detailed analysis of COFs with TEM highly challenging as the samples easily decompose before useful information can be extracted. The destruction of COFs in the electron beam can be ascribed to different damaging mechanisms: One of the defining features of COFs is their composition out of light elements, which makes them difficult to image since such atoms can be significantly affected by

atom displacement, electron-beam sputtering, electron-beam heating, electrostatic charging, and radiolysis.[350]

The TTI- and TTT-COF were analyzed by electron microscopy, where TEM and SEM revealed a morphology of inter-grown crystallites with a slightly anisotropic shape in both COFs (Figure S 128). Imaging TTI- and TTT-COF by TEM suggests significantly increased electron contrast for TTT-COF and improved electron beam stability as compared to TTI-COF and other COFs.[2, 278] First, we quantified the stability of the TTI- and the TTT-COF in the electron beam by taking images at defined time intervals, under otherwise identical conditions. Visual inspection of the images revealed gradual decomposition of the TTI-COF upon electron beam exposure as evident by shrinking of the structure as well as diminished lattice fringes (Figure S 129). Quantitative analysis of these images by means of their fast Fourier transform (FFT) showed a continued broadening and shift to larger d-spacings for the peak corresponding to the 100 reflection in the XRPD. The continuous shift in d-spacing can be fitted by an exponential decay from which half-lives can be extracted. TTI-COF has an average half-life of 1.22 min, while TTT-COF displays a significantly increased half-life in the electron beam of 2.83 min (Figure S 130), thus clearly pointing to the higher stability of TTT-COF in the electron beam (Figure 6-12). While the higher electron contrast in the TEM images of the TTT-COF results from the regular incorporation of sulfur into the lattice, the improved stabilization is likely due to the "aromatization" of the imine bond in the form of a thiazole and the lower number of hydrogen atoms in the structure, which are most susceptible to electron beam damage.[350] This improved stability is crucial for exploring the real structure of the TTT-COF with TEM as described in the following.
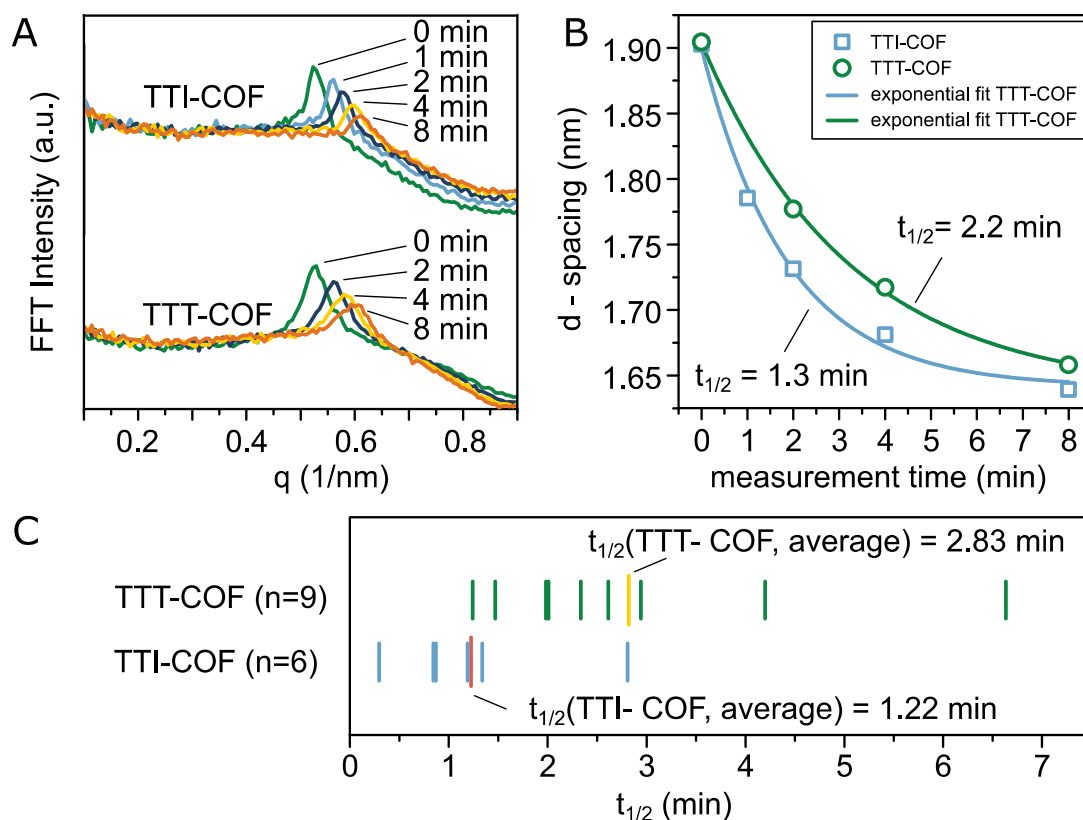
Figure 6-12: A: Electron beam damage seen by the broadening and a shift of the peak in the FFT, corresponding to the 100 reflection in XRPD, of TEM images taken after different exposure times. B: Plotting the exposure time against the peak shift in the FFT shows a decay that can be fitted with an exponential (fit parameters shown in Table S 11). C: Several sets of images were analyzed this way and the results are depicted graphically for better comparison. The average half-life of each system reveals the higher stability of the TTT-COF as compared to TTI-COF.
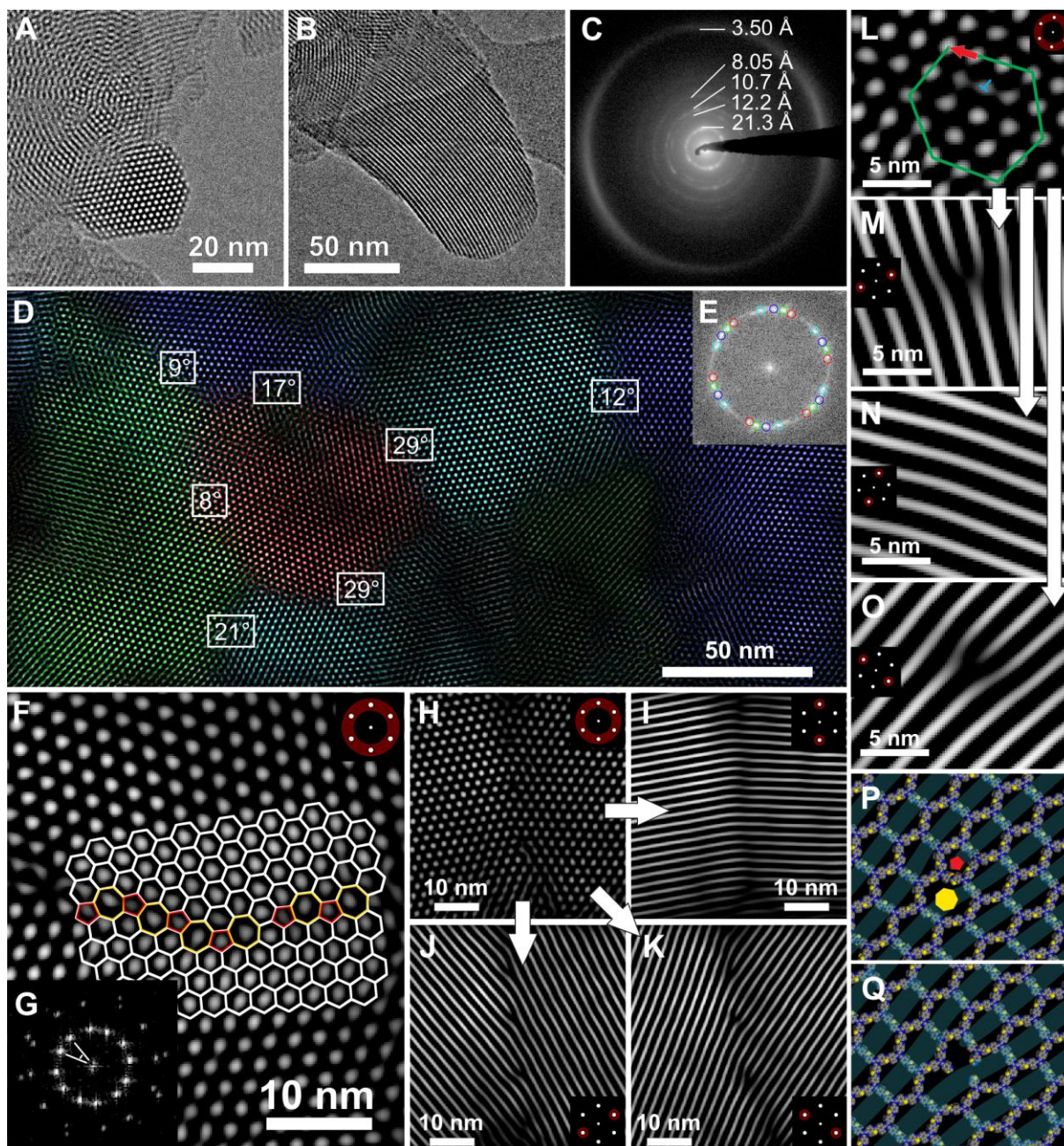
Figure 6-13: TEM images and TEM analysis of TTT-COF. FFT filters applied to the image are indicated by a schematic inset. A, B: Individual crystallites in different orientations. C: SAED with logarithmic contrast showing diffraction rings, which are in agreement with the XRPD pattern. D: Multiple intergrown grains visible by TEM. Indicated angles show the relative orientation of neighboring crystallites. Color overlay indicating the individual grains generated by applying selective hexagonal Fourier filtration (E). F: High angle grain boundary of crystallites with co-aligned c direction with an overlay indicating the interface consisting of five, six and seven membered rings. G: FFT of image F. H, I, J, K: Low angle grain boundary with different Fourier filters applied, visualizing the starting points of edge dislocations. L: Close-up of the start of an edge dislocation. The beginning of the edge dislocation is indicated by the blue T, the Burgers vector (red arrow) is determined from the green hexagon to be (100). M, N, O: visualization of the edge dislocation position from image L with different Fourier filters. P, Q: Modeling of an edge dislocation in Materials Studio utilizing a screw dislocation along the pentagonal (red pentagon) and the heptagonal channel (yellow heptagon) (P) and the edge dislocation visualized as a channel linker vacancy (Q).

TEM images of TTT-COF reveal an overall retention of the crystallite size compared to the precursor TTI-COF (50-200 nm); likewise, the crystallinity seen already for the TTI-COF is clearly retained as well.[278] The hexagonal symmetry of the structure is visible from the real space images (along the

[001] zone axis, Figure 6-13, A), which also show the presence of continuous pore channels when viewed along [hk0] (Figure 6-13, B). Both real space images and selected area electron diffraction (SAED) patterns (Figure 6-13, C) are in agreement with the structural model developed with Rietveld refinement (see also Figure S 131, Figure S 132, Figure S 133).

In addition, TEM reveals a host of real structure details of TTT-COF, including many forms of defects such as disorder, twin and grain boundaries. Several observed grains of the COF have co-aligned *c*-axes but are rotated against each other in the *ab*-plane (Figure 6-13, D). Two main types of boundaries are visible between grains: high angle grain boundaries (HAGB) and low angle grain boundaries (LAGB). HAGB are formed by a corrugated interface of adjacent five and seven membered rings in contrast to the normal six membered rings in the ordered TTT-COF, as shown in Figure 6-13 F. Some crystallites have an angle of 29° between them, previously observed by TEM in covalently connected grain boundaries of single-layer graphene showing "quilt"-like structures,[351] similar to the co-aligned crystallites of TTT-COF. It was not possible to discern unambiguously whether a covalent interface exists between the grains due to increased radiation damage at higher magnifications. However, having this many different crystallites in such an oriented way and intimate contact between the different domains suggests an alignment of these domains during synthesis, which is likely induced by covalent connections.

A likely mechanism for the formation of the observed grain boundaries is the crystallization of grains from an initially amorphous imine gel (Figure 7) as has been proposed as a formation mechanism for imine COFs by Dichtel and coworkers.[144] This mechanism implies that the covalent connectivity between the different grains is present from the initial formation of the polymer on and that the grain boundary is left as a remnant of this amorphous state.
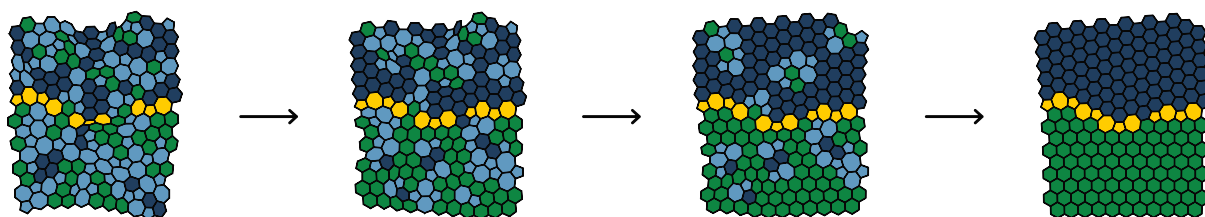
Figure 6-14: Schematic of the proposed mechanism for the formation of grain boundaries by crystallization of an initially amorphous gel.

The intergrowth is even more likely for LAGB as these present a nearly continuous transition from one crystallite to another. Inspection of the LAGB with different Fourier filters shows the presence of several edge dislocations (Figure 6-13 H-K). Details of such an edge dislocation with a Burgers vector of [100] are shown in Figure 6-13 L-O. At the molecular level, such a defect could be described by either a linker vacancy (Figure 6-13 P-Q, and supplemental discussion) or an out-of-plane growth that resembles five- and seven-membered rings such as spirals (see also supplemental discussion). Features such as five membered rings and the growth of spirals have similarly been described in the simulation of the crystallization of COF-5, thus predicting the presence of these features in a COF, which have been observed here.[107]

The observed defects in TTT-COF might have important implications for the properties of the COF. The grain boundaries of the co-aligned crystallites would not obstruct the pore channels and therefore are not expected to influence properties that are primarily contingent on the porous nature of COFs, such as their use as a sorption material or membranes where continuous mass transport is important. The electronic or excitonic conductivity in COFs is assumed to require ordered π-stacking for charge carrier percolation perpendicular to the layers,[152] while the transport of charges is also possible

within the *ab*-plane of the individual layers.[352] In the latter case the covalent connection and co-alignment of the COF layers could still enable charge transport from one grain to another, rendering limitations through reduced grain boundary conductivity less severe. The presence of defects extending beyond one layer such as out-of-plane helices would essentially turn the 2D COF into a covalently connected 3D COF (Figure S 135). This could have important implications for the feasibility of exfoliation of nominal 2D COFs, as covalent bonds would need to be broken in order to separate the individual "layers" of the COF. The presence of an isolated vacancy or a columnar vacancy line defect in the COF structure would influence not only the sorption properties of the COF by the presence of differently sized pores, but it would also present functional groups exposed to larger than regular pores in the COF. Furthermore, we note that size-selective properties such as sorption and catalysis[85] would be influenced in terms of selectivity by the presence of defects, again emphasizing the importance of real structure effects for the properties of COFs.

The reaction of the TTI-COF with sulfur proceeds under conditions that should not allow opening of the imine bonds; the reaction is performed in neat sulfur and no water is present. Furthermore, special solvent mixtures are required to form a porous crystalline covalent organic framework while reversible bonds are formed and broken. Since these conditions are not met during the sulfurization reaction described, the formation of TTT-COF has to happen in a topochemical fashion with minimal structural disruption of the covalent molecular backbone and the retention of the hexagonal structure of the material. While oxidative conditions during the thiazole formation might cause the scission of the covalent backbone, it cannot explain the presence of the observed defects such as grain boundaries and edge dislocations. We thus note that the observed defects in TTT-COF have to be present already in TTI-COF and likely in other COFs as well, especially 2D COFs based on the same topology.

6.2.2. Conclusion

In summary, the reaction of an imine COF with elemental sulfur leads to the topochemical formation of aromatic thiazole moieties as a new and robust linkage group, which causes a change in the symmetry of the COF crystal, but not of its topology or its connectivity. This reaction therefore adds to the synthetic toolbox of post-synthetic "locking" of COFs, which helps to circumvent the inherent limitations imposed by the presence of reversible bonds. The effect of this locking strategy was exemplified by the significantly improved chemical stability of the resulting thiazole COF. In addition, sulfur-assisted generation of thiazoles increases the number of possible COF structures and at the same time opens the door to new COFs with chemical properties not attainable in materials synthesized by reversible reactions.

While crystallinity and porosity of the TTT-COF are fully retained, it shows significantly improved electron contrast compared to the parent COF in addition to improved stability to the electron beam, thus making this system amenable to a study of its real structure by TEM for the first time. Close inspection of the structure of the TTT-COF allowed us to extract valuable information on both its long-range and local structure, including the nature of defects and disorder present in the system. While locked in during TTT-COF formation, these defects have been introduced already during the (reversible) synthesis of the precursor TTI-COF and thus can be considered as lasting fingerprints of the COF formation process. In particular, we find prevalent one-dimensional defects such as edge dislocations as well as co-aligned COF grains with grain boundaries that are likely covalently connected. Unravelling the nature of defects in COFs is not only key to better understand their impact on the optical, electronic and catalytic properties of COFs, but also to control and design new COFs by targeting properties imbued by such defects.

6.2.3. Methods

Additional materials information, synthesis of the TTI-COF, SEM/EXD, FT-IR, Sorption and Elemental Analysis details can be found in the supporting information.

Synthesis. *T*riazine *t*riphenyl *t*hiazole COF (TTT-COF) and *P*yrene tetra(phenyl) *b*iphenyl *t*hiazole (PBT-COF) Synthesis: The respective imine COF was activated under high vacuum at 150 °C and subsequently mixed with the 15-fold amount (by weight) of sulfur in a ball mill. The resulting homogeneous mixture was transferred to a quartz boat in a horizontal tubular furnace and purged at 60 °C under flowing argon. The temperature was increased to 155 °C (60 K/h heating rate) and maintained there for 3 h. Subsequently, the temperature was raised to 350 °C (100 K/h heating rate) and kept for 3 h. After cooling down, the resulting material was washed via Soxhlet extraction with toluene and THF for 24 h, respectively. The samples were dried at 70 °C in an oven and then at 150 °C under high vacuum.

Randomly stacked *T*riazine *t*riazine triphenyl *i*mine COF (rs-TTI-COF): TT-CHO (0.0254 mmol, 10.0mg), TT-NH2 (0.0254 mmol, 9.01 mg), di(n-octly)phthalate (1 ml), triphenyl phosphate (1 ml), aqueous acetic acid (0.318 mmol, 6M, 0.053 ml) were added successively to a Biotage$^{©}$ precision glass vial, sealed and heated under autogenous pressure at 120°C for 72 h. The rs-TTI-COF was worked up in the same manner as TTI-COF.

6.2.3.1. Chemical stability tests

Chemical stability of the TTI- and TTT-COF was assessed by immersing approximately 20 mg of the COF in a solution of each 12.5 M HCl (50°C), 12M KOH, 1M H_2NNH_2 and 1M $NaBH_4$ in water for 16 hours at room temperature unless denoted otherwise. Afterwards, the sample was filtered off and washed thoroughly with water, ethanol, THF, chloroform and DCM. After drying at ambient conditions, the crystallinity was assessed by XRPD.

6.2.3.2. Structure building

The structural models were built successively and based on each other starting from the well defined TTI-COF model.[278] The rs-TTI-COF and the TTT-COF showed no symmetry reduction from a hexagonal to a triclinic unit cell, therefore the highest reasonable symmetry supported by the molecular geometry is $P6_3/m$ which was used to build a unit cell model in BIOVA Materials Studio 2017 (17.1.0.48. Copyright © 2016 Dassault Systèmes). Molecular connectivity was based on geometric considerations and the obtained evidence from FT-IR and ssNMR. The structures and the unit cell was relaxed using Force fields (Forcite, universal force fields with Ewald electrostatic and van der Waals summations method). These models were then used to refine the unit cell parameters by Rietveld refinement.

6.2.3.3. TEM/SAED

TEM was performed with a Philips CM30 ST (300 kV, LaB_6 cathode). The samples were suspended in *n*-butanol and drop-cast onto a lacey carbon film (Plano). Processing of TEM and SAED images was performed with the help of ImageJ 1.47v.

Stability measurements were performed by taking images of the sample after defined time intervals in-between pictures, relative to the first image (t = 0 min).

6.2.3.4.   XRPD

XRPD patterns were collected on a Stoe Stadi P diffractometer (Cu-K$_{\alpha 1}$, Ge(111)) in Debye-Scherrer geometry. The sample was measured inside a sealed glass capillary (1.0 mm) that was spun for improved particle statistics.

The powder patterns were analyzed by Rietveld[326] and Pawley[325] refinement using the range from 2-30 ° 2θ with TOPAS V5, while keeping the atom coordinates fixed. The peak profile was described by applying the fundamental parameter[353] approach as implemented in TOPAS. The background was modeled with a 6th order Chebychev polynomial. Lattice parameters were refined as constrained by the symmetry. The peak broadening was modelled with asymmetry adopted phenomenological model for microstrain.[354] The plotted XRPD patterns were normalized to compare relative peak intensities.

6.2.3.5.   ssNMR

The solid state NMR (ssNMR) spectra were recorded on a Bruker Avance III 400 MHz spectrometer (B0=9.4T) at the frequencies of 400.1, 100.6 and 40.8 MHz, for ^{1}H, ^{13}C and ^{15}N, respectively. The ssNMR experiments were performed on a Bruker double resonance 4 mm MAS probe with the COF samples packed in ZrO_2 rotors. The ^{1}H-^{13}C and ^{1}H-^{15}N cross-polarization (CP) MAS spectra were recorded with a rotation frequency of 10-12 kHz using a ramped-amplitude (RAMP) spin-locking pulse on the proton channel. The contact time for both nuclei was set to 5 ms, which was found to be optimal. The recycle delay in the CP-experiments was 2s, defined primarily by the spin-lattice relaxation of protons. All solid-state experiments were carried out using SPINAL64 composite-pulse proton decoupling with radio frequency power between 70 and 80 kHz. The reported ^{1}H and ^{13}C chemical shifts were referenced to tetramethylsilane (TMS), while the ^{15}N shifts were referenced to nitromethane.

6.2.3.6.   Quantum-chemical calculations

Atom positions and lattices of periodic structures were optimized on PBE-D3/def2‑TZVP[355, 356] level of theory using an acceleration scheme based on the resolution of the identity (RI) technique and the continuous fast multipole method (CFMM)[357] in a developer version of Turbomole.[358]

The CFMM uses multipole moments of maximum order 20 together with a well-separateness value 3 and a basis function extent threshold of 10E-9 a.u. Grid 7 was used for the numerical integration of the exchange-correlation term. The norm of the gradient was converged to 10E-4 a.u. and the total energy is converged to 10E-8 Hartree within the structure optimization using an equidistant 5x5 k-point grid.

NMR chemical shifts were obtained on B97-2/pcS-2//PBE-D3/def2-TZVP level of theory[359, 360] using the Turbomole program package in version 7.0.2 for geometries and the FermiONs++[361] program package for the calculation of NMR chemical shifts performed on excised sections (Figure S 112, Figure S 113; distinction shown in Figure S 114) of the TTT and TTI-COF models. Chemical shifts were then referenced to the experimentally obtained spectra with the triazine peak 1/1' and 6,6'.

6.2.4.   Acknowledgements

6.3. Synthesis of a stilbene based polymer by controlled thermal transformation of an azine covalent organic framework

Frederik Haase proposed the idea, designed the experiments, performed all synthesis, interpreted the data and wrote the manuscript. Florian Pielnhofer performed the theoretical calculations. Rotraut Merkle measured the temperature dependent MS. Willi Hölle measured the TGA. Igor Moudrakovski measured the ssNMR spectra. Bettina V. Lotsch supervised the research.

In this work, the high temperature transformation of azine based COFs to a stilbene based polymer has been investigated. Aromatic azines are known to undergo controlled pyrolysis to form the corresponding stilbenes at high temperatures, a method that has historically been used for preparation of symmetrical stilbenes.[362, 363] This reaction is driven by the formation of molecular nitrogen as the product under the high vacuum and high temperature synthesis conditions. N_3-COF has been employed for this study (Section 4.2).[2]

6.3.1. Results

N_3-COF was employed for this study due to its good crystallinity, high porosity and utility as a photocatalyst as found previously (Chapter 4.2) (Figure 6-15). In addition to generating new COFs, the transformation of azines to stilbenes was motivated by the search for a strategy to lock the azine bond, which can be cleaved under acidic conditions.[364]
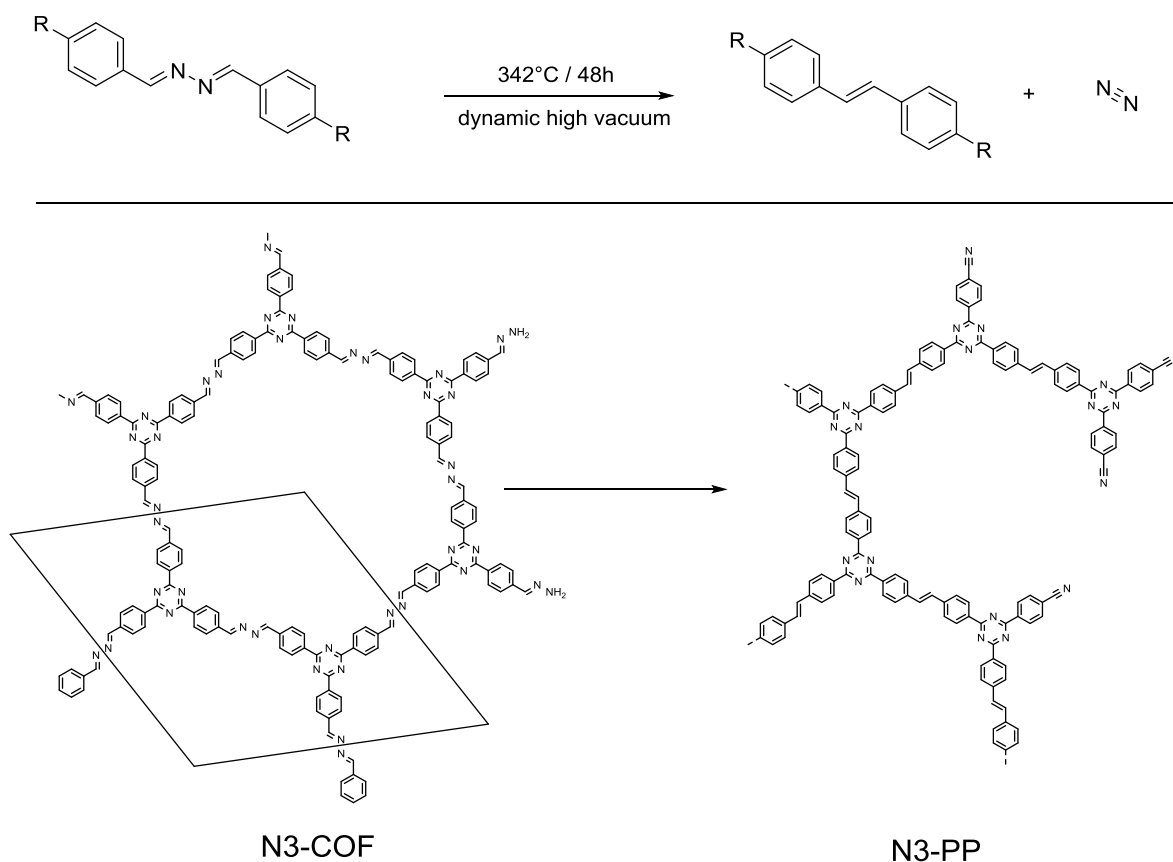
Figure 6-15: Top: Schematic of the pyrolysis reaction of an aromatic azine to a stilbene, by expulsion of a nitrogen molecule. Bottom: Schematic representation of the transformation of crystalline N_3-COF to the amorphous possibly, fragmented N_3-PP.

The first indication that N_3-COF could be thermally transformed was seen with thermogravimetric analysis (TGA). A sharp mass loss during heating in Argon indicates a defined reaction to a pyrolysed polymer (N_3-PP) taking place (Figure 6-16). The observed transition at 342°C was accompanied by a loss of 7.89% of mass, which correlated to the azine to stilbene conversion. However, this is lower than the expected mass loss of 10.84% for the quantitative transformation. Possible explanations could be a low conversion yield, or a side reaction with the decomposition of the azine leading to other reaction products than the desired stilbenes. Previous investigations into the pyrolysis of linear azine polymers have shown that only 79%[363] of the expected nitrogen could be recovered, which matches with the 72% of theoretical mass loss observed here. Further mass loss at higher temperatures might be caused by the uncontrolled decomposition of the N_3-COF and was not further investigated. The azine pyrolysis reaction proceeds through the elimination of molecular nitrogen, which can be observed by mass spectroscopy while the reaction takes place (Figure 6-16). A sharp peak corresponding to the mass/charge ratio for molecular nitrogen (28 m/z) is observed in mass spectroscopy. The peak is most intense at 337°C, close to the reaction temperature extracted from TGA. The determination of CO to N_2 ratio by deconvolution of the 28 m/z to 29 m/z ratio of respective masses was not possible due to the low signal at 29 m/z, however, under air free conditions, the production of CO is deemed to be minimal.
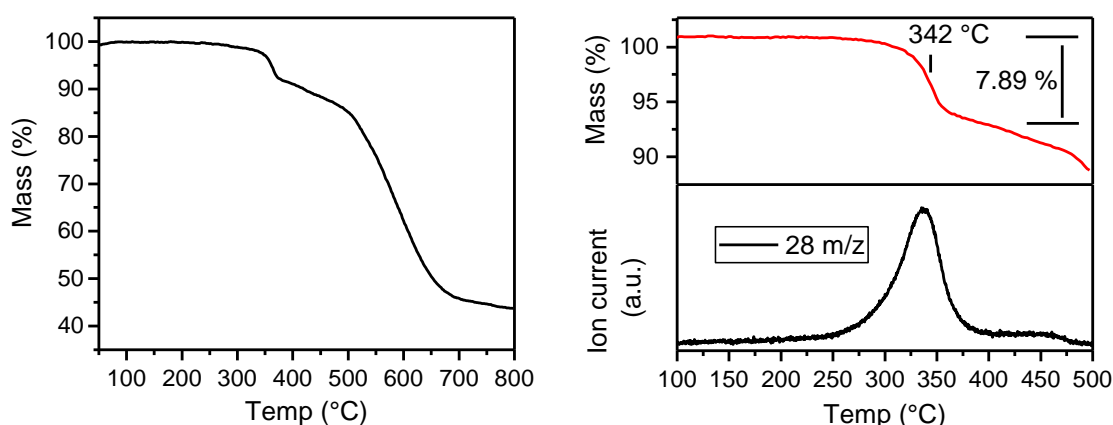
Figure 6-16: Left: Full TGA of N_3-COF in Argon. Right, Top: Close-up of the mass loss step in TGA. Bottom, right: MS of the decomposition process, measured not simultaneously with the shown TGA.

For the bulk transformation of N_3-COF, a temperature slightly higher than the reaction temperature obtained from TGA was chosen. Thus, N_3-COF was transformed to N_3-PP by heating to 350°C under high dynamic vacuum for 48 h to ensure complete transformation.

The obtained material was analyzed by FT-IR after the pyrolysis reaction to trace any significant and well defined changes between the unaltered N_3-COF and the N_3-PP (Figure 6-17). The IR spectra were evaluated by comparison to simulated IR spectra of models of N_3-COF and N_3-PP based on DFT optimized structures, as well as to azine and stilbene model compounds. Bands were assigned by matching peaks of the experimental with the calculated IR spectra. The most notable change in the IR spectra upon transformation to N_3-PP is the disappearance of the peak at 1626 cm^{-1} (Figure 6-17, gray overlay) corresponding to the azine (N=CH) stretching vibration in N_3-COF, confirming the loss of the azine moiety. The band at 1606 cm^{-1} present in the N_3-PP could be attributed to aromatic skeletal vibrations and the ethylene vibration,[363] however the N_3-COF also possesses a band in this region making the assignment to C=C bond ambiguous. Nevertheless, other changes clearly show the transformation of the azine to the stilbene, such as the loss of the peak at 1210 cm^{-1} (Figure 6-17, A), which can be assigned to combined azine C-H rocking motion with a phenyl ring stretching motion.

The significant increase in intensity of the band at 1176 cm^{-1} in the IR spectrum of N$_3$-COF and shift to 1180 cm^{-1} in the N$_3$-PP can be assigned to the phenyl C-H scissoring motion combined with an azine/ethylene C-H rocking motion and this assignment matches well with the calculated spectra (Figure 6-17, A). The newly appeared band at 849 cm^{-1} was confirmed by calculation to be an anti-symmetric stretching deformation of the phenyl-azine and phenyl-ethylene bond with a phenyl ring breathing mode (Figure 6-17, B). A very characteristic peak shift from 513 cm^{-1} to 545 cm^{-1} can be observed for the asymmetric peak corresponding to the anti-symmetric stretching deformation of the phenyl-azine and phenyl-ethylene bond together with a phenyl ring stretching mode (Figure 6-17, C; Figure S 137). These findings are further confirmed by comparison to sets of model azines and stilbenes showing similar characteristic changes in the regions discussed here, such as in p-dimethyl-,[365, 366] p-dinitro-,[367, 368] and benzene[369, 370] based azines and stilbenes (Figure S 138, Figure S 139, Figure S 140).
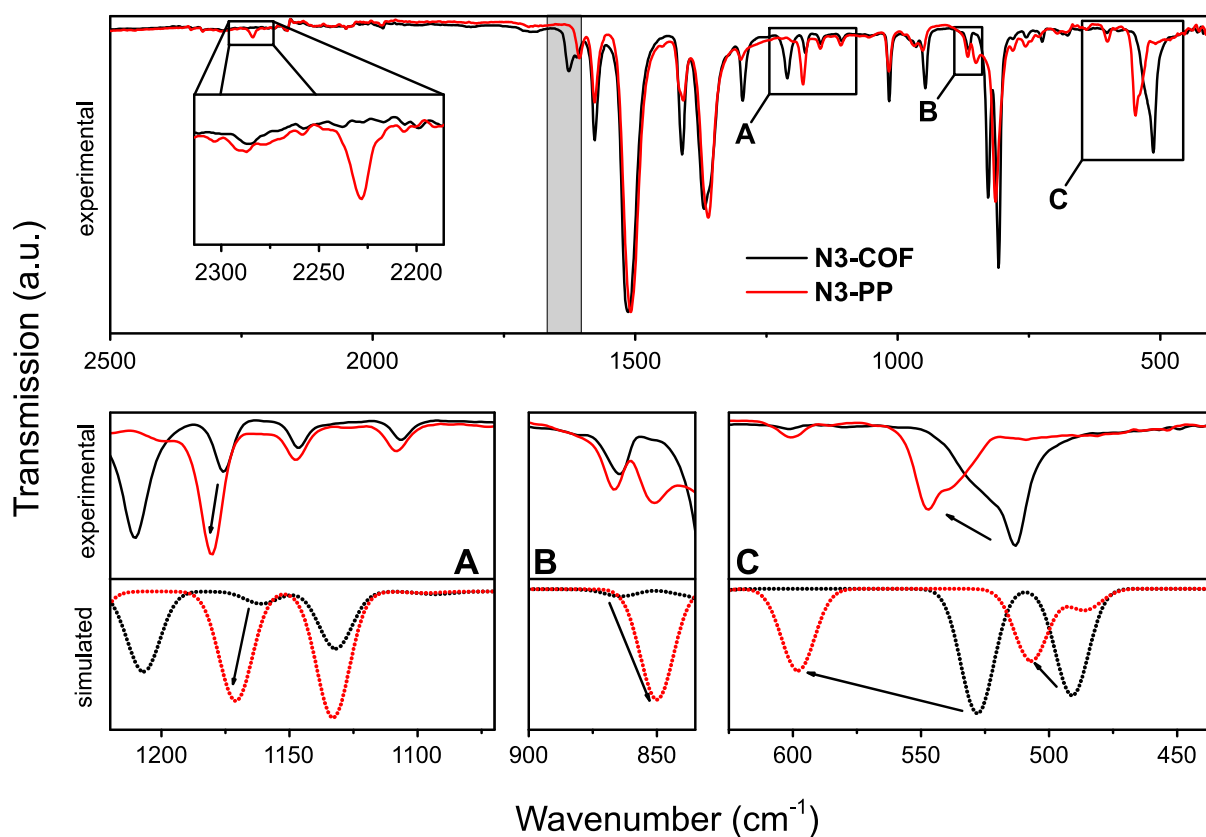
Figure 6-17: Experimental and simulated IR spectra of N$_3$-COF and N$_3$-PP. Simulated IR shown as dotted lines. Disappearance of the N=CH vibration at 1626 cm^{-1} indicated by a gray overlay.

IR provides only little information on the possible side reactions that have previously been found in molecular systems, where the formation of nitrile, imidazole and aldehyde groups were observed.[363, 371] The presence of a weak nitrile band can be confirmed at 2230 cm^{-1}, however, as nitrile bands tend to be very intense in IR, the concentration of nitrile groups are expected to be very small. XRPD measurement of N$_3$-COF and N$_3$-PP showed complete loss of crystallinity upon transformation of the azines to the stilbenes (Figure 6-18).
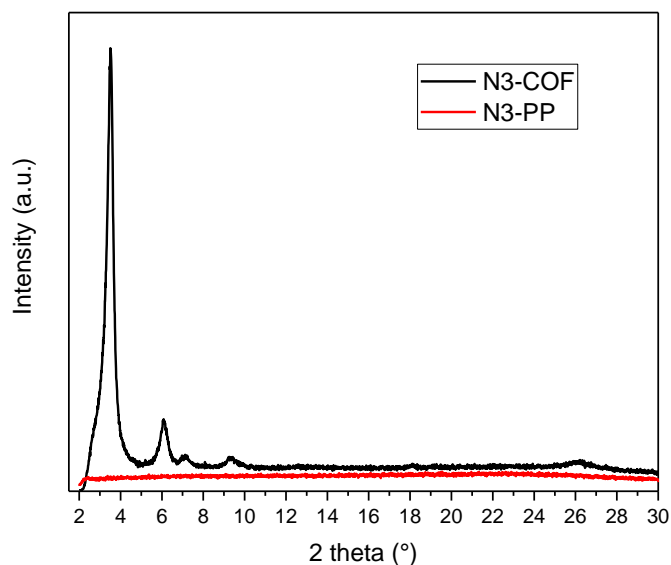
Figure 6-18: XRPD of crystalline N_3-COF and the amorphous N_3-PP.

^{13}C ssNMR of N_3-COF and the N_3-PP shows characteristic peaks. The triazine peak situated at 168.7 ppm (**1**) in N_3-COF is shifted downfield to 170.6 ppm (**1'**) in N_3-PP and broadened,[2] which could be attributed to either the slightly changed chemical environment from the change from azine to stilbene, or a change in packing or strain on the triazine moiety resulting from the structural changes. The characteristic azine carbon peak in N_3-COF at 160.9 ppm (**2**) is lost upon the transformation to the stilbene, which further confirms the transformation of the azine bond. A new peak appears at 115.7 ppm (**2'**), which could be assigned to a vinylic carbon or a nitrile. While some changes are visible in the region 145-120 ppm, it is difficult to assign these signals. However, additional peaks in the range 145-135 ppm would be expected for a stilbene resulting from carbons adjacent to the vinylic carbons (**3'**). The measurement of ^{13}C ssNMR of N_3-PP sample showed residual azine peaks (**2**) after 24 h of reaction time and only after 48 h was the complete loss of the azine peak observed (Figure S 136).
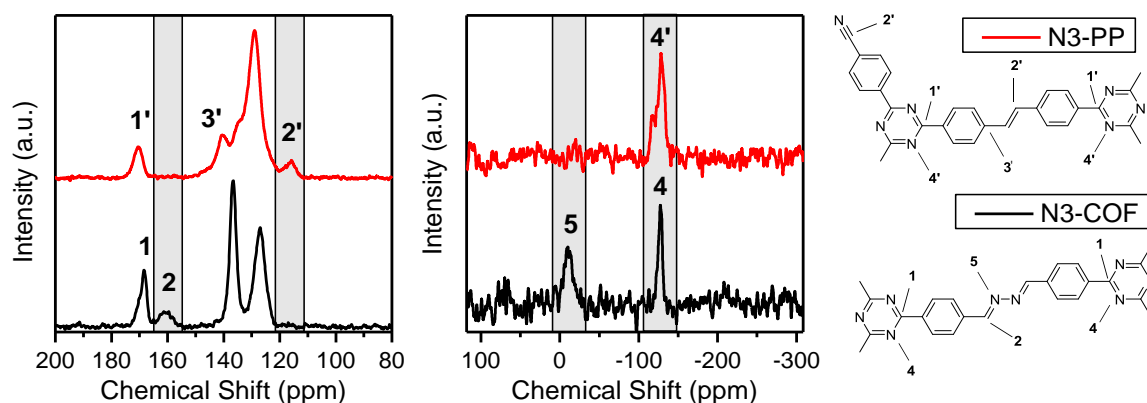
Figure 6-19: Left: ^{13}C ssNMR of N_3-COF and N_3-PP. The gray overlay indicates the position of the azine peak before and the nitrile and vinylic stilbene peaks after the transformation. Middle: ^{15}N ssNMR of N_3-COF and N_3-PP. Right: Assignment of the ssNMR peaks.

^{15}N ssNMR shows the loss of the azine peak of the N$_3$-COF at -9.78 ppm (**5**) upon transformation and the retention of the triazine peak at -128 ppm (**4, 4'**). However, the triazine peak is significantly broadened in N$_3$-PP and has a shoulder at -118 ppm, which could be explained by the structural changes and the thereby induced changes or from overlap with a nitrile nitrogen peak that would be expected in this region.

As triazine COFs as well as polymers and oligomers have successfully been employed for photocatalytic hydrogen evolution, the optical properties of N$_3$-PP were investigated to estimate if this material could be effective for photocatalytic hydrogen evolution. Diffuse reflectance spectra showed that the optical absorption edge was redshifted upon the transformation from N$_3$-COF to N$_3$-PP, corresponding to optical band gaps of 2.73 eV and 2.59 eV for N$_3$-COF and N$_3$-PP, respectively. The band gap of N$_3$-PP would be large enough to facilitate photocatalytic water splitting[232] and the reduction of the optical band gap in comparison to N$_3$-COF might elicit an improved light absorption and thereby overall photocatalysis (Chapter 4.4). Further, work by Schwinghammer et al.[269] has shown that additional nitrile functional groups on the surface of the photocatalyst might be beneficial in facilitating close contact of the co-catalyst and thereby improving photocatlytic hydrogen evolution.
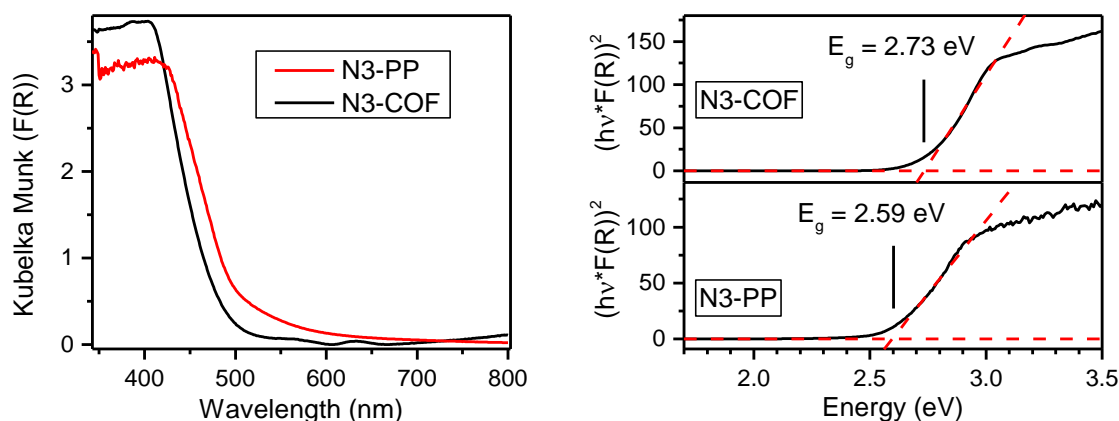
Figure 6-20: Diffuse reflectance spectra of N$_3$-COF and N$_3$-PP showing a 27 nm red shift of the band edge for the pyrolysed polymer.

6.3.2.   Discussion

The pyrolysis of the azine bonds of N$_3$-COF led to a loss of crystallinity. If the azine to stilbene transformation proceeded through a reaction that preserves the connectivity of the backbone throughout the reaction as described in the generation of thiazoles from imines in Chapter 0, it might have been possible to preserve the topology of the COF backbone and thereby the crystallinity. However, in the case of a reaction that proceeds through the scission of the backbone connectivity, it would only be possible to retain the order of the framework, if the covalent bond is reformed before significant conformational rearrangements lead to a loss of order. Otherwise, the irreversible stilbene bond formation would arrest the disorder permanently. Investigations by Zimmerman et al.[371] into the mechanism of azine pyrolysis have shown that stilbene formation proceeds through an ionic chain mechanism. The chain is initiated by thermal scission of the N=C double bond with the formation of a carbene and a phenyl diazomethane, which reacts with an intact azine and forms a stilbene and a new diazomethane leading to the propagation of the chain. This cascade terminates when the carbene and the diazomethane react again to form an azine (Figure 6-21).

chain initiation
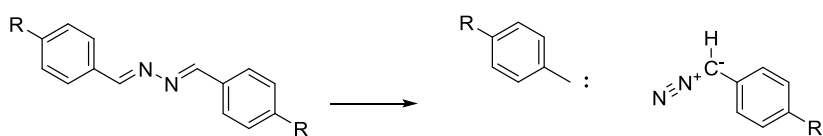
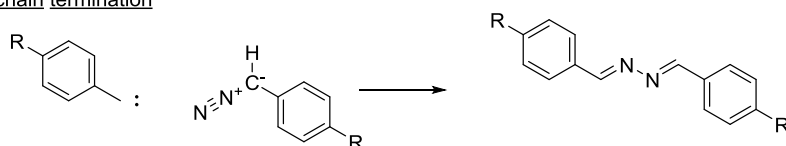chain propagation
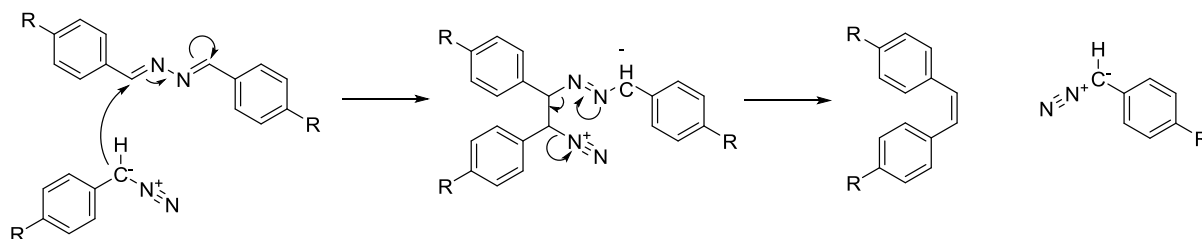
chain termination

Figure 6-21: Mechanism of the chain reaction of the azine pyrolysis.[371]

The confined space in N_3-COF could significantly influence the chain propagation reaction, since the crystalline, ordered nature of N_3-COF places the azine bond of adjacent layers in close proximity (see chapter 4.2). The formation of crystalline stilbene based N_3-PP would require the reaction of diazomethane with an azine that is opposite and in-plane of the layer, to extend the covalent connectivity similarly as in the N_3-COF. The mechanism and the observed loss of crystallinity would suggest that the diazomethane species attacks the azine moiety directly from above or below the layer to form the stilbene (Figure 6-22), leading to an interlayer chain reaction. The result would be the loss of the in-plane connectivity leading to random out of plane connections. Furthermore, the out-of-plane reaction would lead to significant strain and disrupt the stacking, thereby leading to a loss of in- and out-of-plane structure and therefore resulting in a completely amorphous material.
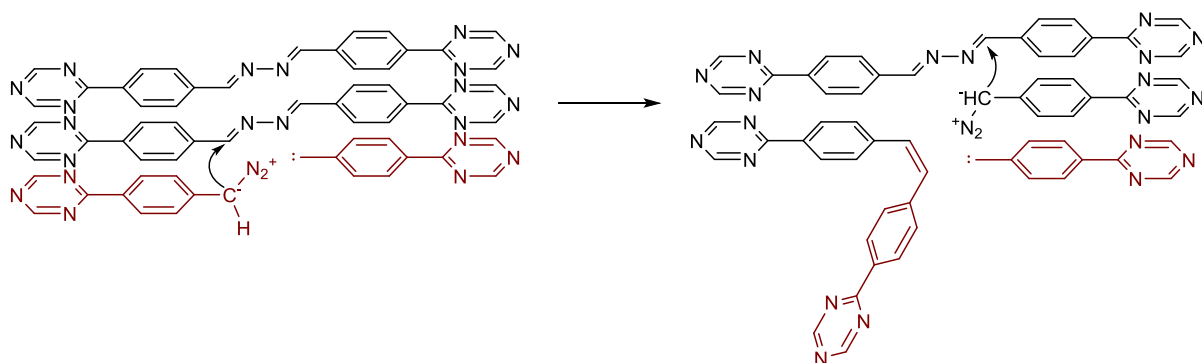
Figure 6-22: Schematic of a possible pathway of azine pyrolysis in N_3-COF, where stacking puts the azines in close proximity.

6.3.3.   Conclusion

The transformation of the azine functional groups in N$_3$-COF to their corresponding stilbenes by thermal treatment only was shown. This high temperature reaction affected the susceptible azine bond but left the rest of the framework molecular structure intact. Due to a possibly high thermal burden and the mechanism of the azine pyrolysis the ordered structure of the N$_3$-COF could not be retained and a completely amorphous polymer was obtained.

6.3.4.   Methods

Synthesis

*T*ris(4-formylphenyl)*t*riazine (TT-CHO)[196] and N$_3$-COF [2] were synthesized according to literature procedures.

N$_3$-PP synthesis: N$_3$-COF (20 mg) was loaded into a Schlenk tube, which was placed into a vertical tube furnace, and then evacuated carefully. As soon as high vacuum was achieved, the temperature of the oven was raised by 100°C/h until 350°C was reached. This temperature was maintained for 48 h. Then the sample was allowed to cool down, removed from the Schlenk container and washed thoroughly with ethanol, water, THF, chloroform and dichloromethane and then dried under high vacuum for 24 h.

MS

MS was measured of the outgassing of the N$_3$-COF heated in argon flow with a temperature ramp of 5K/min on a NETZSCH STA 449C (NETZSCH-Geraetebau GmbH Thermal Analysis) coupled to a mass spectrometry (MS) (Balzers Prisma quadrupol spectrometer).

Simulation of IR spectra

A full structural relaxation (lattice parameters and atomic positions) of the N$_3$-COF and the N$_3$-PP models based on the *P6/m* symmetry was performed in the framework of density functional theory (DFT) using a linear combination of Gaussian-type functions (LCGTF) scheme as implemented in CRYSTAL14.[372, 373] The PBE parametrization[355] of the generalized gradient approximation including Grimme's D2 dispersion correction[374] was applied. The convergence criterion considering the energy was set to 1×10^{-8} a.u. with a k-mesh sampling of $4 \times 4 \times 4$. All-electron basis sets were taken from [375, 376].

Vibrational frequencies calculations with IR intensities were run on fully optimized structural models. Calculated positions and intensities for IR active modes were convoluted with a 15 cm^{-1} Gaussian broadening before plotting them using the J-ICE application.[377] Peak assignment between the experimental and the simulated IR spectra were performed, by first matching modes between the N$_3$-COF and N$_3$-PP, which were then compared to the positon shift and the intensity changes in the experimental spectra.

7. Conclusion

In this thesis, several aspects of designing COFs have been demonstrated that underline the ability to tune the structure and properties in COFs. The work shows the tailoring of the structure on several different levels: the molecular intra-net structure through the design of molecular precursors, the noncovalent interactions between layers of two-dimensional COFs, the post-synthetic modification of the COF linkages and the properties of COFs for photocatalytic hydrogen evolution.

Photocatalysis in COFs

Photocatalytic reduction of water for hydrogen production promises to be a viable method for obtaining clean energy. COFs as a platform for developing highly tailored architectures presents a promising approach for photocatalysis, since the inherent properties of COFs align with many requirements for the design of a successful photocatalyst. The modular nature is of special importance in designing and understanding photocatalytic hydrogen evolution in COFs.

In this thesis, two COF platforms have been developed that can readily be modulated at a molecular level while maintaining the overall structural features and porosity, thereby allowing the tuning of the photocatalytic properties. One platform is based on the substitution of C-H in the aryl rings of the COF platform with nitrogen atoms while in the other the introduction of peripheral hydroxyl groups is used to alter the COF. The translation of structural properties of the precursor aldehydes in the resulting COFs was studied by XRPD, TEM, ssNMR and gas sorption analysis. The optical properties of the COFs were evaluated to analyze their light absorption properties to relate their optoelectronic properties with their photocatalytic hydrogen evolution activity. The synthesized COFs were tested as photocatalysts for the hydrogen evolution reaction and several trends were observed that could be related to structural features of the COFs. In substitution series of four COFs with different nitrogen contents in the central aryl ring a 4-5 fold increase in hydrogen evolution activity was observed with each substitution of C-H in the central aryl ring of the COF platform by nitrogen. This resulted in an overall 75-fold increase in the triply substituted N_3-COF in comparison to the unsubstituted N_0-COF. When the substitution pattern was changed to include the nitrogen substitution in the peripheral aryl rings the resulting PTP-COF performed only 4 times better than the unsubstituted COF. This variation of nitrogen substitution serves to further understand the factors driving photocatalytic hydrogen evolution in this platform, based on an interplay of intrinsic (opto)electronic and geometric properties, as well as extrinsic structural and morphological properties of organic photocatalysts. This work shows that the change in the nitrogen substitution pattern influences on the one hand photocatalytic hydrogen evolution activity, but on the other hand it also influences the crystallization, morphology and electronic properties of the COF, and this will help towards future efforts to predict highly active photocatalysts.

In the second platform the tunability of COFs was used to selectively introduce hydroxyl groups into an imine and triazine based COF to modify its bandgap. The tuning of the band gap to lower energies led to an increased photonic efficiency at wavelengths where solar irradiation is the strongest. Accordingly, the activity of the hydroxylated COF exhibiting the smaller band gap was increased 9-fold with respect to the non-hydroxylated COF. This result shows the possibility of tuning the band gaps of COFs rationally to improve the hydrogen evolution efficiency. Thus, it is this interplay of intrinsic and extrinsic features such as optoelectronic and steric and morphology-related factors, respectively, which likely determines the photocatalytic activity of a COF and therefore the findings presented herein present a fertile ground for further discussions.

This work underlines the tunability of COFs for applications, in a way that the structural and electronic modification can be achieved by rationally designing the structure of COFs from the individual building units to the final framework material. This is especially true for photocatalytic hydrogen evolution studies where many factors play a role in determining the activity. Adjusting the electronic and geometric features of the building blocks can be used to influence the properties of COFs in an incremental, but fundamental fashion. This is beneficial for improving activity and, in combination with insights from theory, also presents a powerful platform for understanding photocatalytic hydrogen evolution through systematic study. The rational design of COFs for such material applications by consequence of the modulation in structural and optoelectronic properties will help in boosting further utilization of COFs in other scientific applications.

Stacking in two-dimensional COFs

The supramolecular assembly of individual COF layers is of significant importance for the optoelectronic properties of COFs, but there is a fundamental lack of understanding regarding the design and control of the stacking structure of COFs. This can largely be attributed to the difficulty of designing highly crystalline COFs and the resulting lack of in-depth structural characterization of the small crystallites which contain many defects.

This thesis addresses both challenges, as the careful analysis of two structurally related COFs enables unprecedented structural insights into two 2D COFs and their stacking polytypes. These insights offer a more general supramolecular design principle that can lead to ordered stacking polytypes and significantly improved crystallinity and domain sizes in COFs. The structural analysis by X-ray powder diffraction in conjunction with Rietveld analysis, complemented by theoretical calculations, and by transmission electron microscopy coupled with selected area electron diffraction shows evidence of the rarely observed slip-stacking mode in TTI-COF. Detailed experimental and theoretical evidence of its interlayer structure showed that rather than adopting the usual apparent eclipsed stacking, the COF shows a uniformly off-set layer sequence, giving rise to distinct Bragg peak splitting in the XRPD pattern.

The stacking structure could be tuned by using a non-flat benzene triphenyl (TBI) building block instead of the triazine triphenyl in TTI-COF. Replacing the flat structure of TTI-COF with the twisted TBI-COF structure leads to a loss of the defined slip stacking, as the COF reverts to the disordered eclipsed structure. The observed stacking preference in TTI-COF can be attributed to the flatness of the structure and donor-acceptor type interactions between adjacent layers that was corroborated by theoretical calculations of the stacking landscape. These results serve as a template for the further design of highly crystalline and well stacked structures. The precise determination of stacking in COFs will provide an accurate descriptor for studying the optoelectronic properties of COFs by theory and experiment, which is of paramount importance to the application of COFs in the field of photovoltaics and photocatalysis.

Transforming COF linkages

The field of COFs is inherently limited by the necessity of dynamic error correction during polymerization to allow crystallization of the material. This not only limits the chemical stability and properties of COFs relevant e.g. for charge transport, but is also the main source of the low crystallinity and high level of structural defects in COFs.

In this thesis, strategies are presented to break free of the limits imposed by this reversibility criterion and modify the structure to obtain unprecedented COF functionalities. This is achieved by a topochemical transformation of the reversible imine linkage - one of the most common COF linkages

- to a thiazole whilst fully preserving the crystallinity and porosity of the COF backbone. This transformation deviates significantly from known COF chemistry and establishes a new class of thiazole-COFs with a fully conjugated and stable backbone, based on "arrested" reversible linkages. This transformation instills a significantly enhanced stability and resilience of the COF to the electron beam as well as improved contrast, which allowed the investigation of the real structure of COFs in an unprecedented detail. Various types of defects were accessible to imaging at an extraordinary level of detail. The nature of point defects, in-plane edge dislocations and inter-grown grain boundaries in COFs, which is crucial for advancing our understanding of both fundamental properties and possible applications of COFs, is verified for the first time.

In addition to the topotactic transformation from imine to thiazole, the transformation of azines to stilbenes was investigated. This reaction showed the limits of how to design a topotactic reaction to preserve crystallinity. The use of an intramolecular reaction for the transformation of a COF linkage can help preserve the crystallinity of the COF, while an intermolecular transformation can lead to a loss of crystallinity as is seen in the azine to stilbene reaction. The investigated reactions are an important starting point for the selection and investigation of further COF linkage transformations.

8. References

[1]   Cote, A.P., Benin, A.I., Ockwig, N.W., O'Keeffe, M., Matzger, A.J., and Yaghi, O.M., *Porous, crystalline, covalent organic frameworks.* Science, **2005**. 310, (5751): 1166-70 DOI: 10.1126/science.1120411.

[2]   Vyas, V.S., Haase, F., Stegbauer, L., Savasci, G., Podjaski, F., Ochsenfeld, C., and Lotsch, B.V., *A tunable azine covalent organic framework platform for visible light-induced hydrogen generation.* Nat Commun, **2015**. 6: 8508 DOI: 10.1038/ncomms9508.

[3]   Dillon, E.C., Wilton, J.H., Barlow, J.C., and Watson, W.A., *Large surface area activated charcoal and the inhibition of aspirin absorption.* Annals of Emergency Medicine, **1989**. 18, (5): 547-552 DOI: 10.1016/s0196-0644(89)80841-8.

[4]   Komvokis, V., Tan, L.X.L., Clough, M., Pan, S.S., and Yilmaz, B., *Zeolites in Fluid Catalytic Cracking (FCC).* **2016**: 271-297 DOI: 10.1007/978-3-662-47395-5_8.

[5]   Kosinov, N., Gascon, J., Kapteijn, F., and Hensen, E.J.M., *Recent developments in zeolite membranes for gas separation.* Journal of Membrane Science, **2016**. 499: 65-79 DOI: 10.1016/j.memsci.2015.10.049.

[6]   Hassan, I. and Grundy, H.D., *The crystal structures of sodalite-group minerals.* Acta Crystallographica Section B Structural Science, **1984**. 40, (1): 6-13 DOI: 10.1107/s0108768184001683.

[7]   Björklund, S. and Kocherbitov, V., *Alcohols react with MCM-41 at room temperature and chemically modify mesoporous silica.* Scientific Reports, **2017**. 7, (1): 9960 DOI: 10.1038/s41598-017-10090-x.

[8]   Rosi, N.L., *Hydrogen Storage in Microporous Metal-Organic Frameworks.* Science, **2003**. 300, (5622): 1127-1129 DOI: 10.1126/science.1083440.

[9]   dos Santos, S.M.L., Nogueira, K.A.B., de Souza Gama, M., Lima, J.D.F., da Silva Júnior, I.J., and de Azevedo, D.C.S., *Synthesis and characterization of ordered mesoporous silica (SBA-15 and SBA-16) for adsorption of biomolecules.* Microporous Mesoporous Mater., **2013**. 180: 284-292 DOI: 10.1016/j.micromeso.2013.06.043.

[10]   Zhou, H.-C., Long, J.R., and Yaghi, O.M., *Introduction to Metal–Organic Frameworks.* Chem. Rev., **2012**. 112, (2): 673-674 DOI: 10.1021/cr300014x.

[11]   Leus, K., Bogaerts, T., De Decker, J., Depauw, H., Hendrickx, K., Vrielinck, H., Van Speybroeck, V., and Van Der Voort, P., *Systematic study of the chemical and hydrothermal stability of selected "stable" Metal Organic Frameworks.* Microporous Mesoporous Mater., **2016**. 226: 110-116 DOI: 10.1016/j.micromeso.2015.11.055.

[12]   Barrer, R.M. and Shanson, V.H., *Dianin's compound as a zeolitic sorbent.* J. Chem. Soc., Chem. Commun., **1976**, (9): 333 DOI: 10.1039/c39760000333.

[13]   Cooper, A.I., *Porous Molecular Solids and Liquids.* ACS Central Science, **2017**. 3, (6): 544-553 DOI: 10.1021/acscentsci.7b00146.

[14]   Sozzani, P., Comotti, A., Simonutti, R., Meersmann, T., Logan, J.W., and Pines, A., *A Porous Crystalline Molecular Solid Explored by Hyperpolarized Xenon.* Angew. Chem. Int. Ed., **2000**. 39, (15): 2695-2699 DOI: 10.1002/1521-3773(20000804)39:15<2695::aid-anie2695>3.0.co;2-m.

[15]   Zentner, C.A., Lai, H.W.H., Greenfield, J.T., Wiscons, R.A., Zeller, M., Campana, C.F., Talu, O., FitzGerald, S.A., and Rowsell, J.L.C., *High surface area and Z[prime or minute] in a thermally stable 8-fold polycatenated hydrogen-bonded framework.* Chem. Commun., **2015**. 51, (58): 11642-11645 DOI: 10.1039/C5CC04219D.

[16]   Mastalerz, M. and Oppel, I.M., *Rational Construction of an Extrinsic Porous Molecular Crystal with an Extraordinary High Specific Surface Area.* Angew. Chem. Int. Ed., **2012**. 51, (21): 5252-5255 DOI: 10.1002/anie.201201174.

[17] Liu, M., Chen, L., Lewis, S., Chong, S.Y., Little, M.A., Hasell, T., Aldous, I.M., Brown, C.M., Smith, M.W., Morrison, C.A., Hardwick, L.J., and Cooper, A.I., *Three-dimensional protonic conductivity in porous organic cage solids.* Nature Communications, **2016**. 7: 12750 DOI: 10.1038/ncomms12750.

[18] Budd, P.M., McKeown, N.B., and Fritsch, D., *Polymers of Intrinsic Microporosity (PIMs): High Free Volume Polymers for Membrane Applications.* Macromolecular Symposia, **2006**. 245-246, (1): 403-405 DOI: 10.1002/masy.200651356.

[19] Liu, Q., Li, G., Tang, Z., Chen, L., Liao, B., Ou, B., Zhou, Z., and Zhou, H., *Design and synthesis of conjugated polymers of tunable pore size distribution.* Mater. Chem. Phys., **2017**. 186: 11-18 DOI: 10.1016/j.matchemphys.2016.06.004.

[20] Slater, A.G. and Cooper, A.I., *Function-led design of new porous materials.* Science, **2015**. 348, (6238): aaa8075 DOI: 10.1126/science.aaa8075.

[21] Budd, P.M., Ghanem, B.S., Makhseed, S., McKeown, N.B., Msayib, K.J., and Tattershall, C.E., *Polymers of intrinsic microporosity (PIMs): robust, solution-processable, organic nanoporous materials.* Chem. Commun., **2004**, (2): 230 DOI: 10.1039/b311764b.

[22] Carta, M., Malpass-Evans, R., Croad, M., Rogan, Y., Jansen, J.C., Bernardo, P., Bazzarelli, F., and McKeown, N.B., *An Efficient Polymer Molecular Sieve for Membrane Gas Separations.* Science, **2013**. 339, (6117): 303-307 DOI: 10.1126/science.1228032.

[23] McKeown, N.B. and Budd, P.M., *Polymers of intrinsic microporosity (PIMs): organic materials for membrane separations, heterogeneous catalysis and hydrogen storage.* Chem. Soc. Rev., **2006**. 35, (8): 675 DOI: 10.1039/b600349d.

[24] Kojima, A., Teshima, K., Shirai, Y., and Miyasaka, T., *Organometal Halide Perovskites as Visible-Light Sensitizers for Photovoltaic Cells.* J. Am. Chem. Soc., **2009**. 131, (17): 6050-6051 DOI: 10.1021/ja809598r.

[25] Grancini, G., Roldán-Carmona, C., Zimmermann, I., Mosconi, E., Lee, X., Martineau, D., Narbey, S., Oswald, F., De Angelis, F., Graetzel, M., and Nazeeruddin, M.K., *One-Year stable perovskite solar cells by 2D/3D interface engineering.* Nature Communications, **2017**. 8: 15684 DOI: 10.1038/ncomms15684.

[26] Cheetham, A.K., Rao, C.N.R., and Feller, R.K., *Structural diversity and chemical trends in hybrid inorganic–organic framework materials.* Chem. Commun., **2006**, (46): 4780-4795 DOI: 10.1039/b610264f.

[27] Furukawa, H., Kim, J., Ockwig, N.W., O'Keeffe, M., and Yaghi, O.M., *Control of Vertex Geometry, Structure Dimensionality, Functionality, and Pore Metrics in the Reticular Synthesis of Crystalline Metal–Organic Frameworks and Polyhedra.* J. Am. Chem. Soc., **2008**. 130, (35): 11650-11661 DOI: 10.1021/ja803783c.

[28] Dincǎ, M., Dailly, A., Liu, Y., Brown, C.M., Neumann, D.A., and Long, J.R., *Hydrogen Storage in a Microporous Metal–Organic Framework with Exposed Mn2+Coordination Sites.* J. Am. Chem. Soc., **2006**. 128, (51): 16876-16883 DOI: 10.1021/ja0656853.

[29] Chasseau, D., Comberton, G., Gaultier, J., and Hauw, C., *Réexamen de la structure du complexe hexaméthylène-tétrathiafulvalène–tétracyanoquinodiméthane.* Acta Crystallographica Section B Structural Crystallography and Crystal Chemistry, **1978**. 34, (2): 689-691 DOI: 10.1107/s0567740878003830.

[30] Chung, H. and Diao, Y., *Polymorphism as an emerging design strategy for high performance organic electronics.* J. Mater. Chem. C., **2016**. 4, (18): 3915-3933 DOI: 10.1039/c5tc04390e.

[31] Varma, C.M., Zaanen, J., and Raghavachari, K., *Superconductivity in the Fullerenes.* Science, **1991**. 254, (5034): 989-992 DOI: 10.1126/science.254.5034.989.

[32] Singleton, J. and Mielke, C., *Quasi-two-dimensional organic superconductors: A review.* Contemporary Physics, **2002**. 43, (2): 63-96 DOI: 10.1080/00107510110108681.

[33] Brown, S.E., *Organic superconductors: The Bechgaard salts and relatives.* Physica C: Superconductivity and its Applications, **2015**. 514: 279-289 DOI: 10.1016/j.physc.2015.02.030.

[34] Jérome, D., Mazaud, A., Ribault, M., and Bechgaard, K., *Superconductivity in a synthetic organic conductor (TMTSF)2PF 6.* Journal de Physique Lettres, **1980**. 41, (4): 95-98 DOI: 10.1051/jphyslet:0198000410409500.

[35] Özçelik, V.O. and Ciraci, S., *Size Dependence in the Stabilities and Electronic Properties of α-Graphyne and Its Boron Nitride Analogue.* The Journal of Physical Chemistry C, **2013**. 117, (5): 2175-2182 DOI: 10.1021/jp3111869.

[36] Tagami, M., Liang, Y.Y., Naito, H., Kawazoe, Y., and Kotani, M., *Negatively curved cubic carbon crystals with octahedral symmetry.* Carbon, **2014**. 76: 266-274 DOI: 10.1016/j.carbon.2014.04.077.

[37] Wang, Z., Zhou, X.-F., Zhang, X., Zhu, Q., Dong, H., Zhao, M., and Oganov, A.R., *Phagraphene: A Low-Energy Graphene Allotrope Composed of 5–6–7 Carbon Rings with Distorted Dirac Cones.* Nano Lett., **2015**. 15, (9): 6182-6186 DOI: 10.1021/acs.nanolett.5b02512.

[38] Adams, G.B., O'Keeffe, M., Sankey, O.F., and Page, J.B., *Polybenzene, A Predicted New Low Energy Form of Carbon.* MRS Proceedings, **2011**. 270 DOI: 10.1557/proc-270-103.

[39] Hirsch, A., *The era of carbon allotropes.* Nature Materials, **2010**. 9, (11): 868 DOI: 10.1038/nmat2885.

[40] Santhiago, M., Strauss, M., Pereira, M.P., Chagas, A.S., and Bufon, C.C.B., *Direct Drawing Method of Graphite onto Paper for High-Performance Flexible Electrochemical Sensors.* ACS Applied Materials & Interfaces, **2017**. 9, (13): 11959-11966 DOI: 10.1021/acsami.6b15646.

[41] Pan, Z., Sun, H., Zhang, Y., and Chen, C., *Harder than Diamond: Superior Indentation Strength of Wurtzite BN and Lonsdaleite.* Phys. Rev. Lett., **2009**. 102, (5): 055503 DOI: 10.1103/Physrevlett.102.055503.

[42] Yu, M.-F., Lourie, O., Dyer, M.J., Moloni, K., Kelly, T.F., and Ruoff, R.S., *Strength and Breaking Mechanism of Multiwalled Carbon Nanotubes Under Tensile Load.* Science, **2000**. 287, (5453): 637-640 DOI: 10.1126/science.287.5453.637.

[43] Rafiee, M.A., Rafiee, J., Wang, Z., Song, H., Yu, Z.-Z., and Koratkar, N., *Enhanced Mechanical Properties of Nanocomposites at Low Graphene Content.* ACS Nano, **2009**. 3, (12): 3884-3890 DOI: 10.1021/nn9010472.

[44] Gojny, F.H., Wichmann, M.H.G., Köpke, U., Fiedler, B., and Schulte, K., *Carbon nanotube-reinforced epoxy-composites: enhanced stiffness and fracture toughness at low nanotube content.* Compos. Sci. Technol., **2004**. 64, (15): 2363-2371 DOI: 10.1016/j.compscitech.2004.04.002.

[45] Voz, C., Puigdollers, J., Cheylan, S., Fonrodona, M., Stella, M., Andreu, J., and Alcubilla, R., *Photodiodes based on fullerene semiconductor.* Thin Solid Films, **2007**. 515, (19): 7675-7678 DOI: 10.1016/j.tsf.2006.11.160.

[46] Lu, X. and Chen, Z., *Curved Pi-Conjugation, Aromaticity, and the Related Chemistry of Small Fullerenes (<C60) and Single-Walled Carbon Nanotubes.* Chem. Rev., **2005**. 105, (10): 3643-3696 DOI: 10.1021/cr030093d.

[47] Buerschaper, R.A., *Thermal and Electrical Conductivity of Graphite and Carbon at Low Temperatures.* J. Appl. Phys., **1944**. 15, (5): 452-454 DOI: 10.1063/1.1707454.

[48] Novoselov, K.S., Geim, A.K., Morozov, S.V., Jiang, D., Zhang, Y., Dubonos, S.V., Grigorieva, I.V., and Firsov, A.A., *Electric Field Effect in Atomically Thin Carbon Films.* Science, **2004**. 306, (5696): 666-669 DOI: 10.1126/science.1102896.

[49] Kim, M., Seo, J.-H., Singisetti, U., and Ma, Z., *Recent advances in free-standing single crystalline wide band-gap semiconductors and their applications: GaN, SiC, ZnO, [small beta]-Ga2O3, and diamond.* J. Mater. Chem. C., **2017**. 5, (33): 8338-8354 DOI: 10.1039/C7TC02221B.

[50] Liu, A.Y. and Cohen, M.L., *Prediction of New Low Compressibility Solids.* Science, **1989**. 245, (4920): 841-842 DOI: 10.1126/science.245.4920.841.

[51]   Wu, M.L., Guruz, M.U., Dravid, V.P., Chung, Y.W., Anders, S., Freire, F.L., and Mariotto, G., *Formation of carbon nitride with sp3-bonded carbon in CNx/ZrN superlattice coatings.* Appl. Phys. Lett., **2000**. 76, (19): 2692-2694 DOI: 10.1063/1.126743.

[52]   Wang, Y., Wang, X., and Antonietti, M., *Polymeric Graphitic Carbon Nitride as a Heterogeneous Organocatalyst: From Photochemistry to Multipurpose Catalysis to Sustainable Chemistry.* Angew. Chem. Int. Ed., **2012**. 51, (1): 68-89 DOI: 10.1002/anie.201101182.

[53]   Baumann, D. and Schnick, W., *High-Pressure Polymorph of Phosphorus Nitride Imide HP4N7 Representing a New Framework Topology.* Inorg. Chem., **2014**. 53, (15): 7977-7982 DOI: 10.1021/ic500767f.

[54]   Marchuk, A., Pucher, F.J., Karau, F.W., and Schnick, W., *A High-Pressure Polymorph of Phosphorus Nitride Imide.* Angew. Chem. Int. Ed., **2014**. 53, (9): 2469-2472 DOI: 10.1002/anie.201309020.

[55]   Marchuk, A., Pucher, F.J., Karau, F.W., and Schnick, W., *A High-Pressure Polymorph of Phosphorus Nitride Imide.* Angew. Chem., **2014**. 126, (9): 2501-2504 DOI: 10.1002/ange.201309020.

[56]   Mahmood, J., Lee, E.K., Jung, M., Shin, D., Jeon, I.-Y., Jung, S.-M., Choi, H.-J., Seo, J.-M., Bae, S.-Y., Sohn, S.-D., Park, N., Oh, J.H., Shin, H.-J., and Baek, J.-B., *Nitrogenated holey two-dimensional structures.* Nat Commun, **2015**. 6: 6486 DOI: 10.1038/ncomms7486.

[57]   Mahmood, J., Lee, E.K., Jung, M., Shin, D., Choi, H.-J., Seo, J.-M., Jung, S.-M., Kim, D., Li, F., Lah, M.S., Park, N., Shin, H.-J., Oh, J.H., and Baek, J.-B., *Two-dimensional polyaniline (C3N) from carbonized organic single crystals in solid state.* PNAS, **2016**. 113, (27): 7414-7419 DOI: 10.1073/pnas.1605318113.

[58]   Vitaku, E. and Dichtel, W.R., *Synthesis of 2D Imine-Linked Covalent Organic Frameworks through Formal Transimination Reactions.* J. Am. Chem. Soc., **2017**. 139, (37): 12911-12914 DOI: 10.1021/jacs.7b06913.

[59]   Jackson, K.T., Reich, T.E., and El-Kaderi, H.M., *Targeted synthesis of a porous borazine-linked covalent organic framework.* Chem. Commun., **2012**. 48, (70): 8823-5 DOI: 10.1039/c2cc33583b.

[60]   Hunt, J.R., Doonan, C.J., LeVangie, J.D., Cote, A.P., and Yaghi, O.M., *Reticular synthesis of covalent organic borosilicate frameworks.* J. Am. Chem. Soc., **2008**. 130, (36): 11872-3 DOI: 10.1021/ja805064f.

[61]   Du, Y., Yang, H., Whiteley, J.M., Wan, S., Jin, Y., Lee, S.H., and Zhang, W., *Ionic Covalent Organic Frameworks with Spiroborate Linkage.* Angew. Chem. Int. Ed. Engl., **2016**. 55, (5): 1737-41 DOI: 10.1002/anie.201509014.

[62]   Roeser, J., Prill, D., Bojdys, M.J., Fayon, P., Trewin, A., Fitch, A.N., Schmidt, M.U., and Thomas, A., *Anionic silicate organic frameworks constructed from hexacoordinate silicon centres.* Nat Chem, **2017**. 9, (10): 977-982 DOI: 10.1038/nchem.2771.

[63]   Nguyen, H.L., Gándara, F., Furukawa, H., Doan, T.L.H., Cordova, K.E., and Yaghi, O.M., *A Titanium–Organic Framework as an Exemplar of Combining the Chemistry of Metal– and Covalent–Organic Frameworks.* J. Am. Chem. Soc., **2016**. 138, (13): 4330-3 DOI: 10.1021/jacs.6b01233.

[64]   Uribe-Romo, F.J., Hunt, J.R., Furukawa, H., Klock, C., O'Keeffe, M., and Yaghi, O.M., *A crystalline imine-linked 3-D porous covalent organic framework.* J. Am. Chem. Soc., **2009**. 131, (13): 4570-1 DOI: 10.1021/ja8096256.

[65]   Uribe-Romo, F.J., Doonan, C.J., Furukawa, H., Oisaki, K., and Yaghi, O.M., *Crystalline covalent organic frameworks with hydrazone linkages.* J. Am. Chem. Soc., **2011**. 133, (30): 11478-81 DOI: 10.1021/ja204728y.

[66]   Dalapati, S., Jin, S., Gao, J., Xu, Y., Nagai, A., and Jiang, D., *An Azine-Linked Covalent Organic Framework.* J. Am. Chem. Soc., **2013**. 135, (46): 17310-17313 DOI: 10.1021/ja4103293.

[67]   Das, G., Biswal, B.P., Kandambeth, S., Venkatesh, V., Kaur, G., Addicoat, M., Heine, T., Verma, S., and Banerjee, R., *Chemical sensing in two dimensional porous covalent organic nanosheets.* Chem Sci, **2015**. 6, (7): 3931-3939 DOI: 10.1039/c5sc00512d.

[68]   Pyles, D.A., Crowe, J.W., Baldwin, L.A., and McGrier, P.L., *Synthesis of Benzobisoxazole-Linked Two-Dimensional Covalent Organic Frameworks and Their Carbon Dioxide Capture Properties.* ACS Macro Letters, **2016**. 5, (9): 1055-1058 DOI: 10.1021/acsmacrolett.6b00486.

[69]   Guo, J., Xu, Y., Jin, S., Chen, L., Kaji, T., Honsho, Y., Addicoat, M.A., Kim, J., Saeki, A., Ihee, H., Seki, S., Irle, S., Hiramoto, M., Gao, J., and Jiang, D., *Conjugated organic framework with three-dimensionally ordered stable structure and delocalized π clouds.* Nat Commun, **2013**. 4: 2736 DOI: 10.1038/ncomms3736.

[70]   Stewart, D., Antypov, D., Dyer, M.S., Pitcher, M.J., Katsoulidis, A.P., Chater, P.A., Blanc, F., and Rosseinsky, M.J., *Stable and ordered amide frameworks synthesised under reversible conditions which facilitate error checking.* Nature Communications, **2017**. 8, (1): 1102 DOI: 10.1038/s41467-017-01423-5.

[71]   Fang, Q., Zhuang, Z., Gu, S., Kaspar, R.B., Zheng, J., Wang, J., Qiu, S., and Yan, Y., *Designed synthesis of large-pore crystalline polyimide covalent organic frameworks.* Nat Commun, **2014**. 5: 4503 DOI: 10.1038/ncomms5503.

[72]   Nagai, A., Chen, X., Feng, X., Ding, X., Guo, Z., and Jiang, D., *A Squaraine-Linked Mesoporous Covalent Organic Framework.* Angew. Chem. Int. Ed., **2013**. 52, (13): 3770-3774 DOI: 10.1002/anie.201300256.

[73]   Zhao, H., Jin, Z., Su, H., Jing, X., Sun, F., and Zhu, G., *Targeted synthesis of a 2D ordered porous organic framework for drug release.* Chem Commun (Camb), **2011**. 47, (22): 6389-91 DOI: 10.1039/c1cc00084e.

[74]   Bojdys, M.J., Wohlgemuth, S.A., Thomas, A., and Antonietti, M., *Ionothermal Route to Layered Two-Dimensional Polymer-Frameworks Based on Heptazine Linkers.* Macromolecules, **2010**. 43, (16): 6639-6645 DOI: 10.1021/ma101008c.

[75]   Kuhn, P., Antonietti, M., and Thomas, A., *Porous, Covalent Triazine-Based Frameworks Prepared by Ionothermal Synthesis.* Angew. Chem. Int. Ed., **2008**. 47, (18): 3450-3453 DOI: 10.1002/anie.200705710.

[76]   Katekomol, P., Roeser, J., Bojdys, M., Weber, J., and Thomas, A., *Covalent Triazine Frameworks Prepared from 1,3,5-Tricyanobenzene.* Chem. Mater., **2013**. 25, (9): 1542-1548 DOI: 10.1021/cm303751n.

[77]   Bojdys, M.J., Jeromenok, J., Thomas, A., and Antonietti, M., *Rational Extension of the Family of Layered, Covalent, Triazine-Based Frameworks with Regular Porosity.* Adv. Mater., **2010**. 22, (19): 2202-2205 DOI: 10.1002/adma.200903436.

[78]   Ren, S., Bojdys, M.J., Dawson, R., Laybourn, A., Khimyak, Y.Z., Adams, D.J., and Cooper, A.I., *Porous, Fluorescent, Covalent Triazine-Based Frameworks Via Room-Temperature and Microwave-Assisted Synthesis.* Adv. Mater., **2012**. 24, (17): 2357-2361 DOI: 10.1002/adma.201200751.

[79]   Beaudoin, D., Maris, T., and Wuest, J.D., *Constructing monocrystalline covalent organic networks by polymerization.* Nat Chem, **2013**. 5, (10): 830-834 DOI: 10.1038/nchem.1730.

[80]   Zhuang, X., Zhao, W., Zhang, F., Cao, Y., Liu, F., Bi, S., and Feng, X., *A two-dimensional conjugated polymer framework with fully sp2-bonded carbon skeleton.* Polymer Chemistry, **2016**. 7, (25): 4176-4181 DOI: 10.1039/c6py00561f.

[81]   Diercks, C.S., Lin, S., Kornienko, N., Kapustin, E.A., Nichols, E.M., Zhu, C., Zhao, Y., Chang, C.J., and Yaghi, O.M., *Reticular Electronic Tuning of Porphyrin Active Sites in Covalent Organic Frameworks for Electrocatalytic Carbon Dioxide Reduction.* J. Am. Chem. Soc., **2017**. 140, (3): 1116-1122 DOI: 10.1021/jacs.7b11940.

[82]   Ding, X.S., Guo, J., Feng, X.A., Honsho, Y., Guo, J.D., Seki, S., Maitarad, P., Saeki, A., Nagase, S., and Jiang, D.L., *Synthesis of Metallophthalocyanine Covalent Organic Frameworks That Exhibit High Carrier Mobility and Photoconductivity.* Angew Chem Int Edit, **2011**. 50, (6): 1289-1293 DOI: 10.1002/anie.201005919.

[83]   Ascherl, L., Sick, T., Margraf, J.T., Lapidus, S.H., Calik, M., Hettstedt, C., Karaghiosoff, K., Döblinger, M., Clark, T., Chapman, K.W., Auras, F., and Bein, T., *Molecular docking sites designed for the generation of highly crystalline covalent organic frameworks.* Nat Chem, **2016**. 8, (4): 310-316 DOI: 10.1038/nchem.2444.

[84]   Alahakoon, S.B., Thompson, C.M., Nguyen, A.X., Occhialini, G., McCandless, G.T., and Smaldone, R.A., *An azine-linked hexaphenylbenzene based covalent organic framework.* Chem. Commun., **2016**. 52, (13): 2843-5 DOI: 10.1039/C5CC10408D.

[85]   Fang, Q., Gu, S., Zheng, J., Zhuang, Z., Qiu, S., and Yan, Y., *3D Microporous Base-Functionalized Covalent Organic Frameworks for Size-Selective Catalysis.* Angew. Chem. Int. Ed., **2014**. 53, (11): 2878-2882 DOI: 10.1002/anie.201310500.

[86]   Zhang, Y.-B., Su, J., Furukawa, H., Yun, Y., Gándara, F., Duong, A., Zou, X., and Yaghi, O.M., *Single-Crystal Structure of a Covalent Organic Framework.* J. Am. Chem. Soc., **2013**. 135, (44): 16336-16339 DOI: 10.1021/ja409033p.

[87]   Wang, C., Wang, Y., Ge, R., Song, X., Xing, X., Jiang, Q., Lu, H., Hao, C., Guo, X., Gao, Y., and Jiang, D., *A 3D Covalent Organic Framework with Exceptionally High Iodine Capture Capability.* Chem. Eur. J., **2018**. 24, (3): 585-589 DOI: 10.1002/chem.201705405.

[88]   Fang, Q., Wang, J., Gu, S., Kaspar, R.B., Zhuang, Z., Zheng, J., Guo, H., Qiu, S., and Yan, Y., *3D Porous Crystalline Polyimide Covalent Organic Frameworks for Drug Delivery.* J. Am. Chem. Soc., **2015**. 137, (26): 8352-8355 DOI: 10.1021/jacs.5b04147.

[89]   Han, S.S., Furukawa, H., Yaghi, O.M., and Goddard, W.A., 3rd, *Covalent organic frameworks as exceptional hydrogen storage materials.* J. Am. Chem. Soc., **2008**. 130, (35): 11580-1 DOI: 10.1021/ja803247y.

[90]   Lin, G., Ding, H., Yuan, D., Wang, B., and Wang, C., *A Pyrene-Based, Fluorescent Three-Dimensional Covalent Organic Framework.* J. Am. Chem. Soc., **2016**. 138, (10): 3302-5 DOI: 10.1021/jacs.6b00652.

[91]   Lin, G., Ding, H., Chen, R., Peng, Z., Wang, B., and Wang, C., *3D Porphyrin-Based Covalent Organic Frameworks.* J. Am. Chem. Soc., **2017**. 139, (25): 8705-8709 DOI: 10.1021/jacs.7b04141.

[92]   Feng, X., Ding, X., and Jiang, D., *Covalent organic frameworks.* Chem. Soc. Rev., **2012**. 41, (18): 6010-22 DOI: 10.1039/c2cs35157a.

[93]   Ding, S.-Y. and Wang, W., *Covalent organic frameworks (COFs): from design to applications.* Chem. Soc. Rev., **2013**. 42, (2): 548-568 DOI: 10.1039/C2CS35072F.

[94]   Yang, D., Momeni, M.R., Demir, H., Pahls, D.R., Rimoldi, M., Wang, T.C., Farha, O.K., Hupp, J.T., Cramer, C.J., Gates, B.C., and Gagliardi, L., *Tuning the properties of metal-organic framework nodes as supports of single-site iridium catalysts: node modification by atomic layer deposition of aluminium.* Faraday Discuss., **2017**. 201, (0): 195-206 DOI: 10.1039/C7FD00031F.

[95]   Janiak, C. and Vieth, J.K., *MOFs, MILs and more: concepts, properties and applications for porous coordination networks (PCNs).* New J. Chem., **2010**. 34, (11): 2366-2388 DOI: 10.1039/C0NJ00275E.

[96]   Wade, C.R. and Dinca, M., *Investigation of the synthesis, activation, and isosteric heats of CO2 adsorption of the isostructural series of metal-organic frameworks M3(BTC)2 (M = Cr, Fe, Ni, Cu, Mo, Ru).* Dalton Transactions, **2012**. 41, (26): 7931-7938 DOI: 10.1039/C2DT30372H.

[97]   Rosi, N.L., Kim, J., Eddaoudi, M., Chen, B., O'Keeffe, M., and Yaghi, O.M., *Rod Packings and Metal–Organic Frameworks Constructed from Rod-Shaped Secondary Building Units.* J. Am. Chem. Soc., **2005**. 127, (5): 1504-1518 DOI: 10.1021/ja045123o.

[98]   Fessner, W.-D., Murty, B.A.R.C., Wörth, J., Hunkler, D., Fritz, H., Prinzbach, H., Roth, W.D., Schleyer, P.v.R., McEwen, A.B., and Maier, W.F., *Dodecahedranes from [1.1.1.1]Pagodanes.* Angewandte Chemie International Edition in English, **1987**. 26, (5): 452-454 DOI: 10.1002/anie.198704521.

[99]   Eaton, P.E. and Cole, T.W., *Cubane.* J. Am. Chem. Soc., **1964**. 86, (15): 3157-3158 DOI: 10.1021/ja01069a041.

[100]   Biegasiewicz, K.F., Griffiths, J.R., Savage, G.P., Tsanaktsidis, J., and Priefer, R., *Cubane: 50 Years Later.* Chem. Rev., **2015**. 115, (14): 6719-6745 DOI: 10.1021/cr500523x.

[101]   Lin, S., Diercks, C.S., Zhang, Y.-B., Kornienko, N., Nichols, E.M., Zhao, Y., Paris, A.R., Kim, D., Yang, P., Yaghi, O.M., and Chang, C.J., *Covalent organic frameworks comprising cobalt porphyrins for catalytic CO2 reduction in water.* Science, **2015**. 349, (6253): 1208 DOI: 10.1126/science.aac8343.

[102]   Diercks, C.S., Lin, S., Kornienko, N., Kapustin, E.A., Nichols, E.M., Zhu, C., Zhao, Y., Chang, C.J., and Yaghi, O.M., *Reticular Electronic Tuning of Porphyrin Active Sites in Covalent Organic Frameworks for Electrocatalytic Carbon Dioxide Reduction.* J. Am. Chem. Soc., **2018**. 140, (3): 1116-1122 DOI: 10.1021/jacs.7b11940.

[103]   Permyakova, A., Skrylnyk, O., Courbon, E., Affram, M., Wang, S., Lee, U.H., Valekar, A.H., Nouar, F., Mouchaham, G., Devic, T., De Weireld, G., Chang, J.-S., Steunou, N., Frère, M., and Serre, C., *Synthesis Optimization, Shaping, and Heat Reallocation Evaluation of the Hydrophilic Metal–Organic Framework MIL-160(Al).* ChemSusChem, **2017**. 10, (7): 1419-1426 DOI: 10.1002/cssc.201700164.

[104]   Lin, K.-S., Adhikari, A.K., Ku, C.-N., Chiang, C.-L., and Kuo, H., *Synthesis and characterization of porous HKUST-1 metal organic frameworks for hydrogen storage.* Int. J. Hydrogen Energy, **2012**. 37, (18): 13865-13871 DOI: 10.1016/j.ijhydene.2012.04.105.

[105]   Leng, K., Sun, Y., Li, X., Sun, S., and Xu, W., *Rapid Synthesis of Metal–Organic Frameworks MIL-101(Cr) Without the Addition of Solvent and Hydrofluoric Acid.* Crystal Growth & Design, **2016**. 16, (3): 1168-1171 DOI: 10.1021/acs.cgd.5b01696.

[106]   Murray, L.J., Dinca, M., and Long, J.R., *Hydrogen storage in metal-organic frameworks.* Chem. Soc. Rev., **2009**. 38, (5): 1294-1314 DOI: 10.1039/B802256A.

[107]   Nguyen, V. and Gruenwald, M., *Microscopic origins of poor crystallinity in the synthesis of covalent organic framework COF-5.* J. Am. Chem. Soc., **2018** DOI: 10.1021/jacs.7b12529.

[108]   Dienstmaier, J.F., Medina, D.D., Dogru, M., Knochel, P., Bein, T., Heckl, W.M., and Lackinger, M., *Isoreticular Two-Dimensional Covalent Organic Frameworks Synthesized by On-Surface Condensation of Diboronic Acids.* ACS Nano, **2012**. 6, (8): 7234-7242 DOI: 10.1021/nn302363d.

[109]   Dong, J., Wang, Y., Liu, G., Cheng, Y., and Zhao, D., *Isoreticular covalent organic frameworks for hydrocarbon uptake and separation: the important role of monomer planarity.* CrystEngComm, **2017**. 19, (33): 4899-4904 DOI: 10.1039/c7ce00344g.

[110]   Biswal, B.P., Chandra, S., Kandambeth, S., Lukose, B., Heine, T., and Banerjeet, R., *Mechanochemical Synthesis of Chemically Stable Isoreticular Covalent Organic Frameworks.* J. Am. Chem. Soc., **2013**. 135, (14): 5328-5331 DOI: 10.1021/Ja4017842.

[111]   Olajire, A.A., *Recent advances in the synthesis of covalent organic frameworks for CO2 capture.* Journal of CO2 Utilization, **2017**. 17: 137-161 DOI: 10.1016/j.jcou.2016.12.003.

[112]   Feng, X., Chen, L., Dong, Y., and Jiang, D., *Porphyrin-based two-dimensional covalent organic frameworks: synchronized synthetic control of macroscopic structures and pore parameters.* Chem Commun (Camb), **2011**. 47, (7): 1979-81 DOI: 10.1039/c0cc04386a.

[113]   Liu, X., Li, H., Zhang, Y., Xu, B., A, S., Xia, H., and Mu, Y., *Enhanced carbon dioxide uptake by metalloporphyrin-based microporous covalent triazine framework.* Polymer Chemistry, **2013**. 4, (8): 2445 DOI: 10.1039/c3py00083d.

[114] Bhunia, S., Das, S.K., Jana, R., Peter, S.C., Bhattacharya, S., Addicoat, M., Bhaumik, A., and Pradhan, A., *Electrochemical Stimuli-Driven Facile Metal-Free Hydrogen Evolution from Pyrene-Porphyrin-Based Crystalline Covalent Organic Framework.* ACS Applied Materials & Interfaces, **2017**. 9, (28): 23843-23851 DOI: 10.1021/acsami.7b06968.

[115] Ding, X., Chen, L., Honsho, Y., Feng, X., Saengsawang, O., Guo, J., Saeki, A., Seki, S., Irle, S., Nagase, S., Parasuk, V., and Jiang, D., *An n-channel two-dimensional covalent organic framework.* J. Am. Chem. Soc., **2011**. 133, (37): 14510-3 DOI: 10.1021/ja2052396.

[116] Ding, X., Guo, J., Feng, X., Honsho, Y., Guo, J., Seki, S., Maitarad, P., Saeki, A., Nagase, S., and Jiang, D., *Synthesis of metallophthalocyanine covalent organic frameworks that exhibit high carrier mobility and photoconductivity.* Angew. Chem. Int. Ed. Engl., **2011**. 50, (6): 1289-93 DOI: 10.1002/anie.201005919.

[117] Ding, X., Feng, X., Saeki, A., Seki, S., Nagai, A., and Jiang, D., *Conducting metallophthalocyanine 2D covalent organic frameworks: the role of central metals in controlling pi-electronic functions.* Chem Commun (Camb), **2012**. 48, (71): 8952-4 DOI: 10.1039/c2cc33929c.

[118] Neti, V.S.P.K., Wu, X., Hosseini, M., Bernal, R.A., Deng, S., and Echegoyen, L., *Synthesis of a phthalocyanine 2D covalent organic framework.* CrystEngComm, **2013**. 15, (36): 7157-7160 DOI: 10.1039/C3CE41091A.

[119] Li, Z.P., Feng, X., Zou, Y.C., Zhang, Y.W., Xia, H., Liu, X.M., and Mu, Y., *A 2D azine-linked covalent organic framework for gas storage applications.* Chem. Commun., **2014**. 50, (89): 13825-13828 DOI: 10.1039/C4cc05665e.

[120] Cai, S.-L., Zhang, K., Tan, J.-B., Wang, S., Zheng, S.-R., Fan, J., Yu, Y., Zhang, W.-G., and Liu, Y., *Rationally Designed 2D Covalent Organic Framework with a Brick-Wall Topology.* ACS Macro Letters, **2016**. 5, (12): 1348-1352 DOI: 10.1021/acsmacrolett.6b00805.

[121] Yu, J.-T., Chen, Z., Sun, J., Huang, Z.-T., and Zheng, Q.-Y., *Cyclotricatechylene based porous crystalline material: Synthesis and applications in gas storage.* J. Mater. Chem., **2012**. 22, (12): 5369-5373 DOI: 10.1039/C2JM15159F.

[122] Xu, L., Ding, S.-Y., Liu, J., Sun, J., Wang, W., and Zheng, Q.-Y., *Highly crystalline covalent organic frameworks from flexible building blocks.* Chem. Commun., **2016**. 52, (25): 4706-4709 DOI: 10.1039/c6cc01171c.

[123] Li, L.-H., Feng, X.-L., Cui, X.-H., Ma, Y.-X., Ding, S.-Y., and Wang, W., *Salen-Based Covalent Organic Framework.* J. Am. Chem. Soc., **2017**. 139, (17): 6042-6045 DOI: 10.1021/jacs.7b01523.

[124] Rabone, J., Yue, Y.-F., Chong, S.Y., Stylianou, K.C., Bacsa, J., Bradshaw, D., Darling, G.R., Berry, N.G., Khimyak, Y.Z., Ganin, A.Y., Wiper, P., Claridge, J.B., and Rosseinsky, M.J., *An Adaptable Peptide-Based Porous Material.* Science, **2010**. 329, (5995): 1053-1057 DOI: 10.1126/science.1190672.

[125] Chen, Q., Chang, Z., Song, W.-C., Song, H., Song, H.-B., Hu, T.-L., and Bu, X.-H., *A Controllable Gate Effect in Cobalt(II) Organic Frameworks by Reversible Structure Transformations.* Angew. Chem. Int. Ed., **2013**. 52, (44): 11550-11553 DOI: 10.1002/anie.201306304.

[126] Mason, J.A., Oktawiec, J., Taylor, M.K., Hudson, M.R., Rodriguez, J., Bachman, J.E., Gonzalez, M.I., Cervellino, A., Guagliardi, A., Brown, C.M., Llewellyn, P.L., Masciocchi, N., and Long, J.R., *Methane storage in flexible metal–organic frameworks with intrinsic thermal management.* Nature, **2015**. 527, (7578): 357-361 DOI: 10.1038/nature15732.

[127] Deria, P., Gómez-Gualdrón, D.A., Bury, W., Schaef, H.T., Wang, T.C., Thallapally, P.K., Sarjeant, A.A., Snurr, R.Q., Hupp, J.T., and Farha, O.K., *Ultraporous, Water Stable, and Breathing Zirconium-Based Metal–Organic Frameworks with ftw Topology.* J. Am. Chem. Soc., **2015**. 137, (40): 13183-13190 DOI: 10.1021/jacs.5b08860.

[128] Krause, S., Bon, V., Senkovska, I., Stoeck, U., Wallacher, D., Többens, D.M., Zander, S., Pillai, R.S., Maurin, G., Coudert, F.-X., and Kaskel, S., *A pressure-amplifying framework material with negative gas adsorption transitions.* Nature, **2016**. 532, (7599): 348 DOI: 10.1038/nature17430.

[129] Das, R.K., Aijaz, A., Sharma, M.K., Lama, P., and Bharadwaj, P.K., *Direct Crystallographic Observation of Catalytic Reactions inside the Pores of a Flexible Coordination Polymer.* Chem. Eur. J., **2012**. 18, (22): 6866-6872 DOI: 10.1002/chem.201200046.

[130] Alhamami, M., Doan, H., and Cheng, C.-H., *A Review on Breathing Behaviors of Metal-Organic-Frameworks (MOFs) for Gas Adsorption.* Materials, **2014**. 7, (4): 3198 DOI: 10.3390/ma7043198.

[131] Carrington, E.J., McAnally, C.A., Fletcher, A.J., Thompson, S.P., Warren, M., and Brammer, L., *Solvent-switchable continuous-breathing behaviour in a diamondoid metal–organic framework and its influence on CO2 versus CH4 selectivity.* Nature Chemistry, **2017**. 9, (9): 882 DOI: 10.1038/nchem.2747.

[132] Du, Y., Calabro, D., Wooler, B., Li, Q., Cundy, S., Kamakoti, P., Colmyer, D., Mao, K., and Ravikovitch, P., *Kinetic and Mechanistic Study of COF-1 Phase Change from a Staggered to Eclipsed Model upon Partial Removal of Mesitylene.* The Journal of Physical Chemistry C, **2013**. 118, (1): 399-407 DOI: 10.1021/jp4097293.

[133] Ma, Y.-X., Li, Z.-J., Wei, L., Ding, S.-Y., Zhang, Y.-B., and Wang, W., *A Dynamic Three-Dimensional Covalent Organic Framework.* J. Am. Chem. Soc., **2017** DOI: 10.1021/jacs.7b01097.

[134] Baldwin, L.A., Crowe, J.W., Shannon, M.D., Jaroniec, C.P., and McGrier, P.L., *2D Covalent Organic Frameworks with Alternating Triangular and Hexagonal Pores.* Chem. Mater., **2015**. 27, (18): 6169-6172 DOI: 10.1021/acs.chemmater.5b02053.

[135] Feng, X., Dong, Y., and Jiang, D., *Star-shaped two-dimensional covalent organic frameworks.* CrystEngComm, **2013**. 15, (8): 1508-1511 DOI: 10.1039/C2CE26371H.

[136] Yang, H., Du, Y., Wan, S., Trahan, G.D., Jin, Y., and Zhang, W., *Mesoporous 2D Covalent Organic Frameworks Based on Shape-Persistent Arylene-Ethynylene Macrocycles.* Chemical Science, **2015**. 6, (7): 4049-4053 DOI: 10.1039/C5SC00894H.

[137] Zhu, Y., Wan, S., Jin, Y., and Zhang, W., *Desymmetrized Vertex Design for the Synthesis of Covalent Organic Frameworks with Periodically Heterogeneous Pore Structures.* J. Am. Chem. Soc., **2015**. 137, (43): 13772-5 DOI: 10.1021/jacs.5b09487.

[138] Pang, Z.-F., Xu, S.-Q., Zhou, T.-Y., Liang, R.-R., Zhan, T.-G., and Zhao, X., *Construction of Covalent Organic Frameworks Bearing Three Different Kinds of Pores through the Heterostructural Mixed Linker Strategy.* J. Am. Chem. Soc., **2016**. 138, (14): 4710-3 DOI: 10.1021/jacs.6b01244.

[139] Qian, C., Qi, Q.-Y., Jiang, G.-F., Cui, F.-Z., Tian, Y., and Zhao, X., *Toward Covalent Organic Frameworks Bearing Three Different Kinds of Pores: The Strategy for Construction and COF-to-COF Transformation via Heterogeneous Linker Exchange.* J. Am. Chem. Soc., **2017**. 139, (19): 6736-6743 DOI: 10.1021/jacs.7b02303.

[140] Jiang, J., Zhao, Y., and Yaghi, O.M., *Covalent Chemistry beyond Molecules.* J. Am. Chem. Soc., **2016**. 138, (10): 3255-3265 DOI: 10.1021/jacs.5b10666.

[141] Yaghi, O.M., O'Keeffe, M., Ockwig, N.W., Chae, H.K., Eddaoudi, M., and Kim, J., *Reticular synthesis and the design of new materials.* Nature, **2003**. 423, (6941): 705 DOI: 10.1038/nature01650.

[142] Rodgers, M.T. and Armentrout, P.B., *Noncovalent metal-ligand bond energies as studied by threshold collision-induced dissociation.* Mass Spectrom. Rev., **2000**. 19, (4): 215-247 DOI: 10.1002/1098-2787(200007)19:4<215::aid-mas2>3.0.co;2-x.

[143] Atkins, P.d.P., J. , *Physical Chemistry for the Life Sciences, 2nd ed.;* . Vol. New York. 2011: W. H. Freeman and Company.

[144]   Smith, B.J., Overholts, A.C., Hwang, N., and Dichtel, W., *Insight Into the Crystallization of Amorphous Imine-Linked Polymer Networks to 2D Covalent Organic Frameworks.* Chem. Commun., **2016**. 52, (18): 3690-3 DOI: 10.1039/C5CC10221A.

[145]   Smith, B.J. and Dichtel, W.R., *Mechanistic Studies of Two-Dimensional Covalent Organic Frameworks Rapidly Polymerized from Initially Homogenous Conditions.* J. Am. Chem. Soc., **2014**. 136, (24): 8783-8789 DOI: 10.1021/ja5037868.

[146]   Matsumoto, M., Dasari, R.R., Ji, W., Feriante, C.H., Parker, T.C., Marder, S.R., and Dichtel, W.R., *Rapid, Low Temperature Formation of Imine-Linked Covalent Organic Frameworks Catalyzed by Metal Triflates.* J. Am. Chem. Soc., **2017** DOI: 10.1021/jacs.7b01240.

[147]   Calik, M., Sick, T., Dogru, M., Döblinger, M., Datz, S., Budde, H., Hartschuh, A., Auras, F., and Bein, T., *From Highly Crystalline to Outer Surface-Functionalized Covalent Organic Frameworks—A Modulation Approach.* J. Am. Chem. Soc., **2016**. 138, (4): 1234-1239 DOI: 10.1021/jacs.5b10708.

[148]   Karak, S., Kandambeth, S., Biswal, B.P., Sasmal, H.S., Kumar, S., Pachfule, P., and Banerjee, R., *Constructing Ultraporous Covalent Organic Frameworks in Seconds via an Organic Terracotta Process.* J. Am. Chem. Soc., **2017**. 139, (5): 1856-1862 DOI: 10.1021/jacs.6b08815.

[149]   Smith, B.J., Parent, L.R., Overholts, A.C., Beaucage, P.A., Bisbey, R.P., Chavez, A.D., Hwang, N., Park, C., Evans, A.M., Gianneschi, N.C., and Dichtel, W.R., *Colloidal Covalent Organic Frameworks.* ACS Central Science, **2017**. 3, (1): 58-65 DOI: 10.1021/acscentsci.6b00331.

[150]   Austin M., E., Lucas R., P., Nathan C., F., Ryan P., B., Edon, V., Lin X., C., Nathan C., G., and William, D., *Seeded Growth of Single-Crystal Two-Dimensional Covalent Organic Frameworks*. 2017.

[151]   DeBlase, C.R., Hernández-Burgos, K., Silberstein, K.E., Rodríguez-Calero, G.G., Bisbey, R.P., Abruña, H.D., and Dichtel, W.R., *Rapid and Efficient Redox Processes within 2D Covalent Organic Framework Thin Films.* ACS Nano, **2015**. 9, (3): 3178-3183 DOI: 10.1021/acsnano.5b00184.

[152]   Bertrand, G.H.V., Michaelis, V.K., Ong, T.-C., Griffin, R.G., and Dincă, M., *Thiophene-based covalent organic frameworks.* PNAS, **2013**. 110, (13): 4923-4928 DOI: 10.1073/pnas.1221824110.

[153]   Artz, J., Mallmann, S., and Palkovits, R., *Selective Aerobic Oxidation of HMF to 2,5-Diformylfuran on Covalent Triazine Frameworks-Supported Ru Catalysts.* ChemSusChem, **2015**. 8, (4): 672-679 DOI: 10.1002/cssc.201403078.

[154]   Bhunia, A., Vasylyeva, V., and Janiak, C., *From a supramolecular tetranitrile to a porous covalent triazine-based framework with high gas uptake capacities.* Chem. Commun., **2013**. 49, (38): 3961 DOI: 10.1039/c3cc41382a.

[155]   Bhunia, A., Boldog, I., Möller, A., and Janiak, C., *Highly stable nanoporous covalent triazine-based frameworks with an adamantane core for carbon dioxide sorption and separation.* Journal of Materials Chemistry A, **2013**. 1, (47): 14990 DOI: 10.1039/c3ta13407e.

[156]   Mo, Y.-P., Liu, X.-H., and Wang, D., *Concentration-Directed Polymorphic Surface Covalent Organic Frameworks: Rhombus, Parallelogram, and Kagome.* ACS Nano, **2017**. 11, (11): 11694-11700 DOI: 10.1021/acsnano.7b06871.

[157]   Zhou, T.-Y., Xu, S.-Q., Wen, Q., Pang, Z.-F., and Zhao, X., *One-Step Construction of Two Different Kinds of Pores in a 2D Covalent Organic Framework.* J. Am. Chem. Soc., **2014**. 136, (45): 15885-15888 DOI: 10.1021/ja5092936.

[158]   Dalapati, S., Jin, E., Addicoat, M., Heine, T., and Jiang, D., *Highly Emissive Covalent Organic Frameworks.* J. Am. Chem. Soc., **2016**. 138, (18): 5797-800 DOI: 10.1021/jacs.6b02700.

[159]   Rabbani, M.G., Sekizkardes, A.K., Kahveci, Z., Reich, T.E., Ding, R., and El-Kaderi, H.M., *A 2D Mesoporous Imine-Linked Covalent Organic Framework for High Pressure Gas Storage Applications.* Chemistry - A European Journal, **2013**. 19, (10): 3324-3328 DOI: 10.1002/chem.201203753.

[160] Leng, W., Peng, Y., Zhang, J., Lu, H., Feng, X., Ge, R., Dong, B., Wang, B., Hu, X., and Gao, Y., *Sophisticated Design of Covalent Organic Frameworks with Controllable Bimetallic Docking for a Cascade Reaction.* Chem. Eur. J., **2016**. 22, (27): 9087-91 DOI: 10.1002/chem.201601334.

[161] Wu, Y., Xu, H., Chen, X., Gao, J., and Jiang, D., *A [small pi]-electronic covalent organic framework catalyst: [small pi]-walls as catalytic beds for Diels-Alder reactions under ambient conditions.* Chem. Commun., **2015**. 51, (50): 10096-10098 DOI: 10.1039/C5CC03457D.

[162] Auras, F., Ascherl, L., Hakimioun, A.H., Margraf, J.T., Hanusch, F.C., Reuter, S., Bessinger, D., Doblinger, M., Hettstedt, C., Karaghiosoff, K., Herbert, S., Knochel, P., Clark, T., and Bein, T., *Synchronized Offset Stacking: A Concept for Growing Large-Domain and Highly Crystalline 2D Covalent Organic Frameworks.* J. Am. Chem. Soc., **2016**. 138, (51): 16703-16710 DOI: 10.1021/jacs.6b09787.

[163] Chen, X., Huang, N., Gao, J., Xu, H., Xu, F., and Jiang, D., *Towards covalent organic frameworks with predesignable and aligned open docking sites.* Chem. Commun., **2014**. 50, (46): 6161-6163 DOI: 10.1039/C4CC01825G.

[164] Pal, N. and Bhaumik, A., *Soft templating strategies for the synthesis of mesoporous materials: Inorganic, organic–inorganic hybrid and purely organic solids.* Adv. Colloid Interface Sci., **2013**. 189-190: 21-41 DOI: 10.1016/j.cis.2012.12.002.

[165] Kresge, C.T., Leonowicz, M.E., Roth, W.J., Vartuli, J.C., and Beck, J.S., *Ordered mesoporous molecular sieves synthesized by a liquid-crystal template mechanism.* Nature, **1992**. 359, (6397): 710 DOI: 10.1038/359710a0.

[166] Zhao, D., Feng, J., Huo, Q., Melosh, N., Fredrickson, G.H., Chmelka, B.F., and Stucky, G.D., *Triblock Copolymer Syntheses of Mesoporous Silica with Periodic 50 to 300 Angstrom Pores.* Science, **1998**. 279, (5350): 548-552 DOI: 10.1126/science.279.5350.548.

[167] Stupp, S.I., Son, S., Lin, H.C., and Li, L.S., *Synthesis of Two-Dimensional Polymers.* Science, **1993**. 259, (5091): 59-63 DOI: 10.1126/science.259.5091.59.

[168] Takami, T., Ozaki, H., Kasuga, M., Tsuchiya, T., Ogawa, A., Mazaki, Y., Fukushi, D., Uda, M., and Aono, M., *Periodic Structure of a Single Sheet of a Clothlike Macromolecule (Atomic Cloth) Studied by Scanning Tunneling Microscopy.* Angewandte Chemie International Edition in English, **1997**. 36, (24): 2755-2757 DOI: 10.1002/anie.199727551.

[169] Mazur, M., Wheatley, P.S., Navarro, M., Roth, W.J., Položij, M., Mayoral, A., Eliášová, P., Nachtigall, P., Čejka, J., and Morris, R.E., *Synthesis of 'unfeasible' zeolites.* Nat Chem, **2016**. 8, (1): 58-62 DOI: 10.1038/nchem.2374.

[170] Baumgartner, B., Bojdys, M.J., and Unterlass, M.M., *Geomimetics for green polymer synthesis: highly ordered polyimides via hydrothermal techniques.* Polymer Chemistry, **2014**. 5, (12): 3771-3776 DOI: 10.1039/C4PY00263F.

[171] Roth, W.J., Nachtigall, P., Morris, R.E., Wheatley, P.S., Seymour, V.R., Ashbrook, S.E., Chlubná, P., Grajciar, L., Položij, M., Zukal, A., Shvets, O., and Čejka, J., *A family of zeolites with controlled pore size prepared using a top-down method.* Nature Chemistry, **2013**. 5, (7): 628 DOI: 10.1038/nchem.1662.

[172] Lange, R.Z., Hofer, G., Weber, T., and Schlüter, A.D., *A Two-Dimensional Polymer Synthesized through Topochemical [2 + 2]-Cycloaddition on the Multigram Scale.* J. Am. Chem. Soc., **2017**. 139, (5): 2053-2059 DOI: 10.1021/jacs.6b11857.

[173] Kissel, P., Murray, D.J., Wulftange, W.J., Catalano, V.J., and King, B.T., *A nanoporous two-dimensional polymer by single-crystal-to-single-crystal photopolymerization.* Nature Chemistry, **2014**. 6, (9): 774-778 DOI: 10.1038/nchem.2008.

[174] Kissel, P., Erni, R., Schweizer, W.B., Rossell, M.D., King, B.T., Bauer, T., Götzinger, S., Schlüter, A.D., and Sakamoto, J., *A two-dimensional polymer prepared by organic synthesis.* Nature Chemistry, **2012**. 4, (4): 287 DOI: 10.1038/nchem.1265.

[175] Kory, M.J., Wörle, M., Weber, T., Payamyar, P., van de PollStan, W., Dshemuchadse, J., Trapp, N., and Schlüter, A.D., *Gram-scale synthesis of two-dimensional polymer crystals and their structure analysis by X-ray diffraction.* Nat Chem, **2014**. 6, (9): 779-784 DOI: 10.1038/nchem.2007.

[176] Huang, N., Ding, X., Kim, J., Ihee, H., and Jiang, D., *A Photoresponsive Smart Covalent Organic Framework.* Angew. Chem. Int. Ed., **2015**. 54, (30): 8704-8707 DOI: 10.1002/anie.201503902.

[177] Liu, Y., Ma, Y., Zhao, Y., Sun, X., Gándara, F., Furukawa, H., Liu, Z., Zhu, H., Zhu, C., Suenaga, K., Oleynikov, P., Alshammari, A.S., Zhang, X., Terasaki, O., and Yaghi, O.M., *Weaving of organic threads into a crystalline covalent organic framework.* Science, **2016**. 351, (6271): 365-369 DOI: 10.1126/science.aad4011.

[178] Zhao, Y., Guo, L., Gándara, F., Ma, Y., Liu, Z., Zhu, C., Lyu, H., Trickett, C.A., Kapustin, E.A., Terasaki, O., and Yaghi, O.M., *A Synthetic Route for Crystals of Woven Structures, Uniform Nanocrystals, and Thin Films of Imine Covalent Organic Frameworks.* J. Am. Chem. Soc., **2017**. 139, (37): 13166-13172 DOI: 10.1021/jacs.7b07457.

[179] Cesario, M., Dietrich-Buchecker, C.O., Guilhem, J., Pascard, C., and Sauvage, J.P., *Molecular structure of a catenand and its copper(I) catenate: complete rearrangement of the interlocked macrocyclic ligands by complexation.* J. Chem. Soc., Chem. Commun., **1985**, (5): 244-247 DOI: 10.1039/C39850000244.

[180] Han, S.S., Mendoza-Cortés, J.L., and Goddard Iii, W.A., *Recent advances on simulation and theory of hydrogen storage in metal–organic frameworks and covalent organic frameworks.* Chem. Soc. Rev., **2009**. 38, (5): 1460 DOI: 10.1039/b802430h.

[181] Mendoza-Cortes, J.L., Goddard, W.A., Furukawa, H., and Yaghi, O.M., *A Covalent Organic Framework that Exceeds the DOE 2015 Volumetric Target for H2 Uptake at 298 K.* The Journal of Physical Chemistry Letters, **2012**. 3, (18): 2671-2675 DOI: 10.1021/jz301000m.

[182] Mendoza-Cortés, J.L., Han, S.S., Furukawa, H., Yaghi, O.M., and Goddard, W.A., *Adsorption Mechanism and Uptake of Methane in Covalent Organic Frameworks: Theory and Experiment.* The Journal of Physical Chemistry A, **2010**. 114, (40): 10824-10833 DOI: 10.1021/jp1044139.

[183] Mendoza-Cortes, J.L., Pascal, T.A., and Goddard, W.A., *Design of Covalent Organic Frameworks for Methane Storage.* The Journal of Physical Chemistry A, **2011**. 115, (47): 13852-13857 DOI: 10.1021/jp209541e.

[184] Furukawa, H. and Yaghi, O.M., *Storage of Hydrogen, Methane, and Carbon Dioxide in Highly Porous Covalent Organic Frameworks for Clean Energy Applications.* J. Am. Chem. Soc., **2009**. 131, (25): 8875-8883 DOI: 10.1021/Ja9015765.

[185] Choi, Y.J., Choi, J.H., Choi, K.M., and Kang, J.K., *Covalent organic frameworks for extremely high reversible CO2 uptake capacity: a theoretical approach.* J. Mater. Chem., **2011**. 21, (4): 1073-1078 DOI: 10.1039/c0jm02891f.

[186] Babarao, R. and Jiang, J., *Exceptionally high CO2 storage in covalent-organic frameworks: Atomistic simulation study.* Energy & Environmental Science, **2008**. 1, (1): 139 DOI: 10.1039/b805473h.

[187] Doonan, C.J., Tranchemontagne, D.J., Glover, T.G., Hunt, J.R., and Yaghi, O.M., *Exceptional ammonia uptake by a covalent organic framework.* Nat Chem, **2010**. 2, (3): 235-8 DOI: 10.1038/nchem.548.

[188] Lee, G.-Y., Lee, J., Vo, H.T., Kim, S., Lee, H., and Park, T., *Amine-Functionalized Covalent Organic Framework for Efficient SO2 Capture with High Reversibility.* Scientific Reports, **2017**. 7, (1): 557 DOI: 10.1038/s41598-017-00738-z.

[189] Stegbauer, L., Hahn, M.W., Jentys, A., Savasci, G., Ochsenfeld, C., Lercher, J.A., and Lotsch, B.V., *Tunable Water and CO2 Sorption Properties in Isostructural Azine-Based Covalent Organic Frameworks through Polarity Engineering.* Chem. Mater., **2015**. 27, (23): 7874-7881 DOI: 10.1021/acs.chemmater.5b02151.

[190] Lu, H., Wang, C., Chen, J., Ge, R., Leng, W., Dong, B., Huang, J., and Gao, Y., *A novel 3D covalent organic framework membrane grown on a porous [small alpha]-Al2O3 substrate under solvothermal conditions.* Chem. Commun., **2015**. 51, (85): 15562-5 DOI: 10.1039/C5CC06742A.

[191] Shan, M., Seoane, B., Rozhko, E., Dikhtiarenko, A., Clet, G., Kapteijn, F., and Gascon, J., *Azine-Linked Covalent Organic Framework (COF)-Based Mixed-Matrix Membranes for CO2 /CH4 Separation.* Chemistry, **2016**. 22, (41): 14467-70 DOI: 10.1002/chem.201602999.

[192] Oh, H., Kalidindi, S.B., Um, Y., Bureekaew, S., Schmid, R., Fischer, R.A., and Hirscher, M., *A Cryogenically Flexible Covalent Organic Framework for Efficient Hydrogen Isotope Separation by Quantum Sieving.* Angew. Chem. Int. Ed., **2013**. 52, (50): 13219-13222 DOI: 10.1002/anie.201307443.

[193] Sun, Q., Aguila, B., Perman, J., Earl, L.D., Abney, C.W., Cheng, Y., Wei, H., Nguyen, N., Wojtas, L., and Ma, S., *Postsynthetically Modified Covalent Organic Frameworks for Efficient and Effective Mercury Removal.* J. Am. Chem. Soc., **2017**. 139, (7): 2786-2793 DOI: 10.1021/jacs.6b12885.

[194] Ding, S.-Y., Dong, M., Wang, Y.-W., Chen, Y.-T., Wang, H.-Z., Su, C.-Y., and Wang, W., *A Thioether-Based Fluorescent Covalent Organic Framework for Selective Detection and Facile Removal of Mercury(II).* J. Am. Chem. Soc., **2016**. 138, (9): 3031-7 DOI: 10.1021/jacs.5b10754.

[195] Bai, L., Phua, S.Z.F., Lim, W.Q., Jana, A., Luo, Z., Tham, H.P., Zhao, L., Gao, Q., and Zhao, Y., *Nanoscale covalent organic frameworks as smart carriers for drug delivery.* Chem. Commun., **2016**. 52, (22): 4128-31 DOI: 10.1039/C6CC00853D.

[196] Vyas, V.S., Vishwakarma, M., Moudrakovski, I., Haase, F., Savasci, G., Ochsenfeld, C., Spatz, J.P., and Lotsch, B.V., *Exploiting Noncovalent Interactions in an Imine-Based Covalent Organic Framework for Quercetin Delivery.* Adv. Mater., **2016**. 28, (39): 8749-8754 DOI: 10.1002/adma.201603006.

[197] Xie, Y.-F., Ding, S.-Y., Liu, J., Wang, W., and Zheng, Q.-Y., *Triazatruxene Based Crystalline Covalent Organic Framework and Its Quick-response Fluorescence-on Nature towards Electron Rich Arenes.* J. Mater. Chem. C., **2015**. 3, (39): 10066-10069 DOI: 10.1039/C5TC02256H.

[198] Kaleeswaran, D., Vishnoi, P., and Murugavel, R., *[3+3] Imine and [small beta]-ketoenamine tethered fluorescent covalent-organic frameworks for CO2 uptake and nitroaromatic sensing.* J. Mater. Chem. C., **2015**. 3, (27): 7159-7171 DOI: 10.1039/C5TC00670H.

[199] Das, G., Biswal, B.P., Kandambeth, S., Venkatesh, V., Kaur, G., Addicoat, M., Heine, T., Verma, S., and Banerjee, R., *Chemical sensing in two dimensional porous covalent organic nanosheets.* Chemical Science, **2015**. 6, (7): 3931-3939 DOI: 10.1039/C5SC00512D.

[200] Li, W., Yang, C.-X., and Yan, X.-P., *A versatile covalent organic framework-based platform for sensing biomolecules.* Chem. Commun., **2017**. 53, (83): 11469-11471 DOI: 10.1039/C7CC06244C.

[201] Wang, T., Xue, R., Chen, H., Shi, P., Lei, X., Wei, Y., Guo, H., and Yang, W., *Preparation of two new polyimide bond linked porous covalent organic frameworks and their fluorescent sensing application for sensitive and selective determination of Fe3+.* New J. Chem., **2017**. 41, (23): 14272-14278 DOI: 10.1039/C7NJ02134H.

[202] Ding, S.-Y., Gao, J., Wang, Q., Zhang, Y., Song, W.-G., Su, C.-Y., and Wang, W., *Construction of Covalent Organic Framework for Catalysis: Pd/COF-LZU1 in Suzuki–Miyaura Coupling Reaction.* J. Am. Chem. Soc., **2011**. 133, (49): 19816-19822 DOI: 10.1021/ja206846p.

[203] Goncalves, R.S.B., de Oliveira, A.B.V., Sindra, H.C., Archanjo, B.S., Mendoza, M.E., Carneiro, L.S.A., Buarque, C.D., and Esteves, P.M., *Heterogeneous Catalysis by Covalent Organic Frameworks (COF): Pd(OAc)(2)@COF-300 in Cross-Coupling Reactions.* Chemcatchem, **2016**. 8, (4): 743-750 DOI: 10.1002/cctc.201500926.

[204] Kaleeswaran, D., Antony, R., Sharma, A., Malani, A., and Murugavel, R., *Catalysis and CO2 Capture by Palladium-Incorporated Covalent Organic Frameworks.* ChemPlusChem, **2017**. 82, (10): 1253-1265 DOI: 10.1002/cplu.201700342.

[205] Sun, Q., Aguila, B., and Ma, S., *A bifunctional covalent organic framework as an efficient platform for cascade catalysis.* Materials Chemistry Frontiers, **2017**. 1, (7): 1310-1316 DOI: 10.1039/C6QM00363J.

[206] Li, H., Pan, Q., Ma, Y., Guan, X., Xue, M., Fang, Q., Yan, Y., Valtchev, V., and Qiu, S., *Three-Dimensional Covalent Organic Frameworks with Dual Linkages for Bifunctional Cascade Catalysis.* J. Am. Chem. Soc., **2016**. 138, (44): 14783-14788 DOI: 10.1021/jacs.6b09563.

[207] Wang, X., Han, X., Zhang, J., Wu, X., Liu, Y., and Cui, Y., *Homochiral 2D Porous Covalent Organic Frameworks for Heterogeneous Asymmetric Catalysis.* J. Am. Chem. Soc., **2016**. 138, (38): 12332-12335 DOI: 10.1021/jacs.6b07714.

[208] Zhu, C., Xia, Q., Chen, X., Liu, Y., Du, X., and Cui, Y., *Chiral Metal–Organic Framework as a Platform for Cooperative Catalysis in Asymmetric Cyanosilylation of Aldehydes.* ACS Catalysis, **2016**. 6, (11): 7590-7596 DOI: 10.1021/acscatal.6b02359.

[209] Xu, H., Gao, J., and Jiang, D., *Stable, crystalline, porous, covalent organic frameworks as a platform for chiral organocatalysts.* Nat Chem, **2015**. 7, (11): 905-912 DOI: 10.1038/nchem.2352.

[210] Zhang, K., Cai, S.L., Yan, Y.L., He, Z.H., Lin, H.M., Huang, X.L., Zheng, S.R., Fan, J., and Zhang, W.G., *Construction of a hydrazone-linked chiral covalent organic framework-silica composite as the stationary phase for high performance liquid chromatography.* J. Chromatogr. A, **2017**. 1519: 100-109 DOI: 10.1016/j.chroma.2017.09.007.

[211] Qian, H.-L., Yang, C.-X., and Yan, X.-P., *Bottom-up synthesis of chiral covalent organic frameworks and their bound capillaries for chiral separation.* Nature Communications, **2016**. 7: 12104 DOI: 10.1038/ncomms12104.

[212] Han, X., Huang, J., Yuan, C., Liu, Y., and Cui, Y., *Chiral 3D Covalent Organic Frameworks for High Performance Liquid Chromatographic Enantioseparation.* J. Am. Chem. Soc., **2018**. 140, (3): 892-895 DOI: 10.1021/jacs.7b12110.

[213] Xu, F., Jin, S., Zhong, H., Wu, D., Yang, X., Chen, X., Wei, H., Fu, R., and Jiang, D., *Electrochemically active, crystalline, mesoporous covalent organic frameworks on carbon nanotubes for synergistic lithium-ion battery energy storage.* Sci. Rep., **2015**. 5: 8225 DOI: 10.1038/srep08225.

[214] Xu, F., Xu, H., Chen, X., Wu, D., Wu, Y., Liu, H., Gu, C., Fu, R., and Jiang, D., *Radical Covalent Organic Frameworks: A General Strategy to Immobilize Open-Accessible Polyradicals for High-Performance Capacitive Energy Storage.* Angew. Chem. Int. Ed., **2015**. 54, (23): 6814-8 DOI: 10.1002/anie.201501706.

[215] DeBlase, C.R., Silberstein, K.E., Truong, T.-T., Abruña, H.D., and Dichtel, W.R., *β-Ketoenamine-Linked Covalent Organic Frameworks Capable of Pseudocapacitive Energy Storage.* J. Am. Chem. Soc., **2013**. 135, (45): 16821-16824 DOI: 10.1021/ja409421d.

[216] Bai, L., Gao, Q., and Zhao, Y., *Two Fully Conjugated Covalent Organic Frameworks as Anode Materials for Lithium Ion Batteries.* Journal of Materials Chemistry A, **2016**. 4, (37): 14106-14110 DOI: 10.1039/C6TA06449C.

[217] Wang, J., Si, L., Wei, Q., Hong, X., Lin, L., Li, X., Chen, J., Wen, P., and Cai, Y., *An imine-linked covalent organic framework as the host material for sulfur loading in lithium–sulfur batteries.* Journal of Energy Chemistry, **2017** DOI: 10.1016/j.jechem.2017.10.021.

[218] Ghazi, Z.A., Zhu, L., Wang, H., Naeem, A., Khattak, A.M., Liang, B., Khan, N.A., Wei, Z., Li, L., and Tang, Z., *Efficient Polysulfide Chemisorption in Covalent Organic Frameworks for High-Performance Lithium-Sulfur Batteries.* Advanced Energy Materials, **2016**. 6, (24) DOI: 10.1002/aenm.201601250.

[219]   Wu, Y., Zhang, Z., Bandow, S., and Awaga, K., *A Novel Strategy to Functionalize Covalent Organic Frameworks for High-Energy Rechargeable Lithium Organic Batteries via Graft Polymerization in Nano-Channels.* Bull. Chem. Soc. Jpn., **2017**. 90, (12): 1382-1387 DOI: 10.1246/bcsj.20170247.

[220]   Wan, S., Gándara, F., Asano, A., Furukawa, H., Saeki, A., Dey, S.K., Liao, L., Ambrogio, M.W., Botros, Y.Y., Duan, X., Seki, S., Stoddart, J.F., and Yaghi, O.M., *Covalent Organic Frameworks with High Charge Carrier Mobility.* Chem. Mater., **2011**. 23, (18): 4094-4097 DOI: 10.1021/cm201140r.

[221]   Feng, X., Liu, L., Honsho, Y., Saeki, A., Seki, S., Irle, S., Dong, Y., Nagai, A., and Jiang, D., *High-rate charge-carrier transport in porphyrin covalent organic frameworks: switching from hole to electron to ambipolar conduction.* Angew. Chem. Int. Ed. Engl., **2012**. 51, (11): 2618-22 DOI: 10.1002/anie.201106203.

[222]   Feng, X., Chen, L., Honsho, Y., Saengsawang, O., Liu, L., Wang, L., Saeki, A., Irle, S., Seki, S., Dong, Y., and Jiang, D., *An ambipolar conducting covalent organic framework with self-sorted and periodic electron donor-acceptor ordering.* Adv. Mater., **2012**. 24, (22): 3026-31 DOI: 10.1002/adma.201201185.

[223]   Dogru, M., Handloser, M., Auras, F., Kunz, T., Medina, D., Hartschuh, A., Knochel, P., and Bein, T., *A Photoconductive Thienothiophene-Based Covalent Organic Framework Showing Charge Transfer Towards Included Fullerene.* Angew. Chem. Int. Ed., **2013**. 52, (10): 2920-2924 DOI: 10.1002/anie.201208514.

[224]   Li, L., Tian, Z., Tang, Z., Chen, Y., Cui, H., Zhang, J., Zhao, K., Ding, D., and Guo, J., *Surface Growth of Highly Oriented Covalent Organic Framework Thin Film with Enhanced Photoresponse Speed.* RSC Advances, **2015**. 5, (112): 92573-92576 DOI: 10.1039/C5RA19430J.

[225]   Feldblyum, J.I., McCreery, C.H., Andrews, S.C., Kurosawa, T., Santos, E.J.G., Duong, V., Fang, L., Ayzner, A.L., and Bao, Z., *Few-layer, large-area, 2D covalent organic framework semiconductor thin films.* Chem. Commun., **2015**. 51, (73): 13894-13897 DOI: 10.1039/C5CC04679C.

[226]   Sun, B., Zhu, C.-H., Liu, Y., Wang, C., Wan, L.-J., and Wang, D., *Oriented Covalent Organic Framework Film on Graphene for Robust Ambipolar Vertical Organic Field-Effect Transistor.* Chem. Mater., **2017**. 29, (10): 4367-4374 DOI: 10.1021/acs.chemmater.7b00800.

[227]   Chandra, S., Kundu, T., Dey, K., Addicoat, M., Heine, T., and Banerjee, R., *Interplaying Intrinsic and Extrinsic Proton Conductivities in Covalent Organic Frameworks.* Chem. Mater., **2016**. 28, (5): 1489-1494 DOI: 10.1021/acs.chemmater.5b04947.

[228]   Chandra, S., Kundu, T., Kandambeth, S., BabaRao, R., Marathe, Y., Kunjir, S.M., and Banerjee, R., *Phosphoric Acid Loaded Azo (−N≡N−) Based Covalent Organic Framework for Proton Conduction.* J. Am. Chem. Soc., **2014**. 136, (18): 6570-6573 DOI: 10.1021/ja502212v.

[229]   Xu, H., Tao, S., and Jiang, D., *Proton conduction in crystalline and porous covalent organic frameworks.* Nat Mater, **2016**. 15, (7): 722-6 DOI: 10.1038/nmat4611.

[230]   Ma, H., Liu, B., Li, B., Zhang, L., Li, Y.-G., Tan, H.-Q., Zang, H.-Y., and Zhu, G., *Cationic Covalent Organic Frameworks: A Simple Platform of Anionic Exchange for Porosity Tuning and Proton Conduction.* J. Am. Chem. Soc., **2016**. 138, (18): 5897-5903 DOI: 10.1021/jacs.5b13490.

[231]   Chen, H., Tu, H., Hu, C., Liu, Y., Dong, D., Sun, Y., Dai, Y., Wang, S., Qian, H., Lin, Z., and Chen, L., *Cationic Covalent Organic Framework Nanosheets for Fast Li-Ion Conduction.* J. Am. Chem. Soc., **2018**. 140, (3): 896-899 DOI: 10.1021/jacs.7b12292.

[232]   Osterloh, F.E. and Parkinson, B.A., *Recent developments in solar water-splitting photocatalysis.* MRS Bull., **2011**. 36, (1): 17-22 DOI: 10.1557/mrs.2010.5.

[233]   Demirbaş, A., *Global Renewable Energy Resources.* Energy Sources, Part A: Recovery, Utilization, and Environmental Effects, **2006**. 28, (8): 779-792 DOI: 10.1080/00908310600718742.

[234] Tuller, H.L., *Solar to fuels conversion technologies: a perspective.* Materials for Renewable and Sustainable Energy, **2017**. 6, (1): 3 DOI: 10.1007/s40243-017-0088-2.

[235] Hill, C.A., Such, M.C., Chen, D., Gonzalez, J., and Grady, W.M., *Battery Energy Storage for Enabling Integration of Distributed Solar Power Generation.* IEEE Transactions on Smart Grid, **2012**. 3, (2): 850-857 DOI: 10.1109/TSG.2012.2190113.

[236] Gamborg, C., Millar, K., Shortall, O., and Sandøe, P., *Bioenergy and Land Use: Framing the Ethical Debate.* Journal of Agricultural and Environmental Ethics, **2012**. 25, (6): 909-925 DOI: 10.1007/s10806-011-9351-1.

[237] Frei, H., *Photocatalytic fuel production.* Current Opinion in Electrochemistry, **2017**. 2, (1): 128-135 DOI: 10.1016/j.coelec.2017.03.009.

[238] Hinnemann, B., Moses, P.G., Bonde, J., Jørgensen, K.P., Nielsen, J.H., Horch, S., Chorkendorff, I., and Nørskov, J.K., *Biomimetic Hydrogen Evolution: MoS2 Nanoparticles as Catalyst for Hydrogen Evolution.* J. Am. Chem. Soc., **2005**. 127, (15): 5308-5309 DOI: 10.1021/ja0504690.

[239] Meng, X., Wang, T., Liu, L., Ouyang, S., Li, P., Hu, H., Kako, T., Iwai, H., Tanaka, A., and Ye, J., *Photothermal Conversion of CO2 into CH4 with H2 over Group VIII Nanocatalysts: An Alternative Approach for Solar Fuel Production.* Angew. Chem., **2014**. 126, (43): 11662-11666 DOI: 10.1002/ange.201404953.

[240] Osterloh, F.E., *Photocatalysis versus Photosynthesis: A Sensitivity Analysis of Devices for Solar Energy Conversion and Chemical Transformations.* ACS Energy Letters, **2017**. 2, (2): 445-453 DOI: 10.1021/acsenergylett.6b00665.

[241] Bolton, J.R., Strickler, S.J., and Connolly, J.S., *Limiting and realizable efficiencies of solar photolysis of water.* Nature, **1985**. 316, (6028): 495-500 DOI: 10.1038/316495a0.

[242] Hu, S., Xiang, C., Haussener, S., Berger, A.D., and Lewis, N.S., *An analysis of the optimal band gaps of light absorbers in integrated tandem photoelectrochemical water-splitting systems.* Energy & Environmental Science, **2013**. 6, (10): 2984 DOI: 10.1039/c3ee40453f.

[243] Rocheleau, R., *Photoelectrochemical production of hydrogen: Engineering loss analysis.* Int. J. Hydrogen Energy, **1997**. 22, (8): 771-782 DOI: 10.1016/s0360-3199(96)00221-2.

[244] Seitz, L.C., Chen, Z., Forman, A.J., Pinaud, B.A., Benck, J.D., and Jaramillo, T.F., *Modeling Practical Performance Limits of Photoelectrochemical Water Splitting Based on the Current State of Materials Research.* ChemSusChem, **2014**. 7, (5): 1372-1385 DOI: 10.1002/cssc.201301030.

[245] Pinaud, B.A., Benck, J.D., Seitz, L.C., Forman, A.J., Chen, Z., Deutsch, T.G., James, B.D., Baum, K.N., Baum, G.N., Ardo, S., Wang, H., Miller, E., and Jaramillo, T.F., *Technical and economic feasibility of centralized facilities for solar hydrogen production via photocatalysis and photoelectrochemistry.* Energy & Environmental Science, **2013**. 6, (7): 1983 DOI: 10.1039/c3ee40831k.

[246] Wilker, M.B., Schnitzenbaumer, K.J., and Dukovic, G., *Recent Progress in Photocatalysis Mediated by Colloidal II-VI Nanocrystals.* Isr. J. Chem., **2012**. 52, (11-12): 1002-1015 DOI: 10.1002/ijch.201200073.

[247] Liu, C.-J., Yang, T.-Y., Wang, C.-H., Chien, C.-C., Chen, S.-T., Wang, C.-L., Leng, W.-H., Hwu, Y., Lin, H.-M., Lee, Y.-C., Cheng, C.-L., Je, J.H., and Margaritondo, G., *Enhanced photocatalysis, colloidal stability and cytotoxicity of synchrotron X-ray synthesized Au/TiO2 nanoparticles.* Mater. Chem. Phys., **2009**. 117, (1): 74-79 DOI: 10.1016/j.matchemphys.2009.05.030.

[248] Schwinghammer, K., Mesch, M.B., Duppel, V., Ziegler, C., Senker, J., and Lotsch, B.V., *Crystalline Carbon Nitride Nanosheets for Improved Visible-Light Hydrogen Evolution.* J. Am. Chem. Soc., **2014**. 136, (5): 1730-1733 DOI: 10.1021/ja411321s.

[249] Kamat, P.V., *Manipulation of Charge Transfer Across Semiconductor Interface. A Criterion That Cannot Be Ignored in Photocatalyst Design.* The Journal of Physical Chemistry Letters, **2012**. 3, (5): 663-672 DOI: 10.1021/jz201629p.

[250] Subramanian, V., Wolf, E., and Kamat, P.V., *Semiconductor–Metal Composite Nanostructures. To What Extent Do Metal Nanoparticles Improve the Photocatalytic Activity of TiO2Films?* The Journal of Physical Chemistry B, **2001**. 105, (46): 11439-11446 DOI: 10.1021/jp011118k.

[251] Dionigi, F., Vesborg, P.C.K., Pedersen, T., Hansen, O., Dahl, S., Xiong, A., Maeda, K., Domen, K., and Chorkendorff, I., *Suppression of the water splitting back reaction on GaN:ZnO photocatalysts loaded with core/shell cocatalysts, investigated using a µ-reactor.* J. Catal., **2012**. 292: 26-31 DOI: 10.1016/j.jcat.2012.03.021.

[252] Hisatomi, T., Takanabe, K., and Domen, K., *Photocatalytic Water-Splitting Reaction from Catalytic and Kinetic Perspectives.* Catal. Lett., **2014**. 145, (1): 95-108 DOI: 10.1007/s10562-014-1397-z.

[253] Abe, R., Sayama, K., Domen, K., and Arakawa, H., *A new type of water splitting system composed of two different TiO2 photocatalysts (anatase, rutile) and a IO3−/I− shuttle redox mediator.* Chem. Phys. Lett., **2001**. 344, (3-4): 339-344 DOI: 10.1016/s0009-2614(01)00790-4.

[254] Teets, T.S. and Nocera, D.G., *Photocatalytic hydrogen production.* Chem. Commun., **2011**. 47, (33): 9268-9274 DOI: 10.1039/C1cc12390d.

[255] Artero, V. and Fontecave, M., *Solar fuels generation and molecular systems: is it homogeneous or heterogeneous catalysis?* Chem. Soc. Rev., **2013**. 42, (6): 2338-2356 DOI: 10.1039/C2cs35334b.

[256] Du, P.W. and Eisenberg, R., *Catalysts made of earth-abundant elements (Co, Ni, Fe) for water splitting: Recent progress and future challenges.* Energy & Environmental Science, **2012**. 5, (3): 6012-6021 DOI: 10.1039/c2ee03250c.

[257] Boddy, P.J., *Oxygen Evolution on Semiconducting TiO2.* J. Electrochem. Soc., **1968**. 115, (2): 199-203 DOI: 10.1149/1.2411080.

[258] Fujishima, A. and Honda, K., *Electrochemical Evidence for the Mechanism of the Primary Stage of Photosynthesis.* Bull. Chem. Soc. Jpn., **1971**. 44, (4): 1148-1150 DOI: 10.1246/bcsj.44.1148.

[259] Fujishima, A. and Honda, K., *Electrochemical Photolysis of Water at a Semiconductor Electrode.* Nature, **1972**. 238, (5358): 37-38 DOI: Doi 10.1038/238037a0.

[260] Esswein, A.J. and Nocera, D.G., *Hydrogen Production by Molecular Photocatalysis.* Chem. Rev., **2007**. 107, (10): 4022-4047 DOI: 10.1021/cr050193e.

[261] Lu, H., Hu, R., Bai, H., Chen, H., Lv, F., Liu, L., Wang, S., and Tian, H., *Efficient Conjugated Polymer–Methyl Viologen Electron Transfer System for Controlled Photo-Driven Hydrogen Evolution.* ACS Applied Materials & Interfaces, **2017**. 9, (12): 10355-10359 DOI: 10.1021/acsami.7b00069.

[262] Zhang, G., Lan, Z.-A., and Wang, X., *Conjugated Polymers: Catalysts for Photocatalytic Hydrogen Evolution.* Angew. Chem. Int. Ed., **2016**. 55, (51): 15712-15727 DOI: 10.1002/anie.201607375.

[263] Hoofman, R.J.O.M., de Haas, M.P., Siebbeles, L.D.A., and Warman, J.M., *Highly mobile electrons and holes on isolated chains of the semiconducting polymer poly(phenylene vinylene).* Nature, **1998**. 392, (6671): 54-56 DOI: 10.1038/32118.

[264] Zhou, Q. and Swager, T.M., *Fluorescent Chemosensors Based on Energy Migration in Conjugated Polymers: The Molecular Wire Approach to Increased Sensitivity.* J. Am. Chem. Soc., **1995**. 117, (50): 12593-12602 DOI: 10.1021/ja00155a023.

[265] Wang, X., Maeda, K., Thomas, A., Takanabe, K., Xin, G., Carlsson, J.M., Domen, K., and Antonietti, M., *A metal-free polymeric photocatalyst for hydrogen production from water under visible light.* Nature Materials, **2008**. 8, (1): 76 DOI: 10.1038/nmat2317.

[266] Liu, J., Liu, Y., Liu, N., Han, Y., Zhang, X., Huang, H., Lifshitz, Y., Lee, S.-T., Zhong, J., and Kang, Z., *Metal-free efficient photocatalyst for stable visible water splitting via a two-electron pathway.* Science, **2015**. 347, (6225): 970-974 DOI: 10.1126/science.aaa3145.

[267]   Schwinghammer, K., Tuffy, B., Mesch, M.B., Wirnhier, E., Martineau, C., Taulelle, F., Schnick, W., Senker, J., and Lotsch, B.V., *Triazine-based Carbon Nitrides for Visible-Light-Driven Hydrogen Evolution.* Angew. Chem. Int. Ed., **2013**. 52, (9): 2435-2439 DOI: 10.1002/anie.201206817.

[268]   Zheng, Y., Lin, L., Wang, B., and Wang, X., *Graphitic Carbon Nitride Polymers toward Sustainable Photoredox Catalysis.* Angew. Chem. Int. Ed., **2015**. 54, (44): 12868-12884 DOI: 10.1002/anie.201501788.

[269]   Schwinghammer, K., Hug, S., Mesch, M.B., Senker, J., and Lotsch, B.V., *Phenyl-triazine oligomers for light-driven hydrogen evolution.* Energy & Environmental Science, **2015**. 8, (11): 3345-3353 DOI: 10.1039/C5EE02574E.

[270]   Sprick, R.S., Bonillo, B., Clowes, R., Guiglion, P., Brownbill, N.J., Slater, B.J., Blanc, F., Zwijnenburg, M.A., Adams, D.J., and Cooper, A.I., *Visible-Light-Driven Hydrogen Evolution Using Planarized Conjugated Polymer Photocatalysts.* Angew. Chem. Int. Ed., **2016**. 55, (5): 1792-1796 DOI: 10.1002/anie.201510542.

[271]   Sprick, R.S., Jiang, J.X., Bonillo, B., Ren, S., Ratvijitvech, T., Guiglion, P., Zwijnenburg, M.A., Adams, D.J., and Cooper, A.I., *Tunable organic photocatalysts for visible-light-driven hydrogen evolution.* J. Am. Chem. Soc., **2015**. 137, (9): 3265-70 DOI: 10.1021/ja511552k.

[272]   Schwartz, B.J., *CONJUGATED POLYMERS AS MOLECULAR MATERIALS: How Chain Conformation and Film Morphology Influence Energy Transfer and Interchain Interactions.* Annu. Rev. Phys. Chem., **2003**. 54, (1): 141-172 DOI: 10.1146/annurev.physchem.54.011002.103811.

[273]   Kuecken, S., Acharjya, A., Zhi, L., Schwarze, M., Schomacker, R., and Thomas, A., *Fast tuning of covalent triazine frameworks for photocatalytic hydrogen evolution.* Chem. Commun., **2017**. 53, (43): 5854-5857 DOI: 10.1039/C7CC01827D.

[274]   Meier, C.B., Sprick, R.S., Monti, A., Guiglion, P., Lee, J.-S.M., Zwijnenburg, M.A., and Cooper, A.I., *Structure-property relationships for covalent triazine-based frameworks: The effect of spacer length on photocatalytic hydrogen evolution from water.* Polymer, **2017**. 126, (Supplement C): 283-290 DOI: 10.1016/j.polymer.2017.04.017.

[275]   Bi, J., Fang, W., Li, L., Wang, J., Liang, S., He, Y., Liu, M., and Wu, L., *Covalent Triazine-Based Frameworks as Visible Light Photocatalysts for the Splitting of Water.* Macromol. Rapid Commun., **2015**. 36, (20): 1799-1805 DOI: 10.1002/marc.201500270.

[276]   Lan, Z.-A., Fang, Y., Zhang, Y., and Wang, X., *Photocatalytic Oxygen Evolution from Functional Triazine-Based Polymers with Tunable Band Structures.* Angew. Chem. Int. Ed., **2017**. 57, (2): 470-474 DOI: 10.1002/anie.201711155.

[277]   Haase, F., Banerjee, T., Savasci, G., Ochsenfeld, C., and Lotsch, B.V., *Structure-property-activity relationships in a pyridine containing azine-linked covalent organic framework for photocatalytic hydrogen evolution.* Faraday Discuss., **2017**. 201: 247-264 DOI: 10.1039/c7fd00051k.

[278]   Haase, F., Gottschling, K., Stegbauer, L., Germann, L.S., Gutzler, R., Duppel, V., Vyas, V.S., Kern, K., Dinnebier, R.E., and Lotsch, B.V., *Tuning the stacking behaviour of a 2D covalent organic framework through non-covalent interactions.* Mater. Chem. Front., **2017**. 1, (7): 1354-1361 DOI: 10.1039/c6qm00378h.

[279]   Chen, X., Addicoat, M., Irle, S., Nagai, A., and Jiang, D., *Control of Crystallinity and Porosity of Covalent Organic Frameworks by Managing Interlayer Interactions Based on Self-Complementary π-Electronic Force.* J. Am. Chem. Soc., **2013**. 135, (2): 546-549 DOI: 10.1021/ja3100319.

[280]   Salonen, L.M., Medina, D.D., Carbo-Argibay, E., Goesten, M.G., Mafra, L., Guldris, N., Rotter, J.M., Stroppa, D.G., and Rodriguez-Abreu, C., *A supramolecular strategy based on molecular dipole moments for high-quality covalent organic frameworks.* Chem. Commun., **2016**. 52, (51): 7986-7989 DOI: 10.1039/C6CC02170K.

[281] Yu, S.-B., Lyu, H., Tian, J., Wang, H., Zhang, D.-W., Liu, Y., and Li, Z.-T., *A polycationic covalent organic framework: a robust adsorbent for anionic dye pollutants.* Polymer Chemistry, **2016**. 7, (20): 3392-3397 DOI: 10.1039/C6PY00281A.

[282] Banerjee, T., Gottschling, K., Savasci, G., Ochsenfeld, C., and Lotsch, B.V., *H2 Evolution with Covalent Organic Framework Photocatalysts.* ACS Energy Letters, **2018**. 3, (2): 400-409 DOI: 10.1021/acsenergylett.7b01123.

[283] Stegbauer, L., Schwinghammer, K., and Lotsch, B.V., *A hydrazone-based covalent organic framework for photocatalytic hydrogen production.* Chemical Science, **2014**. 5, (7): 2789-2793 DOI: 10.1039/C4SC00016A.

[284] Kandambeth, S., Mallick, A., Lukose, B., Mane, M.V., Heine, T., and Banerjee, R., *Construction of Crystalline 2D Covalent Organic Frameworks with Remarkable Chemical (Acid/Base) Stability via a Combined Reversible and Irreversible Route.* J. Am. Chem. Soc., **2012**. 134, (48): 19524-19527 DOI: 10.1021/Ja308278w.

[285] Thote, J., Aiyappa, H.B., Deshpande, A., Díaz Díaz, D., Kurungot, S., and Banerjee, R., *A Covalent Organic Framework–Cadmium Sulfide Hybrid as a Prototype Photocatalyst for Visible-Light-Driven Hydrogen Production.* Chem. Eur. J., **2014**. 20, (48): 15961-15965 DOI: 10.1002/chem.201403800.

[286] Banerjee, T., Haase, F., Savasci, G., Gottschling, K., Ochsenfeld, C., and Lotsch, B.V., *Single-Site Photocatalytic H2 Evolution from Covalent Organic Frameworks with Molecular Cobaloxime Co-Catalysts.* J. Am. Chem. Soc., **2017**. 139, (45): 16228-16234 DOI: 10.1021/jacs.7b07489.

[287] Pachfule, P., Acharjya, A., Roeser, J., Langenhahn, T., Schwarze, M., Schomaecker, R., Thomas, A., and Schmidt, J., *Diacetylene Functionalized Covalent Organic Framework (COF) for Photocatalytic Hydrogen Generation.* J. Am. Chem. Soc., **2017**. 140, (4): 1423-1427 DOI: 10.1021/jacs.7b11255.

[288] Li, Z., Feng, X., Zou, Y., Zhang, Y., Xia, H., Liu, X., and Mu, Y., *A 2D azine-linked covalent organic framework for gas storage applications.* Chem. Commun., **2014**. 50, (89): 13825-13828 DOI: 10.1039/C4CC05665E.

[289] Aly, M.M.A., *Infrared and Raman spectra of some symmetric azines.* Spectrochim Acta A, **1999**. 55, (9): 1711-1714 DOI: 10.1016/S1386-1425(98)00326-6.

[290] Spitler, E.L., Koo, B.T., Novotney, J.L., Colson, J.W., Uribe-Romo, F.J., Gutierrez, G.D., Clancy, P., and Dichtel, W.R., *A 2D covalent organic framework with 4.7-nm pores and insight into its interlayer stacking.* J. Am. Chem. Soc., **2011**. 133, (48): 19416-21 DOI: 10.1021/ja206242v.

[291] Chandra, S., Kandambeth, S., Biswal, B.P., Lukose, B., Kunjir, S.M., Chaudhary, M., Babarao, R., Heine, T., and Banerjee, R., *Chemically Stable Multilayered Covalent Organic Nanosheets from Covalent Organic Frameworks via Mechanical Delamination.* J. Am. Chem. Soc., **2013**. 135, (47): 17853-17861 DOI: 10.1021/ja408121p.

[292] Butchosa, C., McDonald, T.O., Cooper, A.I., Adams, D.J., and Zwijnenburg, M.A., *Shining a Light on s-Triazine-Based Polymers.* The Journal of Physical Chemistry C, **2014**. 118, (8): 4314-4324 DOI: 10.1021/jp411854f.

[293] Kiwi, J. and Gratzel, M., *Hydrogen Evolution from Water Induced by Visible-Light Mediated by Redox Catalysis.* Nature, **1979**. 281, (5733): 657-658 DOI: 10.1038/281657a0.

[294] Wang, C., Cao, S., and Fu, W.-F., *A stable dual-functional system of visible-light-driven Ni(II) reduction to a nickel nanoparticle catalyst and robust in situ hydrogen production.* Chem. Commun., **2013**. 49, (96): 11251-11253 DOI: 10.1039/C3cc46623j.

[295] Martin, D.J., Qiu, K., Shevlin, S.A., Handoko, A.D., Chen, X., Guo, Z., and Tang, J., *Highly Efficient Photocatalytic H2 Evolution from Water using Visible Light and Structure-Controlled Graphitic Carbon Nitride.* Angew. Chem. Int. Ed. Engl., **2014**. 53, (35): 9240-5 DOI: 10.1002/anie.201403375.

[296]   Zhang, J., Chen, X., Takanabe, K., Maeda, K., Domen, K., Epping, J.D., Fu, X., Antonietti, M., and Wang, X., *Synthesis of a Carbon Nitride Structure for Visible-Light Catalysis by Copolymerization.* Angew Chem Int Edit, **2010**. 49, (2): 441-444 DOI: 10.1002/anie.200903886.

[297]   Bunck, D.N. and Dichtel, W.R., *Bulk Synthesis of Exfoliated Two-Dimensional Polymers Using Hydrazone-Linked Covalent Organic Frameworks.* J. Am. Chem. Soc., **2013**. 135, (40): 14952-14955 DOI: 10.1021/Ja408243n.

[298]   Berr, M.J., Wagner, P., Fischbach, S., Vaneski, A., Schneider, J., Susha, A.S., Rogach, A.L., Jackel, F., and Feldmann, J., *Hole scavenger redox potentials determine quantum efficiency and stability of Pt-decorated CdS nanorods for photocatalytic hydrogen generation.* Appl. Phys. Lett., **2012**. 100, (22) DOI: 10.1063/1.4723575.

[299]   Simon, T., Bouchonville, N., Berr, M.J., Vaneski, A., Adrovic, A., Volbers, D., Wyrwich, R., Doblinger, M., Susha, A.S., Rogach, A.L., Jackel, F., Stolarczyk, J.K., and Feldmann, J., *Redox shuttle mechanism enhances photocatalytic H2 generation on Ni-decorated CdS nanorods.* Nat Mater, **2014**. 13, (11): 1013-8 DOI: 10.1038/nmat4049.

[300]   Jin, S., Sakurai, T., Kowalczyk, T., Dalapati, S., Xu, F., Wei, H., Chen, X., Gao, J., Seki, S., Irle, S., and Jiang, D., *Two-Dimensional Tetrathiafulvalene Covalent Organic Frameworks: Towards Latticed Conductive Organic Salts.* Chem. Eur. J., **2014**. 20, (45): 14608-14613 DOI: 10.1002/chem.201402844.

[301]   Gunasinghe, R.N., Reuven, D.G., Suggs, K., and Wang, X.-Q., *Filled and Empty Orbital Interactions in a Planar Covalent Organic Framework on Graphene.* The Journal of Physical Chemistry Letters, **2012**. 3, (20): 3048-3052 DOI: 10.1021/jz301304f.

[302]   Jin, S.B., Ding, X.S., Feng, X., Supur, M., Furukawa, K., Takahashi, S., Addicoat, M., El-Khouly, M.E., Nakamura, T., Irle, S., Fukuzumi, S., Nagai, A., and Jiang, D.L., *Charge Dynamics in A Donor-Acceptor Covalent Organic Framework with Periodically Ordered Bicontinuous Heterojunctions.* Angew Chem Int Edit, **2013**. 52, (7): 2017-2021 DOI: 10.1002/anie.201209513.

[303]   van der Horst, J.-W., Bobbert, P.A., de Jong, P.H.L., Michels, M.A.J., Siebbeles, L.D.A., Warman, J.M., Gelinck, G.H., and Brocks, G., *Predicting polarizabilities and lifetimes of excitons on conjugated polymer chains.* Chem. Phys. Lett., **2001**. 334, (4-6): 303-308 DOI: 10.1016/S0009-2614(00)01476-7.

[304]   Andrew, T.L. and Swager, T.M., *Structure-Property Relationships for Exciton Transfer in Conjugated Polymers.* J Polym Sci Pol Phys, **2011**. 49, (7): 476-498 DOI: 10.1002/Polb.22207.

[305]   Ahlrichs, R., Bar, M., Haser, M., Horn, H., and Kolmel, C., *Electronic-Structure Calculations on Workstation Computers - the Program System Turbomole.* Chem. Phys. Lett., **1989**. 162, (3): 165-169 DOI: 10.1016/0009-2614(89)85118-8.

[306]   Kussmann, J. and Ochsenfeld, C., *Pre-selective screening for matrix elements in linear-scaling exact exchange calculations.* J. Chem. Phys., **2013**. 138, (13): 134114 DOI: 10.1063/1.4796441.

[307]   Kussmann, J. and Ochsenfeld, C., *Preselective Screening for Linear-Scaling Exact Exchange-Gradient Calculations for Graphics Processing Units and General Strong-Scaling Massively Parallel Calculations.* J Chem Theory Comput, **2015**. 11, (3): 918-22 DOI: 10.1021/ct501189u.

[308]   Aradi, B., Hourahine, B., and Frauenheim, T., *DFTB+, a sparse matrix-based implementation of the DFTB method.* J. Phys. Chem. A, **2007**. 111, (26): 5678-5684 DOI: 10.1021/Jp070186p.

[309]   Sangill, R., Rastrupandersen, N., Bildsoe, H., Jakobsen, H.J., and Nielsen, N.C., *Optimized Spectral Editing of 13C MAS NMR Spectra of Rigid Solids Using Cross-Polarization Methods.* Journal of Magnetic Resonance, Series A, **1994**. 107, (1): 67-78 DOI: 10.1006/jmra.1994.1048.

[310] Farley, S.J., Rochester, D.L., Thompson, A.L., Howard, J.A.K., and Williams, J.A.G., *Controlling Emission Energy, Self-Quenching, and Excimer Formation in Highly Luminescent N⋀C⋀N-Coordinated Platinum(II) Complexes.* Inorg. Chem., **2005**. 44, (26): 9690-9703 DOI: 10.1021/ic051049e.

[311] Damiani, A., Giglio, E., and Ripamonti, A., *Crystal and molecular structure of s-triphenyltriazine.* Acta Crystallographica, **1965**. 19, (2): 161-168 DOI: 10.1107/S0365110X65003018.

[312] Shalom, M., Inal, S., Fettkenhauer, C., Neher, D., and Antonietti, M., *Improving Carbon Nitride Photocatalysis by Supramolecular Preorganization of Monomers.* J. Am. Chem. Soc., **2013**. 135, (19): 7118-7121 DOI: 10.1021/ja402521s.

[313] Lau, V.W.-h., Yu, V.W.-z., Ehrat, F., Botari, T., Moudrakovski, I., Simon, T., Duppel, V., Medina, E., Stolarczyk, J., Feldmann, J., Blum, V., and Lotsch, B.V., *Urea-Modified Carbon Nitrides: Enhancing Photocatalytic Hydrogen Evolution by Rational Defect Engineering.* Adv. Energy Mater., **2017**. 7, (12) DOI: 10.1002/aenm.201602251.

[314] Jin, S., Ding, X., Feng, X., Supur, M., Furukawa, K., Takahashi, S., Addicoat, M., El-Khouly, M.E., Nakamura, T., Irle, S., Fukuzumi, S., Nagai, A., and Jiang, D., *Charge Dynamics in A Donor–Acceptor Covalent Organic Framework with Periodically Ordered Bicontinuous Heterojunctions.* Angew. Chem. Int. Ed., **2013**. 52, (7): 2017-2021 DOI: 10.1002/anie.201209513.

[315] de Mello, J.C., Wittmann, H.F., and Friend, R.H., *An improved experimental determination of external photoluminescence quantum efficiency.* Adv. Mater., **1997**. 9, (3): 230-232 DOI: 10.1002/adma.19970090308.

[316] Ahlrichs, R., Bär, M., Häser, M., Horn, H., and Kölmel, C., *Electronic structure calculations on workstation computers: The program system turbomole.* Chem. Phys. Lett., **1989**. 162, (3): 165-169 DOI: 10.1016/0009-2614(89)85118-8.

[317] Gao, Q., Bai, L., Zhang, X., Wang, P., Li, P., Zeng, Y., Zou, R., and Zhao, Y., *Synthesis of Microporous Nitrogen-Rich Covalent-Organic Framework and Its Application in CO2 Capture.* Chin. J. Chem . **2015**. 33, (1): 90-94 DOI: 10.1002/cjoc.201400550.

[318] Zhu, X., An, S., Liu, Y., Hu, J., Liu, H., Tian, C., Dai, S., Yang, X., Wang, H., Abney, C.W., and Dai, S., *Efficient removal of organic dye pollutants using covalent organic frameworks.* AIChE J., **2017**. 63, (8): 3470-3478 DOI: 10.1002/aic.15699.

[319] Luo, H., Xie, W., Tao, J., Inoue, H., Gyenis, A., Krizan, J.W., Yazdani, A., Zhu, Y., and Cava, R.J., *Polytypism, polymorphism, and superconductivity in TaSe2−xTex.* PNAS, **2015**. 112, (11): E1174-E1180 DOI: 10.1073/pnas.1502460112.

[320] Huisman, R. and Jellinek, F., *On the polymorphism of tantalum diselenide.* Journal of the Less Common Metals, **1969**. 17, (1): 111-117 DOI: 10.1016/0022-5088(69)90041-1.

[321] Prasad, R., *Present state of polytypism in cadmium iodide crystals.* physica status solidi (a), **1976**. 38, (1): 11-44 DOI: 10.1002/pssa.2210380102.

[322] Tilford, R.W., Gemmill, W.R., zur Loye, H.C., and Lavigne, J.J., *Facile synthesis of a highly crystalline, covalently linked porous boronate network.* Chem. Mater., **2006**. 18, (22): 5296-5301 DOI: 10.1021/cm061177g.

[323] Koo, B.T., Dichtel, W.R., and Clancy, P., *A classification scheme for the stacking of two-dimensional boronate ester-linked covalent organic frameworks.* J. Mater. Chem., **2012**. 22, (34): 17460-17469 DOI: 10.1039/C2JM32009F.

[324] Lukose, B., Kuc, A., and Heine, T., *The Structure of Layered Covalent-Organic Frameworks.* Chem. Eur. J., **2011**. 17, (8): 2388-2392 DOI: 10.1002/chem.201001290.

[325] Pawley, G., *Unit-cell refinement from powder diffraction scans.* J. Appl. Crystallogr., **1981**. 14, (6): 357-361 DOI: 10.1107/S0021889881009618.

[326] Rietveld, H., *A profile refinement method for nuclear and magnetic structures.* J. Appl. Crystallogr., **1969**. 2, (2): 65-71 DOI: 10.1107/S0021889869006558.

[327] Ojala, C.R., Ojala, W.H., Gleason, W.B., and Britton, D., *The crystal structures of p-iodo-N-(p-cyanobenzylidene)aniline and p-cyano-N-(p-iodobenzylidene)aniline.* J. Chem. Crystallogr., **1999**. 29, (1): 27-32 DOI: 10.1023/a:1009563012943.

[328] Ojala, C.R., Ojala, W.H., Gleason, W.B., and Britton, D., *The crystal structures of p-halo-N-(p-cyanobenzylidene)aniline and p-cyano-N-(p-halobenzylidene)aniline (halo = bromo and chloro).* J. Chem. Crystallogr., **2001**. 31, (7): 377-386 DOI: 10.1023/a:1015799223882.

[329] Ojala, C., Ojala, W., and Britton, D., *Solid-State Intermolecular Contacts Involving the Nitrile Group in p-Cyano-N-(p-cyanobenzylidene)aniline and 4,4'-(azinodimethylidyne)bis-benzonitrile.* J. Chem. Crystallogr., **2011**. 41, (4): 464-469 DOI: 10.1007/s10870-010-9902-8.

[330] Bernstein, J. and Izak, I., *Molecular conformation and electronic structure. II: Crystal and molecular structure ofN-(p-bromobenzylidene)-p-bromoaniline.* J. Cryst. Mol. Struct., **1975**. 5, (4): 257-266 DOI: 10.1007/BF01303084.

[331] Ojala, C.R., Ojala, W.H., and Britton, D., *Solid-State Intermolecular Contacts Involving the Nitrile Group in p-Cyano-N-(p-cyanobenzylidene)aniline and 4,4'-(azinodimethylidyne)bis-benzonitrile.* J. Chem. Crystallogr., **2010**. 41, (4): 464-469 DOI: 10.1007/s10870-010-9902-8.

[332] Bernstein, J. and Schmidt, G.M.J., *Conformational studies. Part IV. Crystal and molecular structure of the metastable form of N-(p-chlorobenzylidene)-p-chloroaniline, a planar anil.* J. Chem. Soc., Perkin Trans. 2, **1972**, (8): 951 DOI: 10.1039/p29720000951.

[333] Marszalek, T., Li, M., and Pisula, W., *Design directed self-assembly of donor-acceptor polymers.* Chem. Commun., **2016**. 52, (73): 10938-10947 DOI: 10.1039/C6CC04523E.

[334] Waller, P.J., Lyle, S.J., Osborn Popp, T.M., Diercks, C.S., Reimer, J.A., and Yaghi, O.M., *Chemical Conversion of Linkages in Covalent Organic Frameworks.* J. Am. Chem. Soc., **2016**. 138, (48): 15519-15522 DOI: 10.1021/jacs.6b08377.

[335] Lanni, L.M., Tilford, R.W., Bharathy, M., and Lavigne, J.J., *Enhanced Hydrolytic Stability of Self-Assembling Alkylated Two-Dimensional Covalent Organic Frameworks.* J. Am. Chem. Soc., **2011**. 133, (35): 13975-13983 DOI: 10.1021/ja203807h.

[336] Kandambeth, S., Shinde, D.B., Panda, M.K., Lukose, B., Heine, T., and Banerjee, R., *Enhancement of Chemical Stability and Crystallinity in Porphyrin-Containing Covalent Organic Frameworks by Intramolecular Hydrogen Bonds.* Angew. Chem. Int. Ed., **2013**. 52, (49): 13052-13056 DOI: 10.1002/anie.201306775.

[337] Kandambeth, S., Venkatesh, V., Shinde, D.B., Kumari, S., Halder, A., Verma, S., and Banerjee, R., *Self-templated chemically stable hollow spherical covalent organic framework.* Nat Commun, **2015**. 6: 6786 DOI: 10.1038/ncomms7786.

[338] Biswal, B.P., Chaudhari, H.D., Banerjee, R., and Kharul, U.K., *Chemically Stable Covalent Organic Framework (COF)-Polybenzimidazole Hybrid Membranes: Enhanced Gas Separation through Pore Modulation.* Chem. Eur. J., **2016**. 22, (14): 4695-9 DOI: 10.1002/chem.201504836.

[339] Rao, M.R., Fang, Y., De Feyter, S., and Perepichka, D.F., *Conjugated Covalent Organic Frameworks via Michael Addition–Elimination.* J. Am. Chem. Soc., **2017**. 139, (6): 2421-2427 DOI: 10.1021/jacs.6b12005.

[340] Hu, X.-Y., Zhang, W.-S., Rominger, F., Wacker, I., Schroder, R.R., and Mastalerz, M., *Transforming a chemically labile [2+3] imine cage into a robust carbamate cage.* Chem. Commun., **2017**. 53, (61): 8616-8619 DOI: 10.1039/C7CC03677A.

[341] Du, Y., Mao, K., Kamakoti, P., Ravikovitch, P., Paur, C., Cundy, S., Li, Q., and Calabro, D., *Experimental and computational studies of pyridine-assisted post-synthesis modified air stable covalent-organic frameworks.* Chem. Commun., **2012**. 48, (38): 4606-4608 DOI: 10.1039/C2CC30781B.

[342] Du, Y., Calabro, D., Wooler, B., Kortunov, P., Li, Q., Cundy, S., and Mao, K., *One Step Facile Synthesis of Amine-Functionalized COF-1 with Enhanced Hydrostability.* Chem. Mater., **2015**. 27, (5): 1445-1447 DOI: 10.1021/cm5032317.

[343]   O'Connor, C., *Acidic and basic amide hydrolysis.* Quarterly Reviews, Chemical Society, **1970**. 24, (4): 553-564 DOI: 10.1039/QR9702400553.

[344]   Böttcher, B. and Bauer, F., *Über die Einwirkung von Schwefel auf Schiffsche Basen.* Justus Liebigs Annalen der Chemie, **1950**. 568, (3): 218-227 DOI: 10.1002/jlac.19505680308.

[345]   Zhu, X., Tian, C., Jin, T., Wang, J., Mahurin, S.M., Mei, W., Xiong, Y., Hu, J., Feng, X., Liu, H., and Dai, S., *Thiazolothiazole-linked porous organic polymers.* Chem. Commun., **2014**. 50, (95): 15055-15058 DOI: 10.1039/C4CC07255C.

[346]   Rabbani, M.G., Islamoglu, T., and El-Kaderi, H.M., *Benzothiazole- and benzoxazole-linked porous polymers for carbon dioxide storage and separation.* Journal of Materials Chemistry A, **2017**. 5, (1): 258-265 DOI: 10.1039/C6TA06342J.

[347]   Sośnicki, J.G., Jagodziński, T.S., Nowak-Wydra, B., and Hansen, P.E., *Complete Assignment of 1H and 13C NMR Spectra and Conformational Analysis of Thioamide Cannabinoids.* Magn. Reson. Chem., **1996**. 34, (9): 667-674 DOI: 10.1002/(SICI)1097-458X(199609)34:9<667::AID-OMR960>3.0.CO;2-F.

[348]   Zhang, J., Peng, Y., Leng, W., Gao, Y., Xu, F., and Chai, J., *Nitrogen ligands in two-dimensional covalent organic frameworks for metal catalysis.* Chinese Journal of Catalysis, **2016**. 37, (4): 468-475 DOI: 10.1016/S1872-2067(15)61050-6.

[349]   Mullangi, D., Dhavale, V., Shalini, S., Nandi, S., Collins, S., Woo, T., Kurungot, S., and Vaidhyanathan, R., *Low-Overpotential Electrocatalytic Water Splitting with Noble-Metal-Free Nanoparticles Supported in a sp3 N-Rich Flexible COF.* Advanced Energy Materials, **2016**. 6, (13): 1600110 DOI: 10.1002/aenm.201600110.

[350]   Egerton, R.F., Li, P., and Malac, M., *Radiation damage in the TEM and SEM.* Micron, **2004**. 35, (6): 399-409 DOI: 10.1016/j.micron.2004.02.003.

[351]   Huang, P.Y., Ruiz-Vargas, C.S., van der Zande, A.M., Whitney, W.S., Levendorf, M.P., Kevek, J.W., Garg, S., Alden, J.S., Hustedt, C.J., Zhu, Y., Park, J., McEuen, P.L., and Muller, D.A., *Grains and grain boundaries in single-layer graphene atomic patchwork quilts.* Nature, **2011**. 469, (7330): 389-92 DOI: 10.1038/nature09718.

[352]   Gutzler, R. and Perepichka, D.F., *pi-Electron Conjugation in Two Dimensions.* J. Am. Chem. Soc., **2013**. 135, (44): 16585-16594 DOI: 10.1021/Ja408355p.

[353]   Coelho, A., *Whole-profile structure solution from powder diffraction data using simulated annealing.* J. Appl. Crystallogr., **2000**. 33, (3 Part 2): 899-908 DOI: 10.1107/S002188980000248X.

[354]   Stephens, P., *Phenomenological model of anisotropic peak broadening in powder diffraction.* J. Appl. Crystallogr., **1999**. 32, (2): 281-289 DOI: 10.1107/S0021889898006001.

[355]   Perdew, J.P., Burke, K., and Ernzerhof, M., *Generalized Gradient Approximation Made Simple.* Phys. Rev. Lett., **1996**. 77, (18): 3865-3868 DOI: 10.1103/PhysRevLett.77.3865.

[356]   Grimme, S., Antony, J., Ehrlich, S., and Krieg, H., *A consistent and accurate ab initio parametrization of density functional dispersion correction (DFT-D) for the 94 elements H-Pu.* The Journal of Chemical Physics, **2010**. 132, (15): 154104 DOI: 10.1063/1.3382344.

[357]   Łazarski, R., Burow, A.M., Grajciar, L., and Sierka, M., *Density functional theory for molecular and periodic systems using density fitting and continuous fast multipole method: Analytical gradients.* J. Comput. Chem., **2016**. 37, (28): 2518-2526 DOI: 10.1002/jcc.24477.

[358]   *TURBOMOLE, developer version based on version V7.1 2017, a development of University of Karlsruhe and Forschungszentrum Karlsruhe GmbH, 1989-2007, TURBOMOLE GmbH, since 2007; available from* http://www.turbomole.com.

[359]   Wilson, P.J., Bradley, T.J., and Tozer, D.J., *Hybrid exchange-correlation functional determined from thermochemical data and ab initio potentials.* The Journal of Chemical Physics, **2001**. 115, (20): 9233-9242 DOI: 10.1063/1.1412605.

[360]   Jensen, F., *Segmented Contracted Basis Sets Optimized for Nuclear Magnetic Shielding.* Journal of Chemical Theory and Computation, **2015**. 11, (1): 132-138 DOI: 10.1021/ct5009526.

[361] Kussmann, J. and Ochsenfeld, C., *Preselective Screening for Linear-Scaling Exact Exchange-Gradient Calculations for Graphics Processing Units and General Strong-Scaling Massively Parallel Calculations.* Journal of Chemical Theory and Computation, **2015**. 11, (3): 918-922 DOI: 10.1021/ct501189u.

[362] Curtius, T. and Jay, R., *Diazo- und Azoverbindungen der Fettreihe. IV. Abhandlung. Ueber das Hydrazin.* Journal für Praktische Chemie, **1889**. 39, (1): 27-58 DOI: 10.1002/prac.18890390102.

[363] d'Alelio, G.F. and Schoenig, R.K., *Polymeric Schiff Bases. XII. The Syntheses and Thermal Stabilities of Polyazines and Derived Polystilbenes.* Journal of Macromolecular Science: Part A - Chemistry, **1968**. 2, (5): 979-1043 DOI: 10.1080/10601326808051454.

[364] Alahakoon, S.B., Occhialini, G., McCandless, G.T., Karunathilake, A.A.K., Nielsen, S.O., and Smaldone, R.A., *Experimental and Theoretical Insight into the Effect of Fluorine Substituents on the Properties of Azine Linked Covalent Organic Frameworks.* CrystEngComm, **2017**. 19, (33): 4882-4885 DOI: 10.1039/C7CE00598A.

[365] Spectral Database for Organic Compounds (SDBS), *p-methylbenzaldehyde azine, SDBS No.: 28416, IR : KBr disc*. Available from: SDBSWeb : http://sdbs.db.aist.go.jp (National Institute of Advanced Industrial Science and Technology). (accessed: 04. Jan 2018).

[366] Spectral Database for Organic Compounds (SDBS), *4,4'-dimethyl-trans-stilbene, SDBS No.: 41222, IR : KBr disc*. Available from: SDBSWeb : http://sdbs.db.aist.go.jp (National Institute of Advanced Industrial Science and Technology). (accessed: 04. Jan 2018).

[367] Spectral Database for Organic Compounds (SDBS), *4,4'-dinitrostilbene, SDBS No.: 19737, IR : KBr disc*. Available from: SDBSWeb : http://sdbs.db.aist.go.jp (National Institute of Advanced Industrial Science and Technology). (accessed: 04. Jan 2018).

[368] Spectral Database for Organic Compounds (SDBS), *trans-4-nitrostilbene, SDBS No.: 28812, IR : KBr disc*. Available from: SDBSWeb : http://sdbs.db.aist.go.jp (National Institute of Advanced Industrial Science and Technology). (accessed: 04. Jan 2018).

[369] Spectral Database for Organic Compounds (SDBS), *benzaldehyde azine, SDBS No.: 7297, IR : KBr disc*. Available from: SDBSWeb : http://sdbs.db.aist.go.jp (National Institute of Advanced Industrial Science and Technology). (accessed: 04. Jan 2018).

[370] Spectral Database for Organic Compounds (SDBS), *trans-1,2-diphenylethylene, SDBS No.: 1844, IR : KBr disc*. Available from: SDBSWeb : http://sdbs.db.aist.go.jp (National Institute of Advanced Industrial Science and Technology). (accessed: 04. Jan 2018).

[371] Zimmerman, H.E. and Somasekhara, S., *The Mechanism of the Thermal Decomposition Reaction of Azines.* J. Am. Chem. Soc., **1960**. 82, (22): 5865-5873 DOI: 10.1021/ja01507a024.

[372] Dovesi, R., Saunders, V.R., Roetti, C., Orlando, R., Zicovich-Wilson, C.M., Pascale, F., Civalleri, B., Doll, K., Harrison, N.M., Bush, I.J., D'Arco, P., Llunell, M., Causà, M., and Noël, Y., *CRYSTAL14 User's Manual*. 2014, University of Torino: Torino, Italy.

[373] Dovesi, R., Orlando, R., Erba, A., Zicovich-Wilson, C.M., Civalleri, B., Casassa, S., Maschio, L., Ferrabone, M., De La Pierre, M., D'Arco, P., Noël, Y., Causà, M., Rérat, M., and Kirtman, B., *CRYSTAL14: A program for the ab initio investigation of crystalline solids.* Int. J. Quantum Chem, **2014**. 114, (19): 1287-1317 DOI: 10.1002/qua.24658.

[374] Grimme, S., *Semiempirical GGA-type density functional constructed with a long-range dispersion correction.* J. Comput. Chem., **2006**. 27, (15): 1787-1799 DOI: 10.1002/jcc.20495.

[375] Gatti, C., Saunders, V.R., and Roetti, C., *Crystal field effects on the topological properties of the electron density in molecular crystals: The case of urea.* The Journal of Chemical Physics, **1994**. 101, (12): 10686-10696 DOI: 10.1063/1.467882.

[376] Dovesi, R., Causa', M., Orlando, R., Roetti, C., and Saunders, V.R., *Ab initio approach to molecular crystals: A periodic Hartree–Fock study of crystalline urea.* The Journal of Chemical Physics, **1990**. 92, (12): 7402-7411 DOI: 10.1063/1.458592.

[377]   Canepa, P., Hanson, R.M., Ugliengo, P., and Alfredsson, M., *J-ICE: a new Jmol interface for handling and visualizing crystallographic and electronic properties.* J. Appl. Crystallogr., **2011**. 44, (1): 225-229 DOI: doi:10.1107/S0021889810049411.

[378]   Yelamaggad, C.V., Achalkumar, A.S., Rao, D.S.S., and Prasad, S.K., *Luminescent, Liquid Crystalline Tris(N-salicylideneaniline)s: Synthesis and Characterization.* The Journal of Organic Chemistry, **2009**. 74, (8): 3168-3171 DOI: 10.1021/jo9001933.

[379]   Alterman, M. and Hallberg, A., *Fast Microwave-Assisted Preparation of Aryl and Vinyl Nitriles and the Corresponding Tetrazoles from Organo-halides.* The Journal of Organic Chemistry, **2000**. 65, (23): 7984-7989 DOI: 10.1021/jo0009954.

[380]   Wang, Z.M., Lu, P., Chen, S.M., Gao, Z., Shen, F.Z., Zhang, W.S., Xu, Y.X., Kwok, H.S., and Ma, Y.G., *Phenanthro[9,10-d]imidazole as a new building block for blue light emitting materials.* J. Mater. Chem., **2011**. 21, (14): 5451-5456 DOI: 10.1039/C1jm10321k.

[381]   Mikroyannidis, J.A., Ye, S.H., and Liu, Y.Q., *Electroluminesent divinylene- and trivinylene-molecules with terminal naphthalimide or phthalimide segments.* Synth. Met., **2009**. 159, (5-6): 492-500 DOI: 10.1016/j.synthmet.2008.11.009.

[382]   Hartman, G.D., Halczenko, W., and Phillips, B.T., *Iminium Ion Mediated Cyclizations of 4-Aryl-1,4-Dihydropyridines - Bridging with Olefins.* J. Org. Chem., **1985**. 50, (14): 2427-2431 DOI: 10.1021/Jo00214a005.

[383]   Achelle, S., Ramondenc, Y., Marsais, F., and Ple, N., *Star- and banana-shaped oligomers with a pyrimidine core: Synthesis and light-emitting properties.* Eur. J. Org. Chem., **2008**, (18): 3129-3140 DOI: 10.1002/ejoc.200800139.

[384]   Tanaka, H., Shizu, K., Nakanotani, H., and Adachi, C., *Twisted Intramolecular Charge Transfer State for Long-Wavelength Thermally Activated Delayed Fluorescence.* Chem. Mater., **2013**. 25, (18): 3766-3771 DOI: 10.1021/cm402428a.

[385]   Peersen, O.B., Wu, X.L., Kustanovich, I., and Smith, S.O., *Variable-Amplitude Cross-Polarization MAS NMR.* Journal of Magnetic Resonance, Series A, **1993**. 104, (3): 334-339 DOI: 10.1006/jmra.1993.1231.

[386]   Fung, B.M., Khitrin, A.K., and Ermolaev, K., *An Improved Broadband Decoupling Sequence for Liquid Crystals and Solids.* Journal of Magnetic Resonance, **2000**. 142, (1): 97-101 DOI: 10.1006/jmre.1999.1896.

[387]   Wu, X.L., Burns, S.T., and Zilm, K.W., *Spectral Editing in CPMAS NMR. Generating Subspectra Based on Proton Multiplicities.* Journal of Magnetic Resonance, Series A, **1994**. 111, (1): 29-36 DOI: 10.1006/jmra.1994.1222.

[388]   *Topas.* 2014, Bruker AXS.

[389]   *Materials Studio v6.0.0.*

[390]   Treacy, M.M.J., Newsam, J.M., and Deem, M.W., *A General Recursion Method for Calculating Diffracted Intensities from Crystals Containing Planar Faults.* Proceedings of the Royal Society of London. Series A: Mathematical and Physical Sciences, **1991**. 433, (1889): 499-520 DOI: 10.1098/rspa.1991.0062.

[391]   Giannozzi, P., Baroni, S., Bonini, N., Calandra, M., Car, R., Cavazzoni, C., Ceresoli, D., Chiarotti, G.L., Cococcioni, M., Dabo, I., Dal Corso, A., de Gironcoli, S., Fabris, S., Fratesi, G., Gebauer, R., Gerstmann, U., Gougoussis, C., Kokalj, A., Lazzeri, M., Martin-Samos, L., Marzari, N., Mauri, F., Mazzarello, R., Paolini, S., Pasquarello, A., Paulatto, L., Sbraccia, C., Scandolo, S., Sclauzero, G., Seitsonen, A.P., Smogunov, A., Umari, P., and Wentzcovitch, R.M., *QUANTUM ESPRESSO: a modular and open-source software project for quantum simulations of materials.* Journal of physics. Condensed matter : an Institute of Physics journal, **2009**. 21, (39): 395502 DOI: 10.1088/0953-8984/21/39/395502.

[392]   Troullier, N. and Martins, J.L., *Efficient pseudopotentials for plane-wave calculations.* Physical review. B, Condensed matter, **1991**. 43, (3): 1993-2006.

[393] Rabbani, M.G., Sekizkardes, A.K., El-Kadri, O.M., Kaafarani, B.R., and El-Kaderi, H.M., *Pyrene-directed growth of nanoporous benzimidazole-linked nanofibers and their application to selective CO2 capture and separation.* J. Mater. Chem., **2012**. 22, (48): 25409-25417 DOI: 10.1039/C2JM34922A.

9.   Appendix

9.1.   Abbreviations

2D	two-dimensional
3D	three dimensional
ALCOF	arrested linkage COF
AM1.5 G	Air mass 1.5 x atmosphere thickness
ATA‑COF	aryl‑triaryl‑azine COF
BET	Brunauer−Emmett−Teller
BTI	triformyl benzene - triphenyl triazine amine imine COF
BTI-COF	benzene triazine imine COF
COF	covalent organic framework
CP-MAS	cross-polarization magic angle-spinning
CTF	covalent triazine framework
CWL	central wavelength
DA	donor acceptor
DA	donor-acceptor
DCM	Dichloromethane
DCvC	dynamic covalent chemistry
DFT	density functional theory
DMAc	N-Dimethyl acetamide
DMF	N-Dimethyl formamide
DMSO	dimethyl sulfoxide
EDTA	ethylenediaminetetraacetic acid
EDX	Energy dispersive X-ray spectroscopy
FFT	fast Fourier transform
FT-IR	Fourier transform infrared spectroscopy
HAGB	high angle grain boundaries
H‑BTI‑COF	hydrogen functionalized BTI COF
HE	hydrogen evolution
HOMO	highest occupied molecular orbital
IR	Infrared spectroscopy
LAGB	low angle grain boundaries

LUMO	lowes unoccupoied molecular orbital
MAS	magic angle spinning
MOF	metal organic framework
MS	mass spectroscopy
N0-CHO	1,3,5-Tris(4-formylphenyl)benzene
N1-CHO	2,4,6-Tris(4-formylphenyl)pyridine
N2-CHO	2,4,6-Tris(4-formylphenyl)pyrimidine
N3-CHO	2,4,6-Tris(4-formylphenyl)-1,3,5-triazine
N3-PP	N3-COF pyrolysed polymer
n-BuLi	n butyl lithium
NLDFT	non-local density functional theory
NMR	nuclear magnetic resonance spectroscopy
Nx-HxAl	Nx- model hexagon aldehyde terminated
Nx-HxHz	Nx- model hexagon hydrazone terminated
Nx-PhAz	Nx-model phenylazines
OH‑BTI‑COF	hydroxy functionalized BTI COF
PBI-COF	Pyrene tetra(phenyl) biphenyl imine-COF
PBT-COF	Pyrene tetra(phenyl) biphenyl thiazole-COF
PCPs	porous conjugated polymers
PE	photonic efficiency
PIMs	polymers of intrinsic micro-porosity
PL	photoluminescence
PTP	phenyl tripyridine
PTP‑CHO	2,2',2''-(1,3,5-benzenetriyl) tris-(pyridine-2-carboxaldehyde)
PTP-COF	phenyl tripyridine azine COF
QD	quantum dot
RASE	radical anion stabilization energy
RLCOF	reversible linkage COF
rs-TTI-COF	Randomly stacked Triazine triazine triphenyl imine COF
SAED	Selected area electron diffraction
sCOF	surface COF
SED	sacrificial electron donor
SEM	Scanning electron microscope

ssNMR	solid state nuclear magnetic resonance spectroscopy
TB	triphenyl benzene
TBI	triphenyl benzene imine
TEM	Transmission electron microscope
TEoA	triethanolamine
TGA	thermogravimetric analysis
THB-CHO	Triformyl phloroclucinol
THF	tetrahydrofuran
TSA	toluene sulfonic acid
TT	triphenyl trizaine
TT-CHO	tris(4-formylphenyl)triazine
TTI	triazine triphenyl imine
TT-NH2	tris(4-aminophenyl)triazine
TTT	Triazine triphenyl thiazole
TTT-COF	Triazine triphenyl thiazole COF
XPS	X-ray photoelectron spectroscopy
XRD	X-Ray diffraction
XRPD	X-Ray powder diffraction

9.2. Methods

9.2.1. Synthesis of molecular precursor compounds

9.2.1.1. Triformyl phloroclucinol (THB-CHO)
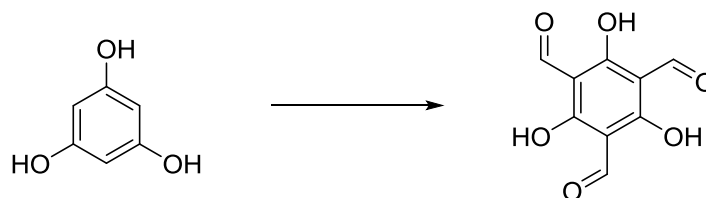
Synthesis was as per a modified literature protocol.[378] Phloroglucinol (3.0 g, 23.6 mmol) and hexamethylenetetramine (7.3 g, 51.9 mmol) were added to trifluoroacetic acid (45 ml) under argon atmosphere. The solution was heated under reflux at 100°C for 2.5 h. Then, hydrochloric acid (3 M, 150 ml) was added slowly and the mixture heated for another 1 h. The solution was allowed to cooled down to room temperature and filtered through celite. The filtrate was extracted with dichloromethane (4 × 100 ml) and the combined organic phases were concentrated to afford a yellow solid, which was

washed with hot acetone to yield THB-CHO as an off-white powder. ^{1}H NMR (CDCl$_3$, 25°C, 300 MHz, ppm) = 14.13 (s, 3H, OH), 10.17 (s, 3H, CHO)

9.2.1.2.   *N*-Phenylacetamide
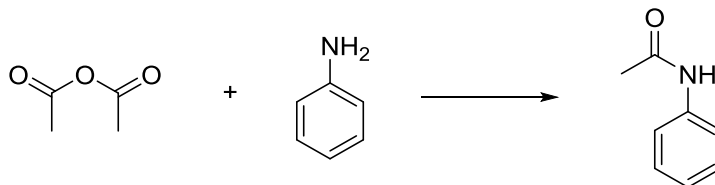
Aniline (5.0 ml, 54.8 mmol) was dissolved in a mixture of hydrochloric acid (38%; 5 ml) with water (150 ml) by stirring. The solution was warmed to 50°C in a water bath, acetic anhydride (7.8 ml, 82.1 mmol) was added and the dissolution affected by swirling the mixture. To this mixture, a solution of potassium acetate (16.1 mg, 164.0 mmol) in water (25 ml) was added. After a brief period of mixing, the mixture was allowed to cool to room temperature. The precipitate was filtered off and recrystallized from water/ethanol to yield *N*-phenylacetamide in quantitative amounts. 1H NMR (CDCl3, 25°C, 300 MHz, ppm) = 7.88 (s, 1H, NH), 7.52 (d, 2H, CH), 7.30 (t, 2H, CH), 7.10 (t, 1H, CH), 2.16 (s, 3H, CH3).

9.2.1.3.   *N*-(4-Bromophenyl)acetamide
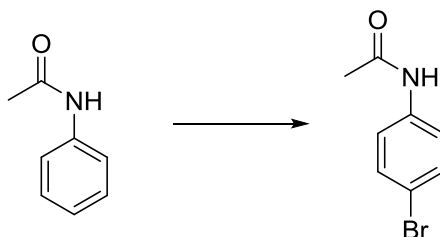
N-Phenylacetamide (7.5 g, 55.5 mmol) was dissolved in acetic acid (15 ml). To this solution a solution of bromine (3.1 ml, 61 mmol) in acetic acid (25 ml) was added dropwise from a dripping funnel while stirring vigorously. After the complete addition of the bromine, the mixture was allowed to stir for 1 h. The remaining bromine in the reaction mixture was quenched by addition of a concentrated sodium bisulfite solution until complete discoloration was achieved. The precipitate was filtered off and washed with addition sodium bisulfite solution, sodium bicarbonate solution and water to yield 7.2 g (white powder, 60 %) of product. 1H NMR (DMSO-d6, 25°C, 300 MHz, ppm) = 10.05 (s, 1H, NH), 7.54 (d, 2H, CH), 7.45 (d, 2H, CH), 2.02 (s, 3H, CH3).

9.2.1.4.   *N*-(4-Cyanophenyl)acetamide
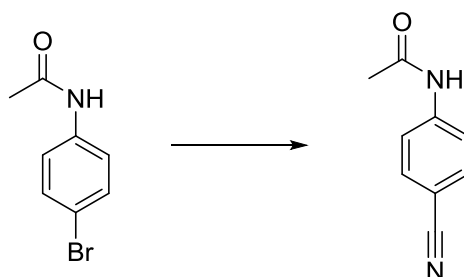
Synthesis was carried out as per a modified literature procedure.[379] DMF (20 ml) was degassed in a microwave vial (20 ml) by bubbling argon for 30 min. *N*-(4-Bromophenyl)acetamide (2 g, 9.3 mmol), zinc cyanide (1.2 g, 10.2 mmol), tetrakis(triphenylphosphin)palladium(0) (50 mg, 43 μmol) and 1,5-bis(diphenylphosphinopentane) (25 mg, 55 μmol) were added and degassed for another 5 min. The vial was sealed under argon and heated in a Biotage Initiator microwave to 150°C for 30 min. The solution was cooled to room temperature, poured onto ice cold water (200 ml) and extracted with dichloromethane (4×100 ml). The solvent was removed under reduced pressure and any residual DMF was removed with stream of air to yield the product (1180 mg, white powder, 79 %). 1H NMR (DMSO-d6, 25°C, 300 MHz, ppm) = 10.36 (s, 1H, NH), 7.74 (s, 4H, CH), 2.08 (s, 3H, CH3). 13C NMR (DMSO-d6, 25°C, 75 MHz, ppm) = 167.89, 141.34, 132.77, 118.90, 118.22, 106.70, 24.23.

9.2.1.5.   2,4,6-Tris(4-aminophenyl)-1,3,5-triazine (TT-NH2)
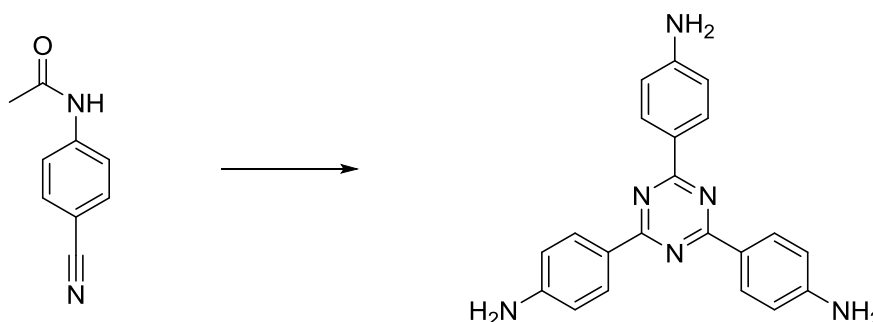
N-(4-Cyanophenyl)acetamide (1.0 g, 6.2 mmol) was added to a Schlenk tube, and degasses by purging with argon. The flask was cooled to -15°C with an acetone ice bath, then triflic acid (4.0 ml, 6.7 g, 44.6 mmol) was slowly added. The mixture was stirred for 1 h at -15°C, then the ice bath was removed and the mixture was allowed to warm up to room temperature over night. The mixture was poured onto 100 g ice and neutralized using 25 % ammonia solution. The precipitate was filtered off, washed with water until no more acid could be detected in the filtrate. The obtained substance was used without further purification for the subsequent hydrolysis. The powder was added to 10 mL of 6 M HCl in 100 mL ethanol and heated under reflux for 4 hours. The reaction mixture was cooled, the precipitate was filtered and washed with small amounts of 10% NaOH and then water to afford the title compound as yellow solid (0.4 g, 54 %).

^{1}H NMR (DMSO, 300 MHz): δ ppm 8.34 (d, J = 8.4 Hz, 6H), 6.68 (d, J = 8.4 Hz, 6H), 5.90 (s, 6H).

^{13}C NMR (DMSO, 75 MHz): δ ppm 169.57, 152.95, 130.14, 122.95, 113.12

9.2.1.6.   1,3,5-Tris(4-formylphenyl)benzene (N$_0$-CHO)
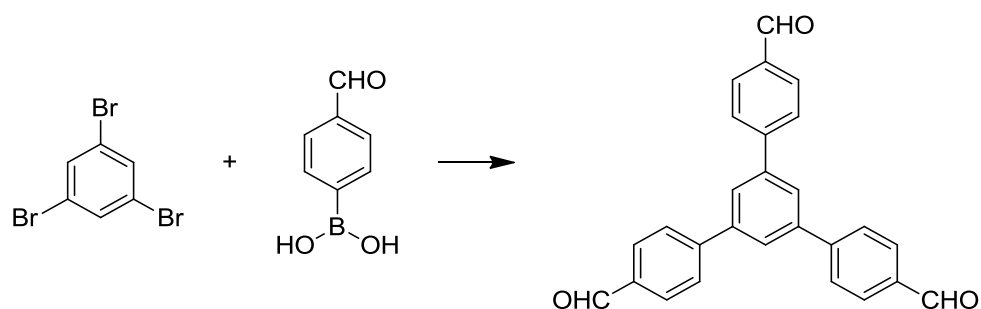
This compound was prepared as per modified literature procedure.[380] In a Schlenk flask equipped with a stir bar and reflux condenser, 1, 3, 5-tribromobenzene (1.0 g, 3.1 mmol), 4-formylphenyl boronic acid (2.2 g, 13.9 mmol), potassium carbonate (2.1 g, 15.0 mmol), and palladiumtetrakis(triphenylphosphine) (0.17 g, 0.15 mmol) were taken. The flask was evacuated and backfilled with argon three times. To this were added toluene (50 mL), ethanol (10 mL) and water (10 mL) and the contents were refluxed for 48 h. The reaction mixture was then cooled to room temperature and water (100 mL) was added. The organic compound was extracted with dichloromethane, dried over anhyd. MgSO$_4$ and then filtered. The solvent was removed under reduced pressure and after column chromatography (silica gel, dichloromethane) pure product was obtained as an off white solid (0.89 g, 73 %).

^{1}H NMR (CDCl$_3$, 300 MHz): δ ppm 10.11 (s, 3H), 8.02 (d, *J* = 8.3 Hz, 6H), 7.91 (s, 3H), 7.87 (d, *J* = 8.3 Hz, 6H). ^{13}C NMR (CDCl$_3$, 75 MHz): δ ppm 191.93, 146.49, 141.81, 135.99, 130.64, 128.19, 126.68. MALDI-TOF-MS for C$_{27}$H$_{18}$O$_3$: 389.8 M$^+$ (calculated: 390.1)

9.2.1.7.   2,4,6-Tris(4-bromophenyl)pyridine (1)
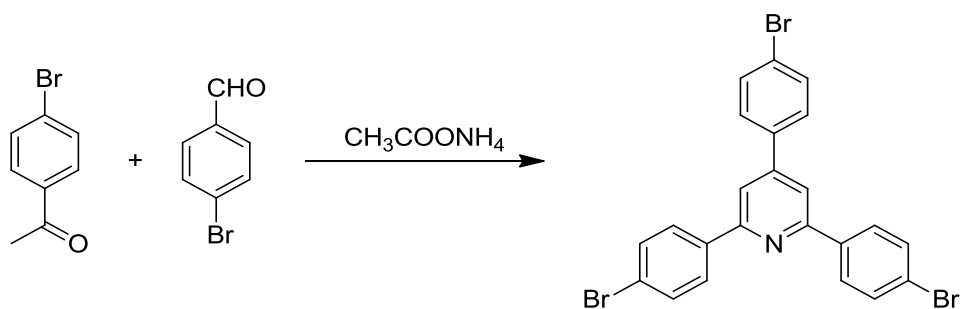
This compound was prepared as per modified literature procedure.[381] In a 20 ml microwave vial equipped with a stir bar was taken a mixture of 4-bromoacetophenone (2.07 g, 10.4 mmol), 4-bromobenzaldehyde (0.97 g, 5.2 mmol), ammonium acetate (14.0 g, 181.6 mmol) and glacial acetic acid (7.3 ml). The contents were flushed with Argon before sealing the vial. The contents were heated in the microwave under autogenous pressure at 220°C for 45 min. The reaction mixture was then cooled to room temperature and water (10 mL) was added. The aqueous suspension was then neutralized by saturated sodium bicarbonate solution. The organic compound was extracted with dichloromethane, dried over anhyd. MgSO$_4$ and then filtered. The solvent was removed under reduced pressure and after recrystallization (acetone), pure product was obtained as off white solid (0.90 g, 31%).

^{1}H NMR (CDCl$_3$, 300 MHz): δ ppm 8.04 (d, J = 8.4 Hz, 4H), 7.80 (s, 2H), 7.62 (m, 8H). ^{13}C NMR (CDCl$_3$, 75 MHz): $δ$ ppm 156.87, 149.64, 138.25, 137.80, 132.62, 132.16, 128.93, 128.87, 124.05, 123.93, 116.97.

9.2.1.8. 2,4,6-Tris(4-formylphenyl)pyridine (N$_1$-CHO)
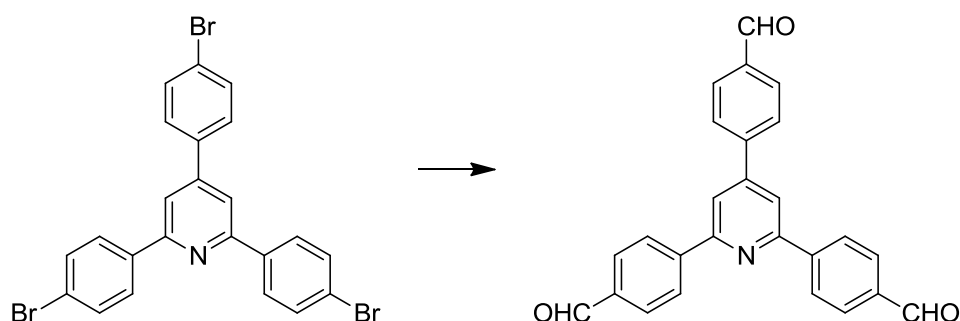
The synthesis was adapted from literature published procedure with modifications.[382] In a Schlenk flask under Argon flow, a suspension of **1** (0.5 g, 0.92 mmol) in dry THF (150 mL) was cooled to -78°C. To this was added a solution of *n*-BuLi (1.1 mL, 2.8 mmol, 2.5 M in hexane). The mixture was stirred for 1 hour and then N-formylpiperidine (0.32 mL, 2.9 mmol) was added. The mixture was stirred for 30 min at -78 °C and then warmed to room temperature. After stirring for an additional 1 h at room temperature, 5 mL of 0.5 M HCl was added. The mixture was extracted with dichloromethane, dried over anhyd. MgSO$_4$ and then filtered. After evaporating the solvent, the product was obtained as an off-white solid (0.34 g, 95 %).

^{1}H NMR (CDCl$_3$, 300 MHz): δ ppm 10.15 (s, 1H), 10.14 (s, 2H), 8.39 (d, J = 8.2 Hz, 4H), 8.05 (m, 8H), 7.92 (d, J = 8.2 Hz, 2H). ^{13}C NMR (CDCl$_3$, 75 MHz): $δ$ ppm 191.77, 191.38, 157.15, 149.96, 144.65, 144.41, 137.41, 137.34, 130.75, 130.41, 128.23, 128.04, 118.89. MALDI-TOF-MS for C$_{26}$H$_{17}$NO$_3$: 391.0 M$^+$ (calculated: 391.1)

9.2.1.9. 2,4,6-Tris(4-formylphenyl)pyrimidine (N2-CHO)
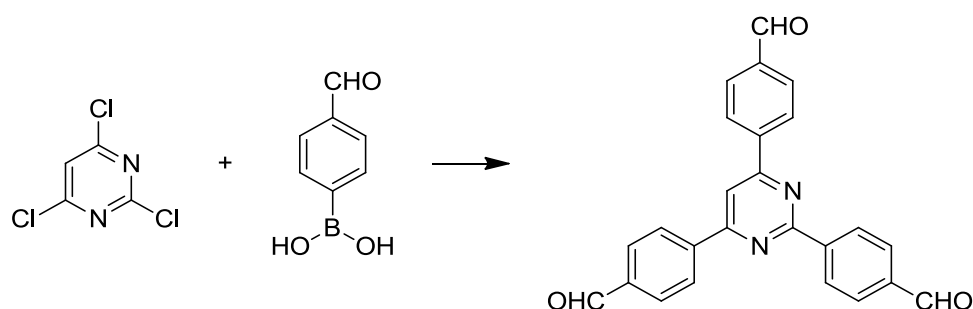
This was prepared as per modified literature procedure.[383] In a Schlenk flask equipped with a stir bar and reflux condenser, 2, 4, 6-trichloropyrimidine (0.15 g, 0.8 mmol), 4-formylphenylboronicacid (0.56 g, 3.6 mmol), potassium carbonate (0.3 g, 2.4 mmol), cesium carbonate (0.78 g, 2.4 mmol), and palladiumtetrakis(triphenylphosphine) (0.14 g, 0.12 mmol) were taken. The flask was evacuated and backfilled with argon three times. To this were added toluene (25 mL), ethanol (5 mL) and water (5 mL) and the contents were refluxed for 72 h. The reaction mixture was then cooled to room temperature and water (100 mL) was added. The organic compound was extracted with dichloromethane, dried over anhyd. MgSO$_4$ and then filtered. The solvent was removed under reduced

pressure and after column chromatography (silica gel, ethylacetate:hexanes (1:3) followed by methanol) pure product was obtained that was further recrystallized from acetone to yield an off white solid (0.15 g, 48 %).

^{1}H NMR (CDCl$_3$, 300 MHz): δ ppm 10.17 (s, 3H), 8.90 (d, J = 8.2 Hz, 2H), 8.48 (d, J = 8.2 Hz, 4H), 8.12 (m, 7H). ^{13}C NMR (CDCl$_3$, 75 MHz): $δ$ ppm 192.24, 191.80, 164.47, 164.16, 143.05, 142.44, 138.36, 138.30, 130.52, 130.16, 129.36, 128.26, 112.42. MALDI-TOF-MS for C$_{25}$H$_{16}$N$_2$O$_3$: 392.0 M$^+$ (calculated: 392.1).

9.2.1.10. 2,4,6-Tris(4-bromophenyl)-1,3,5-triazine (2)
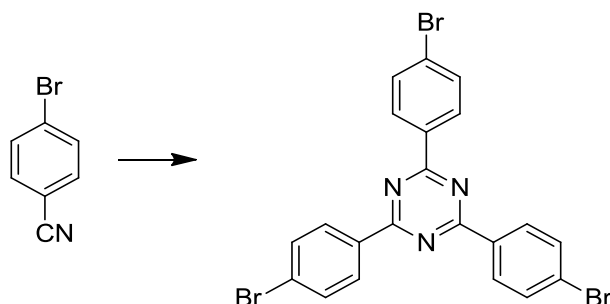
This compound was prepared as per modified literature procedure.[384] In a 15 ml Schlenk tube under Argon, was taken triflic acid (4.0 ml, 6.7 g, 44.6 mmol) and cooled to 0 °C. To this was added 4-bromobenzonitrile (1.5 g, 8.2 mmol) in portions and the solution was continued to stir for an hour at 0 °C and then 16 hours at room temperature. The workup was done by pouring the reaction mixture in 100 mL ice cold water and neutralizing the resulting suspension with 25 % ammonia solution. The precipitate was filtered off, washed with water (2 x 10 mL) acetone (3 x 5 mL) and dried in vacuum to afford the title compound as off white solid (1.4 g, 94 %).

^{1}H NMR (CDCl$_3$, 300 MHz): δ ppm 8.59 (d, J = 8.4 Hz, 6H), 7.72 (d, J = 8.4 Hz, 6H). ^{13}C NMR (CDCl$_3$, 75 MHz): $δ$ ppm 171.37, 135.07, 132.10, 130.55, 127.88.

9.2.1.11. 2,4,6-Tris(4-formylphenyl)-1,3,5-triazine (N$_3$-CHO)
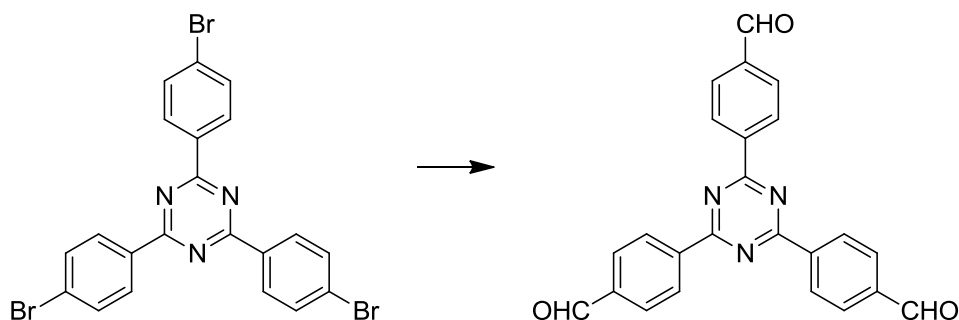
The synthesis was adapted from literature published procedure with modifications.[382] In a Schlenk flask under Argon flow, a suspension of 2 (0.5 g, 0.9 mmol) in THF (150 mL) was cooled to -78 °C. To this was added a solution of n-BuLi (1.1 mL, 2.7 mmol, 2.5 M in hexane). The mixture was stirred for 1 hour and then N-formylpiperidine (0.32 mL, 2.9 mmol) was added. The mixture was stirred for 30 min at -78 °C and then warmed to room temperature. After stirring for an additional 1 h at room temperature, 5 mL of 0.5 M HCl was added. The mixture was extracted with dichloromethane, dried

over anhyd. MgSO$_4$ and then filtered. After evaporating the solvent, the residue was obtained as an off-white solid (0.29 g, 81 %).

^{1}H NMR (C$_2$D$_2$Cl$_4$, 70 °C, 300 MHz): δ ppm 10.20 (s, 3H), 8.94 (d, J = 8.2 Hz, 6H), 8.13 (d, J = 8.2 Hz, 6H). ^{13}C NMR (C$_2$D$_2$Cl$_4$, 70 °C, 75 MHz): $δ$ ppm 191.36, 171.16, 140.57, 139.25, 129.60, 129.45. MALDI-TOF-MS for C$_{24}$H$_{15}$N$_3$O$_3$: 393.0 M$^+$ (calculated: 393.1).

9.2.1.12.   1,3,5- phenyltriboronic acid tris(pinacol) ester (3)
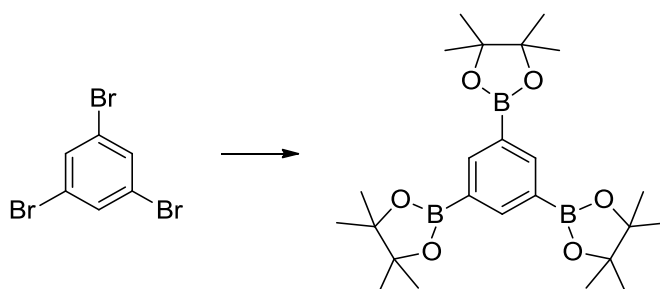
Bis(pinacolato)diboron (4 eq, 10 g, 39 mmol), 1,3,5-tribromobenzene (1 eq, 3.131 g, 9.75 mmol) and potassium acetate (9 eq, 8.6 g, 87.7mmol) were added to 90 ml of 1,4-dioxane in a 250 ml flask and degassed by bubbling argon for 30 min. 1,1'-bis(diphenylphosphino)ferrocene-palladium(II)dichloride dichloromethane adduct (0.059 eq, 0.575 mmol, 470 mg) was then added and the mixture was heated at 90 °C for 16 h under an inert Ar atmosphere. The reaction mixture was then allowed to cool down and 200 ml water was added to it. The resulting solution was extracted with dichloromethane (3×100 ml); the organic layers were combined, dried over magnesium sulfate and the solvent removed. To the obtained solid, 100 ml hot heptane was added and the solution was filtered while hot. The solvent was evaporated and the residue was recrystallized from boiling methanol to obtain large white needles (2.56 g, 57.6%). Further evaporation from the mother liquor improved the yield.

^{1}H NMR (CDCl$_3$, 300 MHz): δ (ppm) 8.38 (s, 3H), 1.34 (s, 36H). ^{13}C NMR (CDCl$_3$, 75 MHz): δ (ppm) 144.33, 106.72, 83.93, 25.11.

9.2.1.13.   2,2',2''- (1,3,5-benzenetriyl) tris-5-bromo pyridine (4)
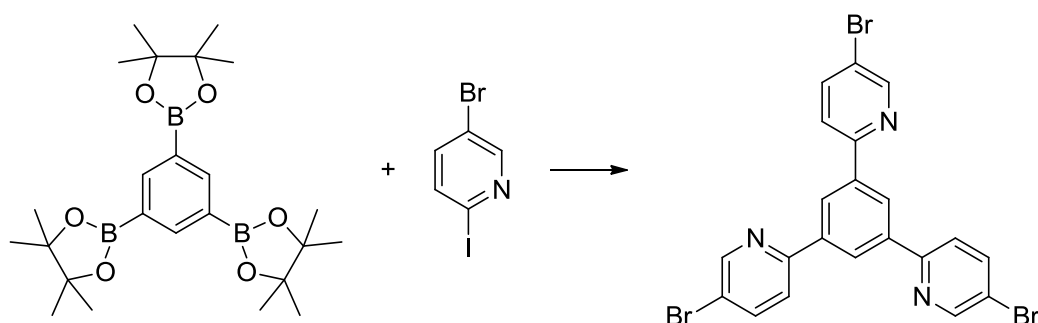
3 (1 eq, 3 g, 6.58 mmol), 5-Bromo-2-iodopyridine (4 eq, 7.62 g , 26.3 mmol), cesium carbonate (3 eq, 6.43 g, 19.7 mmol) and potassium carbonate (3 eq, 2.73 g, 19.7 mmol) were added to a mixture of toluene (193 ml), ethanol (64.3 ml) and water (64.3 ml). The mixture was degassed by bubbling argon for 30 min. Tetrakis(triphenylphospine)palladium(0) (0.141 eq, 1.07 g, 0.925 mmol) was then added and stirred first for 8 h at 25 °C and then for 16 h at 90 °C under an argon atmosphere . The reaction was then allowed to cool down, 200 ml water was added and then extracted with dichloromethane

(3×100 ml). The organic layers were combined, dried over magnesium sulfate and the solvent removed. The product was purified by column chromatography over silica gel (10% dichloromethane in chloroform) and all fractions between the first two yellow bands were collected. To these combined fractions, 1:1 ethanol was added and the solvent was removed under reduced pressure until precipitation started. The solid was filtered off to obtain the product as an off-white dense powder (2.26 g, 62.9%). The product could be further purified by recrystallization from chloroform.

^{1}H NMR (CDCl$_3$, 300 MHz): δ (ppm) 8.79 (d, J = 2.28 Hz, 3H), 8.68 (s, 3H), 7.94 (dd, J = 8.39, 2.38 Hz, 3H), 7.84 (d, J = 8.57 Hz, 3H). ^{13}C NMR (CDCl$_3$, 75 MHz): δ (ppm) 155.2, 150.99, 139.65, 139.62, 126.07, 122.09, 120.10.

9.2.1.14. 2,2',2''-(1,3,5-benzenetriyl) tris-(pyridine-2-carboxaldehyde) (5)
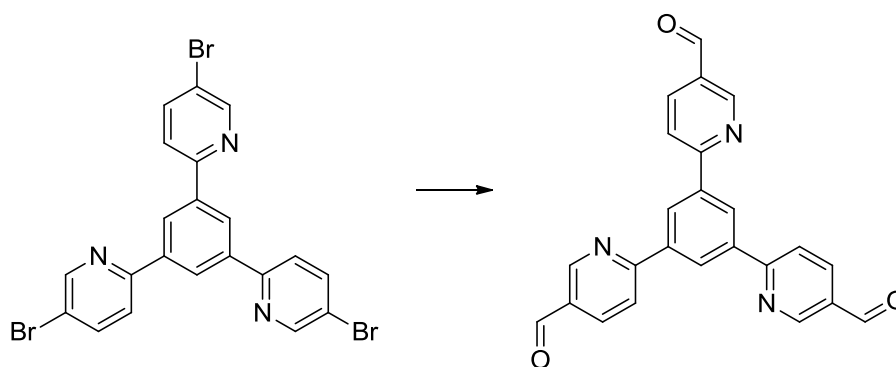
4 (1 eq, 600 mg, 546.06 mmol) was added to 60 ml of dry tetrahydrofuran in an argon atmosphere. The mixture was cooled to -78 °C with a acetone/dry ice bath and *n*-butyllithium (3.3 eq, 2.5 mol/L in hexanes, 1.45 ml, 3.63 mmol) was very slowly added and stirred for 1 h. To the cold reaction mixture, N-formylpiperidine (3.6 eq, 0.439 ml, 3.96 mmol) was added and stirred for another 1 h at -78 °C. The cold bath was then removed and the reaction mixture was allowed to warm to room temperature overnight. 20 ml water was then added to the reaction mixture and to stirred for 30 min. The precipitated solid was filtered off to obtain the crude product which was used for the next step without purification.

9.2.1.15. 2,2',2''-(1,3,5- benzenetriyl) tris-(pyridine-2-carboxaldehyde) dimethyl acetal (6)
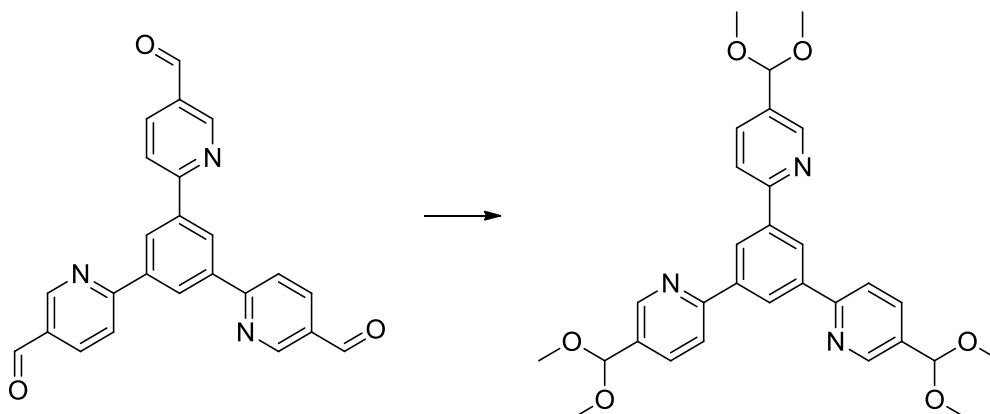
5 (1 eq, 360 mg, 0.916 mmol) was added to a mixture of methanol (50 ml), chloroform (50 ml) and trimethyl orthoformate (100 eq, 10 ml, 91.6 mmol). To this *p*-toluenesulfonic acid monohydrate (0.3 eq, 52.2 mg, 0.275 mmol) was added and heated to reflux for 2 h. The cooled reaction mixture was quenched with 20 ml saturated sodium bicarbonate solution. Water was then added and extracted with dichloromethane (3×50 ml). The combined organic layers were washed with brine and dried over anhydrous magnesium sulfate. The solvent was removed under reduced pressure and the solid product washed with a small amount of diethyl ether (5 ml) and sonicated. After filtration, the product was obtained as a sticky white solid.

^{1}H NMR (CDCl$_3$, 300 MHz): δ (ppm) 8.81 (d, *J* = 2.0 Hz, 3H), 8.78 (s, 3H), 8.01 (d, *J* = 8.08 Hz, 3H), 7.91 (dd, *J* = 8.15, 2.07 Hz, 3H) 5.55 (s, 3H), 3.39 (s, 18H). ^{13}C NMR (CDCl$_3$, 75 MHz): δ (ppm) 157.14, 148.66, 140.32, 135.72, 132.57, 126.53, 120.65, 101.51, 52.87.

9.2.1.16. 2,2',2''-(1,3,5-benzenetriyl) tris-(pyridine-2-carboxaldehyde), (PTP-CHO)
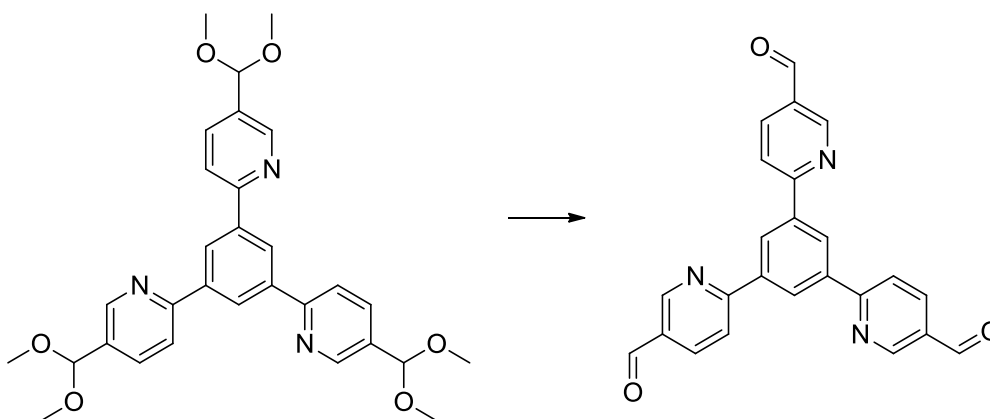
To a solution of 6 (250 mg, 0.47 mmol) in THF (51 ml), hydrochloric acid (aq. 6M, 10 ml) was added. The solution was heated at 50 °C for 20 min and then left to stir at 25°C for 16 h. The precipitate formed was filtered off and washed with water, sodium bicarbonate solution and again with water. After drying in air, the product was obtained as an off-white powder (153 mg, 82.7 %).

^{1}H NMR (CDCl$_3$, 300 MHz): δ (ppm) 10.22 (s, 3H), 9.23 (d, *J* = 1.38 Hz, 3H), 9.02 (s, 3H), 8.34 (dd, *J* = 8.12, 2.18 Hz, 3H), 8.19 (d, *J* = 8.08 Hz, 3H).

9.2.2. Structure Building

Structures were built by considering the molecular geometry of the building blocks, upon which likely nets were considered. Periodic models were built in either Materials Studio v6.0.0 Copyright © 2011 Accelrys Software or BIOVA Materials Studio 2017 (17.1.0.48) Copyright © 2016 Dassault Systémes. The symmetry of the models was based on the highest reasonable symmetry based on experimental and theoretical evidence. Geometry optimizations were performed Forcite using universal force fields with Ewald electrostatic and van der Waals summations methods.

9.2.3. Characterization techniques

Diffuse reflectance UV-Vis Spectra

Diffuse reflectance UV–visible absorption spectra were measured on a Cary 5000 spectrometer and referenced to barium sulphate. Absorption spectra were calculated from the reflectance data using the Kubelka-Munk function.

Diffuse reflectance UV-Vis absorption spectra were collected on a Cary 5000 spectrometer (referenced to barium sulfate). Absorption spectra were calculated from the reflectance data using the Kubelka-Munk function.

Elemental analysis

CHNS elemental analyses were performed with a vario EL elemental analyser (Elementar Analysensysteme GmbH).

IR

Infrared spectra were recorded in attenuated total reflection (ATR) geometry on a PerkinElmer UATR Two Spectrometer equipped with a diamond crystal and a Perkin Elmer Spectrum BX II FT-IR Spectrophotometer equipped with an ATR unit (Smith Detection Dura-Sample IIR diamond).

Raman

Raman spectra were recorded with a Jobin Yvon Type V 010 labRAM single grating spectrometer equipped with a double super razor edge filter and a peltier cooled CCD camera in quasi-backscattering geometry using the linearly polarized 632.817 nm He/Ne gas laser.

SEM/EDX

SEM images were obtained on either a Zeiss Merlin instrument with EsB (energy and angle selective BSE) and SE (secondary electron) detector or with a VEGA TS 5130MM (TESCAN) instrument with a SEM-EDX using a Si/Li detector (10kV acceleration voltage, Oxford).

TEM/SAED

TEM was performed with a Philips CM30 ST (300 kV, LaB_6 cathode). The samples were suspended in *n*-butanol and drop-cast onto a lacey carbon film (Plano).

TGA

TGA measurements were performed on NETZSCH STA 409 C/CD at a heating rate of 5K/minute under Argon and in air.

Solution NMR

Solution ^{1}H and ^{13}C NMR spectra were recorded on a Bruker 300-MHz NMR spectrometer.

Sorption

Ad- and desorption measurements were performed on an Autosorb iQ-MP2 (Quantachrome Instruments, Florida, USA) with argon of 99.9999% purity at 87 K. Prior to the measurements, the sample was outgassed under high vacuum at 120 °C for at least 12 h. In accordance with the ISO recommendations multipoint BET tags equal or below the maximum in $V \cdot (1 - p/p_0)$ were chosen. The pore size distribution was calculated from Ar adsorption isotherms by non-local density functional theory (NLDFT) using the "Ar-zeolite/silica cylindrical pores at 87 K" kernel (applicable pore diameters 3.5 Å – 1000 Å).

ssNMR

The ssNMR spectra were recorded on a Bruker Avance-III 400 MHz spectrometer at magnetic field of 9.4 T at the frequencies of 400.1, 100.6 and 40.8 MHz, for ^{1}H, ^{13}C and ^{15}N, respectively. The sample was packed in a 4-mm ZrO_2 rotor, which was mounted in a standard double resonance MAS probe (Bruker). The ^{13}C chemical shift was referenced to tetramethylsilane (TMS). ^{1}H-^{13}C and ^{1}H-^{15}N cross-polarization (CP) MAS spectra were recorded with a rotation frequency of 10-12 kHz, using a ramped-amplitude contact pulse of 5 ms on ^{1}H channel[385] and SPINAL64 broadband proton decoupling with radio frequency power between 70 and 80 kHz.[386] Cross Polarization with Phase Inversion (CPPI)[387] was performed with polarization inversion time of 40 mks and all other conditions being the same as in the CP. The reported ^{1}H and ^{13}C chemical shifts were referenced to tetramethylsilane (TMS), while the ^{15}N shifts were referenced to nitromethane.

XPS

For X-ray photoelectron spectroscopy (XPS), samples were pressed onto indium foil and the spectra were collected on an Axis Ultra (Kratos Analytical, Manchester) X-ray photoelectron spectrometer with charge neutralization. The spectra were referenced with the adventitious carbon 1s peak at 284.80 eV.

XRPD

XRPD pattern were collected at room temperature on a *Huber* G670 diffractometer or a Stoe Stadi P diffractometer (Cu-Kα1, Johann monochromator Ge(111)) in Debye-Scherrer geometry. The sample was measured in a glass capillary (1.0 mm). The sample was spun for improved particle statistics. The powder patterns were analyzed by Rietveld[326] and Pawley[325] refinement with TOPAS V5.[388] The peak profile was described by applying the fundamental parameter[353] approach as implemented in TOPAS. The background was modeled with Chebychev polynomials and a 1/X background correction function to describe the incoherent scattering at low 2θ. Likely lattice parameters were refined, constrained only by the symmetry. The anisotropic peak shape, caused by stacking faults and mismatches in the microstructure, was modelled by a phenomenological model for microstrain.[354]

9.3. Supplementary Tables

Table S 9.3-1: List of Molecular crystal structures with their extracted layer distances and layer offsets.

Type	CCDC Code	centroid -centroid distance	Distance	Offset
N_0	EXESAC	3.733	3.706	0.448166264
N_0		5.286	3.169	4.230748752
N_0	JOPMEI	5.139	3.878	3.372007859
N_0	MIGRID	4.241	3.827	1.827608273
N_0		5.168	3.206	4.053367489
N_0	NETQOT	4.749	3.468	3.244376211
N_0	NOPFEP	5.030	3.312	3.785704162
N_0		5.026	3.946	3.112837933
N_0	TECNAR	5.453	4.183	3.498245274
N_0	TPHBEN	4.917	3.320	3.626911772
N_0		4.932	4.008	2.874118995
N_0	YIHPOU	4.770	3.033	3.681550081
N_0	ZIMMAL	5.908	4.467	3.866571479
N_0	ZZZTCK01	4.78	3.716	3.006616703
N_0		4.689	3.369	3.261373944
N_1	AJEZOF	4.841	3.721	3.096682095
N_1		4.835	3.695	3.118364956
N_1	DEZKAV	6.667	3.927	5.387723081
N_1	EGUDER	7.579	3.619	6.659135079
N_1	GINXOR	5.557	4.308	3.510183044
N_1	GISGEV	4.795	4.000	2.644243748
N_1		4.797	3.987	2.667403232
N_1	HEVVAF	4.827	3.450	3.37600785
N_1		4.823	3.928	2.79859697
N_1	HUFBIU	6.394	4.191	4.828949679
N_1	SURGAN	5.893	3.658	4.620225644
N_1	SURGER	4.789	3.833	2.870998433
N_1		4.789	3.830	2.874999304
N_1	TAYXEX	5.452	3.655	4.045402205
N_1	TEDVEE	5.607	4.054	3.873439428
N_1	YALRIO	5.371	3.482	4.089415239
N_1	YOHXAW	7.004	3.874	5.835078406
N_1	YOVBAN	6.322	3.585	5.207250618

N$_2$	DALGED	5.275		3.463	3.979102411
N$_3$	FALWEW	3.860		3.480	1.670089818
N$_3$	FALWIA	3.868		3.503	1.640248457
N$_3$	HIQYUB	6.342		3.391	5.359298741
N$_3$	HIQYUB01	4.573		3.349	3.113924855
N$_3$	SIJYIU	6.468		3.276	5.576992738
N$_3$	TPTRAZ	3.910		3.633	1.445479505
PTP	JEFSOD	5.523		3.963	3.846837662

9.4. Supporting information for A Tunable Azine-Covalent Organic Framework Platform for Visible Light-Induced Hydrogen Generation

9.4.1. Supplementary Figures
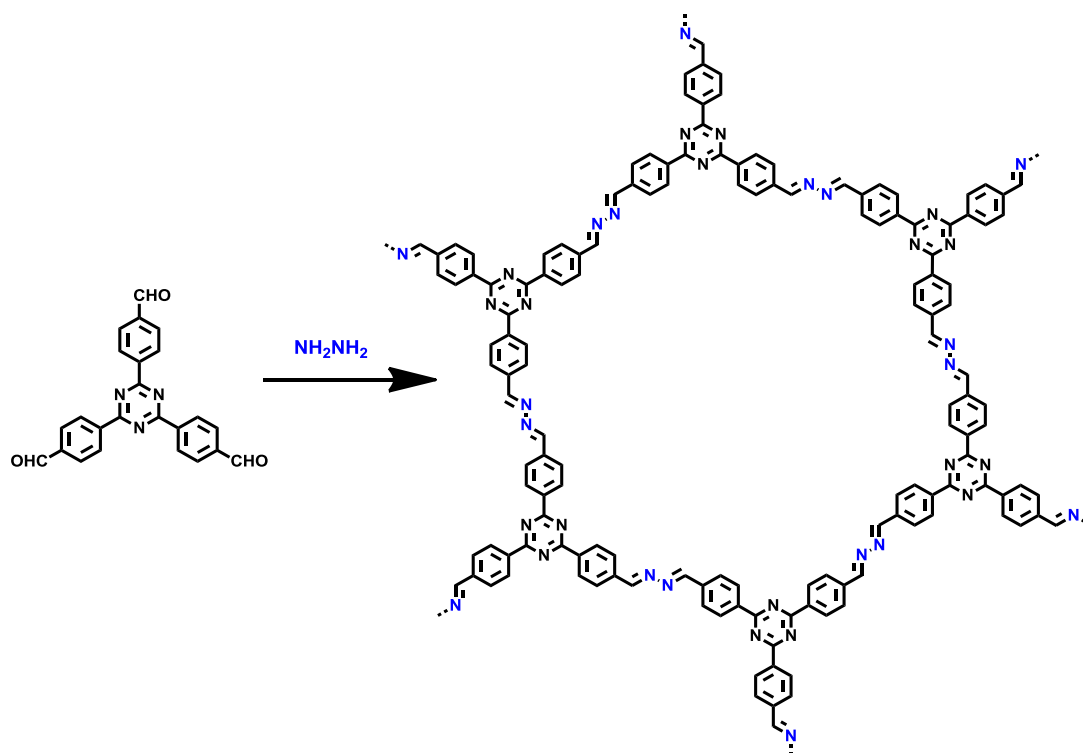
Figure S 1: Synthesis scheme for N$_3$-COF.
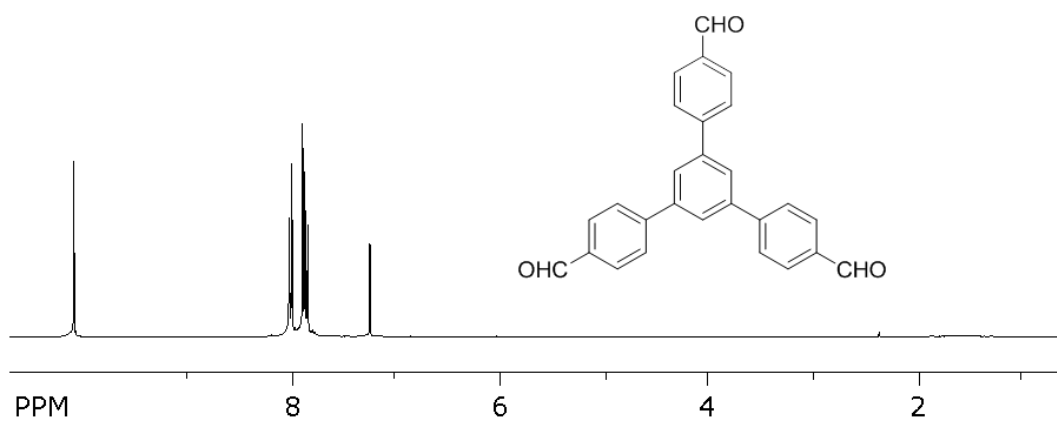
Figure S 2: ^{1}H NMR of 1,3,5-Tris(4-formylphenyl)benzene (N$_0$-CHO).
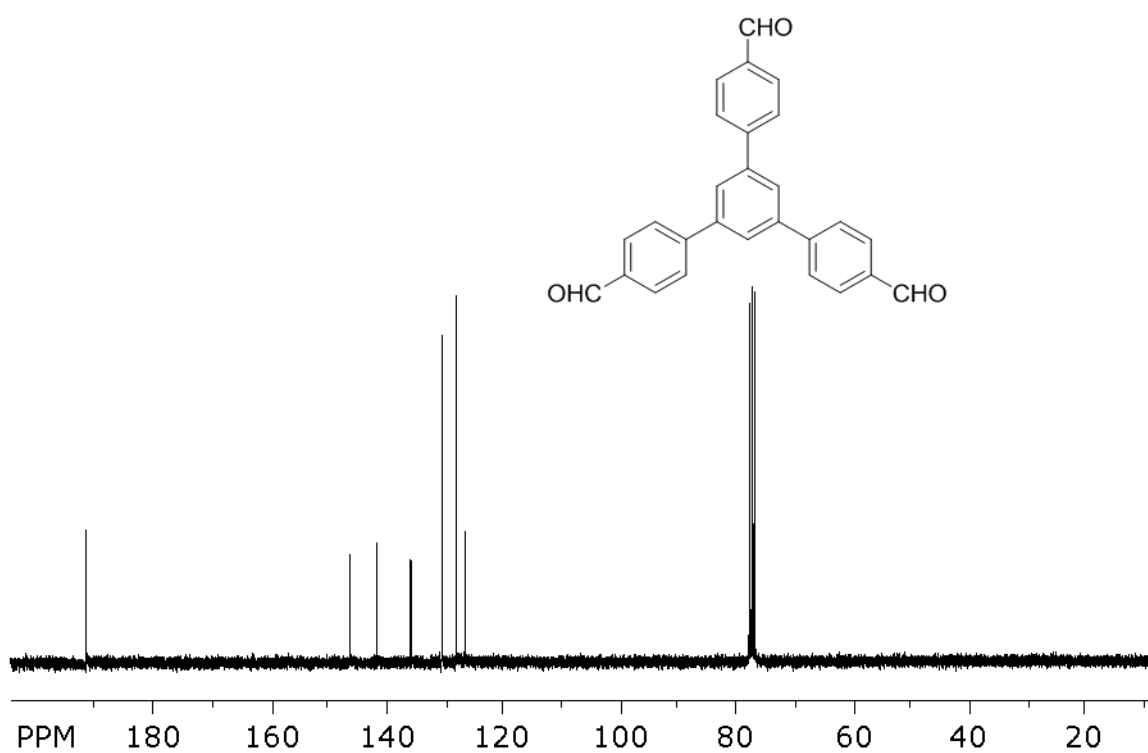
Figure S 3: ^{13}C NMR of 1,3,5-Tris(4-formylphenyl)benzene (N$_0$-CHO).
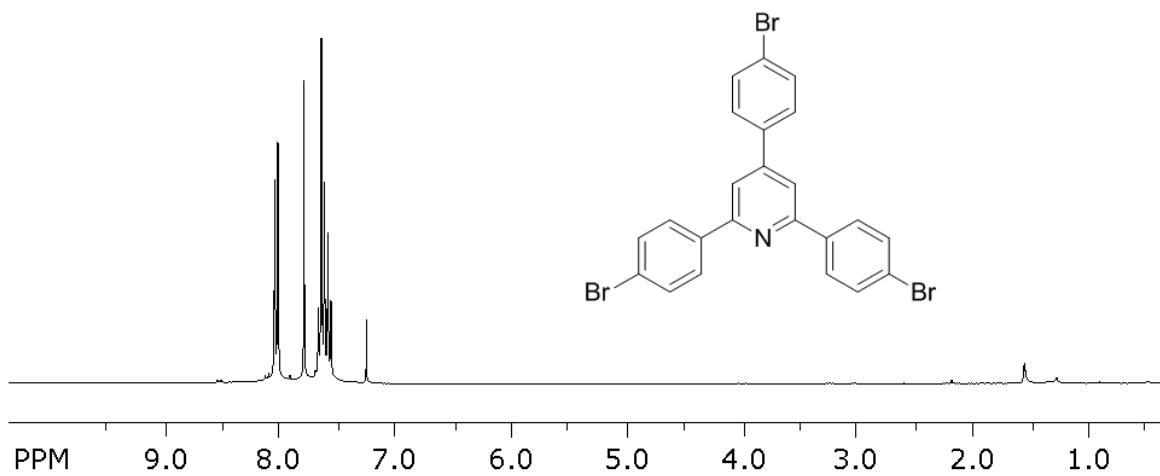
Figure S 4: ^{1}H NMR of 2,4,6-Tris(4-bromophenyl)pyridine (1).

Figure S 5: ^{13}C NMR of 2,4,6-Tris(4-bromophenyl)pyridine (1).

Figure S 6: ^{1}H NMR of 2,4,6-Tris(4-formylphenyl)pyridine (N$_1$-CHO).

Figure S 7: ^{13}C NMR of 2,4,6-Tris(4-formylphenyl)pyridine (N$_1$-CHO).

H-1/X correlation via heteronuclear zero- and
double-quantum coherence

VSV-N1-Aldehyde in CDCl3
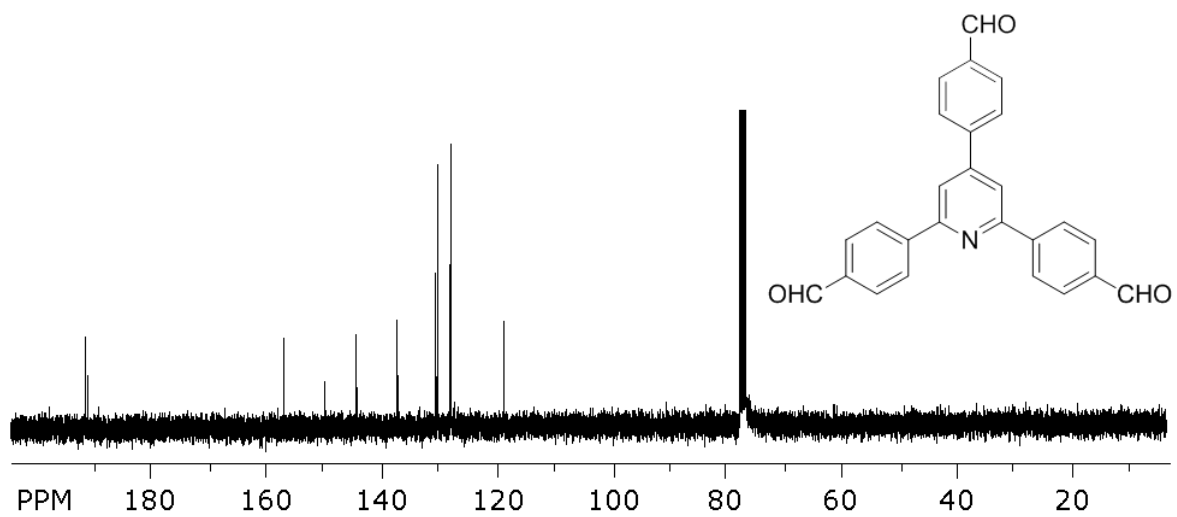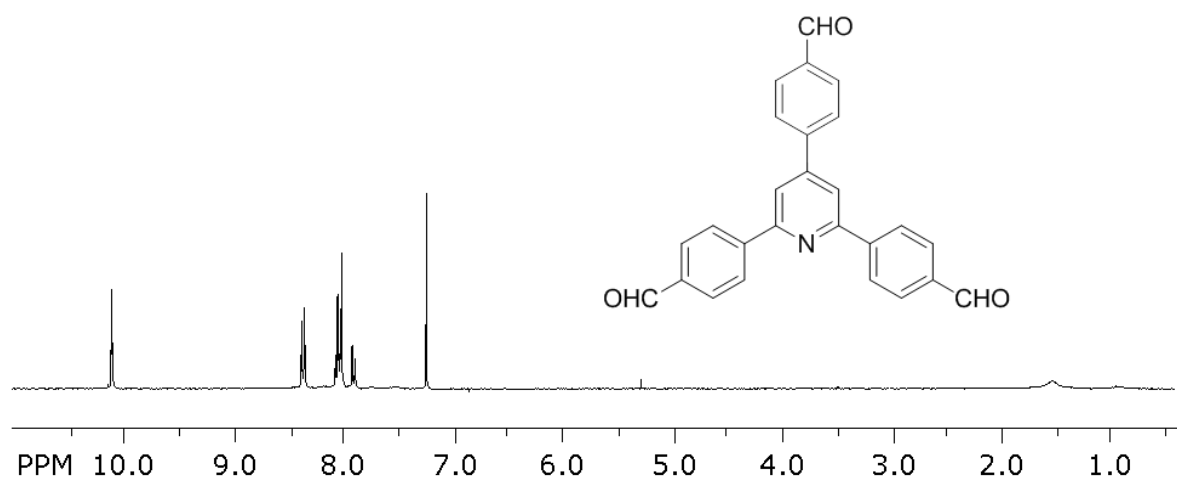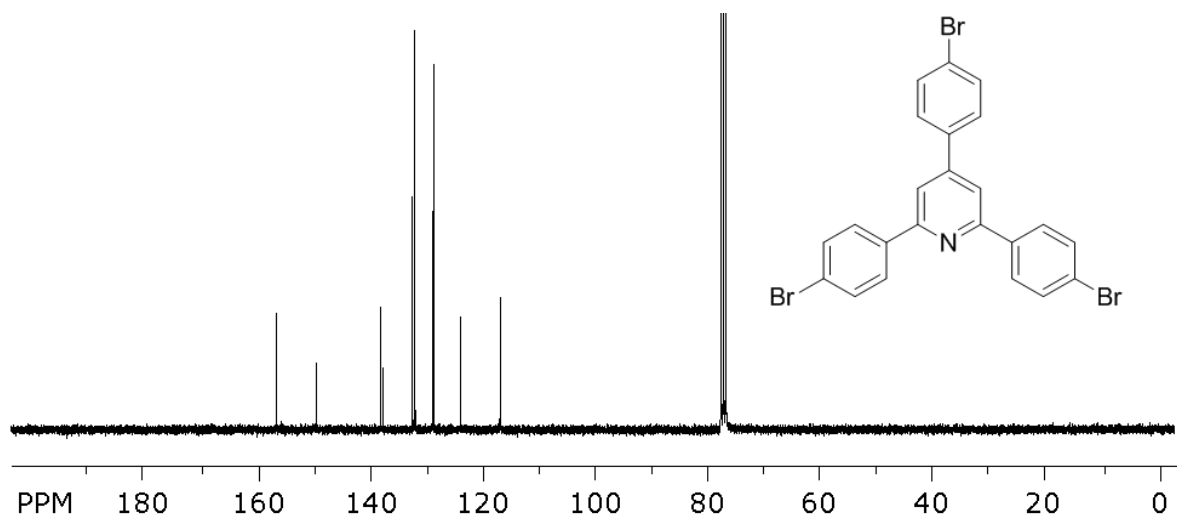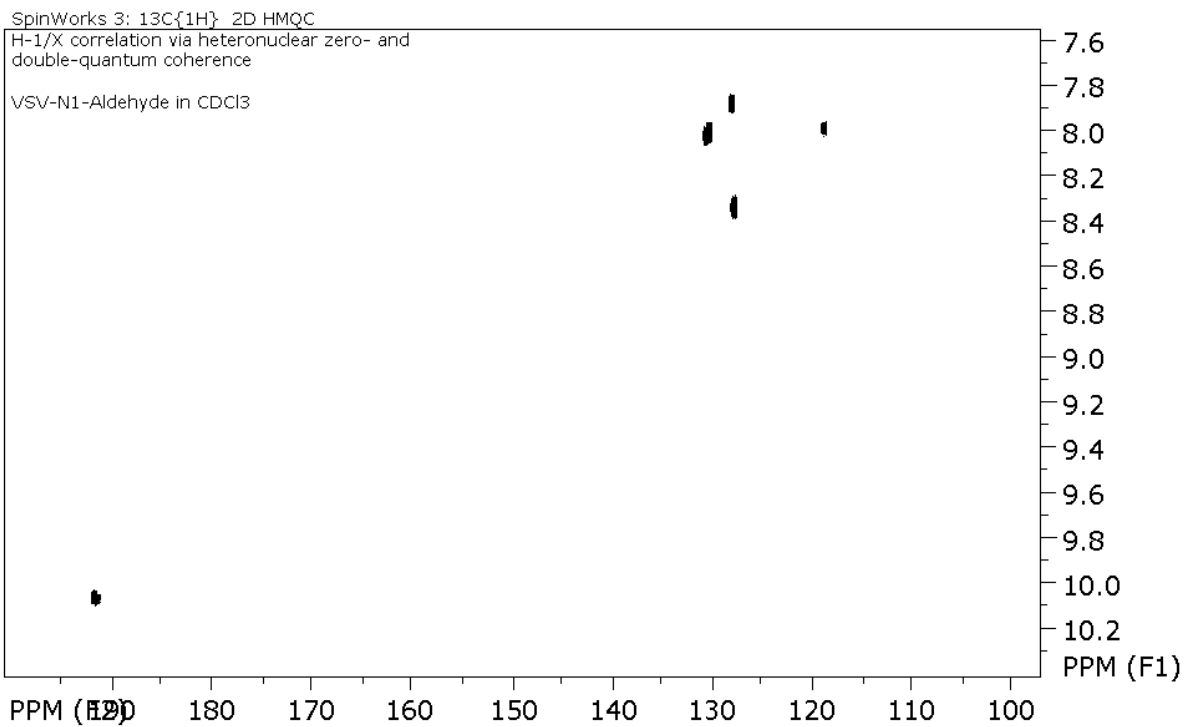
Figure S 8: 2D HMQC NMR of 2,4,6-Tris(4-formylphenyl)pyridine (N₁-CHO).
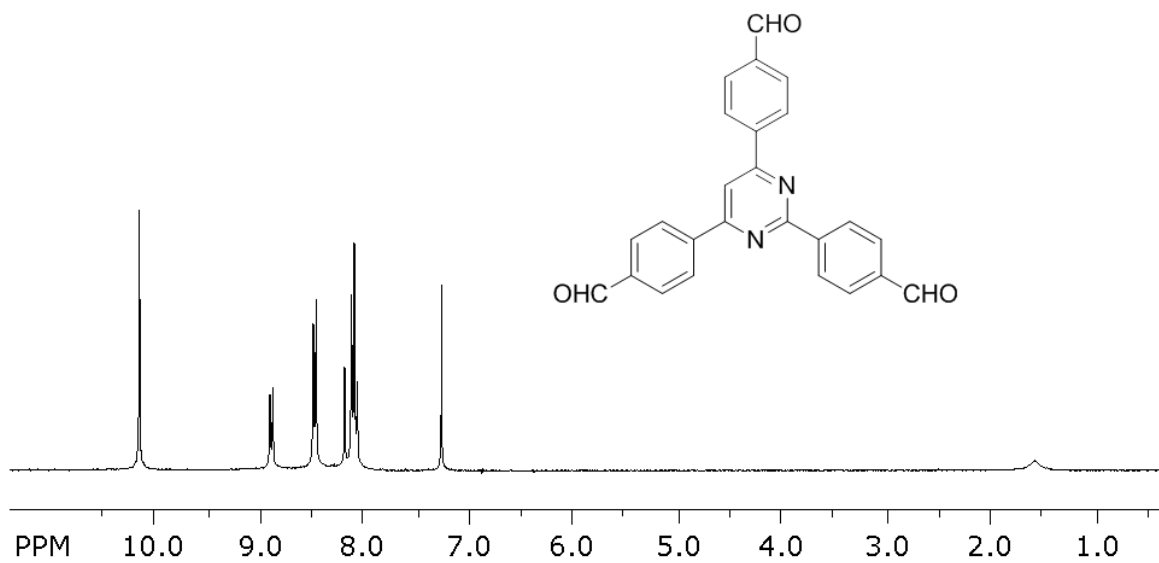
Figure S 9: ¹H NMR of 2,4,6-Tris(4-formylphenyl)pyrimidine (N₂-CHO).
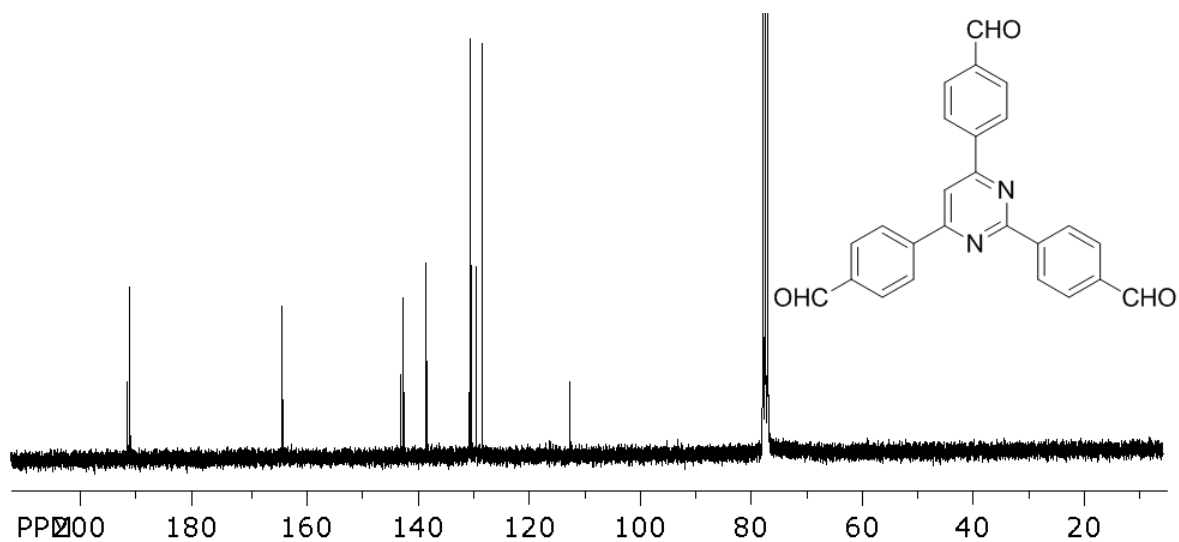
Figure S 10: ^{13}C NMR of 2,4,6-Tris(4-formylphenyl)pyrimidine (N$_2$-CHO).
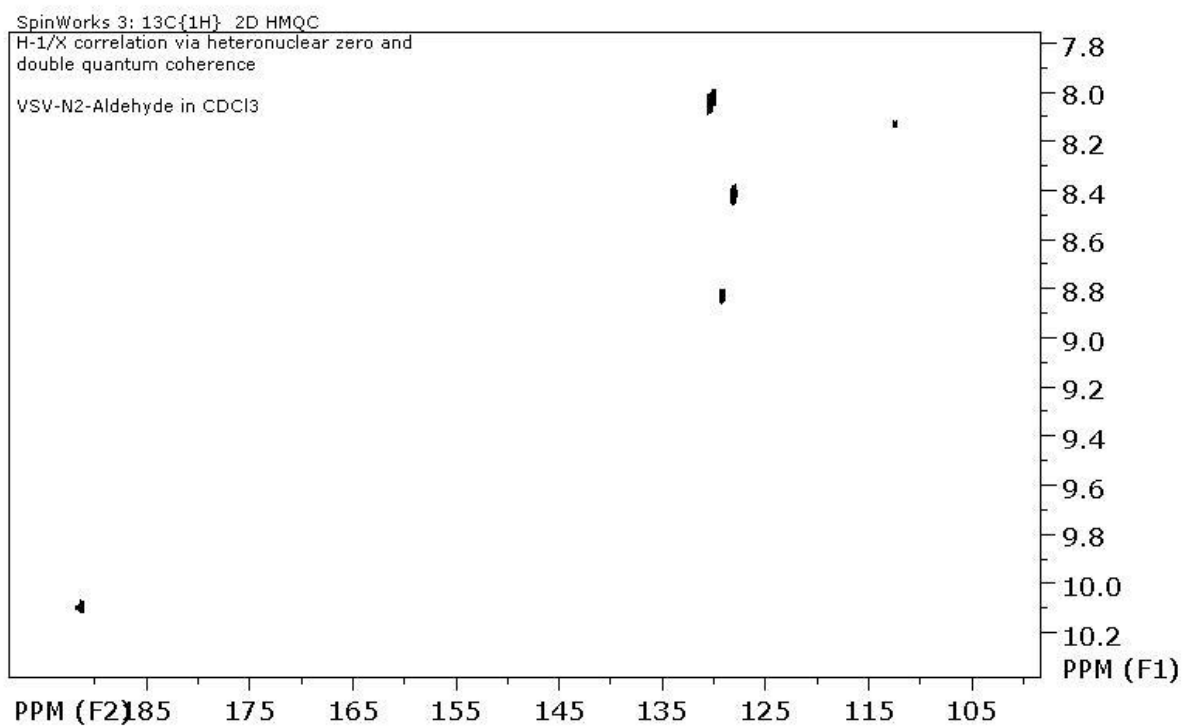
Figure S 11: 2D HMQC NMR of 2,4,6-Tris(4-formylphenyl)pyrimidine (N$_2$-CHO).
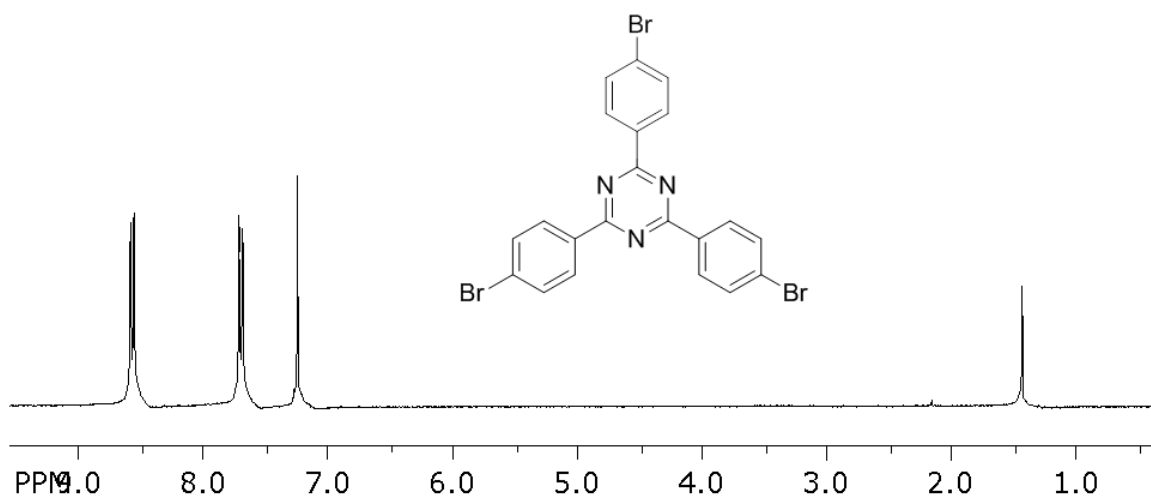
Figure S 12: ^{1}H NMR of 2,4,6-Tris(4-bromophenyl)-1,3,5-triazine (**2**).
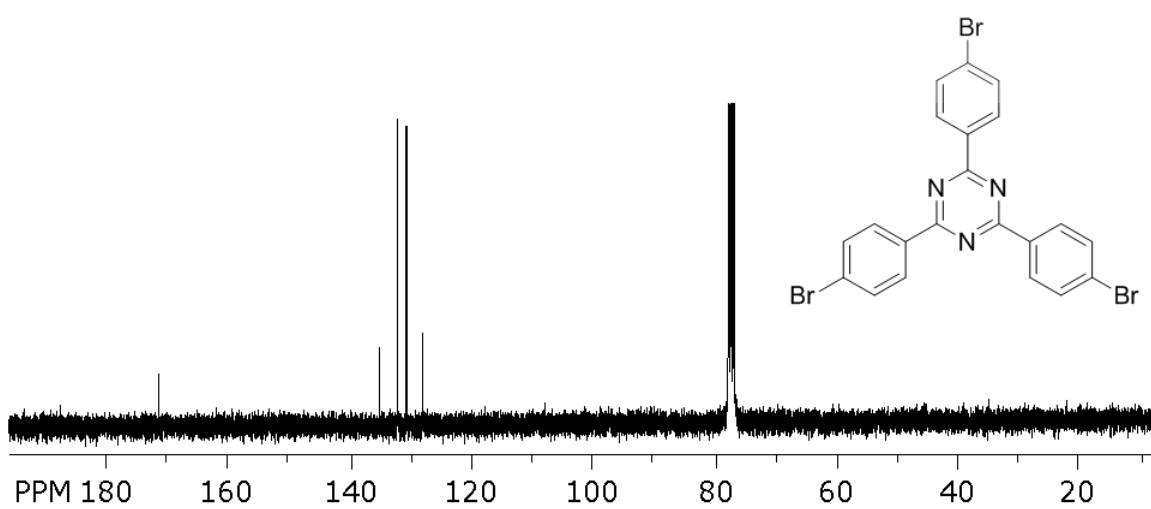
Figure S 13: ^{13}C NMR of 2,4,6-Tris(4-bromophenyl)-1,3,5-triazine (**2**).
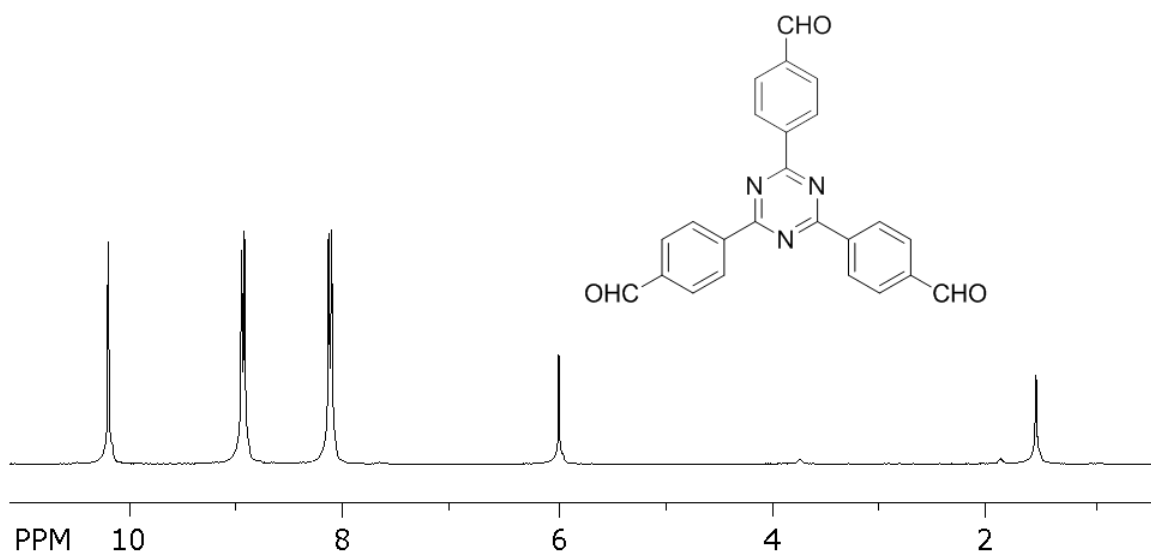
Figure S 14: ^{1}H NMR of 2,4,6-Tris(4-formylphenyl)-1,3,5-triazine (N$_3$-CHO).
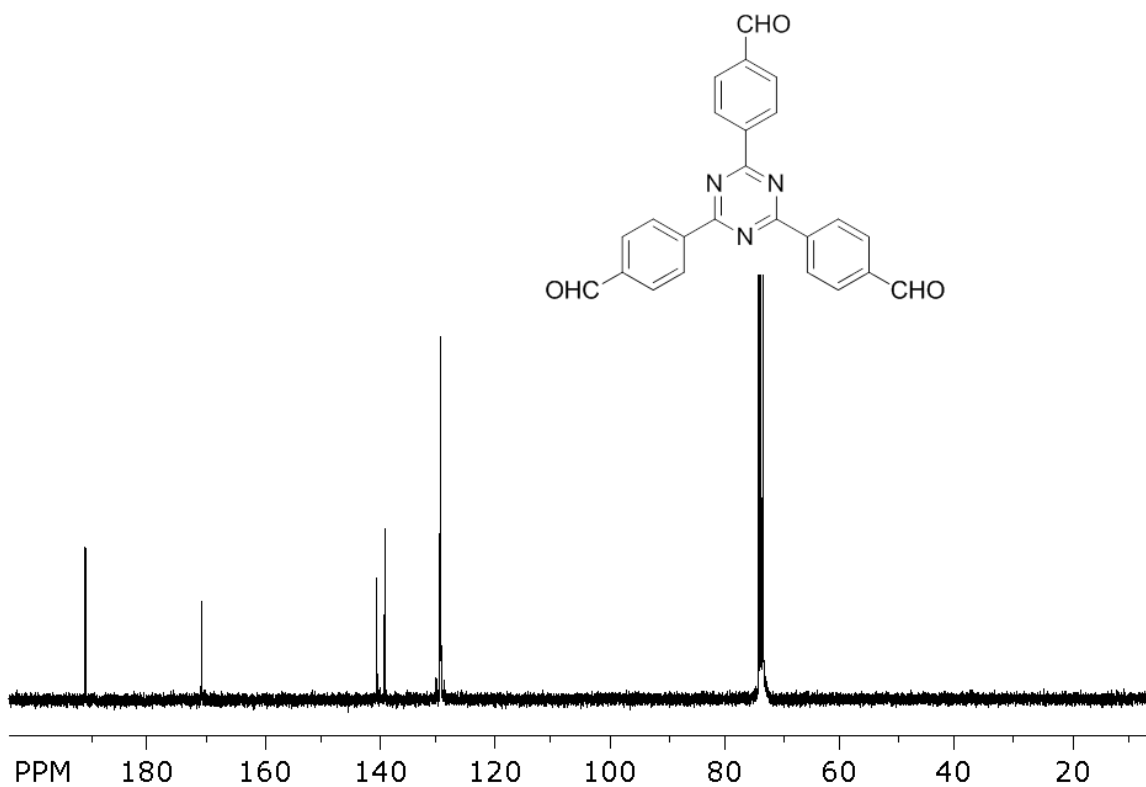
Figure S 15: ^{13}C NMR of 2,4,6-Tris(4-formylphenyl)-1,3,5-triazine (**N₃-CHO**).
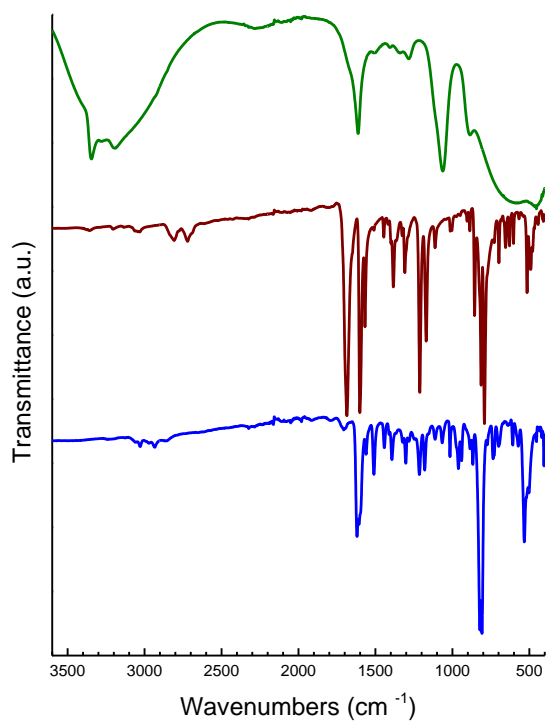
Figure S 16: FT-IR spectra of hydrazine hydrate (green), **N₀-CHO** (brown) and **N₀-COF** (blue).
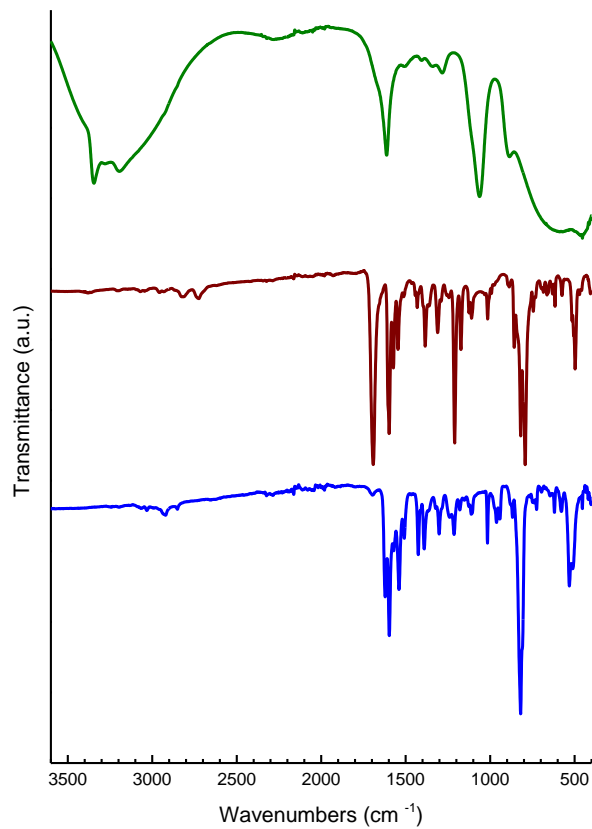
Figure S 17: FT-IR spectra of hydrazine hydrate (green), **N₁-CHO** (brown) and **N₁-COF** (blue).
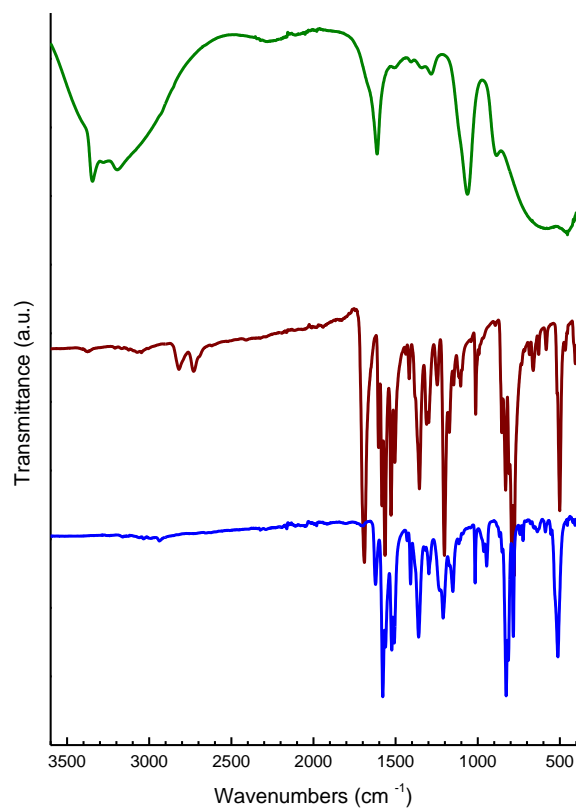
Figure S 18: FT-IR spectra of hydrazine hydrate (green), **N₂-CHO** (brown) and **N₂-COF** (blue).
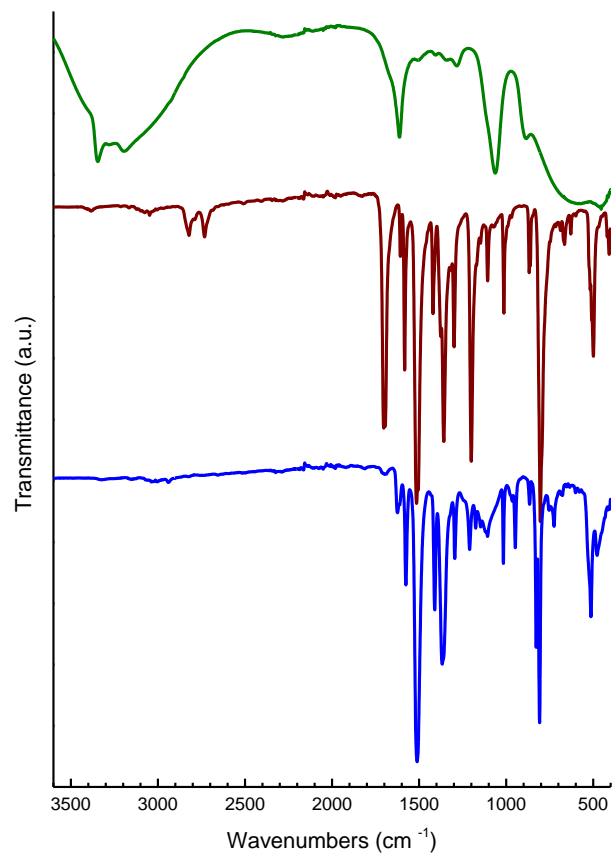
Figure S 19: FT-IR spectra of hydrazine hydrate (green), **N₃-CHO** (brown) and **N₃-COF** (blue).
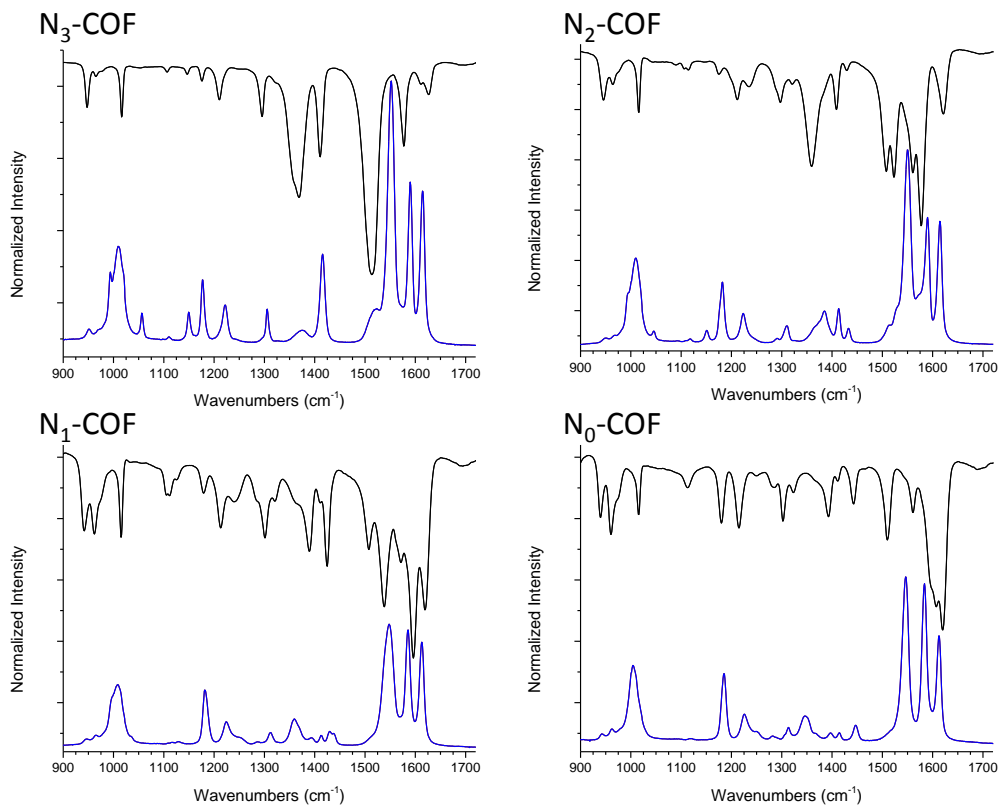
Figure S 20: A comparison of the Raman (blue) and FT-IR (black) spectra of **Nₓ-COFs**.
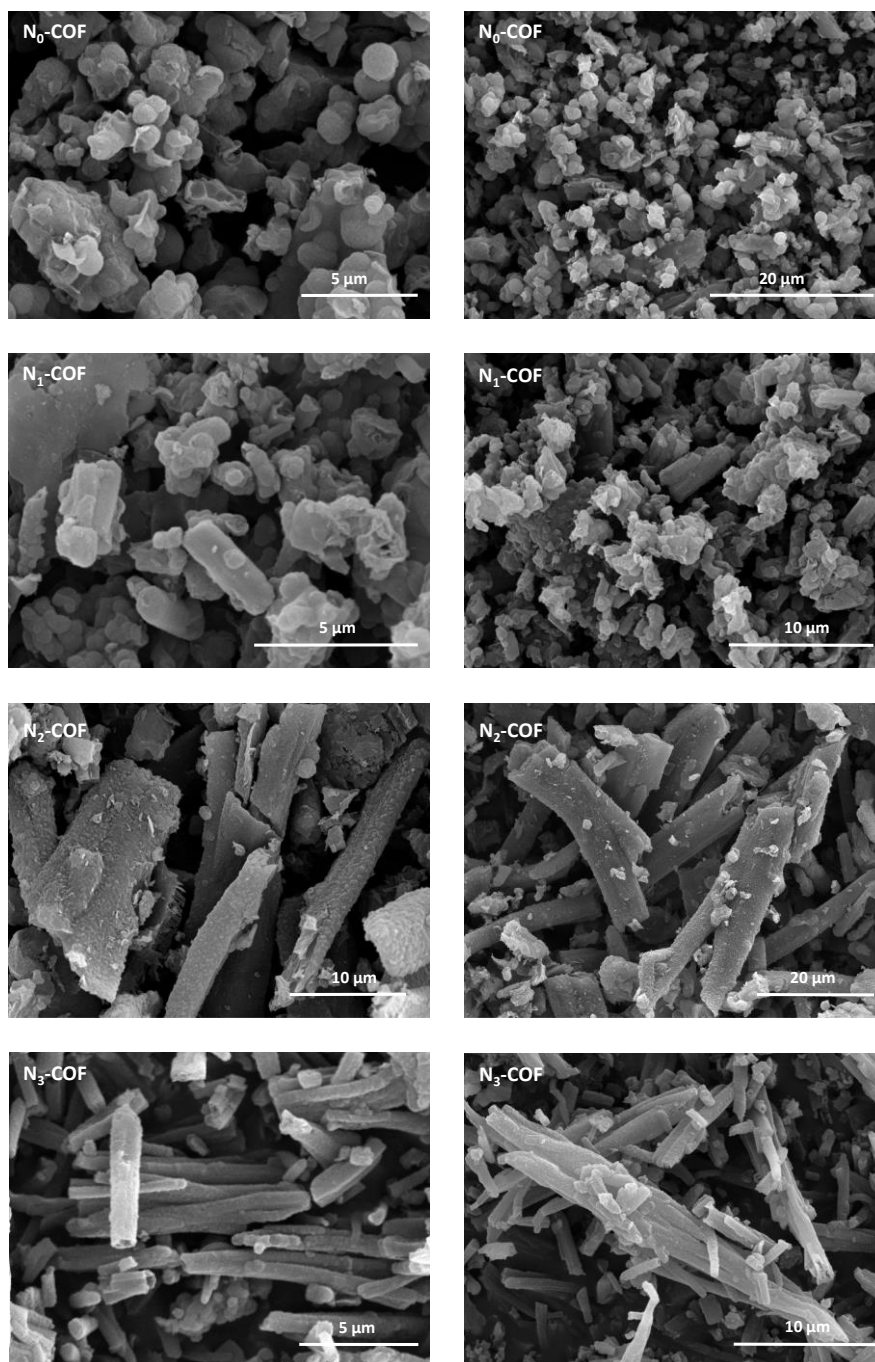
Figure S 21: SEM images of N_x-COFs.
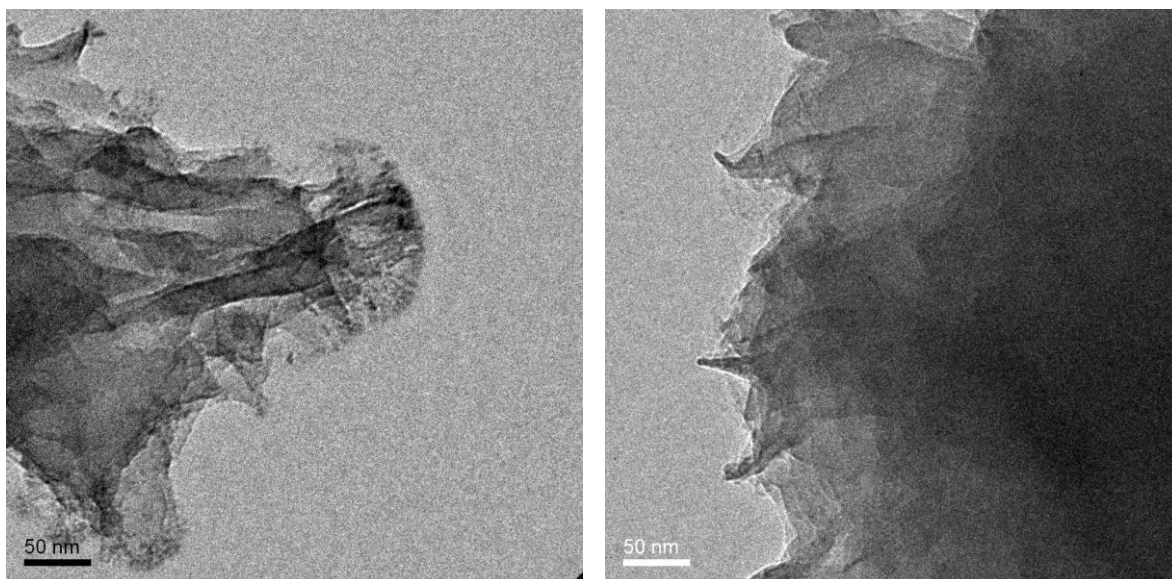
Figure S 22: TEM images of N_0-COF.
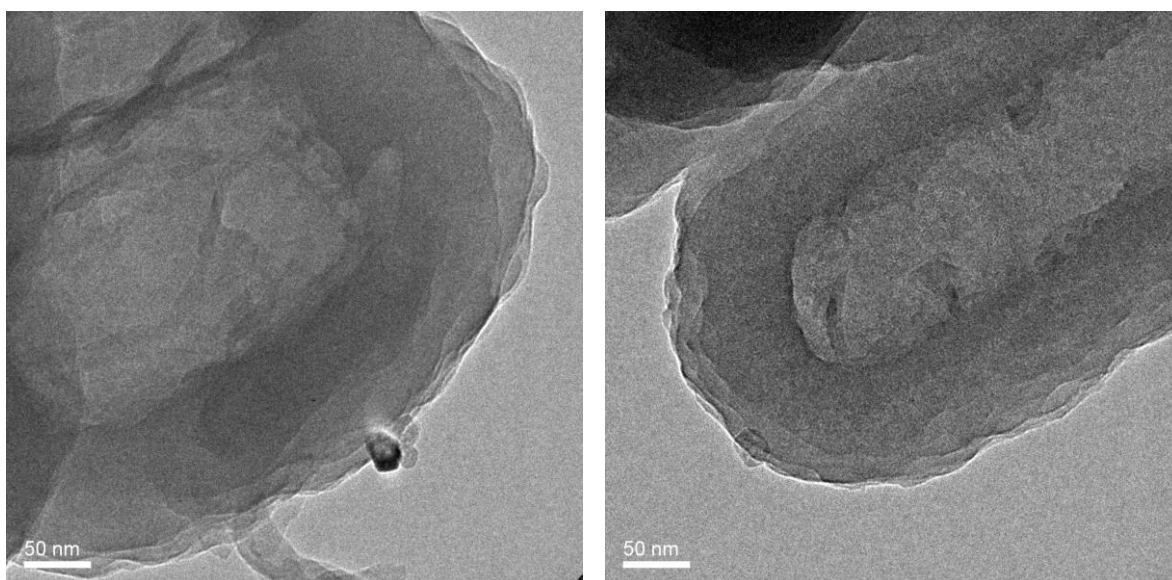
Figure S 23: TEM images of N_1-COF.
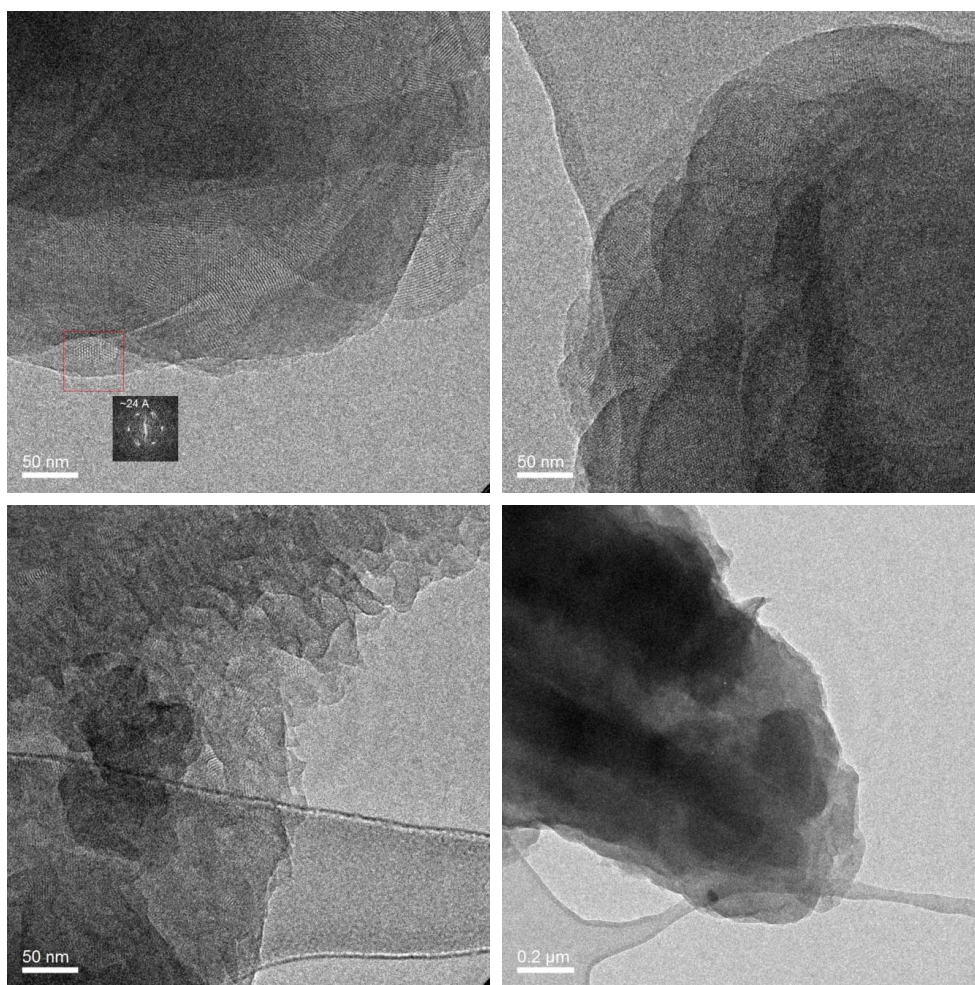
Figure S 24: TEM images of N$_2$-COF.
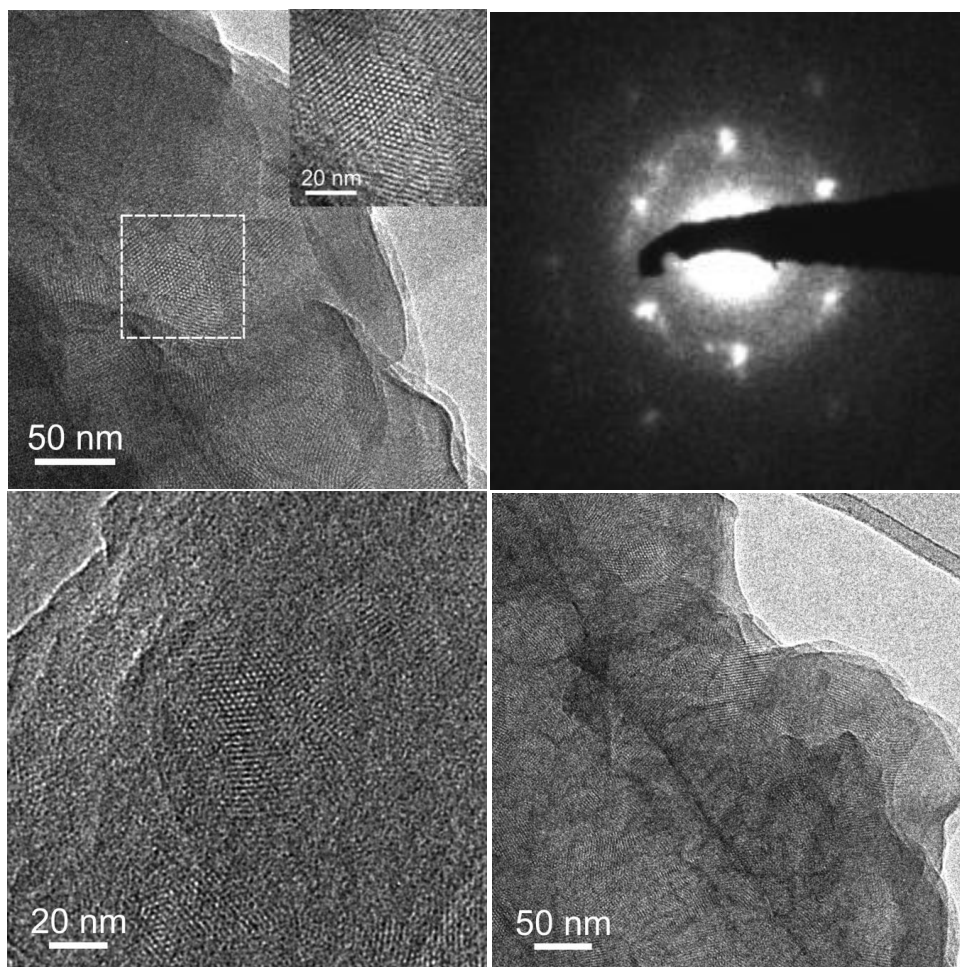
Figure S 25: TEM images of N_3-COF.
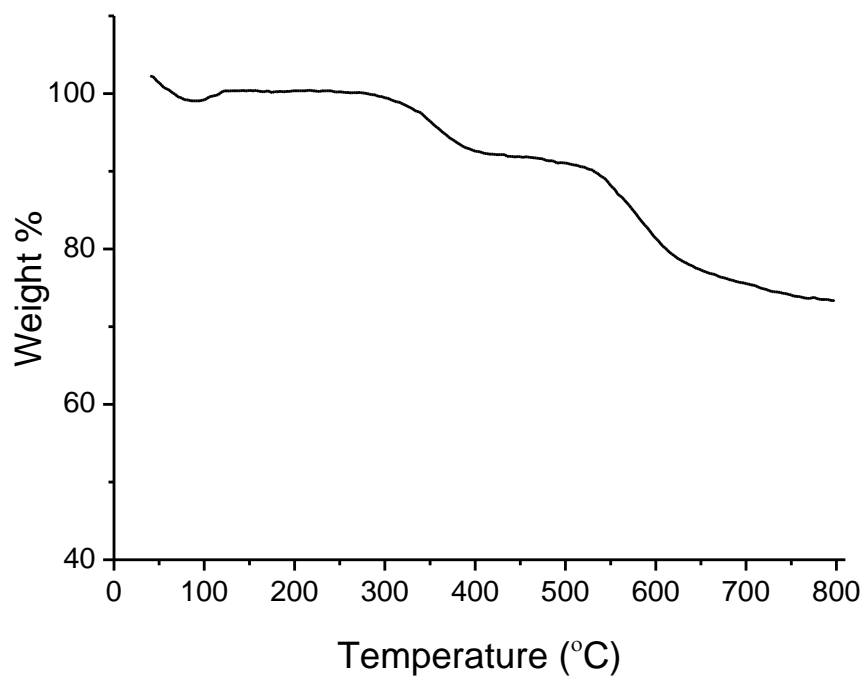
Figure S 26: TGA of N_0-COF in Argon.
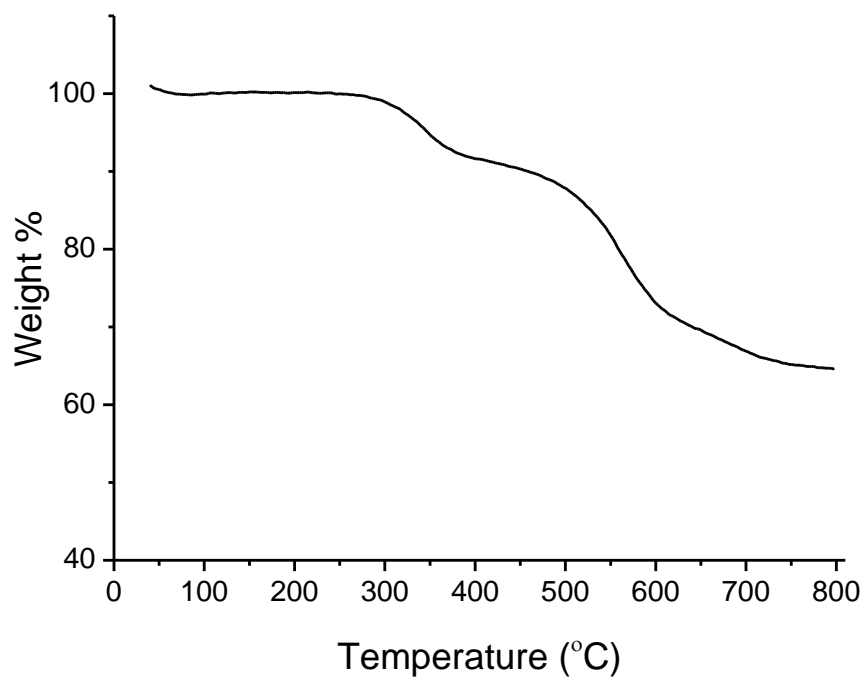
Figure S 27: TGA of N_1-COF in Argon.
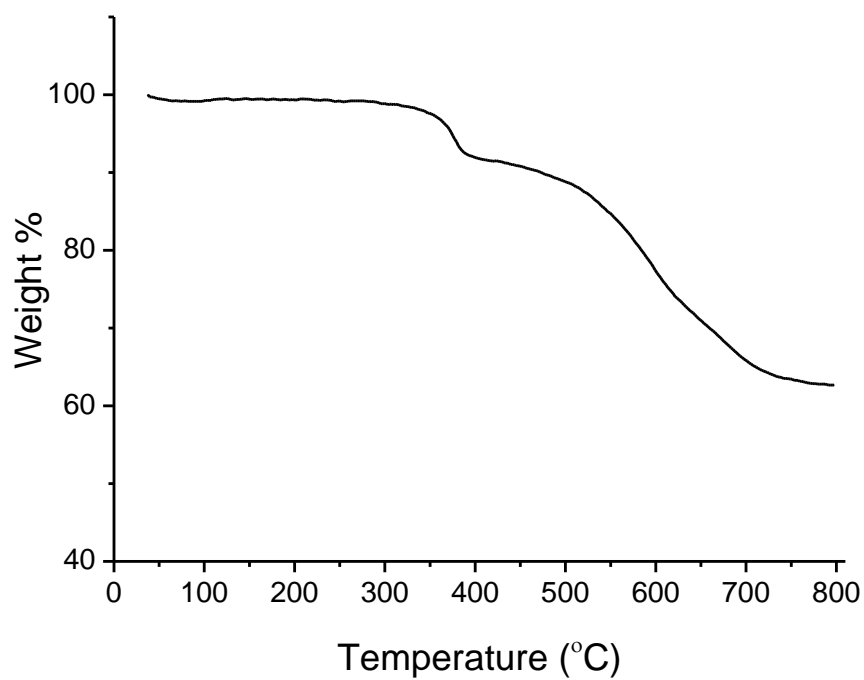
Figure S 28: TGA of N_2-COF in Argon.
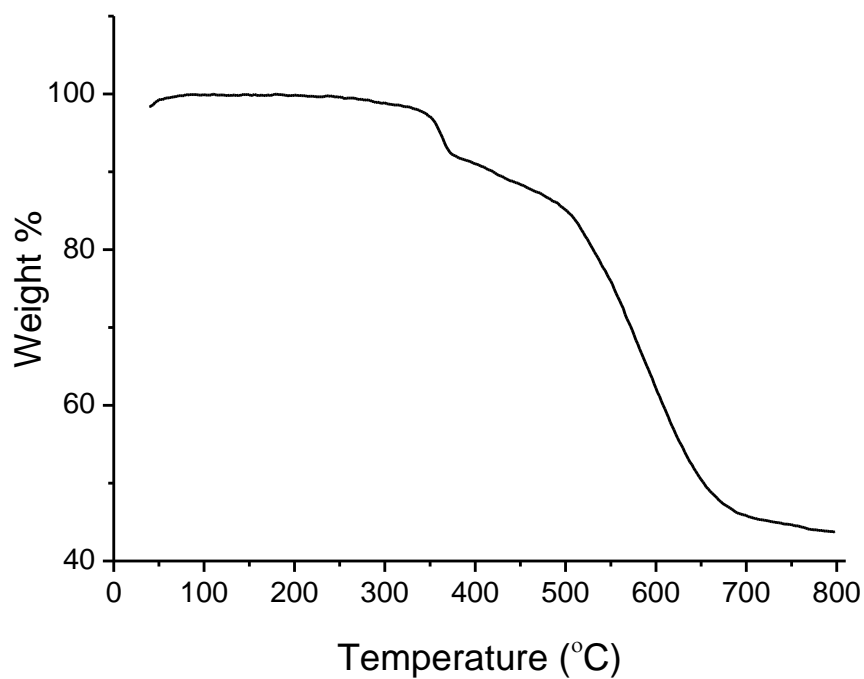
Figure S 29: TGA of N_3-COF in Argon.
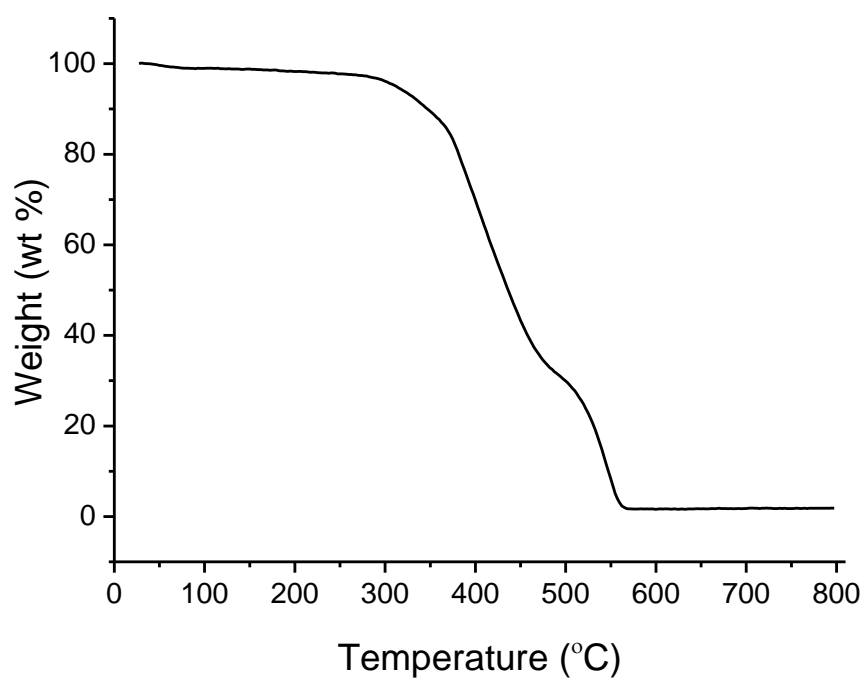
Figure S 30: TGA of N_0-COF in Air.
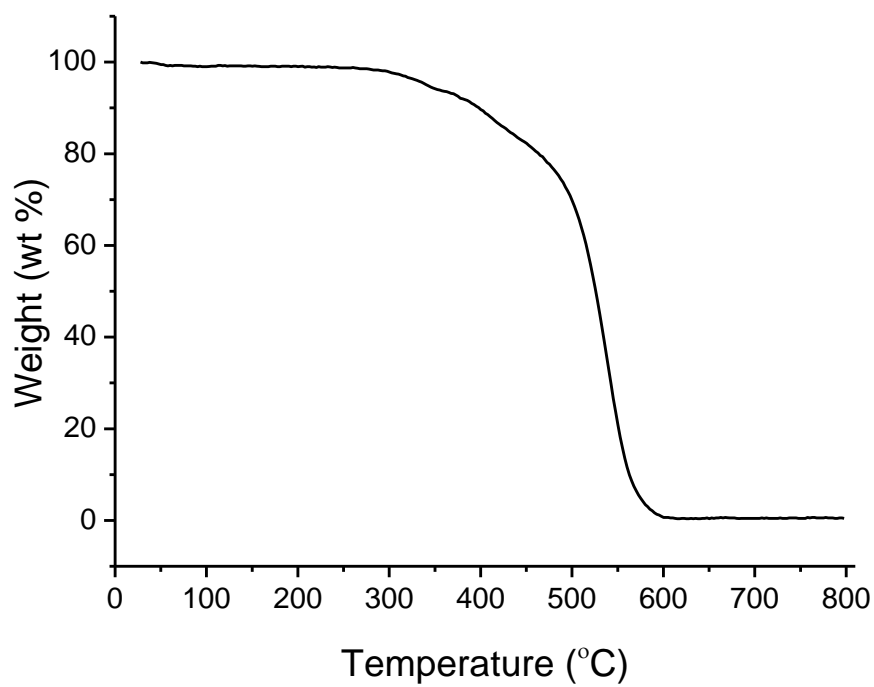
Figure S 31: TGA of N_1-COF in Air.
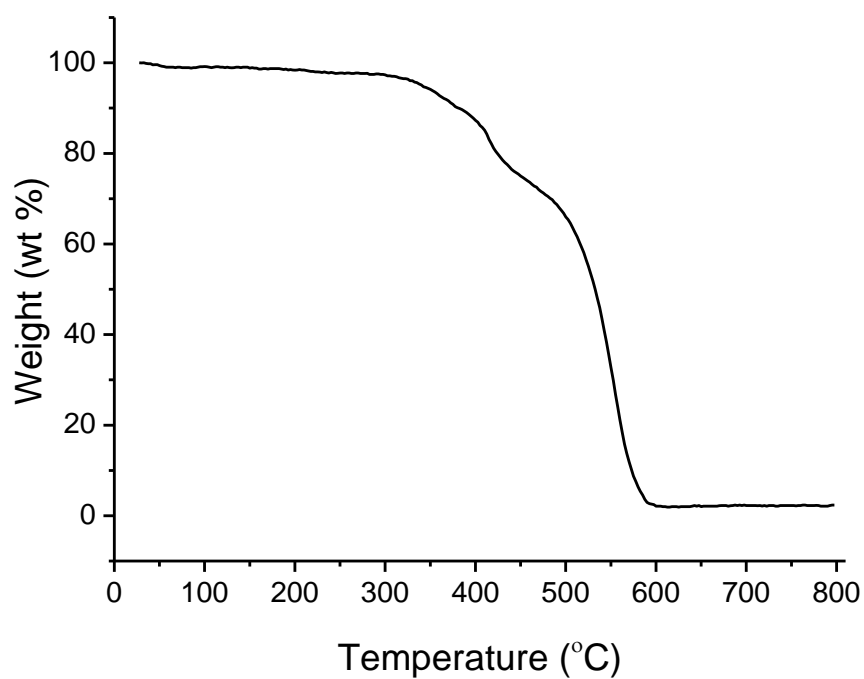
Figure S 32: TGA of N_2-COF in Air.
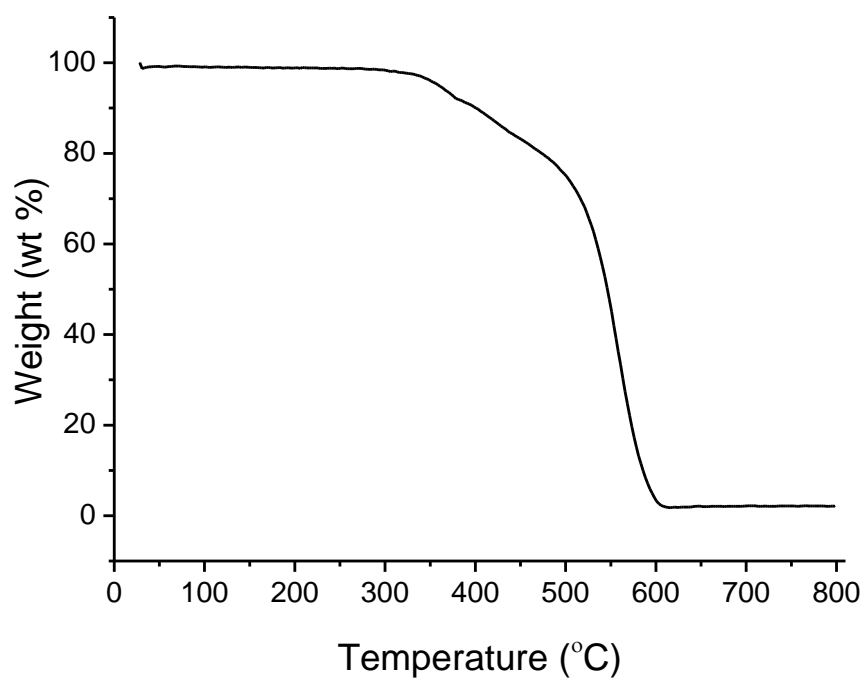
Figure S 33: TGA of N$_3$-COF in Air.
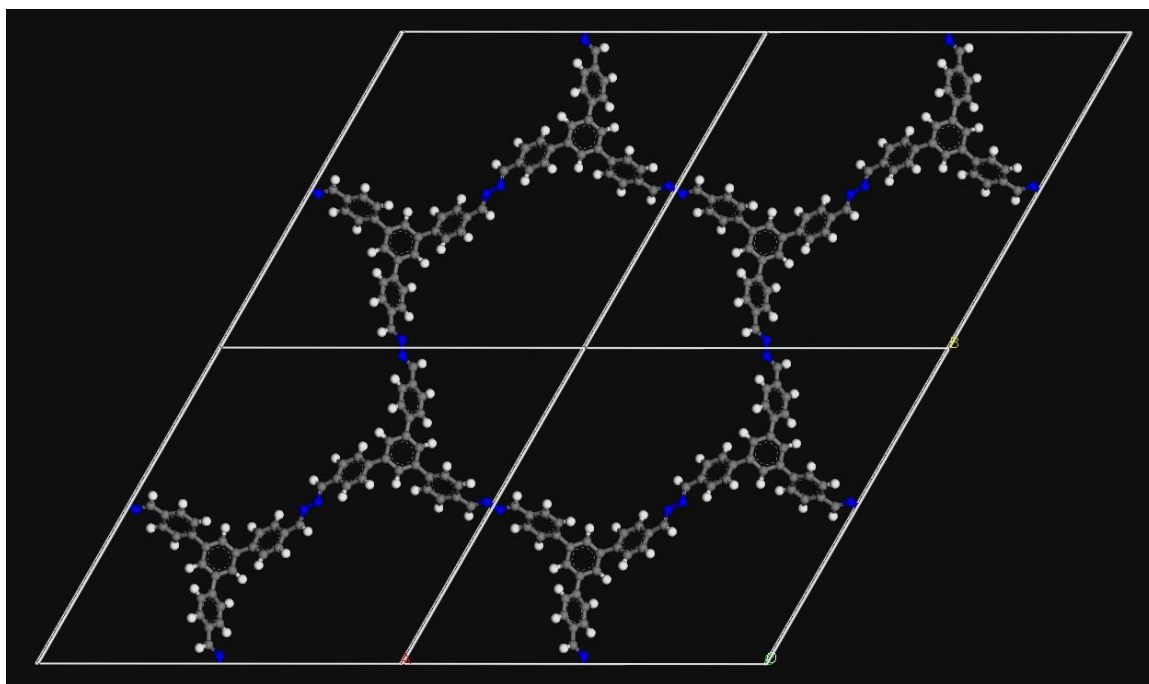
Figure S 34: View of the simulated structure of the N$_0$-COF along the *c* axis.
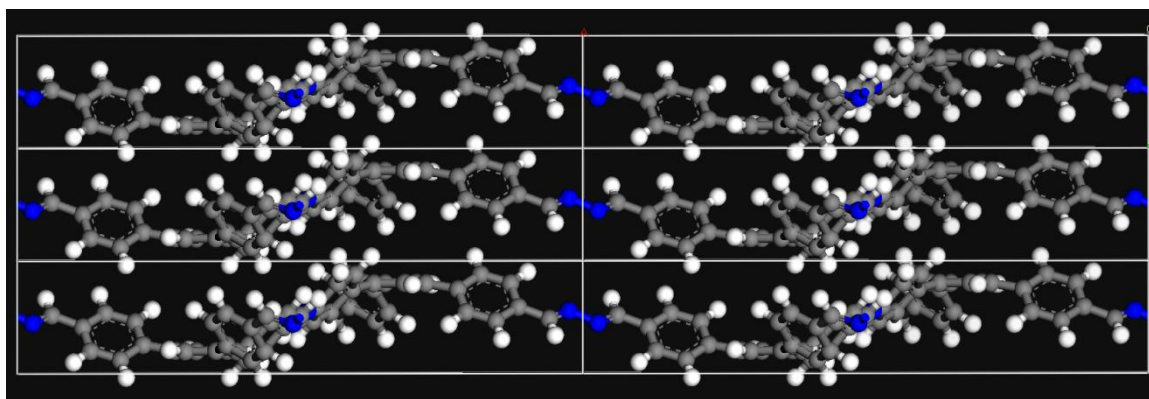
Figure S 35: View of the simulated structure of the **N₀-COF** along the *a* axis.
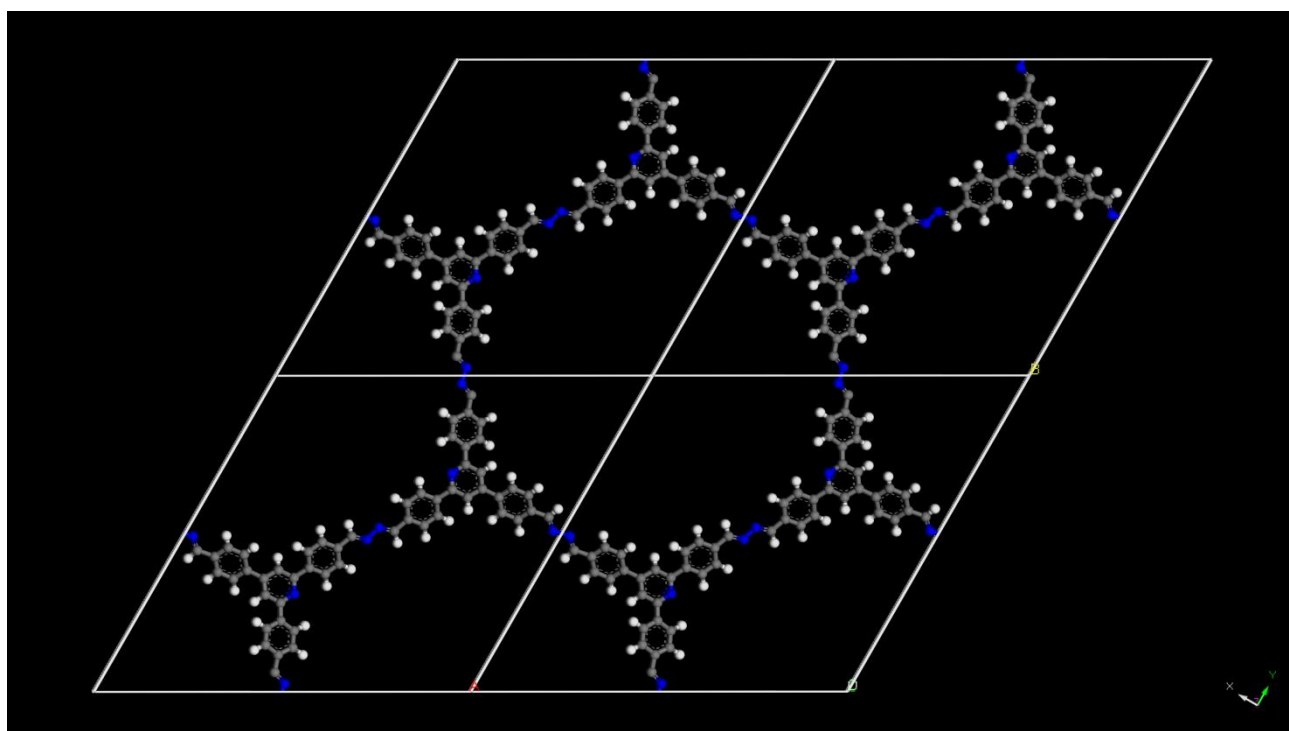
Figure S 36: View of the simulated structure of the N$_1$-COF along the *c* axis.
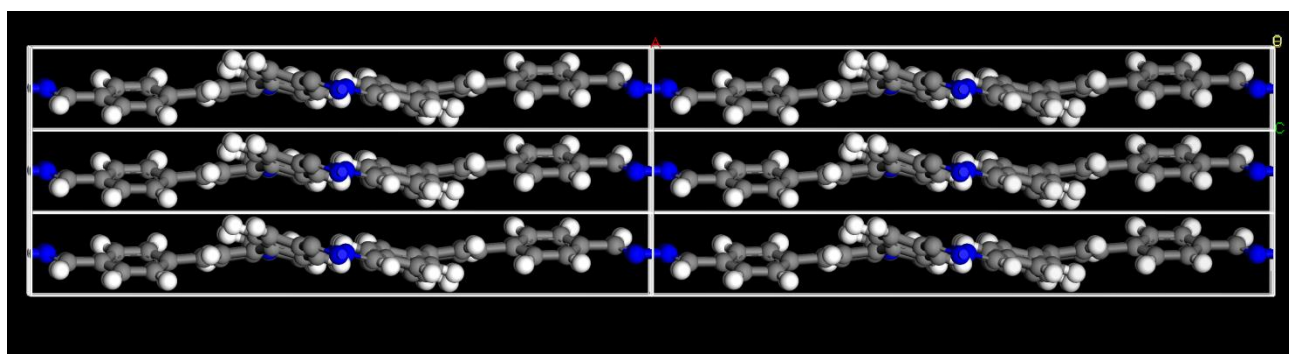
Figure S 37: View of the simulated structure of the N$_1$-COF along the *a* axis.
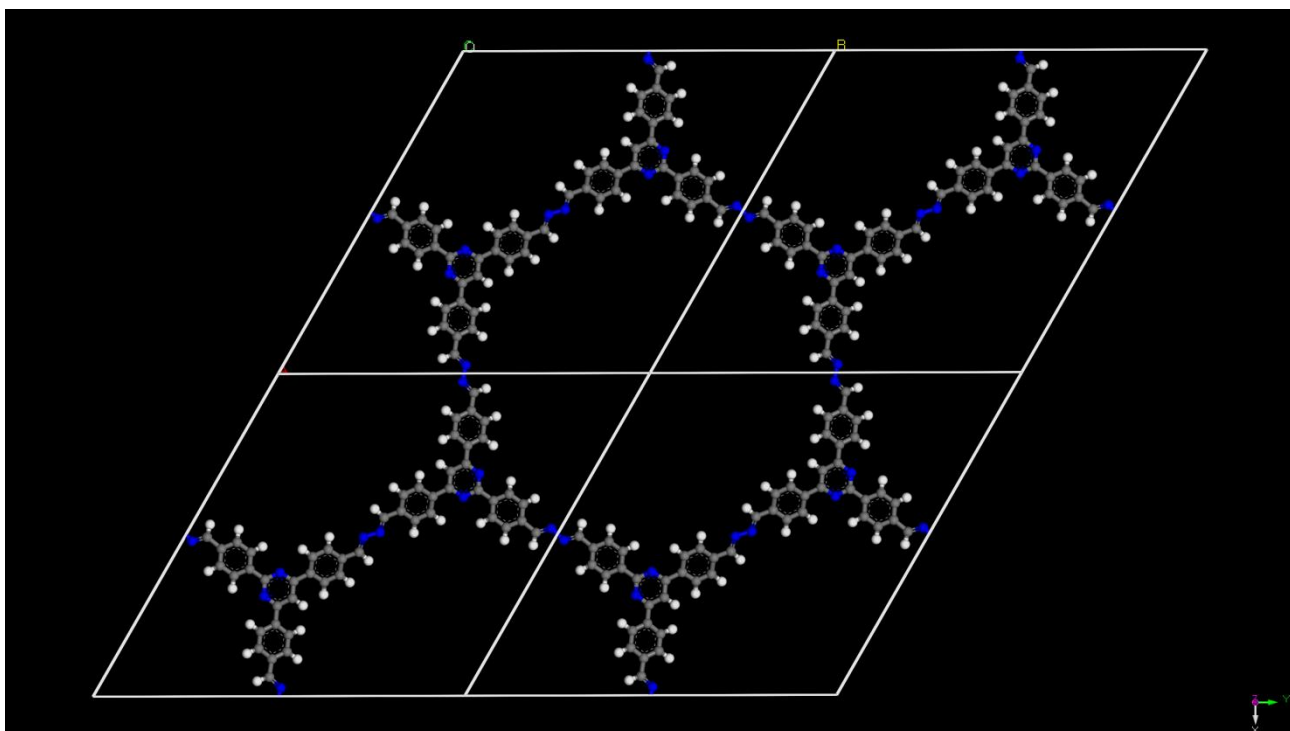
Figure S 38: View of the simulated structure of the N$_2$-COF along the *c* axis.
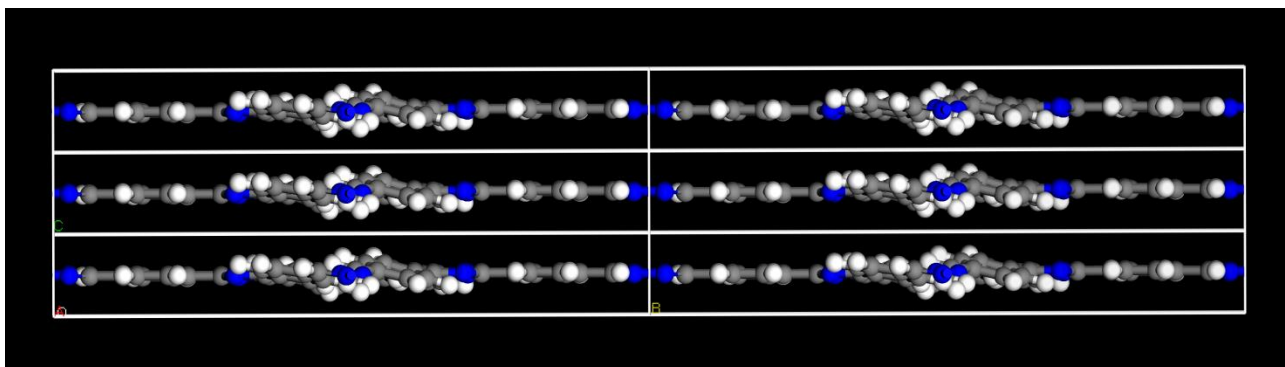
Figure S 39: View of the simulated structure of the **N$_2$-COF** along the *a* axis.
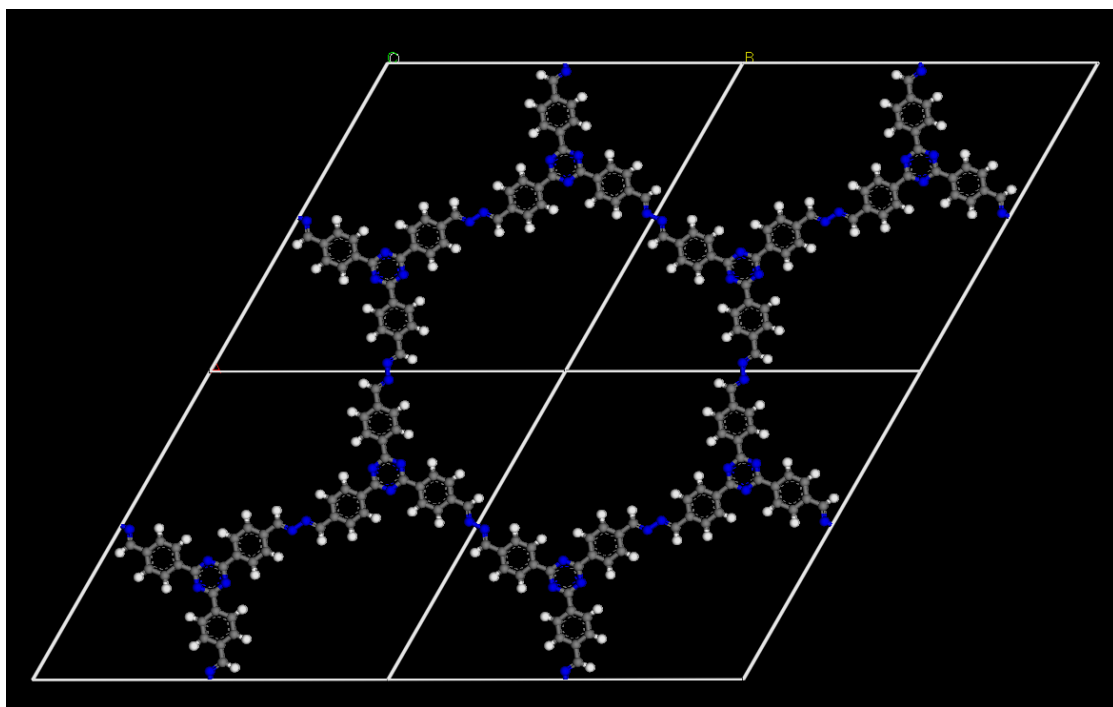
Figure S 40: View of the simulated structure of the **N₃-COF** along the *c* axis.
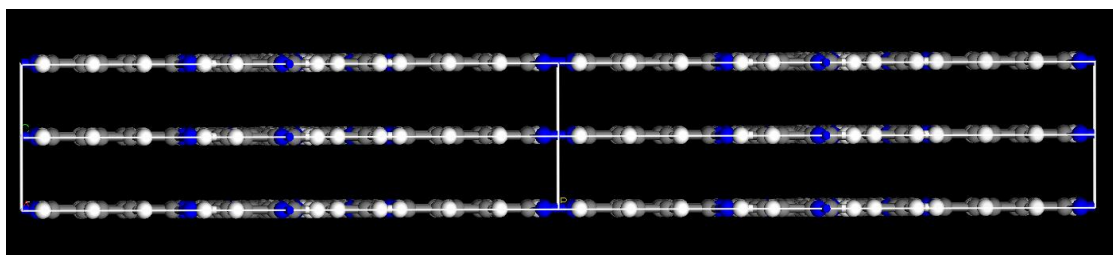
Figure S 41: View of the simulated structure of the N₃-COF along the *a* axis.
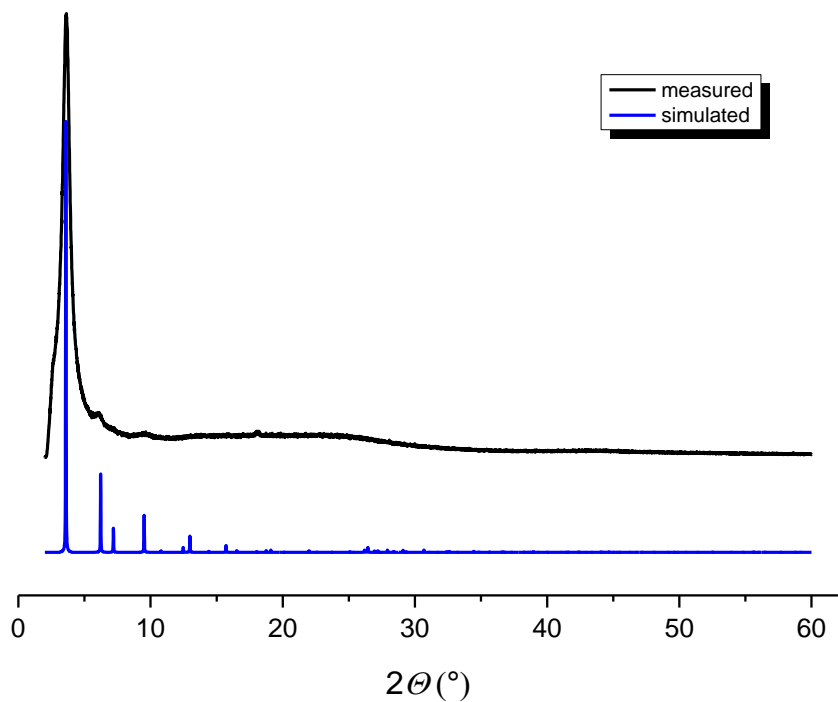
Figure S 42: Experimental X-ray powder diffraction pattern of **N₀-COF** (black), compared with the simulated XRPD pattern assuming $P\bar{3}$ symmetry (blue).
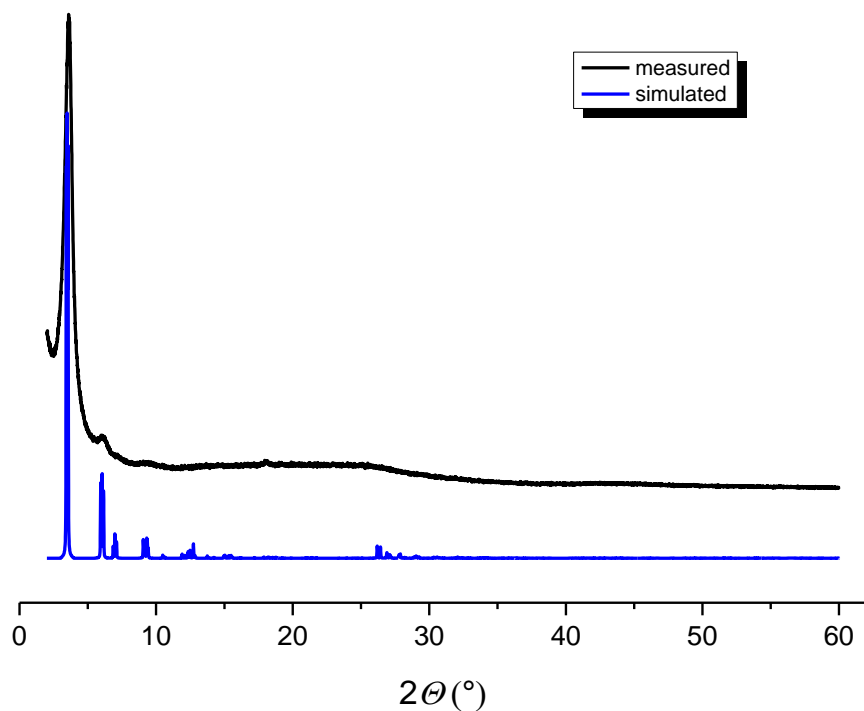
Figure S 43: Experimental X-ray powder diffraction pattern of **N₁-COF** (black), compared with the simulated XRPD pattern assuming $P\bar{1}$ symmetry (blue).
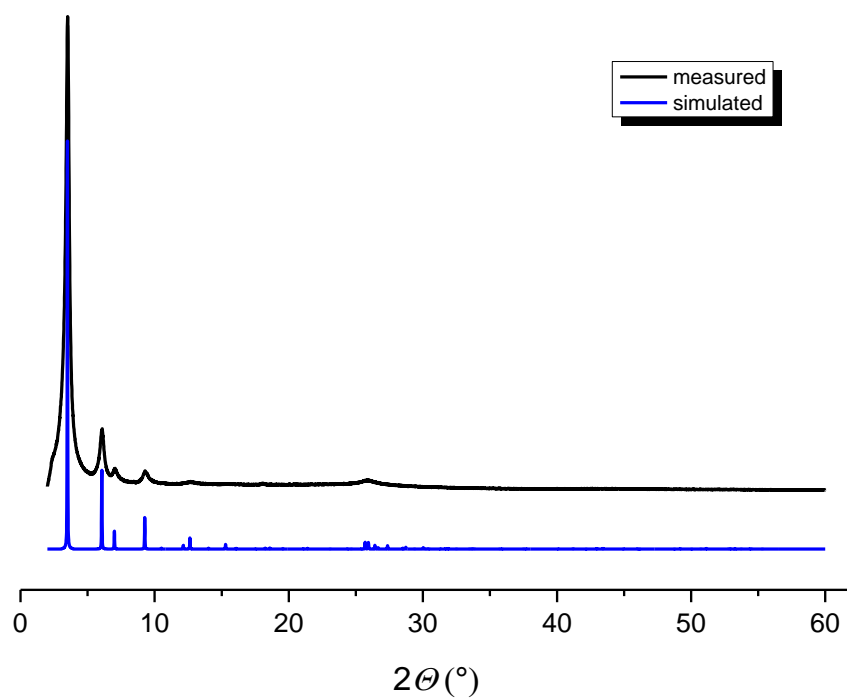
Figure S 44: Experimental X-ray powder diffraction pattern of **N₂-COF** (black), compared with the simulated XRPD pattern assuming $P\bar{1}$ symmetry (blue).
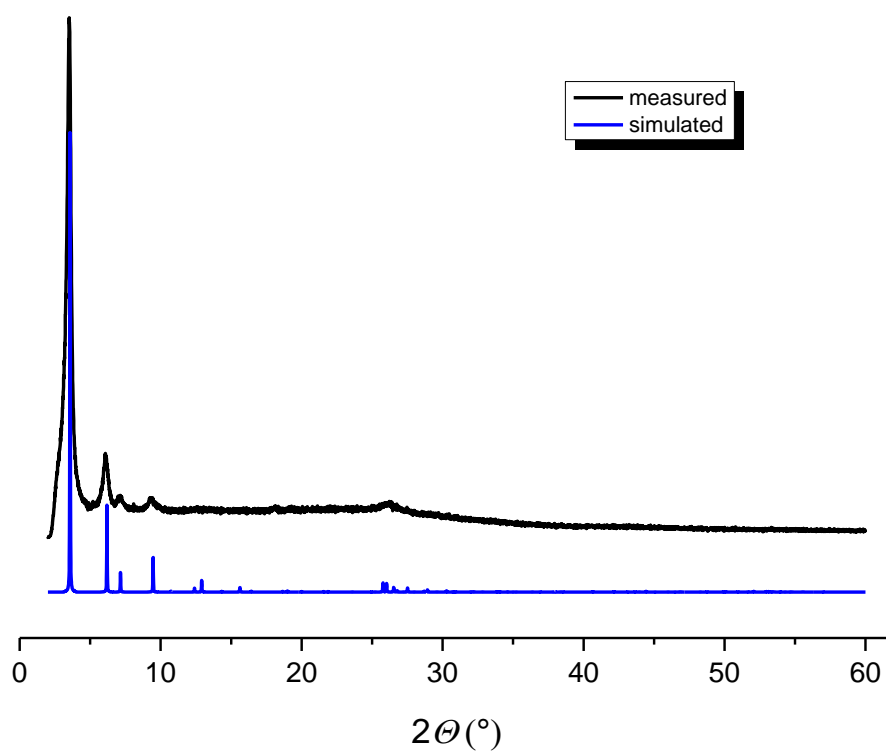
Figure S 45: Experimental X-ray powder diffraction pattern of **N₃-COF** (black), compared with the simulated XRPD pattern assuming $P6/m$ symmetry (blue).
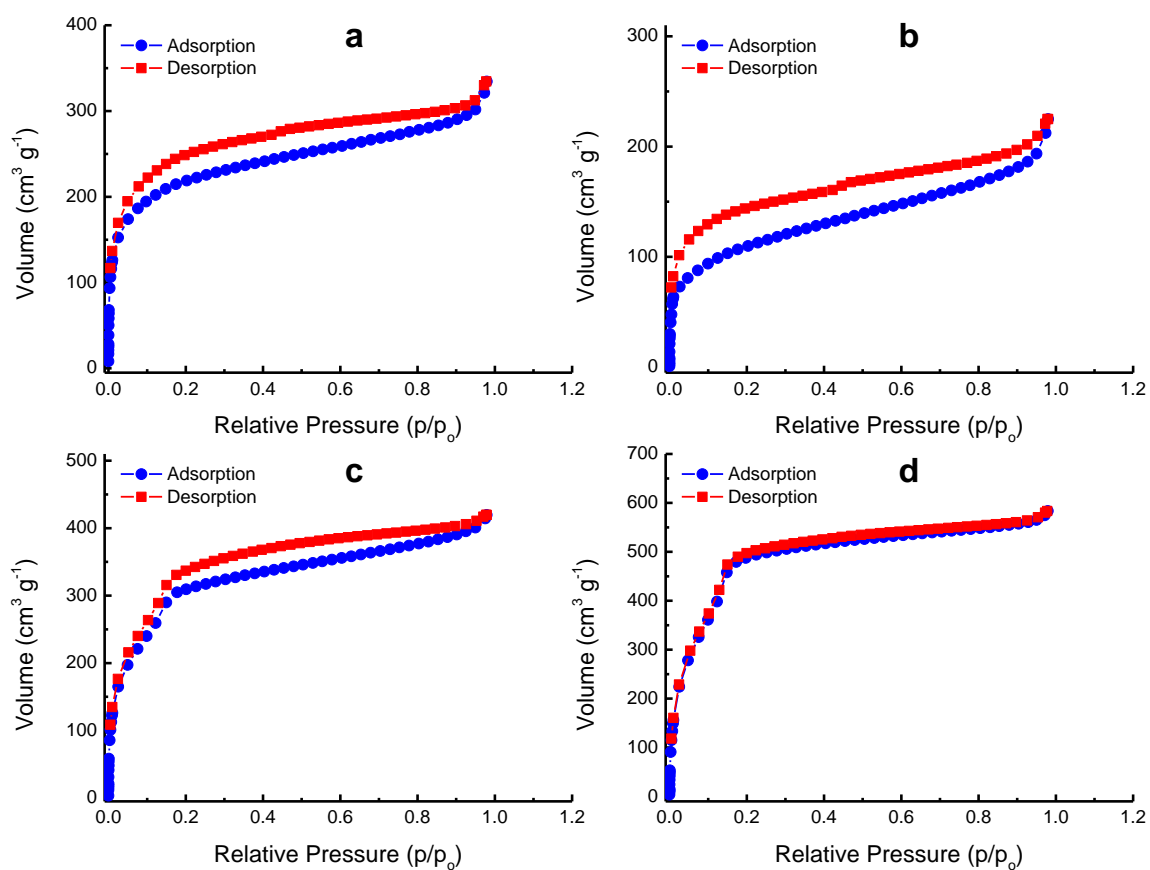
Figure S 46: Argon sorption isotherms of the N_x-COFs measured at 87 K. (a) **N_0-COF**, (b) **N_1-COF**, (c) **N_2-COF**, (d) **N_3-COF**.
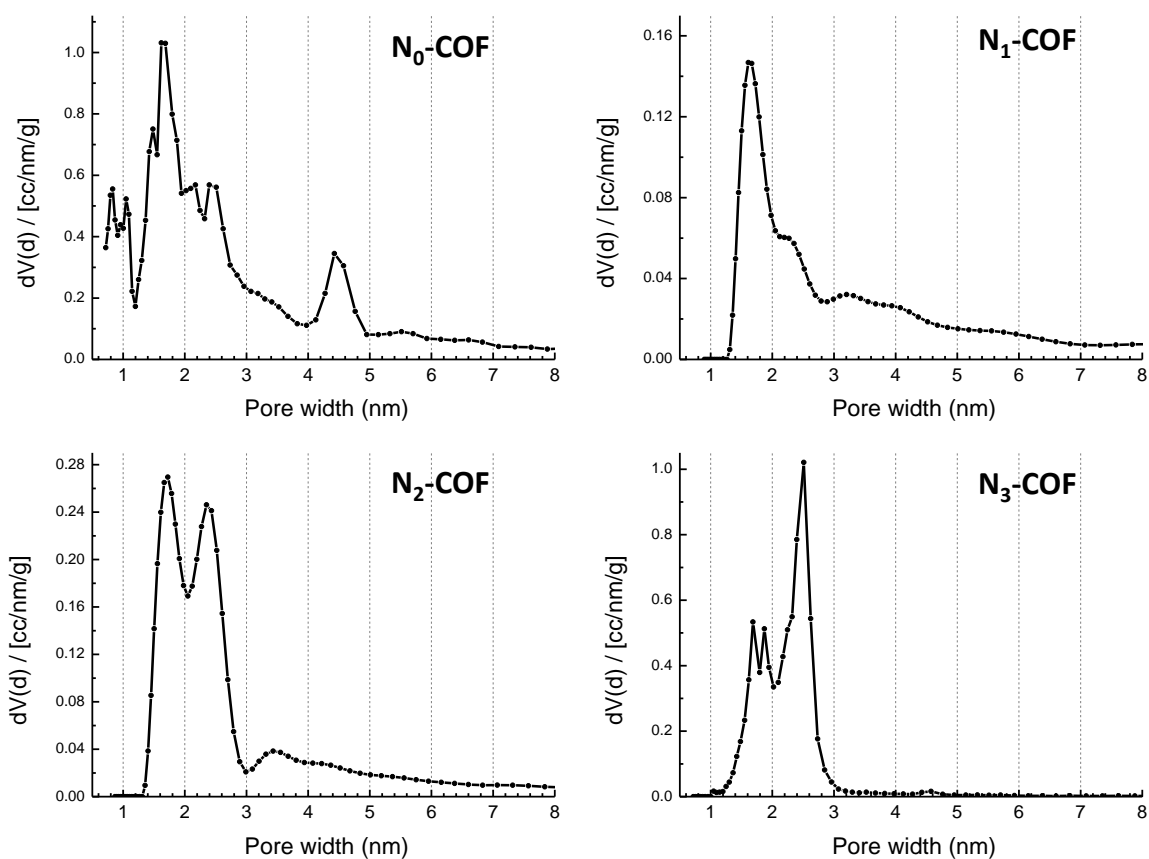
Figure S 47: Pore Size Distribution (PSD) of the COFs calculated by non-local density functional theory (NLDFT) using the "Ar-zeolite/silica cylindrical pores at 87 K" kernel accessible in the ASiQwin software.
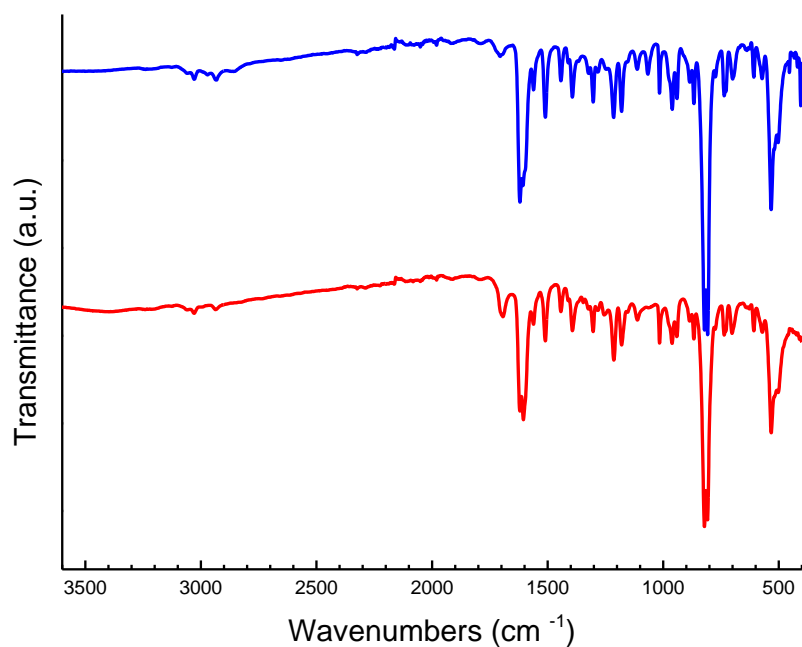
Figure S 48: FT-IR spectra of **N$_0$-COF** before (blue) and after (red) photocatalysis.
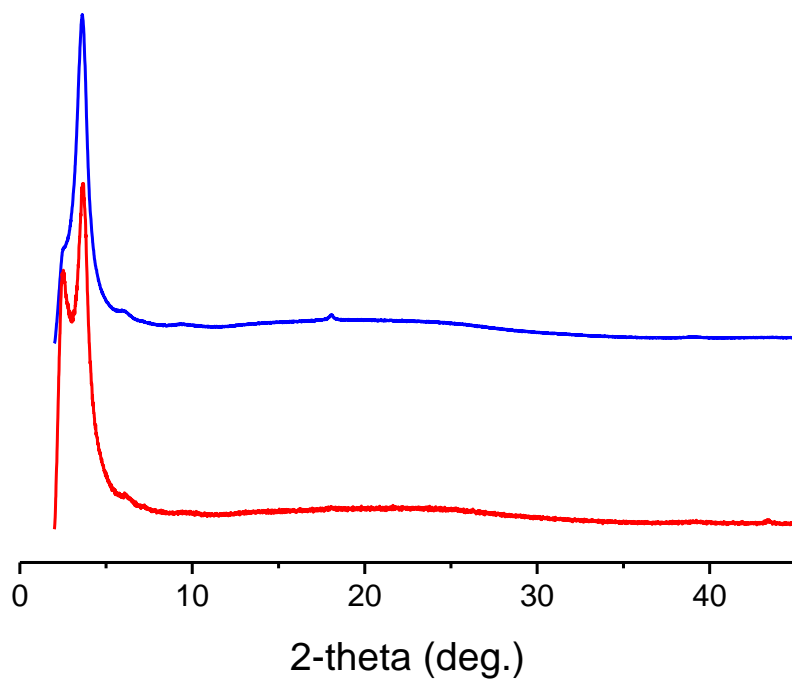
Figure S 49: XRPD of N_0-COF before (blue) and after (red) photocatalysis.
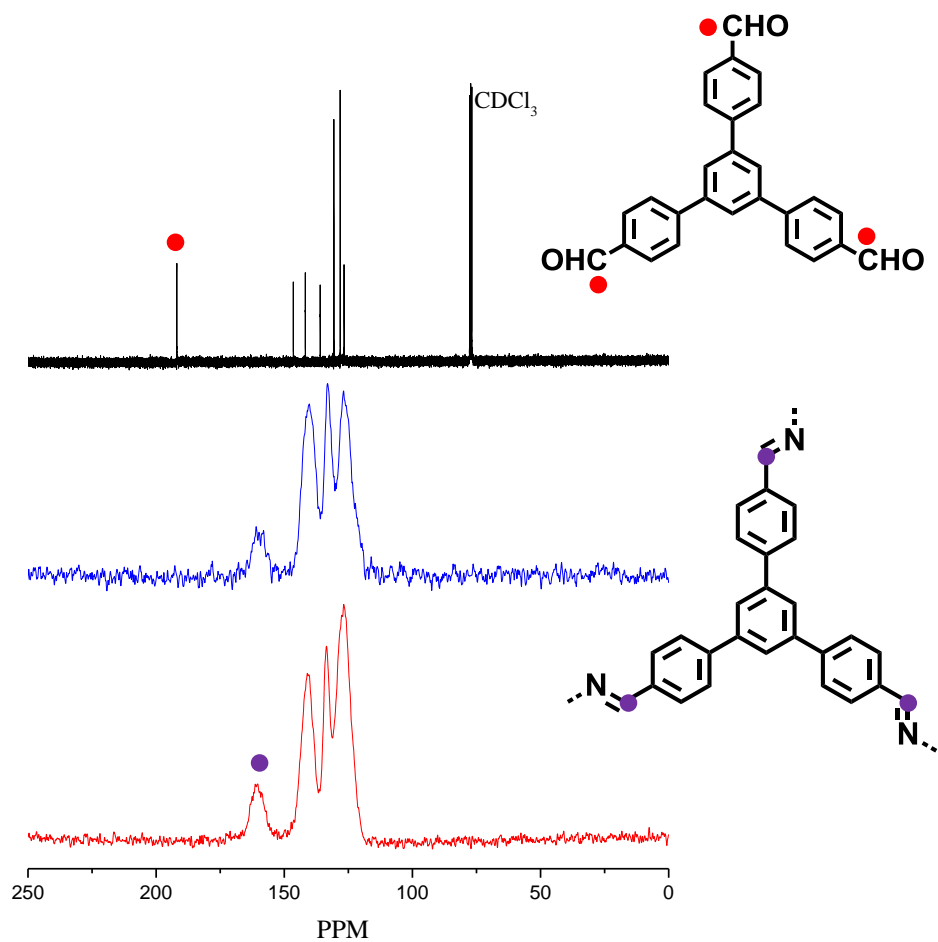
Figure S 50: Solution ^{13}C NMR of the **N$_0$-CHO** (black); ^{13}C ssNMR of **N$_0$-COF** before (blue) and after (red) photocatalysis. The peaks have been assigned to the carbons in the respective structures.
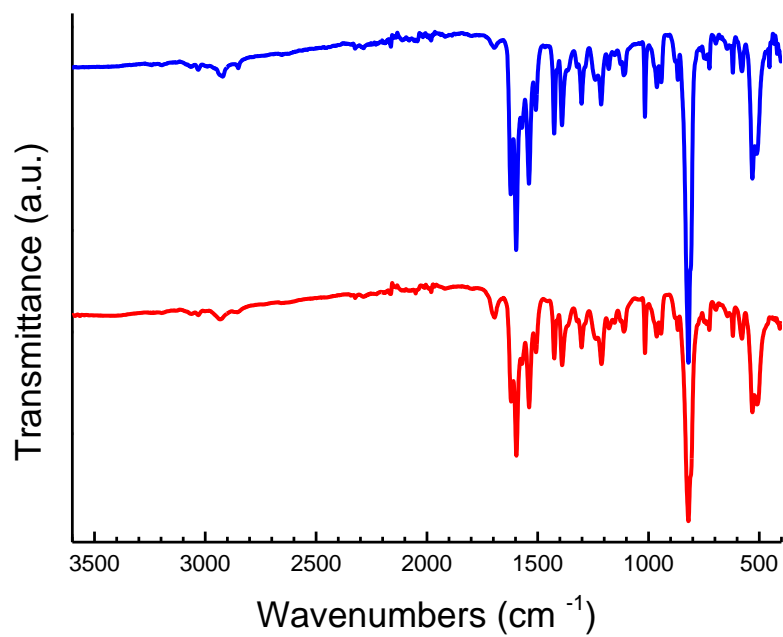
Figure S 51: FT-IR spectra of **N₁-COF** before (blue) and after (red) photocatalysis.
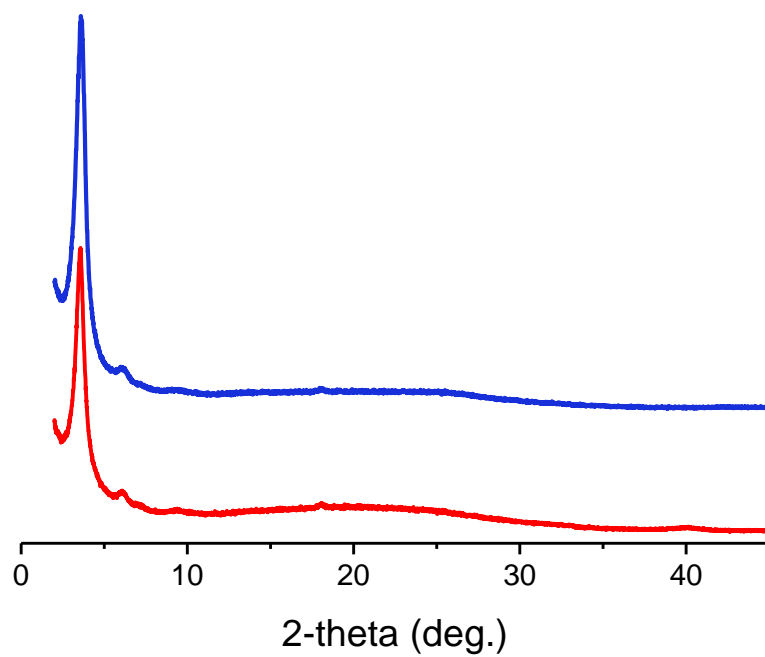
Figure S 52: XRPD N₁-COF before (blue) and after (red) photocatalysis.
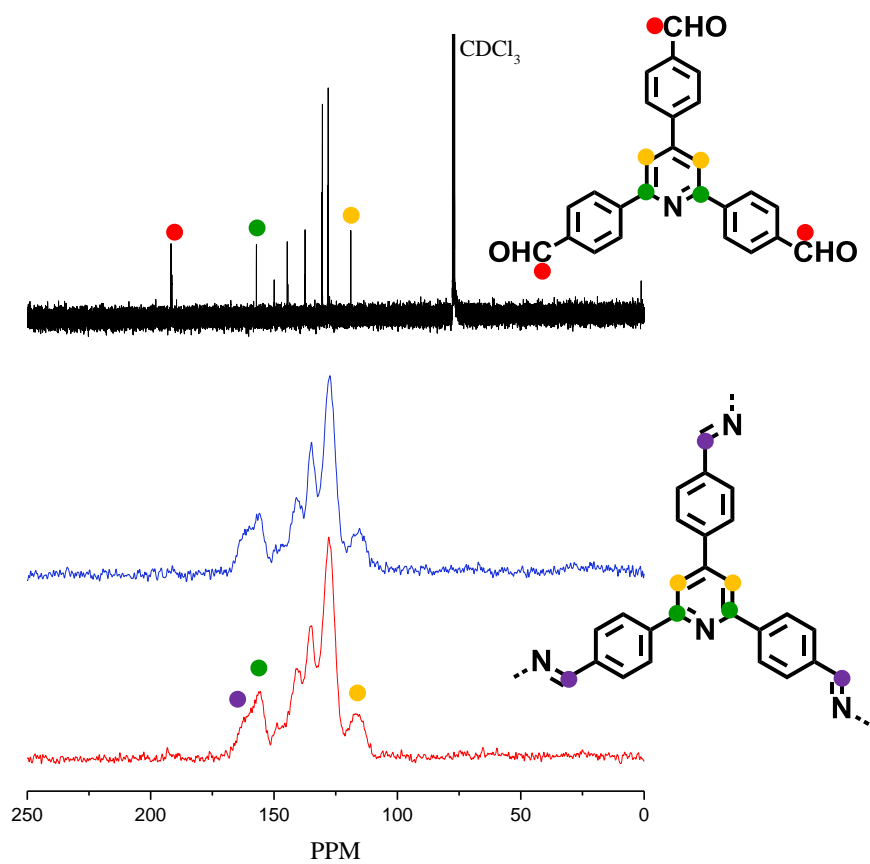
Figure S 53: Solution ^{13}C NMR of the **N₁-CHO** (black); ^{13}C ssNMR of **N₁-COF** before (blue) and after (red) photocatalysis. The peaks have been assigned to the carbons in the respective structures.
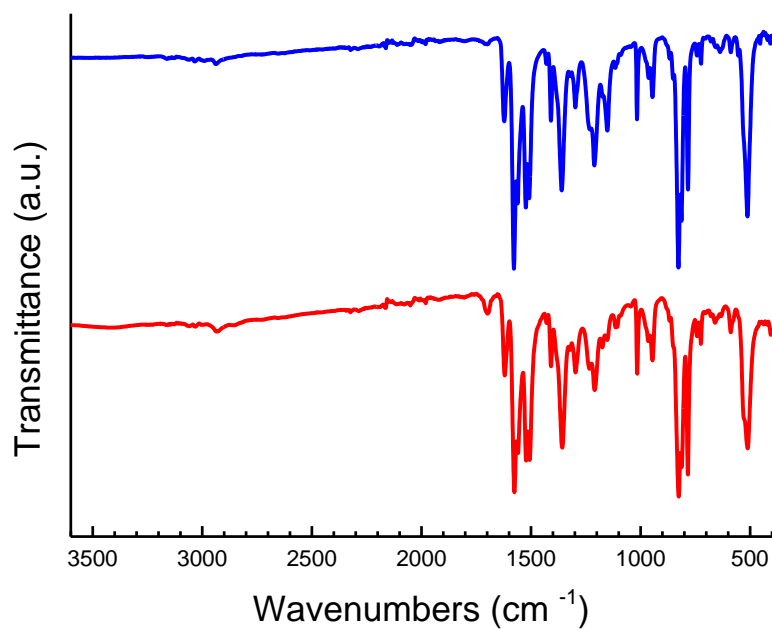
Figure S 54: FT-IR spectra of **N₂-COF** before (blue) and after (red) photocatalysis.
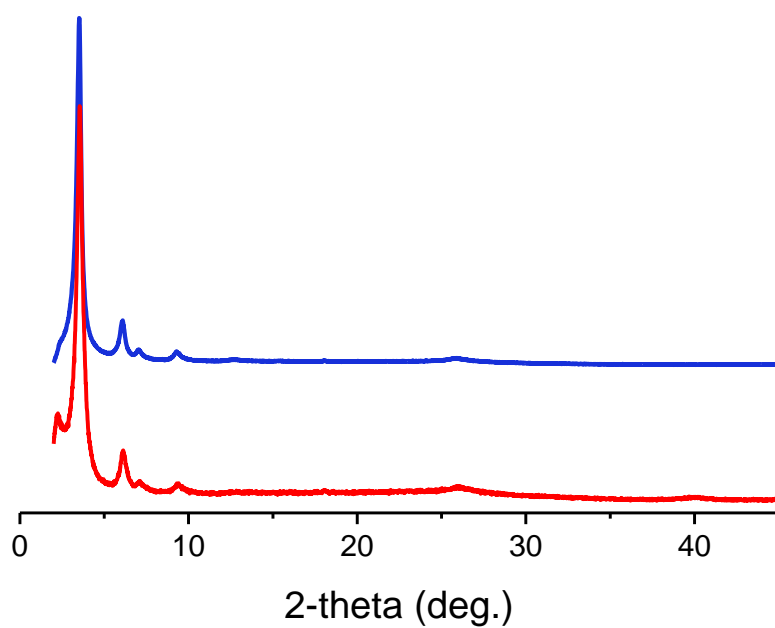
Figure S 55: XRPD N₂-COF before (blue) and after (red) photocatalysis.
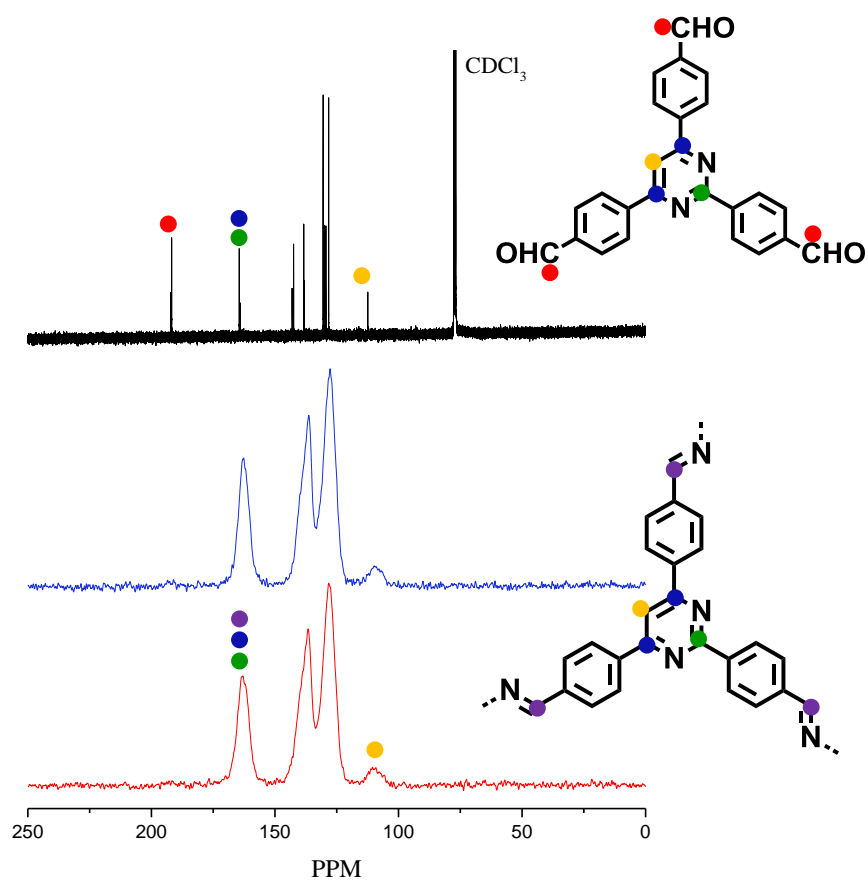
Figure S 56: Solution ^{13}C NMR of the **N$_2$-CHO** (black); ^{13}C ssNMR of **N$_2$-COF** before (blue) and after (red) photocatalysis. The peaks have been assigned to the carbons in the respective structures.
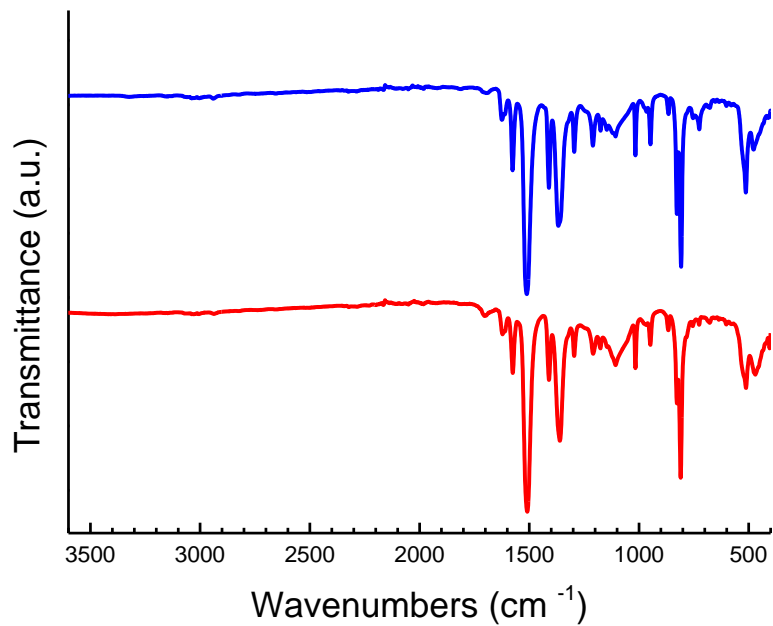
Figure S 57: FT-IR spectra of **N₃-COF** before (blue) and after (red) photocatalysis.
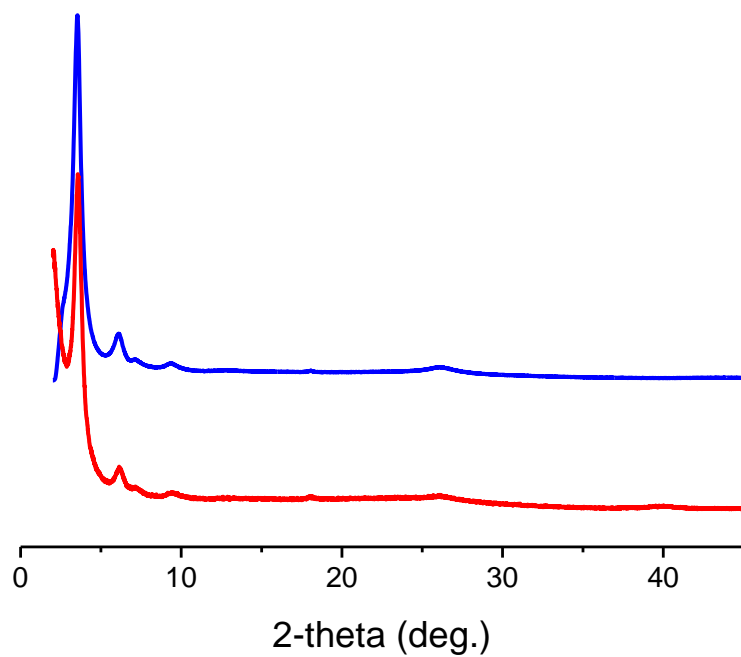
Figure S 58: XRPD of N₃-COF before (blue) and after (red) photocatalysis.
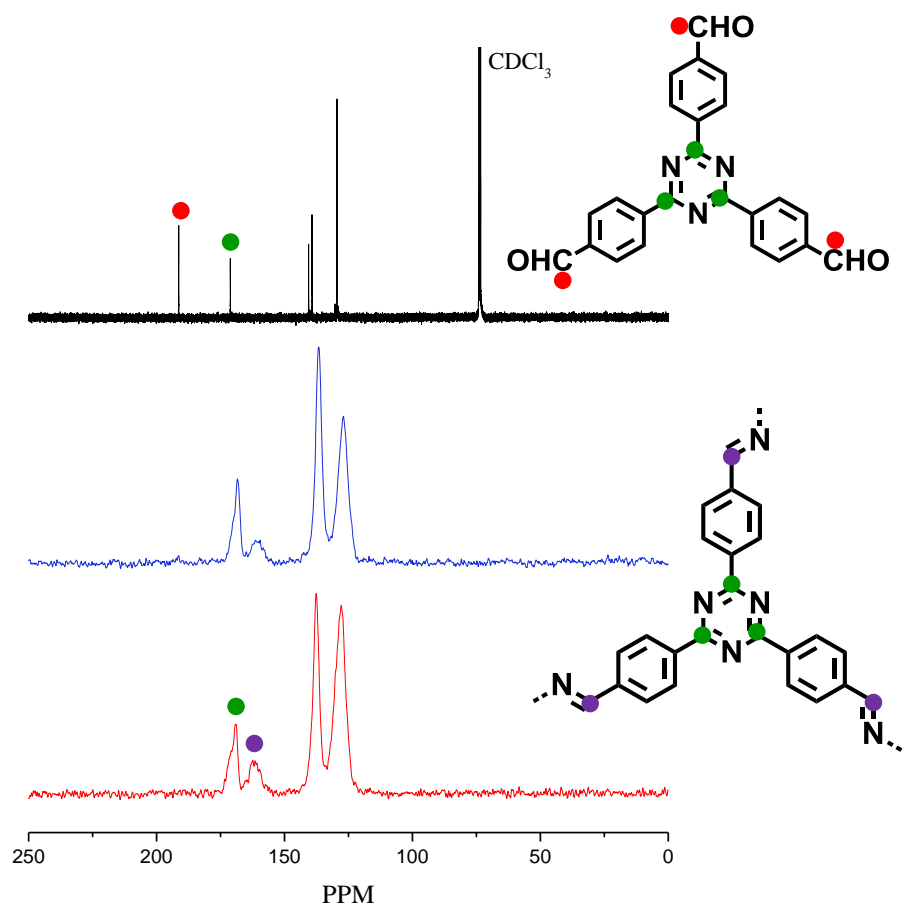
Figure S 59: Solution ^{13}C NMR of the **N$_3$-CHO** (black); ^{13}C ssNMR of **N$_3$-COF** before (blue) and after (red) photocatalysis. The peaks have been assigned to the carbons in the respective structures.
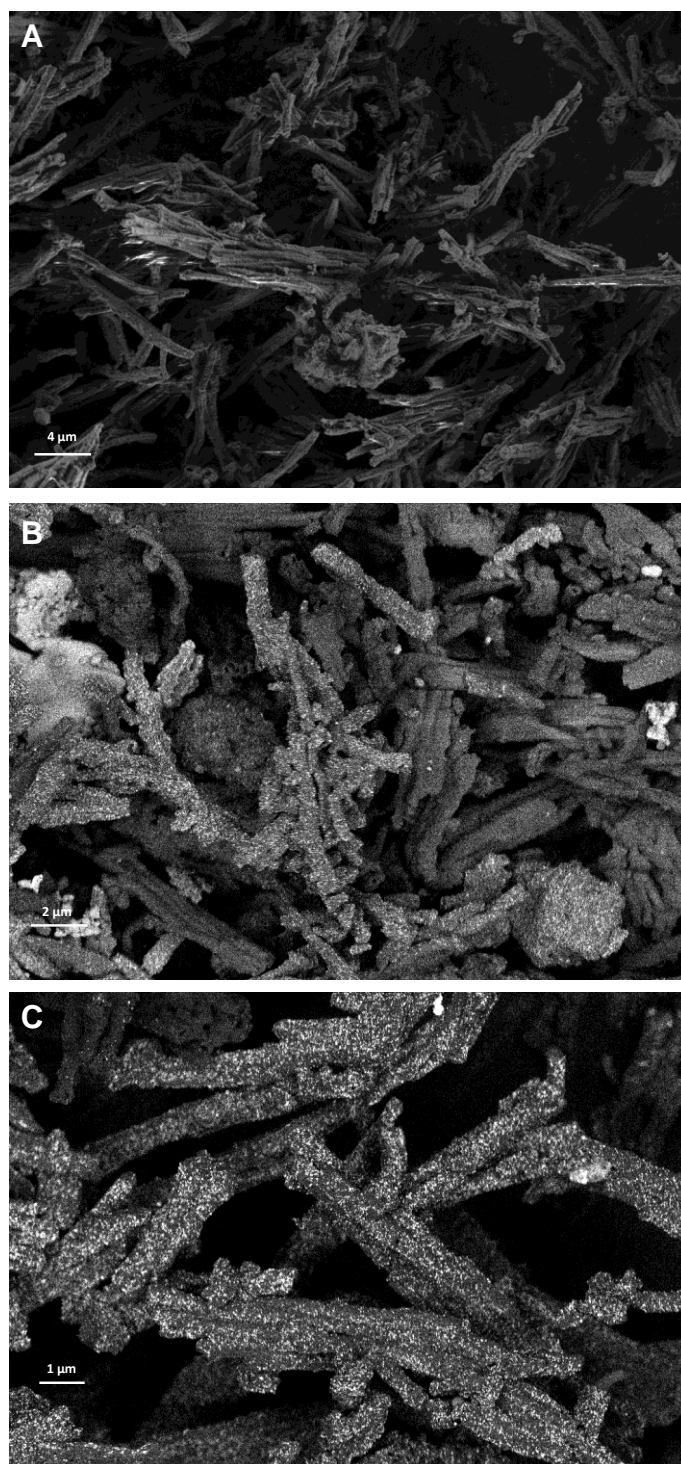
Figure S 60: SEM images of **N₃-COF** after photocatalysis: A. with secondary electron detector; B and C with backscatter detector to provide elemental contrast. The light spots are the Pt nanoparticles, which stay well-dispersed across the sample.
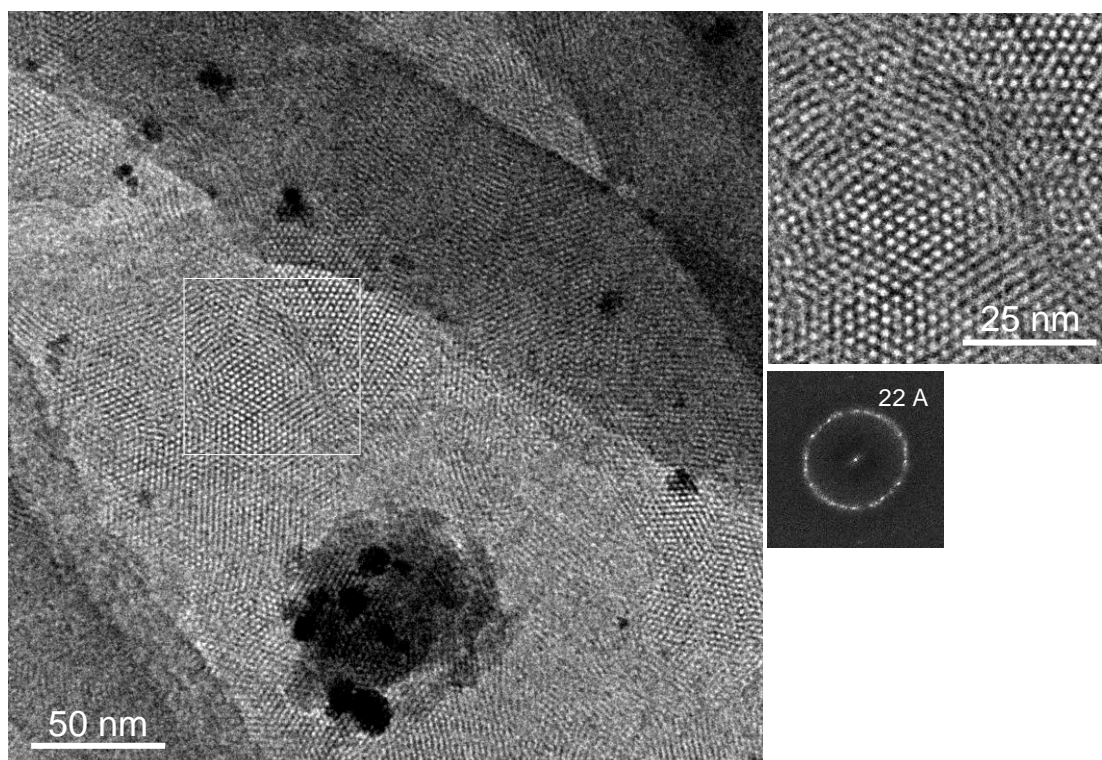
Figure S 61: TEM images of **N₃-COF** after photocatalysis. Bright field images and selected area diffraction pattern were recorded with a CMOS camera (TemCam-F216, TVIPS).
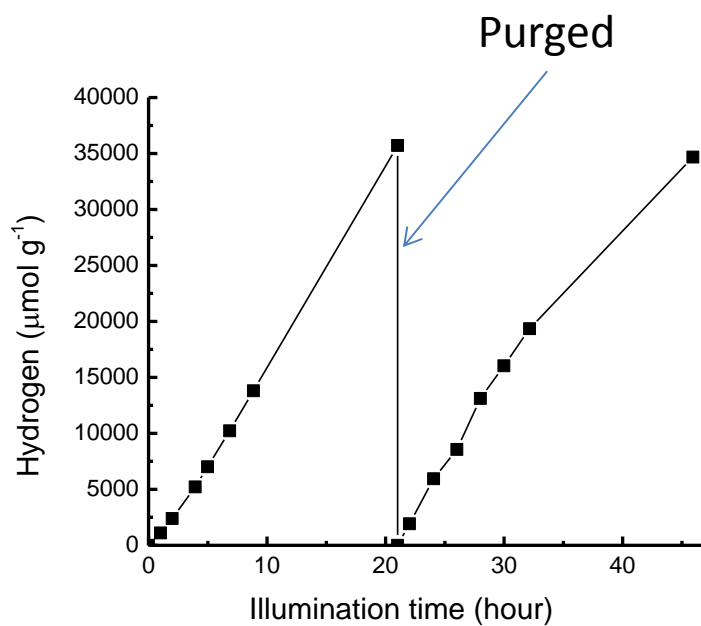
Figure S 62: Long term photocatalysis study of **N₃-COF** using triethanolamine as sacrificial electron donor.
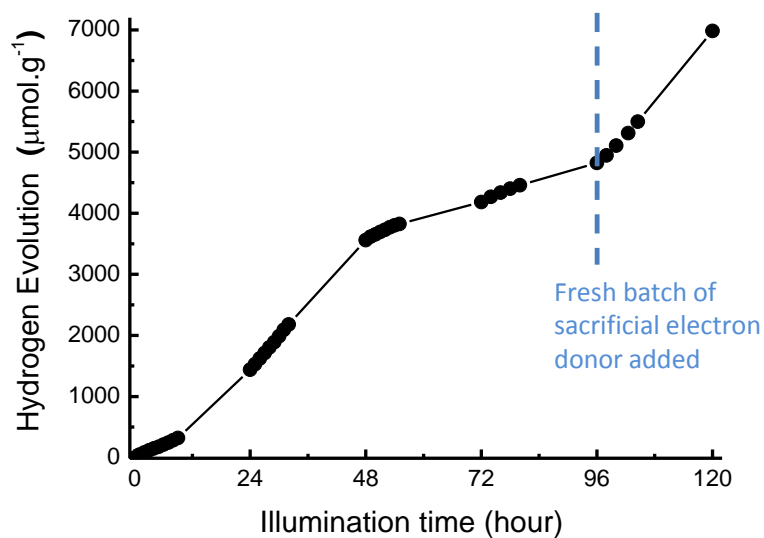
Figure S 63: Long term photocatalysis study of **N₃-COF** using ascorbic acid as sacrificial electron donor.
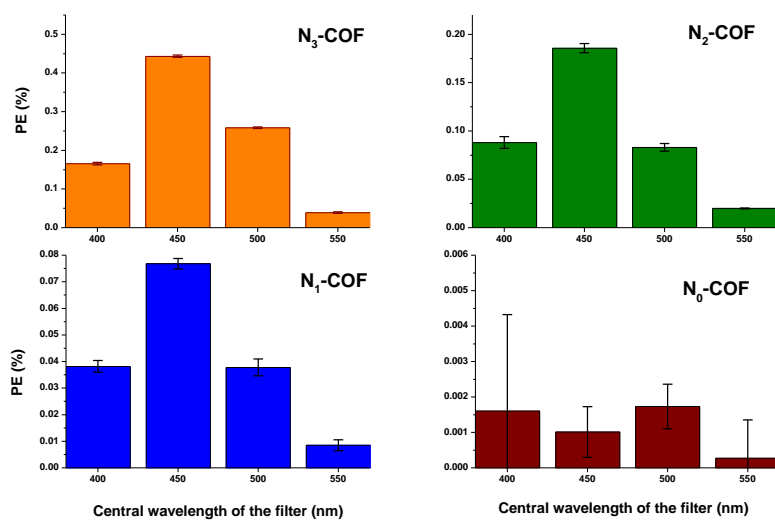
Figure S 64: Comparison of the photonic efficiency of N_x-COFs using different band-pass filters. The error bars represent the error of the gas chromatograph in integrating the amount of hydrogen evolved. The data for N_0-COF is of limited use due to its low photonic efficiency and, hence, large errors.
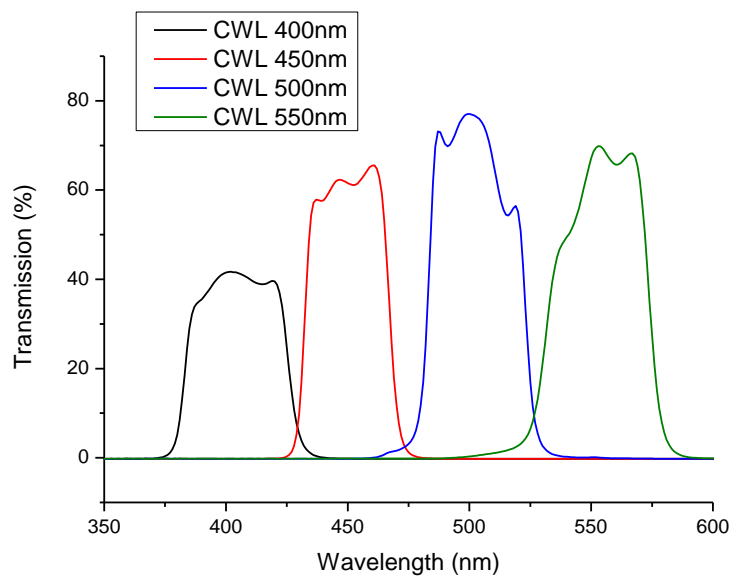
Figure S 65: Transmission spectra of the band-pass filters used for photonic efficiency calculations.
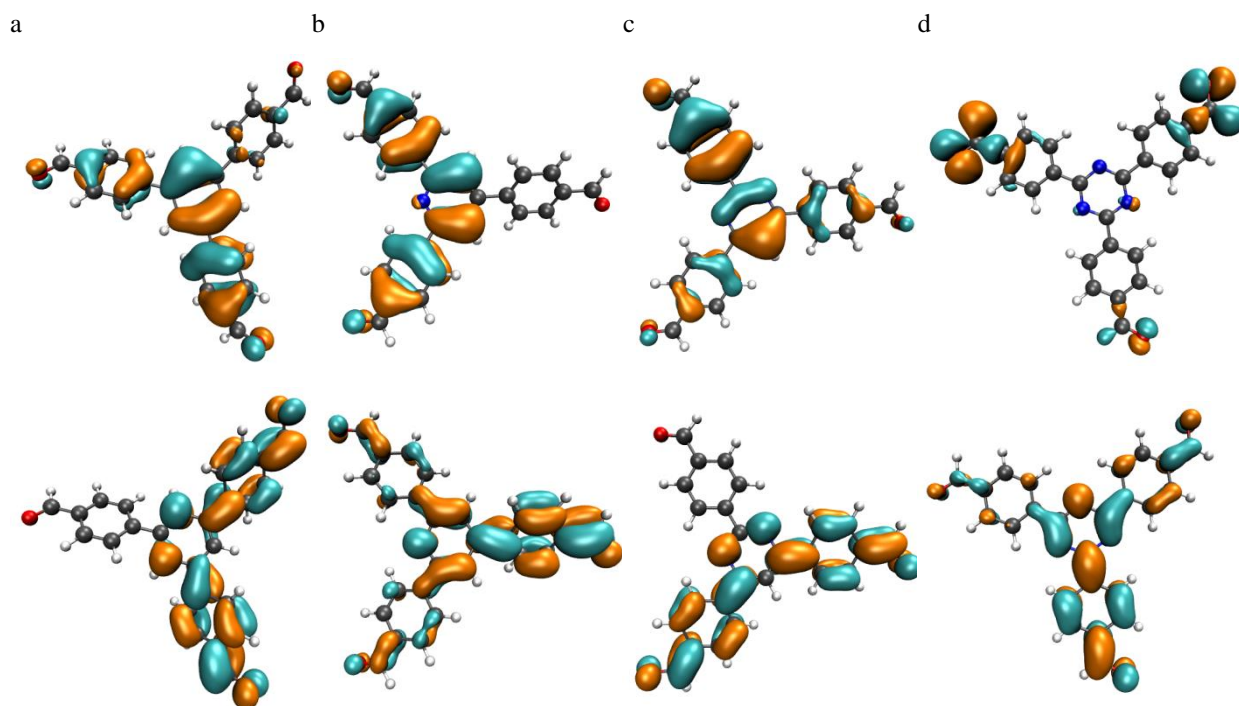
Figure S 66: HOMO and LUMO obtained at the PBE0-D3/def2-SVP level of theory for N_x-Aldehydes. (a) N_0-CHO, (b) N_1- Ald, (c) N_2- Ald, (d) N_3- Ald.
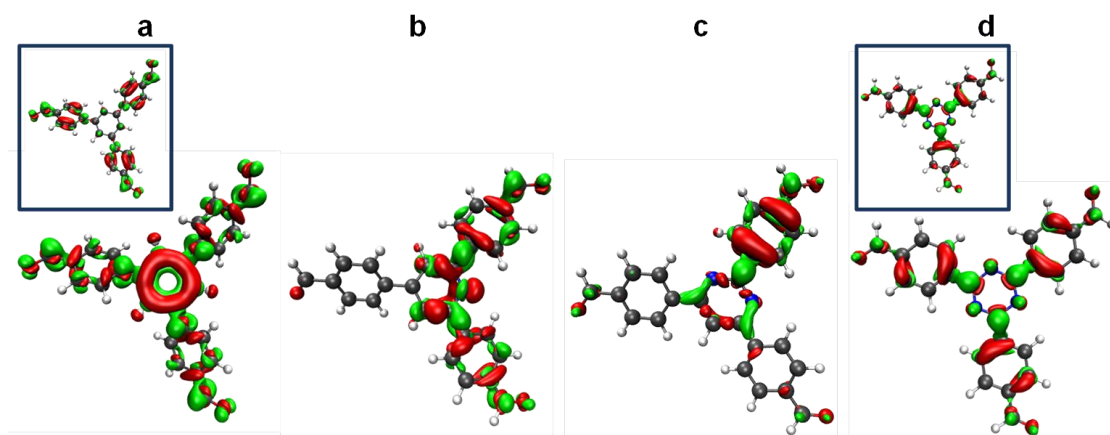
Figure S 67: Difference densities of vertical excitations with highest oscillator strength obtained at the time-dependent (TD)-PBE0/Def2-SVP level of theory for N_x-CHO. (a) N_0-CHO, (b) N_1-CHO, (c) N_2-CHO, (d) N_3-CHO. The red isosurfaces depict regions with lower electron density in the excited state whereas green isosurfaces represent higher electron density in the excited state, both in comparison to the electron density of the ground state. Inset shows the degenerate energy state.
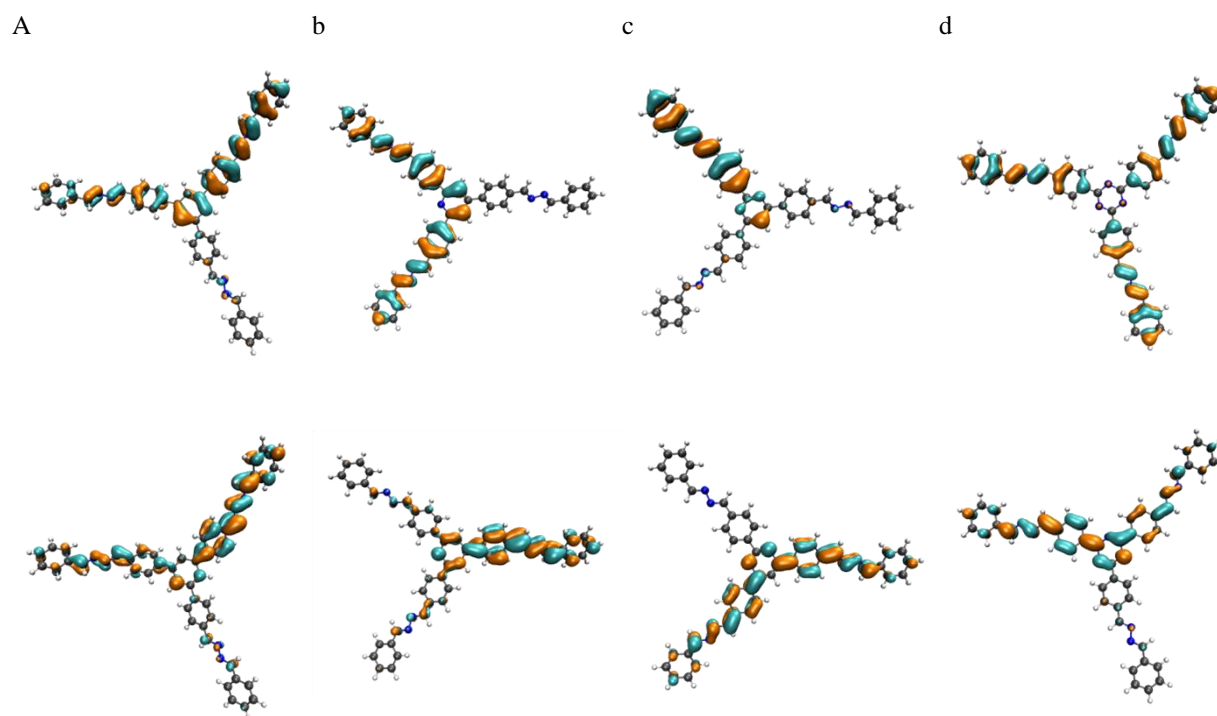
Figure S 68: HOMO and LUMO obtained at the PBE0-D3/def2-SVP level of theory for N_x-Phenylazines. (a) N_0-PhAz, (b) N_1-PhAz, (c) N_2-PhAz, (d) N_3-PhAz.
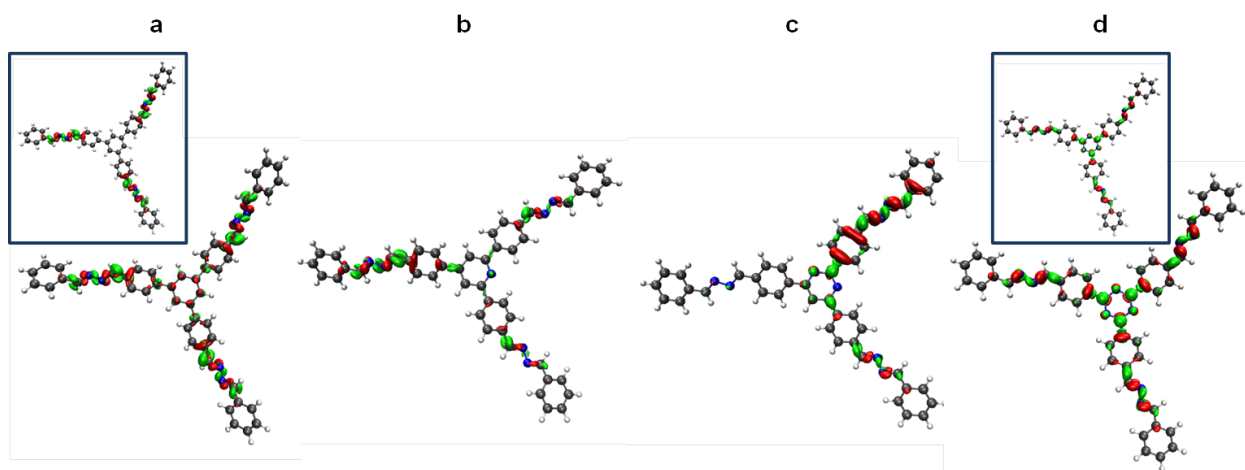
Figure S 69: Difference densities of vertical excitations with highest oscillator strength obtained at time-dependent (TD)-PBE0/def2-SVP level of theory for N_x-Phenylazines. (a) **N_0-PhAz**, (b) **N_1-PhAz**, (c) **N_2-PhAz**, (d) **N_3-PhAz**. The red isosurfaces depict regions with lower electron density in the excited state whereas green isosurfaces represent higher electron density in the excited state, both in comparison to the electron density of the ground state. Inset shows the degenerate energy state.
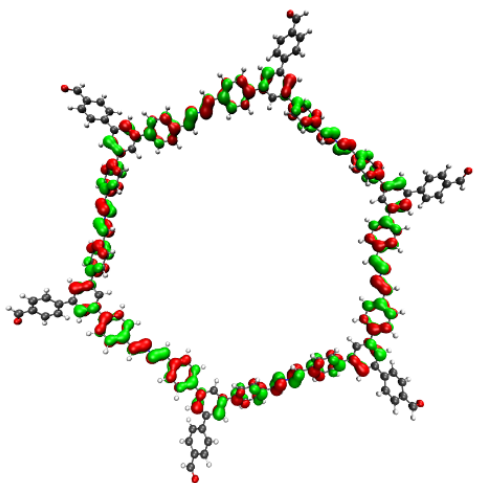
N₀-HxAl
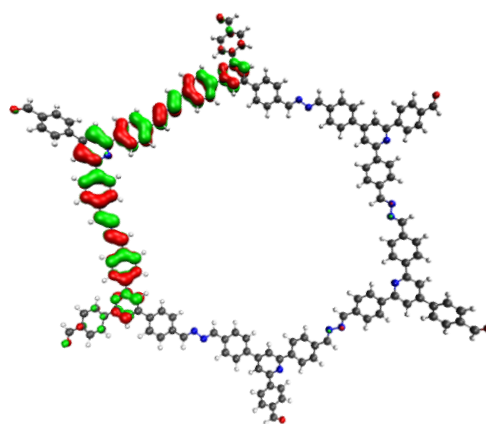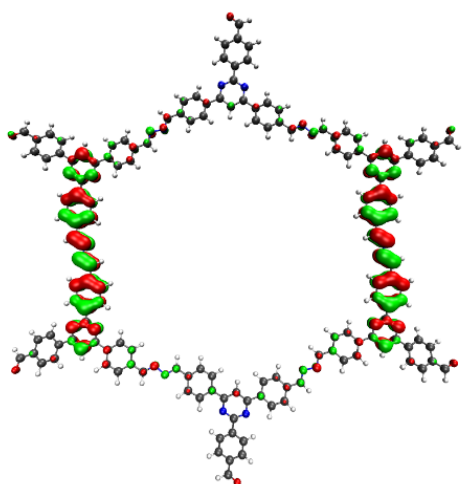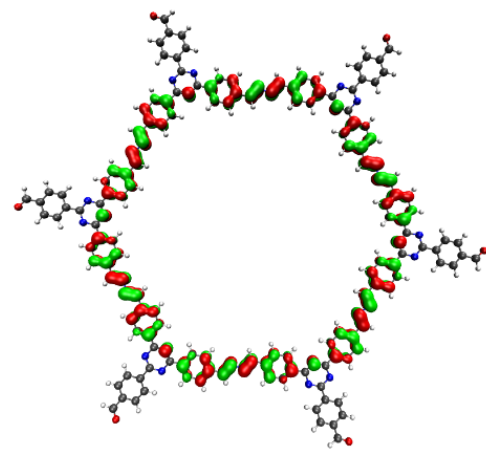
N₁-HxAl

N₂-HxAl

N₃-HxAl

Figure S 70: Localization of the HOMO for selected model hexagons with aldehyde- (HxAl) terminations, calculated at the PBE0-D3/def2-SVP level of theory.
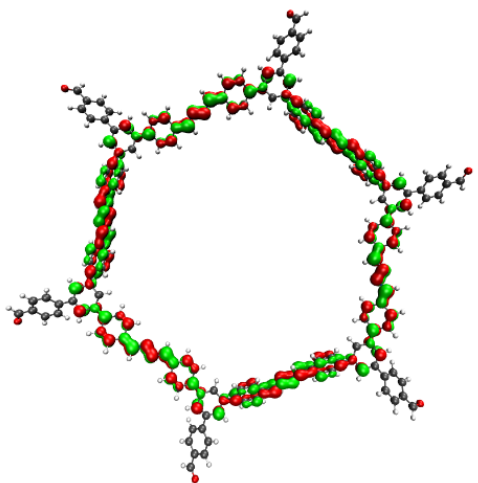
N$_0$-HxAl
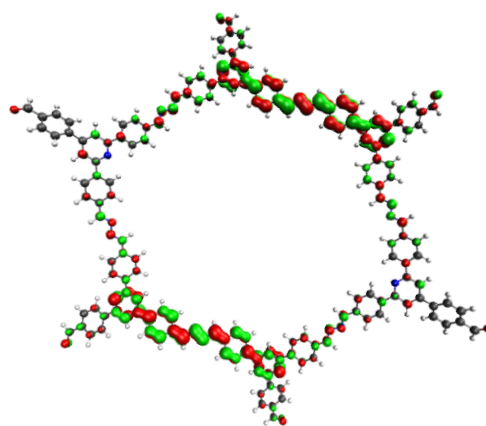
N$_1$-HxAl
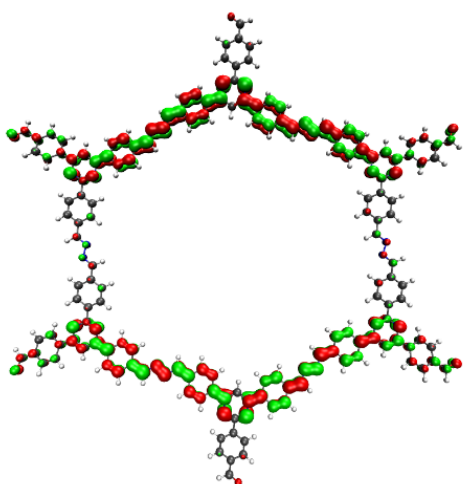
N$_2$-HxAl
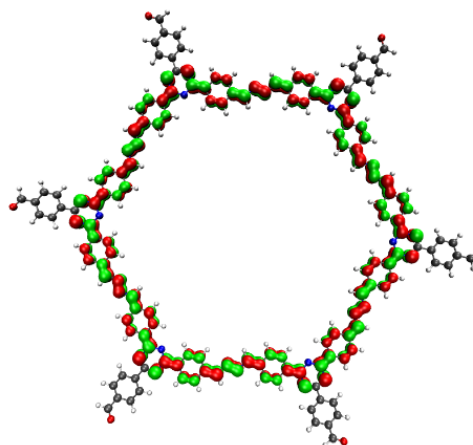
N$_3$-HxAl

Figure S 71: Localization of the LUMO for selected model hexagons with aldehyde-(HxAl) terminations, calculated at the PBE0-D3/def2-SVP level of theory.
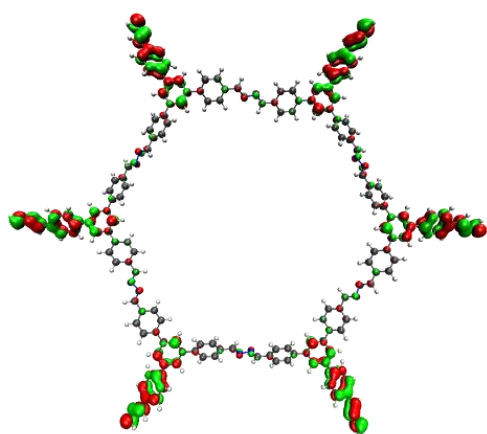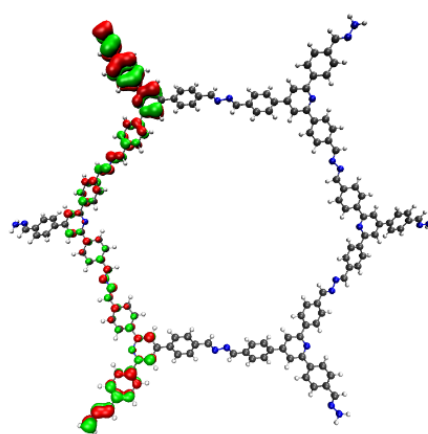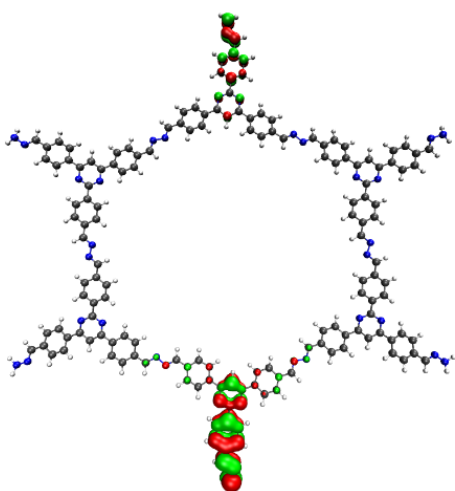
N$_0$-HxHz
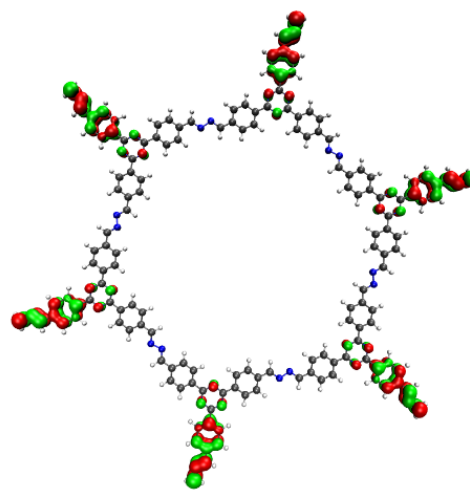
N$_1$-HxHz

N$_2$-HxHz

N$_3$-HxHz

Figure S 72: Localization of the HOMO for selected model hexagons with hydrazone- (HxHz) terminations, calculated at the PBE0-D3/def2-SVP level of theory.
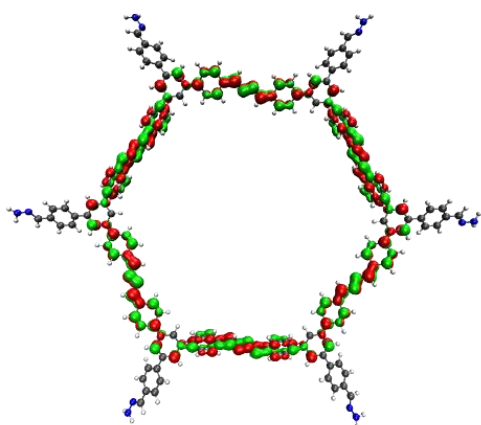
N$_0$-HxHz
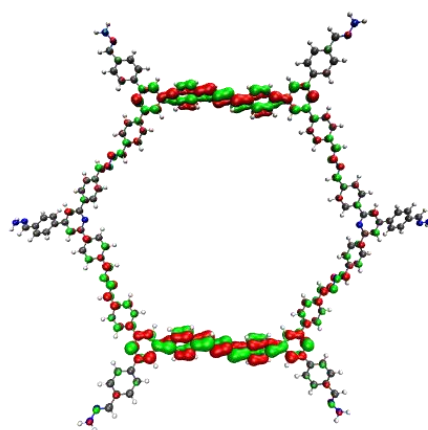
N$_1$-HxHz
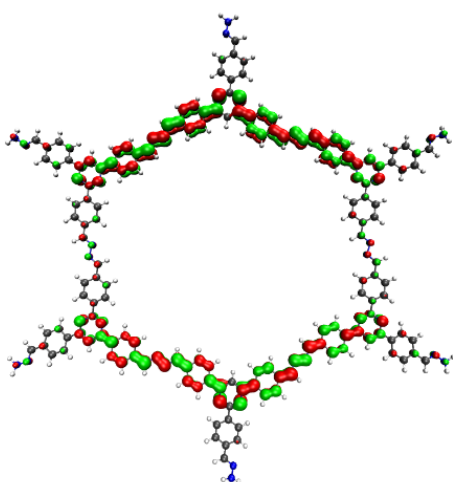
N$_2$-HxHz
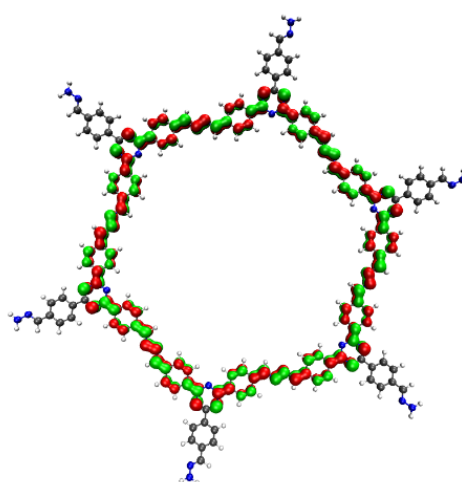
N$_3$-HxHz

Figure S 73: Localization of the LUMO for selected model hexagons with hydrazone- (HxHz) terminations, calculated at the PBE0-D3/def2-SVP level of theory.
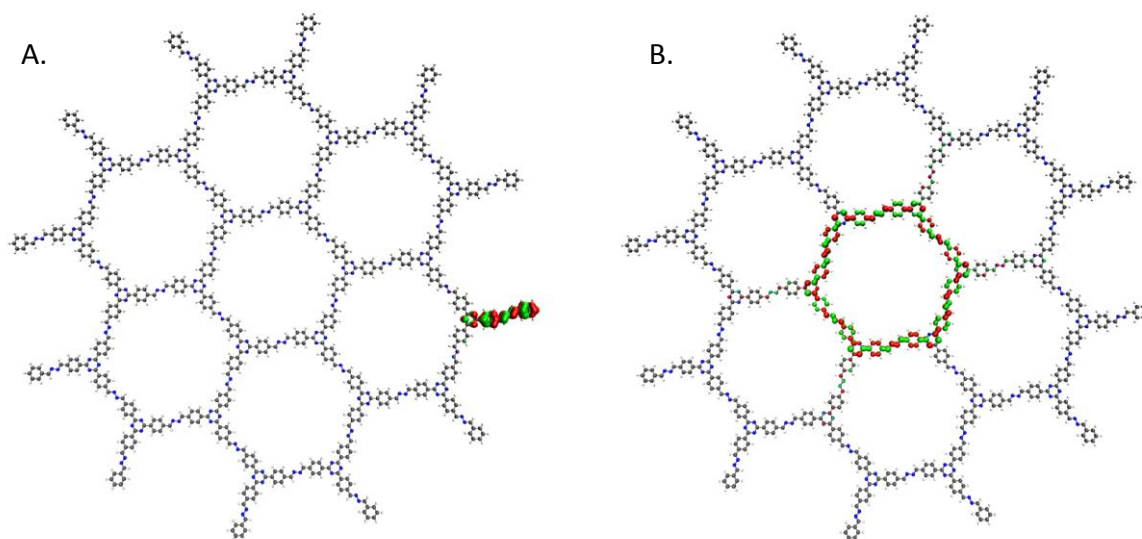
Figure S 74: Localization of the HOMO (left; A) and LUMO (right; B) for **N₃-7H** model hexagons with Phenylazine terminations, calculated at the PBE0-D3/def2-SVP level of theory.
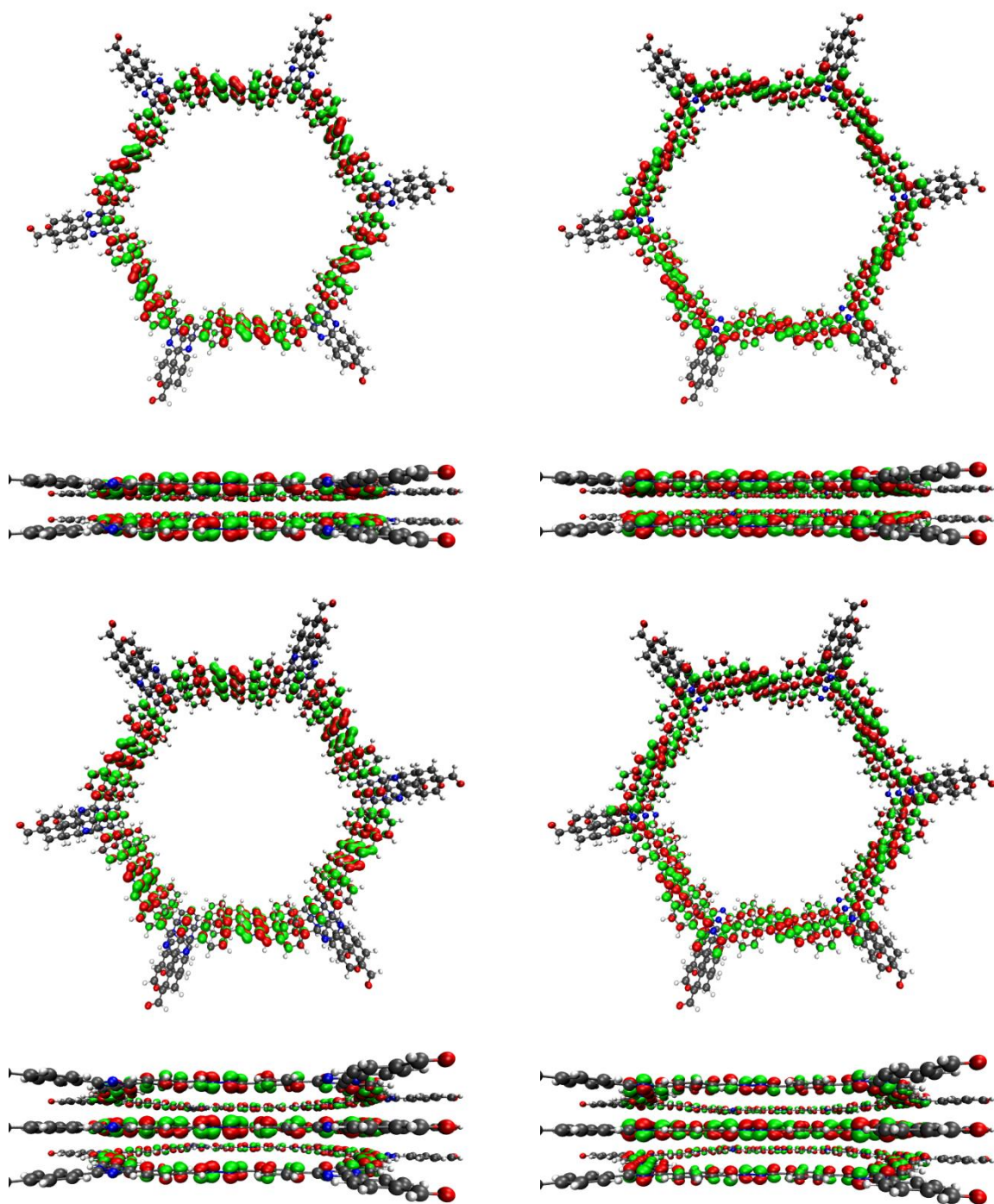
Figure S 75: Localization of the HOMO (left) and LUMO (right) for two/three layers of the **N₃-HxAl** model hexagons with aldehyde terminations, calculated at the PBE0-D3/def2-SVP level of theory.
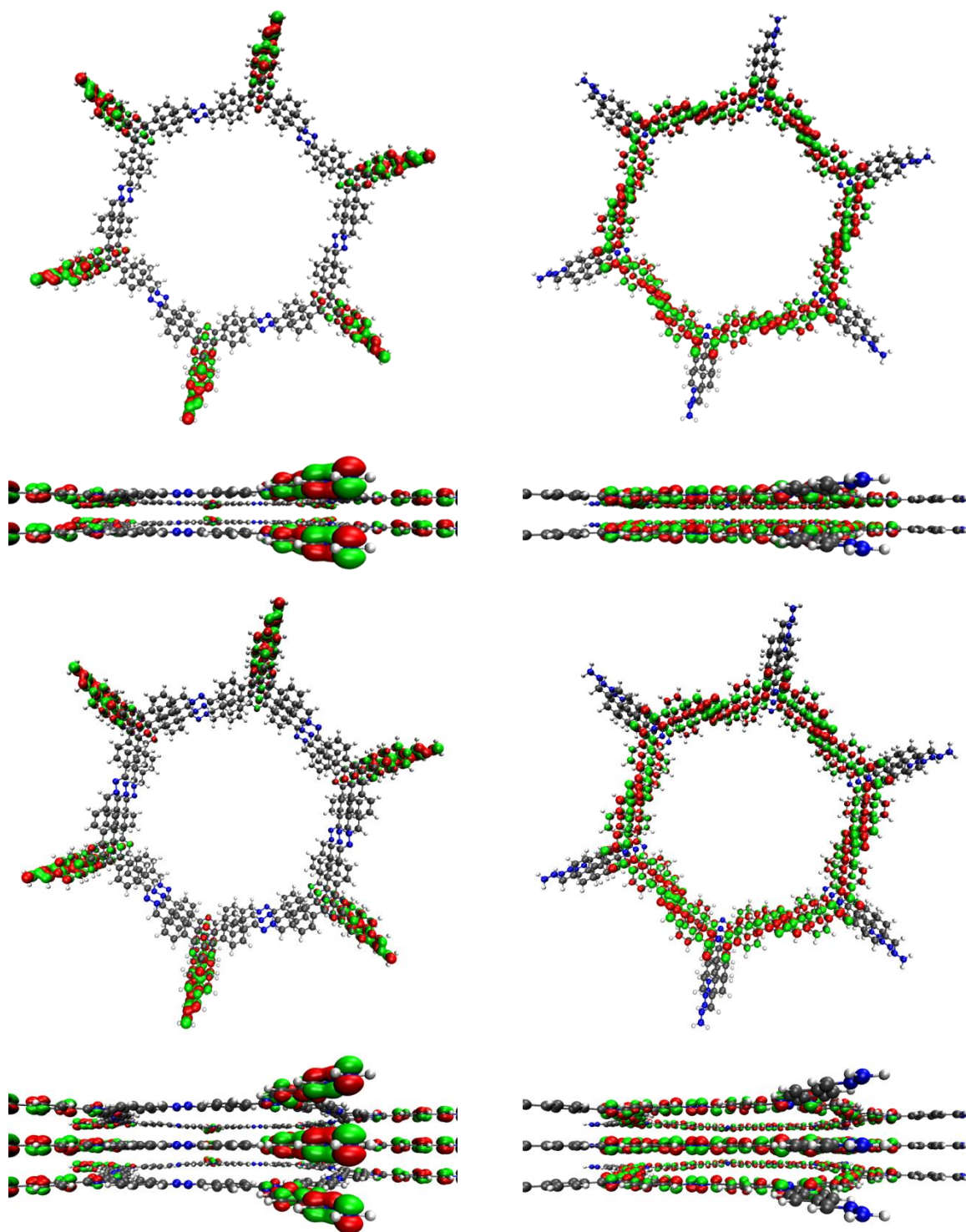
Figure S 76: Localization of the HOMO (left) and LUMO (right) for two/three layers of the **N₃-HxHz** model hexagons with hydrazone terminations, calculated at the PBE0-D3/def2-SVP level of theory.

N₀

N₁

N₂

N₃
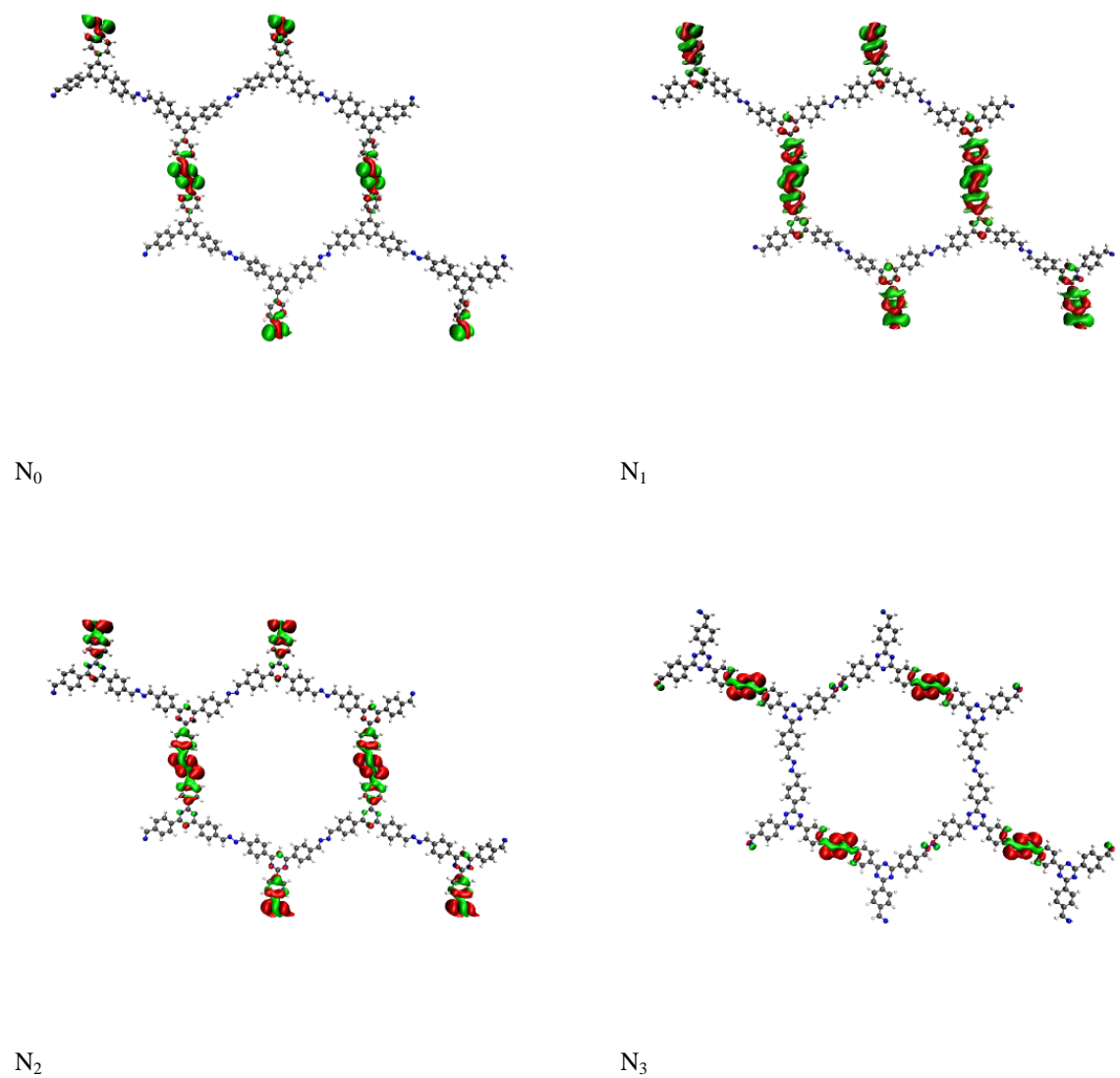
Figure S 77: Localization of the HOMO calculated from periodic single points using optimized unit cells at the DFTB+/mio-1-0 level of theory.
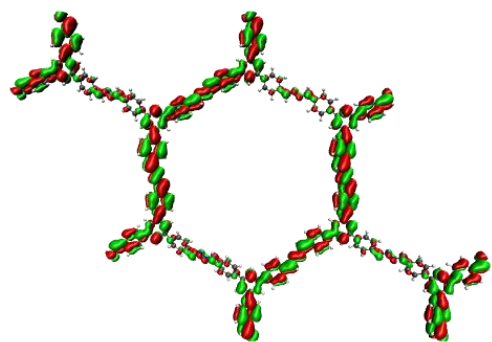
N_0
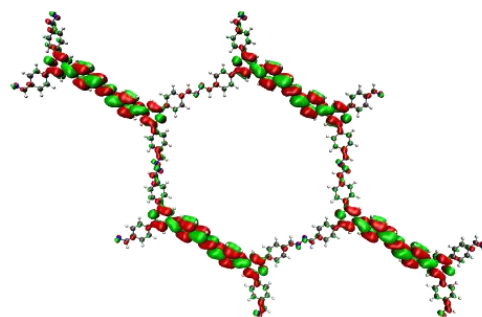
N_1
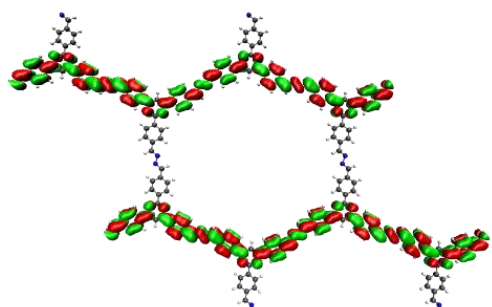
N_2
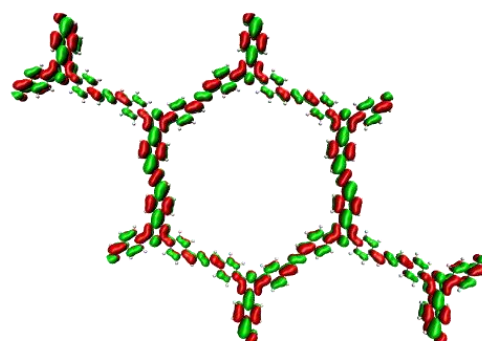
N_3

Figure S 78: Localization of the LUMO calculated from periodic single points using optimized unit cells at the DFTB+/mio-1-0 level of theory.
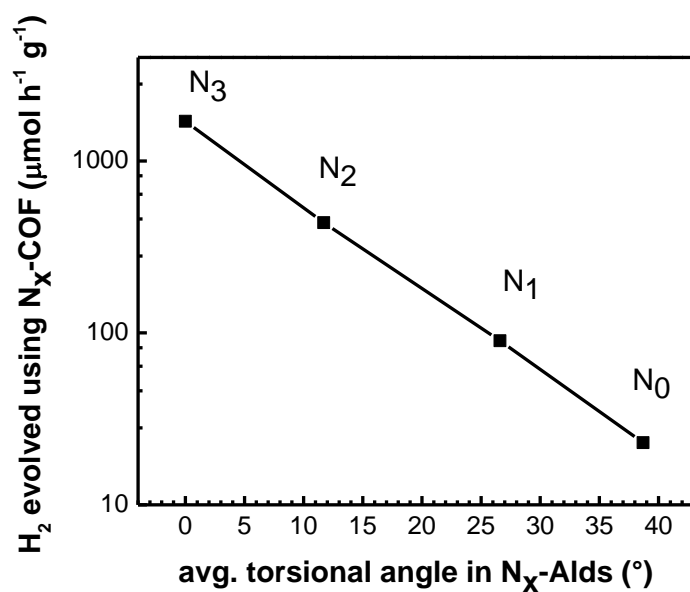
Figure S 79: Plot showing $\log_{10}$ of hydrogen produced (in µmol h^{-1} g^{-1}) by **N$_x$-COFs** against average dihedral angles obtained from the geometry optimized structure of their respective precursor aldehydes.
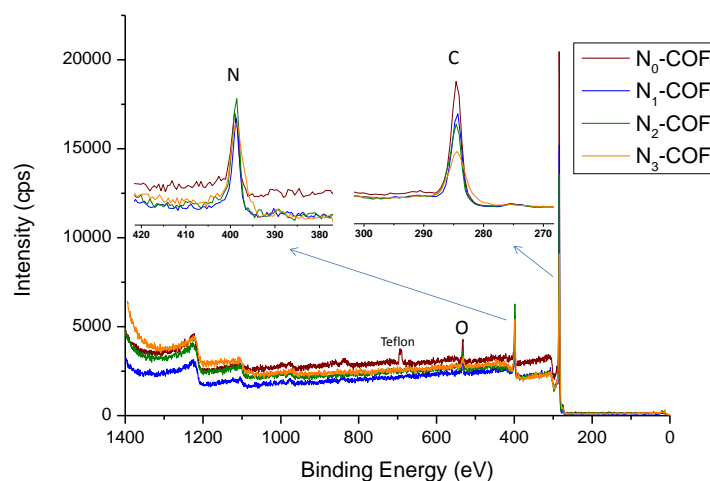
Figure S 80: XPS spectra of the N$_x$-COFs. Note that the C 1s peak at the lower binding energy is assigned to the adventitious carbon and is calibrated to 284.8 eV.

9.4.2. Supplementary Tables

Table S 9.4-1 Unit cell parameters of **N_x-COFs** obtained from the refinement of the XRPD pattern.

	a	b	c	symmetry
N_0	28.91(1)	28.92(1)	3.4	$P\bar{3}$
N_1	28.45(2)	28.45(2)	3.4	$P\bar{1}$
N_2	29.08(8)	29.08(8)	3.481(6)	$P\bar{1}$
N_3	28.541(5)	28.541(5)	3.438(3)	P6/m

Table S 9.4-2 PE of N_x-COFs using four band pass filters.

COF	Filter CWL (nm)	PE (%)
	400	0.17
N_3	450	0.44
	500	0.26
	550	0.039

COF	Filter CWL (nm)	PE (%)
	400	0.088
N_2	450	0.19
	500	0.083
	550	0.020

COF	Filter CWL (nm)	PE (%)
	400	0.038
N_1	450	0.077
	500	0.038
	550	0.0085

COF	Filter CWL (nm)	PE (%)
	400	0.0016
N_0	450	0.0010
	500	0.0017
	550	0.0003

Table S 9.4-3**:** Relationship between evolved hydrogen and the BET surface area of **N_x-COFs**.

1	2	3	4
N_x COF	H_2 evolved(Y) $\mu mol\ h^{-1}\ g^{-1}$	BET area(Z) $m^2\ g^{-1}$	H_2 evolved normalized by surface area (Y/Z ratio)
N_0	23	702	0.0327
N_1	90	326	0.2761
N_2	438	1046	0.4187
N_3	1703	1537	1.1080

Table S 9.4-4: Calculated HOMO and LUMO levels for the N_x-Aldehydes and the Kohn-Sham band gaps.

Compound	HOMO [eV]	LUMO [eV]	Kohn-Sham band gap [eV]
N_0-CHO	-7.16	-2.28	4.89
N_1-CHO	-7.11	-2.58	4.52
N_2-CHO	-7.36	-2.85	4.51
N_3-CHO	-7.71	-2.93	4.78

Table S 9.4-5: Calculated HOMO and LUMO levels for the N_x-Phenylazines and the Kohn-Sham band gaps.

Compound	HOMO [eV]	LUMO [eV]	Kohn-Sham band gap [eV]
N_0-PhAz	-6.27	-2.21	4.06
N_1-PhAz	-6.20	-2.40	3.80
N_2-PhAz	-6.30	-2.57	3.73
N_3-PhAz	-6.50	-2.60	3.89

Table S 9.4-6: Calculated HOMO and LUMO levels for N_x-HxAl model hexagons and the Kohn-Sham band gaps.

Compound	HOMO [eV]	LUMO [eV]	Kohn-Sham band gap [eV]
N_0-HxAl	-5.84	-2.21	3.64
N_1-HxAl	-5.82	-2.45	3.37
N_2-HxAl	-5.88	-2.62	3.26
N_3-HxAl	-5.94	-2.66	3.28

Table S 9.4-7: Calculated HOMO and LUMO levels for N_x-HxHz model hexagons and the Kohn-Sham band gaps.

Compound	HOMO [eV]	LUMO [eV]	Kohn-Sham band gap [eV]
N_0-HxHz	-6.34	-2.50	3.85
N_1-HxHz	-6.32	-2.77	3.55
N_2-HxHz	-6.45	-2.98	3.47
N_3-HxHz	-6.77	-3.08	3.69

Table S 9.4-8: Calculated HOMO and LUMO levels for stacks of N_x-HxAl model hexagons and the Kohn-Sham band gaps.

Compound	HOMO [eV]	LUMO [eV]	Kohn-Sham band gap [eV]
1 Layer N_3-HxAl	-6.77	-3.08	3.69
2 Layer N_3-HxAl	-6.41	-3.47	2.93
3 Layer N_3-HxAl	-6.25	-3.63	2.62

Table S 9.4-9: Calculated HOMO and LUMO levels for stacks of N_x-HxHz model hexagons and the Kohn-Sham band gaps.

Compound	HOMO [eV]	LUMO [eV]	Kohn-Sham Band gap [eV]

1 Layer **N₃-HxHz**	-5.94	-2.66	3.28
2 Layer **N₃-HxHz**	-5.45	-2.82	2.63
3 Layer **N₃-HxHz**	-5.19	-2.80	2.39

Table S 9.4-10: Calculated vertical electron affinities as differences in total energies between radical anionic and neutral states of **N$_x$-HxHz** model systems at the PBE0-D3/def2-SVP level of theory.

Compound	ΔE [eV]	$\Delta\Delta E$ [eV]
N$_0$-HxHz	-1.80	0.00
N$_1$-HxHz	-1.99	-0.19
N$_2$-HxHz	-2.19	-0.39
N$_3$-HxHz	-2.25	-0.45

9.4.3.   Supplementary Methods

General Synthesis of N$_x$-COFs

All COFs were prepared by a procedure identical to the one described for the synthesis of **N₃-COF**.

Synthesis of N$_3$-COF

In a Biotage® 5 mL high precision glass vial, was suspended **N₃-CHO** (50 mg, 0.13 mmol) in a mixture 1.0 mL of mesitylene, 1.0 mL of 1,4-dioxane and 100 μL aqueous 6M acetic acid. To the suspension was then added hydrazine hydrate (10 μL, 50-60 % solution, Sigma Aldrich). The vial was then sealed and heated in an oil bath at 120 °C for 3 days at autogenous pressure. Thereafter, the vial was opened and the suspension was filtered and washed with chloroform (2 x 5 mL), acetone (2 x 5 mL) and THF (2 x 5 mL). The solid was dried in an oven at 60 °C to afford **N₃-COF** as light yellow powder.

Anal. Calcd. for N₃-COF (C$_{24}$N$_6$H$_{15}$)$_n$: C, 74.40; N, 21.69; H, 3.90. Found: C, 72.36; N, 21.32; H, 4.07.

Anal. Calcd. for N₂-COF (C$_{25}$H$_{16}$N$_5$)$_n$: C, 77.70; N, 18.12; H, 4.17. Found: C, 71.85; N, 16.21; H, 4.40.

Anal. Calcd. for N₁-COF (C$_{26}$H$_{17}$N$_4$)$_n$: C, 81.02; N, 14.54; H, 4.45. Found: C, 72.48; N, 12.10; H, 4.55.

Anal. Calcd. for N₀-COF (C$_{27}$H$_{18}$N$_3$)$_n$: C, 84.35; N, 10.93; H, 4.72. Found: C, 80.15; N, 9.99; H, 4.76.

Structure Simulation and X-ray powder Diffraction of COFs

Molecular modeling of the COF was carried out using the Materials Studio (v6.0.0) suite of programs by Accelrys.[389] The structure was geometry optimized using the MS Forcite molecular dynamics module (Universal force fields, Ewald summations), and the unit cell parameters were received from Pawley refinement of the powder pattern. The COFs were modeled with imposed symmetry that is conceived from the native connectivity and geometry of the building blocks. The length of the *c* axis in the refinement of **N₀** and **N₁** was fixed at 3.4 Å, since no stacking peak was observed for these materials that allowed refinement of this value. The **N₁-COF** and **N₂-COF** were simulated with the symmetry $P\bar{1}$, which is the highest symmetry in these COFs if the aryl nitrogens are ordered. Note that assuming disorder for the orientation of the pyridine and pyrimidine rings, a higher symmetry such as $P\bar{3}$ is conceivable.

The obtained unit cell parameters and symmetry constraints are summarized in Table S 9.4-1.

9.5. Supporting information for: Structure-Property-Activity Relationships in a Pyridine containing Azine-linked Covalent Organic Framework for Photocatalytic Hydrogen Evolution

9.5.1. Supporting tables

Table S9.5-1: Parameters of Rietveld refinement

	PTP-COF
Restraints & constraints	a=b≠c; α=β=90°, γ=120°.
Rwp	1.833
a (Å)	27.7(8)
b (Å)	27.7(8)
c (Å)	3.55
α (°)	90
β (°)	90
γ (°)	120

Table S9.5-2: Dihedral angles in PTP-CHO and N_x-CHO building blocks obtained from optimized geometries on the PBE0-D3/def2-TZVP level of theory. Dihedral angles are reported in a clockwise order, starting from the upward pointing ligand A. Structures of the respective aldehydes can be found in Figure 4-4.

	Dihedral Angle [°]			
	A	B	C	Average
PTP-CHO	16.3	16.3	-18.4	17.0
N_0-CHO	39.1	39.1	39.1	39.1
N_1-CHO	39.1	24.2	26.2	29.8
N_2-CHO	7.5	24.4	24.5	18.8
N_3-CHO	0.0	0.0	0.0	0.0

Table S9.5-3: Radiative and non-radiative rates of PTP-COF under different experimental conditions

Sample	Φ[a]	τ, ns (amplitude)	$<\tau>$[b], ns	k_r ($\times 10^7$ s^{-1})[c]	k_{nr} ($\times 10^8$ s^{-1})[d]
Solid sample	0.0415	0.32 (10.58%), 1.13 (58.2%) and 3.54 (31.22%)	1.8	2.306	5.325
Water dispersion	0.0209	0.1 (9.73%), 0.57 (44.28%) and 1.55 (45.99%)	0.97	2.155	10.094
Photocatalytic conditions	0.0087	0.09 (14.86%), 0.37 (51.02%) and 1.07 (34.13%)	0.57	1.526	17.391

Φ - Quantum yield; τ - Fluorscence lifetime fitted to three expoentials; $<\tau>$ - Amplitude-weighted average lifetime;

k_r - radiative rate: k_{nr} - non-radiative rate.

[a] λ_{exc}=380 nm; [b] $<\tau> = \Sigma a_i \tau_i / \Sigma a_i$; [c] $k_r = \Phi/\tau$; [d] $k_{nr} = (1-\Phi)/\tau$

Table S 9.5-4: Excitation energies for the PTP-CHO building block unit calculated on TD-PBE0/def2-TZVP level of theory.

	State	Excitation Energy [eV]	Oscillator Strength [km/mol]	Occupied Orbital	Virtual Orbital	Orbital Contribution [%]
PTP-CHO	6	4.06	0.8081	HOMO	LUMO+1	40.5
N_0-CHO	5	4.30	0.7813	HOMO	LUMO	33.2
N_1-CHO	5	4.22	0.5047	HOMO	LUMO+1	90.4
N_2-CHO	7	4.25	0.5450	HOMO	LUMO+1	81.7
N_3-CHO	9	4.24	0.4739	HOMO-4	LUMO+1	28.1

Table S9.5-5: Calculated vertical radical stabilization energies as differences in total energies between radical anionic, radical cationic and neutral states of the PTP-CHO model system, PBE0-D3/def2-TZVP level of theory.

	Radical Cation				Neutral
	ΔVCSE [eV]	ΔVCSE [H]	VCSE [H]	Total Energy [H]	Total Energy [H]
PTP-CHO	-0.53	-0.01935494	0.30533824	-1312.19120015	-1312.49653838
N_0-CHO	-0.52	-0.01928853	0.30540465	-1264.09669101	-1264.40209566
N_1-CHO	-0.55	-0.02013946	0.30455372	-1280.13258163	-1280.43713535
N_2-CHO	-0.34	-0.01231277	0.31238041	-1296.16429579	-1296.47667619
N_3-CHO	0.00	0.00000000	0.32469318	-1312.19606741	-1312.52076059

	Radical Anion				Neutral
	ΔVASE [eV]	ΔVASE [H]	VASE [H]	Total Energy [H]	Total Energy [H]
PTP-CHO	0.34	0.01253149	-0.05811023	-1312.55464862	-1312.49653838
N_0-CHO	0.59	0.02161944	-0.04902228	-1264.45111794	-1264.40209566
N_1-CHO	0.32	0.01176033	-0.05888139	-1280.49601674	-1280.43713535
N_2-CHO	0.12	0.00442453	-0.06621719	-1296.54289338	-1296.47667619
N_3-CHO	0.00	0.00000000	-0.07064172	-1312.59140231	-1312.52076059

9.5.2. Supporting Figures
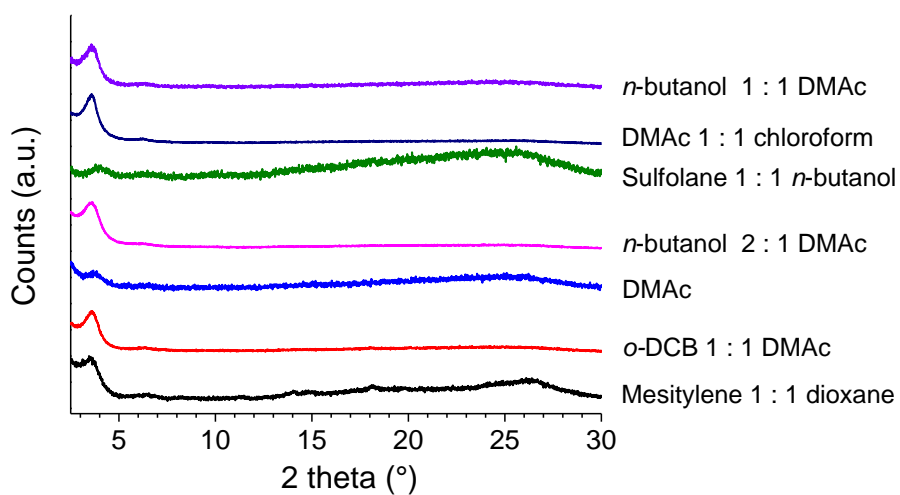
Figure S81: XRPD of PTP-COF synthesized in different solvent systems. DMAc = dimethyl acetamide, *o*-DCB = *o*-dichlorobenzene.
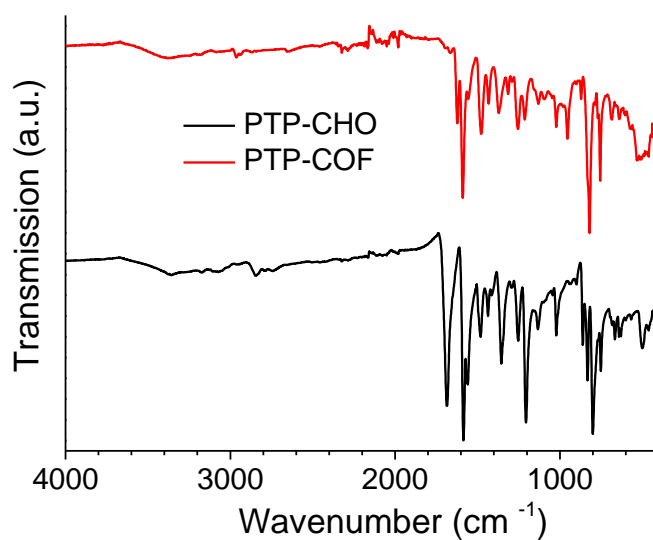
Figure S82: Full IR Spectrum of PTP-CHO and PTP-COF.
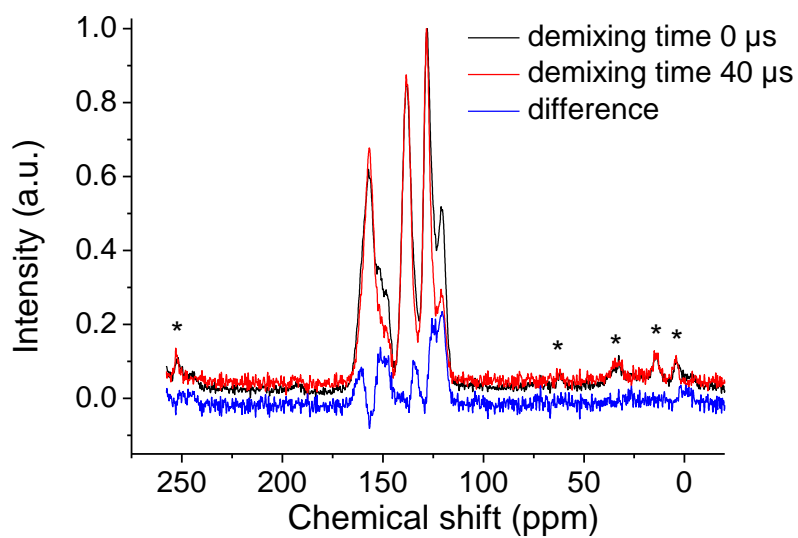
Figure S83: ^{13}C ssNMR of PTP-COF. Asterisks denote spinning side bands.
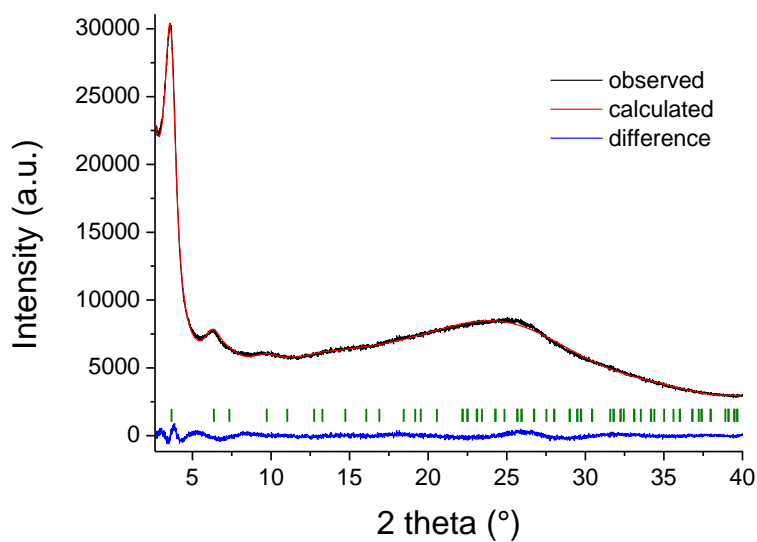
Figure S84: Rietveld refinement of the PTP-COF shows a good fit to the experimentally observed powder pattern (Rwp: 1.833)

Equation	y = a + b*x
Plot	V\+(-1) ((p\-(0) p\+(-1))-1)\+(-1)
Weight	No Weighting
Intercept	3.99085
Slope	21.42785
Residual Sum of Squares	0.18224
Pearson's r	0.98915
R-Square(COD)	0.97843
Adj. R-Square	0.97411
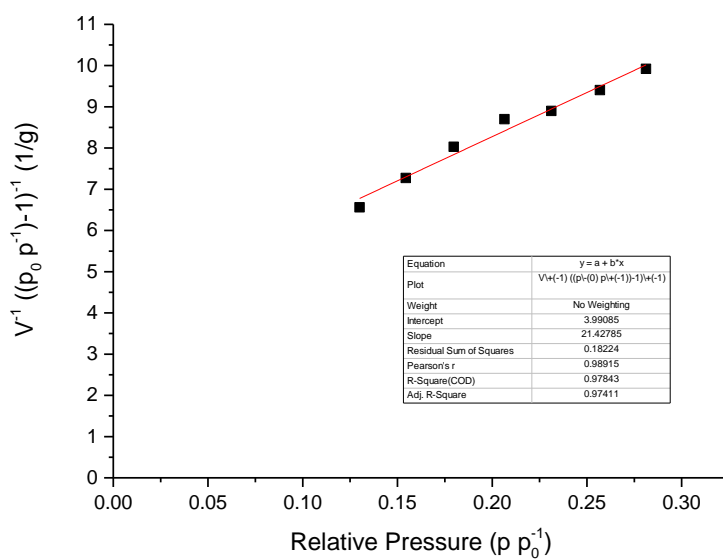
Figure S85: BET fit of the surface area of PTP-COF.
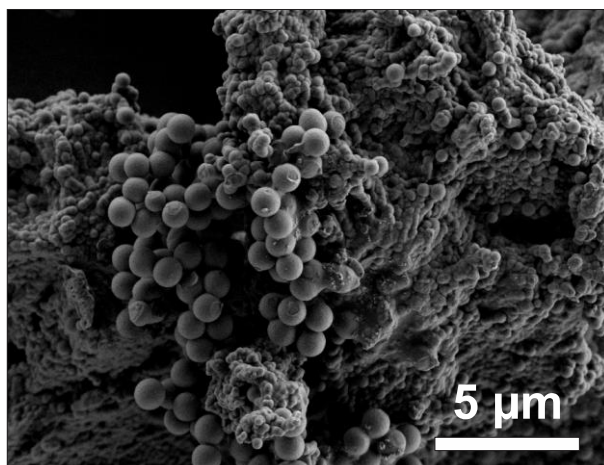
Figure S 86: SEM image of the PTP-COF showing the spherical particles and the intergrown agglomerates.
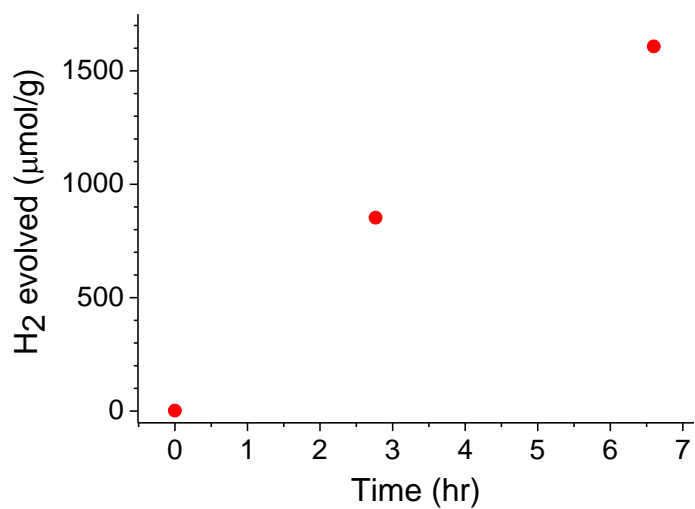
Figure S87: Hydrogen evolution under full spectrum light.
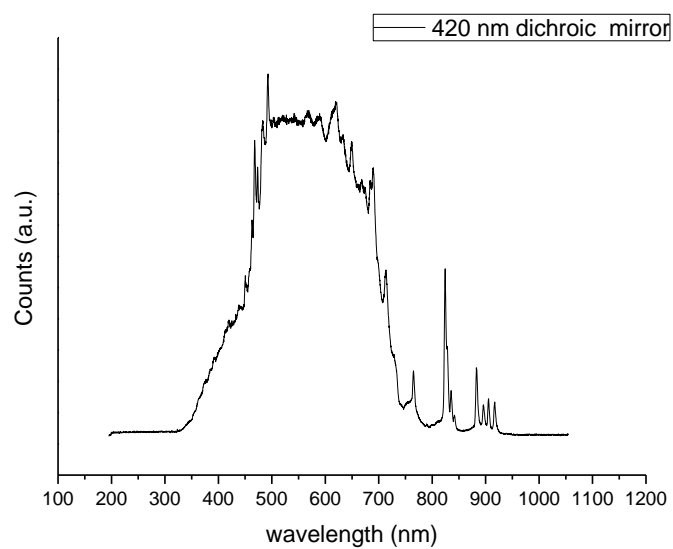
Figure S88: Spectrum of the xenon lamp with the dichroic mirror used for the AM1.5 G photocatalysis experiments.
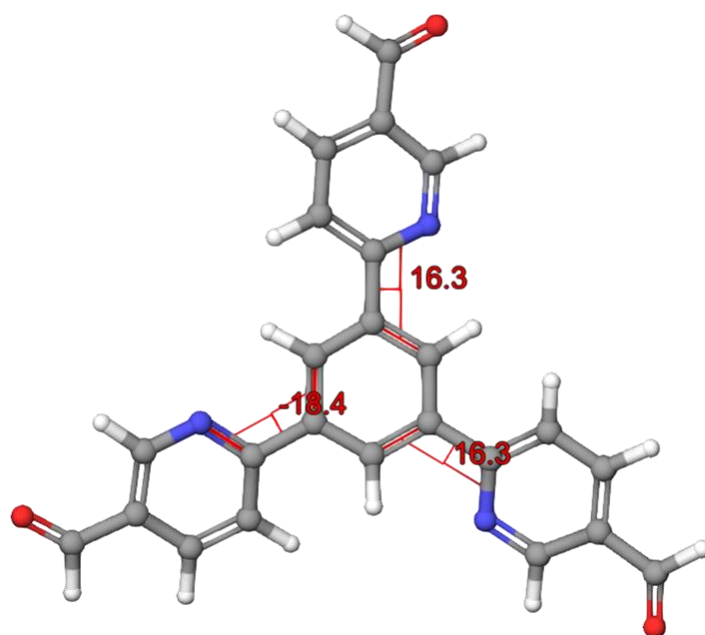
Figure S89: Geometry of the PTP-CHO building block, optimized on PBE0-D3/def2-TZVP level of theory. Representative dihedral angles are marked in red.
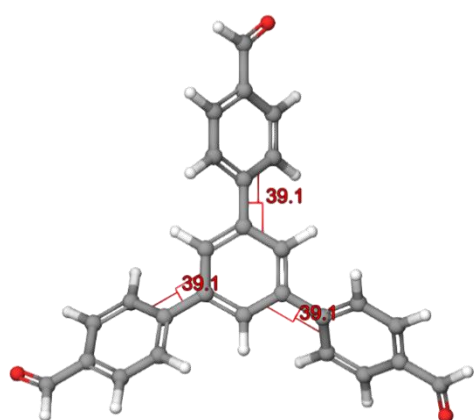
N₀-CHO
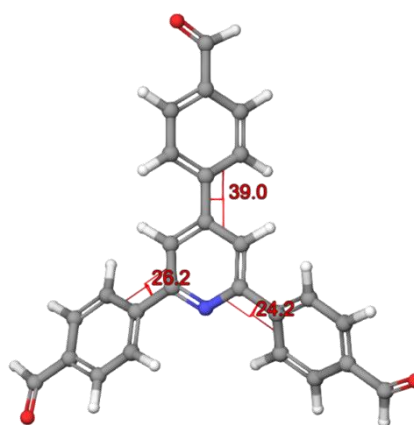
N₁-CHO
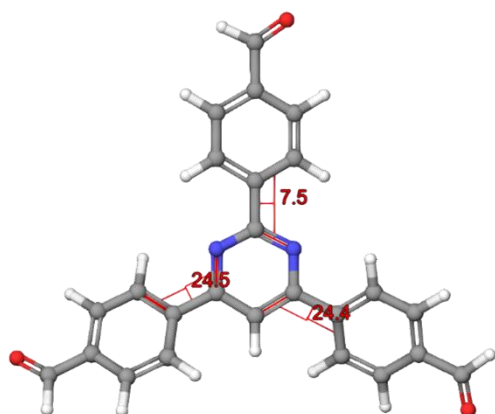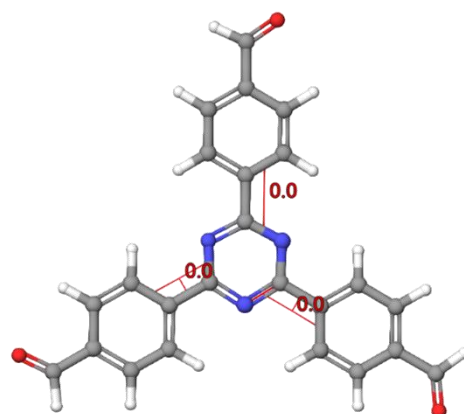
N$_2$-CHO   N$_3$-CHO

Figure S90: Geometries of the N$_x$ building block units optimized on PBE0-D3/def2-TZVP level of theory. Representative dihedral angles are marked in red.
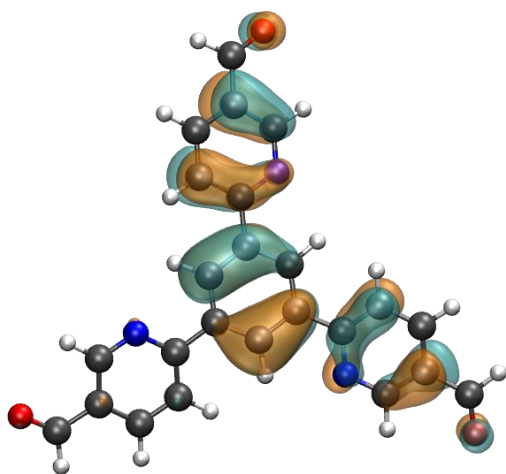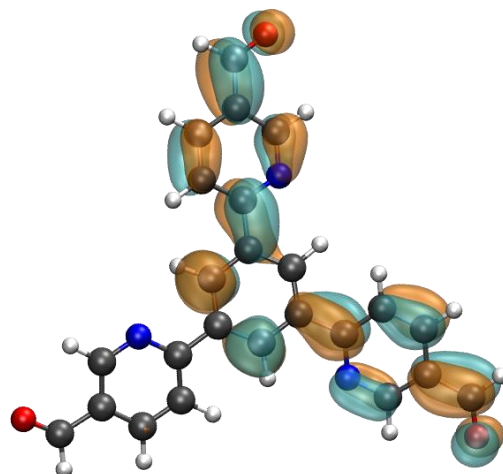
HOMO   LUMO

Figure S91: HOMO and LUMO of the PTP-CHO building block obtained at PBE0/def2-TZVP level of theory.
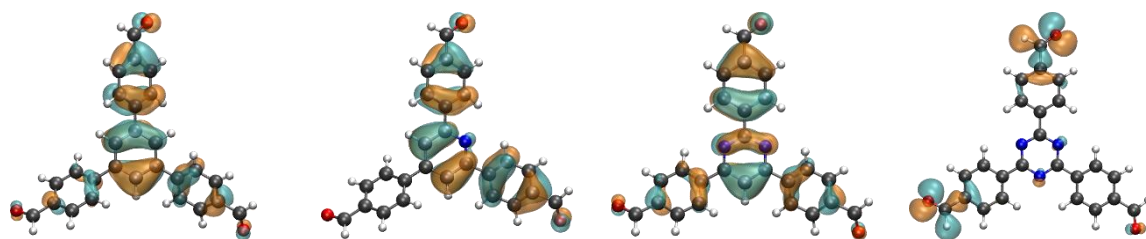
HOMO
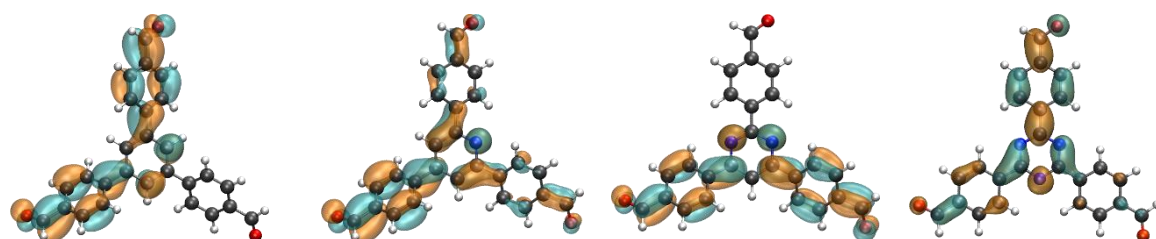
LUMO

N₀-CHO   N₁-CHO   N₂-CHO   N₃-CHO

Figure S92: HOMO and LUMO of the N_x building block units obtained at PBE0/def2-TZVP level of theory.
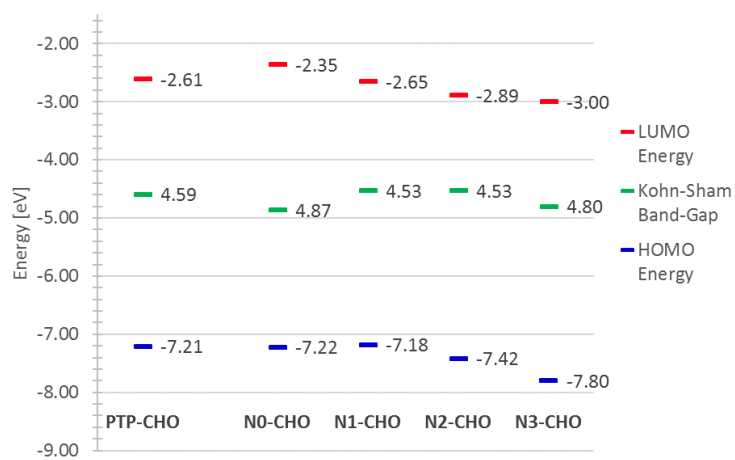
Figure S93: Orbital energies and Kohn-Sham Band-Gaps for the PTP-CHO building block in comparison with the N_x building block units, all data obtained at PBE0/def2-TZVP level of theory.
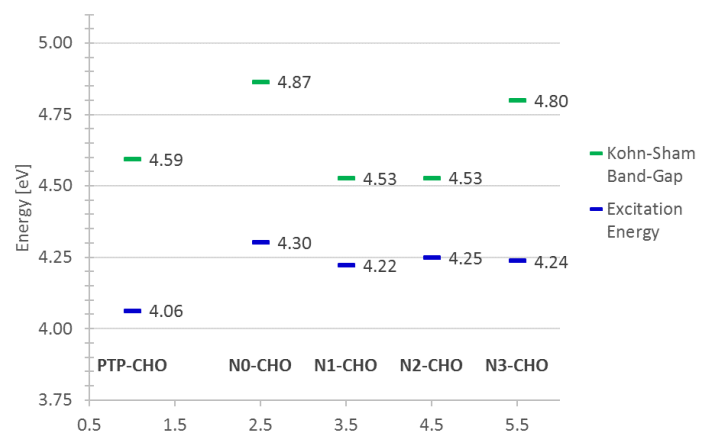
Figure S94: Comparison of Kohn-Sham Band-Gaps and excitation energies on PBE0/def2-TZVP and TD-PBE0/def2-TZVP level of theory.
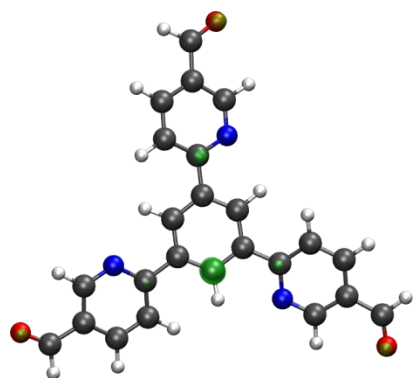
PTP-CHO
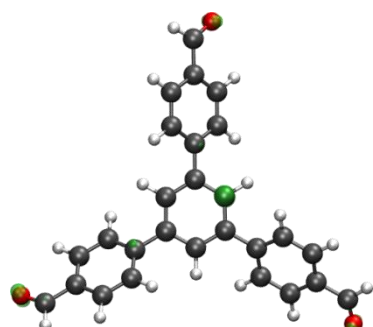
N₀-CHO
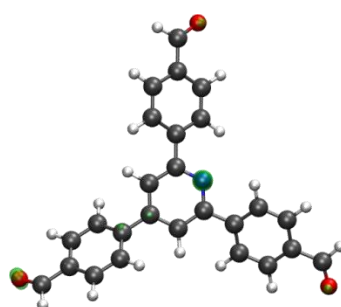
N₁-CHO
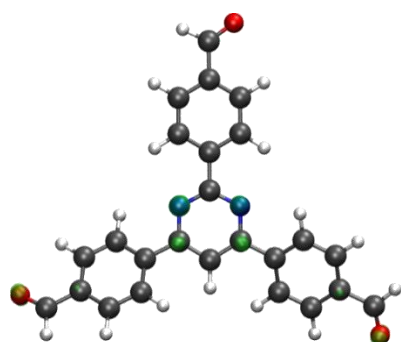
N₂-CHO
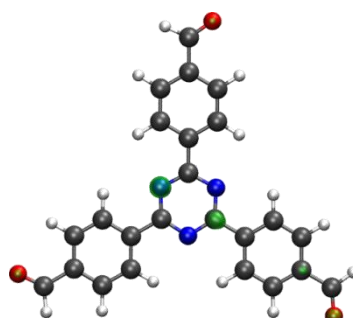
N₃-CHO

Figure S95: Spin densities of the vertical radical anion for the PTP-CHO building block and the N_x building block units, calculated on PBE0-D3/def2-TZVP level of theory.
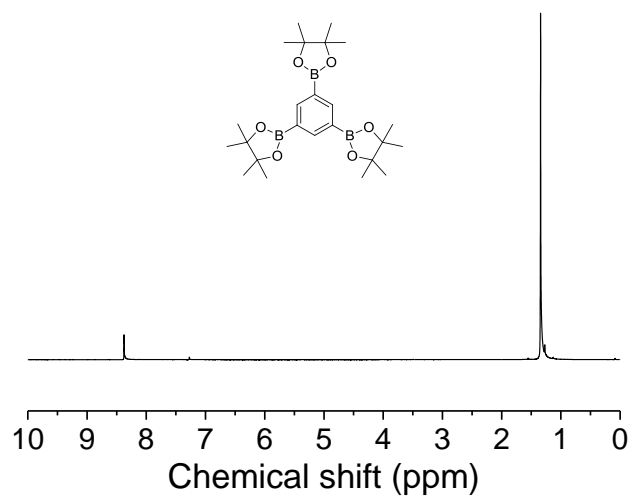
Figure S96: 300 MHz ^{1}H NMR of **2** in CDCl$_3$.
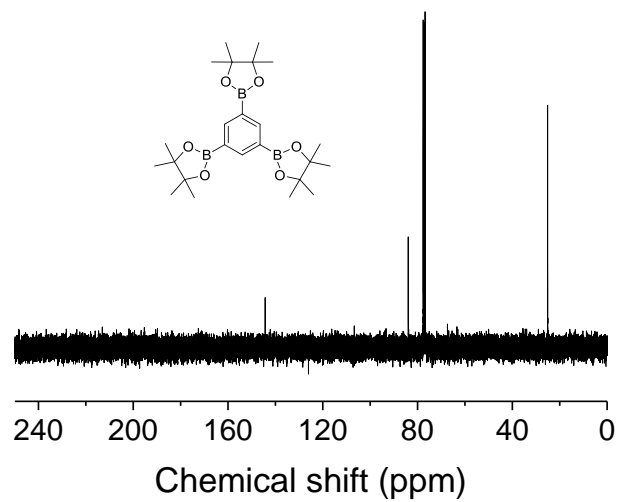
Figure S97: 75 MHz ^{13}C NMR of **2** in CDCl$_3$.
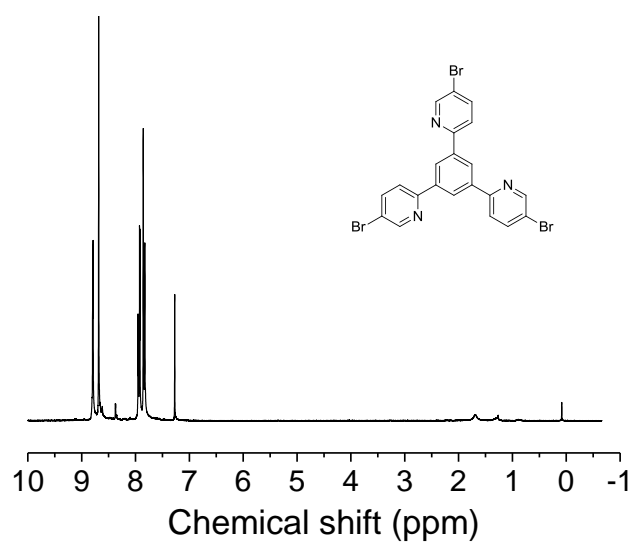
Figure S98: 300 MHz ^{1}H NMR of **3** in CDCl$_3$.
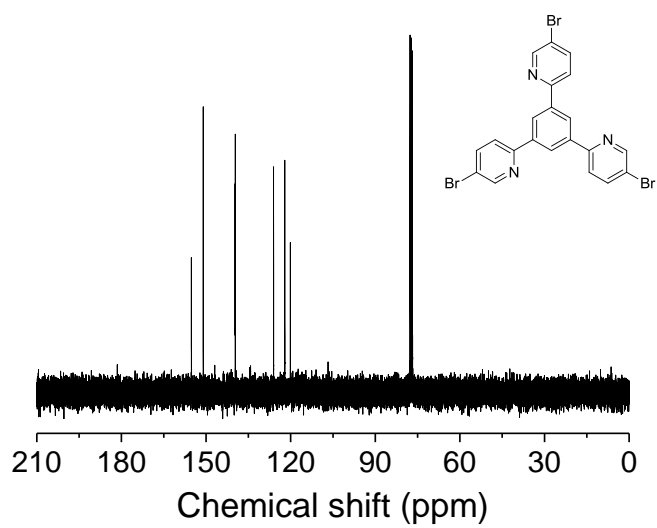
Figure S99: 75 MHz ^{13}C NMR of **3** in CDCl$_3$.
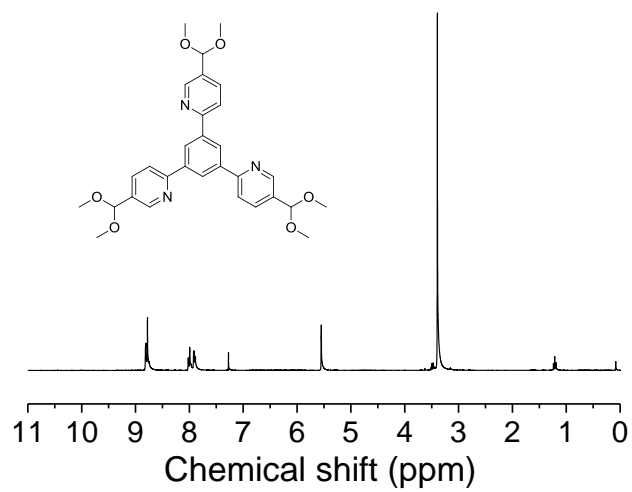
Figure S100: 300 MHz ^{1}H NMR of **5** in CDCl$_3$.
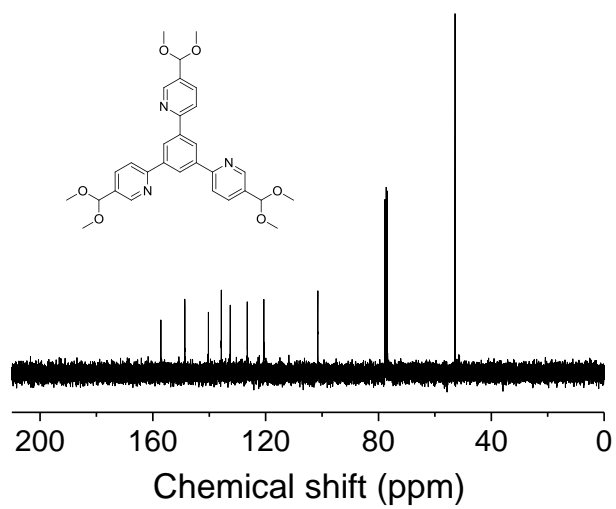
Figure S101: 75 MHz ^{13}C NMR of **5** in CDCl$_3$.
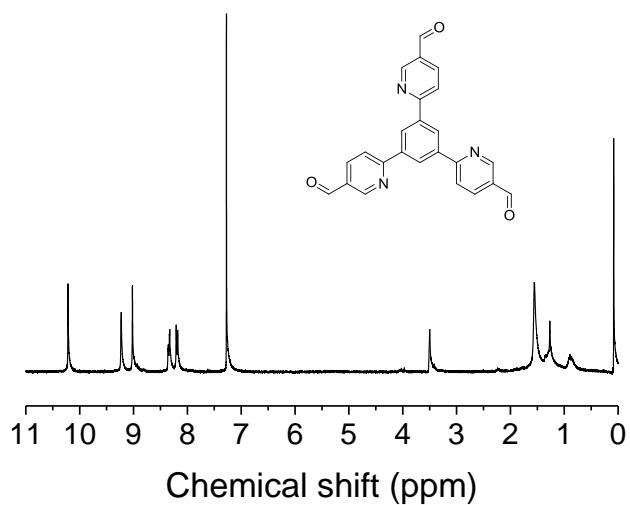
Figure S102: 300 MHz ^{1}H NMR of PTP-CHO in CDCl$_3$.

9.6. Supporting information for Tuning the optical band gaps of Covalent organic frameworks for efficient solar light absorption and photocatalytic hydrogen evolution

Table S 9.6-1: Rietveld refinement of the H-BTI- and OH-BTI-COF showing their respective unit cell parameters for comparison.

Fitted Pattern	H-BTI-COF[278]	OH-BTI-COF
Space group	P-6	P-6
constraints	-	-
Rwp (%)	8.735	2.141
a (Å)	17.733 (4)	17.457 (4)
b (Å)	17.733 (4)	17.457 (4)
c (Å)	3.483 (5)	3.330 (5)
α (°)	90	90
β (°)	90	90
γ (°)	120	120

9.7. Supporting information for: Tuning the Stacking Behaviour of a 2D Covalent Organic Framework through non-covalent Interactions

9.7.1. Methods

Synthesis

*T*ris(4-formylphenyl)*t*riazine (TT-CHO) and *t*ris(4-aminophenyl)*t*riazine (TT-NH2) were synthesized according to literature procedures.[196] *T*ris(4-aminophenyl)*b*enzene (TB-NH2) was obtained from TCI Chemicals.

*T*riazine-*t*riazine-triphenyl-*i*mine (TTI-COF):[196] TT-CHO (0.0635 mmol, 25.0 mg), TT-NH2 (0.0635 mmol, 22.5 mg), mesitylene (2.5 ml), 1,4-dioxane (2.5 ml), aqueous acetic acid (0.794 mmol, 6M, 0.132 ml) were added successively to a Biotage© precision glass vial, sealed and heated under autogenous pressure at 120°C for 72 h. After the reaction was allowed to cool down, the reaction mixture was filtered and washed thoroughly with ethanol, water, tetrahydrofuran and chloroform and then dried in high dynamic vacuum overnight.

*T*riazine *b*enzene triphenyl *i*mine (TBI-COF): TB-NH2 (0.032 mmol, 12.1 mg), TT-CHO (0.032 mmol, 12.6 mg), mesitylene (0.5 ml), 1,4-dioxane (0.5 ml), aqueous acetic acid (6M, 0.5 ml) were added successively to a Biotage© precision glass vial, sealed and heated under autogenous pressure at 155°C for 45 min. Afterwards the reaction vial was placed in a muffle furnace and heated at 120°C for 72 h. After the reaction was allowed to cool down, the reaction mixture was filtered and washed thoroughly with dimethylformamide, tetrahydrofuran and dichloromethane and then dried in a desiccator.

Model construction

Models of the structures were produced in Materials Studio v6.0.0 Copyright © 2011 Accelrys Software using of the Forcite Geometry optimizations with universal force fields with Ewald electrostatic and van der Waals summations methods.

SEM

SEM SE (secondary electron) detector images were obtained on either a Zeiss Merlin or a VEGA TS 5130MM (TESCAN).

TEM/SAED

TEM was performed with a Philips CM30 ST (300 kV, LaB$_6$ cathode). The samples were suspended in *n*-butanol and drop-cast onto a lacey carbon film (Plano). The images were recorded with a CMOSS camera F216 (TVIPS)

XRPD

XRPD patterns were collected at room temperature on a Stoe Stadi-P Diffractometer (Cu-Kα1 (λ = 1.540596 Å), Ge(111) Johann monochromator, Mython 1K detector with an opening angle of 12.5°) in Debye-Scherrer geometry. The samples were measured inside sealed glass capillaries (φ 1.0 mm capillary from Hilgenberg, glass no. 14). For improved particle statistics the samples were spun. The samples were measured from 2° to 60° 2θ over 20 hours.

Structural refinement

The powder patterns were analyzed by Rietveld refinement[326] using the range from 2-30 ° 2θ with TOPAS V5. [388] The peak profile was described by applying the fundamental parameter[353] approach as implemented in TOPAS. The background was modeled with Chebychev polynomials and for the TBI-COF a 1/X background correction function was additionally used to describe the incoherent scattering at low 2θ. Lattice parameters were refined freely for TBI-COF and with constraints (*a=b* and α = β) for TTI-COF. For the TBI-COF a one layer structural model was refined, whereas for TTI-COF two layers were used and their shift with respect to each other was refined. The anisotropic peak shape, caused by stacking faults and mismatches in the microstructure, was modelled by a phenomenological model for microstrain.[354] In order to keep correlation to an absolute minimum the same constraints were used as for the lattice parameters using only used the S400 and S004 parameters.

Rwp is defined in TOPAS as:

$$R_{wp} = \left\{ \frac{\sum w_m (Y_{o,m} - Y_{c,m})^2}{\sum w_m Y_{o,m}^2} \right\}^{1/2} \quad (1)$$

with $Y_{o,m}$ and $Y_{c,m}$ being the observed and calculated data, respectively, at point *m*, w_m is the weighting which accounts for counting statistics by $w_m = 1/\sigma(Y_{o,m})^2$ with the error of intensity ($\sigma(Y_{o,m})$).

Disorder simulations

DIFFaX Simulations[390] were performed by construction of one layer unit cell based on the structural model of TBI-COF obtained by DFT calculations. The optimal stacking was taken from the offset present in the unit cell obtained from DFT. The simulation included Gaussian broadening (0.15 trim). The stacking probability was varied sequentially from 99.9% uniform to 50%-50% random stacking, by the use of layer transition probabilities indifferent directions, as indicated next to the DIFFaX simulated XRPD pattern (Figure 5-9).

Theory

Quantum Espresso 5.1[391] was used for theoretical investigation of geometry-optimized unit cell and energy landscape. The Perdew-Burke-Ernzerhof (PBE) functional[355] was employed together with normconserving Martins-Troullier pseudopotentials.[392] The cut-off was set to 60 Ry and a $2 \times 2 \times 2$ k-point grid was used for the unit cell which included two COF sheets. A semi-empirical van-der-Waals interaction was added to account for dispersive interactions between sheets.[374]

The energy landscape of two sheets displaced from their equilibrium position was calculated by using two isolated layers from the converged structural optimization and displacing laterally one layer with respect to the other by given distances. The layer-layer distance perpendicular to the a-b plane (*c**) was held constant. Single-point energy calculations were performed at each lateral displacement using the Gamma point only. The two layers were separated from the next unit cell along the z-direction by >15 Å of vacuum.

9.7.2.   Supplementary Tables

Table S 9.7-1: Obtained values for the Pawley refinement of the TTI-COF for different models. a) This value could not be refined due to the lack of reflections containing a c component. Therefore this value was fixed at the distance obtained from the force field geometry optimization.

	TTI-eclipsed	TTI-oblong	TTI-slipped	TBI-eclipsed
Schematic representation				
Restraints & constraints	$a=b\neq c$; α = β =90°, γ =120°.	$a\neq b\neq c$; α = β = 90°, γ =120°.	$a=b\neq c$; α = β, γ =120°.	$a=b\neq c$; α = β =90°, γ =120°.
Rwp	9.319	5.359	4.461	1.365
a (Å)	25.272 (19)	25.390 (6)	26.029 (6)	24.359 (3)
b (Å)	25.272 (19)	24.175 (6)	26.029 (6)	24.359 (3)
c (Å)	3.545 (8)	3.4997 (12)	3.5190 (8)	3.5[a]
α (°)	90	90	80.180 (12)	90
β (°)	90	90	80.180 (12)	90
γ (°)	120	120	120	120

Table S9.7-2: Unit cell parameters for the refined and calculated structures. The XRPD refinement was performed with a one layer unit cell. The DFT was done with a two layer unit cell to compare alternate and parallel direction stacking.

	TTI-COF			TBI-COF		
Unit cell parameter	XRPD Rietveld Refinement	DFT (imine parallel)	DFT (imine antiparallel)	XRPD Rietveld Refinement	DFT (imine parallel)	DFT (imine antiparallel)
a (Å)	25.840963	25.488	25.551	24.336(0.003)	25.702	25.780
b (Å)	25.884321	25.476	25.583	24.336(0.003)	25.612	25.500
c (Å)	7.101546	7.084	6.988	7.0	7.126	7.046
α (°)	83.64200	77.616	76.933	90	71.622	73.856
β (°)	82.93933	77.464	77.699	90	88.458	89.380
γ (°)	121.57261	119.882	120.380	120	119.978	119.621

9.7.3.   Supplementary Figures
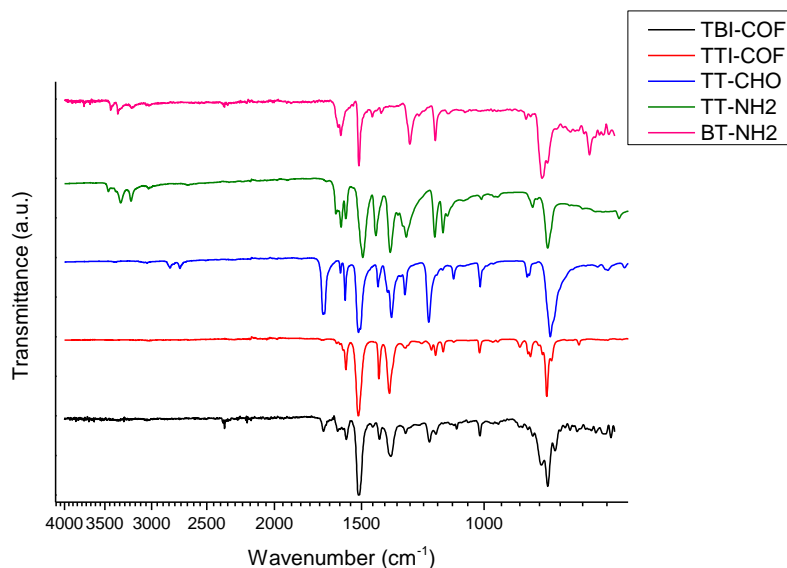
Figure S103: IR spectra of the TTI-COF and the TBI-COF show the transformation of the aldehyde and amine precursors to the corresponding imines. This is evident by the disappearance of the C=O stretch (1698 cm^{-1}) and the CO-H vibrations (2819 and 2730 cm^{-1}) in the precursor aldehyde (TT-CHO), the disappearance of the N-H vibrations (3500-3200 cm^{-1}) of the TT-NH2 precursor and (3500-3200 cm^{-1}) of the TB-NH2 precursor, as well as the appearance of the imine C=N stretch TTI-COF (1628 cm^{-1}) and TBI-COF at (1621 cm^{-1}).
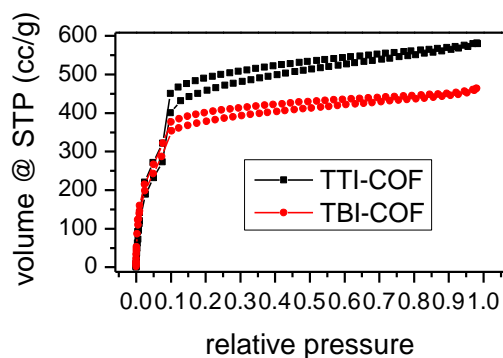
Figure S104: Sorption isotherms with Argon at 87K (right) of the TBI and the TTI-COF
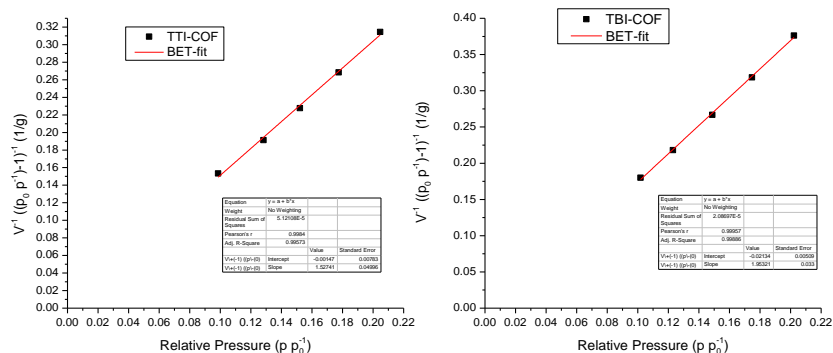
Figure S105: BET fit of the TTI-COF (left) and the TBI-COF (right).
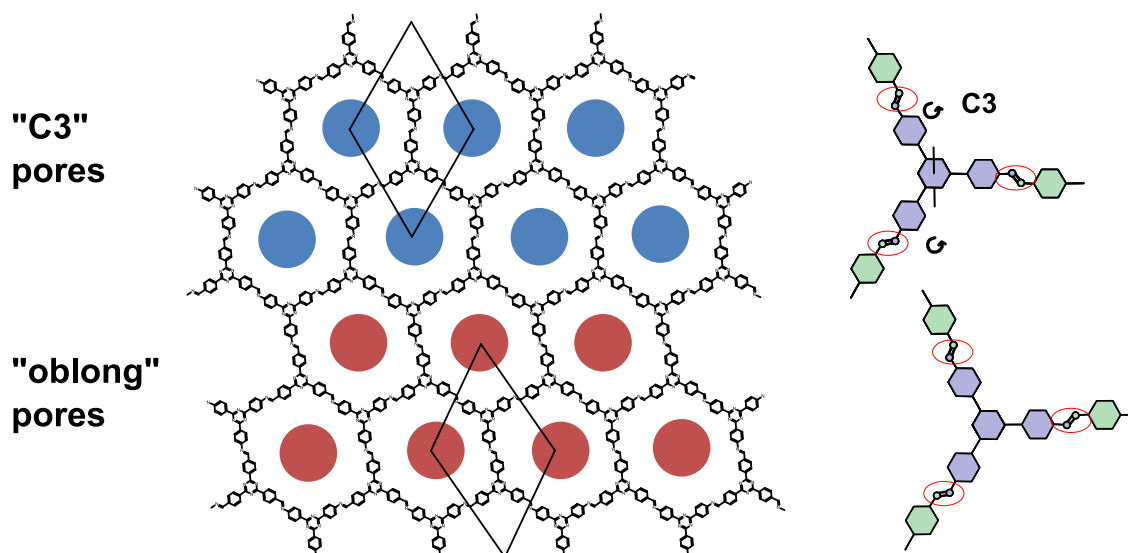
Figure S106: Illustration of the different possible relative orientations of the imine groups that could lead to different conformations. While the "C3" pores are only composed of imines with a rotational symmetry (right drawings), the imines in the "oblong" pores are rotated clockwise and anticlockwise.
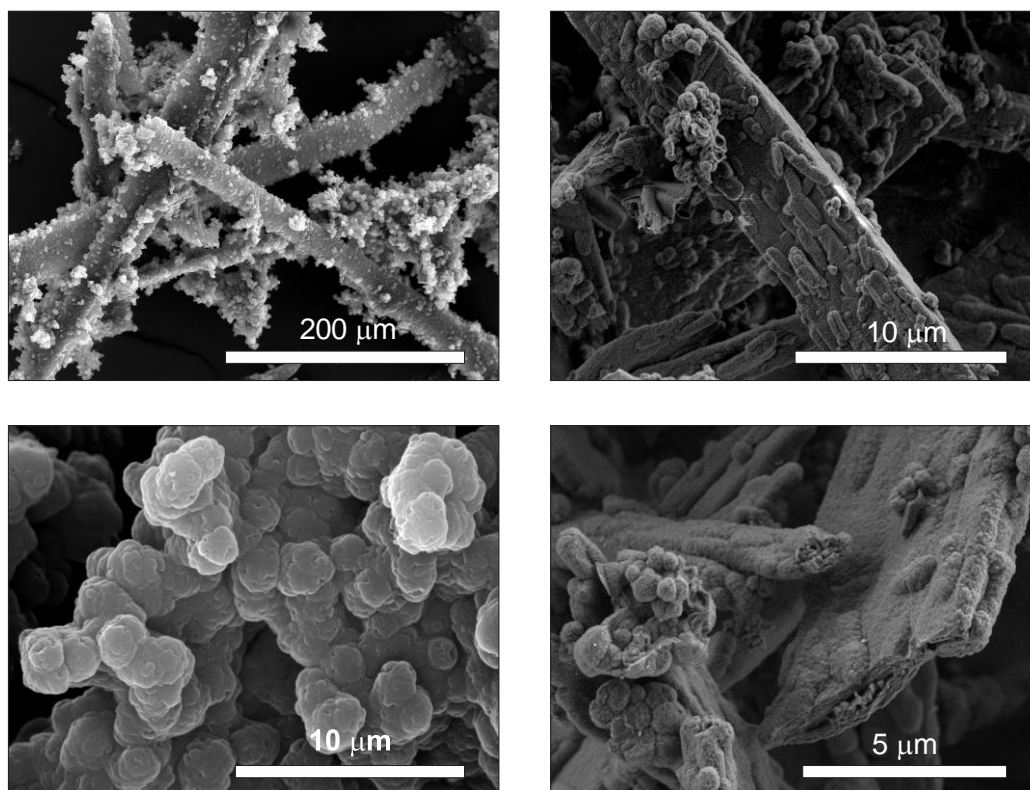
Figure S107: SEM images of the two COFs: TTI-COF on the left, TBI-COF on the right.
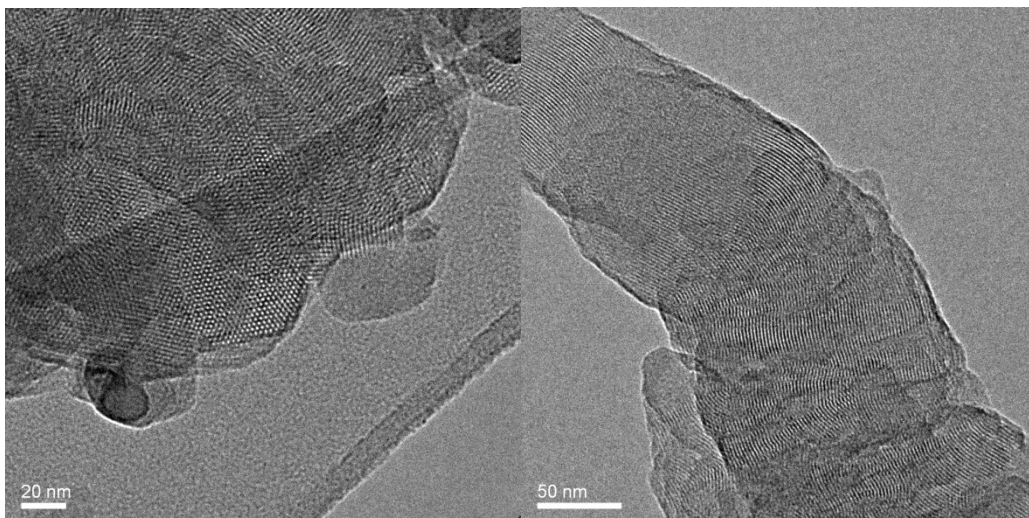
Figure S108: TEM images of the TTI-COF showing the hexagonal pore structure (left) and the bending of the crystallites/pores (right).
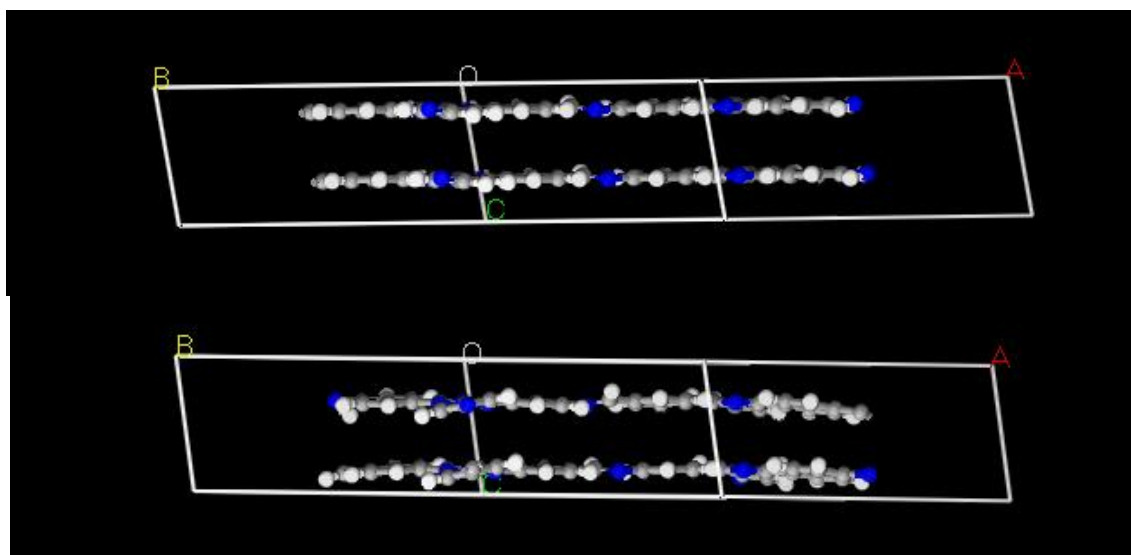
Figure S109: Visualization of the view in the a-b plane of the TTI-COF with parallel imines (top) and antiparallel imines (bottom) as obtained from the periodic boundary DFT calculations.

9.8.   Supporting Information for: Topochemical conversion of an imine- into a thiazole-linked covalent organic framework enabling real-structure analysis

9.8.1.   Supplementary Methods

Materials

*T*ris(4-formylphenyl)*t*riazine (TT-CHO),[196] tris(4-aminophenyl)triazine (TT-NH2),[196] tetra(4-formylphenyl)pyrene[393] were synthesized according to literature procedures. All other chemicals were obtained from commercial sources.

Synthesis

TTI-COF was synthesized as previously described.[196, 278] TT-NH2 (0.0635 mmol, 22.5 mg), TT-CHO (0.0635 mmol, 25.0 mg), 1,4-dioxane (2.5 ml), mesitylene (2.5 ml), aqueous acetic acid (0.794 mmol, 6M, 0.132 ml) were added to a Biotage© precision glass vial, sealed and heated under autogenous pressure at 120°C for 72 h. After the reaction was allowed to cool down, the reaction mixture was filtered and washed thoroughly with ethanol, water, tetrahydrofuran and chloroform and then dried in high dynamic vacuum overnight.

*P*yrene tetra(phenyl) *b*iphenyl *i*mine PBI-COF was synthesized from tetra(4-formylphenyl)pyrene and diaminobiphenyl according to the literature procedure. [160]

SEM/EDX

SEM SE (secondary electron) detector images were obtained on either a Zeiss Merlin or a VEGA TS 5130MM (TESCAN) with a SEM-EDX using a Si/Li detector (10kV acceleration voltage, Oxford).

FT-IR

Infrared spectra were recorded in attenuated total reflection (ATR) geometry on a PerkinElmer UATR Two equipped with a diamond crystal.

Sorption

Sorption measurements were performed on a Quantachrome Instruments Autosorb iQ MP with Argon at 87K. The pore size distribution was determined from argon adsorption isotherms using the QSDFT cylindrical pores in carbon model for argon at 87 K.

Elemental analysis

CHNS elemental analyses were performed with a Vario EL elemental analyser (Elementar Analysensysteme GmbH).

9.8.2.   Supplemental Tables and Figures

Table S 3: ^{15}N-NMR chemical shifts for all three distinct **TTT-COF sections** (Figure S 112, Figure S 113, Figure S 114), obtained on B97-2/def2-TZVP level of theory.

<div align="center">

NMR Chemical Shift [ppm]

</div>

Atom Label	Atom	TTT-Section 1	TTT-Section 2	TTT-Section 3	Average
1 (6')	N	-131.35	-130.90	-133.51	-131.92
10 (5')	N	-76.67	-76.66	-76.72	-76.68
18 (6')	N	-136.41	-134.18	-134.37	-134.99
33 (6')	N	-134.06	-134.64	-132.60	-133.77
38 (6')	N	-134.29	-131.80	-133.79	-133.29

Table S 4: ^{13}C-NMR chemical shifts for all three distinct TTT-COF sections, obtained on B97-2/def2-TZVP level of theory.

NMR Chemical Shift [ppm]

Atom Label	Atom	TTT-Section 1	TTT-Section 2	TTT-Section 3	Average
2 (1')	C	179.89	180.64	179.36	179.96
3	C	146.95	146.97	146.92	146.95
4	C	138.17	138.17	138.09	138.14
5	C	135.46	135.43	135.46	135.45
6	C	145.62	145.69	145.57	145.63
7	C	135.65	135.67	135.71	135.67
8	C	137.88	138.00	137.90	137.92
9 (2')	C	182.95	182.98	183.01	182.98
11 (3')	C	166.48	166.51	166.56	166.52
12	C	146.54	146.55	146.52	146.54
13	C	131.31	131.47	131.40	131.39
14	C	141.05	141.09	141.10	141.08
15	C	135.73	135.70	135.80	135.74
16	C	130.85	130.85	130.85	130.85
17 (1')	C	179.59	180.27	180.90	180.25

Table S 5: ^{15}N-NMR chemical shifts for all three distinct TTI-COF sections, obtained on B97-2/def2-TZVP level of theory.

NMR Chemical Shift [ppm]

Atom Label	Atom	TTI-Section 1	TTI-Section 2	TTI-Section 3	Average
8 (5)	N	-50.84	-51.68	-51.03	-51.18
16 (6)	N	-130.23	-129.46	-129.36	-129.68
26 (6)	N	-128.71	-131.14	-130.75	-130.20
38 (6)	N	-134.33	-134.14	-134.88	-134.45
39 (6)	N	-131.81	-131.58	-131.87	-131.75

Table S 6: ^{13}C-NMR chemical shifts for all three distinct TTI-COF sections, obtained on B97-2/def2-TZVP level of theory.

NMR Chemical Shift [ppm]

Atom Label	Atom	TTI-Section 1	TTI-Section 2	TTI-Section 3	Average
9 (3)	C	164.28	164.13	164.40	164.27
10 (4)	C	122.39	122.32	122.43	122.38
11	C	139.64	139.71	139.71	139.69
12	C	143.12	143.20	142.95	143.09
13	C	139.42	139.38	139.34	139.38
14	C	134.95	135.14	134.86	134.98
15 (1)	C	181.01	181.11	180.82	180.98
27 (1)	C	181.75	180.50	181.14	181.13
28	C	148.13	148.00	148.23	148.12
29	C	138.41	138.28	138.33	138.34
30	C	135.31	135.25	135.29	135.29
31	C	148.44	148.35	148.29	148.36
32	C	140.50	140.69	140.55	140.58
33	C	138.17	138.22	138.27	138.22
34 (2)	C	168.63	168.57	168.68	168.62
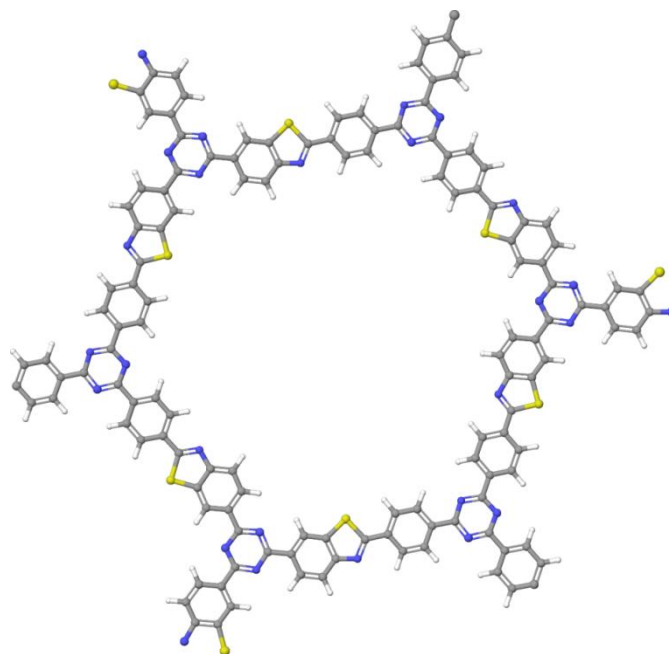
Figure S 110: Optimized geometry for a single TTT-COF pore, excised from a 2x2 supercell obtained from periodic calculations on PBE-D3/def2-TZVP level of theory using 5x5 k-points.
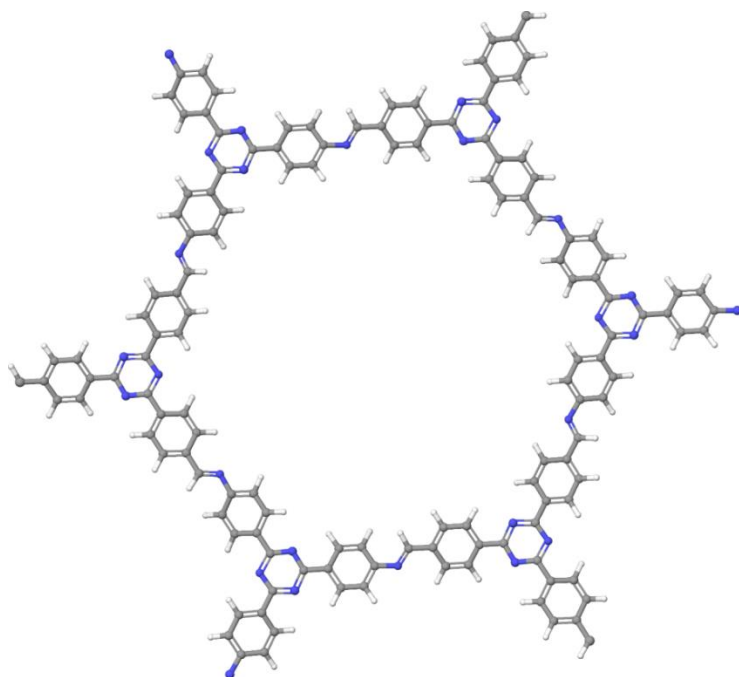
Figure S 111: Optimized geometry for a single TTI-COF pore, excised from a 2x2 supercell obtained from periodic calculations on PBE-D3/def2-TZVP level of theory using 5x5 k-points.
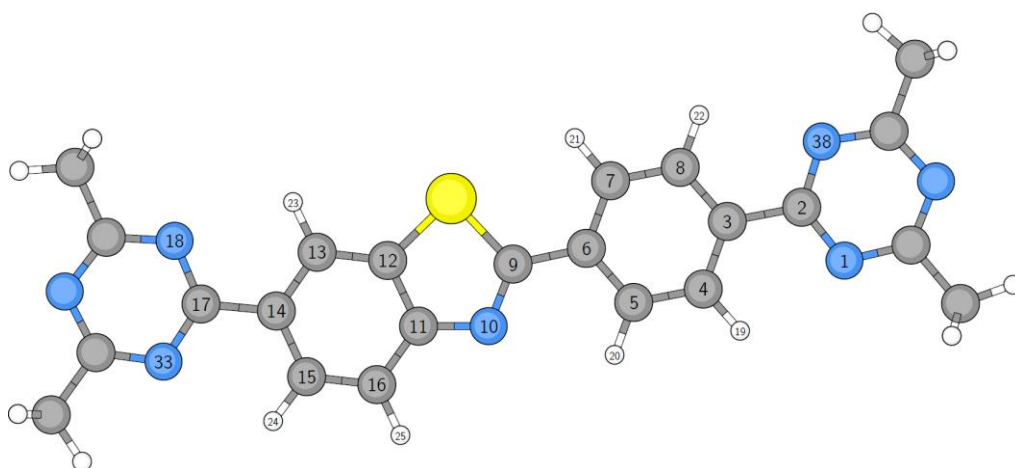
Figure S 112: Relevant atom labels for the excised TTT-Section from the optimized geometry of the COF.
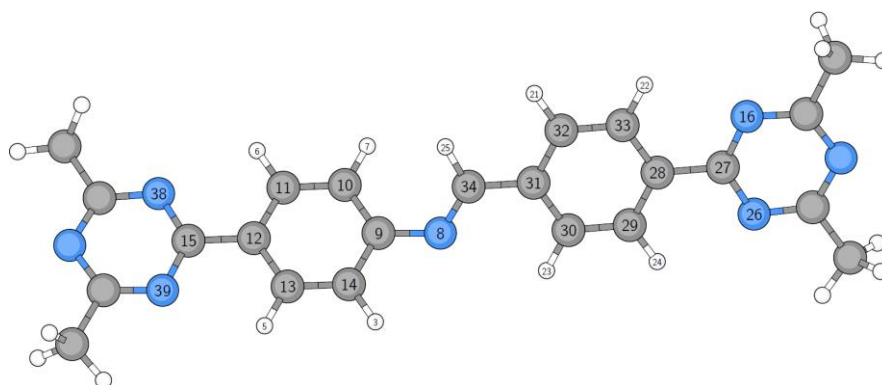
Figure S 113: Relevant atom labels for the excised TTI-Section from the optimized geometry of the COF.
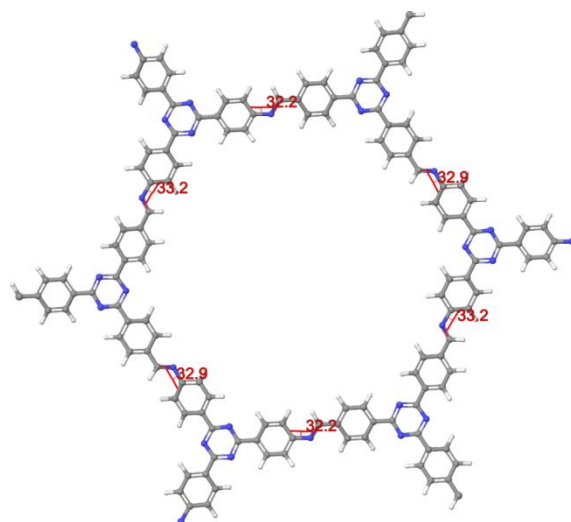
Figure S 114: Dihedral angles for all imine bonds within the optimized geometry of a single TTI-COF ring, identifying three distinct sections: Section-1, 32.9°; Section-2, 32.2°; Section-3, 33.2°. Corresponding sections were also selected for the TTT-COF pore.
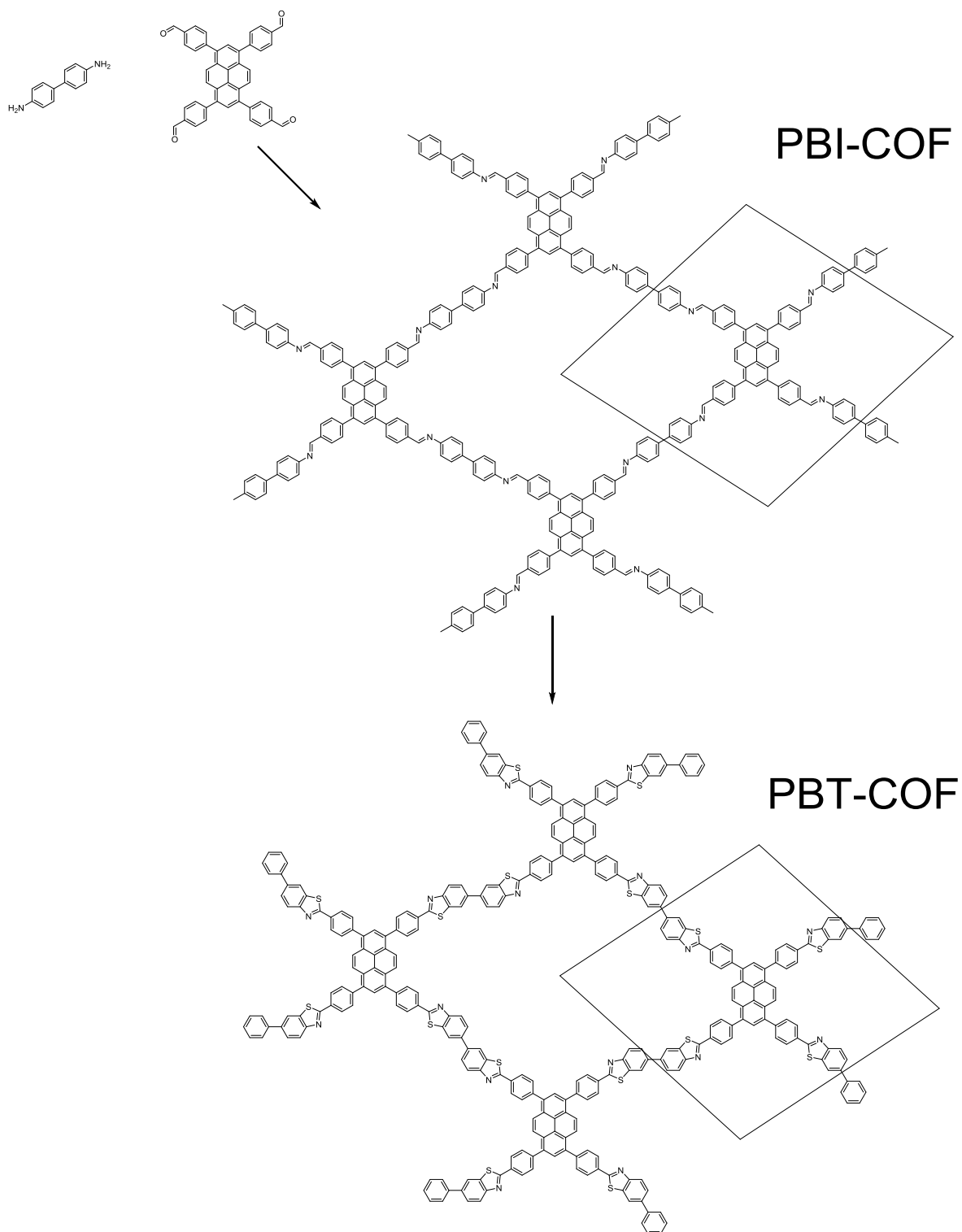
Figure S 115: Schematic of the formation of the PBI-COF from the molecular precursors benzidine and tetra(formylphenyl) pyrene under reversible conditions. The PBI-COF is then transformed into the PBT-COF by reaction with sulfur.
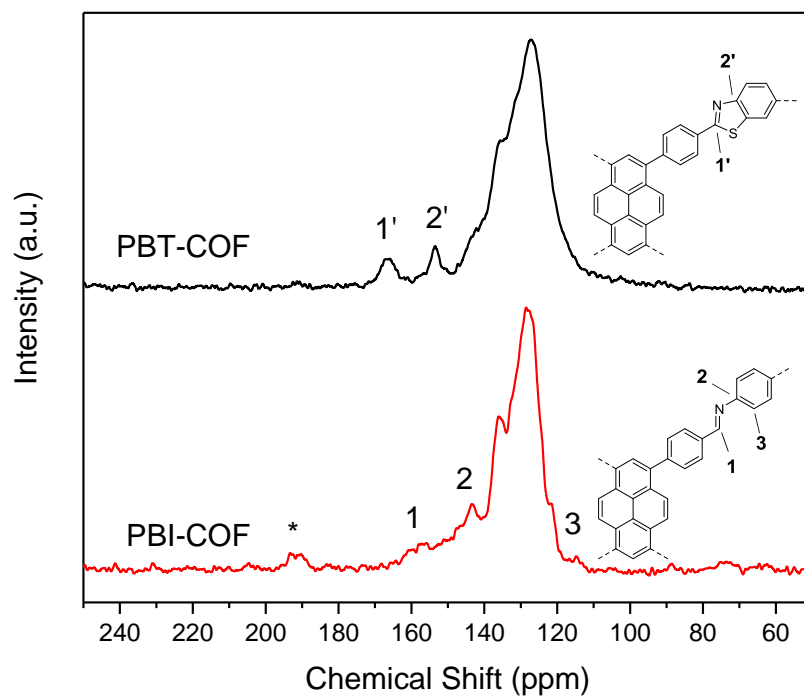
Figure S 116: ^{13}C ssNMR of the PBI-COF (red) and PBT-COF (black) with the tentative assignment of the characteristic peaks. The peak indicated by the asterisk points towards residual aldehyde left from the COF synthesis, which is gone after the sulfur incorporation.
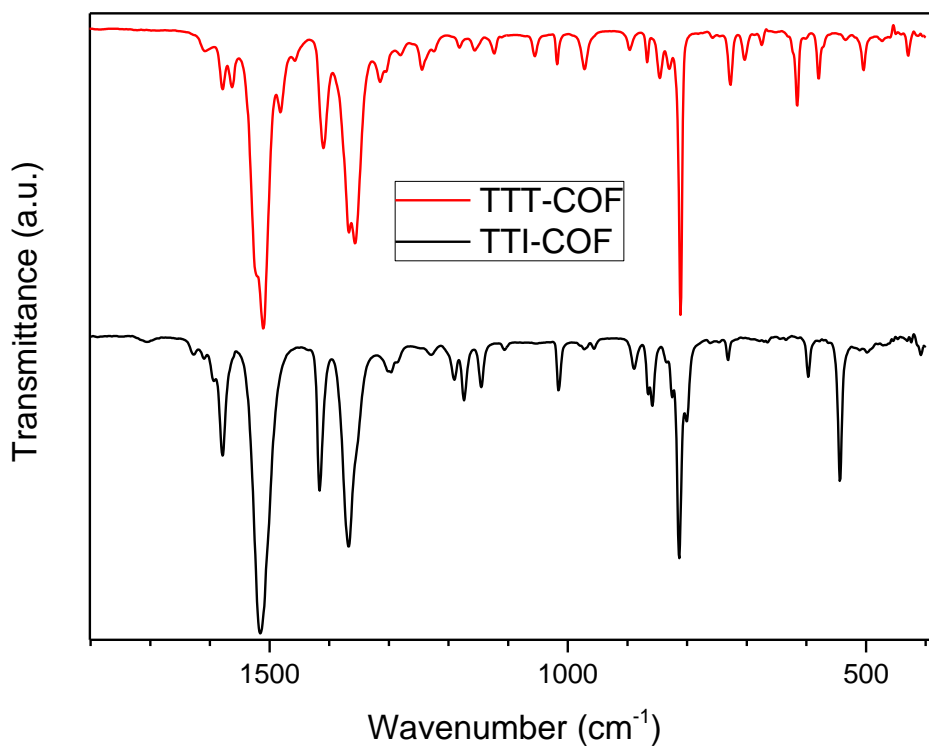
Figure S 117: Zoomed section of the IR spectra of the TTI- and TTT-COF showing significant changes between the imine and the thiazole-based COFs.
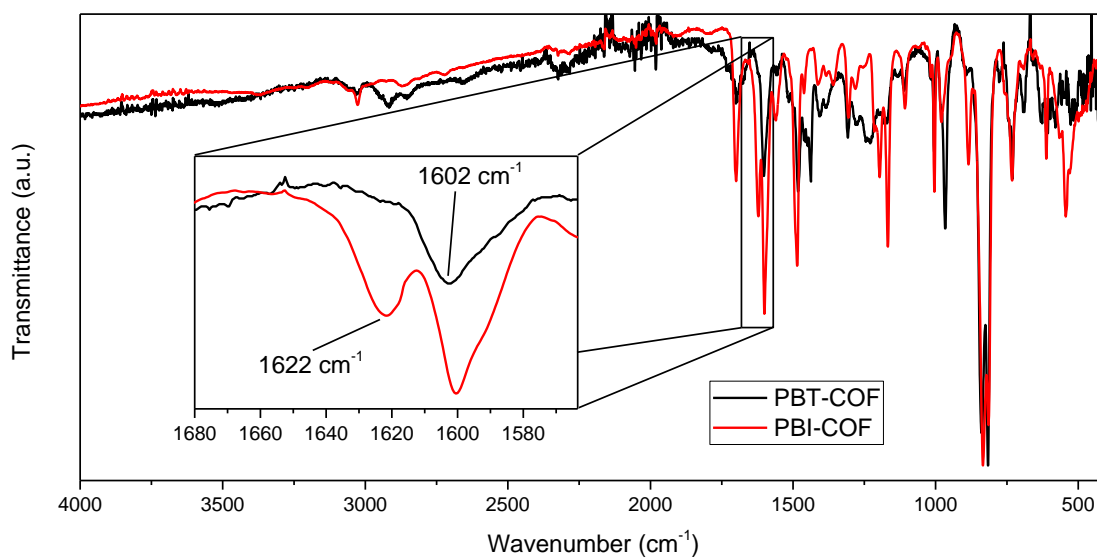
Figure S 118: IR spectra of the PBT- and the PBI-COF, where the enlarged inset shows the region of the characteristic imine vibration (1622 cm^{-1}) in the PBI-COF that is lost upon transformation to the thiazole. The corresponding thiazole vibration can be assigned to the band at 1602 cm^{-1}.

Table S 7: Elemental analysis of the TTT-COF and the TTI-COF.

TTT-COF	C	N	H	S
Measured	66.09 (10)	15.11 (17)	2.68 (14)	13.56 (22)
Expected	68.95	16.08	2.70	12.27

TTI-COF[196]	C	N	H	S
Measured	76.85	18.37	3.79	-
Expected	77.91	18.17	3.92	-
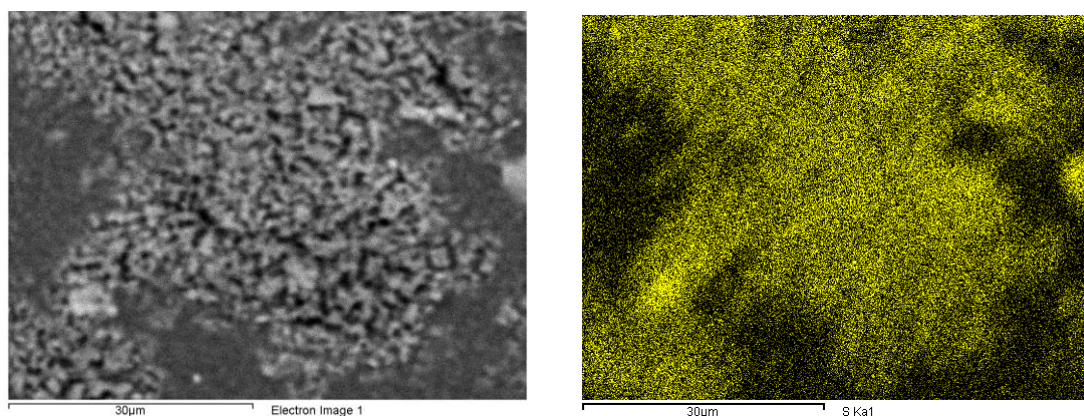
Figure S 119: SEM image of the TTT-COF (left) and the corresponding EDX map of sulfur (right), where the dark areas indicate the substrate. Due to the instrument-inherent drift, higher resolution of the EDX mapping was not possible.
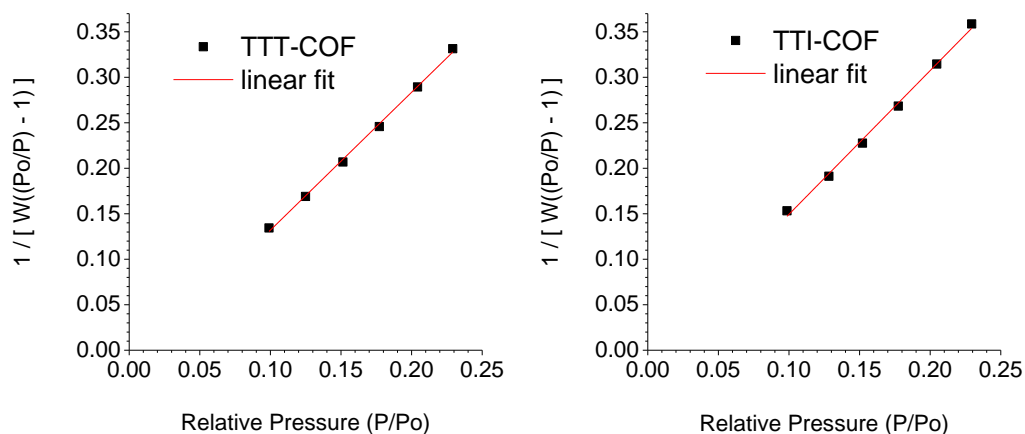
Figure S 120: BET fit of TTT-COF (left) and TTI-COF (right).
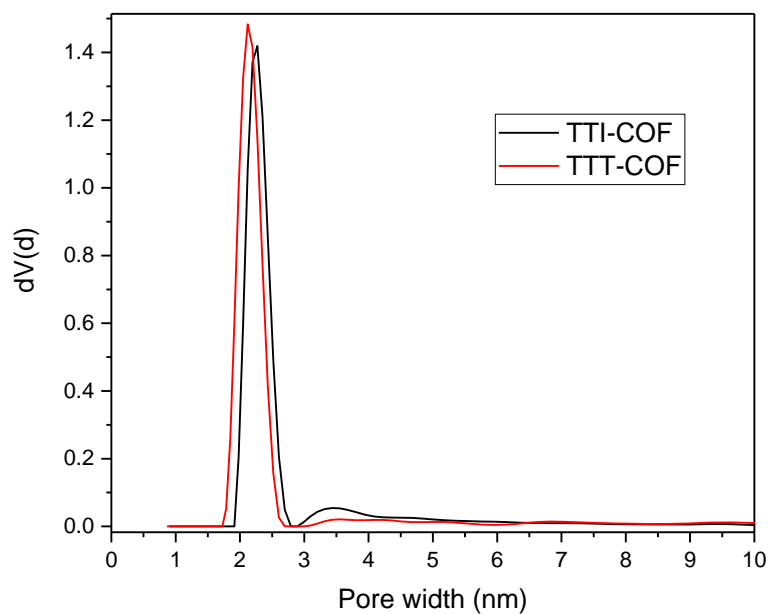
Figure S 121: Pore size distribution (PSD) of the TTI-COF and the TTI-COF calculated from Argon isotherms with a QSDFT model based on carbon. The PSD exhibits a small reduction of the average pore size from the TTI-COF to the TTT- COF that matches well with the respective structure models.
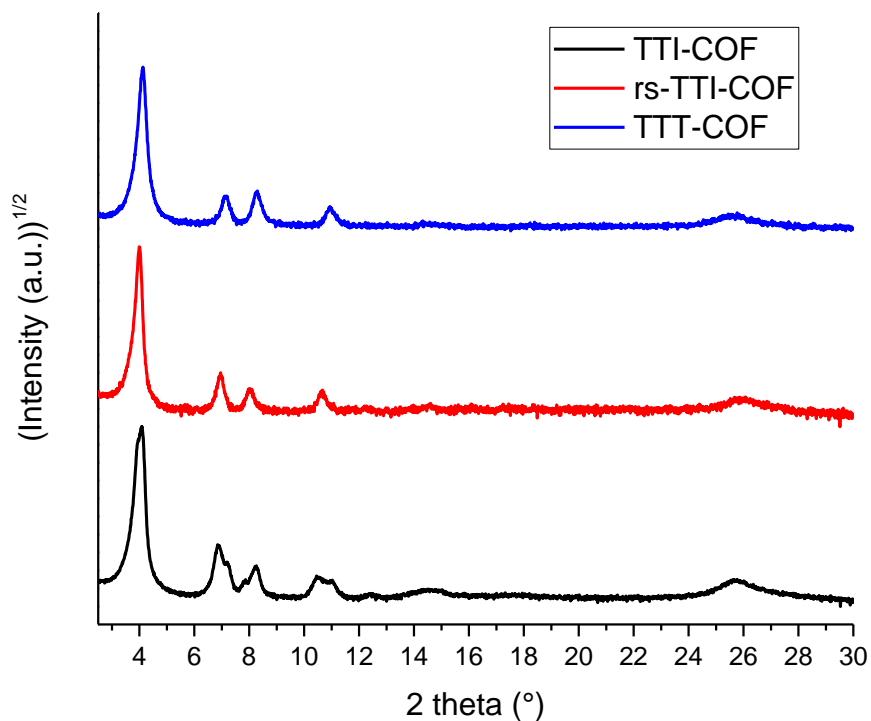
Figure S 122: Comparison of the XRPD patterns of the randomly stacked (rs) TTI-COF, the TTI-COF (see also ref: [278]) and the TTT-COF.

Table S 8: Rietveld refinement of the TTI- and TTT-COF showing their respective unit cell parameters for comparison.

Fitted Pattern	TTI-COF[278]	rs-TTI-COF	TTT-COF
Space group	P1	P6₃/m	P6₃/m
constraints	a=b ; α = β	-	-
Rwp (%)	7.135	11.014	11.091
a (Å)	26.060 (8)	25.244 (8)	24.478 (5)
b (Å)	26.060 (8)	25.244 (8)	24.478 (5)
c (Å)	7.348 (5)	6.905 (7)	7.002 (5)
α (°)	80.151 (3)	90	90
β (°)	80.151 (3)	90	90
γ (°)	120	120	120
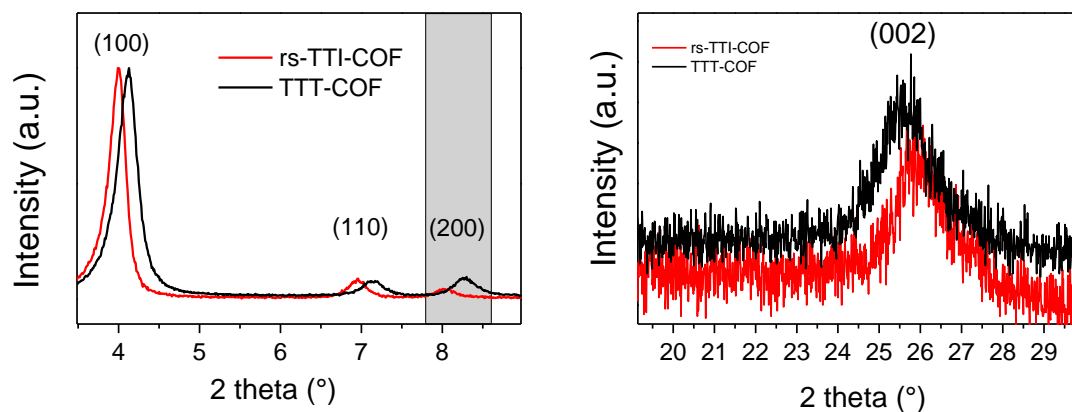
Figure S 123: Close-up of the XRPD patterns of TTI-COF and TTT-COF showing the shift in the unit cell dimensions (left) and in interlayer distance (right).
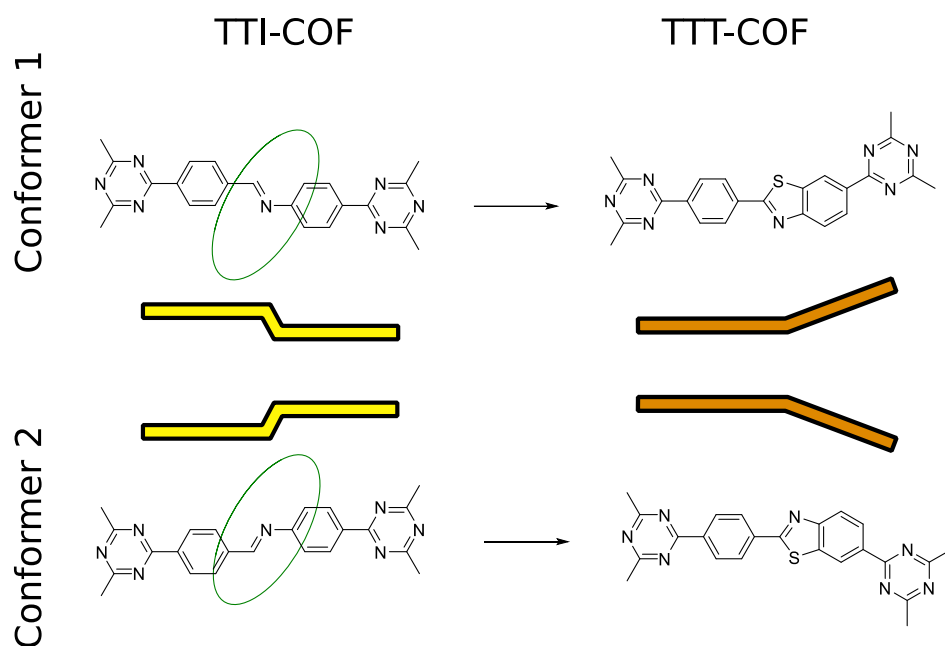
Figure S 124: Two conformational isomers in the TTI-COF showing parallel offset (left), with small structural differences between the conformers. However, transformation of these conformers into their respective thiazoles leads to the generation of bending instead of offsets.

Table S 9 Rietveld analysis of the TTT-COF using different structure models.

Applied Model	imine-model	thiazole-model
Space group	$P6_3/m$	$P6_3/m$
Rwp (%)	16.237	11.091
a (Å)	24.514 (8)	24.478 (5)
b (Å)	24.514 (8)	24.478 (5)
c (Å)	7.013 (6)	7.002 (5)
α (°)	90	90
β (°)	90	90
γ (°)	120	120
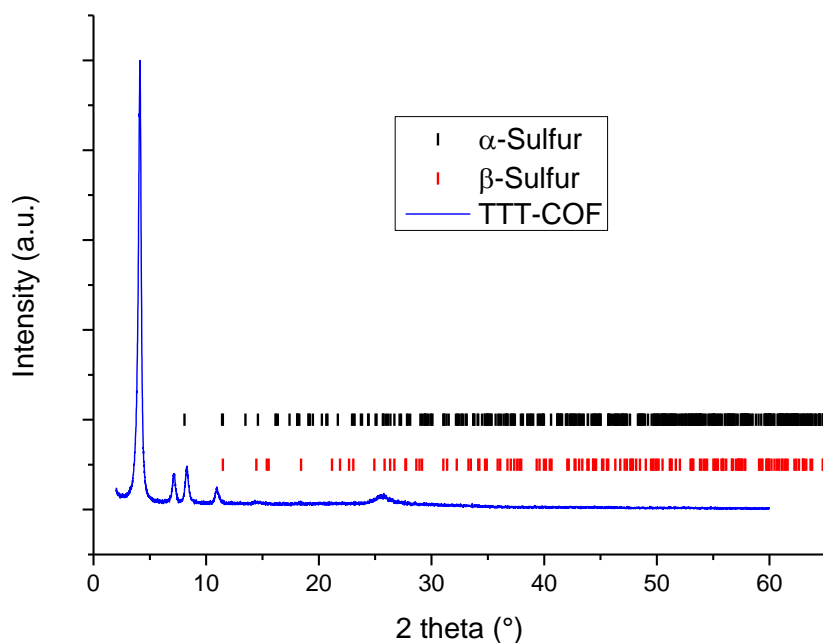
Figure S 125: Full XRPD of the TTT-COF, along with the calculated peak positions of alpha and beta sulfur, shows the absence of sulfur reflections.
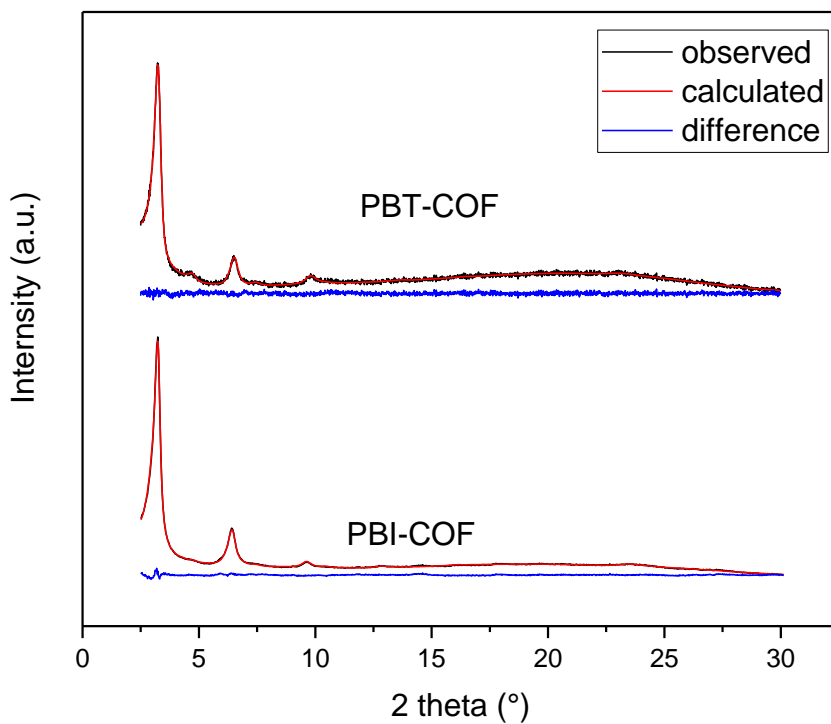
Figure S 126: XRPD of the PBT- (top) and the PBI-COF (bottom) showing the retention of crystallinity after sulfur incorporation and a good match to the Rietveld fit of the respective models.

Table S 10: Rietveld refinement of the PBI- and PBT-COFs showing their respective unit cell parameters for comparison.

Fitted Pattern	PBI-COF	PBT-COF
Space group	*P*1	*P*1
constraints	*a=b* ; α = β	*a=b* ; α = β
Rwp (%)	1.661	3.090
a (Å)	28.37 (13)	27.77 (18)
b (Å)	28.37 (13)	27.77 (18)
c (Å)	3.915 (16)	4.00 (5)
α (°)	78.1 (1.3)	76.4 (1.6)
β (°)	78.1 (1.3)	76.4 (1.6)
γ (°)	82.3 (5)	84.0 (7)
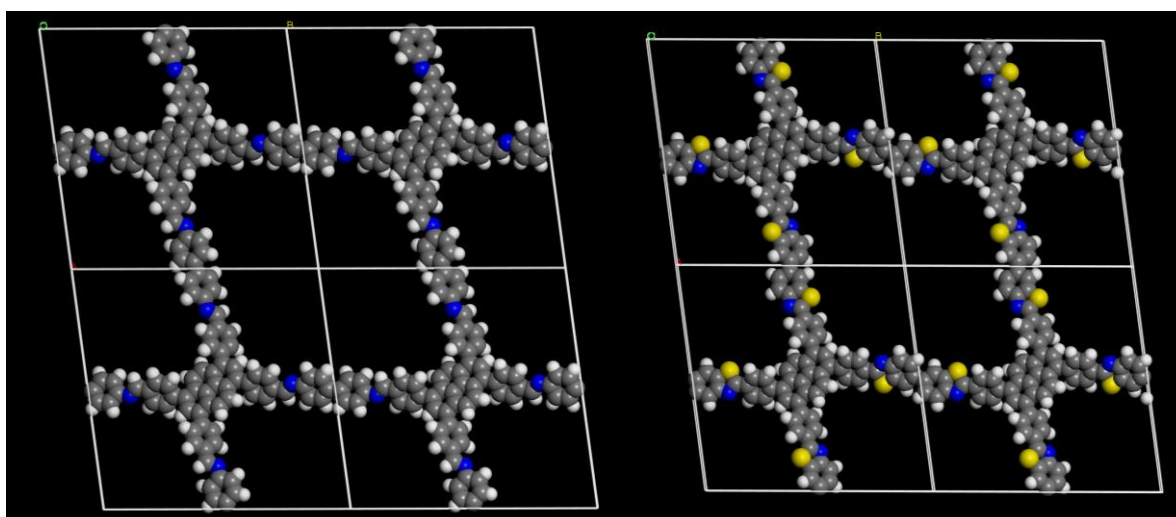
Figure S 127: Simulated unit cells of the PBI-COF (left) and the PBT-COF (right).
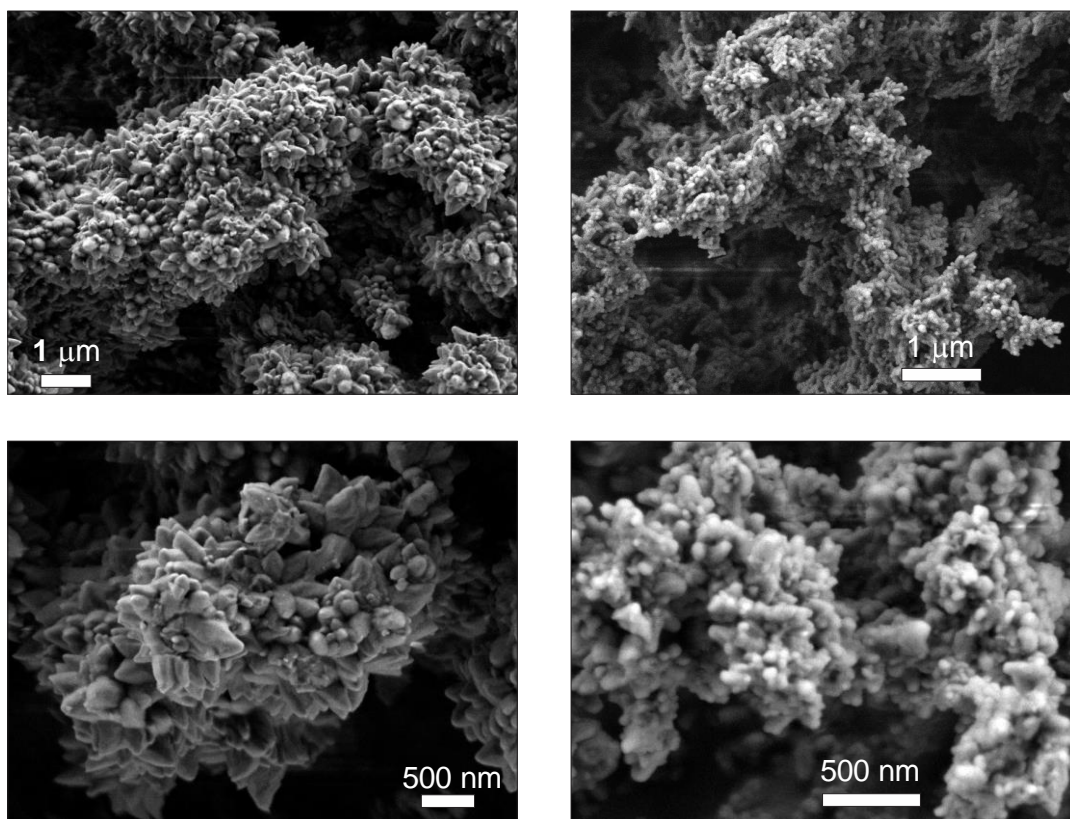
Figure S 128: SEM images of the TTI-COF (left) and the TTT-COF (right).
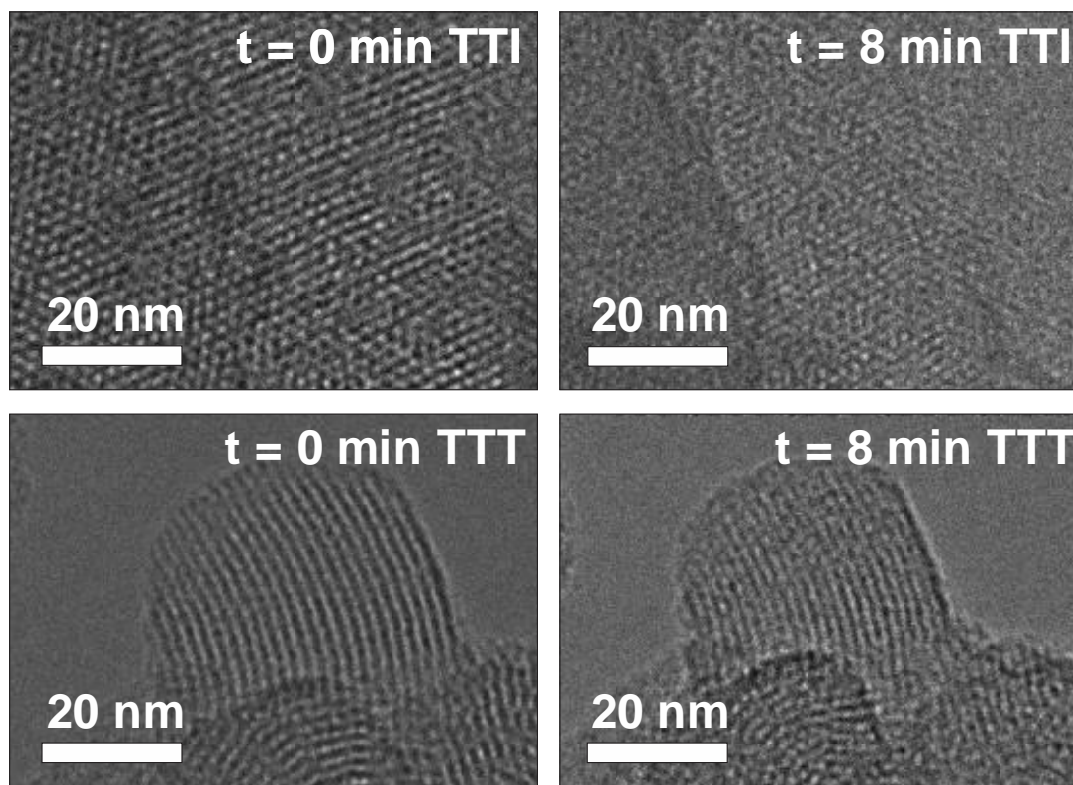
Figure S 129: Different degrees of electron beam damage after 8 minutes of exposure to the electron beam to the TTI-COF (top) and the TTT-COF (bottom) at identical magnifications and electron flux, evident by the reduction of visible lattice fringes.
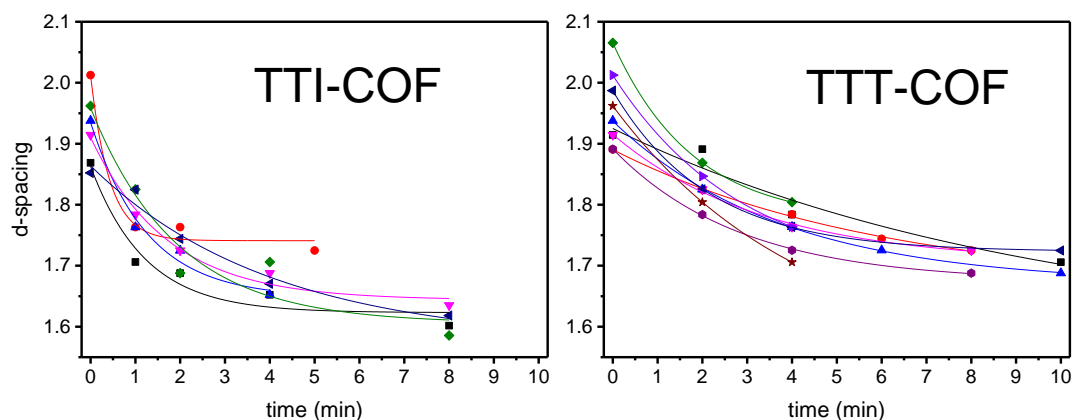
Figure S 130: Fitted exponential decays to the peak positions in the fourier transforms of the TEM images.

Table S 11: Exemplary fit parameters for the exponential decay in Figure 6-12.

Model	ExpDec1	
Equation	$y = A1*exp(-x/t1) + y0$	
Plot	TTI-COF	TTT-COF
y0	1.64151 ± 0.01001	1.63748 ± 0.00889
A1	0.2582 ± 0.01256	0.26629 ± 0.00923
t1	1.87451 ± 0.22461	3.20317 ± 0.26763
$t_{1/2}$ (half life time)	1.29931 ± 0.15568	2.22027 ± 0.18550
Reduced Chi-Sqr	9.14005E-5	2.24183E-5
R-Square(COD)	0.99564	0.99933
Adj. R-Square	0.99127	0.99798
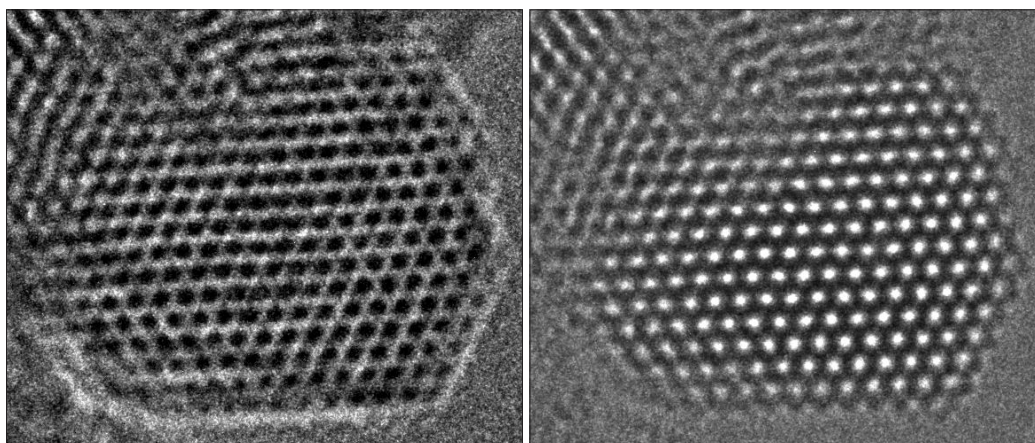
Figure S 131: Defocus series of a crystallite of the TTT-COF in the TEM viewed along [001].
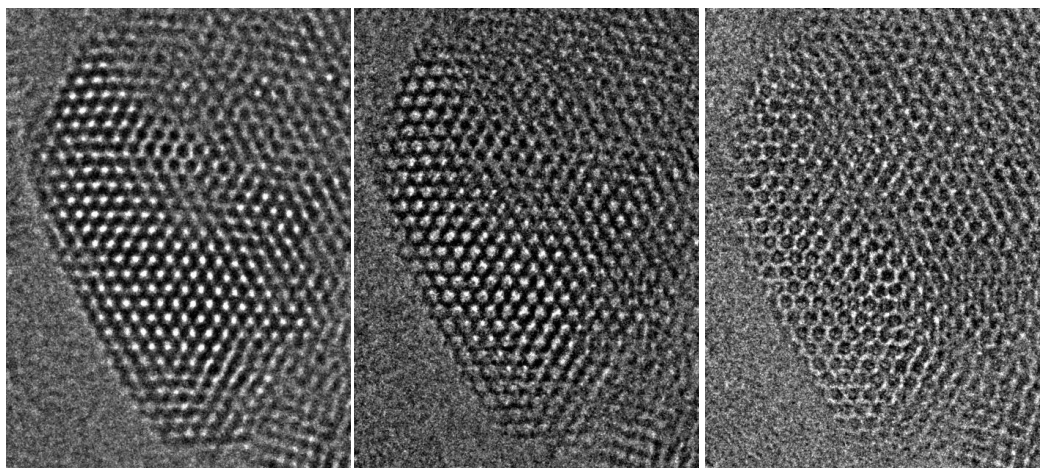
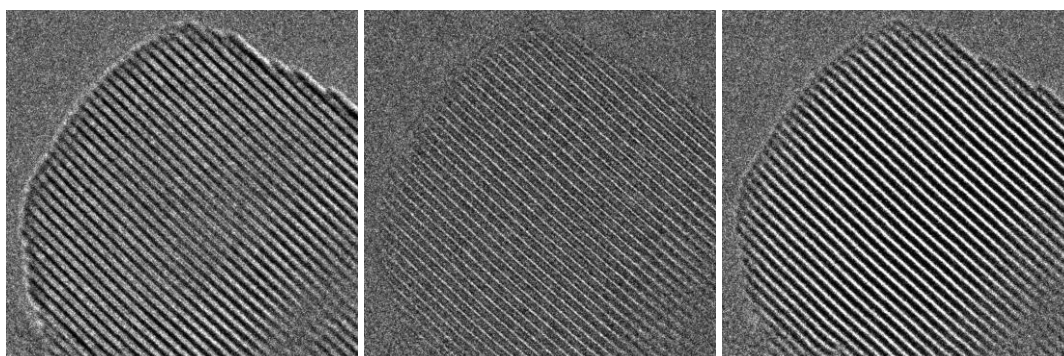Figure S 132: Defocus series of a crystallite of the TTT-COF in the TEM viewed along [001].

Figure S 133: Defocus series of the TTT-COF viewed along [100].

9.8.3. Supplemental Discussion

Molecular nature of edge dislocation in TTT-COF

The molecular nature of the edge dislocation could be described by either a columnar linker vacancy or an out-of-plane growth that resembles a five and a seven membered ring such as spirals (Figure S 134, Figure S 135, Figure 6-13 P-Q). However, the formation of an actual five or a seven membered ring within the COF plane is not possible, since TTI-COF and by extension TTT-COF is composed of two different building blocks that always have to alternate due to their molecular functionalities – the aldehyde building block can only form a bond with the amine and vice versa (Figure 6-14, A). While true (i.e. in-plane) five and seven-membered rings are not possible in C3-C3 linked COFs, the same does not apply for C3-C2 linked COFs. The latter have less binding and geometry constraints that render the formation of rings with five or seven edges possible. The combination of C3-C3 COFs could thus be used as a strategy for improving crystallinity in 2D COFs by making these in-plane defects less favorable.

In C3+C2 systems the formation of pentagonal or heptagonal rings is possible as the alternation is not between corners but between edge and corner nodes (see Figure S 134). Of course an uneven number of building blocks in these structures is also not possible, but the twice as high number of building blocks involved in the ring formation (i.e. building blocks in C2+C3 always have to come "in pairs") results in a higher conformational flexibility that makes these pentagonal and heptagonal rings more likely. However, connecting one layer to the next in C3+C3 systems via a fivefold or a sevenfold

screw axis would allow all valences of the linkers to be saturated (Figure S 135, B, C and D). The introduction of such an edge dislocation into the structure would lead to significant localized strain, caused by the unit cell mismatch as well as the bending strain imposed by the presence of screw axes as they deviate from the ideal angle of 120° in a hexagon. However, such strain and deviation from the ideal structure of the COF matches the observed large reflection broadening that is usually present in COFs. This is in contrast to a model involving a column of vacancies as in Figure 6-13 Q, Figure S 135, Figure 6-14 E, running uniformly along the *c*-direction, where the amount of strain should be much smaller but a large number of linker end groups would remain at the site of the edge dislocation after COF formation. However, it is considered rather unlikely that an in-plane vacancy acts as a "seed" for a column of identical vacancies forming along the out-of-plane direction as sketched in Figure S 135 E.
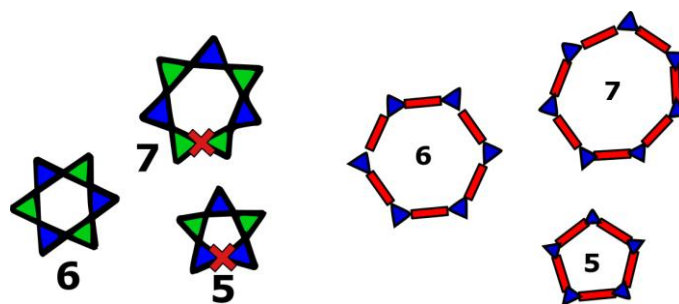

Figure S 134: Comparison of C3+C3 systems with C3+C2 based systems with regard to their ability to produce pentagonal and heptagonal rings.
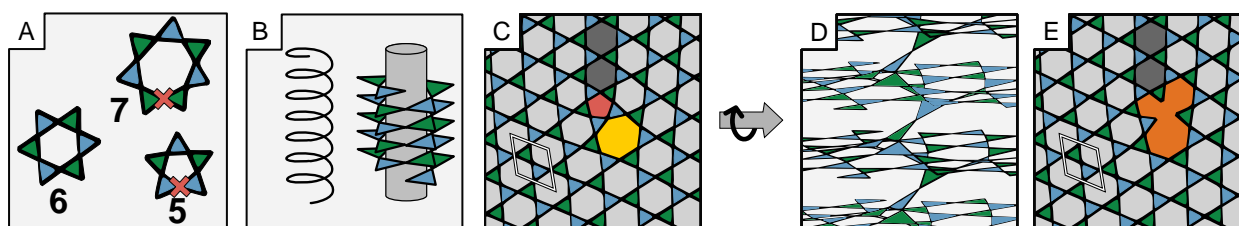

Figure S 135: Visualizing the formation of screw dislocations in COFs. A: Schematic of the different kinds of possible (6) and impossible (5,7) in-plane connectivity in a COF composed of two complementary building blocks (green and blue triangles) where alternation between the blue and green triangles enables only even-membered rings. B: Screw axis with an odd number of members per turn, maintaining both in-plane and out-of plane alternation, which look in projection like an odd numbered ring. C, E: View onto the hexagonal plane of the COF with an edge dislocation composed of a vacancy (E) or a screw axis (C). D: Visualization along the COF layers showing the connection of layers by the screw axis, with a greatly exaggerated interlayer distance.

9.9. Supporting information for: Synthesis of a stilbene based polymer by controlled thermal transformation of an azine covalent organic framework
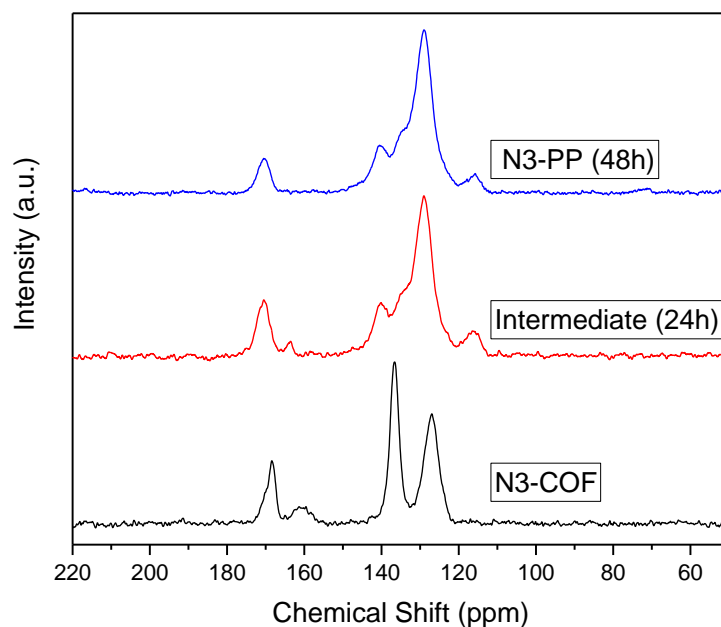

Figure S 136: ssNMR of the reaction progress of the pyrolysis after 0 h (N$_3$-COF), 24 h (intermediate) and 48 h (N$_3$-PP).
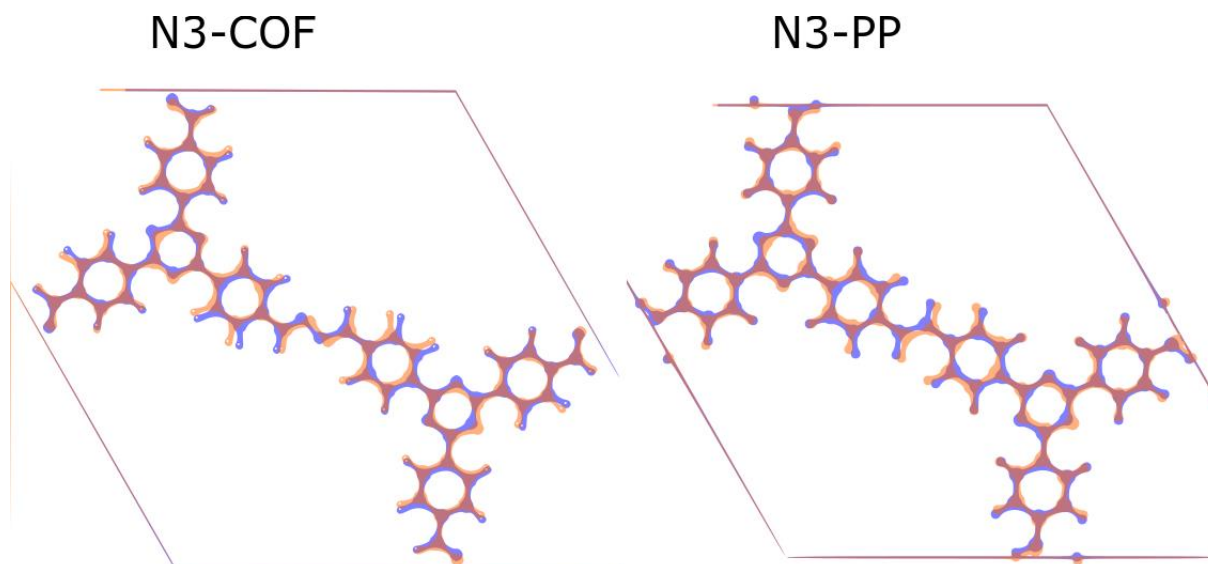

Figure S 137: Schematic anti-symmetric stretching deformation of the phenyl-azine and phenyl-ethyene bond together with a phenyl ring stretching mode bond in N$_3$-COF and N$_3$-PP calculated to be at 514 cm^{-1} and 597 cm^{-1}, respectively.
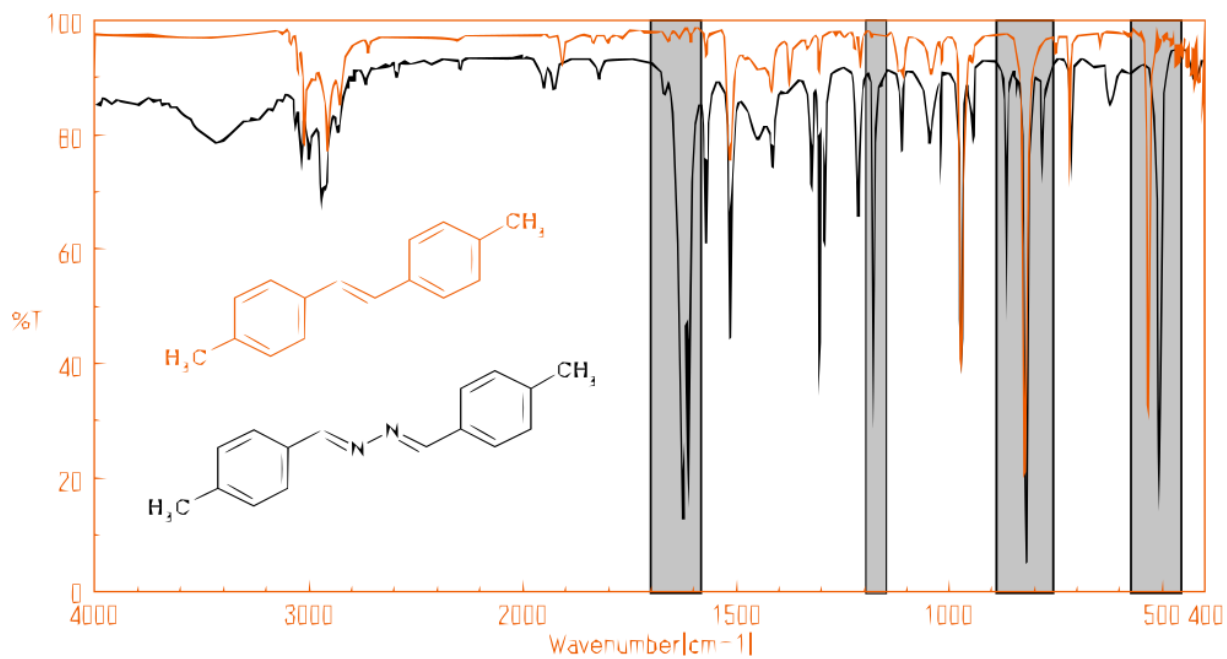
Figure S 138: IR spectra of p-dimethyl-stilbene and -benzaldazine. Data obtained with permission.[365, 366]
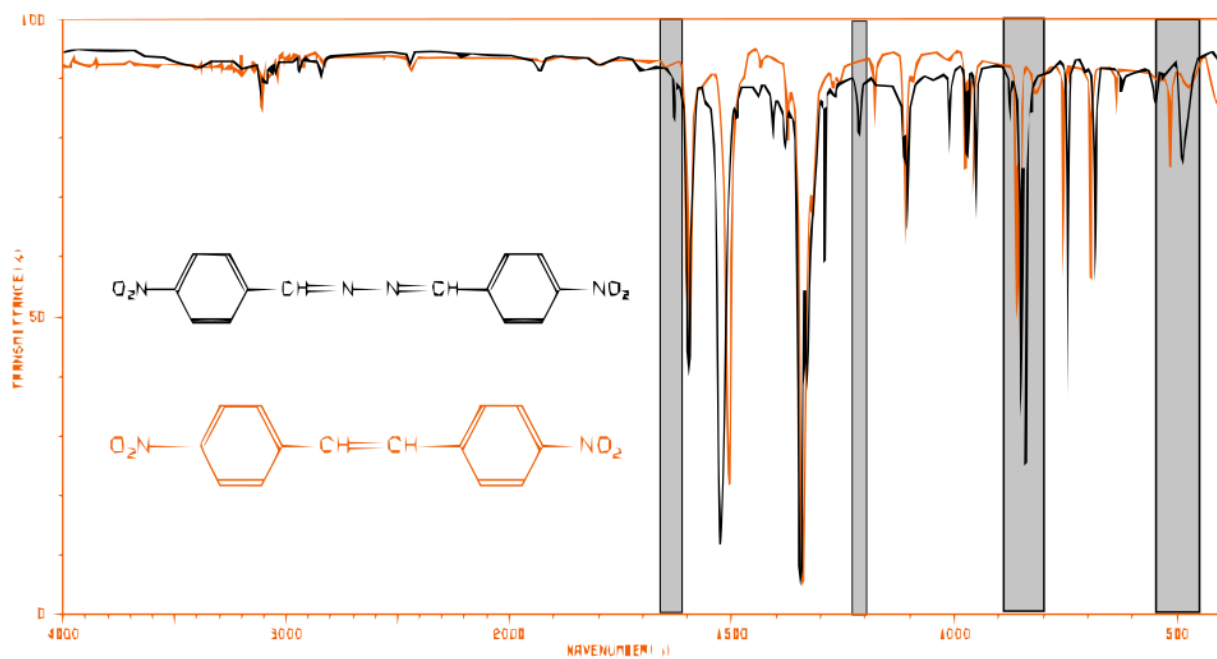

Figure S 139: IR spectra of p-dinitro -stilbene and -benzaldazine. Data obtained with permission.[367, 368]
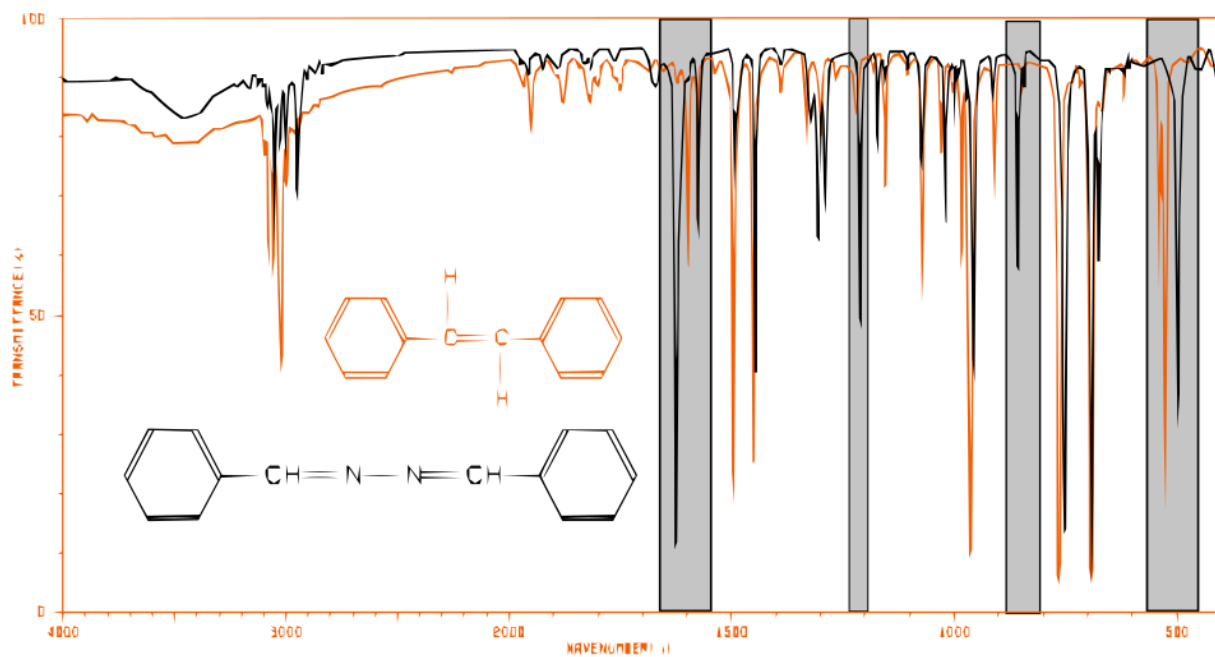
Figure S 140: IR spectra of stilbene and benzaldazine. Data obtained with permission.[369, 370]